Naoki Fukata
Riccardo Rurali *Editors*

Fundamental Properties of Semiconductor Nanowires

Springer

Fundamental Properties of Semiconductor Nanowires

Naoki Fukata · Riccardo Rurali
Editors

Fundamental Properties of Semiconductor Nanowires

Springer

Editors
Naoki Fukata
National Institute for Materials Science
Tsukuba, Ibaraki, Japan

Riccardo Rurali
CSIC
Institut de Ciència de Materials
de Barc CSIC
Bellaterra, Spain

ISBN 978-981-15-9049-8 ISBN 978-981-15-9050-4 (eBook)
https://doi.org/10.1007/978-981-15-9050-4

© Springer Nature Singapore Pte Ltd. 2021
This work is subject to copyright. All rights are reserved by the Publisher, whether the whole or part of the material is concerned, specifically the rights of translation, reprinting, reuse of illustrations, recitation, broadcasting, reproduction on microfilms or in any other physical way, and transmission or information storage and retrieval, electronic adaptation, computer software, or by similar or dissimilar methodology now known or hereafter developed.
The use of general descriptive names, registered names, trademarks, service marks, etc. in this publication does not imply, even in the absence of a specific statement, that such names are exempt from the relevant protective laws and regulations and therefore free for general use.
The publisher, the authors and the editors are safe to assume that the advice and information in this book are believed to be true and accurate at the date of publication. Neither the publisher nor the authors or the editors give a warranty, expressed or implied, with respect to the material contained herein or for any errors or omissions that may have been made. The publisher remains neutral with regard to jurisdictional claims in published maps and institutional affiliations.

This Springer imprint is published by the registered company Springer Nature Singapore Pte Ltd.
The registered company address is: 152 Beach Road, #21-01/04 Gateway East, Singapore 189721, Singapore

Preface

Semiconductor nanowires exhibit novel electrical, optical, and mechanical properties due to their reduced dimensionality and nanoscale size. These novel properties not only can improve device performances but also pave the way to the design of new devices with new functionalities. For the optimization of these novel devices, it is important to understand the growth mechanism of nanowires and how to obtain a tight control on the size (diameter and length), the orientation, the degree of crystallinity, and the crystal structure, first. Functionalization and surface modifications in a broader sense are also an important subject for device applications, particularly those related to chemical sensing. Last, but not least, impurity doping is the cornerstone of device design and is thus indispensable for the use of nanowires in electrical and optical devices. Understanding and governing the novel properties of nanowires relies on accurate characterization techniques. In particular, nanoscale and in situ characterization are key tools to understand the properties of nanowires and finally to realize new devices.

This book aims to present readers with a comprehensive overview of semiconductor nanowires, with a focus on recent developments. It covers the whole spectrum of nanowire-related science, ranging from fundamental to applied research. In Chapter Vapor-Liquid-Solid Growth of Semiconductor Nanowires, the details of nanowire growth are theoretically and experimentally discussed. In Chapters Surface Functionalization of III-V Nanowires and Impurity Doping in Semiconductor Nanowires, functionalization of nanowires by surface modification and impurity doping are introduced. Surface functionalization is one of the ways to obtain new functionalities because of the high surface-to-volume ratio of nanowires. In Chapter Surface Functionalization of III-V Nanowires, standard surface science techniques, such as scanning tunneling microscopy (STM) and X-ray photoemission spectroscopy (XPS), which were modified for effective studies of 1D nanowires are introduced. These techniques reveal the precise structure–function relationship of semiconductor nanowires and their surfaces, resulting in the control of the structure and chemistry of the nanowires with atomic scale. As for impurity doping, several doping methods such as *ex situ*, *in situ*, and surface doping are discussed in terms of their advantages and disadvantages, presenting some illustrative examples in

Chapter Impurity Doping in Semiconductor Nanowires. The characterization methods of dopant atoms, such as their bonding structures and behaviors in nanowires, are also discussed. Chapters X-ray Methods for Structural Characterization of III-V Nanowires: From an *ex-situ* Ensemble Average to Time-resolved Nano-diffraction–Nanowire Field-Effect Transistors focus on various characterization techniques. Chapter X-ray Methods for Structural Characterization of III-V Nanowires: From an *ex-situ* Ensemble Average to Time-resolved Nano-diffraction introduce time-resolved in situ X-ray method. In Chapter Characterisation of Semiconductor Nanowires by Electron Beam Induced Microscopy and Cathodoluminescence, electron beam-induced microscopy and cathodoluminescence (CL) methods. In Chapters Photoluminescence Spectroscopy Applied to Semiconducting Nanowires: A Valuable Probe for Assessing Lattice Defects, Crystal Structures, and Carriers' Temperature and Addressing Crystal Structure in Semiconductor Nanowires by Polarized Raman Spectroscopy, two optical methods, photoluminescence (PL) and Raman spectroscopy, respectively, are introduced and discussed in detail. To predict and understand the novel properties of nanowires, theoretical methods are indispensable. First-principle calculations aimed at the calculation of impurity formation energy, which is important to determine equilibrium concentrations, solubilities, diffusivities, and doping efficiencies, are discussed in Chapter Theoretical Aspects of Point Defects in Semiconductor Nanowires. Finally, in Chapters Nanowire Field-Effect Transistors and InP/InAs Quantum Heterostructure Nanowires Towards Telecom-Band Nanowire Lasers, two examples of applications using nanowires are introduced. In Chapter Nanowire Field-Effect Transistors, next-generation field-effect transistors using nanowires as transistor channels are introduced. In Chapter InP/InAs Quantum Heterostructure Nanowires Towards Telecom-Band Nanowire Lasers, telecom-band single-nanowire lasers are introduced. The NW laser can be operating at room temperature based on multi-quantum disk InP/InAs heterostructure nanowires.

In conclusion, we would like to highlight that this book covers everything from the basics of semiconductor nanowires to cutting-edge applications, and thus we hope that it may be useful to both researchers who are starting and to those who are already doing nanowire research, and many others who are doing research related to nanostructures. Chapters Vapor-Liquid-Solid Growth of Semiconductor Nanowires through Impurity Doping in Semiconductor Nanowires are important for understanding the fundamentals of nanowires, and Chapters X-ray Methods for Structural Characterization of III-V Nanowires: From an *ex-situ* Ensemble Average to Time-resolved Nano-diffraction–Theoretical Aspects of Point Defects in Semiconductor Nanowires are useful for the overall study of nanostructures. Chapters Nanowire Field-Effect Transistors and InP/InAs Quantum Heterostructure Nanowires Towards Telecom-Band Nanowire Lasers detail the superior properties of nanowire-based devices and show how nanowires will be used in devices in the future. Since semiconductor nanowire research is expected to continue to be active, we hope this book will be useful to researchers and students engaged in semiconductor nanowire-related research, or anyone involved in semiconductor nanostructures.

Tsukuba, Japan — Naoki Fukata
Bellaterra, Spain — Riccardo Rurali

Contents

Growth

Vapor–Liquid–Solid Growth of Semiconductor Nanowires 3
Vladimir G. Dubrovskii and Frank Glas

Functionalization

Surface Functionalization of III–V Nanowires 111
Rainer Timm and Anders Mikkelsen

Impurity Doping in Semiconductor Nanowires 143
Naoki Fukata

Characterization

X-ray Methods for Structural Characterization of III-V Nanowires: From an *ex-situ* Ensemble Average to Time-resolved Nano-diffraction 185
Ludwig Feigl and Philipp Schroth

Characterisation of Semiconductor Nanowires by Electron Beam Induced Microscopy and Cathodoluminescence 251
Maria Tchernycheva, Gwénolé Jacopin, and Valerio Piazza

Photoluminescence Spectroscopy Applied to Semiconducting Nanowires: A Valuable Probe for Assessing Lattice Defects, Crystal Structures, and Carriers' Temperature 289
Davide Tedeschi, Marta De Luca, and Antonio Polimeni

Addressing Crystal Structure in Semiconductor Nanowires by Polarized Raman Spectroscopy 307
Claudia Fasolato, Ilaria Zardo, and Marta De Luca

Theoretical Aspects of Point Defects in Semiconductor Nanowires 349
Riccardo Rurali, Maurizia Palummo, and Xavier Cartoixà

Applications

Nanowire Field-Effect Transistors 371
Junichi Motohisa and Shinjiro Hara

InP/InAs Quantum Heterostructure Nanowires Toward Telecom-Band Nanowire Lasers 433
Guoqiang Zhang, Kouta Tateno, Takehiko Tawara, and Hideki Gotoh

Growth

Vapor–Liquid–Solid Growth of Semiconductor Nanowires

Vladimir G. Dubrovskii and Frank Glas

Abstract We discuss the growth of semiconductor nanowires, with an emphasis on the vapor–liquid–solid growth of III–V nanowires. Special attention is paid to modeling of growth and the resulting morphology, crystal phase, composition, nanowire heterostructures, and statistical properties within the nanowire ensembles. We give a general overview of the vapor–liquid–solid growth of nanowires by different epitaxy techniques and the bases for nanowire growth modeling. We discuss the role of surface energetics in the formation of GaAs nanowires, which has an important impact on the nanowire morphology and crystal phase. A detailed description of the nanowire growth kinetics is presented, including the transport-limited growth, chemical potentials, nucleation and growth of two-dimensional islands, and self-consistent growth models combining the material transport equations with the nucleation rate. The nanowire length and diameter distributions are considered along with the methods for narrowing them to sub-Poissonian values. Ternary III–V nanowires and heterostructures based on such nanowires are discussed, including the relaxation of elastic stress at the free sidewalls and the sharpening of the heterointerfaces. We consider polytypism of III–V nanowires and possibilities to control their crystal phase by tuning the growth parameters.

Keywords III–V nanowires · Vapor–liquid–solid growth · Nucleation · Growth modeling

V. G. Dubrovskii
ITMO University, Kronverkskiy pr. 49, 197101 St. Petersburg, Russia
e-mail: dubrovskii@mail.ioffe.ru

F. Glas (✉)
Centre for Nanoscience and Nanotechnology, Université Paris-Saclay, CNRS, 10 bd. Thomas Gobert, 91120 Palaiseau, France
e-mail: frank.glas@c2n.upsaclay.fr

© Springer Nature Singapore Pte Ltd. 2021

N. Fukata and R. Rurali (eds.), *Fundamental Properties of Semiconductor Nanowires*,
https://doi.org/10.1007/978-981-15-9050-4_1

1 Introduction

In this chapter, we discuss the growth of semiconductor nanowires, with an emphasis put on the vapor–liquid–solid growth of III–V nanowires. Particular attention is paid to theoretical understanding and the relevant models for the growth, morphology, crystal phase, composition, and statistical properties within the nanowire ensembles.

The chapter is organized as follows. Section 2 gives a general description of the vapor–liquid–solid growth by different epitaxy techniques, including the role of equilibrium phase diagrams, growth in regular arrays on patterned substrates such as SiO_x/Si(111), Au-catalyzed and self-catalyzed growth of III–V nanowires. We also present some recent examples of shaping GaAs nanowires in the self-catalyzed approach. In Sect. 3, we review the basics for the nanowire growth modeling, including the kinetics of group III and V species, axial growth rate, the role of supersaturation, nucleation-limited and regular growth modes. Section 4 deals with the role of surface energetics in the vapor–liquid–solid growth of GaAs nanowires, which has an important impact on the nanowire morphology and crystal phase. Section 5 presents a brief description of selective area epitaxy of III–V nanowires and a model for such growth. In Sect. 6, we consider a detailed description of the nanowire growth kinetics, including the transport-limited growth, chemical potentials for the vapor–liquid–solid growth of III–V nanowires, nucleation and growth of two-dimensional islands at the liquid–solid interface, and some advanced self-consistent growth models combining the material transport equations with the Zeldovich nucleation rate.

Section 7 describes an interesting effect of radius self-equilibration in self-catalyzed III–V nanowires. Section 8 presents the recent results on the length distributions within the ensembles of different III–V nanowires, including the role of surface diffusion and delayed nucleation of nanowires on the substrate surface, and possibilities to obtain sub-Poissonian length distributions induced by nucleation antibunching. Section 9 deals with ternary alloys in nanowires and describes some theoretical models for the nanowire composition. In Sect. 10, we consider heterostructures within nanowires, in particular, relaxation of elastic stress induced by lattice mismatch, the vapor–liquid–solid growth of axial heterostructures in different III–V material systems, and sharpness of the nanowire heterointerfaces. Section 11 deals with the zincblende-wurtzite polytypism in III–V nanowires and its theoretical understanding achieved to this day.

2 Vapor–Liquid–Solid Growth of Semiconductor Nanowires

The vapor–liquid–solid (VLS) method was introduced by Wagner and Ellis in 1964 to grow sub-micrometer Si "whiskers" on Si(111) substrates with Au catalyst [1]. Many fundamental aspects of the VLS growth of elemental and compound semiconductors

were later developed by Givargizov [2]. At the beginning of the 2000s, a rapid development of semiconductor nanowires (NWs) started, lead by the groups of Lieber [3], Yang [4], and Samuelson [5], soon followed by many others. This has resulted in tremendous progress in the NW synthesis, characterization, and applications (see, for example, Refs. [3, 4, 6, 7] for a review). One important advantage of NWs is that they allow for a very efficient relaxation of elastic stress induced by lattice mismatch on the lateral sidewalls, thus enabling dislocation-free growth on dissimilar substrates (such as Si for III–V NWs), and in NW heterostructures [8–10]. Peculiarities of the VLS growth from nanoscale catalyst droplets in largest measure determine the resulting morphology, crystal quality and phase, and statistical properties within the NW ensembles, which explains the importance of theoretical understanding and modeling [6, 7].

The VLS method makes use of a catalytic effect of a liquid metal droplet such as Au to fabricate semiconductor NWs which grow away from the substrate, with the position determined by the initial location of the droplet on the substrate. Usually, NWs grow in <111> direction perpendicular to (111) substrate. Parasitic growth between the NWs is either completely suppressed (for example, by using lithographically patterned substrates with a mask oxide layer) or proceeds at a lower rate than that of NWs. Radial growth rate of NWs by the vapor–solid (VS) mechanism on the sidewalls or due to non-stationary droplet swelling is much lower than the axial one. In chemical epitaxy techniques, a liquid metal acts as a chemical catalyst which enhances the cracking efficiency of semiconductor precursors at the droplet surface, so ideally NWs would grow only axially [1, 2, 5]. In molecular beam epitaxy (MBE) [11, 12], the droplet acts as a material collector (or a "physical" catalyst) whih directs the materical diffusion fluxes to the NW top. Whatever the epitaxy technique used to grow NWs, the VLS process necessarily involves two phase transitions of a semiconductor material: from vapor (for example, Ga and As_2 beams in MBE) to liquid (Au–Ga–As liquid alloy in the droplet) and from liquid to solid (stoichiometric GaAs NW). This explains the term "vapor–liquid–solid" growth.

The nature of Au-catalyzed VLS growth, particularly for elemental semiconductors such as Si or Ge, can be understood through the equilibrium phase diagrams [1–3]. Let us consider the phase diagram shown in Fig. 1 for a binary alloy of Au with a NW material M. At least in the M-rich region of the diagram (for large enough M fractions x), the solid state is immiscible and consists of pure GaAs and Au crystallites. In this region, above the eutectic temperature T_e and below the liquidus, the system consists of a mixed M–Au liquid and pure M crystallites, with temperature-dependent fractions of liquid and the remaining solid M. Above the liquidus, the M–Au alloy becomes a single liquid melt. Therefore, any growth temperature T between T_e and $T_{\max}$ for a given composition x (determined, say, by material flux) will produce solid M NW, with the remaining liquid melt in the droplet seated on the NW top. In other words, no Au should incorporate to the NW according to the equilibrium phase diagram. This property of the binary Au–Si, Au–Ge, or pseudo-binary Au–GaAs alloys explains why Au is the most common catalyst to grow NWs. According to the lever rule [13], the fraction of liquid equals $(1-x)/(1-x_L)$, while the fraction of solid M equals $(x-x_L)/(1-x_L)$, with x_L the M content in liquid.

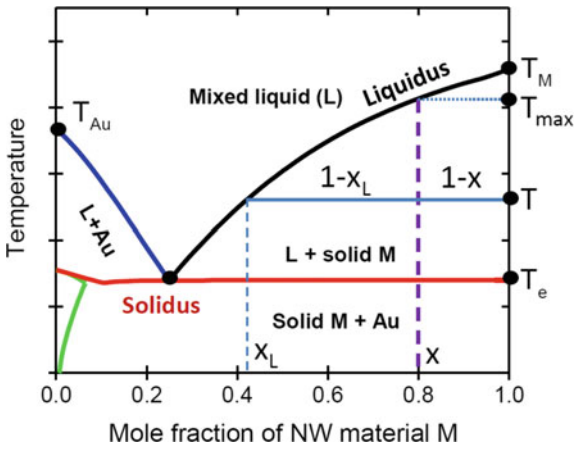

Fig. 1 Liquid–solid phase diagram of M-Au alloy, characterized by an almost horizontal solidus at the eutectic melting temperature T_e, and the two liquidus lines separating a mixture of M–Au liquid with solid Au (for low fractions of M), or solid M (for high fractions of M) for lower temperatures, from a single melt at higher temperatures. The temperatures T_{Au} and T_M correspond to melting of pure Au (1064 °C) and M, respectively. Vertical dashed line corresponds to a fixed M fraction of 0.8. Horizontal blue line is the tie line at the growth temperature T. The M content in liquid M-Au alloy at this temperature is x_L and the fraction of liquid is $(1 - x)/(1 - x_L)$, while the fraction of solid M is $(x - x_L)/(1 - x_L)$

Of course, using pseudo-binary diagrams for Au–III–V alloys (that is, assuming stoichiometric GaAs composition in the liquid phase) is not very relevant due to the known low solubility of highly volatile group V elements such as As and P in liquids [14]. Therefore, Au–III–As or Au–III–P liquid melts contain very small fractions of the group V elements rather than being stoichiometric. This property considerably complicates theoretical treatment as will be explained in what follows.

Specifically for III–V NWs, Au-catalyzed VLS growth with a high degree of control over the position, morphology, composition, and crystal phase has been achieved in a wide range of epitaxy techniques, including metal–organic vapor phase epitaxy (MOVPE, also known as metal–organic chemical vapor deposition, MOCVD) [5, 15, 16], chemical beam epitaxy (CBE, the same as molecular organic MBE, MO-MBE) [17, 18], and MBE [11, 12, 19]. In MOVPE, both group III and V elements are supplied in the form of chemical precursors, such as TMGa [$Ga(CH_3)_3$] for Ga and AsH_3 for As, in a carrier gas flow (H_2). CBE uses metal–organic precursors for the group III and either hydride gases or metal-organics TBAs (TBP) for the group V elements under high vacuum conditions. In MBE (either solid source or gas source), III–V materials are deposited from an atomic beam of the group III element (Ga) and molecular beam of the group V element (As_4 or As_2 after precracking). Hydride vapor phase epitaxy (HVPE), which uses chloride precursors for the group III element (GaCl) and hydride gases for the group V element in a vector vapor of H_2 with some additional HCl, yields a less controlled nucleation but on the other hand enables the highest aspect ratio and crystal quality in the zincblende (ZB)

phase of GaAs NWs [20]. Despite this variety of techniques, the major difference between them is in the different mechanisms and kinetic pathways of delivering the material into the droplet and onto the substrate surface. These differences result in more or less regular nucleation of NWs (which also depends on the substrate preparation), parasitic growth and, most importantly, different group III and V contents in an Au–III–V droplet at the typical temperatures employed in a particular growth method. The latter manifests through different axial growth rates, which are typically on the order of 1 nm/s in MBE, 1–10 nm/s in MOVPE, and reach 40 nm/s in HVPE. However, the liquid–solid phase transition can be understood from a general perspective, because the liquid alloy in any case consists of a mixture of group III and V atoms with Au.

Au-catalyzed VLS growth of III–V NWs usually consists of the following steps:

(1) Preparation of the substrate surface with the Au catalyst particles.
(2) Annealing the surface above the melting temperature of the alloy of Au with a given substrate material to produce liquid droplets.
(3) Deposition of semiconductor material, where the properties of the NW ensembles (surface density, size uniformity, mean length, width, shape, and even the crystal phase) can be tuned by the deposition conditions such as the growth time, temperature, group III and V fluxes.

In particular, Fig. 2 illustrates the Au-catalyzed VLS growth of GaAs NWs by MBE on a GaAs(111)B substrate in the simplest procedure where a thin solid Au layer is pre-deposited onto the substrate outside the MBE growth chamber. Then the substrate is transferred to the growth chamber and annealed above the eutectic temperature of Au-Ga alloy (the influence of As can be ignored in this stage) to break the Au film into an ensemble of liquid droplets, with a broad Gaussian-like size distribution. Deposition of GaAs at a temperature around 550 °C leads to rapid VLS growth of <111> B oriented NWs, and a much slower growth of a rough parasitic GaAs layer between the NWs. The resulting NW ensemble is irregular in terms of random positioning, broad length and radius distributions originating from the initial size inhomogeneity of the droplets, and random character of the NW nucleation.

In order to achieve more regular ensembles of NWs, Au particles can be organized before growth using electron beam [17] or nanoimprint [21] lithographical patterning of a substrate. In particular, Fig. 3 presents the examples of InP/GaP core–shell NW arrays grown by MO-MBE from the organized Au seeds in the openings of a SiN_x mask layer on InP(111)B [17]. Compared to Fig. 2, these NW structures (i) are positioned in regular arrays, with the inter-NW distance and arrangement determined by the lithographically defined pitch; (ii) have no parasitic layer between the NWs, because semiconductor material does not stick onto the inert mask layer; and (iii) are more regular in terms of both radius and length. The latter feature is explained by the fact that the initial growth seeds have a narrower size distribution compared to the case of thermally dewetted Au droplets. It will be shown later that the axial NW growth rate depends on the droplet size and hence more uniform droplets should yield less variation in terms of length. It can be anticipated that the NW nucleation

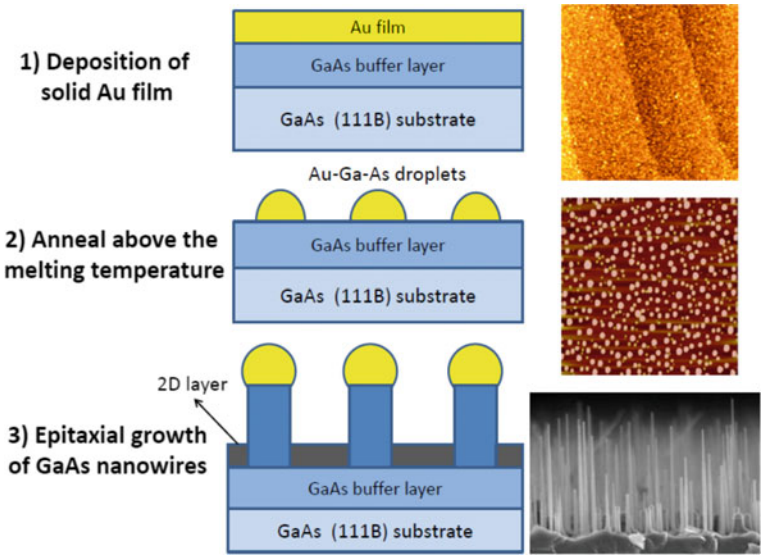

Fig. 2 Illustration of the Au-catalyzed VLS growth of GaAs NWs on a GaAs(111)B substrate by MBE with pre-deposition of ~1 nm thick solid Au layer. Atomic force microscopy (AFM) images show the surface after Au deposition (1st stage) and three-dimensional (3D) droplets after annealing (2nd stage). Scanning electron microscopy (SEM) image shows the vertically aligned GaAs NWs (3rd stage). Reprinted from Semiconductors and Semimetals, vol. 93, V. G. Dubrovskii, Theory of VLS growth of compound semiconductors, pp. 1–78. Copyright (2015), with permission from Elsevier

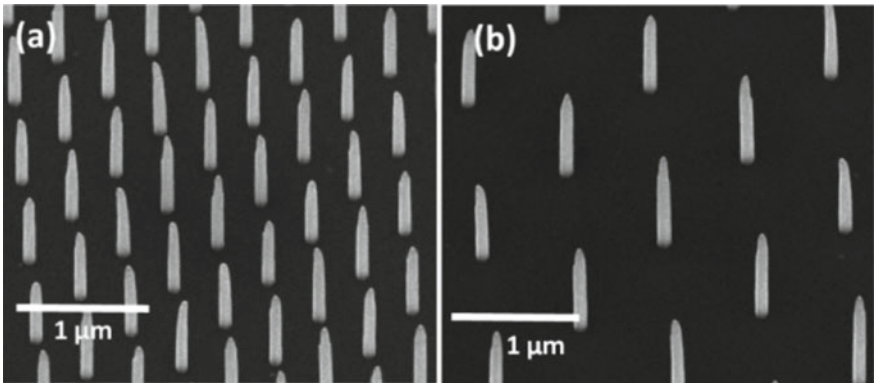

Fig. 3 Tilted SEM images of regular two-dimensional (2D) arrays of InP/GaP core–shell NWs grown by MO-MBE from Au nanoparticles formed prior to epitaxy in the openings of a SiN_x mask, defined by electron beam lithography. The pattern pitches are 0.5 and 1 µm in (**a**) and (**b**), respectively. Reprinted from Journal of Crystal Growth, vol. 463, N. N. Halder, A. Kelrich, Y. Kauffmann, S. Cohen and D. Ritter, Growth of wurtzite InP/GaP core–shell nanowires by metal–organic molecular beam epitaxy pp. 10–13, Copyright (2017), with permission from Elsevier

is better synchronized in time in the case of the VLS growth in regular templates, which also contributes into the resulting size uniformity.

Using Au as the VLS growth catalyst for III–V NWs is not desirable for integration with Si electronics, because Au can contaminate the NWs due to kinetic factors. Consequently, self-catalyzed (or self-assisted) VLS growth has emerged as a promising Au-free alternative, starting from the pioneering works by the group of Fontcuberta i Morral [22] and Jabeen et al. [23], and quickly adopted by other groups [24–32]. In this method, Au is replaced by the group III metal, that is, one of the NW constituents. Self-catalyzed VLS growth of III–V NWs allows one not only to safely avoid the unwanted Au contamination, but also to achieve excellent phase purity [27] and high degree of size homogeneity within the NW ensembles in terms of both radius [28] and length [30, 31]. It should be noted that the self-catalyzed growth of III–V NWs is more easily achieved in MBE. Chemical epitaxy techniques such as MOVPE, CBE, or HVPE are less suited for the self-catalyzed approach, most probably due to the difficulty in maintaining Ga droplets under effectively group V rich conditions typically employed in these growth methods (see Ref. [32] and a discussion therein).

Figure 4 shows the initial stages of self-catalyzed GaAs NW growth in regular arrays on patterned Si [33]. MBE growth was performed on a Si(111) substrate covered with a 10 nm thick thermal oxide, in which nanoscale holes were etched with reactive ion etching. The yield of vertical NWs was higher than 85%. SEM images in Fig. 4a–i show the GaAs NW arrays obtained on 45 nm wide holes as a function of time. For this series of samples, the Ga flux corresponded to a GaAs planar growth rate of 0.1 nm/s, the As_4 beam equivalent pressure (BEP) was 2×10^{-6} Torr, and the substrate temperature was 635 °C. Morphological analysis [33] shows that the NWs elongate axially and extend radially, as shown in Fig. 4j, k. Radial growth occurs due to effectively Ga-rich growth conditions, whereby more Ga atoms arrive at the droplet than used for NW growth [25]. As a consequence, the droplets inflate, first by increasing their contact angle and then by extending the radius of the NW top. Cylindrical geometry is maintained by the step flow growth on the NW sidewalls, following the radial extension of the tip. Very importantly, one can observe a long delay of the NW nucleation, about 4 min, and a wide spread of the nucleation times for different NWs, which explains the broad length distribution within the array. Minimizing the nucleation randomness is crucial for improving the length uniformity [30, 31] as will be discussed in Sect. 8.

One of the most interesting features of self-catalyzed VLS growth is that the droplet serves as a non-stationary reservoir of a group III metal, which can either swell or shrink depending on the V/III flux ratio [25, 28, 34, 35]. Indeed, Ga is always present in the droplet for crystallization of GaAs with the arriving As. Hence, the axial NW growth rate is determined by the As influx and temperature-dependent desorption. Then the droplet will swell under negative and shrink under positive V/III influx imbalance, depending on whether more or less As atoms arrive to the droplet compared to Ga, respectively. The Ga influx usually includes surface diffusion flux of Ga adatoms from the NW sidewalls to the droplet, which is radius-dependent and increases for smaller radii. This may result in an interesting self-equilibration

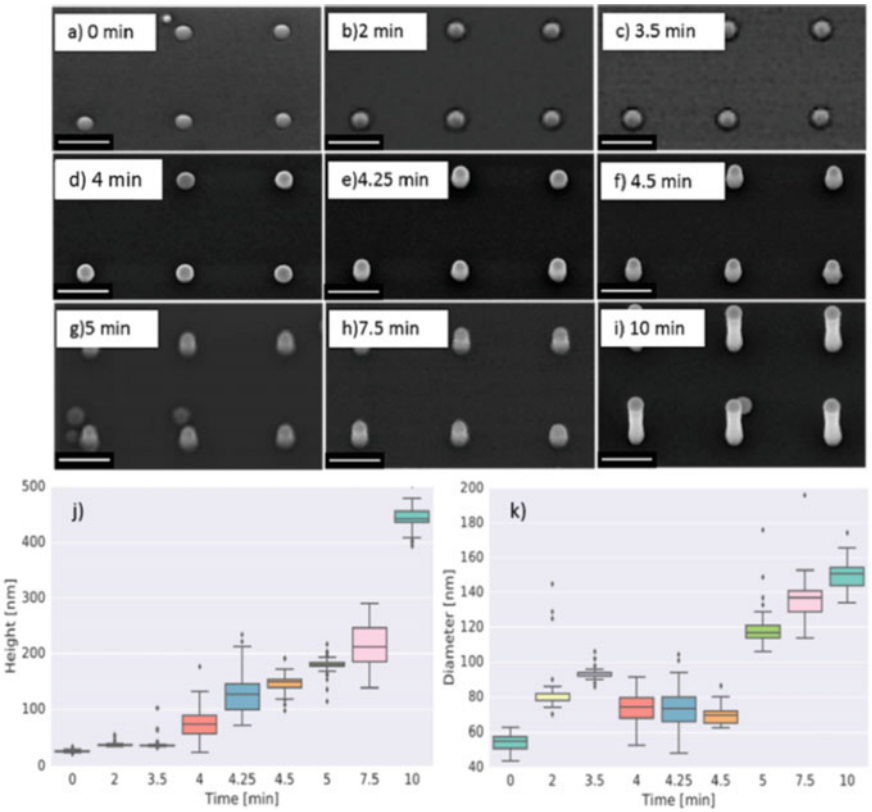

Fig. 4 Time series of Ga-catalyzed GaAs NW arrays: (**a**–**i**) SEM images of the array grown for 0 min (just after the droplet deposition) up to 10 min. Scale bar is 200 nm, and the tilt angle is 20°; the corresponding height (**j**) and diameter (**k**) distributions obtained by AFM. The diameter decrease seen after 4 min of GaAs deposition is due to the shape change as the droplets are lifted from the substrate surface, after which the NWs start to grow radially. Reprinted from J. Vukajlovic-Plestina, W. Kim, V. G. Dubrovskii, G. Tütüncüoğlu, M. Lagier, H. Potts, M. Friedl and A. Fontcuberta i Morral, Engineering the size distributions of ordered GaAs nanowires on silicon, Nano Letters **17**, 4101–4108 (2017), https://pubs.acs.org/doi/10.1021/acs.nanolett.7b00842, with permission from the American Chemical Society, to which further permissions related to the material excerpted should be directed

effect for the NW radius [28, 34]. The effect requires that the influx of As atoms from vapor (minus desorption) is larger than that of Ga. The missing Ga is brought by surface diffusion along the sidewalls. This contribution scales with NW radius whereas Ga consumption (an As input) scales with its square. As a consequence, the droplet size, and consequently the radius of the NW top, will increase with time for thin NWs, and decrease with time for thick NWs. As a result, the NW radii will converge to a stationary value, corresponding to the stable growth at this constant

radius. Therefore, the radius distribution of NWs will self-regulate to an almost delta-like function regardless of the initial size distribution of Ga droplets. Details of this process will be discussed in Sect. 7.

The V/III influx imbalance can easily be regulated by the V/III flux ratio. This can be used for the fine tuning of the morphology of self-catalyzed III–V NWs. Figure 5 shows the example of Ga-catalyzed GaAs NWs grown in regular arrays on patterned SiO_2/Si(111) templates [35]. The initial step is the standard growth under negative V/III influx imbalance, achieved at a low As_4 BEP of 2×10^{-6} Torr for a fixed Ga flux corresponding to 0.11 nm/s planar growth rate of GaAs. All NWs grow radially in this step, reaching an average radius of 75 nm for 4 μm length. Now, the idea is to obtain quantum-thin nanoneedles (NNs) on top of this NWs by engineering the As flux. Increasing the As_4 BEP to 8.9×10^{-6} Torr for 2 min after the standard growth step yields the structures shown in Fig. 5c. Even though the Ga flux is still on, the droplets have decreased to a radius smaller than that of the NW. Keeping these conditions for 3 min longer yields the formation of conical-like NN tops, as shown in Fig. 5d. The top radius of conical-like NNs can be decreased to a very small size, about 5 nm. After that, the VLS growth should stop due to the consumption of Ga and NNs cannot grow any longer.

If, instead of maintaining the As_4 BEP at a constant value of 8.9×10^{-6} Torr in the droplet shrinking stage, it is decreased down to 5.5×10^{-6} Torr from the step shown in Fig. 5c, the morphology changes dramatically. Figure 5e shows a representative SEM image of the structures obtained after 20 min of growth at 5.5×10^{-6} Torr. It is clearly seen that introducing the third growth step with a lower As flux after shrinking the droplets results in the formation of thin NNs that first taper and then acquire a uniform radius of approximately 10 nm. This stationary radius stays constant along ~1 μm of the NN length. These structures show quantum confinement effect as discussed in detail in Ref. [35].

Figure 6a shows the results of Ref. [25], where the Ga-catalyzed VLS growth of GaAs NWs was intentionally stopped and resumed by consuming Ga droplets under As flux and then nucleating a secondary NW. Primary GaAs NWs were fabricated by solid source MBE on Si-treated GaAs(111)B substrates. The NW growth was carried out at 640 °C with a V/III BEP ratio of 5. The Ga flux was set to a BEP of 3.6×10^{-7} Torr, corresponding to a growth rate of 0.28 nm/s on GaAs(100) surface. After 60 min of growth, the Ga shutter was closed and the sample was kept for 10 min under As flux to obtain the complete consumption of the droplet. After this step, the Ga shutter was opened again for different durations. NW A in Fig. 6a represents the starting point of the secondary growth step. After the complete consumption of the Ga droplet, the tip appears flat. After 30 s of exposure to Ga and As beams (NWs B, C, and D) the morphology of the tip changes. A spherical cap droplet, with radius smaller than that of the NW, becomes visible. This droplet is now sitting on top of a pyramid-like structure, which morphology resembles that of NWs terminating with (110) facets. NWs B-D belong to the same sample, and the differences between them can be ascribed to local fluctuations of the effective beam fluxes. After 60 s (NW E) a new NW portion has grown and the droplet has already reached its equilibrium geometry, with a contact angle exceeding 110°. For increased deposition times (NW

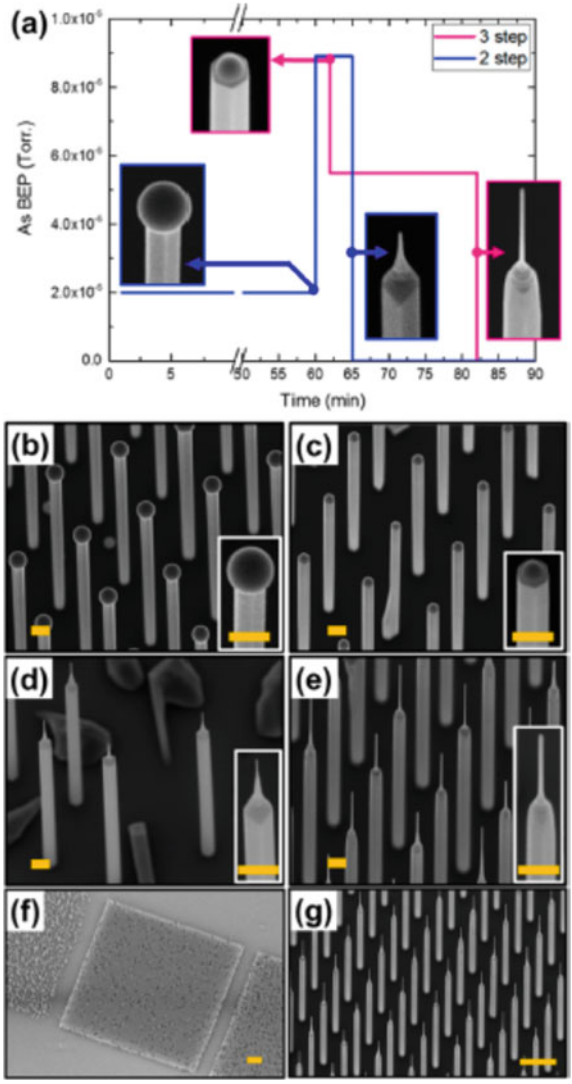

Fig. 5 **a** Schematic morphology evolution of GaAs NWs and 20° tilted SEM images of 800 nm pitch arrays: **b** Standard growth under Ga-rich conditions at an As_4 BEP of 2×10^{-6} Torr; **c** Abrupt droplet shrinkage by increasing the As_4 BEP to $8.9\ 10^{-6}$ Torr for 2 min; **d** Further evolution of the tip under the same As_4 BEP, the tips are conically tapered and the droplets are finally lost; **e** Straight, 10 nm radius NNs on top of NWs obtained via the three-step procedure by decreasing the As_4 BEP to $5.5\ 10^{-6}$ Torr after step (**c**) and growing the NNs for 20 min. The inserts in (**d**) and (**e**) show the tapered tip without any droplet and straight NN with a droplet for higher and lower As_4 BEP, respectively. **f** and **g** Lower magnification SEM images of regular NNs on top of NWs. Scale bars are 200 nm in (**b**) to (**e**), 10 μm in (**f**) and 1 μm in (**g**). Reprinted from W. Kim, V. G. Dubrovskii, J. Vukajlovic-Plestina, G. Tütüncüoglu, L. Francaviglia, L. Güniat, H. Potts, M. Friedl, J.-B. Leran and A. Fontcuberta i Morral, Bistability of contact angle and its role in achieving quantum-thin self-assisted GaAs nanowires, Nano Letters **18**, 49–57 (2018), https://doi.org/10.1021/acs.nanolett.7b03126, with permission from the American Chemical Society, to which further permissions related to the material excerpted should be directed

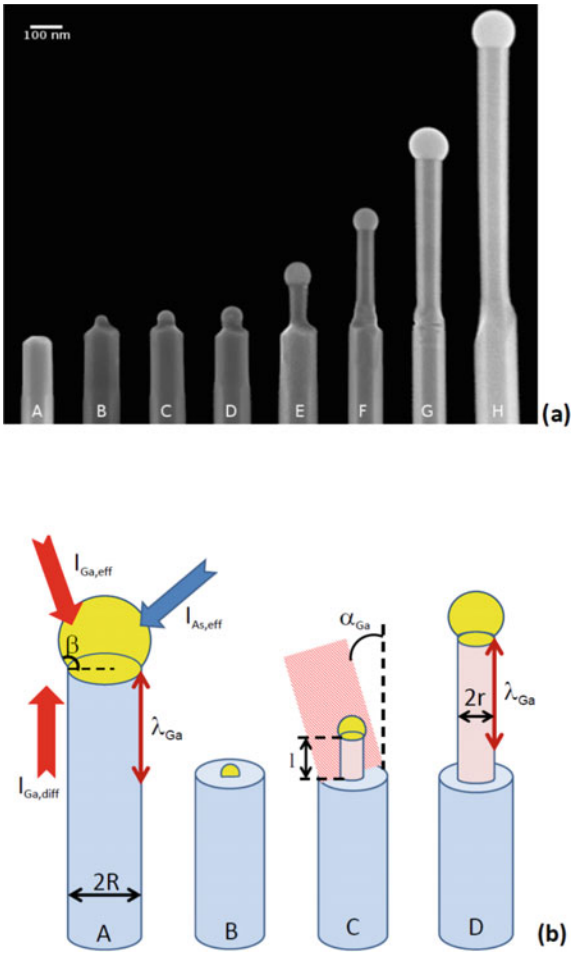

Fig. 6 **a** Collage of SEM images of the GaAs NWs coming from different samples after the consumption of the Ga nanoparticle (A) and after exposure to Ga and As beams for 30 s (B–D), 60 s (E), 150 s (F), 300 s (G) and 420 s (H). **b** Schematics of the NW growth process: Regular growth stage with the radius R increasing linearly with time due to a positive Ga imbalance arising from $I_{\mathrm{Ga,eff}} + I_{\mathrm{Ga,diff}} > I_{\mathrm{As,eff}}$, with I_{eff} denoting the effective incoming fluxes of Ga and As (A); Nucleation of Ga droplet on a flat top facet of the primary NW (B); Fast radial growth of a short secondary NW (with the length l shorter than the diffusion length of Ga adatoms λ_{Ga}) due to additional diffusion flux of Ga from the top surface of the primary NW (C); Regular growth of a long secondary NW with $l > \lambda_{Ga}$ (D). Finally, the radius of secondary NW r will reach the radius of the stem R. Reprinted with permission from G. Priante, S. Ambrosini, V. G. Dubrovskii, A. Franciosi and S. Rubini, Stopping and resuming at will the growth of GaAs nanowires, Crystal Growth & Design **13**, 3976–3984 (2013). Copyright (2013) American Chemical Society

F after 150 s and G after 300 s), the NW continues to elongate. NWs B to F show two diameter discontinuities along their bodies. The first related to the consumption of the droplet, as in A, and the second due to the growth resumption with smaller radius. By increasing the deposition time, the separation between the two discontinuities tends to decrease, and finally the secondary NW reaches the size of the primary one.

The model schematized in Fig. 6b and described in more detail in Ref. [25] is capable of explaining the observed trends, including (i) the linear length–time and radius-time dependences for the primary NWs; (ii) explanation of why Ga nanodroplet reappears on the NW top; and (iii) the non-linear radius-time dependence for the secondary NW, while the length–time correlation remains almost exactly identical to that at the regular growth stage.

Besides engineering the radius of vertical NWs, growth interruptions can be used for changing the NW growth direction. Controllable switching of the NW growth direction opens up new horizons in the bottom-up engineering of self-assembled nanostructures, for example, to fabricate interconnected nanowires used for quantum transport measurements. In Ref. [36], a robust and highly controllable method was proposed for deterministic switching of the growth direction of self-catalyzed GaAs NWs. The method is based on the modification of the droplet-NW interface in the annealing stage without any fluxes and subsequent growth in the horizontal direction by a twin-mediated mechanism with indications of a novel type of interface oscillations. By systematically optimizing the growth parameters, 100% yield of switching the NW growth direction from vertical to horizontal was achieved, and occurring in the same horizontal plane.

In brief, the initial self-catalyzed GaAs NWs were grown by solid source MBE on lithography-free oxide pattern templates fabricated on p-Si(111) substrates via droplet epitaxy, with remarkably narrow length distribution [30]. After growth of the vertical part, the NWs were annealed for 20–70 s at the growth temperature of 640 °C, without any fluxes in order to reshape the droplet-NW interface. After the annealing, the NW growth was resumed by simultaneously providing the Ga and As fluxes. A typical NW sample after 20 min of vertical growth and immediate cool down without any fluxes is shown in Fig. 7a, d. It is clearly seen that the Ga droplets remain stationary on the NW tips just after growth. In contrast, the sample that was annealed for 45 s at the growth temperature prior to cool down [Fig. 7b, e] exhibits 100% yield of droplets falling toward one of the (110) side facets. When the growth is resumed after annealing by simultaneously opening the Ga shutter and As cracker, the NWs continue their growth perpendicular to their initial growth direction [type 1 NWs in Fig. 7c, f], or slightly downward [type 2 NWs in Fig. 7c, g]. The azimuthal direction of the bent NW part is toward one of the <112> directions associated with the corners of the (110) sidewalls, in contrast to the droplet position after the annealing [see the insets in Fig. 7e–g].

It was found that horizontal type 1 NWs have a better crystal quality, exhibiting pure ZB structure throughout the whole NW, with a single twin plane extending along the horizontal section. For type 2 NWs, the downward section is dominated by periodic twinning. Therefore, the yield of type 1 horizontal NWs was carefully optimized by the growth parameter tuning, and reached 100% for smaller diameters

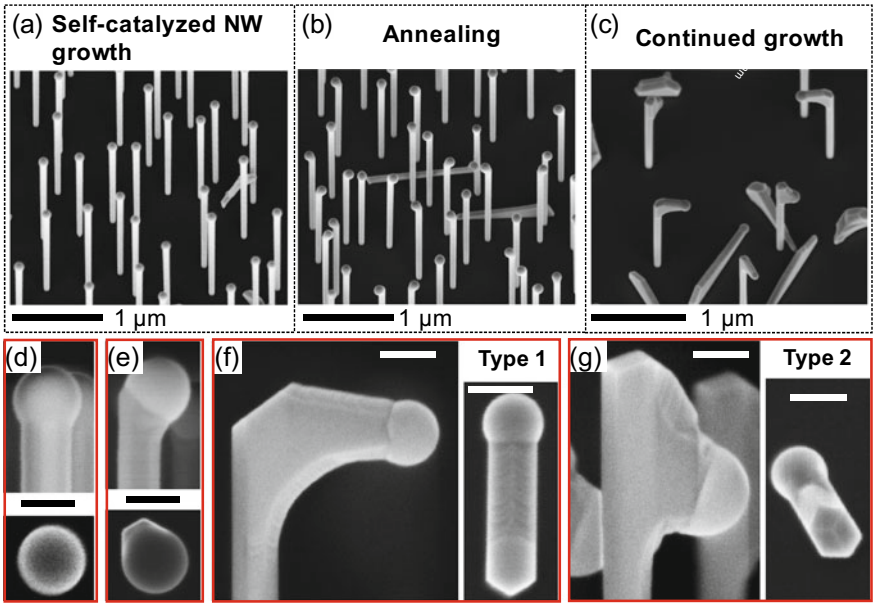

Fig. 7 Growth of bent Ga-catalyzed GaAs NWs: **a** and **d** Vertical NWs grown for 20 min and rapidly cooled down; **b** and **e** NWs annealed at the growth temperature for 45 s prior to cool down; **c** NWs grown for 5 min after 45 s annealing; Side and top-view images of (**f**) type 1 horizontal and (**g**) type 2 downward growth. Scale bars in low magnification 30° tilted images are 1 μm in (**a**)–(**c**) and 100 nm in (**d**)-(**g**) . Reprinted with permission from E. S. Koivusalo, T. V. Hakkarainen, H. V. A. Galeti, Y. G. Gobato, V. G. Dubrovskii and M. D. Guina, Deterministic switching of the growth direction of self-catalyzed GaAs nanowires, Nano Letters **19**, 82–89 (2019). Copyright (2019) American Chemical Society

of the initial NWs (75 nm), higher number density (2.5×10^8 cm^{-2}), or longer annealing times (70 s).

3 Basics of the Nanowire Growth Modeling

These examples demonstrate almost unlimited possibilities for bottom-up design of III–V NWs. Let us now discuss the most important ingredients of the NW growth modeling, leaving the details for the next sections. We start from the kinetic equations describing the time evolution of the total number of group V (N_5) and III (N_3) atoms in a catalyst droplet with base radius R, which equals the radius of the NW top [37]

$$\frac{\mathrm{d}N_5}{\mathrm{d}t} = \chi_5 I_5 (1+\alpha_r)\pi R^2 - I_5^{\mathrm{des}} \frac{2}{(1+\cos\beta)} \pi R^2 - \frac{\pi R^2}{\Omega_S} \frac{dL}{dt}, \qquad (3.1)$$

$$\frac{dN_3}{dt} = \chi_3 I_3 \pi R^2 + j_{3,diff} - \frac{\pi R^2}{\Omega_S}\frac{dL}{dt}. \tag{3.2}$$

Equation (3.1) accounts for (i) the direct (I_5) and re-emitted ($\alpha_r I_5$) atomic fluxes of group V atoms [26] which are entering the droplet seated on the NW top, with χ_5 accounting for the beam geometry and the droplet contact angle in MBE [38] or the precursor cracking efficiency in MOVPE (with $\chi_5 = 2/(1 + \cos\beta)$ for 100% cracking), (ii) the desorption flux I_5^{des} from the surface area of a spherical cap droplet with the contact angle β, and (iii) the sink of group V atoms due to the NW elongation dL/dt, with Ω_S as the elementary volume per III–V pair in solid. We neglect surface diffusion of group V species due to their high volatility. The influx of group III atoms in Eq. (3.2) is the sum of the impinging flux $\chi_3 I_3$ (with the same meaning of the parameters as for group V), and the net diffusion current through the triple-phase line (TPL) of the cylindrical NW (in s^{-1}). The latter is given by $j_{3,\mathrm{diff}} = -2\pi R D_3 (\partial n_3/\partial z)|_{z=L}$, with D_3 as the diffusion coefficient of group III adatoms on the sidewalls, and n_3 their surface concentration as a function of the height z. Desorption of group III atoms from the droplet is neglected. The sink due to NW growth should be exactly the same as for group V atoms to ensure stoichiometric III–V compound in the solid NW.

In the Au-catalyzed case under group V rich conditions, the excess group V atoms will desorb from the droplet. The axial NW growth rate is then obtained from the condition $dN_3/dt = 0$, in which case Eq. (3.2) yields

$$\frac{dL}{dt} = \chi_3 \Omega_S I_3 + \frac{\Omega_S j_{3,\mathrm{diff}}}{\pi R^2}. \tag{3.3}$$

The diffusion flux $j_{3,\mathrm{diff}}$ should depend on the chemical potentials of group III atoms in the droplet (μ_3^L) and group III adatoms on the NW sidewalls at large enough distance from the droplet and may be sensitive to the vapor flux of As atoms and their concentration in the droplet. The simplest approximation $j_3 = 2\pi R \varphi_3 \lambda_3 I_3$ (where φ_3 summarizes the geometrical effect in MBE or the cracking efficiency at the NW sidewalls in MOVPE and the collection length of Ga atoms λ_3 can depend on the group V flux) leads to the typical inverse radius dependence of the NW axial growth rate [5, 11, 37]

$$\frac{dL}{dt} = \Omega_S I_3 \left[\chi_3 + \varphi_3 \frac{2\lambda_3}{R}\right] \tag{3.4}$$

In this transport-limited regime, the NW elongation is independent of the droplet composition. A similar equation is often used to describe the length–radius correlation of elemental semiconductor NWs such as Si [39].

For self-catalyzed VLS growth, or Au-catalyzed VLS growth under As-poor conditions (where the Ga fraction in liquid approaches unity), the axial growth rate is limited by the kinetics of group V species, while dN_3/dt is non-zero as discussed above. Putting $dN_5/dt = 0$ in Eq. (3.1), we obtain

$$\frac{dL}{dt} = \chi_5 \Omega_S I_5 (1 + \alpha_r) - \frac{2}{1 + \cos\beta} \Omega_S I_5^{des} \tag{3.5}$$

However, this equation is not self-consistent because the desorption rate depends on the atomic concentration of group V atoms in the droplet c_5 (here and below, we use the normalization for c_X with $X = 3, 5$, Au such that $c_3 + c_5 + c_{Au} = 1$, which is reduced to $c_3 + c_5 = 1$ for self-catalyzed NWs). According to Refs. [40, 41], if group V species desorb in the form of dimers, we have

$$I_5^{des} = I_{5,0} \exp(2\overline{\mu}_5^L), \tag{3.6}$$

where $\overline{\mu}_5^L = \mu_5^L/(k_B T)$ is the chemical potential of group V atoms in liquid in thermal units, T is temperature, and k_B is the Boltzmann constant. The temperature-dependent pre-exponent $I_{5,0}$ is related to the vapor phase. Finding c_5 requires a second equation for dL/dt, which is determined by the crystallization rate at the liquid–solid interface under the droplet [40, 41].

Theoretical considerations [42–46] and in situ growth monitoring inside a transmission electron microscope (TEM) [47–49] suggest that NWs often grow in the so-called mononuclear regime whereby only one 2D island succeeds in nucleating for each NW monolayer (ML). The probability to nucleate a 2D island on the top facet of cylindrical NW of radius R per unit time equals $\pi R^2 J$, where J is the nucleation rate. On the other hand, the island fills the complete ML slice of a NW after the time R/v, where $v = dr/dt$ is the growth rate of a linear size of the island. The ratio of these characteristic times naturally yields the control parameter $\pi R^3 J/v$ [43]. Mononuclear growth occurs at $\pi R^3 J/v << 1$, which requires small NW radii, slow nucleation rates, and rapid island growth rates. Similar considerations apply when nucleation of 2D islands takes place at the TPL rather than on the whole top facet, as has been proposed [42] to explain polytypism in NWs (see Sect. 10.2), in which case the nucleation probability equals $2\pi R r_c J$, with r_c as the radius of the critical 2D island [41, 42].

Slow nucleation rates correspond to low chemical potentials of III–V pairs in the liquid with respect to the reference solid state, defined as [14]

$$\Delta\mu(c_3, c_5, T) = \mu_3^L(c_3, c_5, T) + \mu_5^L(c_3, c_5, T) - \mu_{35}^S(T). \tag{3.7}$$

Here, the μ_X^L are the chemical potentials of group III and V atoms in liquid, which depend on the two atomic concentrations c_3, c_5 and temperature T, and μ_{35}^S is the temperature-dependent chemical potential per III–V pair in solid. The number of III–V pairs in the critical 2D island (the critical size for brevity) is given by the standard equation of classical nucleation theory (CNT) [6]

$$i_c = \frac{a^2}{4\Delta\overline{\mu}^2}, \tag{3.8}$$

with $\Delta\overline{\mu} = \Delta\mu/(k_B T)$ the chemical potential in thermal units. The energetic constant a is proportional to the effective surface (or edge) energy of 2D island γ_{eff} (see Sect. 6.3 and 11.2). For regular triangle shape of the island, it is given by [7]

$$a = 2 \times 3^{3/4} \frac{\gamma_{eff}}{k_B T} (\Omega_S h)^{1/2}, \tag{3.9}$$

with h the ML height. Using CNT requires that the critical size is macroscopic ($i_c >> 1$). In the mononuclear growth regime, the axial NW growth rate equals

$$\frac{dL}{dt} = \eta \pi R^2 h J, \tag{3.10}$$

with $\eta = 1$ for the center and $\eta = 2r_c/R$ for the TPL nucleation.

The Zeldovich nucleation rate of CNT was studied in Ref. [40] for self-catalyzed and in Ref. [50] for Au-catalyzed III–V NWs. It was argued that the island formation energy $F(i)$ should include the so-called self-consistency renormalization to ensure that $F(i)$ equals zero for the island of size one [51]. The details of calculations can be found in Ref. [50]. The resulting expression in the Au-catalyzed case has the form [50]

$$J = \frac{3^{3/4}}{\sqrt{\pi}} D_5 \left(\frac{h}{\Omega_S}\right)^2 e^{\overline{\mu}_{35}^S} c_5 \Delta\overline{\mu}^{1/2} \exp\left(a - \frac{a^2}{4\Delta\overline{\mu}}\right). \tag{3.11}$$

Here, D_5 is the diffusion coefficient of group V atoms in liquid, and $\overline{\mu}_{35}^S = \mu_{35}^S/(k_B T)$. This expression is consistent with the earlier result of Ref. [40] for self-catalyzed III–V NWs

$$J = J_0 c_5 \Delta\overline{\mu}^{1/2} \exp\left(-\frac{a^2}{4\Delta\overline{\mu}}\right), \tag{3.12}$$

with

$$J_0 = \frac{3^{3/4}}{\sqrt{\pi}} D_5 \left(\frac{h}{\Omega_S}\right)^2 e^{\overline{\mu}_{35}^S + a}. \tag{3.13}$$

For a Ga droplet, the surface energy and the diffusion coefficient of group V atoms in liquid Ga depend only on temperature. Therefore, the J_0 coefficient may depend on temperature but neither on $\Delta\mu$ nor c_5. According to Ref. [40], the values of the two unknowns J_0 and γ_{eff} [related to a in Eq. (3.12) through Eq. (3.9)] for Ga-catalyzed GaAs NWs equal 7 nm^{-2} s^{-1} and 0.123 J m^{-2}, respectively, and can be taken independent of temperature within the range of 570–630 °C. Diffusion coefficient of As in liquid Ga is estimated at $D_{As} \cong 2 \times 10^{-12}$ m^{2}s^{-1} for this temperature range [50].

When the critical size i_c approaches one III–V pair, CNT is no longer valid [6]. Small $i_c \sim 1$ corresponds to high chemical potentials (or supersaturations) of the liquid phase and consequently rapid NW growth rates. This situation may occur in MOVPE and HVPE growth techniques at high material inputs, particularly for group V species. For $i_c \cong 1$, growth of 2D islands becomes regular (or irreversible), meaning that meeting of any group III and V atoms at the liquid–solid growth interface immediately produces a stable III–V pair. The corresponding nucleation rate is then proportional to $c_3 c_5$. The axial growth rate in this case is given by [51–53]

$$\frac{dL}{dt} = K_{35} c_3 c_5, \tag{3.14}$$

with K_{35} as the crystallization rate in nm s^{-1}. Obviously, regular growth is enabled on the entire surface of the top facet. In the regular growth picture, it is reasonable to take the desorption rate in the form

$$I_5^{des} = k_5^{des} c_5^2, \tag{3.15}$$

with a certain temperature-dependent pre-exponent k_5^{des}.

Equations (3.10), (3.11) for $i_c >> 1$ or Eq. (3.14) for $i_c \cong 1$ together with Eqs. (3.1) and (3.2) and the corresponding desorption rates constitute the closed system which allows for the self-consistent determination of all the unknowns entering the equations, namely, the steady-state values of c_3, c_5 and dL/dt in the Au-catalyzed case, or c_5 and dL/dt in the self-catalyzed case. The non-stationary equation for dN_3/dt is separated from the axial growth rate in the latter case and describes the time evolution of the Ga droplet size. The full self-consistency requires determination of (i) chemical potentials as functions of the concentration(s) and temperature, (ii) desorption rate of group V atoms from the droplet, and (iii) diffusion flux of group V atoms into the droplet. This will be discussed in Sect. 6. Furthermore, relating N_X to c_X and β to c_3 by simple geometrical expressions enables one to treat interesting not-stationary problems such as formation of axial NW heterostructures in ternary III–V NWs [53, 54], or evolution of the droplet volume under time-dependent fluxes [55].

4 Role of Surface Energy

Nebol'sin and Shchetinin [56] presented a model for the surface energetics of VLS NWs, in which a stable contact angle of the droplet was introduced related to stable growth of NWs with vertical sidewalls. The model enabled a simple classification of the catalyst metals suitable for the VLS growth of Si NWs [56]. The surface energy criteria were later reconsidered by Tersoff et al. [47, 48, 57] and Dubrovskii [58] and turned out to have an important impact on the droplet stability issues [35, 59],

NW morphologies [57, 58], and related crystal phases of III–V NWs [48, 60, 61]. In particular, in situ monitoring of the VLS growth of GaAs NWs [48, 61] reveal the occurrence of a truncated corner facet at the growth interface at large enough contact angles of the droplet. The amount of truncation oscillates with the period of ML formation. The presence or absence of the truncation is related to the crystal phase of III–V NWs [47, 48, 61], which can be either cubic ZB or hexagonal wurtzite (WZ). Morphology of the growth interface has an interesting connection with the Glas theory of polytypism of VLS III–V NWs [42]. All these factors show the importance of the surface energy constrains in the VLS growth of NWs.

Possible geometries of the VLS growth interface are shown in Fig. 8. The NWs can form in (i) inward tapered geometry with non-wetted (N-W) narrowing (n) facets making a positive angle θ_n with respect to vertical [Fig. 8a]; (ii) outward tapered geometry with non-wetted widening (w) facets inclined at a negative angle θ_w with respect to the vertical [Fig. 8b]; (iii) with truncated (tr) wetted (W) growth interface at an angle θ_{tr} with respect to the vertical, which can grow only to a finite length according to Ref. [47] [Fig. 8c]; or (iv) with non-wetted vertical facets and planar growth interface [Fig. 8d], which is the standard VLS configuration. The solid–vapor surface energies $\gamma_{SV}(\theta)$ depend on the crystal phase (ZB or WZ) [62, 63], while the solid–liquid surface energies $\gamma_{SL}(\theta)$ are usually assumed phase-independent for any θ according to Ref. [42].

Using the results of Ref. [58], the excess surface energy (per unit area) of forming NWs with non-wetted facet at the angle θ to the vertical with respect to the standard non-wetted vertical facet in the ZB phase is given by

$$\Delta\Gamma_{N-W} = \frac{\gamma_{SV}(\theta)}{\cos\theta} - \gamma_{SV}(0) - [\gamma_{SL}(\pi/2) + \gamma_{LV}\cos\beta]\tan\theta. \qquad (4.1)$$

Here, $\theta = \theta_n > 0$ for narrowing or $\theta_w < 0$ for widening facet. The excess surface energy of forming NWs with truncated wetted facet with the angle θ_{tr} equals

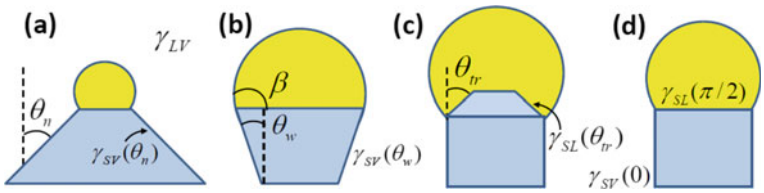

Fig. 8 Non-wetted (**a**) narrowing and (**b**) widening facets, yielding an increasing or decreasing contact angle β, respectively. **c** Truncated wetted facet with the angle θ_{tr}, which will grow only to a finite length. Configurations (**a**)–(**c**) are compared to the standard VLS growth mode with planar liquid–solid interface and vertical side facets, shown in (**d**). Reprinted with permission from V. G. Dubrovskii, N. V. Sibirev, N. N. Halder and D. Ritter, Classification of the morphologies and related crystal phases of III–V nanowires based on the surface energy analysis, Journal of Chemical Physics C **123**, 18,693–18,701 (2019). Copyright (2019) American Chemical Society

$$\Delta\Gamma_W = \frac{\gamma_{SL}(\theta_{tr})}{\cos\theta_{tr}} - \gamma_{SV}(0) - \gamma_{SL}(\pi/2)\tan\theta_{tr} + \gamma_{LV}\sin\beta. \qquad (4.2)$$

We note that these expressions are actually insensitive to whether the VLS growth is considered as instantaneous adding of MLs or at a constant volume of the catalyst droplet [58].

The preferred morphology is now determined by the minimum $\Delta\Gamma$ at a given contact angle β, where the zero level corresponds to the vertical sidewalls and planar liquid–solid interface in the ZB phase. Constructing the structural diagrams for different contact angles requires knowing the types of different facets and their surface energies. Below we consider the best known case of GaAs NWs. The widening facet should be the low energy (111)B facet in the ZB phase, with $\theta_w = -19.5°$. The narrowing facet is the (110) ZB facet according to the in situ data of Ref. [61] (obtained for Ga-catalyzed GaAs NWs), with $\theta_n = 54.7°$. The wetted truncated facet makes the same angle to the vertical, with $\theta_{tr} = 54.7°$. The lowest energy vertical facet in the WZ phase is the $(1\bar{1}00)$ facet, whose surface energy is lower than that of the (110) ZB vertical facet according to the calculations of Refs. [62, 63]. This feature is essential for the WZ phase formation in III–V NWs (see, for example, Ref. [6] for a detailed review). The calculated surface energies of the solid–vapor facets are given in Table 1, along with the corresponding references. The droplet surface energy γ_{LV} should be close to that of pure liquid Ga. This is guaranteed for Ga-catalyzed growth and should also be the case for Au-catalyzed due to the lower surface energy of liquid Ga compared to Au. We take the Ga surface energy at 420 °C, corresponding to the growth temperature employed during in situ measurements [61]. However, the temperature dependence of the surface energy of liquid Ga is very weak [65]. All these considerations show that the structural diagram for a given material should not be much affected by the catalyst type and temperature.

With the known angles θ_w, θ_n, θ_{tr}, and the surface energies γ_{SV} and γ_{LV}, Eqs. (4.1) and (4.2) contain two unknowns, the solid–liquid interface energies $\gamma_{SL}(\pi/2)$ and $\gamma_{SL}(\theta_{tr})$. These values can be deduced based on the results of in situ monitoring of Ga-catalyzed GaAs NWs [61]. These results were obtained under varying Ga and As fluxes, which resulted in different contact angles of Ga droplets. At small contact angles, typically below 100°, the NW morphology was tapered and the liquid–solid interface was planar. This kinetic regime was achieved under high As and low Ga fluxes where the droplet volume was gradually diminishing. At intermediate contact angles, typically between 100° and 125°, stable NW growth was observed, with vertical facets and planar liquid–solid interface. At large contact angles, above 125° the truncated wetted corner facets developed, oscillating with the period of ML growth and increasing their size toward larger β. Soon after the 125° contact angle, the NWs became reverse tapered due to the droplet swelling. Very importantly, these changes of the morphology led to the crystal phase switching—the crystal phase was ZB for small ($\beta < 100°$) and large ($\beta > 125°$) angles and WZ for the intermediate range of β. Fitting the two critical contact angles, $\beta_{\min} = 100°$ and $\beta_{\max} = 125°$ yields the structural diagram of VLS GaAs NWs shown in Fig. 9. From the fits, we deduce the plausible values of $\gamma_{SL} = 0.593$ J/m^2 and $\gamma_{\theta_{tr}L} = 0.566$ J/m^2, which appear close

Table 1 Parameters of GaAs used for modeling the NW morphology

Parameter	$\gamma_{(111)B}$ (J/m^2)	$\gamma_{(110)}$ (J/m^2)	$\gamma_{(1\bar{1}00)}$ (J/m^2)	γ_{Ga} (J/m^2)	$\beta_{\min}$ (deg)	$\beta_{\max}$ (deg)	θ_w (deg)	$\theta_n = \theta_{tr}$ (deg)	$\gamma_{SL}(\pi/2)$ (J/m^2)	$\gamma_{SL}(\theta_{tr})$ (J/m^2)
Value	0.690	0.798	0.700	0.684	100	125	−19.5	54.7	0.593	0.566
Source	Calc. [64]	Calc. [62]	Calc. [62]	Calc. [65]	Exp. [61]	Exp. [61]	Assum	Exp	Fit	Fit

Table 2 Parameters of GaAs NWs used for the fits in Fig. 11

Pore size $2R_0$ (nm)	ε_f	R_c/R_0	t_0 (min)	t_1 (min)	t_* (min)
125	0.522	3.73	22	44	44
150	0.522	3.73	27	46	46.5
175	0.522	3.73	37	47	57.2
200	0.522	3.73	43	47	60
225	0.522	3.73	53.5	47	69

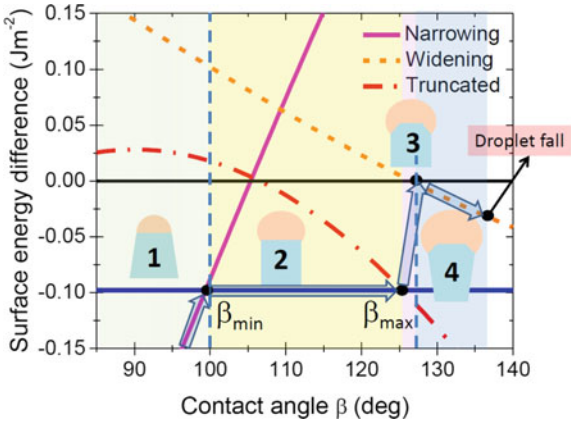

Fig. 9 Structural diagram for VLS GaAs NWs, showing the energetically preferred morphology versus the contact angle of the droplet. Zero energy level corresponds to vertical (110) ZB side facets. Horizontal line at -0.098 Jm^2 corresponds to the negative surface energy difference between $(1\bar{1}00)$ WZ and (110) ZB vertical facets. Structure 1 with tapered NW shape and planar liquid–solid interface is preferred at small contact angles <100°. The stable contact angle $\beta_{\min} \cong 100°$ corresponds to the VLS growth with vertical sidewalls at high V/III flux ratios. Any decrease of the contact angle below this value will introduce the narrowing facet and vertical growth will be resumed. Therefore, contact angles smaller than $\beta_{\min}$ are possible only in the kinetic regime where the droplet volume is gradually decreasing. The crystal phase in zone 1 is cubic ZB. Structure 2, observed between $\beta_{\min} \cong 100°$ and $\beta_{\max} \cong 125°$, corresponds to the VLS growth with vertical sidewalls and planar liquid–solid interface, most probably in the WZ phase. Above $\beta_{\max}$, the truncated corner facets are developed, growing to a finite length. The crystal phase of such NWs should be cubic ZB. There is a narrow range of contact angles, approximately between 125° and 127°, where the truncated top is followed by vertical (110) ZB sidewalls (structure 3). The contact angle of ≅127° can be called the second stable angle for the VLS growth at low V/III flux ratios, because any further increase will be compensated by introduction of the widening facet. If the droplet volume keeps increasing under excessive Ga influx, like in Ga-catalyzed GaAs NWs grown under Ga-rich conditions, the top facet increases its radius. This leads to reverse tapered geometry (structure 4). Subsequent radial growth on the NW sidewalls may resume cylindrical geometry, with the uniform NW radius increasing with time. Further increase of the contact angle to ~137° (in the kinetic regime) leads to the droplet fall onto the NW sidewalls. The arrows show the transformation of morphology with increasing the contact angle. The increase of surface energy in transition from structure 2 to 3 is explained by the fact that the vertical part of the NW must follow the ZB phase, determined by the center nucleation on the top facet

to each other. The entire set of the parameters for GaAs NWs is summarized in Table 1, where "Calc." stands for calculations, "Exp." for the in situ data of Ref. [61], "Assum." for the assumption, and "Fit" for the fits of the surface energy curves with the two critical contact angles corresponding to the morphological transformations.

The structural diagram shown in Fig. 9 reveals the following general trends. There are two critical contact angles, $\beta_{\min} \cong 100°$ and $\beta_{\max} \cong 125°$, between which the droplet changes its volume under varying group V and III fluxes (or the V/III flux ratio) by changing its contact angle. Within this range, the NW sidewalls are vertical and the liquid–solid interface is planar. The crystal phase of such NWs is expected to be WZ (see further details in what follows). In the narrow range of contact angles, between 125° and 127°, the NWs grow with vertical sidewalls and truncated wetted top, in the ZB crystal phase. The two stable contact angles of 100° and 127° correspond to the vertical VLS growth under high and low V/III flux ratios, respectively. Decreasing the contact angle below the first stable value of 100° is possible only in the kinetic regime where the droplet volume rapidly shrinks and leads to tapered NW geometry, planar growth interface, and the ZB phase. Excessive supply of Ga, as in some Ga-catalyzed GaAs NWs, will yield the radial growth at the NW top. Increasing the contact angle even above 127° in the kinetic regime leads to more reverse tapered NWs. Quite interestingly, the two stable angles deduced here (100° and 127°) are very close to the ones obtained in Ref. [35] from ex situ measurements (95° and 130°). The small stable angle in Ref. [35] corresponded to predominantly WZ and the large stable angle to pure ZB crystal phase, which is also consistent with the diagram in Fig. 9. Overall, Fig. 9 explains quite well the known prevalence of the WZ phase in the steady-state growth of Au-catalyzed GaAs NWs, because the ZB phase forms in a very narrow range of contact angles (structure 3), and predominantly ZB phase of Ga-catalyzed GaAs NWs with large contact angles and radial growth at the NW top (structures 3 and 4).

It should be noted that treatment of the crystal phase presented here is based entirely on the surface energetics of ZB or WZ NWs in different morphologies and ignore the influence of chemical potential on the crystal phase switching, which is very important in the Glas theory of polytypism [42]. In this simplified picture, the preferred crystal phase is controlled by a single parameter, the droplet contact angle. While including the chemical potential considerations may refine the picture, the existence of the two critical contact angles for the crystal phase switching in GaAs NWs strongly suggests that phase transitions occur quite abruptly whenever allowed by surface energetics. In other words, chemical potential near the transition points quickly exceeds the energy of stacking fault, which is required for switching from the ZB to WZ phase [42, 43, 60], and do not significantly affect the critical contact angles for the transition. We anticipate that a similar growth picture is relevant for other III–V NWs, but with different contact angles for the morphological transformations and the related crystal phase switching. These contact angles are entirely determined by the surface energies of the relevant facets. It would be very interesting to perform similar in situ growth experiments for other material systems in the future.

5 Selective Area Epitaxy of III–V Nanowires

Selective area epitaxy (SAE) of III–V NWs, pursued by Fukui et al. [66, 67] and other groups [68–73], is another Au-free alternative to the Au-catalyzed VLS growth method. SAE growth of III–V NWs works equally well in MOVPE and MBE techniques. In the true SAE mode with no group III droplets on the NW tops, vertical growth of NWs is directed by the arrays of lithographically defined holes, or pores on patterned substrates such as SiO_x/Si(111). To improve the vertical yield of NWs, a balanced V/III flux ratio should be employed in order to avoid the formation of too large group III droplets in the holes or irregular III–V crystallites [72]. However, the initial stage of the SAE growth of III–V NWs may have the self-catalyzed VLS nature [72, 73], with group III droplets disappearing in a later stage due to a reduced material supply of group III atoms by surface diffusion.

According to the experimental data [66–71], both length L and radius R of the SAE-grown NWs usually increase with time, while the radius of Au-catalyzed VLS III–V NWs is fixed by the initial size of the growth seed and stays constant under optimized conditions. Here, we present a model for the time evolution of the mean length and radius of SAE NWs versus the growth parameters [74]. In particular, we discussed why, after a short incubation stage, the NW length and radius often feature scaling power-law dependencies on the growth time, with the power exponents related to the growth conditions, the NW length, and the array pitch.

Consider the SAE growth from the group III and V atomic fluxes I_3 and I_5, arriving onto the top NW facet and its sidewalls with the efficiencies χ_3, χ_5 and χ_3', χ_5', respectively. Group III adatoms are able to migrate from the NW sidewalls to the top, with the corresponding net diffusion flux j_3, as in Eq. (3.2). For highly volatile group V atoms such as As and P, we account for desorption in the form of dimers (As_2 or P_2). We use Eq. (3.14) for the growth rate on both top and side facets of the NW, and Eq. (3.15) for the desorption rates of group V species. For SAE growth, it is more natural to consider the surface concentrations of group III and V atoms on the NW top (n_3, n_5) and sidewalls (n_3', n_5'), in nm^{-2}. Under the steady-state conditions, we thus have

$$\chi_3 I_3 + \frac{j_3}{\pi R^2} = k_{35} n_3 n_5, \quad \chi_5 I_5 = 2k_5 n_5^2 + k_{35} n_3 n_5; \tag{5.1}$$

$$\chi_3' I_3 - \frac{j_3}{2\pi R L_*} = k_{35}' n_3' n_5', \quad \chi_5' I_5 = 2k_5' (n_5')^2 + k_{35}' n_3' n_5', \tag{5.2}$$

with k_5 and k_5' the desorption rates of group V atoms from the NW top and sidewalls, and k_{35} and k_{35}' the crystallization rates of III–V pairs on the NW top and sidewalls, respectively. The latter are measured in $nm^2 s^{-1}$, and related to K_{35} in Eq. (3.14) as $k_{35} = K_{35}\Omega_S/h^2$ due to $n_X = c_X h/\Omega_S$ for $X = 3, 5$.

The net diffusion current arriving at the top should be divided by the surface area of the top facet πR^2 to give the diffusion-induced contribution to the adatom surface

concentration. The same current should be divided by the collection area $2\pi RL_*$ to describe the corresponding decrease in the surface concentration of the group III adatoms on the NW sidewalls. The collection length for group III adatoms can equal either the entire NW length L or only the effective diffusion length λ_3 at the NW top [6, 7]. In the directional deposition techniques such as MBE, this λ_3 can be limited by the shadowing effect [75], with $\lambda_3 \cong P \cot \alpha_3$ related to the inter-wire spacing (pitch) P and the angle α_3 of the group III beam with respect to the vertical. Therefore, the expression

$$L_* = \min\{L, \lambda_3\} \tag{5.3}$$

can be used in the first approximation. Then the axial and radial NW growth rates are given by

$$\frac{dL}{dt} = \Omega_S k_{35} n_3 n_5; \quad \frac{dR}{dt} = \frac{L_*}{L} \Omega_S k_{35}^{'} n_3^{'} n_5^{'}, \tag{5.4}$$

In the equation for the radial growth rate, the L_*/L factor accounts for the fact that crystallization of III–V pairs occurs only at the NW areas exposed to the vapor fluxes but contributes into the radial growth of the entire NW (under the assumption of cylindrical NW having a uniform radius from base to top at any moment of time).

Kinetic Eqs. (5.1), (5.2) and (5.4) should be valid for the SAE NW growth under rather general conditions. In Ref. [74], two additional simplifications were used. First, it was assumed that the SAE growth proceeds under group V rich conditions—otherwise, it would quickly transition to a self-catalyzed mode with a group III droplet appearing on the NW top [73]. Then, much more group V atoms should desorb than crystallize in solid, corresponding to large desorption terms compared to the crystallization rates in Eqs. (5.1) and (5.2) for group V atoms. Second, the diffusion current j_3 should be presented as a function of n_3. In the absence of desorption of a group III element, the simplest approximation used in Ref. [74] writes

$$j_3 = 2\pi RL_* \chi_3^{'} I_3 (1 - \varepsilon_f). \tag{5.5}$$

Here, the most important parameter of the model

$$\varepsilon_f = \frac{\chi_3 I_3 \tau_5}{\chi_3^{'} I_3 \tau_5^{'}} = \frac{\chi_3 k_{35}^{'}}{\chi_3^{'} k_{35}} \left(\frac{\chi_5^{'} k_5}{\chi_5 k_5^{'}} \right)^{1/2} \tag{5.6}$$

is given by the ratio of the group III adatom activities on the NW top facet over the sidewalls.

Under these assumptions, Eqs. (5.1), (5.2), and (5.4) yield the kinetic equations for the axial and radial NW growth rates of the form

$$\frac{dL}{dt} = v_3\left[\chi_3 + \chi_3^{'}\frac{2L_*}{R}(1-\varepsilon_f)\right],\ \frac{dR}{dt} = v_3\chi_3^{'}\frac{L}{L_*}\varepsilon_f \tag{5.7}$$

where $v_3 = \Omega_S I_3$ is the vapor flux of group III species in nm/s. This model should be relevant for sufficiently long NWs, while for shorter ones we should additionally account for a diffusion flux from the substrate surface [73]. While negligible for the growth on rough substrates with a parasitic layer [76], this flux can be much more important in the case of atomically flat patterned SiO_x/Si(111) substrates, and essential for understanding of the growth start.

Equation (5.7) for dL/dt is similar to the conventional expression for the axial growth rate of VLS III–V NWs [5, 11, 41, 65, 76–80] or self-induced GaN NWs [81] under group V rich conditions. For small $\varepsilon_f << 1$, it gives the exponential elongation with time at $L < \lambda_3$, followed by the linear elongation at $L > \lambda_3$, and almost negligible radial growth. The smallness of ε_f for VLS NWs can be due to fast crystallization rate from liquid compared to the VS crystallization rate on the NW sidewalls ($k_{35} >> k_{35}^{'}$), slower desorption of group V atoms from liquid compared to the NW sidewalls ($k_5 << k_5^{'}$), or their better adsorption at the liquid surface ($\chi_5 >> \chi_5^{'}$). The ε_f values for the SAE NWs are expected to be larger, and highly dependent on the material composition. This explains, for example, why InSb NWs grown on InAs stems become nano-disks at high Sb fluxes [71], that is, grow faster in radius than in length.

Solutions to Eq. (5.7) for short NWs ($L < \lambda_3$) are given by

$$L = (L_0 + R_c)\left(1 + \frac{t}{t_0}\right)^a - R_c\left(1 + \frac{t}{t_0}\right),\ R = R_0\left(1 + \frac{t}{t_0}\right) \tag{5.8}$$

with $a = 2(1-\varepsilon_f)/\varepsilon_f$, $R_c = R_0\chi_3/[\varepsilon_f(a-1)\chi_3^{'}]$, $t_0 = R_0/(\varepsilon v_3\chi_3^{'})$, and R_0, L_0 the initial NW radius and length at $t = 0$, respectively. For long NWs ($L \geq \lambda_3$), the solutions change to

$$L \cong \lambda_3\left(1 + \frac{t - t_*}{t_1}\right)^{\frac{a}{a+1}},\ R = R_*\left(1 + \frac{t - t_*}{t_1}\right)^{\frac{1}{a+1}} \tag{5.9}$$

with $t_1 = R_*/[(2-\varepsilon_f)v_3\chi_3^{'}]$ and R_* as the NW radius at the moment of time t_* where L becomes equal λ_3. With the known deposition rate v_3 and geometry (the χ coefficients and the pore radius R_0), these simple expressions are controlled by the single parameter ε_f. It determines the power exponents in the scaling power-law dependencies of the length and radius on the growth time as well as the characteristic times t_0 and t_1 for the axial elongation and radial extension in different stages. After an incubation stage, the NW radius evolves linearly with time as long as $L < \lambda_3$, while the length increases super-linearly for $\varepsilon_f < 2/3$, or $a > 1$. The limiting case of the highest $\varepsilon_{f,\max} = 2/3$, or the lowest $a_{\min} = 1$, corresponds to the linear time

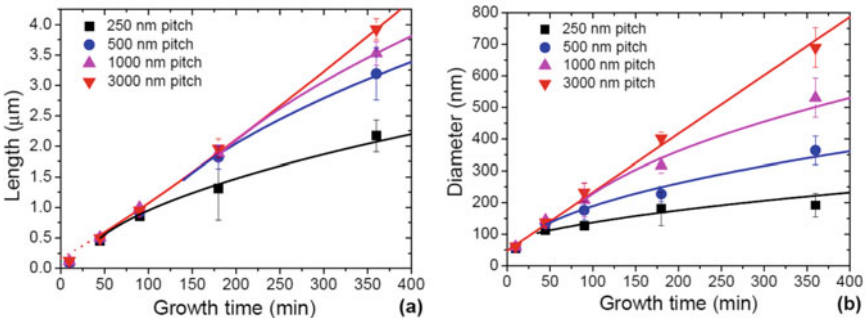

Fig. 10 Time evolution of (**a**) length and (**b**) diameter of SAE InAs NWs grown by MBE in patterned arrays on SiO_x/Si(111) with different pitches from 250 to 3000 nm (symbols) [69], fitted by the model (lines). For the largest pitch of 3000 nm, the length evolution is slightly super-linear and the diameter is linear in time in the absence of shadowing. Decreasing the pitch leads to the decrease of the In collection length due to the shadowing effect, from more than 3500 nm for 3000 nm pitch down to 500 nm for 250 nm pitch. This leads to sub-linear behavior of both length and diameter after the NW length exceeds the collection length of In. Reprinted from V. G. Dubrovskii, Evolution of the length and radius of III–V nanowires grown by selective area epitaxy, ACS Omega **4**, 8400–8405 (2019), https://pubs.acs.org/doi/10.1021/acsomega.9b00525, with permission from the American Chemical Society, to which further permissions related to the material excerpted should be directed

dependence of the NW length. At $L > \lambda_3$, both length and radius increase sub-linearly with time. At $\varepsilon_{f,\max} = 2/3$, the power exponent for both length and radius at $L > \lambda_3$ equals 1/2.

We now consider experimental data on the SAE InAs NWs grown by MBE in patterned arrays on SiO_2/Si(111) at 480 °C, with As-BEP fixed at 3.5×10^{-6} Torr, and In flux corresponding to 0.024 nm/s, in 18 nm deep pores with a fixed radius of 40 nm and variable pitches [69]. Figure 10a, b shows the time evolution of the NW length and diameter, respectively, for pitches varying from 250 to 3000 nm. In MBE, the collection length of In should be limited by shadowing, which is expected to be almost negligible for 3000 nm pitch. Therefore, these data points were fitted by Eq. (5.8) at $L < \lambda_3$, yielding the linear time dependence of the NW diameter (with $R_0 = 24$ nm and $t_0 = 26$ min). This corresponds to the effective deposition rate on the NW sidewalls $\chi_3' v_3 \cong 1.45$ nm/min. As discussed in detail in Ref. [69], the axial NW growth rate is faster at the beginning of growth, which can be attributed to the additional collection of In from the oxide surface. Leaving aside this initial stage, Eq. (5.8) was used for the NW length starting from $L_0 = 170$ nm. The best fit to the length data for 3000 nm pitch shown in Fig. 10a is obtained with $R_c = 17.5$ nm and $a = 1.14$, corresponding to $\varepsilon_f = 0.637$. This large ε_f value yields only a slight super-linearity of the length versus time. The data for smaller pitches clearly show sub-linear behavior of the NW length and diameter, both decreasing with decreasing the pitch. All sets of data for 250 to 1000 nm pitches are well fitted by Eq. (5.9) at $L > \lambda_3$ if we assume that the In collection length decreases from ~1.85 μm for 1000 nm pitch to ~0.5 μm for 250 nm pitch. All the curves in Fig. 10 correspond to the same $\varepsilon_f = 0.637$, related to a fixed V/III flux ratio, with the characteristic times

t_1 in the range from 24 to 76 nm/min. Overall, the model reproduces very well the data, explaining why the length and diameter are almost linear in time for the largest pitch and become more and more sub-linear for smaller pitches after the NW length exceeds the collection length of In.

Next, we discuss the data of Ref. [70] for the length and diameter evolution of GaAs NWs grown by SAE MOVPE at 750 °C on patterned SiO_2/GaAs substrates, with a 600 nm pitch and variable pore diameter from 125 to 225 nm. These data show that the NW length first increases super-linearly with time, converging to a sub-linear behavior for longer times (Fig. 11). This effect should be due to a limited diffusion length of Ga adatoms on the NW sidewalls. At a high temperature of 750 °C, a fraction of Ga adatoms desorb before reaching the NW top, corresponding to the transition from the growth regime at $L > \lambda_3$ to the one at $L < \lambda_3$. The pronounced super-linear increase of the NW length for shorter times requires sufficiently large a according to Eq. (5.8). The NW diameter in this stage is linear in time regardless of a. All theoretical curves shown in Fig. 11 correspond to a fixed $a = 1.83$, or $\varepsilon_f = 0.522$, at $L_0 = 0$. Other parameters are summarized in Table 2 and provide the excellent fits to all data. From the fits, we can deduce the values of $\chi_3' v_3 = 5.44$ nm/min and $\chi_3/\chi_3' = 1.78$, showing that the adsorption of gallium is more effective on the top NW facet than on the sidewalls. The observed decrease of the NW length for larger pore size is explained simply by the fact that the NW elongation is controlled by

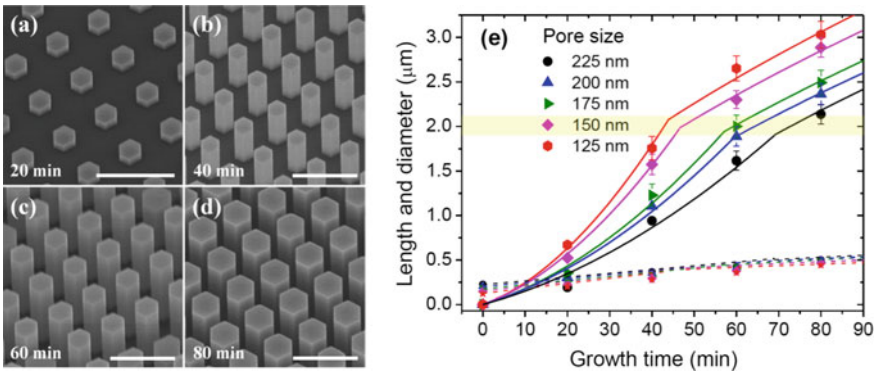

Fig. 11 Length and diameter evolution of SAE GaAs NWs grown by MOVPE in patterned arrays on SiO_2/GaAs. SEM images in (**a**)–(**d**) show the time-dependent morphology of NWs after 20, 40, 60, and 80 min of growth, respectively, for a 600 nm pitch and 225 nm diameter pore array. All scale bars represent 1 μm. **e** Time-dependent mean length and diameter in the arrays with different pore sizes from 125 to 225 nm (symbols), fitted by the model (solid lines for the length and dashed lines for the diameter) with the parameters summarized in Table 2. Time dependence of the NW length converges from super-linear to sub-linear at around 2 μm, corresponding to the diffusion length of Ga adatoms on the NW sidewalls (shown by the shaded zone). The NW diameters increase linearly before and slightly sub-linearly after 2 μm of length. The diffusion-like character of growth leads to the increase of length for thinner NWs. Reprinted from K. P. Bassett, P. K. Mohseni and X. Li, Evolution of GaAs nanowire geometry in selective area epitaxy, Applied Physics Letters **106**, 133,102 (2015)., with the permission of AIP Publishing

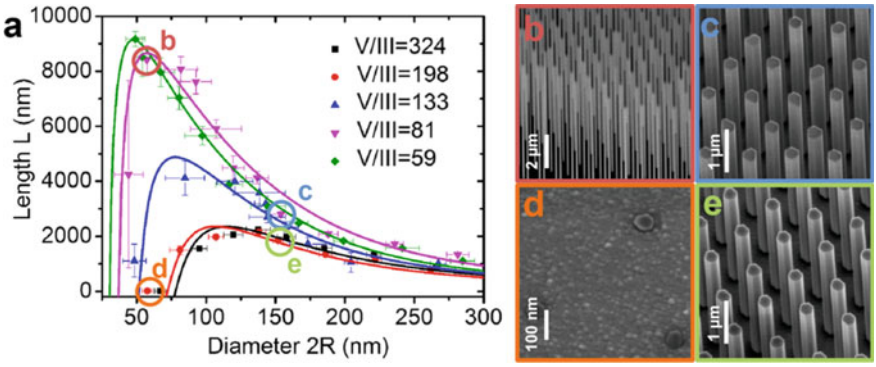

Fig. 12 **a** Average NW length (after 5 min of growth time) of <111> A-oriented InP NWs grown by MOVPE in patterned arrays on SiO_x/InP(111) A substrates with variable pore size, as a function of their diameter under different V/III ratios obtained by varying only group V flow. Panels (**b**, **c**) and (**d**, **e**) show 30° tilted SEM images of the InP NWs grown with a V/III ratio of 81 and 198, respectively, as indicated in (**a**). The NW diameters are around 60 nm in (**b**), 150 nm in (**c**), 60 nm in (**d**), and 150 nm in (**e**). Lines in (**a**) are theoretical fits by the model. Reprinted with permission from Q. Gao, V. G. Dubrovskii, P. Caroff, J. Wong-Leung, L. Li, Y. Guo, L. Fu, H. H. Tan and C. Jagadish, Simultaneous selective-area and vapor–liquid–solid growth of InP nanowire arrays, Nano Letters **16**, 4361–4367 (2016). Copyright (2016) American Chemical Society

surface diffusion of Ga, which contributes more to the axial growth rate of thinner NWs. The Ga diffusion length on the sidewalls appears very close to 2 μm in all cases.

In Ref. [73], it was shown that true SAE growth without droplets on top can coexist with the In-catalyzed VLS growth for InP NWs fabricated by MOVPE, even in the same sample. The actual growth mode of NWs depends on the initial radius of the pores, V/III flow ratio and growth time. The VLS growth mode becomes more probable for thinner NWs (which start from smaller pores), lower V/III flow ratios and shorter times. In particular, Fig. 12 shows the length-diameter correlation for InP NWs grown for 5 min with different V/III ratios, which can only be understood by considering simultaneous SAE and VLS growth. The growth rate of thin, 50–60 nm diameter NWs is tremendously enhanced by the presence of an In droplet, forming spontaneously at the tip due to surface diffusion of In. Medium diameter NWs evolve in a combined mode, with In droplets appearing and then disappearing in the course of growth. Only thick, ~150 nm diameter NWs grow in the true SAE mode from the very beginning. The coexistence of the VLS and SAE mechanism was also observed in Ref. [72] for InAs NWs grown by MBE in patterned arrays on SiOx/Si(111) substrates. It was found that most NWs start with In droplets that nucleated in the pores and disappeared in a later stage due to insufficient In supply from the oxide surface.

6 Growth Kinetics of III–V Nanowires

As already discussed in Sect. 3, the main kinetic processes governing the VLS growth of III–V NWs include (i) material transport of the group III and V species into the droplet by different kinetic pathways, including surface diffusion of group III atoms, (ii) desorption of group V atoms, and (iii) nucleation of 2D islands on the liquid–solid interface or at the TPL (at low supersaturations) or their regular crystallization (at high supersaturations). Here, we briefly discuss theoretical understanding and modeling methods for these processes achieved to this end.

6.1 Transport-Limited Nanowire Growth

Models based on the mass transport equations do not consider 2D nucleation and hence are relevant in the case of Au-catalyzed VLS growth of III–V NWs under group V rich conditions, self-induced growth of GaN NWs, or true SAE growth of III–V NWs. The axial NW growth rate in this case is limited by the mass transport of group III atoms into the droplet according to Eq. (3.3). Similar models can also be used for NWs of elemental semiconductors. The main problem is in finding the diffusion-induced contribution to the axial NW growth rate, given by

$$\left(\frac{dL}{dt}\right)_{diff} = -\frac{2\Omega_S}{R} D_f \left.\frac{dn_f}{dz}\right|_{z=L}. \tag{6.1}$$

Here, subscript "f" is introduced instead of "3" in order to distinguish group III adatoms on the NW sidewalls ("f") or on the substrate surface ("s").

Diffusion-limited growth of NWs was considered in many original papers and reviews, for example, in Refs. [2, 6, 7, 11, 65, 77–81]. The most general result is given by [78]

$$\frac{1}{V_3}\left(\frac{dL}{dt}\right)_{diff} = \frac{BU(L/\lambda_f) + C}{U'(L/\lambda_f)}, \tag{6.2}$$

where $V_3 \equiv I_3 \Omega_S \cos\alpha_3$ is the 2D equivalent growth rate in MBE, α_3 is the angle of the group III beam to the vertical, and λ_f is the diffusion length of group III adatoms on the NW sidewalls. The functions U and U' are defined as follows

$$U(L/\lambda_f) = \sinh\left(\frac{L}{\lambda_f}\right) + Q\delta\left(\frac{R}{\lambda_s}\right)\left[\cosh\left(\frac{L}{\lambda_f}\right) - 1\right], \tag{6.3}$$

$$U'(L/\lambda_f) \equiv \frac{dU}{d(L/\lambda_f)} = \cosh\left(\frac{L}{\lambda_f}\right) + Q\delta\left(\frac{R}{\lambda_s}\right)\sinh\left(\frac{L}{\lambda_f}\right). \tag{6.4}$$

Here, $\delta(R/\lambda_s) = K_1(R/\lambda_s)/K_0(R/\lambda_s)$, with $K_m(x)$ the modified Bessel functions of order m, R the radius of the NW top, and λ_s the diffusion length of group III adatoms on the substrate surface. The kinetic coefficients B and C stand for the diffusion fluxes into the droplet which originate from the NW sidewalls and the substrate, respectively

$$B = \frac{2\lambda_f \tan\alpha_3}{\pi R}(1-\varepsilon_f),\ C = \frac{2\lambda_s}{R}\delta\left(\frac{R}{\lambda_s}\right)(1-\varepsilon_s) \tag{6.5}$$

The parameters ε_f and ε_s describe the differences between chemical potentials of group III atoms on the two surfaces and in liquid, similarly to Eq. (5.6):

$$\varepsilon_f = \exp\left(-\frac{\Delta\mu_{fl}}{k_B T}\right),\ \varepsilon_s = \exp\left(-\frac{\Delta\mu_{sl}}{k_B T}\right). \tag{6.6}$$

Here, $\Delta\mu_{fl} = \mu_f - \mu_3^L$, $\Delta\mu_{sl} = \mu_s - \mu_3^L$ are the chemical potential differences for group III atoms on the surfaces (μ_f on the NW sidewalls and μ_s on the substrate) and in the liquid phase (μ_3^L). The coefficient Q in Eqs. (6.3) and (6.4) is given by

$$Q = \frac{\lambda_s}{\lambda_f}\frac{\varepsilon_s}{\varepsilon_f}\frac{\pi}{\tan\alpha_3}, \tag{6.7}$$

and does not contain the chemical potential in the liquid.

The total group III limited axial NW growth rate is obtained by summing up Eq. (6.2) with the flux originating from the direct impingement from vapor. If NWs grow on unpatterned substrates, we should subtract the 2D growth rate of the parasitic layer between the NWs. Without desorption, all group III atoms deposited from vapor should be distributed in the parasitic layer and NWs. Then the final result for the axial growth rate takes the form [77]

$$\frac{1}{V_3}\frac{dL}{dt} = \left(A + \frac{BU(L/\lambda_f)+C}{U'(L/\lambda_f)}\right)\left(1+\frac{R^2}{S_{NW}}\right) - 1, \tag{6.8}$$

with S_{NW} the mean substrate area per NW (the reverse of the NW surface density). The vapor flux in the MBE case is given by

$$A = \frac{\chi_3(\alpha_3,\beta)}{\cos\alpha_3}, \tag{6.9}$$

where the geometrical function $\chi_3(\alpha_3,\pi/2) = (1+\cos\alpha_3)/2$ at $\beta = \pi/2$, $\chi_3 = 1/\sin^2\beta$ when $\beta \geq \alpha_3 + \pi/2$, and has a more complex form for intermediate contact angles β [38]. Thus, the transport-limited elongation rate generally contains four unknown parameters: the two adatom diffusion lengths on the substrate surface and

the NW sidewalls (λ_s and λ_f), and the two chemical potential differences between the surface and sidewall adatoms and group III atoms in liquid ($\Delta\mu_{sl}$ and $\Delta\mu_{fl}$).

The transport-limited growth model given by Eq. (6.8) was used for modeling the growth kinetics of a single $InP_{1-x}As_x$ NW with modulated composition in Ref. [77]. The NWs were grown at 420 °C by the Au-catalyzed MBE on InP (111)B substrates. These growth conditions produced NWs of WZ structure which grow in the [0001] direction without stacking faults, with a uniform diameter. A periodic modulation of the incident As_4:P_2 flux ratio was achieved by using the non-uniformity of the fluxes on the substrate area. The $InP_{1-x}As_x$ NWs were removed from their substrate and imaged by high angle annular dark-field scanning TEM (HAADF STEM). The image of a NW segment of 45 nm diameter is presented in Fig. 13. The modulation of the HAADF intensity profile integrated over the whole diameter is superimposed [Fig. 13a]. The FFT-filtered HAADF image with the corresponding intensity profile is shown in Fig. 13b. The oscillation amplitude is about 0.7% of the total HAADF intensity. The corresponding variation Δx of the As concentration x was determined to be about 0.03 around the mean value of 0.66. Such a small variation of composition is not expected to influence the NW elongation.

The distance between any two concentration extrema equals the increase of the NW length during one time period. Therefore, it is straightforward to determine the instantaneous growth rate at each oscillation. This procedure was applied to a 21 nm diameter NW. The dependence with time of the NW length counted from the cleaved end is shown in Fig. 14. The measured NW length clearly displays a non-linear behavior with time. In this growth experiment, the flux modulation was stopped

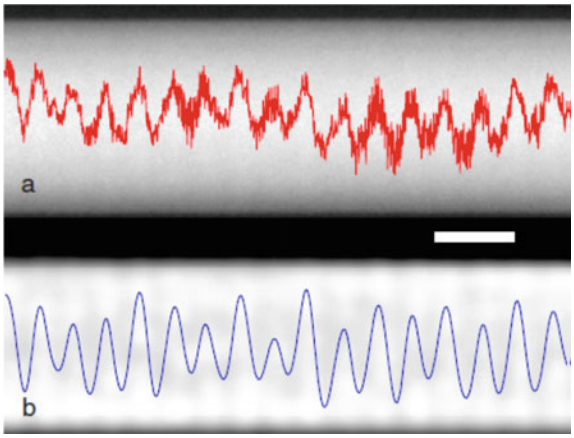

Fig. 13 **a** HAADF STEM image of an $InP_{1-x}As_x$ NW segment grown with a modulated As_4:P_2 flux ratio. Scale bar represents 20 nm. The HAADF signal is integrated over the whole diameter and the profile is plotted along the growth axis. **b** FFT-filtered HAADF image and corresponding profile. Reprinted with permission from J. C. Harmand, F. Glas and G. Patriarche, Physical Review B **81**, 235,436 (2010), https://doi.org/10.1103/PhysRevB.81.235436. Copyright (2010) by the American Physical Society

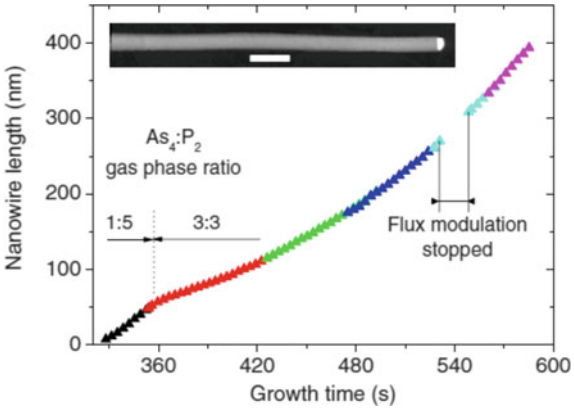

Fig. 14 Growth chronology of a single $InP_{1-x}As_x$ NW. The length of the NW shown in the inset (scale bar is 50 nm), is plotted as a function of time, as deduced from the composition oscillations along its axis. The different colors correspond to overlapping HAADF images. During growth, the flux modulation was stopped for 12 time periods. The corresponding region serves as a time reference. At 355 s, the nominal As_4:P_2 flux ratio was changed abruptly from 1:5 to 3:3. Reprinted with permission from J. C. Harmand, F. Glas and G. Patriarche, Physical Review B **81**, 235,436 (2010), https://doi.org/10.1103/PhysRevB.81.235436. Copyright (2010) by the American Physical Society

for 12 time periods. The corresponding region without compositional modulation, indicated in Fig. 14, may serve as a time reference. At some point during growth, the nominal As_4:P_2 ratio was changed abruptly from 1:5 to 3:3, while the total average group V flux was kept constant. Thanks to the former time reference, this event can be accurately dated, as shown in Fig. 14. The impact of this large change of flux ratio is strong and immediate—as seen from the change of the slope in Fig. 14, the growth rate was suddenly reduced by a factor of 2.

The obtained length-time dependence was fitted by Eq. (6.8). The value of λ_f has little influence on the results, provided that it is larger than the final NW length. Therefore, it was chosen to be 2 μm. Concerning λ_s, it was found that very small values (a few nm) are necessary to fit the experiment. The best fit is obtained with $\lambda_s = 2$ nm. This very short length can be understood as a limitation of adatom diffusion by atomic steps of the rough parasitic layer. The abrupt change of As_4:P_2 flux ratio is expected to modify significantly the composition and chemical potential of the catalyst droplet. Accordingly, two sets of chemical potential differences were adjusted, valid before and after this change. The best fit for the first part of growth at As_4:P_2 flux ratio of 1:5 was obtained with $\Delta\mu_{fl} = 270$ meV and $\Delta\mu_{sl} = 18.2$ meV. The contribution from the substrate surface is very small due to the combination of low λ_s and moderate $\Delta\mu_{sl}$. Very quickly, the contribution from the sidewalls dominates largely. After the change of As_4:P_2 flux ratio to 3:3, $\Delta\mu_{fl}$ must be reduced to 160 meV, which indicates that the flow from the sidewalls to the droplet is less efficient when P_2 is replaced by As_4. At the same time, $\Delta\mu_{sl}$ takes a negative value of −145 meV, showing that a significant part of the atoms intercepted by the NW

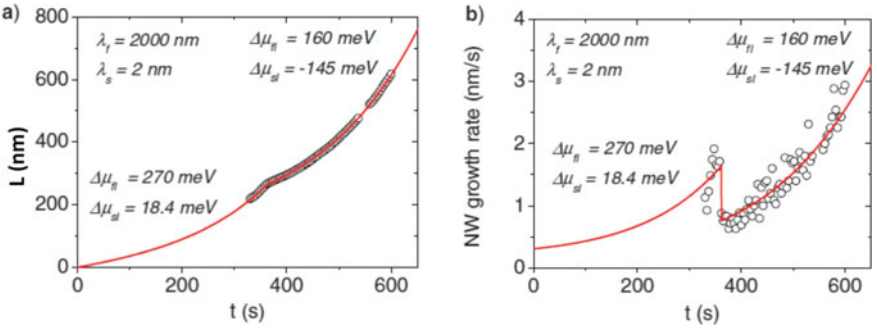

Fig. 15 **a** Experimental NW elongation and **b** axial growth rate (circles), fitted with the diffusion transport model with the four parameters shown in the legends. Different chemical potentials are used for each As_4:P_2 ratio, before and after $t = 355$ s. Reprinted figure with permission from J. C. Harmand, F. Glas and G. Patriarche, Physical Review B **81**, 235,436 (2010), https://doi.org/10.1103/PhysRevB.81.235436. Copyright (2010) by the American Physical Society

now migrates to the substrate surface. With these parameters, the diffusion transport model describes fairly well the experimental $L(t)$ dependence, as shown in Fig. 15. For both As_4:P_2 flux ratios, NW length increases almost exponentially with time, because the diffusion-induced contribution is proportional to the length at $\lambda_f >> L$.

As regards the length–radius dependencies of different semiconductor NWs, they were measured and modeled by many authors (see Refs. [6] and [7] for a detailed review). The diffusion transport into the droplet given by the general Eq. (6.2) can be reduced to the inverse power-law dependence on the NW radius and becomes independent of length in some important particular cases (see Ref. [7] for a systematization of such growth modes). For thin NWs, the chemical potential of group III atoms in the catalyst droplet can be elevated by the Gibbs–Thomson effect due to the curvature of the droplet surface according to [65, 82]

$$\mu_3^{eff} = \mu_3^L + \frac{2\gamma_{LV}\tilde{\Omega}_L \sin\beta}{R}. \tag{6.10}$$

Here, $\tilde{\Omega}_L$ is the elementary volume per group III atom in the liquid phase and $R_d = R/\sin\beta$ is the droplet radius, with R as the radius of the NW top. We can then obtain the growth equation which describes surface diffusion of adatoms to the NW top and the Gibbs-Thomson effect in the form

$$\frac{1}{V_3}\frac{dL}{dt} = A_* + \left(\frac{\Lambda_3}{R}\right)^p \left(1 - be^{R_{GT}/R}\right). \tag{6.11}$$

Here, A_* stands for the vapor flux and accounts for possible growth on the substrate surface. $b = \exp[(\mu_3^L - \mu_a)/k_BT]$ is a radius-independent constant (with index "a" corresponding to sidewall or surface adatoms), Λ_3 is the effective diffusion length of group III adatoms and p is the growth index which typically ranges from ½ to 2.

For example, $p = 1$ corresponds to the collection of group III atoms from the top part of the NW as discussed above, and $p = 2$ to the collection from the substrate surface. The characteristic Gibbs–Thomson radius is given by

$$R_{GT} = \frac{2\tilde{\Omega}_L \gamma_{LV} \sin\beta}{k_B T}, \tag{6.12}$$

and equals a few nanometers in the typical cases [65].

Integration of Eq. (6.11) at a time-independent NW radius gives

$$L = H\left[A_* + \left(\frac{\Lambda_3}{R}\right)^p \left(1 - be^{R_{GT}/R}\right)\right], \tag{6.13}$$

with $H = V_3 t$ the effective deposition thickness. This simplified expression shows that the length decreases with increasing radius for thick enough NWs where the Gibbs–Thomson effect becomes negligible, while for thin NW the growth rate tends to zero at a certain minimum droplet size. NWs cannot be grown thinner than this minimum size due to the Gibbs–Thomson effect [65, 82]. Therefore, the length–radius correlation is generally composed of an increasing part for thin NWs, then reaching a maximum and further decreasing toward larger R in the pure diffusion-controlled regime [65]. The probability to observe non-monotonic length–radius correlation increases for smaller radii and larger μ_3^L, while the length of thicker NWs decreases inversely proportional to R^p. Figures 16 and 17 present the examples of the inverse $L(R)$ correlations with $p = 1$ and 2, where the influence of the Gibbs–Thomson effect is not visible.

6.2 *Chemical Potentials for the VLS Growth of III–V Nanowires*

Chemical potentials of group III and V atoms in a ternary Au–III–V liquid are given by

$$\begin{aligned}
\mu_3^L &= \mu_3^{PL} + k_B T \ln c_3 + \omega_{35} c_5^2 + \omega_{3Au}(1 - c_3 - c_5)^2 \\
&\quad + (\omega_{35} + \omega_{3Au} - \omega_{5Au}) c_5 (1 - c_3 - c_5) + \ldots \\
\mu_5^L &= \mu_5^{PL} + k_B T \ln c_5 + \omega_{35} c_3^2 + \omega_{5Au}(1 - c_3 - c_5)^2 \\
&\quad + (\omega_{35} + \omega_{5Au} - \omega_{3Au}) c_3 (1 - c_3 - c_5) + \ldots,
\end{aligned} \tag{6.14}$$

Here, the μ_X^{PL} are the temperature-dependent chemical potentials of pure liquids and ω_{XY} are the binary interaction parameters between X and Y atoms accounting for deviations from ideality, for $X, Y = 3, 5$ and Au. The written terms with composition-independent interaction constants correspond to the regular solution model. In the so-called sub-regular solution model, ω_{XY} are allowed to depend on concentrations, as

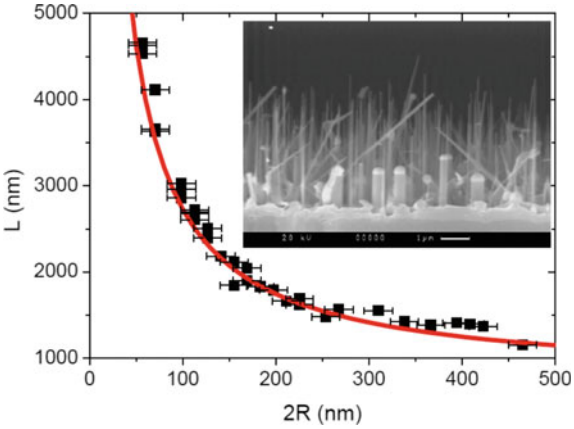

Fig. 16 Length-diameter correlation of Au-catalyzed WZ GaAs NWs grown by MBE on a GaAs(111)B substrate at 585 °C, with Ga flux corresponding to 1 ML/s, and GaAs deposition thickness of 1000 nm (symbols). The insert shows a typical SEM image. The line shows the fit by $L = H(A_* + \Lambda_3/R)$, with $A_* = 0.75$ and $\Lambda_3 = 100$ nm. Reprinted figure with permission from V. G. Dubrovskii, G. E. Cirlin, L. P. Soshnikov, A. A. Tonkikh, N. V. Sibirev, Yu. B Samsonenko and V. M. Ustinov, Physical Review B **71**, 205,325 (2005), https://doi.org/10.1103/PhysRevB.71.205325. Copyright (2005) by the American Physical Society

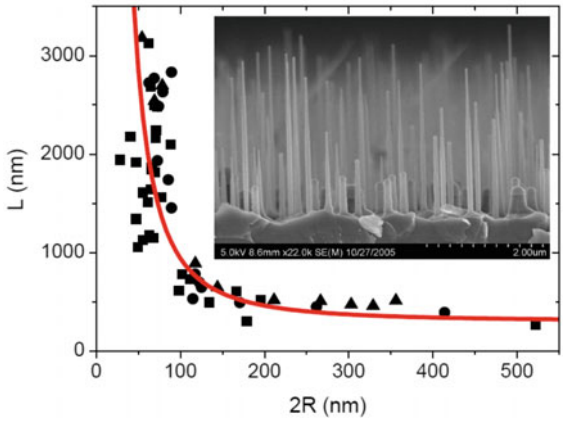

Fig. 17 Length-diameter correlation of Au-catalyzed WZ GaAs NWs grown by MBE on a GaAs(111)B substrate at 560 °C, with Ga flux corresponding to 1 ML/s, and GaAs deposition thickness of 1000 nm (squares, dots, and triangles correspond to different parts of the same sample). The insert shows a typical SEM image. The line shows the fit by $L = H(A_* + \Lambda_3^2/R^2)$, with $A_* = 0.3$ and $\Lambda_3 = 40$ nm. Reprinted from Surface Science, vol. 601, V. G. Dubrovskii, N. V. Sibirev, R. A. Suris, G. E. Cirlin, J. C. Harmand and V. M. Ustinov, Diffusion controlled growth of semiconductor nanowires: vapor pressure versus high vacuum deposition, pp. 4395–4401, Copyright (2007), with permission from Elsevier

in Refs. [14] or [84]. In Ref. [14], the ω_{XY} were calculated according to Stringfellow [85]. Johansson et al. [84] took the ω_{XY} in the form $\omega_{XY} = \omega^0_{XY} + \omega^1_{XY}(c_X - c_Y)$, where ω^0_{XY} and ω^1_{XY} denote the zero-order and first-order binary interaction parameters, respectively. Higher order terms include ternary interactions, described by the (composition-independent) ternary interaction parameter ω_{35Au}(more parameters appear if ternary interactions are considered in a quaternary liquid during the Au-catalyzed growth of ternary III–V NWs [84]). To compute the chemical potential difference with respect to the solid state as given by Eq. (3.7), one needs to know the interaction parameters and the temperature-dependent $\mu_3^{PL}(T)$, $\mu_5^{PL}(T)$, and $\mu_{35}(T)$. The latter values are usually referred to the standard reference states of pure elements at temperature $T_0 = 298.15$ K. The reader may refer to Refs. [14, 40, 84] for the parameters of different material systems.

Due to a low solubility of As and P atoms in liquid, their concentrations should be a few percent at most, and undetectable by compositional measurements. Conversely, group III atoms may take a significant fraction of the liquid. Figures 18 and 19 present chemical potentials $\Delta\mu$ for Au-catalyzed GaAs NWs calculated by Glas in Ref. [14]. Figure 18 shows chemical potential as a function of atomic concentration of As $c_5 = c_{As}$ between 0.001 and 0.06 at three different temperatures within the typical growth domain, and for three different Ga concentrations $c_3 = c_{Ga}$ of 0.2 0.35 and 0.7. Figure 19 shows chemical potential as a function of c_{Ga}, for three different $c_{As} = 0.005, 0.02$, and 0.05, and at two different temperatures. It is seen $\Delta\mu_{LS}$ is most sensitive to the group V concentration when the latter is less than ~0.01, whereas the variations with group III concentrations are more uniform. $\Delta\mu$ increases with group III and group V concentrations in the range considered. However, this property is not critical and some calculations show that chemical potential may decrease with

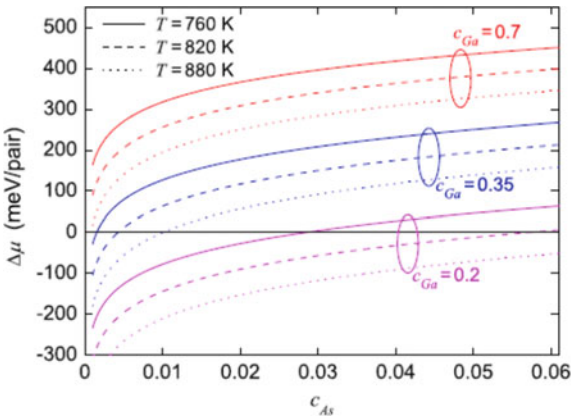

Fig. 18 Variation with the atomic concentration of As of the difference of chemical potential per Ga–As pair between a ternary Au-Ga–As liquid and solid ZB GaAs, calculated for a set of temperatures and Ga concentrations. Reprinted from F. Glas, Chemical potentials for Au-assisted vapor–liquid–solid growth of III–V nanowires, Journal of Applied Physics **108**, 073,506 (2010), with the permission of AIP Publishing

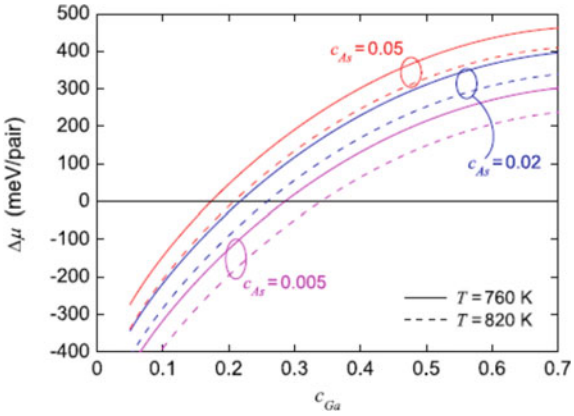

Fig. 19 Variation with the atomic concentration of Ga of the difference of chemical potential per Ga–As pair between a ternary Ga–As–Au liquid and solid ZB GaAs, calculated for a set of temperatures and As concentrations. Reprinted from F. Glas, Chemical potentials for Au-assisted vapor–liquid–solid growth of III–V nanowires, Journal of Applied Physics **108**, 073,506 (2010), with the permission of AIP Publishing

c_3 in group III rich regions [54]. At fixed concentrations, $\Delta\mu$ always decreases with increasing temperature. These trends remain the same for other Au–III–V systems such as Au–In–As, Au–In–P, and Au–Ga–P [14]. For WZ III–V NWs, all the curves will be shifted down by a constant value $\psi = \mu_{35}^{WZ} - \mu_{35}^{ZB}$ ($\psi = 24$ meV per pair for GaAs [7]).

6.3 Nucleation and Growth of 2D Islands

Figure 20 illustrates the VLS growth model for Au-catalyzed III–V NWs in the case of TPL nucleation. Let us first consider the change of the surface energy upon island nucleation, assumed for the moment to be instantaneous. The edge of an island formed at the TPL comprises a solid–liquid interface with surface energy $(1 - x_{TPL})Ph\gamma_{SL}$ and a solid–vapor interface with surface energy $x_{TPL}Ph\gamma_{SV}$, where P is the island perimeter and x_{TPL} its fraction along the TPL [42]. The surface energy of the droplet changes by $-x_{TPL}Ph\gamma_{LV}\sin\beta$ due to elimination of its portion replaced by the ML edge (this results in an effective areal energy $\gamma_{eff} = \gamma_{SV} - \gamma_{LV}\sin\beta$ for that portion of the TPL located at the TPL [42]; see also Sect. 11.2) and by $\gamma_{\mathrm{LV}}\Delta\mathrm{S} = 2\gamma_{\mathrm{LV}}\sin\beta\Delta\mathrm{V}/\mathrm{R}$ due to the volume variation $\Delta\mathrm{V} = (\Omega_{\mathrm{S}} - \Omega_{\mathrm{L}})\mathrm{i}$ in the liquid–solid phase transition of i III–V pairs having the elementary volumes Ω_S and Ω_L in the solid and liquid phases, respectively [40, 42, 44]. This gives the additional Gibbs–Thomson term $2\gamma_{LV}\sin\beta(\Omega_S - \Omega_L)i/R$ (which is positive when $\Omega_S > \Omega_L$, as in the Au-Ga–As system [44]), proportional to the island size i (which is why it modifies the chemical potential). The total surface energy change thus equals [44]

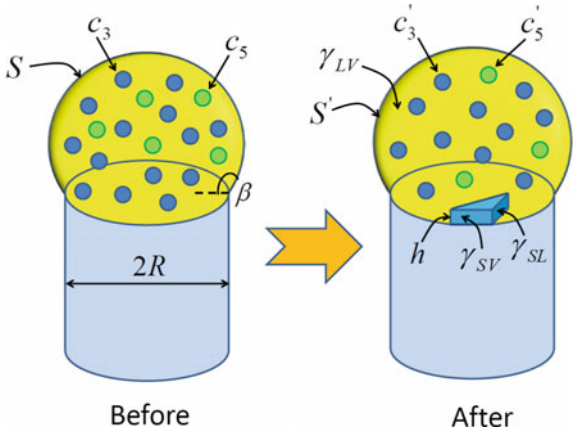

Fig. 20 III–V VLS system with an Au–III–V droplet having the atomic concentrations c_3 of group III and c_5 of group V atoms before nucleation, decreasing to c_3' and c_5', respectively, after nucleation of a 2D island at the TPL. For highly volatile As or P species, the group V concentration is always much lower than the group III one. The island of height h consists of i III–V pairs. The contact angle of the droplet with respect to the horizontal equals β. The droplet base radius equals the NW radius R. The surface energies of interest are those of the liquid–vapor interface (γ_{LV}), solid–vapor lateral interface for one-third of the island perimeter (γ_{SV}) and solid–liquid lateral interface for two-thirds of the island perimeter (γ_{SL}) [86, 87]. Reprinted with permission from V. G. Dubrovskii, Refinement of nucleation theory for vapor–liquid–solid nanowires, Crystal Growth & Design **17**, 2589–2593 (2017). Copyright (2017) American Chemical Society

$$\Delta G_{surf} = [(1 - x_{TPL})\gamma_{SL} + x_{TPL}(\gamma_{SV} - \gamma_{LV}\sin\beta)]Ph + \frac{2\gamma_{LV}\sin\beta}{R}(\Omega_S - \Omega_L)i. \tag{6.15}$$

For $x_{TPL} = 1$, $P = 2\pi R$ and $i = \pi R^2 h/\Omega_s$, this yields the exact result for the complete ML slice in the non-wetting growth mode (where the droplet sits entirely above the ML), namely, $\Delta G_{surf} = [\gamma_{SV} - (\Omega_L/\Omega_S)\gamma_{LV}\sin\beta]2\pi Rh$ (Ref. [6]). Note that x_{TPL} generally changes during the island growth, which is considered in the generalized expression for the surface energy of Ref. [86]. In any case, the last, Gibbs–Thomson term in Eq. (6.15) is proportional to the difference between elementary volumes in the solid and liquid phase $\Omega_S - \Omega_L$ and becomes negligible when $\Omega_S \cong \Omega_L$, as in the case of GaAs NWs [40, 44].

Let us now include the volume energy change upon island formation [86]. For the fast growth stage of island that occurs before refill, let j_0 be the initial number of As atoms in the droplet, j_{eq} the number of As atoms corresponding to its equilibrium concentration with the solid phase, and i the number of As atoms (or GaAs pairs) in the single island growing in the mononuclear growth regime. In the closed system, the number of group V (As) atoms remaining in the droplet simply equals $j = j_0 - i$. The concentration of As atoms in the droplet is $c = (j_0 - i)/j_{tot}$, where $j_{tot} \cong const$ is the total number of all atoms in the droplet, hence $c/c_{eq} = j/j_{eq}$. We introduce

the dimensionless free energy of forming an island (formation energy for brevity) consisting of i III–V pairs (size for brevity), $F(i) = \Delta G(i)/k_B T$. According to the general result [86], its derivative with respect to size is given by

$$\frac{\partial F(i)}{\partial i} = -\left[\mu(j_0 - i) - \mu_{eq}\right] + \frac{\partial \Gamma(i)}{\partial i}. \tag{6.16}$$

Here, $\mu(j_0 - i)$ is the chemical potential (in thermal units) of a III–V pair in a droplet containing $j_0 - i$ As atoms, μ_{eq} the equilibrium chemical potential, and $\Gamma(i) = \Delta G_{surf}/k_B T$ the island surface energy (with the Gibbs–Thomson term now removed from ΔG_{surf}) which scales as $i^{1/2}$ for small enough islands and in any case does not grow faster than $i^{1/2}$ [86]. The stopping size introduced in Ref. [87] corresponds to the minimum of the formation energy [86], while the critical size of CNT (which is of course smaller) is determined by its maximum. After reaching the stopping size, the island cannot continue growing from liquid; its further extension requires refill from vapor (for wurtzite GaAs NWs) or developing an interface truncation (for zincblende GaAs NWs), as described in Sect. 4 [86].

Let us derive Eq. (6.16) directly in the specific case of self-catalyzed GaAs NWs growing from a binary Ga–As liquid alloy droplet, in which the chemical potentials depend on a single concentration, for instance that of As. Then, the initial state of the liquid consists of j_0 As atoms (labeled "5"), with chemical potential $\mu_5(c_5)$, and $j_{tot} - j_0$ Ga atoms (labeled "3"), with chemical potential $\mu_3(c_5)$. Here, j_{tot} is the total number of atoms in liquid before nucleation and $c_5 = j_0/j_{tot}$ is the initial As concentration in liquid. The final state after nucleation and formation of a fractional ML consists of $j_0 - i$ As atoms in liquid, with chemical potential $\mu_5(c_5^{'})$, $j_{tot} - j_0 - i$ Ga atoms in liquid, with chemical potential $\mu_3(c_5^{'})$, and i GaAs pairs in solid, with chemical potential μ_{eq}. The As and Ga concentrations in the final state are $c_5^{'} = (j_0 - i)/(j_{tot} - 2i)$, and $c_3^{'} = (j_{tot} - j_0 - i)/(j_{tot} - 2i)$, respectively, with $j_{tot} - 2i$ the total number of atoms remaining in liquid after removing i GaAs pairs. The free energy change upon forming the island of size i therefore equals

$$\begin{aligned} F(i) = &- i\left[\mu_3\left(c_5^{'}\right) + \mu_5\left(c_5^{'}\right) - \mu_{eq}\right] + \Gamma(i) \\ &+ j_0\left[\mu_5\left(c_5^{'}\right) - \mu_5(c_5)\right] + (j_{tot} - j_0)\left[\mu_3\left(c_5^{'}\right) - \mu_3(c_5)\right]. \end{aligned} \tag{6.17}$$

Differentiating this with respect to i, we get

$$\begin{aligned} \frac{\partial F(i)}{\partial i} = &- \left[\mu_3\left(c_5^{'}\right) + \mu_5\left(c_5^{'}\right) - \mu_{eq}\right] + \frac{\partial \Gamma(i)}{\partial i} \\ &+ \left[(j_{tot} - j_0 - i)\frac{\partial \mu_3}{\partial c_5^{'}} + (j_0 - i)\frac{\partial \mu_5}{\partial c_5^{'}}\right]\frac{\partial c_5^{'}}{\partial i}. \end{aligned} \tag{6.18}$$

The first term in the right-hand side of Eq. (6.18) is indeed the same as in Eq. (6.16). The second bracket in Eq. (6.18) equals zero regardless of the specific form of chemical potentials. This is a consequence of the equality $d\mu_3 = -(c_5^{'}/c_3^{'})d\mu_5$ following from the Gibbs–Duhem equation for a binary system [86]. Using the

expressions of $c_5^{'}$ and $c_3^{'}$, we get $d\mu_3 = -[(j_0 - i)/(j_{tot} - j_0 - i)]d\mu_5$ and hence the second bracket term cancels. It can be shown that this result remains valid in the more general case of metal (Au)-catalyzed VLS growth of III–V NWs [86].

We now recall that the chemical potential of a III–V pair in the droplet is well approximated by a logarithmic function of the group V concentration (due to the low value of this concentration) [86], therefore

$$\mu_3(c_5') + \mu_5(c_5') - \mu_{eq} = \ln[(j_0 - i)/j_{eq}], \tag{6.19}$$

(this also holds for Au-catalyzed VLS growth, but then j_{eq} depends also on the Ga concentration). As recalled above, the stopping size i_s corresponds to the minimum of the formation energy [86, 87]. Neglecting the variation of edge energy Γ(which is a good approximation if i_s is much larger than the critical size of CNT and smaller than a full ML [86]), it simply equals

$$i_s = j_0 - j_{eq}. \tag{6.20}$$

This corrects the result of Ref. [87], obtained under unnecessarily restrictive assumptions.

Using Eqs. (6.18) and (6.19), the formation energy itself is obtained by integration:

$$F(i) = -\int_0^i du \ln\left(\frac{j_0 - u}{j_{eq}}\right) + \Gamma(i). \tag{6.21}$$

The result is

$$F(i) = -i \ln\left(\frac{j_0 - i}{j_{eq}}\right) + j_0 \ln\left(\frac{j_0 - i}{j_0}\right) + i + \Gamma(i). \tag{6.22}$$

This can be rewritten

$$F(i) = F_\infty(i) + (j_0 - i)\ln\left(1 - \frac{i}{j_0}\right) + i, \tag{6.23}$$

with

$$F_\infty(i) = -i \ln(j_0/j_{eq}) + \Gamma(i) \tag{6.24}$$

$F_\infty(i)$ is the CNT result for infinite systems (not affected by depletion), which is indeed recovered from Eq. (6.23) at $i/j_0 \to 0$. Equation (6.23) thus separates the CNT result $F_\infty(i)$ from a size-dependent correction which vanishes at $i/j_0 \to 0$.

Accounting for the refill from vapor and neglecting As desorption from liquid, the number of As atoms in the droplet by time t equals $j_0 - i + vt$, where v is the rate of refill and i the number of GaAs pairs in the island, as above. Note that between

nucleation and time *t,* the volume enclosed by the droplet surface (liquid and island) increases by $\Delta V = (vt - i)\Omega_L + i\Omega_S$

Using Eq. (6.22), and presenting the result in terms of the ML coverage $\theta = i/i_{ML}$ (with $i_{ML} = (3\sqrt{3}/2)R^2 h/\Omega_S$ the number of GaAs pairs in the complete ML and R the radius of the hexahedral NW), we obtain the normalized formation energy in the form

$$f = \frac{F}{i_{ML}} = (\theta - x)ln\left(\frac{\theta_0 - \theta + x}{\theta_{eq}}\right) + \theta_0 ln\left(1 - \frac{\theta - x}{\theta_0}\right) + \theta - x + \gamma(\theta) - x\left(\Delta\mu_{VS} - \frac{2\gamma_{LV}\Omega_S \sin\beta}{R}\right) \tag{6.25}$$

Here, $\theta_0 = j_0/i_{ML}$ is the initial As content at nucleation, $\theta_{eq} = j_{eq}/i_{ML}$ the equilibrium As content, $x = vt/i_{ML}$ the coverage equivalent to refill (which is proportional to time), $\Delta\mu_{VS}$ the chemical potential difference per Ga–As pair between vapor and solid, and $\gamma(\theta) = \Gamma(i)/i_{ML}$. In Ref. [86], we derived a representation of the ML edge energy from modeling in situ experiments [49], namely,

$$\gamma(\theta) = \alpha\left[A\theta^{1/2} + B(1-\theta)^{1/2} - B + (1 - A + B)\theta\right]. \tag{6.26}$$

with $\alpha = 4\gamma_{eff}\Omega_S/\left(\sqrt{3}k_B T R\right)$ and γ_{eff} the effective surface energy of the island edge defined earlier. Equation (6.26) correctly accounts for the non-monotonous variation of the edge energy with ML size and for leading terms $\sim i^{1/2}$ and $\sim(i_{ML} - i)^{1/2}$ at small and large sizes, respectively [86]. This functional form is expected to be general but coefficients A and B should vary with catalyst and contact angle (fits to in situ experiments on Au-catalyzed NWs [49] yield A = 3.3748 and B = 2.2993 [86]).

The NW ML is completed at $\theta = 1$ whereas the ML formation cycle ends at $x = 1$, after a full equivalent ML of GaAs is added to the droplet from vapor. Since $\partial F/\partial i = \partial f/\partial\theta$, the minimum of the formation energy obtained by differentiating Eq. (6.25) at given refill yields the size θ_s of the island as a function of time. The extrema of the formation energy are given by

$$-ln\left(\frac{\theta_0 - \theta + x}{\theta_{eq}}\right) + \alpha\frac{d\gamma}{d\theta} = 0. \tag{6.27}$$

At $\alpha \ll 1$, corresponding to large NW radius R and low values of γ_{eff}, the influence of the surface energy term on island size is negligible. In this case, this size equals $\theta_s = \theta_0 - \theta_{eq} + x$, which is reduced to $\theta_s = \theta_0 - \theta_{eq}$ for instantaneous growth from liquid. Figure 21a shows the behavior of $f + x(\Delta\mu_{VS} - 2\gamma_{LV}\Omega_S \sin\beta/R)$ as a function of θ at different x (and hence times) for a 20 nm radius GaAs NW, at a growth temperature of 610 °C, in the case of a low surface energy $\gamma_0 = 0.037$ J/m^2. For instance, values of θ_{eq}= 0.34 and $\theta_0 = 0.7$ yield the stopping size $\theta_s = 0.36$ in the absence of refill. Then, the minimum of the formation energy shifts to the right as

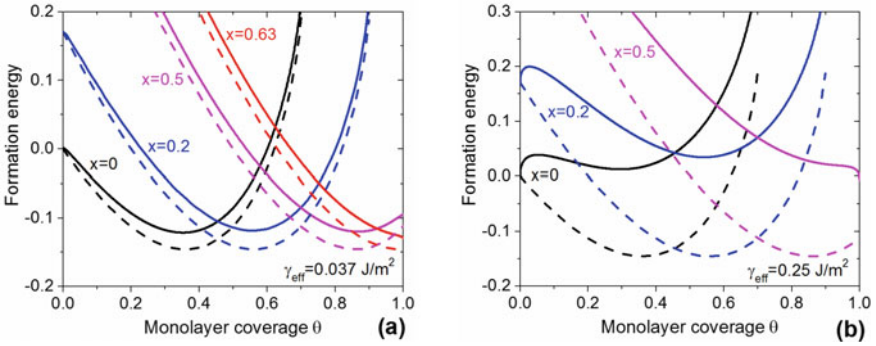

Fig. 21 **a** Normalized island formation energy $f + x(\Delta\mu_{VS} - 2\gamma_{LV}\Omega_S \sin\beta/R)$ versus θ for different initial As droplet contents x indicated near each curve (solid lines). The curves are obtained from Eqs. (6.25) and (6.26) for a GaAs NW with $R = 20$ nm, at $T = 610$ °C, $\theta_{eq} = 0.34$, $\theta_0 = 0.7$ at a low $\gamma_{eff} = 0.037$ J/m^2, corresponding to $\alpha = 0.01584$. Dotted lines show the volume part of the formation energy and correctly describe the stopping size in all cases. **b** Same as (**a**) at a high $\gamma_{eff} = 0.25$ J/m^2, corresponding to $\alpha = 0.1056$. A minimum of the formation energy is observed only at small x and disappears above $x = 0.5$, due to a decrease of the ML surface energy [86]. The volume part of the formation energy gives an incorrect behavior at large x

x increases. This describes the slow growth stage at the rate of refill. The minimum of the formation energy is well approximated by the volume part of the formation energy shown by the dashed lines, which indicates a negligible effect of the island surface energy. The situation changes at a high surface energy, *e.g.*, $\gamma_{eff} = 0.25$ J/m^2. According to Fig. 21b, the minimum of the formation energy then disappears for large enough x, meaning that fractional ML can grow even from equilibrium liquid. This effect is due to a decrease of the surface energy at high coverage, partly explained by a decrease of the island perimeter, which enables fast ML growth from undersaturated liquid [86]. These questions are investigated in detail in Ref. [86], where the present thermodynamic treatment is complemented by a kinetic model taking into account As desorption and a possible hindered incorporation to the growing ML.

The stopping effect does not change the NW axial growth rate given by Eq. (3.10), which still equals the nucleation rate times the available area for nucleation at the maximum chemical potential within the ML growth cycle. However, it may affect the oscillations of the truncated facet [47] and nucleation statistics in VLS NWs [88] which in turn influence some important properties such as the preferred crystal phase and length uniformity within the NW ensembles. One important conclusion is that the nucleation probability in VLS NWs exponentially decreases immediately after nucleation, which makes the next nucleation improbable until the droplet is refilled from vapor [88]. In III–V NWs, this nucleation "antibunching" is critically sensitive to the concentration of group V atoms in the catalyst droplet.

6.4 Self-Consistent Growth Models

The first fully self-consistent VLS growth model was developed by Glas et al. in Ref. [40] for Ga-catalyzed GaAs NWs grown by MBE. The NW growth rate given by the As input, desorption, and nucleation [stationary Eq. (3.1)] was solved numerically using Eq. (3.10) in the case of center nucleation. The Zeldovich nucleation rate was used given by Eq. (3.12). The model reproduces quantitatively all salient features of Ga-catalyzed VLS growth, namely, the variations of the axial NW growth rate with the As flux, temperature, and NW radius.

Figure 22a shows the calculated nucleation barrier $\Delta G_c = 3\sqrt{3}\Omega_S h\gamma_e^2/\Delta\mu$, chemical potential $\Delta\mu$, As concentration in the droplet c_{As}, and axial growth rate dL/dt as a function of As_4 BEP at a constant temperature of 610 °C. The As_4 BEP P_{As_4} was converted into the atomic As influx I_5 using the linear relationship

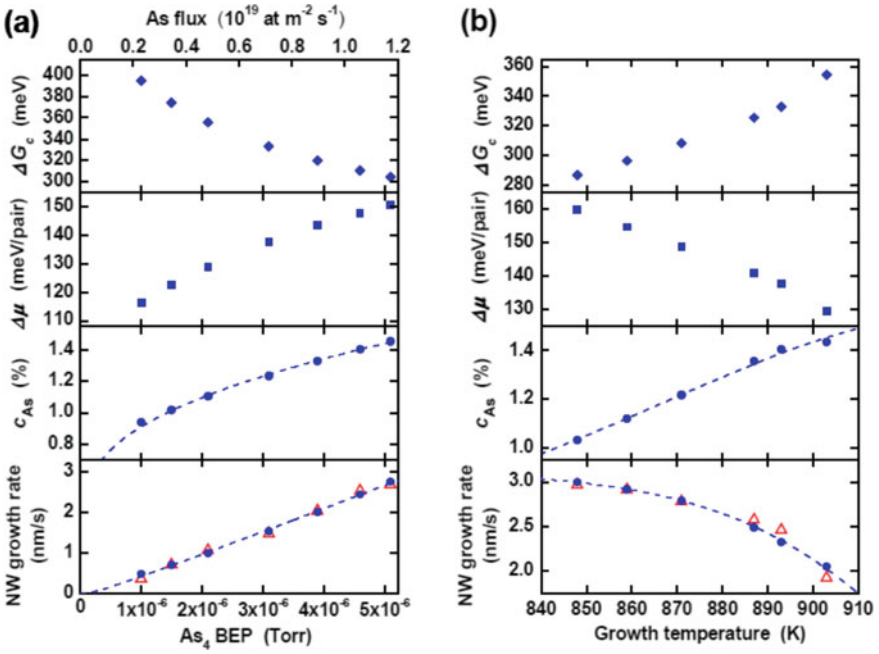

Fig. 22 **a** Bottom panel: growth rates measured (triangles) and calculated (disks) for NW1, as a function of incoming As flux, at temperature $T = 883$ K. Three upper panels: As concentration in the droplet, difference of chemical potential between liquid of composition c_{As} and solid ZB GaAs, and nucleation barrier, calculated for each discrete data point of bottom panel. In the two bottom panels, the dashed lines are calculations extended to the whole pressure range, made for NW1 using the best model parameters. The As flux is expressed as BEP (lower scale) and as absolute atomic flux (top scale). **b** Same as (**a**) for NW2, as a function of growth temperature. Reprinted figure with permission from F. Glas, M. R. Ramdani, G. Patriarche and J. C. Harmand, Physical Review B **88**, 195,304 (2013), https://doi.org/10.1103/PhysRevB.88.195304. Copyright (2013) by the American Physical Society

$I_5 = \nu P_{As_4}$, with $\nu = 2.3 \times 10^{24}$ atoms $\times$ m^{-2} $\times$ s^{-1} $\times$ Torr^{-1} for this MBE system [26]. Experimental data shown in the bottom panel were obtained for NW1 having a constant radius R of 32 nm, with $\beta \cong 125°$. Figure 22b shows the same quantities for NW2 grown under $P_{As_4} = 4.8 \times 10^{-6}$ Torr and different temperatures. For this NW, $R = 37$ nm and $\beta = 125°$. The crystal phase of both NWs was ZB. It is interesting to note that this contact angle is close to the one corresponding to vertical growth of ZB GaAs NWs in Fig. 9 (between 125° and 127°). The best fits to the data were obtained with the re-emission coefficient $\alpha_r = 3.25$ and temperature-independent J_0 and γ_{eff} given in Sect. 3.

According to these calculations, the As concentration increases almost linearly with the As flux and temperature, and varies only from ~0.01 to 0.015 in the experimental range. The chemical potential also does not vary much over the experimental range, remaining within the interval of 115–160 meV. These small variations result in an almost linear correlation of the axial growth rate with As flux, as observed earlier in Ref. [22]. The decrease of dL/dt with temperature is stronger than linear. The radius dependence of the axial growth rate will be discussed shortly.

In Ref. [41], an analytic approach was developed for the self-consistent description of Au-catalyzed and self-catalyzed VLS growth of III–V NWs, based on some earlier results [78]. Using the simplified diffusion flux of group III adatoms as given by Eq. (6.11), it is easy to obtain

$$\frac{dR}{dt} = \frac{\tilde{\Omega}_L}{\Omega_S f(\beta)}\left[\chi_3 v_3 + \left(\frac{\Lambda_3}{R}\right)^p \left(\phi_3 v_3 - \frac{h}{\tau_3} e^{\overline{\mu}_3^L}\right) - \frac{dL}{dt}\right], \tag{6.28}$$

$$\overline{\mu}_5 = \frac{1}{\nu} \ln\left(\frac{\chi_5 v_5 - dL/dt}{v_5^{des}}\right). \tag{6.29}$$

Equation (6.28) describes the time evolution of the NW radius (at a fixed contact angle β), with v_3 the deposition flux in nm/s and τ_3 the characteristic time constant for the reverse diffusion flux from the droplet to the NW sidewalls, which is proportional to $\exp(\overline{\mu}_3^L)$. Equation (6.29) gives the chemical potential of group V atoms in the droplet, for gaseous precursor incorporating ν As atoms, with v_5 the vapor flux including re-emitted species and v_5^{des} the pre-exponent in the desorption rate. The NW elongation rate in the mononuclear regime is given by Eq. (3.10), with the Zeldovich nucleation rate of CNT $J \propto \exp[-a^2/(4\Delta\overline{\mu})]$, as in Eq. (3.11).

Under certain assumptions, solution to the closed system of stationary Eqs. (6.28), (6.29) and (3.11) can be approximated by the following analytical formula for the growth rate

$$\frac{dL}{dt} = \frac{\nu \chi_5 v_5}{(1+\Delta)(1+G)}, \tag{6.30}$$

with

$$G = \frac{i_*}{W[(R/R_*)^2\eta(1+\Delta)]}, \tag{6.31}$$

$$\Delta = \frac{\nu\chi_5 v_5}{\chi_3 v_3 + (\Lambda_3/R)^p \phi_3 v_3} = \frac{\nu F_{53}}{1 + (\phi_3/\chi_3)(\Lambda_3/R)^p}, \tag{6.32}$$

Here, $W(y)$ is the Lambert function, such that $W\exp(W) = y$ and F_{53} stands for the effective V/III flux ratio, defined as $F_{53} = \chi_5 v_5/(\chi_3 v_3)$. The "nucleation" radius R_* is given by

$$R_* = \left(\frac{\nu\chi_5 v_5}{\pi h i_* J(\Delta\overline{\mu}_0)}\right)^{1/2} \tag{6.33}$$

with chemical potential $\Delta\overline{\mu}_0$ containing characteristics of the vapor phase and becoming radius-independent in many practical cases,

$$\Delta\mu_0 = \ln\left(\frac{\chi_3 v_3 + (\Lambda_3/R)^p \phi_3 v_3}{(\Lambda_3/R)^p (h/\tau_3)}\right) + \frac{1}{\nu}\ln\left(\frac{\chi_5 v_5}{v_5^{des}}\right) - \mu_{35}. \tag{6.34}$$

In Eq. (6.33), $i_* = i_c(\Delta\mu_0)$ denotes the critical size at this chemical potential.

The axial growth rate given by Eq. (6.30) is reduced to the transport-limited growth rate when $\Delta >> 1$ and $G << 1$, while at $G >> 1$ it yields the nucleation-limited growth rate. In some regimes, this model is further reduced to the result of Ref. [78], providing explicitly the NW length in the form.

$$L = H\left(\frac{\tilde{\Lambda}_3}{R}\right)^p W\left[\left(\frac{R}{R_n}\right)^{p+q}\right]. \tag{6.35}$$

Here, H is the deposition thickness, $\tilde{\Lambda}_3$ is the re-normalized diffusion length of group III adatoms, R_n is the re-normalized nucleation radius (which depends on the kinetics of group V species), and the index q equals 2 for the center and 1 for the TPL nucleation position.

Similarly to Eq. (6.30), Eq. (6.35) describes the diffusion-limited regime (for sufficiently thin NWs) at small R_n, transitioned to the nucleation-limited regime at large R_n. The $L(R)$ correlation transitions from non-monotonic to monotonically increasing, as shown in Fig. 23. The limitation of the axial growth rate at small R is explained, roughly, by a small facet area available for nucleation even without the Gibbs–Thomson effect. Figure 24 shows the example of non-monotonic length–radius curve for Au-catalyzed InP NWs grown by MOVPE at 470 °C [89]. The NW length first increases with R, then saturates at about 22 nm, and starts to slightly decrease after that. The fit obtained from Eq. (6.35) with $p = q = 2$, $H\Lambda^2 = 1340$ nm^3 and $R_* = 23$ nm provides a better fit than the Gibbs–Thomson curve [65], particularly for thinner NWs. More examples of different length–radius correlations

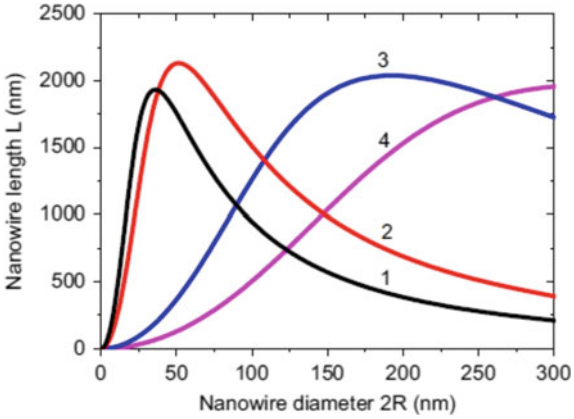

Fig. 23 Transition from non-monotonic to increasing length-diameter correlation with increasing nucleation radius R_n, obtained from Eq. (6.35) at $p = q = 2$: curve 1—$R_n = 14$ nm, $\tilde{\Lambda}_3 = 50$ nm; curve 2—$R_n = 40$ nm, $\tilde{\Lambda}_3 = 75$ nm; curve 3—$R_n = 75$ nm, $\tilde{\Lambda}_3 = 225$ nm; curve 4—$R_n = 125$ nm, $\tilde{\Lambda}_3 = 450$ nm. Reprinted from Journal of Crystal Growth, vol. 401, V. G. Dubrovskii and Yu. Yu. Hervieu, Diffusion-induced growth of nanowires: generalized boundary conditions and self-consistent kinetic equation, pp. 431–440, Copyright (2014), with permission from Elsevier

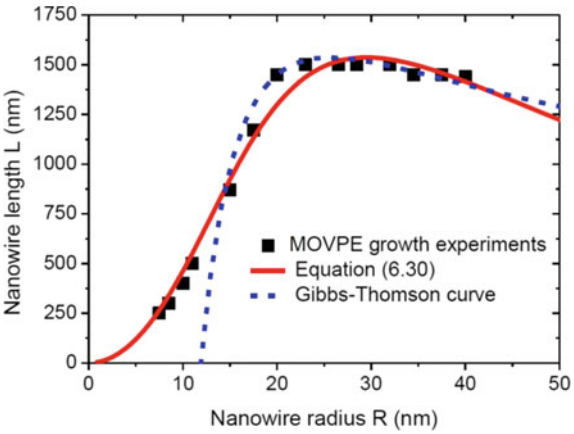

Fig. 24 Length–radius correlation of MOVPE-grown InP NWs [89], fitted by Eq. (6.35) (solid line) and by the Gibbs–Thomson curve [65] (dashed line). Reprinted from Journal of Crystal Growth, vol. 401, V. G. Dubrovskii and Yu. Yu. Hervieu, Diffusion-induced growth of nanowires: generalized boundary conditions and self-consistent kinetic equation, pp. 431–440, Copyright (2014), with permission from Elsevier

of III–V NWs, related to their crystal phase, fitted by a more general Eq. (6.30), can be found in Ref. [41]. It turns out that WZ GaAs NWs usually exhibit the transport-limited inverse length–radius correlations, while ZB GaAs NWs often show lengths

that increase with the radius, and in this sense become similar to the self-catalyzed case.

For self-catalyzed III–V NWs, the analytic approximation for the axial growth rate is given by [41]

$$\frac{dL}{dt} = \frac{\chi_5 v_5}{1+\delta}, \tag{6.36}$$

with

$$\delta = \frac{i_c}{\nu W[(R/R_*)^2]}. \tag{6.37}$$

The nucleation radius R_* is given by Eq. (6.33) but at the different, radius-independent chemical potential

$$\Delta\mu_0 = \mu_3(1) + \frac{1}{\nu}\ln\left(\frac{\chi_5 v_5}{v_5^{des}}\right) - \mu_{35}. \tag{6.38}$$

Here, the value of $\mu_3(1)$ now relates to pure Ga droplet and hence cannot regulate the overall diffusion flux of Ga adatoms.

Because of that, there is no steady-state solution to Eq. (6.28) for R and instead the NW top radius becomes time-dependent. When $\delta << 1$, Eq. (6.36) yields $dL/dt = \chi_5 v_5$, that is, the NW growth rate is simply proportional to the total As influx, including re-emitted flux. If we also assume $p = 1$ and $\phi_3 v_3 >> h\exp(\overline{\mu}_3)/\tau_3$, Eq. (6.28) yields the result of Ref. [25]

$$\frac{dR}{dt} = a + \frac{b}{R}, \tag{6.39}$$

with the coefficients

$$a = g(\chi_3 v_3 - \chi_5 v_5),\ \ b = g\phi_3 v_3 \Lambda_3. \tag{6.40}$$

Here, $g = \Omega_L/[\Omega_S f(\beta)]$ is the shape constant, which can be treated as time-independent at $\beta = const$. Integrating this with the initial condition $R(t = t_0) = R_0$, one obtains

$$t = t_0 + \frac{R - R_0}{a} + \frac{b}{a^2}\ln\left(\frac{R_0 + b/a}{R + b/a}\right). \tag{6.41}$$

Using $dL/dt = \chi_5 v_5$, the shape of Ga-catalyzed GaAs NWs can be put as

$$L = L_0 + \frac{F_{53}}{g(F_{53}-1)}\left[R_0 - R + R_s\ln\left(\frac{R_0 - R_s}{R - R_s}\right)\right]. \tag{6.42}$$

From Eqs. (6.39) and (6.40), we have

$$R_s = -\frac{b}{a} = \frac{\phi_3 \Lambda_3}{\chi_3 (F_{53} - 1)}. \tag{6.43}$$

Here, R denotes the NW top radius corresponding to its length L at a given moment of time, but can also be treated as the radius at a given position along the NW ("height") without subsequent VS radial growth on the sidewalls. The radius increases with time, or with the height when $a > 0$, corresponding to the case of positive Ga to As imbalance ($F_{53} < 1$ and $R_s < 0$). When $F_{53} > 1$, positive R_s gives the stable NW radius as will be discussed shortly.

Figure 25 shows the excellent correlation between the model given by Eqs. (6.36) and (6.37) and the numerical calculations of Glas et al. [40] for the growth rates of MBE-grown, Ga-catalyzed GaAs NWs versus the NW radius at two different temperatures. The calculations of Ref. [40] were performed under the assumption of a time-independent NW radius, for an As flux of 0.498 nm/s, a droplet contact angle of 125° and a re-emission coefficient of 3.1, yielding $\chi_5 v_5 = 3.04$ nm/s. The best fits by the analytic expressions yield a nucleation radius R_* of 20 nm at 610 °C and 27 nm at 640 °C. This should be due to a higher As desorption coefficient v_5^{des} which decreases the $\Delta\mu_0$ in Eq. (6.38) toward higher temperatures. While the fits by the analytic expressions are good, we note that they require very small values of the critical sizes (~2 GaAs pairs) where CNT reaches its limit.

In Ref. [90], the shapes of Ga-catalyzed GaP NWs grown at 600 °C by gas source MBE in patterned arrays on Si(111) substrates were analyzed as a function of V/III flux ratio. The shape of these NWs was not considerably affected by radial VS growth

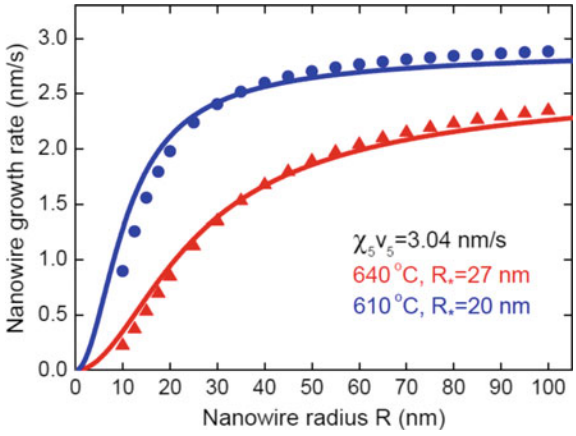

Fig. 25 Growth rate of Ga-catalyzed GaAs NWs grown by MBE versus the NW radius at two different temperatures. Numerical calculations of Ref. [40] (symbols) and fits by Eqs. (6.36) and (6.37) with the parameters listed in the insert [90]. Reprinted from Journal of Crystal Growth, vol. 440, V. G. Dubrovskii, Group V sensitive vapor–liquid–solid growth of Au-catalyzed and self-catalyzed III–V nanowires, pp. 62–68, Copyright (2016), with permission from Elsevier

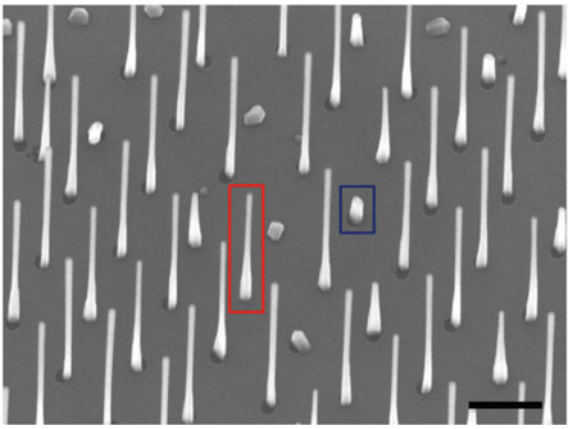

Fig. 26 30° tilted SEM image of an array of self-catalyzed GaP NWs for a V/III flux ratio of 4. Two types of NWs, with (red box) and without (blue box) Ga droplets are indicated. Scale bar is 440 nm. Reprinted from E. D. Leshchenko, P. Kuyanov, R. R. LaPierre and V. G. Dubrovskii, Tuning the morphology of self-assisted GaP nanowires. Nanotechnology **29**, 225,603 (2018); https://doi.org/10.1088/1361-6528/aab47b. © IOP Publishing. Reproduced with permission. All rights reserved

on the sidewalls. In particular, Fig. 26 shows an example of a NW array grown with a V/III flux ratio of 4, whose shape is tapered toward the top. For high V/III flux ratios, some shorter NWs were systematically observed without any droplets on top. Figure 27 shows the measured shapes of NWs for different V/III flux ratios changing from 1 to 6. It is seen that the NWs are reverse tapered for at V/III = 1, almost straight at V/III = 3, and tapered for V/III > 3, with the degree of tapering increasing for higher V/III. These results are fully consistent with the model presented above, and well fitted by Eqs. (6.41) and (6.42) with the parameters detailed in Ref. [90]. In particular, the stable radius R_s was found in the range 12–18 nm for the V/III flux ratios from 3 to 6.

7 Self-equilibration of the Radius of Self-catalyzed Nanowires

Equations (6.41) and (6.42) demonstrate that the radius distribution of self-catalyzed III–V NWs can be narrowed during growth to an almost delta-like shape due to the unusual self-focusing effect. This effect can be observed if the group V atomic flux into the droplet, including re-emitted species, is larger than that of group III ($F_{53} > 1$). A positive diffusion flux of group III atoms from the NW sidewalls contributes more to the increase of droplet volume for thinner NWs and less for thicker NWs. Therefore, larger droplets will grow and smaller droplets will shrink until the diffusion flux equalizes the positive group V to III imbalance. As a result,

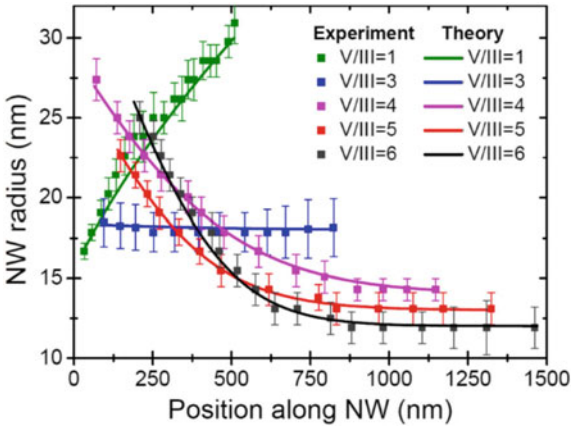

Fig. 27 Experimental (symbols) and theoretical (lines) morphologies of GaP NWs at a fixed pitch of 360 nm and different V/III flux ratios. Experimental morphologies correspond to a fixed growth time of 870 s under different V/III flux ratios after the initial growth step of 435 s at a fixed V/III = 2 to form the NW stems. The measured and calculated shapes correspond only to the upper NW parts, with the initial conditions $R_0(L_0)$ relating to the initial stems. Reprinted from E. D. Leshchenko, P. Kuyanov, R. R. LaPierre and V. G. Dubrovskii, Tuning the morphology of self-assisted GaP nanowires. Nanotechnology **29**, 225,603 (2018); https://doi.org/10.1088/1361-6528/aab47b. © IOP Publishing. Reproduced with permission. All rights reserved

the droplet volume will converge to a certain stationary one regardless of the initial size distribution of the growth seeds. For a fixed contact angle of the droplet, increase or decrease of the droplet volume leads to extending or diminishing the radius of the NW top. This was predicted theoretically in Ref. [25] and later in Ref. [34] and confirmed experimentally in Ref. [28] for Ga-catalyzed GaAs NWs.

These NWs were grown by MBE on Si(111) substrates through three steps: (i) patterning of a hole array in a thin SiO_2 layer, (ii) pre-deposition of Ga to form droplets in the etched holes, and (iii) growth of NWs at a temperature of 630 °C, As/Ga growth rate equivalent ratio of 1.8 and 2D equivalent growth rate of GaAs of 1 ML/s for 5 min. Figure 28 shows the SEM images obtained after steps (ii) and (iii) for an array of holes with a diameter of 60 nm and a pitch of 100 nm. It is seen that the Ga pre-deposition leads to the formation of Ga droplets in the oxide-free openings only, resulting in the growth of NWs at the position of the holes. While the diameter of the Ga droplets varies significantly from hole to hole (the droplet diameter distribution may depend on the droplet preparation process but is never uniform), a high degree of uniformity of the NW diameters is noticed.

This difference between the droplet size distribution and the NW diameter distribution was reproducible, whatever the initial size and the pitch between the holes in the array. For example, Fig. 29 compares the size distribution of the Ga droplets with the distribution of the NW diameters for an array with a hole size of 60 nm and a pitch of 250 nm. Again, the NWs in the array are quite uniform and the NW diameter distribution appears clearly much narrower than the hole size distribution.

Fig. 28 30° tilted SEM image of Ga droplets obtained after pre-deposition of Ga onto a hole array in a SiO_2 on Si(111) substrate. The diameter of the holes is 60 nm and the pitch between the holes is 100 nm. **b** and **c** show top view and 30° tilted SEM images of self-catalyzed GaAs NWs grown from the array of Ga droplets shown in (**a**). Scale bar corresponds to 100 nm. Reprinted with permission from V. G. Dubrovskii, T. Xu, A. Díaz Álvarez, G. Larrieu, S. R. Plissard, P. Caroff, F. Glas, B. Grandidier, Self-equilibration of the diameter of Ga-catalyzed GaAs nanowires, Nano Letters 15, 5580–5584 (2015). Copyright (2015) American Chemical Society

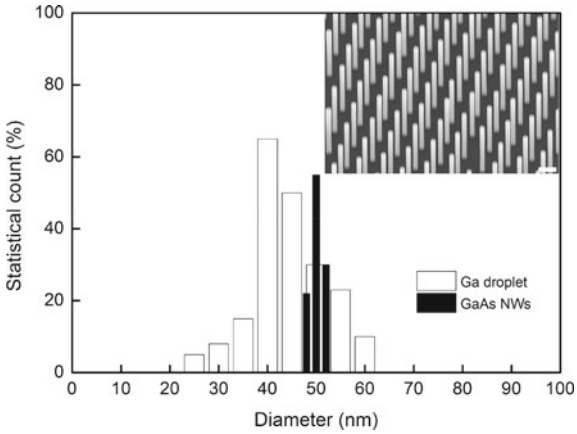

Fig. 29 Histograms of the Ga droplet size distribution and the NW diameter distribution. Inset: 30°tilted SEM images of the corresponding array of GaAs NWs with the hole size and pitch of 60 nm and 250 nm, respectively. Scale bar in the insert corresponds to 100 nm. Reprinted with permission from V. G. Dubrovskii, T. Xu, A. Díaz Álvarez, G. Larrieu, S. R. Plissard, P. Caroff, F. Glas, B. Grandidier, Self-equilibration of the diameter of Ga-catalyzed GaAs nanowires, Nano Letters **15**, 5580–5584 (2015). Copyright (2015) American Chemical Society

The Ga-catalyzed growth of NWs leads to a focusing effect towards a diameter of ~50 nm, slightly bigger than the peak value of the droplet size distribution, but still smaller than the hole size.

Figure 30 shows the time evolution of the NW diameters for the array shown in Fig. 29. These curves are obtained from Eq. (6.41) with a = -0.30 nm/s and b = 7.50 nm^2/s, corresponding to the stable radius R_s = 25 nm for the given MBE growth conditions. These curves can equivalently be presented in the form of $R(L)$ dependence using Eq. (6.42) with the known NW axial growth rate of 3.33 nm/s. It is seen that the initial inhomogeneity of the droplet diameters, ranging from 25 to 60 nm, converges to the size-uniform array of NW after only 5 min of MBE growth.

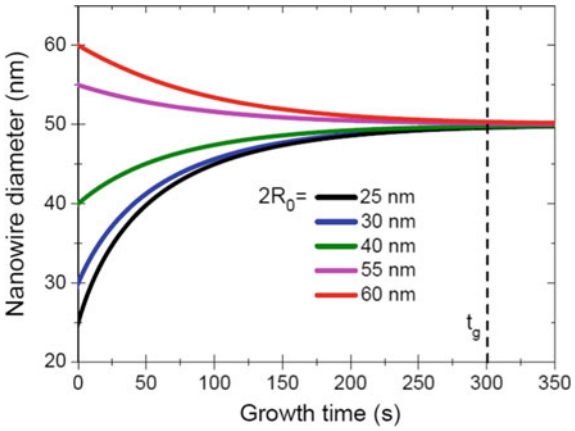

Fig. 30 Time dependences of the NW diameters obtained from Eq. (6.41) with $t_0 = 0$, different R_0, $a = -0.30$ nm/s and $b = 7.50$ nm^2/s. The vertical dash segment indicates the experimental growth time of 300 s, where full self-equilibration of the NW diameter is reached. Reprinted with permission from V. G. Dubrovskii, T. Xu, A. Díaz Álvarez, G. Larrieu, S. R. Plissard, P. Caroff, F. Glas, B. Grandidier, Self-equilibration of the diameter of Ga-catalyzed GaAs nanowires, Nano Letters **15**, 5580–5584 (2015). Copyright (2015) American Chemical Society

8 Length Distributions of Nanowires

Consider an ensemble of VLS NWs growing from pre-existing catalyst droplets on a substrate. Then the number density of NWs having the length of $s = L/h$ MLs, with $s = 0, 1, 2\ldots$, including free droplets (at $s = 0$), equals the number density of the initial droplets at any time t. Therefore, the length distribution (LD) of NWs $f_s(t)$ can be normalized to unity, $\sum_{s=0}^{\infty} f_s)(t) = 1$. The set of rate equations describing the time evolution of the LD has the form [91–96]

$$\begin{aligned} \frac{df_0}{dt} &= -p_0 f_0 \\ \frac{df_s}{dt} &= p_{s-1} f_{s-1} - p_s f_s, \;\; s = 1, 2, 3... \end{aligned} \tag{8.1}$$

Here, $p_s(t)$ are the probabilities of adding 1 ML to the NW of length s per unit time (or the instantaneous growth rate of the NW of length s), including the probability of forming the very first ML from the droplet lying on the substrate surface, $p_0(t)$. These probabilities generally depend on s and t. From the first equation, $f_0(t) = \exp(-p_0 t)$ for a time-independent p_0, and the nucleation rate of NWs on the substrate is given by $J(t) = p_0 \exp(-p_0 t)$.

The continuum approximation reduces the discrete set of Eq. (8.1) at $s >> 1$ to the Fokker–Planck type equation in partial derivatives [92, 95, 96]

$$\frac{\partial f(s,t)}{\partial t} = -\frac{\partial}{\partial s}[p(s,t)f(s,t)] + \frac{1}{2}\frac{\partial^2}{\partial s^2}[p(s,t)f(s,t)], \tag{8.2}$$

If Green's function $F(s,t)$ of this equation is obtained, the resulting LD is given by the convolution of Green's function with the nucleation rate [96]

$$f(s,t) = \int_0^t d\tau F(s,t-\tau)J(\tau). \tag{8.3}$$

The simplest case corresponds to the so-called Poissonian growth, where

$$p_s = v,\ s = 0, 1, 2... \tag{8.4}$$

Here, v is the vapor flux onto the droplet surface in ML/s, which determines the probabilities of adding the MLs to NWs of any length. Then the exact solution to Eq. (8.1) is given by the Poisson LD [91]

$$f_s(t) = e^{-vt}\frac{(vt)^s}{s!} \cong \frac{1}{\sqrt{2\pi vt}}\exp\left[-\frac{(s-vt)^2}{2vt}\right]. \tag{8.5}$$

The discrete Poisson LD rapidly converges to the continuum Gaussian (the approximate expression). The mean length $\langle s\rangle$ and variance σ^2 of this LD equal vt, corresponding to the standard deviation (width) which spreads with time as $\sigma = \sqrt{vt}$, or

$$\langle s\rangle = \tau,\ \sigma^2 = \tau \tag{8.6}$$

with $\tau = vt$.

The measured [30, 31, 92, 93, 97] and modeled [30, 31, 92–97] NW LDs are commonly compared to this Poissonian case.

Without one specific effect which will be discussed later on, the Poisson LD is the best case regarding the length uniformity. There are several effects contributing into the LD broadening, including (i) a nucleation delay due to difficult nucleation of NWs emerging from the substrate; (ii) continuing nucleation of the seed droplets during the NW growth, as in the Ga-catalyzed growth of GaAs NWs without Ga predeposition [97], (iii) surface diffusion of group III adatoms, (iv) collective effects in the NW growth such as shadowing in the directional MBE method, and (v) initial size inhomogeneity of the droplets.

To account for the nucleation delay for NWs whose growth rate is controlled by the direct impingement from vapor, the probabilities $p_s(t)$ are written in the form

$$p_0 = \alpha v,\ p_s = v,\ s =, 1, 2, 3... \tag{8.7}$$

Here, $\alpha < 1$ describes difficult nucleation of the very first NW ML relative to the upper layers. The corresponding continuum LD is now given by [92]

$$f(s,\tau) = \frac{\alpha}{2} e^{\alpha(s-\tau)+\alpha^2\tau/2} \mathrm{erfc}\left[\frac{s-\tau+\alpha\tau}{\sqrt{2\tau}}\right]. \tag{8.8}$$

where erfc is the complimentary error function defined by

$$\mathrm{erfc}(y) = \frac{2}{\sqrt{\pi}} \int_y^\infty dt e^{-t^2}. \tag{8.9}$$

The mean length and variance of this LD, assuming that it is fully formed ($f(s = 0, \tau) \to 0$), equal

$$\langle s \rangle = \tau - \frac{1}{\alpha}, \ \sigma^2 = \tau + \frac{1}{\alpha^2}, \tag{8.10}$$

showing that the mean length decreases and the variance increases with respect to the Poisson case.

The Poisson LDs were obtained in Ref. [92] for InAs NWs grown at 380 °C on InAs(111)B substrates with Au nanopartciles formed by thermal dewetting of a thin Au film. These data are shown in Fig. 31 and confirm that the VLS growth of these InAs NWs is controlled by the direct vapor flux. Figure 32 shows the LDs of InAs NWs grown for 60 and 130 min from 40 nm Au colloids annealed at 500 °C,

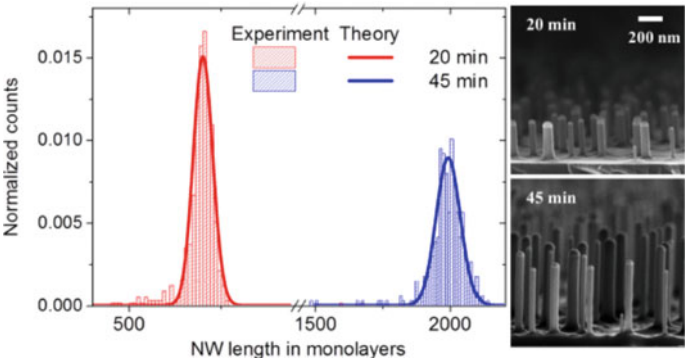

Fig. 31 **a** Normalized LDs (histograms) fitted by the Poissonian shapes (lines) for Au-catalyzed InAs NWs grown by CBE for 20 and 45 min from Au nanoparticles obtained by thermally dewetting of a 0.5 nm thick Au film at 510 °C for 20 min, along with their plan view SEM images. Reprinted from V. G. Dubrovskii, N. V. Sibirev, Y. Berdnikov, U. P. Gomes, D. Ercolani, V. Zannier and L. Sorba, Length distributions of Au-catalyzed and In-catalyzed InAs nanowires, Nanotechnology **27**, 375,602 (2016); https://doi.org/10.1088/0957-4484/27/37/375602. © IOP Publishing. Reproduced with permission. All rights reserved

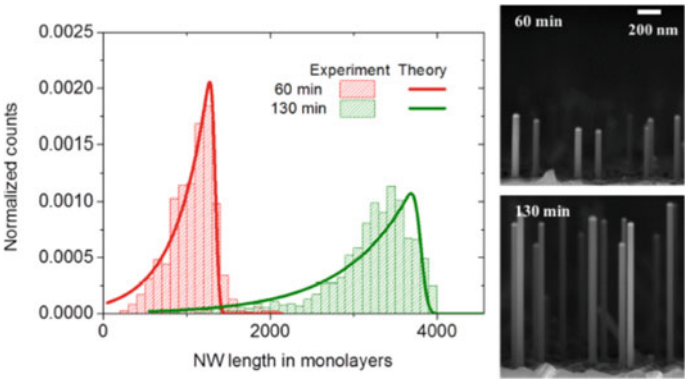

Fig. 32 Normalized LDs (histograms) of Au-catalyzed InAs NWs grown from 40 nm colloids annealed at 500 °C for 60 and 130 min, along with their side view SEM images. The fits (lines) are obtained from Eq. (8.8) with $\alpha = 0.0025$ for 60 min and 0.0013 for 130 min. Reprinted from V. G. Dubrovskii, N. V. Sibirev, Y. Berdnikov, U. P. Gomes, D. Ercolani, V. Zannier and L. Sorba, Length distributions of Au-catalyzed and In-catalyzed InAs nanowires, Nanotechnology **27**, 375,602 (2016); https://doi.org/10.1088/0957-4484/27/37/375602. © IOP Publishing. Reproduced with permission. All rights reserved

along with the corresponding SEM micrographs. These NWs clearly feature much broader LDs with a long left tail that spread with the growth time. Clearly, no new Au nanoparticles can emerge after starting the InAs deposition. and thus the striking difference in the LD shapes between Figs. 31 and 32 should be associated with a much longer nucleation step of InAs NWs grown from Au colloidal nanoparticles.

It was noticed that during the standard annealing step (temperature ramp up to ~500 °C and substrate kept at this temperature for 20 min under TBAs = 1.0 Torr), the Au colloidal nanoparticles dig deep into the substrate, as shown in the SEM micrographs in Fig. 33a. The holes are formed as a result of interaction between Au nanoparticle and InAs substrate to form an Au–In alloy, accompanied by the evaporation of As. The nucleation delay causing the wide and asymmetric LDs in Fig. 32 should be due to a slow re-emerging of Au nanoparticles from the holes when the NW growth is started. In fact, it is evident from the early stages of growth from 3 to 12 min illustrated in Figs. 33d–f that there is a significant delay in the NW nucleation due to the presence of holes. In order to minimize this effect, the annealing step was removed by just ramping the temperature up to 380 °C under TBAs = 4.0 Torr which reduced the size of the holes, as shown in Fig. 33b. InAs NWs were then grown at the same temperature. The measured LDs of these InAs NWs are shown in Fig. 33g. It is clearly seen that the NWs grown without the annealing step feature much narrower and symmetric LDs, in comparison to the LDs of InAs NWs grown under exactly identical conditions but with the standard annealing step as shown in Fig. 32, confirming that the nucleation delay is mainly due to the burial of Au nanoparticles during the annealing.

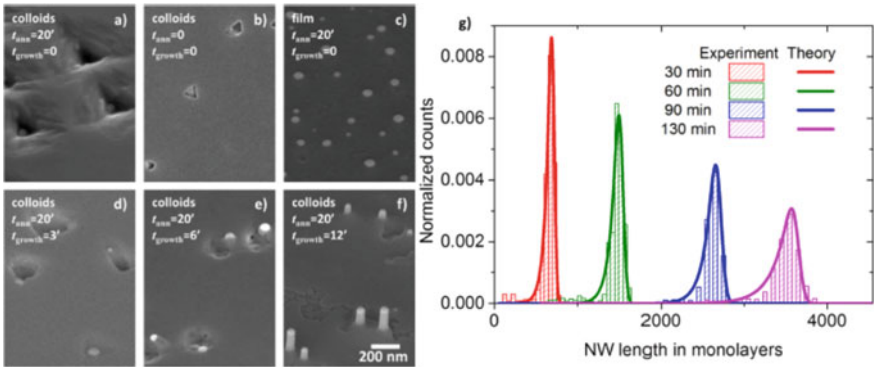

Fig. 33 45° tilted SEM image of (**a**) Au colloidal nanoparticles after the standard annealing step (20 min at 500 °C under TBAs = 1.0 Torr), compared to (**b**) Au colloidal nanoparticles with just ramping the temperature up to 380 °C under TBAs = 4.0 Torr and removing the annealing step; **c** the reference sample with thermally dewetted 0.5 nm thick Au film after the standard annealing step; **d**–**f** slow emerging of InAs NWs during the early stages of NW growth (3–12 min); (**g**) normalized LDs (histograms) of Au-catalyzed InAs NWs grown from Au colloids at 380 °C without the annealing step for 30, 60, 90 and 130 min respectively. The fits (lines) are obtained from Eq. (8.8) with α ranging from 0.0053 to 0.017. Reprinted from V. G. Dubrovskii, N. V. Sibirev, Y. Berdnikov, U. P. Gomes, D. Ercolani, V. Zannier and L. Sorba, Length distributions of Au-catalyzed and In-catalyzed InAs nanowires, Nanotechnology **27**, 375,602 (2016); https://doi.org/10.1088/0957-4484/27/37/375602. © IOP Publishing. Reproduced with permission. All rights reserved

In full agreement with this observation, the NW LDs shown in Figs. 32 are best fitted by Eq. (8.8) with $\alpha = 0.0025$ for 60 min and 0.0013 for 130 min. This corresponds to a very long delay in nucleation of the very first NW ML, ~1000 times slower than in the upper layers. The best fits of the LDs shown in Fig. 33 correspond to α between 0.0053 and 0.017, which are one order of magnitude larger than for the standard annealing step but still two orders of magnitude lower than in the best Poissonian case achieved for thermally dewetted Au film.

In-catalyzed InAs NWs [92] and Ga-catalyzed GaAs NWs [97], whose growth is accompanied by simultaneous nucleation of the group III droplets, feature much broader LDs than shown here, because the NWs continue to emerge from the newly formed droplets.

In Ref. [93], it was demonstrated experimentally and explained theoretically that NWs growing by surface diffusion of group III adatoms exhibit very broad LDs, with the variance increasing proportionally to the squared mean length. Theoretical work [94] considered simultaneous effects of surface diffusion and nucleation delay on the LDs and predicted even larger broadening than in Ref. [93]. Figure 34 shows the model with its main ingredients, a delayed nucleation and the diffusion flux of adatoms collected from the entire length of the NW, which equals s MLs. As a result, the instantaneous growth rates become linear in s. Such size-linear model was discussed earlier in connection with the scaling regime of growth of 2D islands competing for the diffusion flux of adatoms (see Ref. [98] and references therein).

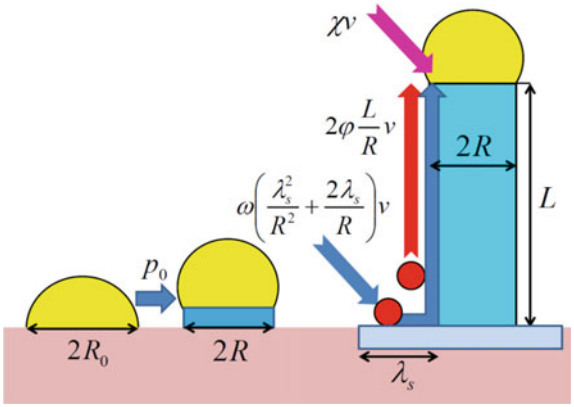

Fig. 34 Schematics of the VLS NW growth from pre-existing Au droplets with radius R_0. The nucleation probability of the very first NW ML equals p_0. Upon the formation of the first ML, the droplet changes its shape and the NW acquires a steady-state radius R. Subsequent elongation rate of the NW contains three contributions: (i) the vapor flux χv, (ii) the diffusion flux $\omega(\lambda_s^2/R^2+2\lambda_s/R)v$ of adatoms collected by the substrate area of width λ_s, and (iii) the diffusion flux $2\varphi(L/R)v$ of adatoms collected by the NW sidewalls of length $L = hs$. Coefficients χ, ϕ and ω are on the order of unity. Reprinted from Journal of Crystal Growth, vol. 463, V. G. Dubrovskii, Length distributions of nanowires: effects of surface diffusion versus nucleation delay, pp. 139–144, Copyright (2017), with permission from Elsevier

Introducing the dimensionless time τ and the model parameters a and b according to

$$\tau = \frac{2\varphi h v t}{R},\ a = \frac{\chi R + \omega(\lambda_s^2/R + 2\lambda_s)}{2\varphi h},\ b = \frac{p_0 R}{2\phi h v}, \tag{8.11}$$

with t the growth time and other parameters illustrated in Fig. 34, Eq. (8.1) take the form

$$\begin{aligned} \frac{df_0}{d\tau} &= -bf_0, \\ \frac{df_1}{d\tau} &= bf_0 - (a+1)f_1, \\ \frac{df_s}{d\tau} &= (a+s-1)f_{s-1} - (a+s)f_s,\ s \geq 2. \end{aligned} \tag{8.12}$$

Here, b describes the nucleation probability of the first ML [in a different normalization compared to α in Eq. (8.7)], while a appears due to normalization of the diffusion flux (to make it equal s at $s \to \infty$). This a is usually much larger than unity due to the presence of the R/h term in the corresponding Eq. (8.11), which equals the NW radius in the units of lattice spacing.

The exact solution to Eq. (8.12), given in Ref. [94], is expressed through the incomplete beta-function. The particular case of this LD at $a = b$ is reduced to the Polya distribution [93, 94]. In the continuum limit $s >> 1$, the beta-distribution converges to

$$f(s,\tau) = \frac{be^{-\tau}}{\Gamma(a+1)}(se^{-\tau})^{b-1}\Gamma(se^{-\tau}, a-b+1), \tag{8.13}$$

with

$$\Gamma(y,q) = \int_y^\infty dt t^{q-1}e^{-t}. \tag{8.14}$$

as the upper incomplete gamma-function and $\Gamma(y)$ the gamma-function. The mean value of such LD equals

$$\langle s\rangle = c(e^\tau - 1) \cong ce^\tau,\ c = \frac{(a+1)b}{(b+1)}, \tag{8.15}$$

where the approximate expression corresponds to the continuum LD. The variance of the continuum LD is given by

$$\sigma = \frac{[a+2+b(b+2)]}{(a+1)b(b+2)}\langle s\rangle^2. \tag{8.16}$$

For $a = b$, corresponding to the case of NWs growing by surface diffusion from their entire length without nucleation delays, the mean length and variance become

$$\langle s\rangle = a(e^\tau - 1),\ \sigma^2 = \frac{\langle s\rangle^2}{a}. \tag{8.17}$$

At $s >> a >> 1$, the continuum Polya LD is reduced to the symmetric Gaussian

$$f(s,\langle s\rangle) \cong \frac{1}{\langle s\rangle}\sqrt{\frac{a}{2\pi}}\exp\left[-\frac{a}{2}\frac{(s-\langle s\rangle)^2}{\langle s\rangle^2}\right]. \tag{8.18}$$

Figure 35 shows how the symmetric Polya LD transitions to much broader LDs, which are asymmetric toward their longer left tails, with increasing the nucleation delay. The LDs can even become monotonically decreasing for very difficult nucleation from the substrate ($b < 1$). But even for the best case without any delays for NWs emerging from the substrate, the variance scales as $\langle s\rangle^2/a$, leading to the extreme broadening of the LDs due to the surface diffusion effect.

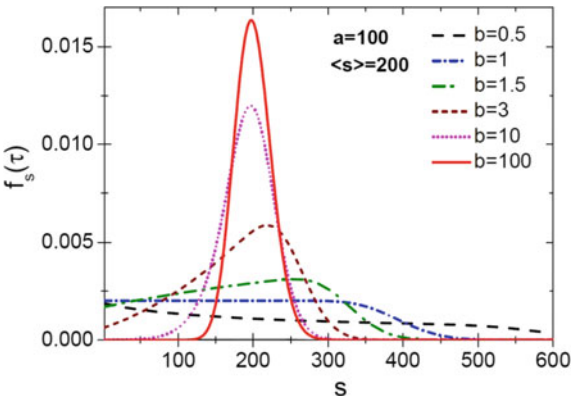

Fig. 35 Discrete beta-distribution at a fixed a of 100, which is very well approximated by the continuum LD given by Eq. (8.13), transitioning from the symmetric Polya LD at $a = b$ to much broader and asymmetric LDs with decreasing b, and finally becoming monotonically decreasing at $b < 1$. Reprinted from Journal of Crystal Growth, vol. 463, V. G. Dubrovskii, Length distributions of nanowires: effects of surface diffusion versus nucleation delay, pp. 139–144, Copyright (2017), with permission from Elsevier

The Au-catalyzed InAs NWs of Ref. [93] were grown by MOVPE. Before MOVPE growth, patterns of Au particles were prepared by means of electron beam lithography (EBL) followed by thermal evaporation of Au and lift-off. The distance between the Au particles was 1000 nm and by varying the EBL dose the nominal NW diameter was varied between 20 and 100 nm. The NWs were grown at 450 °C and the investigated growth times were 7.5, 15, 22.5, 30, and 60 min. SEM images of the NW arrays were recorded at specific tilt angles and NW length and diameter statistics were extracted using the SEM image analysis. Figure 36 shows the typical SEM images of differently sized InAs NWs after 7.5 min of growth. It is clearly seen

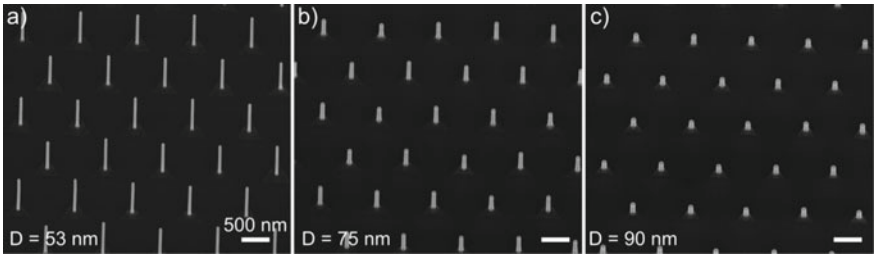

Fig. 36 30° tilted SEM images of InAs NW arrays with 1000 nm pitch, growth time of 7.5 min and NW diameters around (**a**) 53 nm, (**b**) 75 nm, and (**c**) 90 nm. Scale bar is the same in all three images. Reprinted with permission from V. G. Dubrovskii, Y. Berdnikov, J. Schmidtbauer, M. Borg, K. Storm, K. Deppert, J. Johansson, Length distributions of nanowires growing by surface diffusion, Crystal Growth & Design **16**, 2167–2172 (2016). Copyright (2016) American Chemical Society

that the NW length decreases for larger diameters, which confirms that their VLS growth is controlled by surface diffusion of In adatoms.

Figures 37 and 38 show the measured mean length $\langle s \rangle$ and LD width 2σ (expressed in MLs) of 100–110 nm diameter NWs. It is seen that the mean length increases

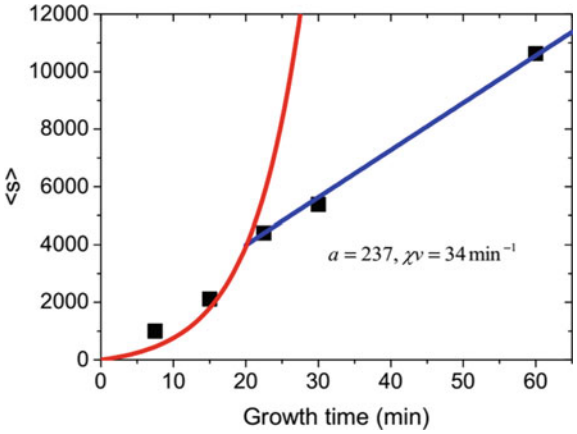

Fig. 37 Transition from the exponential to the linear growth regime of the 100–110 nm diameter InAs NWs (symbols). The fitting parameters in Eq. (8.19) for the lines are: $a = 237$, $\chi v = 34\ \mathrm{min}^{-1}$ and $C = 0.247$. Reprinted with permission from V. G. Dubrovskii, Y. Berdnikov, J. Schmidtbauer, M. Borg, K. Storm, K. Deppert, J. Johansson, Length distributions of nanowires growing by surface diffusion, Crystal Growth & Design **16**, 2167–2172 (2016). Copyright (2016) American Chemical Society

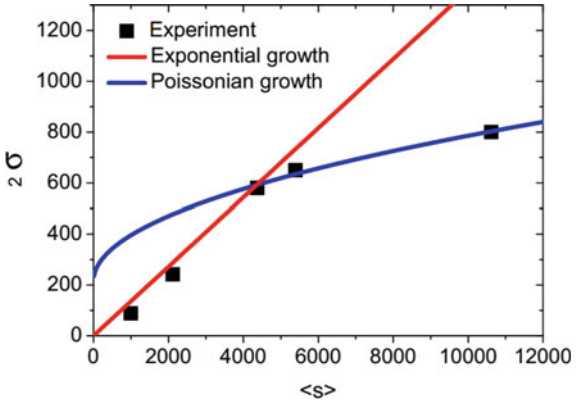

Fig. 38 Best fits by Eqs. (8.19) (lines) of the experimental standard deviations of the 100–110 diameter NW LDs (symbols) versus the mean length at different growth times. Reprinted with permission from V. G. Dubrovskii, Y. Berdnikov, J. Schmidtbauer, M. Borg, K. Storm, K. Deppert, J. Johansson, Length distributions of nanowires growing by surface diffusion, Crystal Growth & Design **16**, 2167–2172 (2016). Copyright (2016) American Chemical Society

exponentially with the growth time for $t < 22.5$ min and linearly for longer times. The standard deviation is proportional to the mean length for $t < 22.5$ but becomes sub-linear for longer times. Such changes are attributed to the transition from the length-linear to length-independent NW growth rates, as discussed previously. Therefore, these data were fitted with

$$\langle s \rangle = s_{\max} + \left(1 + \frac{s_{\max}}{a}\right) C\chi v(t - t_{\max});\ \sigma^2 = < s > - s_{\max} \tag{8.19}$$

Here, $t_{\max}$ is the time at which the mean NW length reaches the diffusion length $s_{\max}$(4400 MLs, or about 1500 nm according to Fig. 37) and C is a constant deduced from the fit.

The solution for the NW LDs at $t > t_{\max}$ is then obtained by convoluting the two Gaussians representing the Poissonian Green function and the Polya LD at $t = t_{\max}$, given by Eq. (8.18). The resulting LD has the form

$$f(s, \langle s \rangle) \cong \frac{1}{\sqrt{2\pi}\sigma} \exp\left[-\frac{(s - \langle s \rangle)^2}{2\sigma^2}\right],\ \sigma^2 = \begin{cases} \dfrac{\langle s \rangle^2}{a}, \langle s \rangle \le s_{\max} \\ \dfrac{s_{\max}^2}{a} + < s > - s_{\max}, < s > \ge s_{\max} \end{cases} . \tag{8.20}$$

This solution holds for any $< s >$, while the mean length is given by Eq. (8.17) in the exponential stage for $\langle s \rangle < s_{\max}$ and by the corresponding Eq. (8.19) when $\langle s \rangle > s_{\max}$. Since no difference in the growth rate of very short NWs was noticed, the diffusion flux from the substrate was neglected. From Eq. (8.11), this gives $a = \chi R/(2\phi h)$, showing that a scales as R.

Figure 39 shows the experimental LDs and their best fits by Eq. (8.20) for NWs with different diameters grown for the same time of 7.5 min. The fitting values of a indeed scale linearly with the NW diameter, as predicted by the model [93]. It is noteworthy that the fits are obtained with rather high $a \ge 140$. This is not surprising because the a parameter contains a large value of R/h in the range of 140–300, while the coefficient $\chi/(2\phi)$ is expected to be of the order of one. This confirms the assumption $\langle s \rangle >> a >> 1$, which allows us to use the Gaussian LD given by Eq. (8.18) instead of the exact solution for the discrete LD. Figure 40 shows the experimental LDs and their Gaussian fits for NWs of 100–110 nm diameter at different growth times. The mean length and width of these LDs are given in Figs. 37 and 38. The fits are obtained with the same $a = 237$ for each growth time, which again confirms the validity of the model. One of the main conclusions is that the LDs acquire the broad Polya-like shape already at the initial stage of growth, in which In adatoms are collected from the entire NW length. Therefore, the VLS growth regimes controlled by the diffusion transport of group III adatoms are not desirable for obtaining narrow NW LDs.

Up to now, we have discussed different mechanisms of broadening the Poisson LDs of NWs. Let us now see if it is possible to achieve sub-Poissonian narrowing of the LDs. The only effect which is expected to be beneficial from this perspective is nucleation antibunching observed experimentally and explained theoretically in

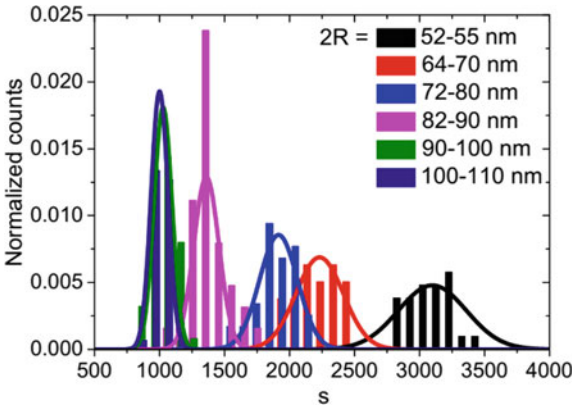

Fig. 39 Normalized experimental LDs (histograms) of differently sized InAs NWs grown for 7.5 min. The data for 52–55, 64–70, 72–80, 82–90, 90–100, and 100–110 nm diameter NWs are fitted by Eq. (8.20) (lines) with $a = 140$, $< s >= 3098$, $a = 160$ $< s >= 2231$ MLs, $a = 180$, $\langle s \rangle = 1915$ MLs, $a = 200$, $\langle s \rangle = 1472$ MLs, $a = 220$, $\langle s \rangle = 1027$ MLs, and $a = 237$, $\langle s \rangle = 1000$ MLs, respectively. For this growth time, all the LDs are Polya-like because the mean length is shorter than $s_{\max} = 4400$ MLs. Reprinted with permission from V. G. Dubrovskii, Y. Berdnikov, J. Schmidtbauer, M. Borg, K. Storm, K. Deppert, J. Johansson, Length distributions of nanowires growing by surface diffusion, Crystal Growth & Design **16**, 2167–2172 (2016). Copyright (2016) American Chemical Society

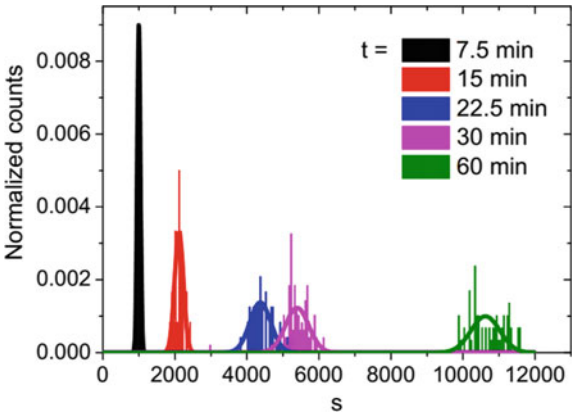

Fig. 40 Broadening of the LD of 100–110 nm diameter InAs NWs with the growth time: experimental LDs (histograms), fitted by the Gaussian distributions (lines) with $a = 237$ and $\langle s \rangle = 1000$, 2110, 4400, 5400, and 10600 MLs for the growth times of 7.5, 15, 22.5, 30, and 60 min, respectively. Reprinted with permission from V. G. Dubrovskii, Y. Berdnikov, J. Schmidtbauer, M. Borg, K. Storm, K. Deppert, J. Johansson, Length distributions of nanowires growing by surface diffusion, Crystal Growth & Design **16**, 2167–2172 (2016). Copyright (2016) American Chemical Society

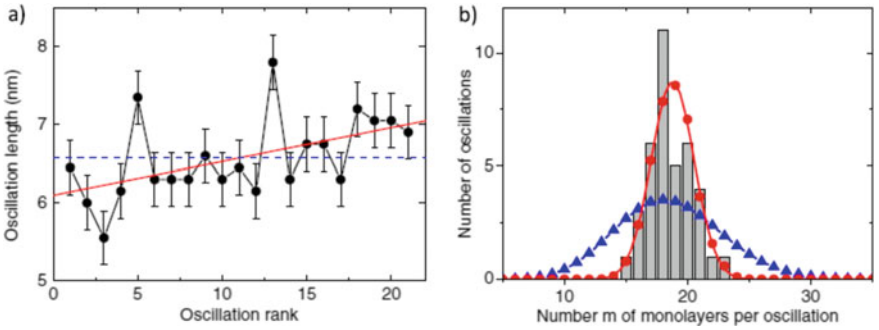

Fig. 41 **a** Length of successive oscillations. The dashed line gives the mean length; the solid line is a linear regression $dL/dt \propto t$. **b** Histogram of the numbers of nucleation events per oscillation. The two curves represent distributions calculated for a large number of nucleation events and normalized to the total number of experimental counts: Poissonian statistics (triangles), self-regulated statistics (disks). Reprinted figure with permission from F. Glas, J. C. Harmand and G. Patriarche, Physical Review Letters **104**, 135,501 (2010), https://doi.org/10.1103/PhysRevLett.104.135501. Copyright (2010) by the American Physical Society

Ref. [88]. Using the method described in Sect. 6 for $InP_{1-x}As_x$ NWs with modulated composition, the nucleation statistics in individual NW was analyzed as shown in Fig. 41. The length of each oscillation of composition in an individual NW is measured to within 1 ML [Fig. 41a]. In the mononuclear growth regime, the NW axial growth rate is fixed by the rate of nucleation at the catalyst-solid interface and the number of MLs grown equals the number of nucleation events. The length of each oscillation (in MLs) thus equals the number of nucleation events in the time period Δt. If these nucleation events occurred independently of each other, the probability of a given number m of nucleations taking place during Δt should follow the Poisson statistics. Figure 41b compares the distribution of the oscillation lengths with a Poisson distribution, normalized to the same total number of oscillations. The nucleation statistics are markedly sub-Poissonian. In three NW segments studied (see Ref. [88] for the details), the measured standard deviations are less than half the Poisson standard deviations. This proves that the nucleation events are not independent.

This effect was explained by nucleation antibunching, whereby the probability to nucleate the next ML decreases exponentially immediately after nucleation of the previous ML [88]. Therefore, the next nucleation event becomes improbable until the droplet is refilled from vapor with the missing As. The measure of nucleation antibunching is readily obtained from the following considerations. The chemical potential decrease immediately after nucleation of one ML equals

$$\delta\Delta\overline{\mu} = c_5 \frac{\partial \Delta\overline{\mu}}{\partial c_5}(1-2c_5)\frac{1}{N_5}\frac{\pi R^2}{\Omega_S}. \tag{8.21}$$

Approximating the nucleation barrier under the exponent of the Zeldovich nucleation rate [Eq. (3.11)] as

$$\frac{a^2}{4(\Delta\overline{\mu}-\delta\Delta\overline{\mu})} \cong \frac{a^2}{4\Delta\overline{\mu}} + \frac{a^2}{4\Delta\overline{\mu}^2}\delta\Delta\overline{\mu} \tag{8.22}$$

and using Eq. (3.8) for the critical size i_c, we note that the decrease in the nucleation probability immediately after nucleation equals $\exp(-\varepsilon)$, with

$$\varepsilon = c_5\frac{\partial\Delta\overline{\mu}}{\partial c_5}(1-2c_5)i_c(\Delta\overline{\mu})\frac{1}{N_5}. \tag{8.23}$$

This ε is called the antibunching parameter in what follows. It can equivalently be presented in the form

$$\varepsilon = \frac{3\tilde{\Omega}_L}{f(\beta)\Omega_S}c_5\frac{\partial\Delta\overline{\mu}}{\partial c_5}i_c(\Delta\overline{\mu})\frac{h}{c_5 R}. \tag{8.24}$$

In these expressions, the chemical potential, its derivative with respect to c_5, and c_5 itself should be taken before nucleation. Clearly, the antibunching effect is stronger for thinner NWs and low group V concentrations in the droplet (small R and c_5), and disappears at large R. As an example, ε equals 0.2 for <111> GaAs NWs ($\tilde{\Omega}_L = 0.02$ nm^3, $\Omega_S = 0.0452$ nm^3, $h = 0.326$ nm) with $R = 50$ nm and $\beta = 127°$ if we assume $\overline{c}(\partial\Delta\mu/\partial\overline{c}) = 1$, $\overline{c} = 0.03$ and $i_c(\Delta\overline{\mu}) = 5$.

Glas [99] presented the exact solution for sub-Poissonian nucleation statistics in individual VLS NWs, controlled by the sole parameter ε. Later, Glas and Dubrovskii [95] considered the effect of nucleation antibunching on the LDs within ensembles of NWs by using three different methods: (i) numerical simulations in a large ensemble of NWs, (ii) exact analytical solution for the LD and its statistical properties based on the results obtained for an individual NW [99], and (iii) simplified analytic approach based on the continuum rate equation. The main goal was to obtain the LD as a function of two parameters, ε for antibunching and $\alpha = p_0/v$ for the nucleation delay, assuming the NW nucleation rate in the form of exponential decay $p_0\exp(-p_0 t)$ as discussed earlier.

For the exact analytical calculations, the central object is the probability $\pi_s(T|p_I)$ that exactly s nucleations occur during a time interval of length T, conditional to the fact that the nucleation probability was p_I at the beginning of this interval. According to Ref. [99], $\pi_s(T|p_I)$ is given by

$$\pi_s(T|p_I) = \sum_{m=0}^{s}\frac{g_{s-m}}{(\gamma;\gamma)_m}\exp\left[-\gamma^m E(T)p_I/(\varepsilon v)\right] \tag{8.25}$$

Here, $\gamma = \exp(-\varepsilon)$, $(\gamma;\gamma)_m = (1-\gamma)\left(1-\gamma^2\right)\ldots(1-\gamma^m)$ is the q-Pochhammer symbol (for $m \geq 1$, with $(\gamma;\gamma)_0 = 1$), $g_m = (-1)^m\gamma^{\frac{m(m-1)}{2}}/(\gamma;\gamma)_m$,

and $E(T) = e^{\varepsilon vT} - 1$. The probability p_I corresponds to the beginning of growth, just after forming the first ML of the NW (the third parameter which is not required in the continuum theory).

The conditional probability $\pi_s(T|p_I)$ is a powerful tool for calculating the time evolution of ensembles of NWs. Indeed, the ensemble LD is simply given by the convolution of this probability with the distribution of times of formation of the first ML, which equals $p_0 \exp(-p_0 T)$. After some calculations (see Ref. [95] for the details), the LD can be expressed in terms of the incomplete gamma functions $\Gamma(x, y)$ as

$$f_s(\tau) = \theta\rho^{-\theta} \sum_{m=0}^{s-1} \frac{g_{s-1-m}}{(\gamma;\gamma)_m} \exp\left[\alpha(m-\tau) + \rho e^{-m\varepsilon}\right]\left[\Gamma\left(\theta, \rho e^{\varepsilon(\tau-m)}\right) - \Gamma\left(\theta, \rho e^{-\varepsilon m}\right)\right] \quad (8.26)$$

for $s \geq 1$, with $\theta = \varepsilon^{-1}\alpha = \varepsilon^{-1} p_0/v$, $\rho = \varepsilon^{-1} p_I/v$ and $\tau = vT$ the normalized growth time. These formulas are exact for any non-zero values of parameters α, p_I and time τ and are computationally efficient unless ε is very small. The LDs so calculated agree extremely well with those obtained from numerical simulations [95]. This confirms that for identical and non-interacting NWs, the statistics of the ensemble may be calculated from those of the single NW.

The average length (in MLs) of the NW ensemble at time τ equals

$$\langle s\rangle = (\gamma;\gamma)_\infty \sum_{m=0}^{\infty} \frac{1}{(\gamma;\gamma)_m} \left\{ \begin{array}{l} 1 - e^{-\alpha\tau} - \theta\rho^{-\theta} \exp\left[\alpha(m-\tau) + \rho e^{-m\varepsilon}\right] \\ \left[\Gamma\left(\theta, \rho e^{\varepsilon(\tau-m)}\right) - \Gamma\left(\theta, \rho e^{-\varepsilon m}\right)\right] \end{array} \right\} + 1 - e^{-\alpha\tau}. \quad (8.27)$$

The variance of the LD is given by

$$\begin{aligned} \sigma^2 =& 2(\gamma;\gamma)_\infty \sum_{m=0}^{\infty} \frac{m - \mathcal{L}(\gamma)}{(\gamma;\gamma)_m} \left\{ \begin{array}{l} 1 - e^{-\alpha\tau} - \theta\rho^{-\theta} \exp\left[\alpha(m-\tau) + \rho e^{-m\varepsilon}\right] \\ \left[\Gamma\left(\theta, \rho e^{\varepsilon(\tau-m)}\right) - \Gamma\left(\theta, \rho e^{-\varepsilon m}\right)\right] \end{array} \right\} \\ &+ 3s - \langle s\rangle^2 - 2\left(1 - e^{-\alpha\tau}\right), \end{aligned} \quad (8.28)$$

where $\mathcal{L}(\gamma) = \sum_{p=1}^{\infty} \gamma^p/(1-\gamma^p)$ is the Lambert series with unit coefficients. It turns out that the parameter p_I has no influence on the LDs of sufficiently long NWs of interest, so the statistical properties of the ensemble are controlled by the two parameters ε and α.

In the continuum approach, the asymptotic method of Ref. [100] was used, which formally requires $\varepsilon << 1$. The instantaneous growth rates in the continuum Eq. (8.2) for $s >> 1$ were taken in the form

$$p_s(t) = p(vt - s) = ve^{\varepsilon(vt-s)}, \quad (8.29)$$

describing the exponential growth of the nucleation probability with time due to incoming flux and its exponential decrease immediately after the ML formation. The Green's function of Eq. (8.2) is obtained in the form

$$F(\rho, z) = \frac{1+\varepsilon\rho}{\sqrt{2\pi}\sigma}\exp\left[-\frac{(\rho-z)^2}{2\sigma^2}\right], \tag{8.30}$$

with

$$\rho = \frac{e^{\varepsilon s}-1}{\varepsilon},\ z = \frac{e^{\varepsilon\tau}-1}{\varepsilon},\ \sigma^2 = z + \frac{\varepsilon z^2}{2} \tag{8.31}$$

This solution is quite interesting as it combines the Poissonian LD at $\varepsilon \to 0$ with self-regulated LD at $\varepsilon > 0$. In the latter case, Green's function becomes a universal function of $s - \tau$:

$$F(s-\tau) = \sqrt{\frac{\varepsilon}{\pi}}e^{\varepsilon(s-\tau)}\exp\left[-\frac{1}{\varepsilon}\left(e^{\varepsilon(s-\tau)}-1\right)^2\right]. \tag{8.32}$$

This property directly shows that the Green's function does not broaden with time due to nucleation antibunching. For small enough ε and large s, it is well approximated by the Gaussian

$$F(s-\tau) = \sqrt{\frac{\varepsilon}{\pi}}\exp\left[-\varepsilon(s-\tau)^2\right] \tag{8.33}$$

Clearly, the mean length of this LD remains τ but the variance is time-independent and equals $1/(2\varepsilon)$ rather than growing infinitely as in the Poissonian case. The variance $1/(2\varepsilon)$ exactly equals the one obtained in Ref. [99] for the individual NW.

Convolution of Green's function given by Eq. (8.33) with the nucleation rate $J(\tau) = \alpha\exp(-\alpha\tau)$ according to Eq. (8.3) yields the asymptotic LD in the form

$$f(s-\tau) = \frac{\alpha}{2}e^{\alpha(s-\tau)+\alpha^2/(4\varepsilon)}\mathrm{erfc}\left[\sqrt{\varepsilon}(s-\tau)+\frac{\alpha}{2\sqrt{\varepsilon}}\right]. \tag{8.34}$$

This universal LD depends only on the difference $x = s - \tau$ and hence its shape does not change with time. The mean length and variance of the fully formed LD given by Eq. (8.34) equal

$$\langle s\rangle = \tau - \frac{1}{\alpha},\ \sigma^2 = \frac{1}{2\varepsilon} + \frac{1}{\alpha^2}. \tag{8.35}$$

It is interesting to note that the Poissonian growth with nucleation delay can be recovered from these results by setting $\varepsilon = 1/(2\tau)$, which transforms Eqs. (8.34) and (8.35) to Eqs. (8.8) and (8.10), respectively.

Figure 42 shows how the universal LD $f(x)$ at a fixed ε of 0.1 is broadened for smaller α, corresponding to longer NW nucleation delays. Figure 43 shows the narrowing of the LDs due to increasing the antibunching parameter ε, at a given

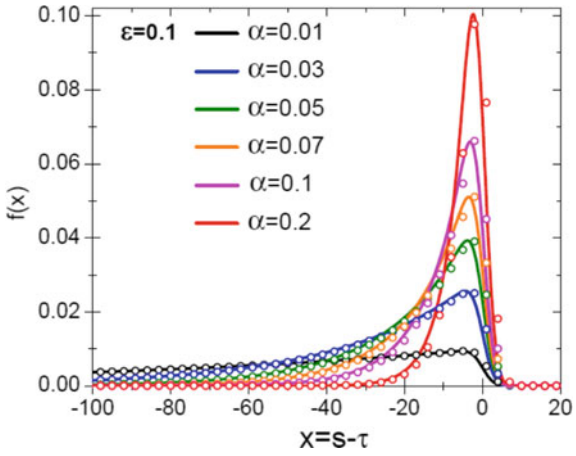

Fig. 42 Shapes of the universal LD at a fixed $\varepsilon = 0.1$ and different α ranging from 0.01 to 0.2. Lines: continuum approximation [Eq. (8.34)]. Symbols: exact solution [Eq. (8.26)], for $p_s = v$. Reprinted figure with permission from F. Glas and V. G. Dubrovskii, Physical Review Materials **1**, 036,003 (2017), https://doi.org/10.1103/PhysRevMaterials.1.036003. Copyright (2017) by the American Physical Society

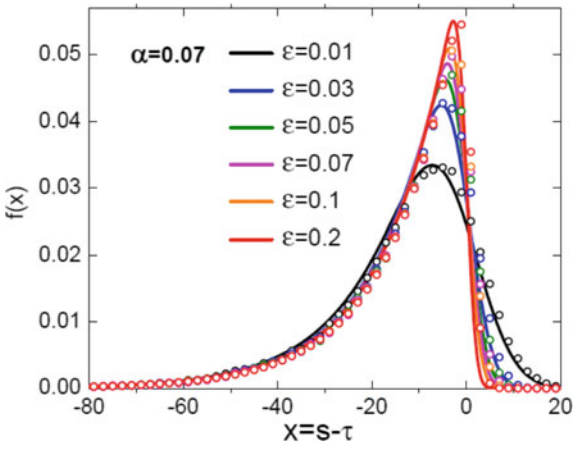

Fig. 43 Shapes of the universal LD at a fixed $\alpha = 0.07$ and different ε ranging from 0.01 to 0.2. Lines: continuum approximation [Eq. (8.34)] Symbols: exact solution for $p_s = v$, using Eq. (8.26) for $\varepsilon \geq 0.1$ and numerical simulation for $\varepsilon \leq 0.07$. Reprinted figure with permission from F. Glas and V. G. Dubrovskii, Physical Review Materials **1**, 036,003 (2017), https://doi.org/10.1103/PhysRevMaterials.1.036003. Copyright (2017) by the American Physical Society

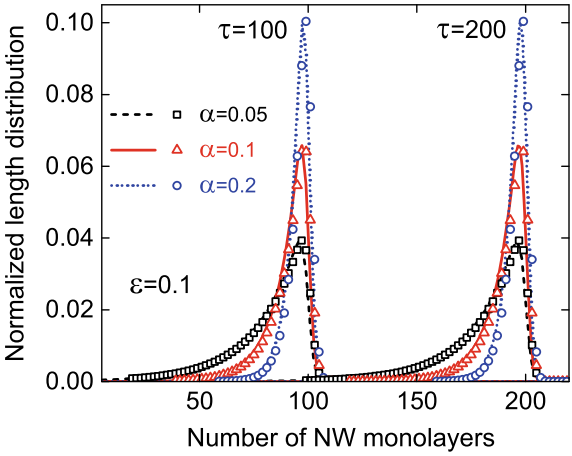

Fig. 44 Discrete (symbols) and continuum (lines) LDs obtained from Eq. (8.26) and Eq. (8.34), respectively, for two different growth times and three different values of α (0.05, 0.1, and 0.2), at a fixed $\varepsilon = 0.1$ and for $p_s = v$ in Eq. (8.26). Reprinted figure with permission from F. Glas and V. G. Dubrovskii, Physical Review Materials **1**, 036,003 (2017), https://doi.org/10.1103/PhysRevMaterials.1.036003. Copyright (2017) by the American Physical Society

$\alpha = 0.07$. This effect is stronger for smaller ε, while for larger ε the LDs converge to a shape that is simply determined by the duration of the NW nucleation step. In both figures, an excellent quantitative agreement is obtained between the exact LDs given by Eq. (8.26) and the continuum LD given by Eq. (8.34).

Figure 44 shows the comparison between the LDs obtained from discrete Eq. (8.26) and continuum Eq. (8.34) and demonstrates again their excellent quantitative correlation. The LD shapes are almost identical; however, the continuum LDs are slightly shifted toward smaller lengths. This is explained by the fact that in the continuum approximation, the NWs are assumed to emerge with zero length while actually they nucleate with a minimum length of 1 ML. The variances of the LDs obtained numerically as the long time asymptotics to the exact Eq. (8.28) and from Eq. (8.35) are also extremely close (see Ref. [95] for a more detailed discussion).

Summarizing the results of Ref. [95], it was demonstrated by three different methods that nucleation antibunching in individual NWs, described by the antibunching parameter ε, completely suppresses the Poissonian broadening of LDs within ensembles of NWs. The initial nucleation randomness, described by the parameter α, affects the LDs forever, which is why the asymptotic variances and the LD shapes depend on the two parameters ε and α. However small these parameters may be, the LDs finally acquire time-independent shapes rather than spread infinitely with the growth time. Numerical simulations over large ensembles of NWs and two different analytical approaches based on discrete and continuum rate equations yield very similar results. Recent experimental results confirm qualitatively these predictions by showing markedly sub-Poissonian LDs of Ga-catalyzed GaAs NWs [30, 31]. However, quantitative comparison with these data requires some care. In theoretical analysis, we used a time-independent antibunching parameter throughout the entire growth process, while the GaAs NWs of Ref. [30] grow also in diameter, which affects the ε value according to Eq. (8.24). In addition, we assumed a time-independent nucleation probability for forming the first NW ML. This corresponds to the VLS regimes with long incubation times for NW growth (small α). Surface

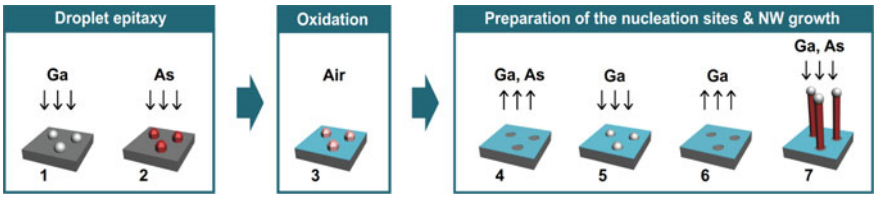

Fig. 45 Description of the NW growth process. Steps 1 and 2: formation of GaAs nanocrystals on oxide-free Si(111) by droplet epitaxy; Step 3: spontaneous oxidation of the Si surface by air exposure; Step 4: removal of the GaAs nanocrystals by annealing; Steps 5 and 6: formation of Ga droplets inside the holes and subsequent evaporation of the Ga droplets by annealing; Step 7: Ga-catalyzed NW growth. Reprinted with permission from E. S. Koivusalo, T. V. Hakkarainen, M. Guina and V. G. Dubrovskii, Sub-Poissonian narrowing of length distributions realized in Ga-catalyzed GaAs nanowires, Nano Letters **17**, 5350–5355 (2017). Copyright (2017) American Chemical Society

diffusion effects may affect this picture, which seems more relevant for self-catalyzed III–V NWs. All these questions require further studies.

We now present one example of sub-Poissonian LDs observed in ensembles of self-catalyzed GaAs NWs [30] (more examples are given in Ref. [31]). The Ga-catalyzed GaAs NWs of Ref. [30] were grown by MBE on p-Si(111) substrates by the procedure which is presented step-by-step in Fig. 45. Before the first growth step, the Si(111) substrates were dipped in HF in order to remove the native oxide and immediately transferred to vacuum where they were first annealed at 275 °C for 1 h and then at 700 °C for 10 min. Then GaAs nanocrystals were grown by droplet epitaxy; (1) Ga droplets were first formed by depositing 0.09 MLs of Ga at 550 °C and then (2) crystallized into GaAs by a 10 min As_2 exposure. The sample temperature in step 1 is a critical parameter that defines the density of the nucleation sites. In step 3, the sample was removed from vacuum and exposed to air for 18 h in order to form an oxide layer on the Si(111) surface. In the following step (4), the sample was transferred back to vacuum where it was annealed at 660 °C for 30 min in order to remove the GaAs nanocrystals and reveal oxide-free nucleation sites. In the final surface preparation steps (5) Ga droplets were formed in the nucleation sites by depositing Ga for 60 s at 640 °C using a growth rate of 0.3 ML/s, and (6) subsequently removed by annealing at 660 °C for 10 min. The purpose of steps 5 and 6 is to prepare the nucleation sites for subsequent NW growth. By introducing these additional steps to the process presented in Ref. [101], a high vertical yield of 70% is obtained, without having to use Ga pre-deposition at the beginning of the NW growth. Finally, in step (7) the NW growth was initiated by simultaneously opening the Ga shutter and As valve and using a sample temperature of 640 °C. The Ga growth rate was 0.3 ML/s and As_2/Ga flux ratio 9. The NW samples were grown for different times : 3 min, 6 min, 20 min, 40 min, 50 min, and 80 min. The 50 min sample was grown on a template having nucleation site density of 2×10^8 cm^{-2} while a slightly higher density of 4×10^8 cm^{-2} was used for the other samples, resulting in NW densities of 0.7×10^8 cm^{-2} and 1.5×10^8 cm^{-2}, respectively.

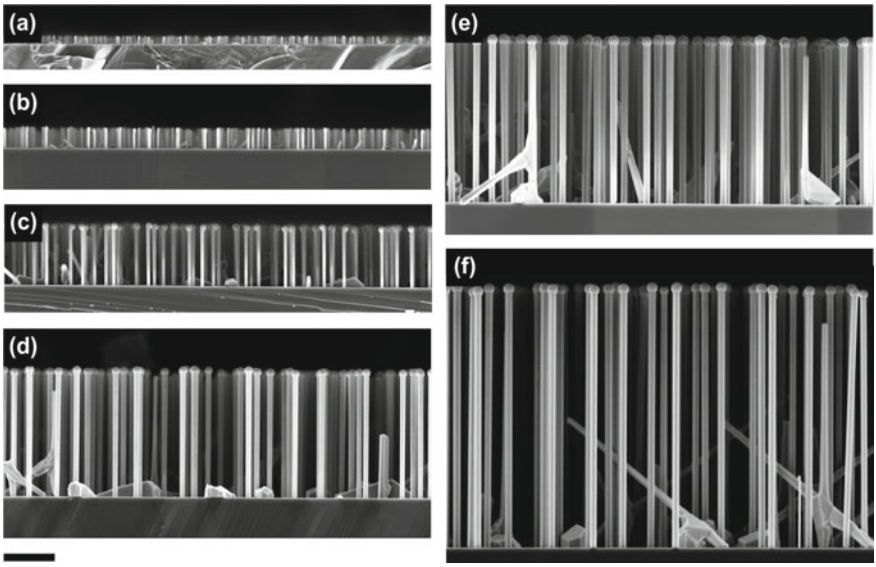

Fig. 46 Cross-sectional SEM images of Ga-catalyzed GaAs NWs grown for 3 min (**a**), 6 min (**b**), 20 min (**c**), 40 min (**d**), 50 min (**e**), and 80 min (**f**). Scale bar is 1 μm. Reprinted with permission from E. S. Koivusalo, T. V. Hakkarainen, H. V. A. Galeti, Y. G. Gobato, V. G. Dubrovskii and M. D. Guina, Deterministic switching of the growth direction of self-catalyzed GaAs nanowires, Nano Letters **19**, 82–89 (2019). Copyright (2019) American Chemical Society

Figure 46 shows cross-sectional SEM images of the NWs after different growth durations. It is evident from the SEM images that the NWs obtained by this method remains remarkably uniform throughout the growth process from 3 min up to 80 min growth duration. Statistical analysis shows the linear time dependence of the NW length, with the axial growth rate V of 62.8 nm/min. The NW diameter increases first linearly and then saturates as the NW length increases, probably reaching the stable diameter as described in Sect. 7. The measured LDs of these NWs after different growth times remain surprisingly narrow as shown in Fig. 47, particularly for longer growth times. The mean NW length is given by $\langle L \rangle = Vt$, with $V = 62.8$ nm/min as the effective influx of As. The measured LDs after 40, 50, and 80 min of growth are markedly sub-Poissonian, as shown in Fig. 48. For example, the variance of 2480 nm long NWs obtained after 40 min of growth is only 367 nm^2, which is more than twice smaller than the Poisson variance of 808 nm^2 for this mean length.

$$\sigma_P^2 = h\langle L \rangle \tag{8.36}$$

It is clear from Fig. 48 that the LD variance first increases with time, then almost saturates at the sub-Poissonian value and starts to increase again for longer NWs, remaining, however, sub-Poissonian even for ~5200 nm long NWs. The model of Ref. [30] thus assumed (i) the initial nucleation-induced broadening of the LD induced

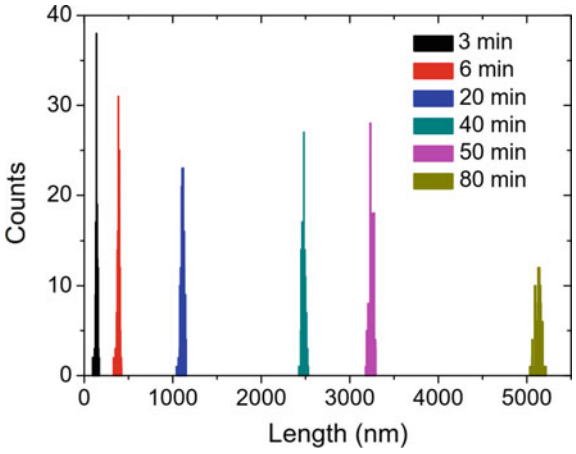

Fig. 47 Measured length histograms of Ga-catalyzed GaAs NWs at $t = 3$, 6, 20, 40, 50, and 80 min. Reprinted with permission from E. S. Koivusalo, T. V. Hakkarainen, H. V. A. Galeti, Y. G. Gobato, V. G. Dubrovskii, and M. D. Guina, Deterministic switching of the growth direction of self-catalyzed GaAs nanowires, Nano Letters **19**, 82–89 (2019). Copyright (2019) American Chemical Society

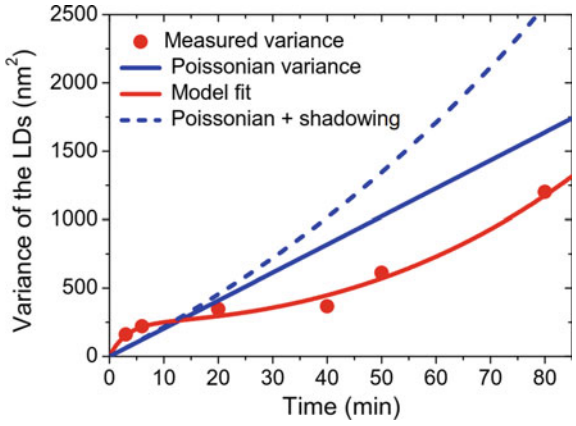

Fig. 48 Measured variance of the GaAs NW LDs versus the growth time (symbols). Solid straight line shows the corresponding Poisson variance $\sigma_P^2 = h\langle L\rangle = hVt$, with $V = 62.8$. The red line shows theoretical fit by Eq. (8.37) which includes the shadowing effect. The dashed blue line corresponds to the Poissonian growth with shadowing. Reprinted with permission from E. S. Koivusalo, T. V. Hakkarainen, H. V. A. Galeti, Y. G. Gobato, V. G. Dubrovskii and M. D. Guina, Deterministic switching of the growth direction of self-catalyzed GaAs nanowires, Nano Letters **19**, 82–89 (2019). Copyright (2019) American Chemical Society

by random nucleation from the substrate surface, (ii) the complete suppression of the fluctuation-induced broadening by nucleation antibunching, and (iii) additional broadening due to the shadowing effect, which becomes important for longer NWs. Broadening of the LDs by partial shadowing of the As flux, including re-emitted flux, can be understood simply from the fact that longer NWs are less shadowed and hence grow faster, while shorter NWs are more shadowed and grow slower than the longer ones. As a result (see Ref. [30] for the details), the model expression for the variance is given by

$$\sigma^2 = \sigma_*^2\left(1 - e^{-\langle L\rangle/L_*}\right) + hL_0\left(e^{\langle L\rangle/L_0} - 1 - \langle L\rangle/L_0\right). \tag{8.37}$$

This equation shows that, in the absence of Poissonian broadening, the length variation is determined by the two factors—the initial nucleation randomness of the NWs emerging from the substrate (leading asymptotically to the time-independent variance σ_*^2 with the characteristic saturation length L_*) and the additional broadening due to the shadow effect (which becomes important for long NWs having a mean length on the order of the shadowing length L_0).

The line in Fig. 48 demonstrates the excellent fit to the measured variance obtained from Eq. (8.37) with $\sigma_*^2 = 250$ nm^2, $L_* = 200$ nm, and $L_0 = 6000$ nm. The dashed line in Fig. 48 corresponds to the Poissonian growth influenced by the shadow effect, with the same L_0 of 6000 nm and shows that the LDs without nucleation antibunching would be even broader than Poissonian in this case. Saturation of the variance in the intermediate growth stage requires that the nucleation step is fast (a short L_*) and the shadowing length L_0 is large. The nucleation variance σ_*^2 depends on the preparation technique used for Ga droplets, the type of the substrate/oxide, and the nucleation rate of stable NWs emerging from Ga droplets which may be changed by the As flux. In comparison to the previous work [101], by eliminating the Ga pre-deposition step in the beginning of the NW growth, we were able to reduce the incubation time and significantly reduce the saturation level of the variance.

Overall, the results presented in this section and in Sect. 7 suggest that remarkable size uniformity can be achieved within ensembles of III–V NWs, particularly those obtained in the self-catalyzed approach. Together with a tremendous progress in growing such NWs on Si substrates, and introducing high quality heterostructures in NWs, this may open a new path for monolithically integrated NW-based photonic devices and optoelectronic circuits, with a high degree of NW ordering in terms of both radii and length.

9 Semiconductor Alloys in Nanowires

9.1 Introduction

In the field of planar (2D) epitaxial structures, it is well known that the range of possible applications is vastly extended by using alloys instead of pure elemental semiconductors or simple stoichiometric binary III–V or II–VI compounds. This allows one to access band gap energies intermediate between those of the end components of the alloy. Moreover, in the frequent case where alloy composition variations induce changes of lattice parameter, one can play on the strain exerted by a substrate or by various parts of a heterostructure on each other to tune further the electronic and optical properties of the alloys. In this respect, the 1D geometry has two important consequences that distinguish NWs from planar structures: first, because of strain relaxation at the free sidewalls, one can associate without creating extended defects, materials that are much more lattice-mismatched than would be possible in the 2D case; second, the strain fields are generally less homogeneous and more complex. These points will be treated in Sect. 10.

Many semiconductor alloys have been fabricated in the form of NWs. This includes alloys between group IV elements, primarily Si–Ge [102] but also Ge–Sn [103], and many III–V and II–VI ternary and even quaternary alloys (for an overview, see, e.g., Ref. [104]). The aim may be to obtain fully or locally homogeneous NWs, or else to create a controlled composition gradient along the axis. Alloys may also form unwantedly when growth fluxes are switched to form an axial heterostructure between nominally non-alloyed sections (e.g., Si_xGe_{1-x} forms at the interface between pure Si and pure Ge sections) or when, despite steady growth conditions, the relative influx of the various components changes with time (for instance, because of different diffusion lengths).

Quite generally, the major question is that of the dependence of the alloy composition on the growth conditions, which here include, in addition to what we considered before, the growth fluxes of all the elements that are alloyed in the NW (or at least their ratios). Alloys may form in NW shells but these grow in the vapor–solid mode, whereas we concentrate on VLS growth. A key point is then to describe theoretically the relationship between liquid and solid compositions. This in turn is an essential step in the modeling of the effect of the growth conditions (fluxes and temperature) on the solid formed; however, this all-important question requires in addition the description of how the liquid droplet is fed by the external fluxes, which is in itself a complicated question (see Sect. 6).

9.2 Description of the Vapor, Liquid and Solid Phases

For each phase ϕ, the number n_φ of constituents must be distinguished from the number of independent compositional parameters i_φ required to describe the thermodynamic state of this phase. Usually, $n_V = n_S$, since each element of the solid is provided by a separate vapor flux, be it single atoms or molecules. For self-catalyzed III–V growth, $n_L = n_S$ but $n_L > n_S$ when a foreign catalyst is used. The vapor state is characterized by fluxes or partial pressures, so that in general $i_V = n_V$ (3 for self-catalyzed growth of ternary alloys, 2 for Ge_xSi_{1-x}).

We shall consider the simplest case, $i_S = 1$, of a solid composition defined by a single atomic concentration x (for species A, that of the other species B being $1 - x$). This holds for binary alloys of elementary semiconductors, such as Ge_xSi_{1-x}, and for ternary alloys of compound semiconductors (in the latter case, the numbers of atoms on each sublattice are equal: atomic species A, B sharing a sublattice while the other is fully occupied by species C produce a pseudo-binary $A_xB_{1-x}C$ alloy). With $i_S = 1$, we have $n_L = 3$, $i_L = 2$ for self-catalyzed growth: the liquid is a genuine ternary alloy, but its state is defined by two atomic concentrations that add up to 1 (e.g., y_{Al} and y_{As} for $Al_xGa_{1-x}As$ NWs, with $y_{Ga} = 1 - y_{Al} - y_{As}$). With a foreign catalyst, $i_L = 3$ or more (if a mixture of foreign metals is used).

9.3 Dependence of Alloy Composition on Vapor Fluxes

It is only in the simplest cases that one can model how the alloy composition x depends on the vapor fluxes. In particular, in stationary VLS growth, the rate at which each component enters the droplet must equal its rate of consumption. However, an element may reach the liquid via various pathways (vapor, surface diffusion, re-emission; see Sect. 3); conversely, in addition to solid growth, it may be removed from the liquid by desorption or reverse diffusion along the sidewalls.

Following Dubrovskii [105], if the vapor composition is defined by

$$z = \frac{I_A}{I_A + I_B}, \tag{9.1}$$

with I_A and I_B the atomic contents of the MBE fluxes or CVD flows, the fraction of element A effectively available for growth is

$$Z = \frac{V_A}{V_A + V_B}, \tag{9.2}$$

where V_A or V_B is given by the right sides of Eq. (3.4) for group III elements and of Eq. (3.5) for group V elements. The two cases are however quite different. Equation (3.4) assumes a constant surface diffusion flux to the droplet, independent of the liquid composition. This may be acceptable for mixed group III alloys. In

this case, the stationary growth constraint $x = Z$ solves the problem. If however surface diffusion depends on the chemical potentials in the liquid, or if the liquid also loses atoms by desorption, with a desorption flux that depends strongly on the concentration of the desorbing species in the droplet, as in the case of mixed group V alloys, then equation $x = Z$ is still valid, but Z now depends on liquid composition and the equation needs to be solved self-consistently.

The simple group III case is a rare instance where we can ignore the state of the liquid. In general, during steady-state growth, the liquid composition will adjust to provide a nucleation rate (or more generally a growth rate) that balances the influx of the various elements, but we have to determine this composition.

9.4 *Dependence of Solid Composition upon Liquid Composition*

Except in the simplest cases treated in Sect. 9.3, determining which solid composition a liquid of a given composition will produce is an essential step of VLS growth modeling. This will in particular give the solid composition profile in a NW as a function of evolving liquid composition, for instance, during heterostructure formation. This can in turn be related in a self-consistent fashion to the changes in the growth fluxes, as will be illustrated in Sect. 10. We now review briefly several approaches (items (a) to (d)) for the solid–liquid composition dependence. Note that all quantities of interest, in particular the chemical potentials, depend on temperature in addition to compositions. This dependence is kept implicit, the calculations being performed at a given temperature.

(a) For a ternary compound semiconductor $A_xB_{1-x}C$, a simple description of the solid–liquid dependence is derived in the regular growth model (Sect. 3). Generalizing Eq. (3.14), the rates of formation of the AC and BC pairs from a liquid with atomic concentrations y_i are assumed to be $K_A y_A y_C$ and $K_B y_B y_C$, respectively, with K_A, K_B the appropriate rate constants. It follows that

$$x = \frac{\varepsilon\, y}{1 + (\varepsilon - 1)y}, \tag{9.3}$$

with $y = \frac{y_A}{y_A + y_B}$ and $\varepsilon = \frac{K_A}{K_B}$. Equation (9.3) is analogous to the Everett isotherm for adsorption and becomes the Langmuir isotherm for $\varepsilon >> 1$.
Dubrovskii showed that, within this model and assuming that the rates of loss of the various NW components by the droplet (via desorption or diffusion) are proportional to their respective concentrations, the steady-state relation between solid (x) and vapor (z) can be determined analytically [52].
The other approaches make use, in various ways, of the differences of chemical potential $\Delta\mu_k$ of each alloy constituent unit k between liquid and solid phases (these units are atoms for group IV alloys and pairs for ternary compounds; see

Eq. (3.7) and Ref. [14]). The calculation of the chemical potentials of use for VLS growth of III–V NWs, with or without foreign catalyst, has been discussed in Sect. 6.2. We describe briefly these approaches.

(b) It may simply be assumed that the rate of incorporation of each unit is proportional to the relevant difference of chemical potential [107]. A difficulty is that the proportionality constants are a priori unknown. The underlying idea is that ML composition is defined not at nucleation stage (since critical nuclei are very small) but during its extension over the top facet.

(c) Another approach, on the contrary, makes use of equilibrium thermodynamics. Let us illustrate this in the case of mixed group III self-catalyzed III–V NWs, such as $A_xB_{1-x}As$. Since $i_S = 1$ and $i_L = 2$, there are in total three independent compositions for the L–S system. Equilibrium fixes $\Delta\mu_{AC} = 0$, $\Delta\mu_{BC} = 0$ for the two pairs. This gives the well-known result that the solid composition x is fixed by a single concentration in the liquid, for instance y_A. The method consists in using this equilibrium relationship also during growth. This may look too simplistic, since NWs grow well out of equilibrium. The underlying idea is that, for such systems, the growth rate is set by the group V concentration y_C in the liquid whereas the relative incorporation of A and B into the solid is more likely to be governed by group III concentrations in the liquid phase and barriers for attachment to the solid, which presumably depend only weakly on y_{As}. Note that this does not make any assumption about the composition of the solid nucleus that mediates the formation of each ML, but simply supposes that this nucleus is sufficiently small for the ML composition to be determined by post-nucleation attachment kinetics [108, 109]. This effective 'decoupling' between group III and group V atoms was checked experimentally for MBE-grown $Al_{1-x}Ga_xAs$ NWs [108, 109].

(d) Probably the most sophisticated models proposed so far rely on a version of the CNT (see Sect. 3) developed to handle the nucleation of a phase of a priori unknown composition. The formation energy F of any 2D island (Sects. 3 and 6) now depends not only on its size but also on its composition (or alternatively, on the absolute numbers of both types of atoms or pairs that it contains). Accordingly, the critical island is defined by critical size (Sect. 3) and critical composition. In 1950, this problem was solved elegantly by Reiss, albeit in quite a different context [110]. The formation energy of an island of radius r and composition x is

$$F(r, x) = -c_1 r^2 h \, \Delta\mu \, (y_A, y_C, x) + c_2 \gamma_e r h, \tag{9.4}$$

where c_1, c_2 are constants depending on nucleus geometry and γ_e the surface (or edge) energy of the 2D island, introduced in Sect. 3. Note that, in this out of equilibrium situation, we retain the full dependence of $\Delta\mu$ on three independent compositions. Reiss shows that the size and composition of the critical island are the coordinates of the saddle point, solutions of system $\frac{\partial F}{\partial r} = 0$, $\frac{\partial F}{\partial x} = 0$, with $\frac{\partial^2 F}{\partial r^2} < 0$, $\frac{\partial^2 F}{\partial x^2} > 0$.

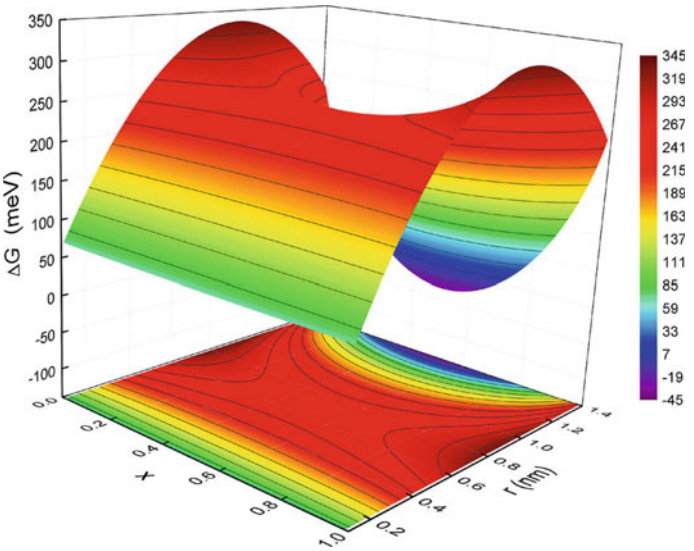

Fig. 49 Variation of the formation energy F of an $Al_xGa_{1-x}As$ nucleus as a function of its size r and fractional AlAs content x, calculated at temperature $T = 883$ K using the thermodynamic data of Li et al. [147]. Nucleus edge energy is $\gamma_e = 0.123$ J m^{-2} independently of x. Fixed liquid composition: $y_{Al} = 0.002$, $y_{As} = 0.01$. Reprinted with permission from F. Glas, Comparison of modeling strategies for the growth of heterostructures in III–V nanowires, Crystal Growth & Design **17**, 4785–4794 (2017). Copyright (2017) American Chemical Society

The conditions on the r derivatives are similar to the standard CNT conditions. In turn, the composition of the critical island minimizes the standard nucleation barrier calculated for any fixed island composition. Note that all derivatives should be taken at given liquid composition. Figure 49 gives an example of such a saddle point in the formation energy surface for the self-catalyzed (Al,Ga,As) system. Only introduced in 2017 in the field of alloy NW growth, this nucleation-based approach is now used in systems of ever increasing complexity [84, 105, 106, 109, 111–113].

However, finding the critical island is not the end of the story, since its size is usually much smaller than that of the NW top facet. What is required is the composition of the full ML that forms by lateral growth of the critical island. The simplest assumption is that the whole ML adopts the critical island composition [105, 106, 109] (note that this assumption is opposite to that underlying approach (b)). Although difficult to justify, it was shown to lead to accurate predictions of the composition profiles in $Al_xGa_{1-x}As$ NWs, measured with ML axial resolution [109] (see Sect. 10). Based on the discussion by Dubrovskii and coworkers of the growth rate of supercritical islands in the non-alloyed case [6, 50], Johansson and Ghasemi calculated formally the rates of incorporation to the island of the two species constituting the alloy [114]. However, they concentrated on the limit of large islands. An accurate description of the average composition of the ML will require further investigations.

Another issue is that of the possible dependence of edge energy γ_e (Eq. 9.4) on island composition x, the so-called Renninger-Wilemski problem. This option was eliminated by Reiss in the case of liquid droplets growing from a vapor, for reason of surface segregation of the constituent with lowest surface tension [110]. It is not clear that this argument should hold for the very small solid nuclei that are typical of VLS growth. However, Glas showed that the already mentioned composition profiles in $Al_xGa_{1-x}As$ NWs were better fitted under this assumption than by supposing that γ_e increases with the Al content of the island [109].

In any case, assuming a composition-independent edge energy simplifies the problem of the liquid–solid composition dependence. From Eq. (9.4), maximizing F is then equivalent to minimizing $\Delta\mu\,(y_A, y_C, x)$ as a function of x for the given liquid composition (y_A, y_C). This difference reads

$$\Delta\mu\,(y_A, y_C, x) = x\,\Delta\mu_{AC} + (1-x)\,\Delta\mu_{BC}, \tag{9.5}$$

with:

$$\Delta\mu_{AC} = \mu_A^L + \mu_C^L - \mu_{AC}^S, \quad \Delta\mu_{BC} = \mu_B^L + \mu_C^L - \mu_{BC}^S. \tag{9.6}$$

In these expressions, at a given temperature, the chemical potentials μ_i^L in the liquid (Eq. (6.14)) depend only on liquid composition whereas the chemical potentials μ_{AC}^S, μ_{BC}^S of the two III–V pairs in the solid depend only on x. In the regular solution model (see Sect. 6.2), which has been widely used for compound semiconductors, the mixing enthalpy of the solid alloy simply writes $\omega_S x\,(1-x)$, with ω_S the interaction parameter, and the entropy of mixing is $-k_B[x\ln x + (1-x)\ln(1-x)]$. Then

$$\mu_{AC}^S = \mu_{AC}^{AC} + \omega_s(1-x)^2 + k_BT\ln x, \quad \mu_{BC}^S = \mu_{BC}^{BC} + \omega_s x^2 + k_BT\ln(1-x), \tag{9.7}$$

where μ_{AC}^{AC} and μ_{BC}^{BC} are the chemical potentials of AC and BC pairs in binaries AC and BC, which depend only on temperature. From Eqs. (9.5)–(9.7), we find that condition $\partial\Delta\mu/\partial x = 0$ is equivalent to $\Delta\mu_{AC} = \Delta\mu_{BC}$. Note that these two quantities depend on liquid and solid compositions and that this constraint is a priori weaker than the equilibrium condition $\Delta\mu_{AC} = \Delta\mu_{BC} = 0$. Using Eqs. (9.6)–(9.7), the saddle point condition $\Delta\mu_{AC} = \Delta\mu_{BC}$ can be rewritten as an implicit relation between the liquid and solid compositions [105–107]:

$$\phi(y_A,\ y_C) = k_BT\ln\left(\frac{x}{1-x}\right) - \omega_s(2x-1), \tag{9.8}$$

with:

$$\phi(y_A,\ y_C) = \mu_A^L - \mu_B^L - \left(\mu_{AC}^{AC} - \mu_{BC}^{BC}\right). \tag{9.9}$$

Dubrovskii noted that, if the liquid is also assumed to be a regular solution (see Sect. 6.2), which means (in the self-catalyzed case) that its mixing enthalpy contains only the three interaction terms $\omega_{ij}^L y_i^L y_j^L$ associated to the three pairs of unlike atoms (with ω_{ij}^L the interaction parameter for pair $(i,\ j)$), Eq. (9.9) becomes a simple implicit relation linking the compositions of liquid and solid:

$$\frac{y}{1-y}\exp\left(-2\,y_{tot}\,\frac{\omega_{AB}^L}{k_BT}\,y\right)=\frac{x}{1-x}\exp\left[-\frac{\omega_s}{k_BT}\,(2x-1)-\alpha\right], \tag{9.10}$$

where $y=\frac{y_A}{y_A+y_B}$, $y_{tot}=y_A+y_B$ and

$$\alpha=\mu_A^A-\mu_B^B-\left(\mu_{AC}^{AC}-\mu_{BC}^{BC}\right)+\omega_{AB}y_{tot}+\left(\omega_{AC}-\omega_{BC}\right)(1-y_{tot}) \tag{9.11}$$

with μ_i^i the chemical potential of element i in its pure liquid form [105, 106].

The concentrations of the volatile group V elements (except possibly Sb) are known to be very low in any catalyst liquid. Hence, for mixed P–As systems, $y_{tot}<<1$ and Eq. (9.10) becomes an explicit relation between atomic fractions in liquid and solid:

$$y=\frac{x}{x+(1-x)\ \exp\left[\frac{\omega_s\,(2x-1)+\alpha'}{k_BT}\right]}, \tag{9.12}$$

with $\alpha'=\mu_A^A-\mu_B^B-\left(\mu_{AC}^{AC}-\mu_{BC}^{BC}\right)+\omega_{AB}+\omega_{AC}-\omega_{BC}$ independent on compositions.

For mixed group III systems, the full calculations show that very wide ranges of solid compositions can be achieved with very composition-asymmetric liquids: any $Al_xGa_{1-x}As$ solid (except nearly pure AlAs) can be obtained with a very low Al concentration in the liquid (Fig. 50, left) and any $In_xGa_{1-x}As$ or $In_xGa_{1-x}P$ solid (save nearly pure GaAs or GaP) with a very low Ga concentration in the liquid (Fig. 50, right). This is related to the very different affinities of the three group III atoms for a given group V atom (P or As), themselves related to the differences of cohesive energies of the three solid binaries (these affinities increase from In to Ga to Al). Moreover, for self-catalyzed systems, $y_{tot}\approx 1$. Then, Eq. (9.12) with a constant α' is again a very good approximation; specifically, $\alpha'=\mu_A^A-\mu_B^B-\left(\mu_{AC}^{AC}-\mu_{BC}^{BC}\right)+\omega_{AB}$ for $Al_xGa_{1-x}As$ and $\alpha'=\mu_A^A-\mu_B^B-\left(\mu_{AC}^{AC}-\mu_{BC}^{BC}\right)-\omega_{AB}$ for $In_xGa_{1-x}As$ or $In_xGa_{1-x}P$.

Hence, for ternary III–V alloys, in the liquid, one NW element is much more abundant than all the others (namely, the group III element for mixed group V systems, In for mixed In–Ga or In–Al systems, Ga for mixed Al–Ga systems). An important consequence is that the regular solution model (with only pair interactions, possibly in a reduced number) is usually very accurate, since higher order concentration products are extremely small. This analysis was developed rigorously in references [105, 106], where more details can be found.

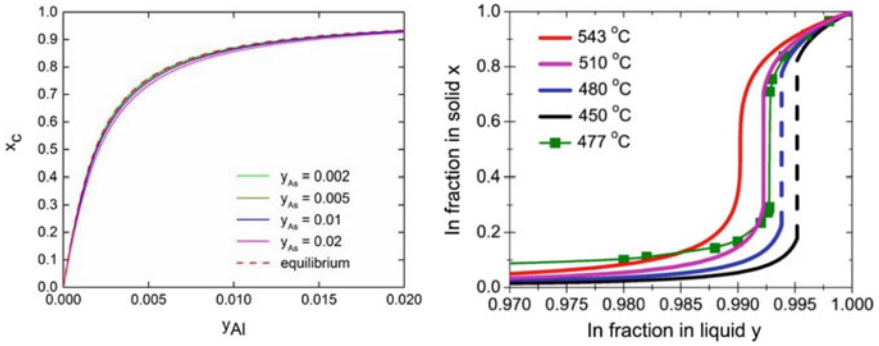

Fig. 50 Left: (Al,Ga,As) system at $T = 873$ K. Variation of the Al concentration in the critical $Al_xGa_{1-x}As$ nucleus as a function Al concentration in liquid, for various As concentrations y_{As} in the liquid. The dashed curve gives the variation at equilibrium. Reprinted with permission from F. Glas, Comparison of modeling strategies for the growth of heterostructures in III–V nanowires, Crystal Growth & Design **17**, 4785–4794 (2017). Copyright (2017) American Chemical Society. Right: (Ga,In,As) system. Variation of the In concentration in the critical $In_xGa_{1-x}As$ nucleus as a function In concentration in liquid at different temperatures for $c_{tot} = 0.99$. Reprinted from Material & Design, Vol. 132, V. G. Dubrovskii, A. A. Koryakin and N. V. Sibirev, Understanding the composition of ternary III–V nanowires and axial nanowire heterostructures in nucleation-limited regime, pp. 400–408, Copyright (2017), with permission from Elsevier

This said, it is remarkable that, at least for mixed group III alloy, the simple quasi-equilibrium model (c) and the nucleation model (d) often give very similar results. This has been studied in detail for the lattice-matched $Al_xGa_{1-x}As$ system [109] (see Fig. 50, left) but it is also the case for the $In_xGa_{1-x}As$ or $In_xGa_{1-x}P$ systems [115]. This can be understood as follows. From Eq. (9.6), the saddle point condition $\Delta\mu_{AC} = \Delta\mu_{BC}$, which yields nucleus composition x for a given liquid composition (y_A, y_C), rewrites $\mu_A^L - \mu_B^L = \mu_{AC}^S - \mu_{BC}^S$, where the left-hand side depends only on (y_A, y_C) and the right-hand side only on x. If the chemical potentials μ_A^L, μ_B^L of the group III species depend little on the group V concentration y_C, then x depends effectively only on y_A, and this dependence can be computed for an arbitrary value of y_C, for instance, that corresponding to equilibrium. This explains the near-coincidence between the equilibrium and nucleation models for mixed group III alloys.

10 Heterostructures in Nanowires

NWs offer great flexibility for associating different materials in a single nanostructure, which opens broad fields of basic research and applications. The 1D geometry of NWs lends itself to two elementary types of combinations: in axial heterostructures, material B is stacked on top of material A; in radial heterostructures, a shell of material

B is wrapped around a core of material A. These can be elaborated into superlattice-type multiple axial or core–shell structures but also into mixed heterostructures, for instance, a quantum size section inserted axially between two barriers can be wrapped in a barrier shell, to produce a genuine quantum dot. In addition to these compositional heterostructures, crystal phase heterostructures, associating the cubic and hexagonal crystalline forms of the same material can be formed in NWs [116, 117].

Standard axial heterostructures may be fabricated in the VLS mode by switching the growth fluxes. This is not possible for radial heterostructures, which are fabricated in the VS mode, with solid B nucleating on an already formed A NW directly from the vapor phase. Since this chapter deals with VLS, we will only consider axial heterostructures.

Heterostructures frequently associate materials with different lattice parameters. We first recall briefly the specific features and advantages of axial heterostructures in terms of strain relaxation, as compared with 2D structures, although these features are not specific to VLS-grown NWs. In the rest of this section, we will then discuss the VLS growth of axial heterostructures.

10.1 Elastic and Plastic Strain Relaxation in Axial Heterostructures—Critical Dimensions

The sidewalls of the NWs are free surfaces which permit a very efficient elastic relaxation. This has two main consequences: the strain field is more complex and less homogeneous than in planar heterostructures and the usually deleterious plastic relaxation is hindered. Let us assume that, on top of a NW stem of radius R of material A, we grow a "layer" of thickness h of material B with larger stress-free (intrinsic) lattice parameter (this applies to elastically isotropic or cubic materials; for hexagonal crystals, several lattice parameters come into play). We first assume that strain relaxation remains elastic (no extended defect forms). At the very beginning of growth, since $h << R$, the system is in a quasi-2D state: the layer contracts in-plane to adapt to the stem lattice parameter and expands quadratically along the NW axis. Very soon, however, strain starts distributing between layer and stem because strain relaxation of both parts is possible at the sidewalls while maintaining a coherent interface; the elastic energy stored in the system is, therefore, lower than in the 2D case (for the same volume of layer). This makes less likely the formation of interfacial dislocations. When h becomes of the order of R, the in-plane parameter at the top of the layer approaches its strain-free value and further deposit is virtually unstrained. Following Glas [8, 10], this effect may be quantified by introducing function $f(\rho) = W_e^{NW} \big/ W_e^{2D}$ of aspect ratio $\rho = h \big/ (2R)$, with W_e^{NW} the elastic energy stored in the whole system and W_e^{2D} the elastic energy in a cylinder of radius R cut in a 2D system with the same layer thickness h (for a semi-infinite substrate, W_e^{2D} is entirely stored in the layer) (Fig. 51). Then, $f(\rho) \rightarrow 1$ when $\rho \rightarrow 0$. Conversely, for $h >> R$, W_e^{NW} saturates while W_e^{2D} still scales with the volume

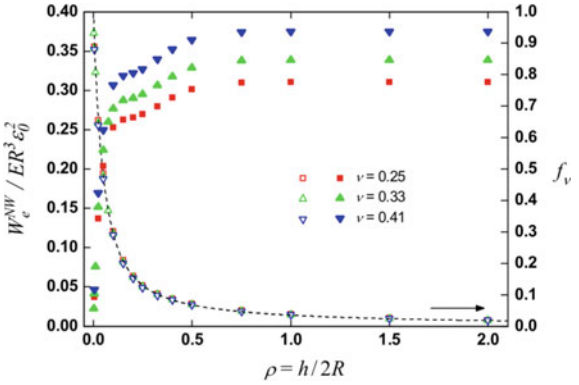

Fig. 51 Full symbols, left scale: Variation with layer aspect ratio ρ of the total elastic energy stored in the NW (without plastic relaxation), for an isotropically elastic system with identical elastic parameters in stem and layer, and for three values of Poisson ratio ν. This energy is normalized as indicated, with E Young's modulus, R the NW radius, and ε_0 the relative misfit between stem and layer. Empty symbols, right scale: Ratio between this energy and the energy in the same volume of a 2D system. Reprinted from Semiconductors and Semimetals, vol. 93, F. Glas, Strain in nanowires and nanowire heterostructures, pp. 79–123, Copyright (2015), with permission from Elsevier

$\pi R^2 h$ of the layer, hence $f(\rho) \sim \rho^{-1}$. By performing numerous finite elements numerical calculations, Glas showed that a very good approximation of function f, for elastically isotropic materials with identical elastic constants, is given by

$$f(\rho) = \frac{1 + \tau_1 \rho \ \exp(-\tau_3 \rho)}{1 + \tau_2 \rho}. \tag{10.1}$$

where parameters τ_i ($i = 1, 2, 3$) depend only on Poisson's ratio of the materials [10, 118]. This is a refinement of Glas' original approximation, with numerator equal to 1 [8]. The elastic energy is considerably reduced with respect to the 2D case, for instance, to about a tenth of its 2D value for $\rho \approx 0.12$ (Fig. 51).

Let us now consider the plastic relaxation of this system, which may occur via the introduction of dislocations with an edge-type component in the stem/layer interface. For given NW radius R and layer thickness h, we compare W_e^{NW} with W_p^{NW}, the energy of the system with one or several interfacial dislocations. The critical layer thickness, if any, is the thickness beyond which $W_e^{NW} > W_p^{NW}$. Indeed, W_p^{NW} includes (in addition to a reduced elastic energy) an energy associated with the dislocation core, which (neglecting possible atomic rearrangements at the intersection with the sidewalls) is proportional to the total dislocation length, and hence to R, and independent of h, of the precise location of the defects in the interface and even of their number. Hence, for small h, $W_p^{NW} > W_e^{NW}$. Calculations of the variation of the critical layer thickness h_c with NW radius have been performed by Glas [8, 10]. h_c tends to the 2D critical thickness when $R \to \infty$ and increases with decreasing R. Whereas in the 2D case, W_e^{2D} scales indefinitely with h and always becomes larger than the energy in presence of dislocations (which increases only as $\ln(h)$), this is

not necessarily the case for a NW. Actually, for any misfit ε_0, $h_c(R)$ becomes infinite for some critical radius $R_c(\varepsilon_0)$. When $R < R_c(\varepsilon_0)$, it should be possible to grow a layer of arbitrary thickness without introducing dislocations.

Glas gave a simple analytical formulas that allows one to determine the critical radius as a function of misfit. Since R_c typically amounts to several tens of nm even for misfits of several % (for which the 2D critical thickness may be subnanometric), NWs having this radius (or less) are easily fabricated in most systems. Moreover, the very existence of a critical radius can be demonstrated on purely dimensional arguments [8]. We saw that, at large h, the layer (and hence the stem) are substantially strained only over a height of order R. Hence, the limit of W_e^{NW} at large h scales with R^3. We also saw that, on the other hand, W_p^{NW} contains a part scaling with R. From these different power-law dependences in R, it follows that, if the layer is thick enough, the dislocation energy always dominates, provided R is small enough. This proves the existence of a critical radius R_c below which plastic relaxation is unfavorable, whatever the layer thickness.

To conclude, lateral relaxation at the free sidewalls is a characteristic feature of NWs that enables very efficient stress relaxation. This allows for a much larger range of defect-free structures than in planar heterostructures or even in standard quantum dots structures.

10.2 VLS Growth of Axial Heterostructures

Heterostructures in NWs have been fabricated for more than 20 years. A great variety of combinations has been achieved, associating elementary semiconductors [107, 119, 120], binary III–V compounds with alternating elements of either group III [121, 122] or group V [59, 123–132, 142], as well as mixed group III [108, 133–137], group V [138, 139] or group VI [140, 141] alloys. The epitaxy techniques standardly used for the VLS growth of homogeneous NWs (see Sect. 2) have also been used for heterostructures, including MBE [119] and chemical vapor deposition (CVD) [107, 120] for Si–Ge, and MOVPE [121–124, 126–129, 132–134, 138, 139], solid source and gas source MBE [108, 131, 136, 137, 140, 141] and CBE [142, 143, 159] for compound semiconductors.

In addition to the great flexibility in terms of misfit discussed in Sect. 10.1, axial heterostructures also offer, in principle, freedom of design and ease of control, for instance, a section of material B can be sandwiched between sections of material A, its diameter set by the NW stem diameter, its height by the growth time. In practice, controlling the section height, the sharpness of the interfaces and even the composition of the material in the case of alloys, may however be challenging.

A major difficulty is commonly associated with the “reservoir effect” (Fig. 52). We mentioned in Sect. 2 that the liquid droplet acts as a reservoir of NW atoms. Whereas this is usually not a problem during the growth of a homogeneous NW, this may cause trouble for heterostructures. Indeed, during the growth of elementary semiconductor B or compound BC, B atoms reside in the droplet to ensure adequate

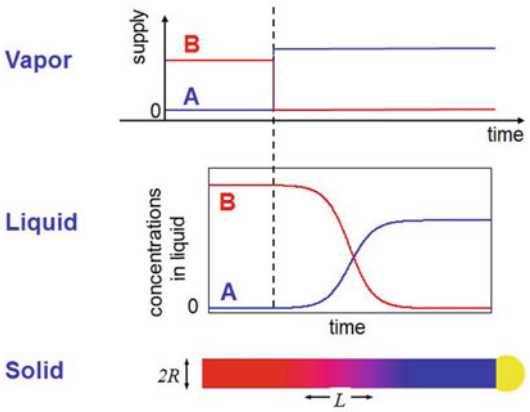

Fig. 52 Schematics of the reservoir effect, illustrating the time variations of compositions of vapor, liquid, and solid

supersaturation. Even if one switches abruptly the growth flux to A (in order to grow material A or compound AC), B will remain for some time in the droplet before it is eliminated. Elimination occurs via desorption or sidewall surface diffusion but also by incorporation in the growing NW. The joint presence of A and B in the liquid, in a proportion varying over time, thus leads to forming an A_xB_{1-x} or $A_xB_{1-x}C$ alloy, which composition evolves during growth, in other words a composition gradient. As a rule of thumb, before switching to B, the number of A atoms in the droplet scales as $\overline{y}_A R^3$, with $\overline{y}_A$ the (average) steady-state concentration for A growth. In the graded solid section, this number will distribute over a length L and hence a volume of order $L R^2$. Hence, $L \sim \overline{y}_{Al}/R$. This readily gives simple recipes for growing sharp interfaces: use small NW radii and elements diluted in the droplet. One way to reduce the solubility and the concentration of a NW element in the seed particle is to use solid catalysts. This is effective but it generates its own problems, in particular a low growth rate. Anyway, the VSS growth mode lies out of the scope of this review.

The simple linear dependence of the length of the transition region upon NW radius was checked for instance in the case of Au-catalyzed Ge/Si heterostructures [107, 119]. In Ref. [119], the proportionality constant between R and L was found to be on the order of 1. This confirms that the concentrations of group IV elements in the catalyst are of several tens of percent, as expected from the equilibrium phase diagrams of the Au–Si and Au–Ge systems [144] (see the discussion at beginning of Sect. 2 and generic Fig. 1).

According to the same simple estimate, it was long thought that heterostructures of III–V compounds alternating group V atoms offered the best prospect of interface sharpness, simply because the steady-state concentrations of As or P in the liquid catalyst (whatever it is) are much smaller than those of group III elements or elementary semiconductors. Experimentally, sharp interfaces have indeed been obtained in alternating group V systems based on the (P,As) couple [123–125, 128, 131, 139, 154]. Since P is present at an even lower concentration in the liquid than As (its equilibrium concentration is typically 5 times smaller), the P → As interface tends

to be sharper than the As → P interface [131], as expected from our simple estimate of interface width. Interfaces tend to be broader when one of the group V elements is Sb, especially at the top of the Sb-rich segments [127, 138]. This can be related to the much higher concentration of Sb in the catalyst droplet as compared with the other group V elements [145]. Since the group V species desorb from the droplet, growth interruptions further reduce the amount of species A stored in the droplet before introducing species B and hence sharpen the interfaces. This was demonstrated in the case of GaAs-GaP heterostructures [131]. Technical specificities may however degrade interface sharpness even in this favorable case, for instance, the relatively long residence time of residual group V species in the MBE growth chamber after shutter closure, due to poor pumping efficiency [131].

On the other hand, given the high group III concentrations in the liquid, the same simple argument seemed to preclude sharp transitions in mixed group III systems (and especially so in the self-catalyzed scheme, when the droplet is made of at least 99% group III atoms). Recent experimental work [108] and theoretical studies of the liquid–solid composition dependence, summarized in Sect. 9.4, have demonstrated that this is fortunately not the case: reasonably sharp interfaces may be obtained even in mixed group III heterostructures (Fig. 53). This can be understood as follows. As discussed in Sect. 9.4, the liquid is overwhelmingly composed of one of the group III elements, In the case of (In,Ga) or (In,Al) systems, Ga for the (Al,Ga) system.

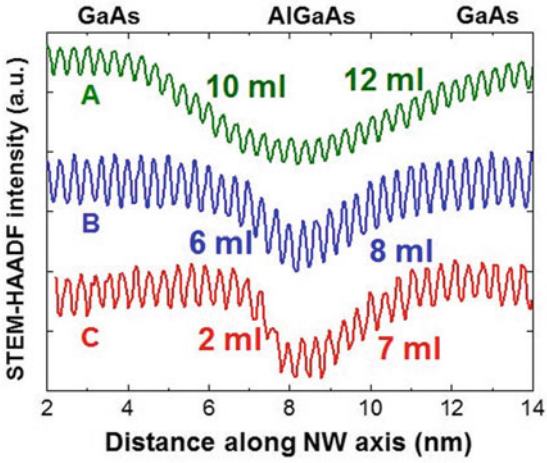

Fig. 53 STEM-HAADF intensities measured across three $Al_xGa_{1-x}As$ axial insertions grown by MBE for 5 s in a GaAs NW. Each oscillation corresponds to a single ML and the intensity averaged over an oscillation decreases when x increases. Sample A and B were grown by simply switching the Al flux on and off while maintaining the Ga and As fluxes (the latter lower for sample B than for sample A). Sample C was grown using the pre-filling technique described in the text. Reprinted with permission from G. Priante, F. Glas, G. Patriarche, K. Pantzas, F. Oehler, J.-C. Harmand, Sharpening the interfaces of axial heterostructures in self-catalyzed AlGaAs nanowires: experiment and theory, Nano Letters **16**, 1917–1924 (2016). Copyright (2016) American Chemical Society

This means, for instance, that when growing an $Al_xGa_{1-x}As$ section atop a GaAs stem, little Al is needed in the liquid to reach high Al concentrations in the solid. The necessary y_{Al} will thus be reached rapidly and the GaAs $\rightarrow$ $Al_xGa_{1-x}As$ interface will be sharp. Moreover, since little Al is stored in the droplet during alloy growth, it will be consumed rapidly when forming the reverse $Al_xGa_{1-x}As \rightarrow$ GaAs interface, which will also be sharp. This is rather satisfactory, but the interface widths measured by Priante et al. in samples with simple Ga-Al switches were still about 10 MLs (for rather thick NWs) [108] (Fig. 53, samples A and B). The interface sharpness can be improved by implementing appropriate growth strategies. In this case, Priante et al. performed a growth interruption after GaAs growth, during which the droplet was pre-filled with Al so that the first subsequently grown $Al_xGa_{1-x}As$ MLs were richer in Al. This produced a spectacular decrease of interface width to about 2 MLs [108] (Fig. 53, sample C). Other methods of manipulation of the liquid composition have been devised to improve interface abruptness [146].

10.3 Modeling the Formation of Axial Heterostructures

Modeling the dynamics of heterostructure formation, with the aim of obtaining the axial composition profile generated by non-steady growth conditions and finding conditions insuring sharp interfaces, relies on coupling the dependence of solid composition upon liquid composition (discussed in Sect. 9.4), which in itself is time-independent, with the rates at which the various elements are added to the droplet (by direct fluxes, re-emission, surface diffusion…) or removed from it (by growth, desorption…).

Let us consider again a ternary $A_xB_{1-x}C$ compound semiconductor alloy. Very generally, we may write, reasoning on full MLs, equations governing the variations of the numbers N_i of each species i in the liquid:

$$\frac{dN_A}{dt} = -\rho(\mathbf{y})\ x(\mathbf{y})\ N^{ML} + \left(\frac{dN_A}{dt}\right)_{in}(\phi_A, \mathbf{y}), \tag{10.2a}$$

$$\frac{dN_B}{dt} = -\rho(\mathbf{y})\ \left[1 - x(\mathbf{y})\right]\ N^{ML} + \left(\frac{dN_B}{dt}\right)_{in}(\phi_B, \mathbf{y}), \tag{10.2b}$$

$$\frac{dN_C}{dt} = -\rho(\mathbf{y})\ N^{ML} + \left(\frac{dN_C}{dt}\right)_{in}(\phi_C, \mathbf{y}). \tag{10.2c}$$

The first terms on the right-hand side are the rates at which each species is removed from the liquid by incorporation into the solid, with ρ the rate of ML formation (which depends on liquid composition $\mathbf{y}$, this vector representing the i_L independent compositions characterizing a given liquid; see Sect. 9.2), N^{ML} the number of atoms of each group (i.*e.,* III or V) in a ML, and $x(\mathbf{y})$ the time-independent function relating solid composition to liquid compositions, discussed in Sect. 9.4. In turn, $\left(dN_i/dt\right)_{in}$

is the net rate at which species i is added to the droplet, or removed from it, by any process except incorporation to the solid. Each rate may depend not only on the corresponding vapor flux ϕ_i but also on the composition of the liquid, which governs desorption and diffusion. All these contributions were discussed in the previous sections.

If the NW radius and the droplet contact angle are constant, the numbers N_i relate straightforwardly to concentrations y_i. A time-dependent geometry can be accounted for by adding extra equations. Note also that the rate of ML formation may depend on NW radius (this is the case for nucleation-mediated growth; see Sect. 3); the rates of input/output via diffusion or desorption also depend on NW radius.

Solving system (10.2a, b, c) yields the time dependence of the composition of the liquid and hence of the solid via the $x(\mathbf{y})$ relation. One is usually more interested in the variation of the NW composition along the NW axis. For this, in principle, the absolute growth rate ρ and input rates $\left(dN_i/dt\right)_{in}$ are not needed, but their ratios must be known. Discrete versions giving the various compositions at each ML step are sometimes used [107]. As will be seen below, additional hypotheses may reduce the number of equations.

We now briefly illustrate various ways of modeling the composition profile in heterostructures, either numerically or analytically, and using any of the four types (a)–(d) of liquid–solid composition relationship reviewed in Sect. 9.4.

System (10.2a, b, c) (or its equivalents in simpler or more complex cases) can be solved in a purely numerical fashion. This was done by Periwal et al. for Ge_xSi_{1-x} heterostructures using a type (b) composition relationship [107]. The authors show that the Si/Ge_xSi_{1-x} and Ge_xSi_{1-x}/Si are always asymmetric, irrespective of the Ge concentration or NW diameter. Another numerical solution was developed by Priante et al. for heterostructures based on self-catalyzed $Al_xGa_{1-x}As$ alloys [108]. Within the type (c) equilibrium scheme, a single concentration, *e.g.*, y_{Al}, defines the state of the liquid at a given temperature. From Eq. (10.2a), it obeys equation:

$$\frac{d\,y_{Al}}{dt} = -g\,\rho\;x(y_{Al}) + \frac{I_{Al}}{N^L}, \tag{10.3}$$

with I_{Al} the Al current (atoms per unit time) entering the droplet, g a geometrical factor and N^L the total number of atoms in the liquid. In separate experiments, the growth rate ρ was checked to be independent of solid composition for long sections of $Al_xGa_{1-x}As$ NWs, and this was assumed to hold during heterostructure formation. For an $Al_xGa_{1-x}As$ barrier inserted in a GaAs NW, post-growth ML-resolved STEM-HAADF composition measurements (see Sect. 6.1 and circles in Fig. 54, left) yielded precise values of growth rate and of total number of Al atoms delivered to the system, from which I_{Al} is easily obtained, knowing the delivery time. The observed NW geometry gave access to parameters g and N^L. Equation (10.3) could then be solved using the $x\,(y_{Al})$ relation obtained from available thermodynamic data [147]. The authors showed that the computed profiles reproduce the experiments very well [108] (Fig. 54, left). The same experiments were later modeled within the nucleation scheme (d). Equation (10.3) was used again but now the solid composition depends

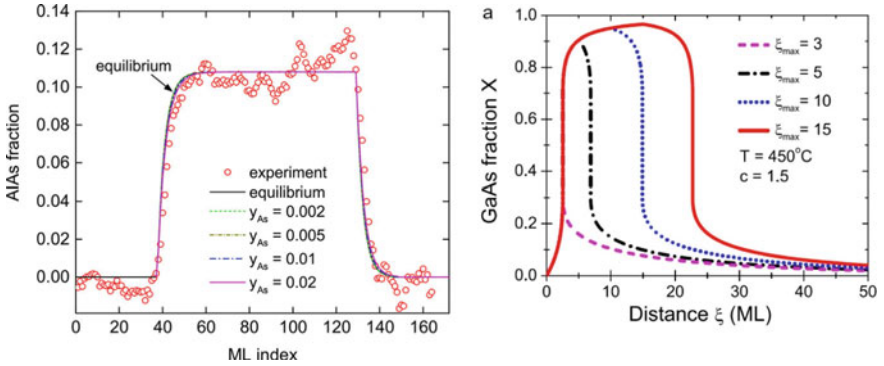

Fig. 54 Left: Composition profiles through a GaAs–$Al_xGa_{1-x}As$–GaAs heterostructure calculated numerically using the nucleation model with different values of y_{As}, compared with equilibrium calculation and experimental data (circles, Ref. [108]), at temperature $T = 873$ K. Reprinted with permission from F. Glas, Comparison of modeling strategies for the growth of heterostructures in III–V nanowires, Crystal Growth & Design **17**, 4785–4794 (2017). Copyright (2017) American Chemical Society. Right: Composition profiles through a GaAs–$Ga_xIn_{1-x}As$–GaAs heterostructure calculated analytically using the nucleation model. To form the heterostructure, the GaAs supply was replaced by an InAs supply during a time corresponding to the growth of ξ_{max} MLs. The different curves correspond to different values of this parameter. Reprinted from Material & Design, Vol. 132, V. G. Dubrovskii, A. A. Koryakin and N. V. Sibirev, Understanding the composition of ternary III–V nanowires and axial nanowire heterostructures in nucleation-limited regime, pp. 400–408, Copyright (2017), with permission from Elsevier. In both cases, the nucleus edge energy is assumed to be composition-independent

on both y_{Al} and y_{As} (see Sect. 9.4). Modeling was thus carried out assuming different constant low values of y_{As} and it was shown that the profiles depend little on this concentration [109] (Fig. 54, left panel). As mentioned in Sect. 9.4, this somehow validates the equilibrium scheme (c), at least in this system.

Turning now to analytical solutions, the simplest of these is derived within the regular growth scheme (a). Dubrovskii showed that, for simple A–B vapor flux commutation (without growth interruption), the concentrations of A and B in the solid vary exponentially at the interface (and independently of each other when a foreign catalyst is used). This solution can easily incorporate growth interruptions, which are confirmed to sharpen the interfaces in mixed group V systems (as discussed in Sect. 10.2).

Within the nucleation scheme (d), numerical solutions of system (10.2), as discussed above, may easily handle the accurate thermodynamic descriptions of the liquid available in the literature for some systems, in particular, the self-catalyzed ones [84, 109, 111, 112, 147–149]. However, as mentioned in Sect. 9.4 and discussed in depth by Dubrovskii et al. [106], for many III–V alloys at least, using such multi-parameter descriptions may be unnecessary given the specificities of these systems. Instead, analytical liquid–solid relationships based on the regular solution model, such as discussed in Sect. 9.4, may lead to analytical descriptions of the axial composition profile in the NW.

This is shown by the analytical solutions obtained for interfaces in the $Al_xGa_{1-x}As$ system [106]. For this alloy without size effect (AlAs and GaAs are nearly lattice-matched), it is often assumed that the solid interaction parameter ω_S is effectively null (see, *e.g.,*[151]). In absence of growth interruption, with a simple switch of the Al and Ga fluxes, an equation linking explicitly axial coordinate and Al content can be derived [106]. This confirms that the interface width is dominated by the reservoir effect and proportional to a quantity scaling with R, which agrees with both experiments and numerical modeling based either on equilibrium (c) or nucleation (d) [108, 109]. Further analytical results confirm the benefit of performing growth interruptions when switching the growth fluxes.

Systems based on mismatched binaries, with non-zero interaction parameter ω_S, present a miscibility gap below critical temperature $T_c = \omega_S/(2k_B)$ [151]. At any temperature $T < T_c$ exists a range of instable solid composition, say $[x_1, x_2]$; any solid within this range will tend to decompose in solids of compositions x_1 and x_2. Consider such a ternary $A_xB_{1-x}C$ system grown self-catalytically below T_c (Fig. 54, right). Starting from $y_A = 0$, the liquid will be in equilibrium with solids with continuously increasing AC content x up to a certain critical value y_A^c. This particular liquid is in equilibrium with both solids of compositions x_1 and x_2. Liquids with A concentration further increasing from y_A^c will again be in equilibrium with solids with AC contents increasing smoothly from x_2. It can then be expected that the interface profile will be driven by the reservoir effect for $y \leq y_A^c$ and $y \geq y_A^c$; however, the abrupt shift from x_1 to x_2 driven by an infinitesimal change of liquid composition around y_A^c should produce a locally very sharp interface. Dubrovskii showed that this is also the case not only in the equilibrium scheme (c) but also in the nucleation scheme (d) [105, 106]. In this case, for each liquid composition within a certain range, there are actually two saddle points, hence two critical solid compositions, corresponding to different nucleation barriers, the lower of which is expected to give the composition of the critical nucleus giving rise to the ML. Since no nucleus ever adopts a composition within the miscibility gap, the formation of a locally very sharp interface is also predicted in this case. Atomically sharp interfaces in such lattice-mismatched were indeed observed [152]. The right panel of Fig. 54 demonstrates this effect. If, however, the growth time of the insertion is too short, the remaining reservoir effect may prevent the solid composition to reach the edge of the miscibility gap and no sharp interface is obtained (see profiles for low values of $\xi_{\max}$ in right panel of Fig. 54).

11 Polytypism

11.1 Introduction

One of the most puzzling features of semiconductor NWs is that they frequently exhibit polytypism. Namely, several crystalline forms with the same composition

coexist either in different NWs of the same ensemble or, most often, in a single NW. This is all the more surprising since, for many materials, in particular the III–V compounds, polytypism is specific of NWs: it appears neither in their bulk counterpart (or only in extreme pressure or temperature conditions) nor in other types of nanostructures. As far as growth is concerned, polytypism raises two main questions: Why does it appear? Is it possible to control it?

We will discuss polytypism in NWs of III–V compounds based on P, As, or Sb, for which it is best documented. In bulk or quantum dot form, these III–V materials invariably adopt the cubic ZB structure. We exclude N-based compounds, which lowest energy structure is hexagonal WZ and which growth mode is usually non-VLS, catalyst-free. Polytypism also occurs in NWs of II–VI compounds [141], but this is less specific to NWs, and in Si NWs [153]. In addition to ground-state cubic ZB, the other structure most frequently encountered is hexagonal WZ (other hexagonal polytypes may be observed in some systems, but usually as transitory forms between ZB and WZ [154]). The differences in cohesive energy between the ZB and WZ forms are given in Table 3 for various semiconductors.

NWs usually grow along a ZB <111> direction (Sect. 2) or WZ <0001 > direction (the latter sometimes called c-axis). Along these axes, the two structures consist in different stackings of the same biatomic III–V planes (MLs). In ZB (a FCC structure), the three lateral positions of the planes, called A,B,C, occur periodically, producing an ABCABC… sequence, while only two positions occur in WZ, which produces an ABABAB… stacking (the A,B,C labeling is arbitrary; only the relative positions of the planes matter). Hence, these structures are easily distinguished when observing the NWs by high resolution TEM with the electron beam along a properly chosen zone axis normal to the growth axis (see e.g. Fig. 56), or by electron or X-ray diffraction.

The coexistence of ZB and WZ was first observed in InAs and GaAs NWs by Hiruma and coworkers, more than 25 years ago [155, 156]. However, explanations of the formation of WZ were first proposed much later and remain few. In the next section, we review the models that have been devised so far. We summarize the main features of these models and the key parameters involved, namely surface, interface, and edge energies, supersaturation of the droplet medium, contact angle of the catalyst particle, and interfacial structure of the liquid.

Table 3 Difference of cohesive energy ΔE_{coh} between the ZB and WZ structures for various materials, in meV per atom pair. Second row: ab initio calculations from references [157] (a) and [158] (b) (for GaSb, see Ref. [150]). Third row: estimate based on the measured stacking fault energies collected in Ref. [159] (see Ref. [160]). Fourth row: estimated errors on third-row values

Material	GaP	InP	GaAs	InAs	GaSb	InSb	ZnS	ZnSe	ZnTe	Si
ΔE_{coh}	18.4[a]	5.8[b]	24.0[a]	12.4[b]	29.8	16.2[b]	6.2[b]	10.6[b]	12.8[b]	23.4[b]
ΔE_{coh}	21.5	9	22.5	15	26.5	19	≤ 3	6.5	8	27.5
	1.5	1.5	3.5	1.5	3.5	2		0.5	1	3.5

11.2 Models

In principle, the formation of ZB in NWs of the materials considered does not require any explanation. For any model explaining the formation of WZ, care should however be taken that it does not predict its occurrence in conditions where experiments show ZB to form!

(1) ***Total energy models***

The first model proposed for the formation of WZ in NWs is not growth-related [161, 162]. The idea is to consider the total energy of fully formed ZB and WZ NWs. This includes the bulk energy, which favors ZB, and energies associated with the sidewall surfaces and with the vertical edges between these facets. For a section of height H of a NW of radius R, these energies scale respectively as $H\,R^2$, $H\,R$, and H. For sufficiently small radii, the terms of lowest orders in R dominate the total energy. Hence, if the sidewall surface energy density or the edge line energy density is lower for WZ than for ZB, the total energy of the NW will be lower in the WZ form than in the ZB form, provided R is small enough. Qualitatively, Akiyama et al. argue that the ZB edges have more dangling bonds, and hence a larger specific energy, than the corresponding WZ edges [161]. This is substantiated by calculating the total energies using an empirical interaction potential between neighbor atoms [161, 162], with the conclusion that, indeed, for all our III–V binaries, there exists a critical radius R_c below which the total energy of the NW is lower in the WZ structure. These ideas were elaborated by others, who performed ab initio calculations for GaAs NWs with different radii. From the variation of the total energy, they could extract the specific energies of facets and edges [62, 63]. These calculations show that, on purely energetic grounds, narrow NWs should adopt the WZ structure. However, the critical radii thus found are all very small. For GaAs, the three groups find critical radii between 2 and 8 nm [62, 63, 162]. For the nine III–V binaries considered, the critical radii range between 6 and 15 nm [162].

Although the Akiyama-Ito theory was adduced to explain some systematic observations of pure WZ in NWs of very small radii [163], it cannot account for the numerous observations of NWs of totally or partially WZ structure, with radii of many tens of nm. This is why, in 2007, Glas proposed a nucleation-based model of the formation of WZ that does not suffer from such NW radius restrictions [42]. This will be reviewed in the next section.

(2) ***Nucleation-based model***

From the very early days of the theory of VLS growth, the mechanism of 2D nucleation of new MLs at the solid–liquid interface was deemed to operate at intermediate supersaturations [164]. Many theoretical investigations indicate that 2D nucleation actually mediates NW growth and that the mononuclear regime, whereby each ML requires a single nucleation event, is very frequent (although polynucleation and regular growth cannot be entirely excluded for wide NWs; see Sect. 3). Recent in situ TEM observations have brought strong support to this idea: all show NWs growing ML by ML and detailed quantitative analysis of the videos indicates that each ML starts with a nucleation event, even if the event itself is too elusive to be captured [49].

Glas noted that each new ML could form in ZB or WZ position with respect to the already formed NW: calling AB the sequence of the two last formed MLs, the new ML will be in ZB position if it adopts the C position, in WZ position if it adopts the A position (position B is forbidden). It is reasonable to assume that this position is actually fixed by the position adopted by the nucleus and then by the whole ML that grows laterally from it [42].

Then, explanation of WZ formation reduces to that of 2D nucleation in WZ position. Glas argued that if the nucleus is formed anywhere at the S-L interface, the ZB and WZ positions are not much different (in terms of atomic environment) so that ZB position should be favored on energetics grounds (interaction with the underlying MLs). However, this might not be the case if the nucleus forms at the TPL: part of its perimeter is then in contact with the vapor instead of the liquid and this might favor the WZ position [42]. This is akin to the idea at the basis of the total energy models (1), but, since the nucleus is always found to be very small (Sect. 6.4), its perimeter has a very strong impact on its formation energy F (see Sects. 3 and 9.4).

The expression of the nucleation barrier given in Sect. 3 must be adapted to differentiate between nuclei positions (ZB or WZ) and locations with respect to the TPL. Very simply, for ZB and WZ, we find barriers:

$$\Delta G_c^{ZB} = A\,\frac{\left(\gamma^{ZB}\right)^2}{\Delta\mu}, \qquad \Delta G_c^{WZ} = A\,\frac{\left(\gamma^{WZ}\right)^2}{\Delta\mu - \Delta E_{coh}}. \tag{11.1}$$

Here, A is a constant depending on material and nucleus geometry (assumed to be the same for ZB and WZ nuclei) and $\Delta\mu > 0$ is the difference of chemical potential between liquid and bulk ZB solid, which has to be diminished for a nucleus in WZ position. This reduction relates to the interaction of the nucleus with the underlying MLs; taking it equal to the difference of cohesive energy between bulk WZ and ZB (counted positive, as in Table 3) is only an approximation. γ^{ZB} and γ^{WZ} are the specific energies of the step bordering the nucleus (in line with the CNT, these are usually taken as energies per unit area, even though the nucleus is only 1 ML high). According to what we just mentioned, we take $\gamma^{WZ} = \gamma^{ZB} = \gamma_e$ for nuclei away from the TPL, γ_e being the energy of a step in contact with the liquid (Fig. 55a). If

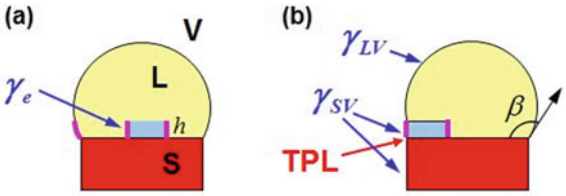

Fig. 55 Schematics of nucleation away from the TPL (a) and at the TPL (b), with relevant interface energies indicated. The crystal phase is not specified

however the nucleus forms at the TPL, a fraction x_{TPL} of its perimeter is in contact with the vapor (Sect. 6.3), which should have a different energy depending on the type of the nucleus (Fig. 55b). A key point of the model is that this energy is not simply the phase-dependent energy γ_{SV}^{j} of the interface between the sidewall of a NW of structure j (ZB or WZ) and vapor: when forming at the TPL, the nucleus indeed acquires an interface with the vapor but this interface "replaces" part of the liquid–vapor that preexisted (this part is indicated by a thick curved line in Fig. 55a), the energy of which should be subtracted from the formation energy. We are thus lead to affect to this portion of the nucleus perimeter a phase-dependent *effective energy*, a simple expression of which is [42]:

$$\gamma_{eff}^{j} = \gamma_{SV}^{j} - \gamma_{LV} \sin\beta. \tag{11.2}$$

Here, γ_{LV} is the specific energy of the liquid–vapor interface, a portion of which is deleted for TPL nucleation (hence the minus sign), and this portion depends on the contact angle β of the droplet [42]. Finally, the edge energies of ZB and WZ nuclei (to be inserted in Eq. (11.1)), with standard contributions from those parts of the perimeter in contact with the liquid and phase-dependent effective contributions (11.2) from those parts at the TPL, are

$$\gamma^{j} = (1 - x_{TPL})\,\gamma_e + x_{TPL}\,\gamma_{eff}^{j}. \tag{11.3}$$

Solid–vapor interface energies are probably larger than the energies γ_e of edges in contact with the liquid [40]. If so, it is only thanks to the destruction of part of the liquid–vapor interface that TPL nucleation may be favored. Equation (11.2) predicts that this is more likely to happen for contact angles around $\pi/2$.

From Eqs. (11.1)–(11.3), it becomes clear that, provided $\gamma_{SV}^{WZ} < \gamma_{SV}^{ZB}$ and TPL nucleation is favored, the nucleation barrier for WZ formation at the TPL may be lower than the nucleation barriers for ZB formation at the TPL or away from the TPL. Given the strong dependence of the nucleation rate on the nucleation barrier (Sect. 3), this will largely advantage, on kinetics ground, the formation of a nucleus in WZ position, and therefore of a WZ ML. However, from Eq. (11.1), condition $\Delta G_c^{WZ} < \Delta G_c^{ZB}$ requires in addition that the chemical potential be large enough. Specifically, comparing, for instance, the two barriers for nucleation at the TPL, and assuming to simplify $\Delta\mu$ large with respect to ΔE_{coh} and a small relative difference $\Delta\gamma_{SV}$ of solid–vapor energies between the two phases, we find that $\Delta\mu$ must be larger than a critical value:

$$\Delta\mu* \approx 2\, x_{TPL}\ \Delta E_{coh}\, \frac{\gamma^{ZB}}{\Delta\gamma_{SV}}. \tag{11.4}$$

Whereas the condition $\gamma_{SV}^{WZ} < \gamma_{SV}^{ZB}$ is mainly related to the NW material (but also possibly to the growth conditions, since the solid–vapor interface energies may depend on the composition of the vapor), condition $\Delta\mu > \Delta\mu*$ is mainly related to growth conditions set by the experimenter, which determine the supersaturation in the liquid (Sect. 6.4).

This theory was initially developed in Ref. [42], where it was argued that the conditions for WZ formation might easily be met in NW growth. It has become the basis of the vast majority of models discussing the formation of the WZ phase in NWs. It has of course been refined in many ways (for instance, to take into account that, whereas nucleation away from the TPL can occur on most of the NW top facet, nucleation at the TPL can occur only on a small ring at the TPL [44]). We will not describe these developments, for which the reader may refer to Sect. 6.6 of Ref. [6]. Instead, we discuss how theory and experiments have confirmed virtually all the assumptions on which it is founded.

A key condition for WZ nucleation (at the TPL) is that $\gamma_{SV}^{WZ} < \gamma_{SV}^{ZB}$. Ab initio calculations have indeed confirmed that this is the case at least for several materials, such as GaAs and InAs, and for some of their sidewall facets commonly found in real NWs [62, 63, 165]. Simpler calculations based on broken bonds lead to the same conclusions, although they produce larger surface energies [166]. Even though the surface energy differences so calculated are rather small (typically only a few %), the corresponding critical values of the difference of chemical potential (Eq. 11.4) seem to be easily attainable given the chemical potentials deduced from comparison of other experiments with models (*e.g.,* regarding the kinetics of self-catalyzed GaAs growth; see Ref. [40], Sect. 6.4 and Fig. 22).

A very striking confirmation of a key point of the model was recently brought by in situ TEM experiments. Harmand et al. observed the VLS growth of Au-catalyzed GaAs NWs by solid source MBE in a dedicated TEM [49]. Both ZB and WZ MLs were found to grow in the mononuclear regime. Whereas ZB MLs extend very quickly after nucleation, WZ MLs advance slowly (as already reported in Ref. [48]) and, by tilting the solid–liquid interface with respect to the electron beam, it is possible to follow the evolution of the geometry of their edge as the coverage of the NW top facet increases. The first fraction of ML that is observed forms very quickly after nucleation and it is systematically located at the TPL, and even at the corner between two sides of the hexagon that constitutes the TPL. In the experiments, this fraction is about 10% of a full ML, which is probably larger than the nucleus. However, probabilistic arguments indicate that these observations make nucleation at the TPL of the WZ MLs extremely likely [49].

As already mentioned, Eq. (11.2) predicts that nucleation at the TPL, and hence WZ formation, is more likely to happen for contact angles around $\pi/2$. Conversely, in situ TEM reveals another correlation between structure and contact angle. Namely, for GaAs at least, at large contact angle (β over about 125°), the solid–liquid interface

is truncated and ZB grows. At angles closer to $\pi/2$ (although maybe still larger than that value), the solid–liquid interface is flat and WZ grows. A model has been devised that shows that, irrespective of the solid structure and depending on surface and interface energies, the truncated shape may be favored at large β and the flat shape around $\pi/2$ [48] (see also Sec. 4). It is then tempting to reason that, for large contact angles, the interface is truncated so that the (111) top facet (where nucleation occurs) is not in contact with the vapor anymore. Obviously, in absence of a proper TPL (as considered in the nucleation-based model; of course, there is still a TPL, but at the edge of the truncation facet; see Fig. 8c), nucleation cannot occur at the TPL, hence, WZ does not form and ZB prevails. This simple interpretation is however questionable. First, it only holds if truncation is present all around the NW, which is not clear at all at the moment. Second, although nucleation at the TPL and planar solid–liquid interface are both predicted to occur for angles around $\pi/2$ [42, 48], the corresponding critical angles depend partially on different parameters and have no reason to be equal. This leaves open the question of the exact coincidence between WZ formation and vanishing of truncation observed experimentally. These questions are further discussed in Sect. 4.

Finally, we note that the nucleation-based model describes stacking defects in otherwise perfect structures as well as polytypism. In both case, we are concerned with the position (WZ or ZB) adopted by the new ML. For instance, in the ZB structure, a stacking fault corresponds to a local AB**A**BC sequence, a twin boundary to a change of stacking direction ABCAB**C**BACBA, with only the single ML in bold wrongly stacked. Of course, forming a WZ segment requires that all successive form in WZ position.

(3) ***Ordering at the solid–liquid interface***

The only other explanation of WZ formation seems to be that of Algra et al. [167]. These authors propose that WZ formation in Au-catalyzed InP NWs results from the peculiar arrangement adopted by the heavy Au and In atoms in the liquid in the very vicinity of the top facet of the NW. Such liquid ordering is a well-known phenomenon [168]. Typically, the density of the liquid is modulated over a few atomic layers in the direction normal to the interface but there is also some solid-like lateral ordering, especially in the first layer.

Based on surface X-ray diffraction measurements on macroscopic interfaces between solid InP and (Au,In,P) liquids supplemented by ab initio calculations, the authors were able to show that, in the liquid, the heavy atoms close to the solid tend to occupy specific positions. They argue that, when a new InP ML forms, this hinders the atom to occupy the ZB positions and channels them to the WZ positions.

This mechanism is not specific to NWs. It should produce WZ crystals even if growth of wide crystals is carried out from the appropriate liquids. However, such growth has not been carried out in these experiments. Somewhat surprisingly, this interesting alternative route to WZ formation during VLS growth has not been further investigated.

11.3 Crystal Phase Heterostructures

Polytypism enables a NW-specific type of heterostructure very different from those that associate different materials or different alloy compositions (Sect. 10). Instead, these heterostructures combine different crystalline structures of the same material. Such ZB/WZ mixed structures have long been observed to form spontaneously and more or less randomly in III–V NWs [155] and for many years, it was rather the fabrication of single phase NWs that was a challenge. One of the interests of such heterostructures is that the interfaces may be ideally abrupt, although mixed structures or higher order polytypes [154] may form between two pure phase sections. Another one is that, for each material, the ZB and WZ forms have different electronic structures, in particular different band gap energies. The phrase "crystal phase heterostructure" (or "crystal phase quantum dot") actually appeared when one started studying their optical properties (in GaAs [116] or InP [117]) or their transport properties (in InAs [169]). The control of the lengths of the sections of each phase became a new challenge and spectacular early results were obtained in fabricating periodic ZB/WZ stacks controlled to the ML [169] (Fig. 56).

Recent in situ TEM experiments have demonstrated that, as discussed in Sect. 4, the droplet contact angle is a key parameter for phase selection [48], with ZB forming at large and small contact angles and WZ in an intermediate range [61]. It is likely that the painstaking studies that allowed Dick et al. blindfoldly to form nearly perfect ZB/WZ superlattices [169] amounted primarily to controlling this parameter. As discussed in Sect. 11.2, both the nucleation-based model of WZ formation [42, 44] and the more recent models describing the morphology of the NW sidewalls and of the solid–liquid interface (Sect. 4) attribute a prominent role to contact angle, with WZ predicted to form at intermediate angles. As yet, a full understanding of the interplay between these various parameters and of the role of the chemical potential has however not been achieved.

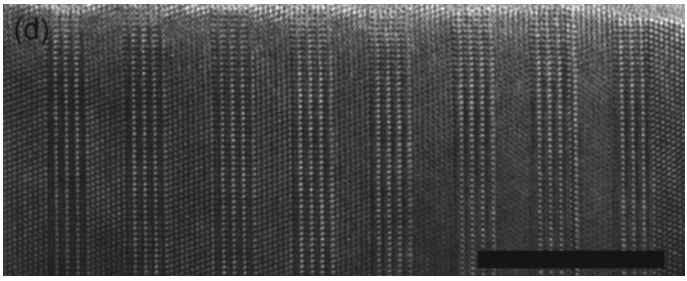

Fig. 56 Periodic crystal phase heterostructure fabricated by Dick et al. in an InAs NW (growth axis is horizontal). The period consists of 2 MLs of WZ (strong contrast) and 3 MLs of ZB (lower contrast). Scale bar is 20 nm. Reprinted with permission from K. A. Dick, C. Thelander, L. Samuelson, P. Caroff, Crystal phase engineering in single InAs nanowires, Nano Letters **10**, 3494–3499 (2010). Copyright (2010) American Chemical Society

Acknowledgments The long-established collaboration between the authors is currently supported by InternationalResearch Project "Physics of nanostructures and innovative devices based on compound semiconductors" (PHYNICS) established between Centre National de la Recherche Scientifique (CNRS) and the Russian Foundation for Basic Research (RFBR). The authors acknowledge fruitful discussions with their colleagues Jean-Christophe Harmand, Gilles Patriarche, Fabrice Oehler, Federico Panciera Giacomo Priante, George Cirlin, and Nikolai Sibirev. VGD thanks the Russian Science Foundation for financial support under the Grant 19-72-30004. FG acknowledges financial support from Agence Nationale de la Recherche within projects ESPADON ANR-15-CE24-0029 and NanoMAX 10-EQPX-0050, and from the European Commission within Marie Skodowska-Curie Innovative Training Network INDEED (No 722176).

References

1. R.S. Wagner, W.C. Ellis, Vapor-liquid-solid mechanism of single crystal growth. Appl. Phys. Lett. **4**, 89–90 (1964)
2. E.I. Givargizov, *Highly Anisotropic Crystals* (Springer, 1987)
3. A. Zhang, G. Zheng, C.M. Lieber, *Nanowires: Building Blocks for Nanoscience and Nanotechnology* (Springer, 2016)
4. P. Yang, P.R. Yan, M. Fardy, Semiconductor nanowires: what's next? Nano Lett. **10**, 1529–1536 (2010)
5. W. Seifert, M. Borgström, K. Deppert, K.A. Dick, J. Johansson, M.W. Larsson, T. Mårtensson, N. Sköld, C.P.T. Svensson, B.A. Wacaser, L.R. Wallenberg, L. Samuelson, Growth of one-dimensional nanostructures in MOVPE. J. Cryst. Growth **272**, 211–220 (2004)
6. V.G. Dubrovskii, *Nucleation Theory and Growth of Nanostructures* (Springer, 2014)
7. V.G. Dubrovskii, Theory of VLS growth of compound semiconductors, in *Semiconductors and Semimetals*, vol. 93, ed. by A. Fontcuberta i Morral, S.A. Dayeh, C. Jagadish (Burlington, Academic Press, 2015), pp. 1–78
8. F. Glas, Critical dimensions for the plastic relaxation of strained axial heterostructures in free-standing nanowires. Phys. Rev. B **74**, 121302R (2006)
9. X. Zhang, V.G. Dubrovskii, N.V. Sibirev, X. Ren, Analytical study of elastic relaxation and plastic deformation in nanostructures on lattice mismatched substrates. Cryst. Growth Des. **11**, 5441–5448 (2011)
10. F. Glas, Strain in nanowires and nanowire heterostructures, in *Semiconductors and Semimetals*, vol. 93, ed. by A. Fontcuberta i Morral, S.A. Dayeh, C. Jagadish (Burlington, Academic Press, 2015), pp. 79–123
11. V.G. Dubrovskii, G.E. Cirlin, I.P. Soshnikov, A.A. Tonkikh, N.V. Sibirev, Yu.B. Samsonenko, V.M. Ustinov, Diffusion-induced growth of GaAs nanowhiskers: theory and experiment. Phys. Rev. B **71**, 205325 (2005)
12. J.C. Harmand, G. Patriarche, N. Péré-Laperne, M.-N. Mérat-Combes, L. Travers, F. Glas, Analysis of vapor-liquid-solid mechanism in Au-assisted GaAs nanowire growth. Appl. Phys. Lett. **87**, 203101 (2005)
13. Smith, W. F.; Hashemi, J.: Foundations of materials science and engineering (4th ed.). McGraw-Hill, 2006, pp. 318–320.
14. F. Glas, Chemical potentials for Au-assisted vapor-liquid-solid growth of III-V nanowires. J. Appl. Phys. **108**, 073506 (2010)
15. H.J. Joyce, Q. Gao, H.H. Tan, C. Jagadish, Y. Kim, M.A. Fickenscher, S. Perera, T.B. Hoang, L.M. Smith, H.E. Jackson, J.M. Yarrison-Rice, X. Zhang, J. Zou, Unexpected benefits of rapid growth rate for III–V nanowires. Nano Lett. **9**, 695–701 (2009)
16. L.C. Chuang, M. Moewe, C. Chase, N.P. Kobayashi, C. Chang-Hasnain, Critical diameter for III-V nanowires grown on lattice-mismatched substrates. Appl. Phys. Lett. **90**, 043115 (2007)

17. N.N. Halder, A. Kelrich, Y. Kauffmann, S. Cohen, D. Ritter, Growth of wurtzite InP/GaP core-shell nanowires by metal-organic molecular beam epitaxy. J. Cryst. Growth **463**, 10–13 (2017)
18. E. Husanu, D. Ercolani, M. Gemmi, L. Sorba, Growth of defect-free GaP nanowires. Nanotechnology **25**, 205601 (2014)
19. M.C. Plante, R.R. LaPierre, Growth mechanisms of GaAs nanowires by gas source molecular beam epitaxy. J. Cryst. Growth **286**, 394–399 (2006)
20. E. Gil, V.G. Dubrovskii, G. Avit, Y. André, C. Leroux, K. Lekhal, J. Grecenkov, A. Trassoudaine, D. Castelluci, G. Monier, M.R. Ramdani, C. Robert-Goumet, L. Bideux, J.C. Harmand, F. Glas, Record pure zincblende phase in GaAs nanowires down to 5 nm in radius. Nano Lett. **14**, 3938 (2014)
21. T. Mårtensson, P. Carlberg, M. Borgström, L. Montelius, W. Seifert, L. Samuelson, Nanowire arrays defined by nanoimprint lithography. Nano Lett. **4**, 699–702 (2004)
22. C. Colombo, D. Spirkoska, M. Frimmer, G. Abstreiter, A. Fontcuberta i Morral, Ga-assisted catalyst-free growth mechanism of GaAs nanowires by molecular beam epitaxy. Phys. Rev. B **77**, 155326 (2008)
23. F. Jabeen, V. Grillo, S. Rubini, F. Martelli, Self-catalyzed growth of GaAs nanowires on cleaved Si by molecular beam epitaxy. Nanotechnology **19**, 275711 (2008)
24. S.J. Gibson, J.P. Boulanger, R.R. LaPierre, Opportunities and pitfalls in patterned self-catalyzed GaAs nanowire growth on silicon. Semicond. Sci. Technol. **28**, 105025 (2013)
25. G. Priante, S. Ambrosini, V.G. Dubrovskii, A. Franciosi, S. Rubini, Stopping and resuming at will the growth of GaAs nanowires. Cryst. Growth Des. **13**, 3976–3984 (2013)
26. M.R. Ramdani, J.C. Harmand, F. Glas, G. Patriarche, L. Travers, Arsenic pathways in self-catalyzed growth of GaAs nanowires. Cryst. Growth Des. **13**, 91–96 (2013)
27. V.G. Dubrovskii, G.E. Cirlin, N.V. Sibirev, F. Jabeen, J.C. Harmand, P. Werner, New mode of vapor-liquid-solid nanowire growth. Nano Lett. **11**, 1247–1253 (2011)
28. V.G. Dubrovskii, T. Xu, A. Díaz Álvarez, G. Larrieu, S.R. Plissard, P. Caroff, F. Glas, B. Grandidier, Self-equilibration of the diameter of Ga-catalyzed GaAs nanowires. Nano Lett. **15**, 5580–5584 (2015)
29. F. Bastiman, H. Küpers, C. Somaschini, L. Geelhaar, Growth map for Ga-assisted growth of GaAs nanowires on Si(111) substrates by molecular beam epitaxy. Nanotechnology **27**, 095601 (2016)
30. E.S. Koivusalo, T.V. Hakkarainen, M. Guina, V.G. Dubrovskii, Sub-Poissonian narrowing of length distributions realized in Ga-catalyzed GaAs nanowires. Nano Lett. **17**, 5350–5355 (2017)
31. T. Tauchnitz, Y. Berdnikov, V.G. Dubrovskii, H. Schneider, M. Helm, E. Dimakis, A simple route to synchronized nucleation of self-catalyzed GaAs nanowires on silicon for sub-Poissonian length distributions. Nanotechnology **29**, 504004 (2018)
32. Z. Dong, Y. André, V.G. Dubrovskii, C. Bougerol, C. Leroux, M.R. Ramdani, G. Monier, A. Trassoudaine, D. Castelluci, E. Gil, Self-catalyzed GaAs nanowires on silicon by hydride vapor phase epitaxy. Nanotechnology **27**, 455601 (2017)
33. J. Vukajlovic-Plestina, W. Kim, V.G. Dubrovskii, G. Tütüncüoğlu, M. Lagier, H. Potts, M. Friedl, A. Fontcuberta i Morral, Engineering the size distributions of ordered GaAs nanowires on silicon. Nano Lett. **17**, 4101–4108 (2017)
34. J. Tersoff, Stable self-catalyzed growth of III–V nanowires. Nano Lett. **15**, 6609–6613 (2015)
35. W. Kim, V.G. Dubrovskii, J. Vukajlovic-Plestina, G. Tütüncüoglu, L. Francaviglia, L. Güniat, H. Potts, M. Friedl, J.-B. Leran, A. Fontcuberta i Morral, Bistability of contact angle and its role in achieving quantum-thin self-assisted GaAs nanowires. Nano Lett. **18**, 49–57 (2018)
36. E.S. Koivusalo, T.V. Hakkarainen, H.V.A. Galeti, Y.G. Gobato, V.G. Dubrovskii, M.D. Guina, Deterministic switching of the growth direction of self-catalyzed GaAs nanowires. Nano Lett. **19**, 82–89 (2019)
37. V.G. Dubrovskii, Influence of the group V element on the chemical potential and crystal structure of Au-catalyzed III-V nanowires. Appl. Phys. Lett. **104**, 053110 (2014)

38. F. Glas, Vapor fluxes on the apical droplet during nanowire growth by molecular beam epitaxy. Phys. Status Solidi B **247**, 254–258 (2010)
39. L. Schubert, P. Werner, N.D. Zakharov, G. Gerth, F.M. Kolb, L. Long, U. Gösele, T.Y. Tan, Silicon nanowhiskers grown on <111> Si substrates by molecular beam epitaxy. Appl. Phys. Lett. **84**, 4968–4970 (2004)
40. F. Glas, M.R. Ramdani, G. Patriarche, J.C. Harmand, Predictive modeling of self-catalyzed III-V nanowire growth. Phys. Rev. B **88**, 195304 (2013)
41. V.G. Dubrovskii, Group V sensitive vapor-liquid-solid growth of Au-catalyzed and self-catalyzed III-V nanowires. J. Cryst. Growth **440**, 62–68 (2016)
42. F. Glas, J.C. Harmand, G. Patriarche, Why does wurtzite form in nanowires of III-V zinc-blende semiconductors? Phys. Rev. Lett. **99**, 146101 (2007)
43. V.G. Dubrovskii, N.V. Sibirev, Growth rate of a crystal facet of arbitrary size and the growth kinetics of vertical nanowires. Phys. Rev. E **70**, 031604 (2004)
44. V.G. Dubrovskii, N.V. Sibirev, J.C. Harmand, F. Glas, Growth kinetics and crystal structure of semiconductor nanowires. Phys. Rev. B **78**, 235301 (2008)
45. D. Kashchiev, Dependence of the growth rate of nanowires on the nanowire diameter. Cryst. Growth Des. **6**, 1154–1156 (2006)
46. E.K. Mårtensson, S. Lehmann, K.A. Dick, J. Johansson, Simulation of GaAs nanowire growth and crystal structure. Nano Lett. **19**, 1197–1203 (2019)
47. C.-Y. Wen, J. Tersoff, K. Hillerich, M.C. Reuter, J.H. Park, S. Kodambaka, E.A. Stach, F.M. Ross, Periodically changing morphology of the growth interface in Si, Ge, and GaP nanowires. Phys. Rev. Lett. **107**, 025503 (2011)
48. D. Jacobsson, F. Panciera, J. Tersoff, M.C. Reuter, S. Lehmann, S. Hofmann, K.A. Dick, F.M. Ross, Interface dynamics and crystal phase switching in GaAs nanowires. Nature **531**, 317–322 (2016)
49. J.C. Harmand, G. Patriarche, F. Glas, F. Panciera, I. Florea, J.-L. Maurice, L. Travers, Y. Ollivier, Atomic step flow on a nanofacet. Phys. Rev. Lett. **121**, 166101 (2018)
50. V.G. Dubrovskii, J. Grecenkov, Zeldovich nucleation rate, self-consistency renormalization, and crystal phase of Au-catalyzed GaAs nanowires. Cryst. Growth Des. **15**, 340–347 (2015)
51. A.S. Ameruddin, P. Caroff, H.H. Tan, C. Jagadish, V.G. Dubrovskii, Understanding the growth and composition evolution of gold-seeded ternary InGaAs nanowires. Nanoscale **7**, 16266 (2015)
52. V.G. Dubrovskii, Fully analytical description for the composition of ternary vapor-liquid-solid nanowires. Cryst. Growth Des. **15**, 5738–5743 (2015)
53. V.G. Dubrovskii, N.V. Sibirev, Factors influencing the interfacial abruptness in axial III-V nanowire heterostructures. Cryst. Growth Des. **16**, 2019–2023 (2016)
54. V.G. Dubrovskii, Compositional control of gold-catalyzed ternary nanowires and axial nanowire heterostructures based on $\mathrm{IIIP}_{1-x}\mathrm{As}_x$. J. Cryst. Growth **498**, 179–185 (2018)
55. V.G. Dubrovskii, Zh.V. Sokolova, M.V. Rylkova, A.A. Zhiglinsky, Composition and contact angle of Au-III-V droplets on top of Au-catalyzed III-V nanowires. Materials Physics and Mechanics **36**, 1–7 (2018)
56. V.A. Nebol'sin, A.A. Shchetinin, Role of surface energy in the vapor–liquid–solid growth of silicon. Inorg. Mater. **39**, 899–903 (2003)
57. F.M. Ross, J. Tersoff, M.C. Reuter, Sawtooth faceting in silicon nanowires. Phys. Rev. Lett. **95**, 146104 (2005)
58. V.G. Dubrovskii, Development of growth theory for vapor-liquid-solid nanowires: contact angle, truncated facets and crystal phase. Cryst. Growth Des. **17**, 2544–2548 (2017)
59. V. Zannier, F. Rossi, V.G. Dubrovskii, D. Ercolani, S. Battiato, L. Sorba, Nanoparticle stability in axial InAs−InP nanowire heterostructures with atomically sharp interfaces. Nano Lett. **18**, 167–174 (2018)
60. J. Johansson, L.S. Karlsson, K.A. Dick, J. Bolinsson, B.A. Wacaser, K. Deppert, L. Samuelson, Effects of supersaturation on the crystal structure of gold seeded III–V nanowires. Cryst. Growth Des. **9**, 766–773 (2009)

61. F. Panciera, Z. Baraissov, G. Patriarche, V.G. Dubrovskii, F. Glas, L. Travers, U. Mirsaidov, J.-C. Harmand, Phase selection in self-catalyzed GaAs nanowires. Nano Lett. **20**, 1669–1675 (2020)
62. V. Pankoke, P. Kratzer, S. Sakong, Calculation of the diameter-dependent polytypism in GaAs nanowires from an atomic motif expansion of the formation energy. Phys. Rev. B **84**, 075455 (2011)
63. M. Rosini, R. Magri, Surface effects on the atomic and electronic structure of unpassivated GaAs nanowires. ACS Nano **4**, 6021–6031 (2010)
64. N. Moll, A. Kley, E. Pehlke, M. Scheffler, GaAs equilibrium crystal shape from first principles. Phys. Rev. B **54**, 8844–8855 (1996)
65. V.G. Dubrovskii, N.V. Sibirev, G.E. Cirlin, I.P. Soshnikov, W.H. Chen, R. Larde, E. Cadel, P. Pareige, T. Xu, B. Grandidier, J.-P. Nys, D. Stievenard, M. Moewe, L.C. Chuang, C. Chang-Hasnain, Gibbs-Thomson and diffusion-induced contributions to the growth rate of Si, InP and GaAs nanowires. Phys. Rev. B **79**, 205316 (2009)
66. P. Mohan, J. Motohisa, T. Fukui, Controlled growth of highly uniform, axial/radial direction-defined, individually addressable InP nanowire arrays. Nanotechnology **16**, 2903 (2005)
67. K. Tomioka, P. Mohan, J. Noborisaka, S. Hara, J. Motohisa, T. Fukui, Growth of highly uniform InAs nanowire arrays by selective-area MOVPE. J. Cryst. Growth **298**, 644–647 (2007)
68. D. Dalacu, A. Kam, D.G. Austing, X. Wu, J. Lapointe, G.C. Aers, P.J. Poole, Selective-area vapour–liquid–solid growth of InP nanowires. Nanotechnology **20**, 395602 (2009)
69. S. Hertenberger, D. Rudolph, M. Bichler, J.J. Finley, G. Abstreiter, G. Koblmüller, Growth kinetics in position-controlled and catalyst-free InAs nanowire arrays on Si(111) grown by selective area molecular beam epitaxy. J. Appl. Phys. **108**, 114316 (2010)
70. K.P. Bassett, P.K. Mohseni, X. Li, Evolution of GaAs nanowire geometry in selective area epitaxy. Appl. Phys. Lett. **106**, 133102 (2015)
71. M. Robson, K.M. Azizur-Rahman, D. Parent, P. Wojdylo, D.A. Thompson, R.R. LaPierre, Multispectral absorptance from large-diameter InAsSb nanowire arrays in a single epitaxial growth on silicon. Nano Futures **1**, 035001 (2017)
72. M.T. Robson, V.G. Dubrovskii, R.R. LaPierre, Conditions for high yield of selective-area epitaxy InAs nanowires on SiOx/Si(111) substrates. Nanotechnology **26**, 465301 (2015)
73. Q. Gao, V.G. Dubrovskii, P. Caroff, J. Wong-Leung, L. Li, Y. Guo, L. Fu, H.H. Tan, C. Jagadish, Simultaneous selective-area and vapor-liquid-solid growth of InP nanowire arrays. Nano Lett. **16**, 4361–4367 (2016)
74. V.G. Dubrovskii, Evolution of the length and radius of III-V nanowires grown by selective area epitaxy. ACS Omega **4**, 8400–8405 (2019)
75. N.V. Sibirev, M. Tchernycheva, M.A. Timofeeva, J.C. Harmand, G.E. Cirlin, V.G. Dubrovskii, Influence of shadow effect on the growth and shape of InAs nanowires. J. Appl. Phys. **111**, 104317 (2012)
76. V.G. Dubrovskii, N.V. Sibirev, G.E. Cirlin, A.D. Bouravleuv, Y.B. Samsonenko, D.L. Dheeraj, H.L. Zhou, C. Sartel, J.C. Harmand, G. Patriarche, F. Glas, Role of non-linear effects in nanowire growth and crystal phase. Phys. Rev. B **80**, 205305 (2009)
77. J.C. Harmand, F. Glas, G. Patriarche, Growth kinetics of a single $InP_{1-x}As_x$ nanowire. Phys. Rev. B **81**, 235436 (2010)
78. V.G. Dubrovskii, Y. Hervieu, Diffusion-induced growth of nanowires: generalized boundary conditions and self-consistent kinetic equation. J. Cryst. Growth **401**, 431–440 (2014)
79. J. Johansson, C.P.T. Svensson, T. Mårtensson, L. Samuelson, W. Seifert, Mass transport model for semiconductor nanowire growth. J. Phys. Chem. B **109**, 13567–13571 (2005)
80. L.E. Fröberg, W. Seifert, J. Johansson, Diameter-dependent growth rate of InAs nanowires. Phys. Rev. B **76**, 153401 (2007)
81. V. Consonni, V.G. Dubrovskii, A. Trampert, L. Geelhaar, H. Riechert, Quantitative description for the growth rate of self-induced GaN nanowires. Phys. Rev. B **85**, 155313 (2012)
82. S.A. Dayeh, S.T. Picraux, Direct observation of nanoscale size effects in Ge semiconductor nanowire growth. Nano Lett. **10**, 4032–4039 (2010)

83. V.G. Dubrovskii, N.V. Sibirev, R.A. Suris, G.E. Cirlin, J.C. Harmand, V.M. Ustinov, Diffusion controlled growth of semiconductor nanowires: vapor pressure versus high vacuum deposition. Surf. Sci. **601**, 4395–4401 (2007)
84. E.D. Leshchenko, M. Ghasemi, V.G. Dubrovskii, J. Johansson, Nucleation-limited composition of ternary III-V nanowires forming from quaternary gold based liquid alloys. CrystEngComm **20**, 1649–1655 (2018)
85. G.B. Stringfellow, Calculation of ternary phase diagrams of III–V systems. J. Phys. Chem. Solids **33**, 665–677 (1972)
86. F. Glas, V.G. Dubrovskii, Energetics and kinetics of monolayer formation in vapor-liquid-solid nanowire growth. Phys. Rev. Mater. **4**, 083401 (2020)
87. V.G. Dubrovskii, Refinement of nucleation theory for vapor-liquid-solid nanowires. Cryst. Growth Des. **17**, 2589–2593 (2017)
88. F. Glas, J.C. Harmand, G. Patriarche, Nucleation antibunching in catalyst-assisted nanowire growth. Phys. Rev. Lett. **104**, 135501 (2010)
89. M. Moewe, L.C. Chuang, V.G. Dubrovskii, C. Chang-Hasnain, Growth mechanisms and crystallographic structure of InP nanowires on lattice-mismatched substrates. J. Appl. Phys. **104**, 044313 (2008)
90. E.D. Leshchenko, P. Kuyanov, R.R. LaPierre, V.G. Dubrovskii, Tuning the morphology of self-assisted GaP nanowires. Nanotechnology **29**, 225603 (2018)
91. V.G. Dubrovskii, Self-regulated pulsed nucleation in catalyzed nanowire growth. Phys. Rev. **87**, 195426 (2013)
92. V.G. Dubrovskii, N.V. Sibirev, Y. Berdnikov, U.P. Gomes, D. Ercolani, V. Zannier, L. Sorba, Length distributions of Au-catalyzed and In-catalyzed InAs nanowires. Nanotechnology **27**, 375602 (2016)
93. V.G. Dubrovskii, Y. Berdnikov, J. Schmidtbauer, M. Borg, K. Storm, K. Deppert, J. Johansson, Length distributions of nanowires growing by surface diffusion. Cryst. Growth Des. **16**, 2167–2172 (2016)
94. V.G. Dubrovskii, Length distributions of nanowires: effects of surface diffusion versus nucleation delay. J. Cryst. Growth **463**, 139–144 (2017)
95. F. Glas, V.G. Dubrovskii, Self-narrowing of size distributions of nanostructures by nucleation antibunching. Phys. Rev. Mater. **1**, 036003 (2017)
96. V.G. Dubrovskii, Analytic form of the size distribution in irreversible growth of nanoparticles. Phys. Rev. E **99**, 012105 (2019)
97. F. Matteini, V.G. Dubrovskii, D. Rüffer, G. Tütüncüoğlu, Y. Fontana, A. Fontcuberta i Morral, Tailoring the diameter and density of self-catalyzed GaAs nanowires on silicon. Nanotechnology **26**, 105603 (2015)
98. V.G. Dubrovskii, N.V. Sibirev, Analytic scaling function for island-size distributions. Phys. Rev. E **91**, 042408 (2015)
99. F. Glas, Statistics of sub-Poissonian nucleation in a nanophase. Phys. Rev. B **90**, 125406 (2014)
100. V.G. Dubrovskii, Fluctuation-induced spreading of size distribution in condensation kinetics. J. Chem. Phys. **131**, 164514 (2009)
101. T.V. Hakkarainen, A. Schramm, J. Mäkelä, P. Laukkanen, M. Guina, Lithography-free oxide patterns as templates for self-catalyzed growth of highly uniform GaAs nanowires on Si(111). Nanotechnology **26**, 275301 (2015)
102. S.G. Choi, P. Manandhar, S.T. Picraux, Vapor-liquid-solid epitaxial growth of $Si_{1-x}Ge_x$ alloy nanowires: Composition dependence on precursor reactivity and morphology control for vertical forests. J. Appl. Phys. **118**, 014303 (2015)
103. S. Biswas, J. Doherty, D. Saladukha, Q. Ramasse, D. Majumdar, M. Upmanyu, A. Singha, T. Ochalski, M.A. Morris, J.D. Holmes, Non-equilibrium induction of tin in germanium: towards direct bandgap $Ge_{1-x}Sn_x$ nanowires. Nature Comm. **7**, 11405 (2016)
104. A. Pan, P.L. Nichols, C.Z. Ning, Semiconductor alloy nanowires and nanobelts with tunable optical properties. IEEE J. Select. Topics Quant. Electron. **17**, 808–818 (2011)

105. V.G. Dubrovskii, Understanding the vapor-liquid-solid growth and composition of ternary III-V nanowires and nanowire heterostructures. J. Phys. D: Appl. Phys. **50**, 453001 (2017)
106. V.G. Dubrovskii, A.A. Koryakin, N.V. Sibirev, Understanding the composition of ternary III-V nanowires and axial nanowire heterostructures in nucleation-limited regime. Mater. Des. **132**, 400–408 (2017)
107. P. Periwal, N.V. Sibirev, G. Patriarche, B. Salem, F. Bassani, V.G. Dubrovskii, T. Baron, Composition-dependent interfacial abruptness in Au-catalyzed $Si_{1-x}Ge_x$/Si/$Si_{1-x}Ge_x$ nanowire heterostructures. Nano Lett. **14**, 5140–5147 (2014)
108. G. Priante, F. Glas, G. Patriarche, K. Pantzas, F. Oehler, J.-C. Harmand, Sharpening the interfaces of axial heterostructures in self-catalyzed AlGaAs nanowires: experiment and theory. Nano Lett. **16**, 1917–1924 (2016)
109. F. Glas, Comparison of modeling strategies for the growth of heterostructures in III-V nanowires. Cryst. Growth Des. **17**, 4785–4794 (2017)
110. H. Reiss, The kinetics of phase transitions in binary systems. J. Chem. Phys. **18**, 840–848 (1950)
111. J. Johansson, M. Ghasemi, Composition of gold alloy seeded InGaAs nanowires in the nucleation limited regime. Cryst. Growth Des. **17**, 1630–1635 (2017)
112. M. Ghasemi, M. Selleby, J. Johansson, Thermodynamic assessment and binary nucleation modeling of Sn-seeded InGaAs nanowires. J. Cryst. Growth **478**, 152–158 (2017)
113. J. Johansson, E.D. Leshchenko, Zinc blende and wurtzite crystal structure formation in gold catalyzed InGaAs nanowires. J. Cryst. Growth **509**, 118–123 (2019)
114. J. Johansson, M. Ghasemi, Kinetically limited composition of ternary III-V nanowires. Phys. Rev. Mater. **1**, 040401 (2017)
115. A. Scaccabarozzi, A. Cattoni, G. Patriarche, L. Travers, S. Collin, J.-C. Harmand, F. Glas, F. Oehler, Stable and high yield growth of GaP and $In_{0.2}Ga_{0.8}As$ nanowire arrays using In as a catalyst. Nanoscale **12**, 18240-18248 (2020)
116. D. Spirkoska, J. Arbiol, A. Gustafsson, S. Conesa-Boj, F. Glas, I. Zardo, M. Heigoldt, M.H. Gass, A.L. Bleloch, S. Estrade, M. Kaniber, J. Rossler, F. Peiro, J.R. Morante, G. Abstreiter, L. Samuelson, A. Fontcuberta i Morral, Structural and optical properties of high quality zinc-blende/wurtzite GaAs nanowire heterostructures. Phys. Rev. B **80**, 245325 (2009)
117. N. Akopian, P. Patriarche, L. Liu, J.-C. Harmand, V. Zwiller, Crystal phase quantum dots. Nano Lett. **10**, 1198–1201 (2010)
118. F. Glas, B. Daudin, Stress-driven island growth on top of nanowires. Phys. Rev. B **86**, 174112 (2012)
119. N.D. Zakharov, P. Werner, G. Gerth, L. Schubert, L. Sokolov, U. Gösele, Growth phenomena of Si and Si/Ge nanowires on Si (1 1 1) by molecular beam epitaxy. J. Cryst. Growth **290**, 6–10 (2006)
120. S.A. Dayeh, J. Wang, N. Li, J.Y. Huang, A.V. Gin, S.T. Picraux, Growth, defect formation, and morphology control of germanium-silicon semiconductor nanowire heterostructures. Nano Lett. **11**, 4200–4206 (2011)
121. K. Hiruma, H. Murakoshi, M. Yazawa, T. Katsuyama, Self-organized growth of GaAs/InAs heterostructure nanocylinders by organometallic vapor phase epitaxy. J. Cryst. Growth **163**, 226–231 (1996)
122. M. Paladugu, J. Zou, Y.-N. Guo, X. Zhang, Y. Kim, H.J. Joyce, Q. Gao, H.H. Tan, C. Jagadish, Nature of heterointerfaces in GaAs/InAs and InAs/GaAs axial nanowire heterostructures. Appl. Phys. Lett. **93**, 101911 (2008)
123. M.T. Björk, B.J. Ohlsson, T. Sass, A.I. Persson, C. Thelander, M.H. Magnusson, K. Deppert, L.R. Wallenberg, L. Samuelson, One-dimensional steeplechase for electrons realized. Nano Lett. **2**, 87–89 (2002)
124. L.E. Fröberg, B.A. Wacaser, J.B. Wagner, S. Jeppesen, B.J. Ohlsson, K. Deppert, L. Samuelson, Transients in the formation of nanowire heterostructures. Nano Lett. **8**, 3815–3818 (2008)
125. J.P. Boulanger, R.R. LaPierre, Polytype formation in GaAs/GaP axial nanowire heterostructures. J. Cryst. Growth **332**, 21–26 (2011)

126. M. Pozuelo, H. Zhou, S. Lin, S.A. Lipman, M.S. Goorsky, R.F. Hicks, S. Kodambaka, Self-catalyzed growth of InP/InSb axial nanowire heterostructures. J. Cryst. Growth **329**, 6–11 (2011)
127. P. Caroff, J.B. Wagner, K.A. Dick, H.A. Nilsson, M. Jeppsson, K. Deppert, L. Samuelson, L.R. Wallenberg, L.-E. Wernersson, High-quality InAs/InSb nanowire heterostructures grown by metal-organic vapor-phase epitaxy. Small **4**, 878–882 (2008)
128. M.T. Borgström, M.A. Verheijen, G. Immink, T. de Smet, E.P.A.M. Bakkers, Interface study on heterostructured GaP-GaAs nanowires. Nanotechnology **17**, 4010–4013 (2006)
129. M. Jeppsson, K.A. Dick, J.A. Wagner, P. Caroff, K. Deppert, L. Samuelson, L.-E. Wernersson, GaAs/GaSb nanowire heterostructures grown by MOVPE. J. Cryst. Growth **310**, 4115–4121 (2008)
130. J.P. Boulanger, R.R. LaPierre, Unveiling transient GaAs/GaP nanowire growth behavior using group V oscillations. Cryst. Growth **388**, 116–123 (2014)
131. G. Priante, G. Patriarche, F. Oehler, F. Glas, J.-C. Harmand, Abrupt GaP/GaAs interfaces in self-catalyzed nanowires. Nano Lett. **15**, 6036–6041 (2015)
132. K. Tateno, G. Zhang, M. Takiguchi, H. Gotoh, T. Sogawa, VLS growth of alternating InAsP/InP heterostructure nanowires for multiple-quantum-dot structures. Nano Lett. **12**, 2888–2893 (2012)
133. L. Ouattara, A. Mikkelsen, N. Sköld, J. Eriksson, T. Knaapen, E. Cavar, W. Seifert, L. Samuelson, E. Lundgren, GaAs/AlGaAs nanowire heterostructures studied by scanning tunneling microscopy. Nano Lett. **7**, 2859–2864 (2007)
134. J. Guo, H. Huang, X. Ren, Y. Xin, S. Cai, Y. Huang, Q. Wang, X. Zhang, W. Wang, Stacking-faults-free zinc blende GaAs/AlGaAs axial heterostructure nanowires during vapor-liquid-solid growth. Chinese Opt. Lett. **9**, 041601 (2011)
135. K. Tateno, G. Zhang, H. Nakano, Growth of GaInAs/AlInAs heterostructure nanowires for long-wavelength photon emission. Nano Lett. **8**, 3645–3650 (2008)
136. M. Heiß, A. Gustafsson, S. Conesa-Boj, F. Peiró, J.R. Morante, G. Abstreiter, J.G. Arbiol, L. Samuelson, A. Fontcuberta i Morral, Catalyst-free nanowires with axial $In_xGa_{1-x}As$/GaAs heterostructures. Nanotechnology **20**, 075603 (2009)
137. P. Krogstrup, J. Yamasaki, C.B. Sørensen, E. Johnson, J.B. Wagner, R. Pennington, M. Aagesen, N. Tanaka, J. Nygård, Junctions in axial III-V heterostructure nanowires obtained via an interchange of group III elements. Nano Lett. **9**, 3689–3693 (2011)
138. S. Plissard, K.A. Dick, X. Wallart, P. Caroff, Gold-free GaAs/GaAsSb heterostructure nanowires grown on silicon. Appl. Phys. Lett. **96**, 121901 (2010)
139. K. Tateno, G. Zhang, M. Takiguchi, H. Gotoh, Alternating InAsP/InP heterostructure nanowires grown with tertiarybutyl chloride. Nano Futures **2**, 045006 (2018)
140. C.H. Hsiao, S.J. Chang, S.C. Hung, Y.C. Cheng, B.R. Huang, S.B. Wang, B.W. Lan, S.H. Chih, ZnSe/ZnCdSe heterostructure nanowires. J. Cryst. Growth **312**, 1670–1675 (2010)
141. E. Bellet-Amalric, M. Elouneg-Jamroz, P. Rueda-Fonseca, S. Bounouar, M. Den Hertog, C. Bougerol, R. André, Y. Genuist, J.P. Poizat, K. Kheng, J. Cibert, S. Tatarenko, Growth of II–VI ZnSe/CdSe nanowires for quantum dot luminescence. J. Cryst. Growth **378**, 233–237 (2013)
142. D. Ercolani, F. Rossi, A. Li, S. Roddaro, V. Grillo, G. Salviati, B. Beltram, L. Sorba, InAs/InSb nanowire heterostructures grown by chemical beam epitaxy. Nanotechnology **20**, 505605 (2009)
143. V. Zannier, F. Rossi, D. Ercolani, L. Sorba, Growth dynamics of InAs/InP nanowire heterostructures by Au-assisted chemical beam epitaxy. Nanotechnology **30**, 094003 (2019)
144. P.-Y. Chevalier, A thermodynamic evaluation of the Au-Ge and Au-Si systems. Thermochim. Acta **141**, 217–226 (1989)
145. R.A. Burke, X. Weng, M.-W. Kuo, Y.-W. Song, A.M. Itsuno, T.S. Mayer, S.M. Durbin, R.J. Reeves, J.M. Redwing, Growth and characterization of unintentionally doped GaSb nanowires. J. Electron. Mater. **39**, 355–364 (2010)
146. K.A. Dick, J. Bolinsson, B.M. Borg, J. Johansson, Controlling the abruptness of axial heterojunctions in III−V nanowires: Beyond the reservoir effect. Nano Lett. **12**, 3200–3206 (2012)

147. C. Li, J.B. Li, Z. Du, L. Lu, W. Zhang, A thermodynamic reassessment of the Al-As-Ga system. J. Phase Equilib. **22**, 26–33 (2001)
148. J.-B. Li, W. Zhang, C. Li, Z. Du, A thermodynamic assessment of the Ga-As-Sb system. J. Phase Equil. **19**, 466–472 (1998)
149. C. Li, J.-B. Li, Z. Du, W. Zhang, A thermodynamic assessment of the Ga-In-P system. J. Phase Equil. **21**, 357–363 (2000)
150. I. Ansara, C. Chatillon, H.L. Lukas, T. Nishizawa, H. Ohtani, K. Ishida, M. Hillert, B. Sundman, B.B. Argent, A. Watson, T.G. Chart, T. Anderson, A binary database for III-V compound semiconductor systems. Calphad **18**, 177–222 (1994)
151. F. Glas, Elastic strain relaxation: thermodynamics and kinetics, in *Mechanical stress on the nanoscale - Simulation, material systems and characterization techniques*, ed. by M. Hanbücken, P. Müller, R.B. Wehrspohn (Wiley-VCH, Weinheim, 2011), pp. 3–26
152. V. Zannier, F. Rossi, V.G. Dubrovskii, D. Ercolani, S. Battiato, L. Sorba, Nanoparticle stability in axial InAs-InP nanowire heterostructures with atomically sharp interfaces. Nano Lett. **18**, 167–174 (2018)
153. J. Tang, J.-L. Maurice, F. Fossard, I. Florea, W. Chen, E.V. Johnson, M. Foldyna, L. Yu, P. Roca i Cabarrocas, Natural occurrence of the diamond hexagonal structure in silicon nanowires grown by plasma assisted vapour-liquid-solid method. Nanoscale **9**, 8113–8118 (2017)
154. D.L. Dheeraj, G. Patriarche, H. Zhou, T.B. Hoang, A.F. Moses, S. Grønsberg, A.T.J. van Helvoort, B.O. Fimland, H. Weman, Growth and characterization of wurtzite GaAs nanowires with defect-free zinc blende GaAsSb inserts. Nano Lett. **8**, 4459–4463 (2008)
155. M. Koguchi, H. Kakiyabashi, M. Yazawa, K. Hiruma, T. Katsuyama, Crystal structure change of GaAs and InAs whiskers from zinc-blende to wurtzite type. Jpn. J. Appl. Phys. **31**, 2061–2065 (1992)
156. K. Hiruma, M. Yazawa, T. Katsuyama, K. Ogawa, K. Haraguchi, M. Koguchi, H. Kakiyabashi, Growth and optical properties of nanometer-scale GaAs and InAs whiskers. J. Appl. Phys. **77**, 447–462 (1995)
157. C.-Y. Yeh, Z.W. Lu, S. Froyen, A. Zunger, Zinc-blende-wurtzite polytypism in semiconductors. Phys. Rev. B **46**, 10086–10097 (1992)
158. C.-Y. Yeh, Z.W. Lu, S. Froyen, A. Zunger, Predictions and systematizations of the zinc-blende-wurtzite structural energies in binary octet compounds. Phys. Rev. B **45**, 12130–12133 (1992)
159. Takeuchi, S., Suzuki, K., Stacking fault energies of tetrahedrally coordinated crystals. phys. stat. sol. (a) **171**, 99–103 (1999)
160. F. Glas, A simple calculation of energy changes upon stacking fault formation or local crystalline phase transition in semiconductors. J. Appl. Phys. **104**, 093520 (2008)
161. T. Akiyama, K. Nakamura, T. Ito, Structural stability and electronic structures of InP nanowires: Role of surface dangling bonds on nanowire facets. Phys. Rev. B **73**, 235308 (2006)
162. T. Akiyama, K. Sano, K. Nakamura, T. Ito, An empirical potential approach to wurtzite-zinc-blende polytypism in group III–V semiconductor nanowires. Jpn. J. Appl. Phys. **45**, L275–L278 (2006)
163. H. Shtrikman, R. Popovitz-Biro, A. Kretinin, L. Houben, M. Heiblum, M. Bukala, M. Galicka, R. Buczko, P. Kacman, Method for suppression of stacking faults in wurtzite III-V nanowires. Nano Lett. **9**, 1506–1510 (2009)
164. B. Mutaftschiev, R. Kern, C. Georges, Sur le mécanisme VLS de croissance des whiskers. Phys. Lett. **16**, 32–33 (1965)
165. E. Hilner, U. Håkanson, L.E. Fröberg, M. Karlsson, P. Kratzer, E. Lundgren, L. Samuelson, A. Mikkelsen, Direct atomic scale imaging of III-V nanowire surfaces. Nano Lett. **8**, 3978–3982 (2008)
166. N.V. Sibirev, M.A. Timofeeva, A.D. Bol'shakova, M.V. Nazarenko, V.G. Dubrovskii, Surface energy and crystal structure of nanowhiskers of III–V semiconductor compounds. Phys. Sol. State **52**, 1531–1538 (2010)

167. R.E. Algra, V. Vonk, D. Wermeille, W.J. Szweryn, M.A. Verheijen, W.J.P. van Enckevort, A.A.C. Bode, W.L. Noorduin, E. Tancini, A.E.F. de Jong, E.P.A.M. Bakkers, E. Vlieg, Formation of wurtzite InP nanowires explained by liquid-ordering. Nano Lett. **11**, 44–48 (2011)
168. W.D. Kaplan, Y. Kauffmann, Structural order in liquids induced by interfaces with crystals. Annu. Rev. Mater. Res. **36**, 1–48 (2006)
169. K.A. Dick, C. Thelander, L. Samuelson, P. Caroff, Crystal phase engineering in single InAs nanowires. Nano Lett. **10**, 3494–3499 (2010)

Functionalization

Surface Functionalization of III–V Nanowires

Rainer Timm and Anders Mikkelsen

Abstract The physical and chemical properties of semiconductor nanowires are significantly influenced by their surface structure and morphology. This can be understood in that surfaces make out a much larger part of the total structure as compared to macroscale objects. An immediate consequence is that the lack of surface control can result in poor performance and reproducibility of any nanowire device. It is clear that bad performance is problematic, but it must be stressed that without performance reproducibility across millions of nanowires they can never become a useful real technology. This is indeed why many promising nanostructures and materials lost interest of both the scientific and commercial communities. However, surface control also can be used to strongly enhance nanowire performance and even introduce new functionality. As a result, surface functionalization is a key issue for nanowire science and technology. In this chapter, we describe in detail how standard surface science techniques such as Scanning Tunneling Microscopy (STM) and X-ray Photoemission Spectroscopy (XPS) can be modified for effective studies of 1D nanowires despite that they have been originally invented only for large and flat 2D surfaces. We go on to give a number of examples on how these techniques have revealed the precise structure–function relationship in particular of III–V semiconductor nanowires and their surfaces. We further discuss, how this can be used to control the structure and chemistry of the wires down to the atomic scale enabling new functionality for (opto)electronics, sensors, and many other device types. While we focus on III–V nanowires, the examples and techniques put forward should be applicable to many other material systems and types of nanostructures.

Keywords Surface · III–V · Semiconductors · Oxides · Scanning tunneling microscopy · X-ray photoemission spectroscopy

R. Timm · A. Mikkelsen (✉)
Division of Synchrotron Radiations Research, Department of Physics and NanoLund, Lund University, Professorsgatan 1, 22362 Lund, Sweden
e-mail: anders.mikkelsen@sljus.lu.se

© Springer Nature Singapore Pte Ltd. 2021

N. Fukata and R. Rurali (eds.), *Fundamental Properties of Semiconductor Nanowires*,
https://doi.org/10.1007/978-981-15-9050-4_2

1 Introduction

Structures confined to the nanoscale in one or more dimensions are characterized by a fundamental particular property, which is their large surface to bulk ratio. In its most simple form, this is defined as the number of atoms in the outermost single layer of the object divided by the total number of atoms in the object. For a macroscopic object, this number will be very small, for example, for a 0.25 carat diamond (affordable even on a professor salary) with a diameter of 4 mm, the surface to the bulk ratio will be only ~0.000002%. While the presence of the surface still matters for the functionality, because it acts as the interface to the surrounding air, metal embedding, etc., the atomic-scale structure is of little relevance for central physical properties such as color and strength. Thus, for the 0.25 carat diamond, we would only need to care about the surface if it would participate in surface reactions—which could be chemical processes in relation to adhesion to metal surfaces such as gold and silver. However, as we scale down to the nanoscale we realize that already for a 50 nm diameter diamond nanowire (NW), the outermost layer of surface atoms makes out 3% of the total volume. At this point, only a few optically or electrical active defects at the surface will correspond to significant doping levels and will influence electrical and optical performance very strongly—in the case of our diamond, for example, the color. Finally, as we go even smaller, we end up at the Carbon nanotube or Graphene, in which case the object is 100% surface—there is nothing else. And even small atomic-scale rearrangements in the surface can completely alter important properties such as conductivity or mechanical strength [1, 2].

From a technological point of view, the surface of nanostructures is then also very important. Any NW-based gas or liquid sensor being developed for medical or security application depends on adsorption on the surface or surface interactions—making the surface structure and stability of central importance. Important is, of course, the ability of the molecule to adsorb and induce an electrical/optical signal, but also issues such as dissolution in the fluid are important if the nanostructure is to be implanted in the body [3]. For electronic devices, defects on the surface will influence effective doping and transport properties, which can be used to improve nanostructure performance, and must definitely be controlled to realize the efficient and reproducible behavior needed. For photonics, surface recombination can dominate over other processes in suppressing carrier extraction, and for resonant optical enhancement, plasmon surface resonances and dynamic behavior can be influenced by the surface [4, 5]. It is fair to state that one of the central issues hindering the application of NWs in mass produced devices is the ability to consistently control their surface properties. It can be noted that this is a challenge for all types of nanostructures, not least 2D materials, in which the issues of atomic-scale surface defect control are very underappreciated when considering that the object is 100% surface. Finally, for the synthesis of NWs, diffusion, incorporation, and stability of the substrate and NW surfaces will be central in steering the growth. This is very fundamental as one can argue that NW growth is generally based on some particular surface area having a faster growth rate than all others. All of this might seem mostly as issues of concern

that may hamper the usefulness of NWs (or any other type of nanostructures). Indeed, if surfaces are not controlled it might severely limit the functionality of the structure, but on the other hand, surfaces can also be the key to the superior performance of the nanostructure. This is certainly true for catalysis where the large surface to bulk ratio "enhances" the catalytic activity per gram of material and the inherently large number of step sites on a nanostructure (see next section) enhances reactivity [6, 7]. For chemical sensors, the same holds true [8], and for electronic devices, the surface can be used as a special conduction channel. So, without surface control, we are lost, but with tailored nanostructure surfaces we open up for incredibly enhanced materials functionality.

Many of the observations we describe below could be found for all kinds of nanostructures, be it NWs as covered here, 2D materials, quantum dots or other types of nanomaterials. Even the area of NWs is vast with a plethora of materials encompassing most of the periodic table. However, given that the literature on nanostructures and NWs, in particular, is so large, we have chosen to focus in particular on III–V semiconductor NWs in this chapter. The III–V NWs have many exciting technological applications, and they also present a very instructive example of surface functionalization and the use of techniques to characterize this. So if you study other types of NWs or nanostructures, you should not put this chapter away now. The messages and general lessons that can be learned by the III–Vs are likely transferable to many material systems. Finally, we note that the substrate surfaces are also extremely important for the NW growth as it has, for example, been found that the detailed surface chemistry is important for tailoring the growth of both Au seeded and In seeded NWs [9–11], but this will not be treated in detail here.

III–V NWs are mixed ion and covalently bonded binaries consisting of materials from the group III and group V of the periodic table. This group of NWs is particularly useful in that the many different combinations of III–Vs have quite similar crystal structures (to be discussed in Sect. 2) and are thus readily combined. Further, the bandgap, which is a defining property for semiconductors, can be varied smoothly over a very wide range using different combinations of III–V materials [12]. Finally, since the growth of these materials has been studied for many years, a very high level of control and quality is possible. As a result, a wide range of applications of these wires has been demonstrated. Photovoltaic cells based on NWs have shown excellent performance [13–16], and since III–Vs with different bandgaps can be combined in a single wire, tandem solar cells with efficiency beyond the Shockley–Queisser limit are possible. Here surface recombination and the influence of the surface in doping control are especially relevant phenomena for the performance of the structures and the ability to reach efficiencies far beyond, for example, Silicon. NWs of InAs and combinations of InAs and GaSb have shown great promise for Tunnel Field Effect Transistors that could go beyond the theoretical limit of conventional MOSFET technology [17, 18]. For these, the NW-oxide interfaces in the device play a crucial role in defining performance as mobility can be reduced if interface defects pin the position of the Fermi level. Excessive losses can also be experienced at the surface that increases heat losses, which is a crucial issue in modern electronics. Of important practical implication is light-emitting diode (LED) technology based on

the III-Nitrides. NWs can in a superior fashion accommodate defects, and surface roughness and defects can again play an important role for efficiencies and possibly the performance over the lifetime of the device—in particular at the interface of the contacts. Despite the many III–V NW technologies under current development, be it solar cells and LEDs or high speed/low power electronics [14, 17, 19], their surface structure, chemistry, and morphology at the interface with other materials, air, or liquids is still poorly understood. Information is lacking both at the atomic scale as well as on the larger morphological level. As argued above, the surfaces play a central role in determining the functionality and this situation is thus quite unfortunate. Without a proper structure–function understanding, surface functionalization essentially depends on trial and error design coupled with knowledge from bulk surfaces. However, as will be seen below, knowledge from the bulk surfaces does not suffice to describe NW surfaces and proper studies give us clear design advantages.

Since it can be clearly argued that surfaces are important for NW functionality, one can wonder why the number of surface studies is far smaller than for bulk materials. The main reason is likely that the 1D nature of the NWs is a poor match for most surface science techniques. These have originally been developed with flat "infinite" 2D surfaces in mind. For averaging techniques such as electron spectroscopy and diffraction, the NW surfaces are much smaller than the typical beam radius. Focusing is one option that introduces a number of difficulties while any averaging over many wires introduces errors if any variation in wire structure from wire-to-wire is present. Scanning Tunneling Microscopy (STM) which can provide atomic resolution in principle has no problem with the small size of the NW terraces, but the large difference in height between the NWs and their atomic-scale surface corrugation introduce challenges, as well as the attempt to locate wires and keep them still during scanning. The good news is that all of these problems can and have been solved, which we will describe further below.

2 Fundamentals of III–V Nanowire Surface Structure and Morphology

To understand the surface structure of the III–V NWs, we have to start with the bulk crystal structures and identify the most favorable facet truncations that can be observed. Generally, the III–V materials either form in cubic Zincblende (Zb) or the hexagonal Wurtzite (Wz) structures.

From a bulk symmetry point of view, these structures at a first inspection appear quite different as the Zb is cubic while the Wz is of hexagonal symmetry. However, the NWs usually grow in the <111> (Zb) or <0001> (Wz) directions, in which the difference, as seen in Fig. 1, is only in the stacking sequence. In both cases, the NWs consist of stacked hexagonal layers with one group III and one group V atom. For Zb the stacking sequence is ABCABC while for the Wz the stacking sequence is

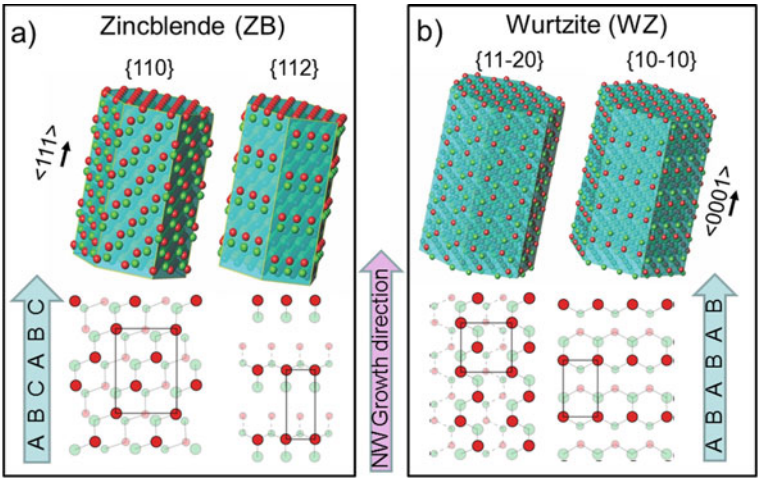

Fig. 1 Atomic models of prototypical III–V NWs. Red and green balls correspond to the group III and V atoms. **a** Zincblende cubic crystal structure which can be described as an ABCABC stacking sequence of hexagonal III–V planes in the <111> direction. The two most close-packed sets of facets that are perpendicular to the growth direction are the {110} and {112} planes. Only the {110} planes are usually observed. **b** Wurtzite hexagonal crystal structure which is can be described as an ABAB stacking sequence of hexagonal III–V planes in the <0001> direction. The two most close-packed sets of facets that are perpendicular to the growth direction are the {11-20} and {10-10} planes. Both planes are observed for NWs

ABAB. Interestingly, while the bulk materials usually favor either the Wz or the Zb depending on the specific elements, the small areas and particular growth modes of the NWs allow the growth of both crystal types for most elemental combinations [20]. In fact, even more complex stacking patterns can be found in the NWs [21]. The growth direction and the crystal structure have significant implications for the surface facets found on the NWs. The most common surfaces for any type of nano crystallite are usually related to the low index surfaces perpendicular to the growth direction. Indeed, as seen in Fig. 2, we can identify these surfaces for the Zb and Wz crystal faces. For the Zb, in particular, the {110} surfaces are relevant, as this facet type is non-polar and presumably has the lowest total energy in general for many III–Vs even in the bulk crystallites. This can be exemplified by the point that for many III–V materials, cleaving along the {110} directions leads to highly flat and step free surfaces [22]. This has been utilized in so-called cross sectional STM, a technique that has been employed with significant success on embedded III–V NWs [23, 24], as well as other nanostructures [25–27]. The {112} surface, which is found at a 30° angle to the {110}, has not been observed as a major facet. In contrast, both the {10-10} and {11-20} type of surfaces have been observed for Wz NWs [28–30]. In particular, for the Wz crystal structure, it has been demonstrated for both GaAs and InAs that a particular facet can be made to dominate by careful control of the growth conditions [29, 30]. This control can both be facilitated by varying III–V

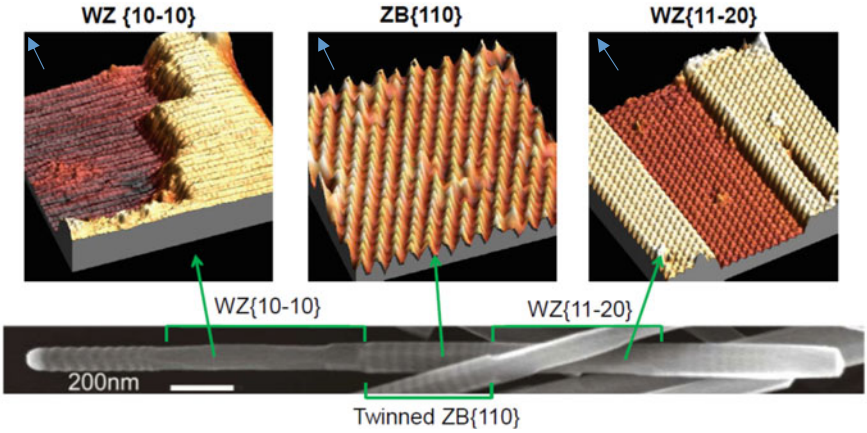

Fig. 2 Top: 3D STM images of the three main facets found on the III–V NW surfaces. In all three cases, the periodic protrusions are individual group V atoms. Surface steps are also observed for the Wz {10-10} and Wz {11-20} surfaces. Blue arrows in each of the images indicate the NW growth direction. Bottom: Scanning Electron Microscopy (SEM) image of a NW with all of these facets found in the same wire, with all three areas from which the STM images have been recorded are indicated.

pressures and temperature during growth or by an overgrowth of the NW through so-called core–shell growth. Originally, the ideal NW has a hexagonal morphology, but if radial overgrowth favors specific surface facets, all 12 possible orientations of the {10-10} and {11-20} facets might be present, with a surface angle of 30° between them, leading to an almost round NW. Interestingly, for all the three main surfaces found, the clean oxide free surfaces are usually unreconstructed [28] (as seen in Fig. 2), as will be discussed more below.

Since both Wz and Zb can be created in the NWs by altering growth parameters, it is also possible to switch between these two types of structures during growth in a seamless fashion as the nearest neighbor bonding is the same in the two types of stacking. While the change can be provoked intentionally, the effect is a very common unintentional effect upon NW growth. Thus, stacking faults as stacking sequences of ABCBABC instead of ABCABCA, or ABCAB instead of ABABA are often observed. These stacking faults can also influence surface morphology as discussed in [31]. A situation can even occur in which the surface step structure is altered by a stacking fault. When switching from a larger Zb to a larger Wz segment, a rather dramatic change in surface morphology has also been observed. As seen in Fig. 3a, while the (110) Zb terrace is completely flat, the following (11–20) surface of the Wz segment has a step structure with elongated steps in the growth direction. The various step morphologies can then be induced during growth, leading to both tapering and in some cases, as, e.g., for Au-free grown NWs, to large sections with no surface steps [32]. For certain instances, periodic fluctuations of the morphology

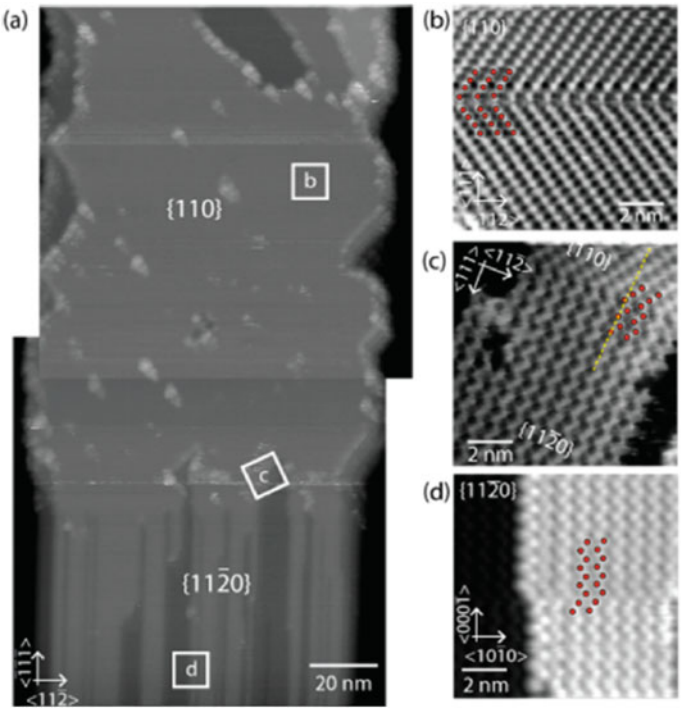

Fig. 3 STM imaging of a Wz and Zb InAs NW. **a** Overview image of a {1120} to {110}-type Wz to Zb interface on a NW. It can be seen how the overall step morphology changes between the two facets. **b** STM image of As atoms on part of the rotationally twinned {110} facet as indicated in **a**. Here essentially the ABCABC stacking of one twin changes into a CBACBA stacking of the other. **c** Atomically sharp interface between {110} and {1120} facets. **d** Atomic arrangement on the {1120} facet, one can notice a single stacking fault in which the Wz ABAB stacking in most of the facet goes into one single segment of a Zb ABC stacking. Reprinted with permission from [30]. Copyright 2014 American Chemical Society

along the NW can also be found. This has been observed on InP pn-junctions with minor terraces elongated along the growth direction [33].

However, for the Zb crystal structure, a further crystallographic feature can induce significant morphological fluctuations. In Fig. 3b, one can see the phenomena of twinning in which a Zb crystal segment is rotated 180° with respect to the previous segment to give its twin. Two twins can be seamlessly joined along the <111> growth direction of the NW. In terms of lattice plains, this corresponds to stacking ABCABC for one twin and CBACBA for the other twin. Under certain growth conditions [34], an oscillatory switching between the two twins will occur as described in Fig. 4a. This will usually result in the formation of small {111} facets on the side of the NW as seen in Fig. 4b, left. Overgrowth of this structure can be performed to create flat {110} facets, as seen in Fig. 4b, middle and right. The small {111} facets have also been studied with STM as seen in Fig. 4d, and it is found that the (111)A is

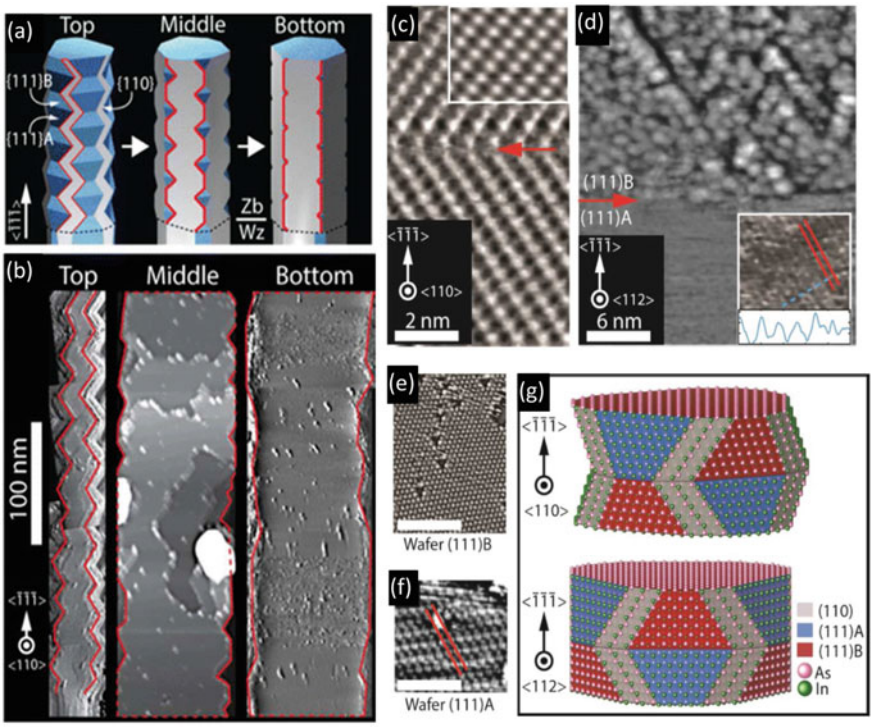

Fig. 4 **a** Illustration of NW with Zb structure alternating between the two possible twins (a so-called twin superlattice) in different stages of overgrowth, displaying the {111}A/B-type facets (blue), as well as the {110}-type overgrowth facets (gray with red borders). **b** STM images of {110} facet from the top, middle, and bottom Zb segment, respectively. Top and bottom image have been differentiated to make height variations more clearly visible. **c** Atomically resolved image of a twin boundary (red arrow) on a {110}-type facet of the NW. Inset shows an analogously treated surface of an InAs(110) wafer. **d** High-resolution image of the {111}A/B-type facets (interface marked with red arrow) of a top Zb segment as observed in stages I–III. The image is differentiated for ease of viewing. The inset shows a portion of the {111}A with enhanced contrast, same scale as the main image. **e**, **f** Depicts the corresponding {111}B- and {111}A-type surfaces from analogously treated InAs(111)A/B wafers, respectively. Same scale as in **d**. **g** Depicts a basic atomic model, i.e., no surface reconstructions are shown, of a Zb twin plane in a NW illustrating the relative orientation of relevant surface planes. Reprinted with permission from [35]. Copyright 2015 American Chemical Society

unreconstructed while the (111)B presumably has a limited version of a sqrt(19) reconstruction. The overgrowth phenomena has been studied in some detail [35]. As is seen in Fig. 4a, growth proceeds more easily on the edges between neighboring {111} facets to start to form {110} facets. Since these are much more stable, growth slows down once they have formed. As a result, overgrowth at higher temperatures (which overcomes kinetic barriers) will favor the presence of {110} facets and lead to a smoothening of the NW surfaces. If a different material (for example AlGaAs

instead of GaAs) is provided during growth, this can be used to form ordered quantum dot pockets along the NW as demonstrated previously [36].

Generally, most film and dot growth on III–Vs is performed on the {100} Zb surfaces, with high growth rates and good control. The surfaces of the NWs are much less explored for overgrowth of thin films and quantum dot growth, but there are a number of recent examples of this also being possible [37, 38]. Here it can be noted that both diffusion rates, surface incorporation rates, and overgrowth rates are very different between the facets. An example of this is found in [23, 36, 39], here it was found that the sidewall overgrowth was a factor 5 slower than substrate growth and material would be lost to the substrate.

3 Methods for Surface Characterization; STM, XPS, PEEM

While the influence of the atomic-scale surface structure on NW physical and chemical properties can be clearly argued (see Sect. 1), the available number of studies that directly address this are considerably fewer than what can be found about the interior structural properties and general morphology as obtained by Transmission Electron Microscopy (TEM) or Scanning Electron Microscopy (SEM). An important side note is that both of these techniques cannot give real surface information on the wires, only for layers beyond ~1 nm in thickness will they give reliable information. A central reason for the lack of "real" surface studies is that while a large number of widely used surface characterization techniques exists, they are generally developed for "infinite" 2D surfaces. Employing these on 1D objects as the III–V NWs presents several new challenges. Firstly, standard techniques such as X-ray Photoemission Spectroscopy (XPS) for chemical analysis or Low Energy Electron Diffraction (LEED) for surface crystal structure analysis average over areas of tens to hundreds of micrometers. As a result, we will need many NWs spread over an area of this size to record a signal. Any inhomogeneity from wire-to-wire can introduce a broadening in obtained XPS spectra and the diffraction pattern obtained in LEED will be smeared out if wires are not all perfectly (atomic level) aligned with respect to both translational and rotational symmetry. To resolve this, either samples with a high degree of perfection and order have to be fabricated, or we turn to the imaging versions of XPS and LEED in form of the Spectroscopic Photoemission and Low Energy Electron Microscope (SPELEEM).

As seen in Fig. 5, XPS studies of ensembles of NWs have been successfully performed with high spectral resolution. To realize a homogeneous sample it was not possible to achieve a coverage of much more than 10% wire on the surface. This results in a small signal from the wires compared to the substrate they have been placed on. To still obtain meaningful results, the superior intensity provided by modern synchrotron facilities must be used, as was done in the work seen in Fig. 5, as well as others [33, 40, 41]. Further, a substrate with no significant peaks

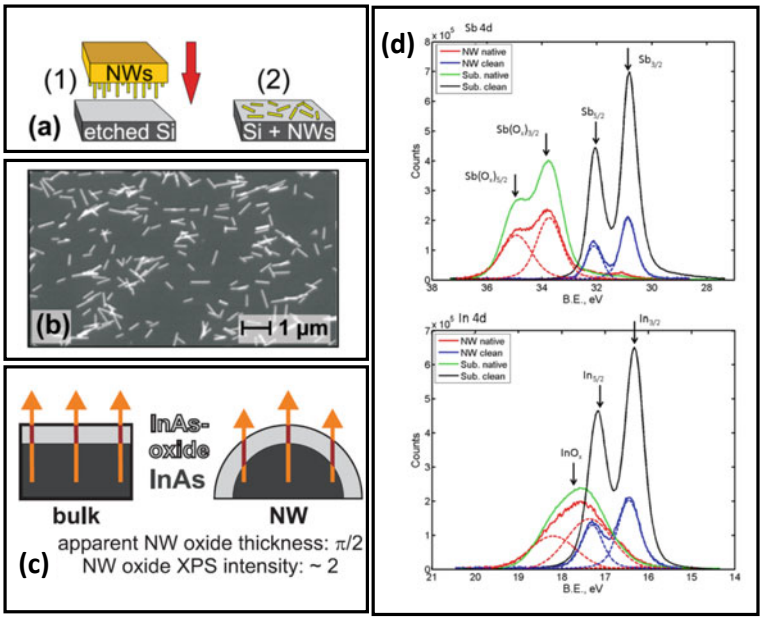

Fig. 5 **a** Sketch of the NW deposition: The growth sample containing vertical NWs is gently pushed onto a Si substrate, resulting in **b** InAs NWs deposited on a Si substrate, imaged by SEM after XPS measurements. **c** Sketch comparing XPS intensities from planar substrates and NWs. Reprinted from [40], with the permission of AIP Publishing. **d** Sb 4d (top) and In 4d (bottom) core-level XPS spectra of an InSb substrate and InAs/InSb NWs with (native) oxide before and after exposure to atomic hydrogen (clean), with background subtracted. Data was recorded using a 350 eV photon energy. We show the fitted peaks (dashed, red) for NW native oxide before cleaning, using a single SbOx and InOx doublet, and for the clean InSb after cleaning (dashed, blue). The oxide peaks are fully removed by the cleaning process. The nanowire peaks are scaled (5 × for Sb 4d, 10 × for In 4d) to ease comparison with the stronger substrate signal. Reprinted with permission from [41]. Copyright 2015 American Chemical Society

in the region of the main photoemission core-level peaks of the III–V NWs must be used. Silicon works well for many III–Vs, graphite samples could potentially be even better due to the quite featureless photoemission spectra, but problems of depositing NWs in a good fashion on this surface have held back the use of this substrate. It can be seen from Fig. 5d, that NW spectra appear broader than for a flat clean surface, however, this is a rather unavoidable trait as the wire surfaces are naturally confined by their nanoscale diameter resulting in more step and kink atoms compared to flat bulk surfaces—which broadens the XPS spectra. For example, a 30 nm wide NW with perfect hexagonal symmetry will have naturally limited terrace sizes as an individual facet will only be about 20 nm wide. An additional issue to regard is that the curvature of the wires also introduces an extra geometric factor if depth profiling using XPS is considered. We mostly obtain electrons emitted towards the direction of the analyser, i.e., normal to the substrate, which is not necessarily normal to the surface in the case of curved NW facets, as sketched for a round NW in Fig. 5c.

Due to the short mean free path of the photoelectrons (that also give us high surface sensitivity), this will lead to an overestimation of the amount of material in the top surface layers compared to layers further down. This geometric factor can, however, be calculated and taken into account [40]. The chemical composition and electronic structure analysis possible with this type of XPS analysis is demonstrated in Sect. 5.

To image individual NWs, SPELEEM can be used, which essentially is an electron microscopy technique that gives 2–20 nm lateral resolution of XPS or LEED. Thus, the resolution vertically is extremely high, with sensitivities of <10% of a monolayer of atoms. For high-resolution imaging using this instrument in XPS imaging mode, a lot of emitted electrons are required, and so again a synchrotron is needed as X-ray excitation source. A more detailed description of the method can be found in Ref. [42], that touches upon NWs, and more generally in a recent book by Ernst Bauer [43].

Another avenue is to turn to scanning probe imaging techniques such as STM which can give you a local (atomically resolved) picture of the surface and thus in principle of the atoms on single NWs (Fig. 6a). The two main challenges, in this case, are firstly to locate NWs dispersed on the surface and secondly that the tens to hundreds of nanometer height of the dispersed wires compared to the desired sub-nanometer resolution has been seen as incompatible (and deterred many people from attempting STM on such objects). However, it has been shown that these challenges can be successfully solved and high quality STM and Scanning Tunneling Spectroscopy (STS) can be performed on the wires [28–33, 35, 41, 44]. To study NWs using STM, the NWs are typically placed on a substrate of similar III–V material

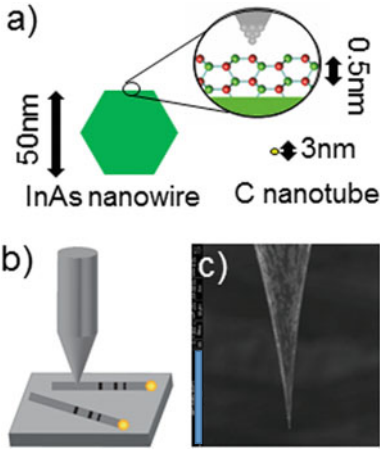

Fig. 6 Description of STM on NWs imaging concept and problems. **a** Scanning on a 50 nm wide NW with the aim to achieve a resolution of 0.01 nm to clearly see the atoms on the III–V surfaces. The large dynamic range for the STM tip is a significant challenge. This is in contrast to, for example, Carbon Nanotubes that are much closer to the atomic scale. **b** The STM tip is approached to a III–V substrate with the III–V NWs that have been hydrogen cleaned. **c** SEM image of an etched W tip that can be used for NW scanning. Scale bar is 50 μm

and then cleaned with atomic Hydrogen (as described in Sect. 4) or decapped from an As protection layer [45]. This is necessary as the NW growth is usually carried out in a chamber separate from the STM system and the in air transport will result in the formation of a native oxide. The density of wires is an important consideration if a sample with no markers is used. A too large density will result in large agglomerations of NWs in piles that will be difficult to scan on, and too few wires will make it impossible to locate them. A density of 1 NW/μm^2 has previously been found to be a good compromise. A good strategy is to deposit wires using the close proximity deposition (CPD) method [46], from a sample with a wire density around $1/\mu m^2$. In the CPD method, a sample with upright standing, as-grown NWs is taken upside-down and briefly touched on the substrate one wants to use for scanning. That the correct wire density has been obtained can be verified using an optical microscope with $\times$ 100 magnification. If the spot where the wires have been deposited on the substrate is larger than 50 $\mu m \times 50$ μm, it can also be seen in most of the optical positioning systems provided with an STM which are used for placing the tip on the sample. These areas will have a matte appearance which is different from the mirror-like surfaces usually found on the III–V substrate wafers. For locating a NW with the STM tip, low currents and high settings for the gain of the PID loop of the STM should be used. Line scans of several micron length allow for quick identification of a NW on the otherwise flat substrate. Some movements using the coarse positioning system of the STM might be needed to find a place with a suitable wire, but with practice and good coverage, a NW can be located within <1 h. Upon finding a NW, one can zoom in on the top facet of the wire and imaging can commence (Fig. 6a, b). Here it is worth noting that in contrast to "standard" STM in wide 2D surfaces, not only a good structure of the outermost few atoms of the tip matters for good results, but also the tip shape on a larger scale of tens to hundreds of nanometers matters. If the tip is too blunt or too awkwardly curved, the wire will look extremely distorted in STM images and it can be difficult to identify the wire facets. Tips with the shape as shown in Fig. 6c are preferable as they give the best results, these can be fabricated by DC electrochemical etching as described in Ref. [47]. After verification of a functioning procedure for good tip shapes, these will no longer present a problem. As measurements have also been performed on top of upright standing NWs [48–50], this issue has been given some consideration as seen in Ref. [48]. Finally, we note that both the top facet and the side facets are possible to image, and with a good tip even the bottom of the grooves created by {111} side facets can be imaged as seen in Fig. 4b.

A further important refinement of STM/S on NW surfaces in order to develop and elucidate their properties would be to image them during device operation. This is relevant for several reasons. Firstly, surfaces can change during device fabrication and thus the final devices could have very different structure and properties compared to the unprocessed wires. Secondly, the NW surfaces might well change during device operation. This type of effect is well known in semiconductor devices where electromigration is a serious issue [51]. This effect can, however, also be useful, in particular, in devices that are developed for network learning as the physical alteration

can act as a memory in the circuit [52]. To perform device measurements under well-controlled surface conditions, it would again be relevant to clean the surfaces to have a single crystalline and oxide free starting point. Here it is interesting to note that the Hydrogen cleaning described in the next section is performed at so low temperatures that it should be possible to retain device functionality. It has indeed been shown that with some modification of standard device designs, it is possible to create devices that can both survive hydrogen cleaning and can be scanned by STM [53]. An important factor to consider here is thermal stress during the heating which can tear apart the device. In particular, the Au contacts that are usually placed on top of the NW can expand differently than the NW and lead to rupture. This is not a problem for devices with a short distance between terminals, but short distances preclude scanning as the STM tip will come into contact with the metal contacts instead of the NW. Both these problems can be solved by placing the NW on top of the contacts instead of using either random dispersion [53], or SEM/optical microprobes. To fix the NW to the contacts and get good conduction through them, in-vacuum annealing (which anyway occurs during hydrogen cleaning) [41], or the addition of a thin top fixation layer can be used. An additional important benefit of a top design is that the devices can be placed on top of a conducting substrate as seen in Fig. 7. Only beneath the contacts, one will find an insulating dielectric. As a result, STM scanning is possible everywhere on the device in contrast to "standard" devices where considerable areas have nonconducting SiO_2 where the tip might crash. Initial results with such systems have indeed confirmed that considerable rearrangements on the NW surfaces can occur during device operation [53]. Both reformation of the complete device or, surprisingly, removal of individual defects can happen. It should be noted that even for NWs deposited on non-conductive surfaces and contacted with metal pads defined by lithography, STM/S can be possible if combined with Atomic Force Microscopy (AFM) by using a so-called qPlus probe tip [54, 55]. However, here a somewhat limited quality of qPlus tips as compared with the ideal STM tips and the limitations given by the metal contacts described above give additional challenges to the STM/S experiment, which can be avoided by using the design described previously and sketched in Fig. 7. Still, if slightly lower resolution can be tolerated, this can give very relevant and interesting results.

4 Initial Formation and Control of the Clean Crystalline NW Surface

A central starting point for proper control and studies of NWs is the creation of initial crystalline and well-ordered surfaces on them. This will form the basis of reproducible scientific studies, as well as for reproducible manipulation of surface functionality. Preparation of clean ordered crystalline NW surfaces is possible on the III–Vs using at least two different strategies. The fundamental problem for any such semiconductor surface is that exposure to air for transport between equipment will

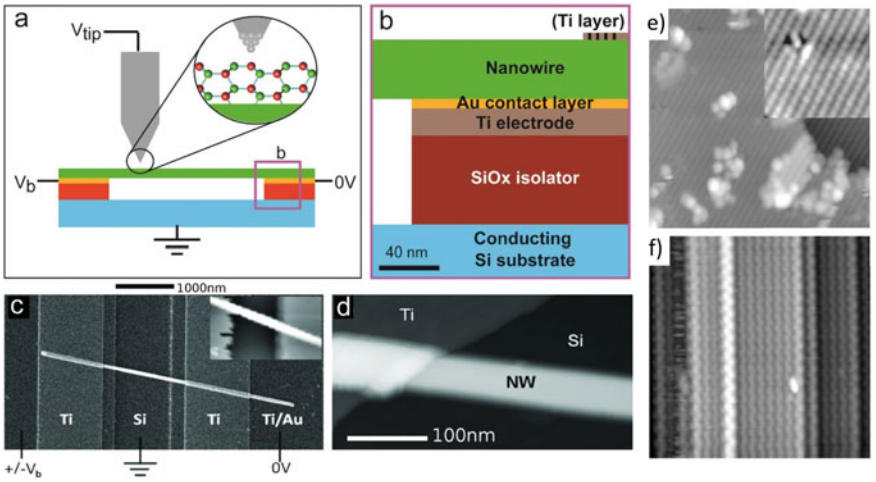

Fig. 7 Nanowire device for atomically resolved STM. **a** Schematic of the STM device experiment. The NW (in green) has been cleaned and atomic resolution is possible as illustrated in the zoom in. V_b is defined as the bias applied across the NW, V_{tip} the bias on the STM tip with respect to the ground. The NW contacts can be independently grounded which prevents electrical shorting and defines a reference ground level (and reference height for the STM tip). **b** Profile of the NW-contact area in **a**. The NW crosses a conducting Si trench contacted by Ti/Au electrodes and separated from the conducting Si substrate by thermally deposited SiO_x (or sputter grown SiO_2). The Si substrate can either be grounded or used as a back gate. The NW can be held in position by an optional thin Ti 'holding' layer deposited on top of it parallel to the trench, but significantly away from the trench edge. **c** A top-down SEM image of the completed device, showing the NW above a 1 μm wide Si trench and contact electrodes (labeled). Inset: Fast scan overview STM image of Ti/Au contacts and nanowire, the image is $3 \times 2\ \mu m^2$. **d** Higher resolution STM image of a NW device, showing the Ti/Au contact and the NW above the Si substrate. All regions of the device can be scanned by the STM tip at a tip bias of −1.5 V in constant current mode at a setpoint of 60 pA. **e**, **f** STM imaging with an atomic resolution on both InAs and GaAs NW devices. **e** $20 \times 20\ nm^2$ STM image of the (110) surface of a GaAs NW with Zb structure. The figure inset more clearly shows the atomic resolution from the top layer As atoms (bright dots) and a defect consisting of several As vacancies (missing dots). **f** $20 \times 20\ nm^2$ STM image of a Wz {11-20} facet showing the atomic resolved zigzag pattern observed on the surface of an InAs NW device. In this specific session, the surface was imaged for about 3 h under varying bias conditions. Reprinted from [53], under a Creative Commons BY4.0 license

lead to the formation of a 1–2 nm thick surface oxide [56, 57]. Removing this oxide thermally is problematic since the desorption temperature of the oxide is higher than the non-congruent evaporation temperature and sometimes even the melting temperature of the III–V surface. Most annealing attempts will thus lead to either formation of group III droplets [58, 59] or roughening of the surface. Sputtering is not useful since it is problematic to obtain a crystalline ordered surface afterwards via annealing and it will introduce unwanted defects [57, 60].

One strategy to solve this could be to transport the sample between experimental equipment without breaking the vacuum. This option is, however, rarely available.

Instead, several transport strategies adopted from bulk surfaces can be used. If Molecular Beam Epitaxy (MBE) growth is used, the wire growth can be finalized by an overgrowth with elemental Arsenic at low temperature. Transport in the air will lead to the partial oxidation of the As layer, however, upon insertion into a characterization chamber, containing, for example, an STM, the As can be desorbed by low-temperature annealing leading to a clean crystalline surface. Such a strategy has been adopted with success in Refs. [45, 61]. However, it is limited to MBE type of growth and specific compound nanowire materials (besides As, a similar capping scheme has, e.g., been applied using Sb [62]). For Metal Organic Chemical Vapor phase Deposition (MOCVD) type of growth that is commonly used in industry, As capping cannot be used and another more general strategy has to be adopted. Here atomic hydrogen cleaning has been shown to provide an excellent alternative. By exposing the surface to atomic hydrogen, the temperature for desorption of the oxides on the surfaces is significantly lowered, whereas it does not affect the crystalline III–V surfaces [28, 29, 32, 41]. This allows the removal of the oxide formed during transport without damaging the crystalline surface. Since the oxidation is very homogenous, it has been shown that the surface that remains after transport and cleaning is very close in morphology to the original surface with a change of only a single atomic layer [32]. This can lead to the formation of the small islands and holes of one atomic layer thickness even on the bulk {110} substrates [32], but the original morphology can be recognized underneath since the disturbance is only a single layer. Due to the small size of the wire facets, perfectly flat island free facets have been obtained for several facets as seen, e.g., in Fig. 2b. Still for larger wires phenomena as the ones seen in Fig. 8, for a very thick (bulk like) InAs NW can be observed. It indicates that single atomic layer features on the NWs with certainty cannot be related to the growth of the wire, but could be a result of the subsequent oxide formation/removal. So, we note that the holes in the surface are a result of that the oxide formation can vary within 1 atomic layer. We assume that the presence of monolayer flat islands on the surface is due to the group III and V materials that did not evaporate upon oxide removal, but instead formed III-V islands. However, such monolayer thin islands induced upon oxide removal can well be distinguished from growth-related surface features. In the example shown in Fig. 8, presenting thick InAs NWs grown with an Indium catalyst, it was still possible to an extremely low step density on the surface of 0.3 steps per micron [32, 63]. In conclusion, atomic Hydrogen cleaning is an extremely powerful method for achieving perfect single crystal NW surfaces for further processing or fundamental studies. In addition, the temperature is low enough to allow the treatment on NW devices without the devices breaking due to melting or thermal stress. As discussed in Ref. [41], this leads to significant changes in the electrical performance of the NW devices and could potentially be used to improve the performance of NW devices by controlling their surfaces. However, for the case of devices, it should be noted that also the contacts to the NWs are affected, which leads to additional complications in interpreting observed results. Again this might, however, be used to improve the device. In this area, significant research will, however, be necessary to further proceed.

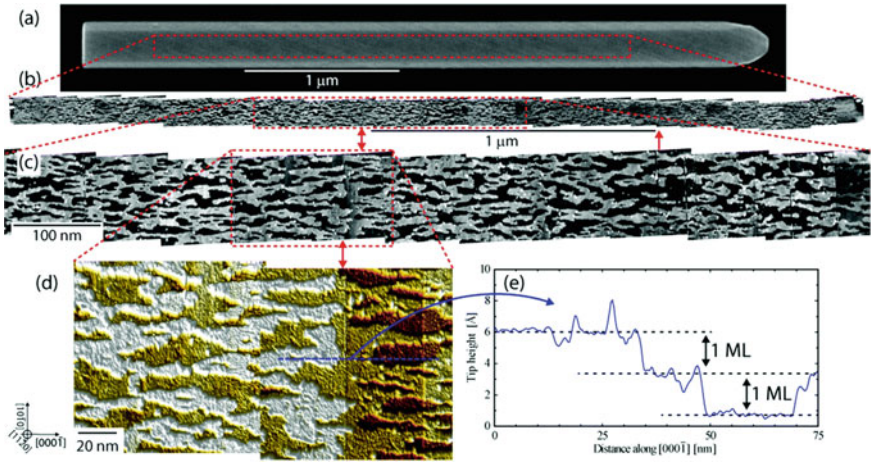

Fig. 8 Imaging of the surfaces a large Au-free grown InAs NWs which shows the pattern on the surface presumably caused by cleaning, as well as surface steps caused by growth. **a** Scanning electron microscopy image of an InAs NW grown for 16 min. **b** STM images stitched together showing more than 3 μm along a NW. Red arrows mark the position of steps perpendicular to the NW growth direction, [000-1]. **c** Magnified version of the area marked by the red rectangle in **b** showing a winding pattern of 1 monolayer high terraces extending along the NW. **d** Magnified version of the area marked by the red rectangle in **c**. Towards the right of the image, the surface pattern continues to be one monolayer below, marking a step perpendicular to [000-1]. **e** Line scan along the blue line in **d** showing the monolayer step height of both the winding pattern and the perpendicular step. The dashed black lines indicate the height of the terraces. Reproduced from [32], by permission of the Royal Society of Chemistry

5 Surface Functionalization and Electronic Properties: Native Oxide Versus High-k Dielectric Layer

III–V NWs are highly promising for electronic and optoelectronic application: Metal–oxide–semiconductor field effect transistors (MOSFETs) make use of the superior charge carrier mobility in, e.g., InAs (electrons) or GaSb (holes), as compared to traditionally used semiconductors such as Si and Ge [56]. The NW geometry thereby enables a wrap-around gate design with very high electrostatic control. The small footprint of NWs further allows the vertical stacking of materials with significantly different lattice constants employing epitaxial growth without the formation of dislocations, unlike in bulk semiconductors. This even enables epitaxial growth of III–V NWs directly on Si, thus integrating high-mobility materials with relatively cheap and industrially compatible substrates [17]. Tunneling field effect transistors (tFETs) based on InAs/GaSb nanowires grown on Si have proven world-record performance regarding on/off current ratios and a subthreshold slope below the thermal limit of 60 mV/decade [18]. Solar cells based on GaAs and InP *pn*-junction NWs have shown photovoltaic efficiencies at 1 sun illumination of 15.3% [15] and 15.0% [16], respectively, thereby exceeding classical light conversion limits

by several times due to resonant light adsorption in NW arrays with optimized NW diameters and distances [64]. The abovementioned possibility to directly stack NWs of different materials on top of each other can be utilized to enable multi-junction solar cells without the need for additional buffer layers. Many more examples of NW-based (opto)electronic devices, including light-emitting diodes or photodetectors, can be found in the literature [13, 65–68].

All these devices have in common that their (opto)electronic performance critically depends on the NW surface properties, mostly due to surface band bending, Fermi level pinning, and surface and interface defects.

A clear example of the electronic effect of an oxide layer on the NW surface is presented in Fig. 9: XPS data acquired from as-grown p-doped InP NWs under surface-sensitive conditions show dominating P-oxide (Fig. 9a) and In-oxide (Fig. 9b) components, in addition to the bulk InP signal. Cleaning the sample by annealing under exposure to atomic hydrogen, as discussed in Sect. 4, almost completely removes the oxide components, but it also shifts the InP bulk components towards smaller binding energies. This behavior can be understood as a shift of the Fermi level energy towards the valence band, i.e., the NW surface becomes more p-type. In other words, the effect of p-doping is significantly degraded at the surface of as-grown InP NWs due to the surface oxide leading to Fermi level pinning, which induces surface band bending. This will cause carrier depletion at the NW surface, which can extend significantly into the interior of the NW, depending on the doping level. Figure 10a shows the calculated depletion layer thickness depending on the dopant concentration for p- and n-doped InP NWs, based on Fermi level, conduction band edge, and valence band edge positions which were experimentally observed in a combined STM/S, XPS, and PEEM study [29]. It is worth mentioning that for typical NW radii in the range of 25–50 nm, surface band bending can deplete the entire NW from charge carriers if the doping level is too low, especially for p-doped NWs. The situation becomes even more complex in the case of NWs with a thin radial shell layer, where the band bending effects at the core/shell interface have to be taken into account as well [69].

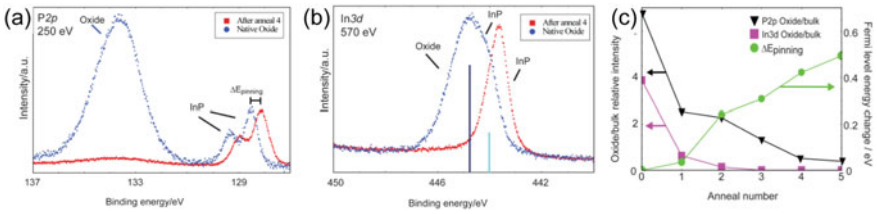

Fig. 9 XPS spectra showing the **a** P 2p and **b** In 3d core-level of p-doped InP NWs with native oxide (blue) and after oxide removal by annealing in atomic Hydrogen (red). Beside the oxide removal, a shift of the binding energy towards lower values can be seen, which corresponds to a shift of the Fermi level energy (**c**). Reprinted with permission from [33]. Copyright 2012 American Chemical Society

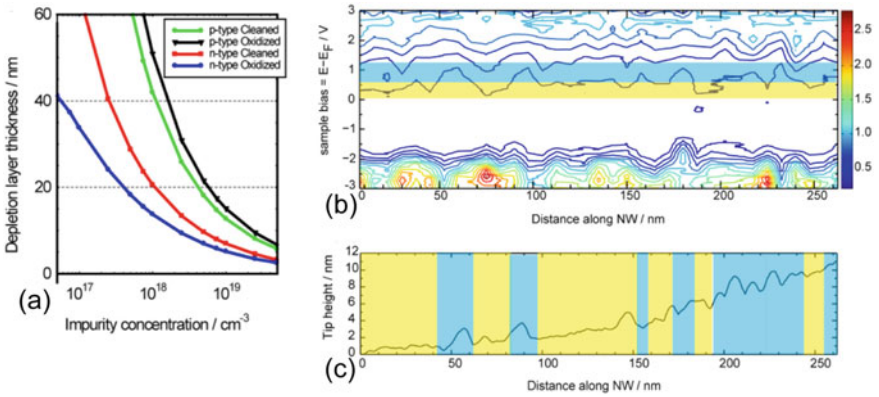

Fig. 10 **a** Surface depletion layer thickness depending on doping levels, for p- and n-type InP NWs with native oxide layers and clean surfaces, based on measurements of Fermi level and band edge energies. **b** The local density of states map of an n-doped InP NW, obtained from averaged STS point spectra acquired in steps of 7 nm distance along the NW, is shown as a contour plot of the $(dI/dV)/(\overline{I/V})$ intensity. The energy range slightly below (above) the average conduction band edge is marked yellow (blue). **c** Height profile measured by STM along the same NW region as in **b**. Areas colored yellow (blue) correspond to areas in **b** where empty states are observed already below (only above) the average conduction band edge. Reprinted with permission from [33]. Copyright 2012 American Chemical Society

In addition to the surface chemistry, also the nm-scale topography and the atomic structure of the NW surface influences the electronic properties. Surface steps, defects, and surface reconstructions will give rise to electronic surface states. Interestingly, the most common surface facets for III–V NWs, including the {110} Zb facet and the {11-20} and {10-10} facets of the Wz structure, are unreconstructed, as can be seen in Fig. 2 [28–30]. Figure 10b, c correlates the local density of states along an InP NW, obtained by a series of scanning tunneling spectroscopy (STS) measurements, with the surface topography measured by STM. Here, areas with a rather rough NW surface come along with a depletion of electronic states at the CB edge.

The crystal phase has a unique importance for the electronic performance of III–V semiconductor NW-based devices, since it can change between Zb and Wz, unlike in bulk (see Sect. 2). A Zb/Wz interface within, e.g., an InAs NW will impose a barrier for electron transport. Measurements based on electron transport through single NWs in a FET geometry obtained a staggered type-II band alignment with conduction band offsets in the range of 100 meV between Wz and Zb InAs NW segments [70, 71]. These values are in qualitative agreement with band structure calculations based on density functional theory [30, 72]. The interface between a Zb and a Wz segment of an InAs NW can be seen with atomic resolution in the STM image of Fig. 3c. STS measurements were performed at both sides of the interface, i.e., on the Zb {110} and on the Wz {11-20} surface facet, with sufficient distance to the interface itself to avoid possible band bending effects. The obtained normalized

differential conductivity plots, representing the local density of states at the sample surface [73], are shown in Fig. 11. The Wz facet shows a larger bandgap than the Zb facets, as expected, but interestingly the conduction band onset of both the Wz {11-20} and the Zb {110} facets are found at exactly the same energy, showing a flat-band condition at the conduction band [30]. This result is in strong discrepancy with the electrical transport measurements. However, the latter measurements are typically performed with the NWs being exposed to ambient conditions, while the STS results of Fig. 11 have been obtained in an ultrahigh vacuum after cleaning the NW surface from its native oxide. Accordingly, the native oxide on the III–V semiconductor NW surface can have a critical influence on the formation of a conduction band offset and therewith a barrier for electron transport at Zb/Wz interfaces. This observation has recently been confirmed by systematic transport measurements of InAs NWs under ultrahigh vacuum conditions before and after native oxide removal [74].

Besides this influence on the surface band alignment, the native surface oxide has another more technical, but still detrimental effect on NW devices, that is the challenge of contact formation. It is well-known that it is difficult to process Ohmic contacts to, e.g., *p*-doped InP NWs, or also to InSb NWs in general. Here, native oxide removal by annealing in atomic Hydrogen can be a very efficient tool for increasing the conductance of lithographically defined nanowire-metal contacts, even after the processing. Figure 12 shows an example of how the conductance of a single NW device containing an axial InAs/InSb material stack can improve over several orders of magnitude upon cleaning and native oxide removal [41].

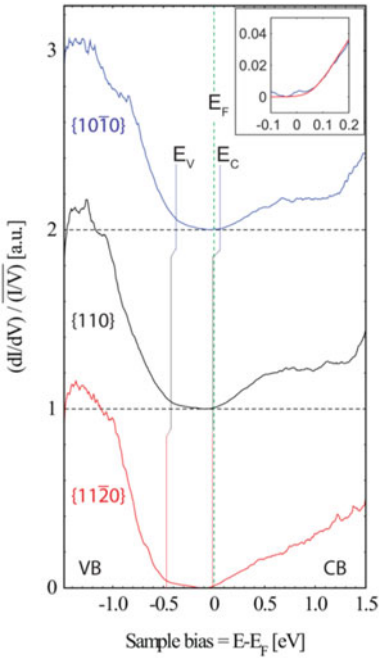

Fig. 11 Scanning tunneling point spectra, representing the local density of states, obtained on neighboring {11-20} (red) and {110} (black) facets of the same InAs NW with the same STM tip conditions, and from a {10-10} facet (blue) measured separately. Energy positions of the valence band edge (E_V), the conduction band edge (E_C) and the Fermi level (E_F) are indicated. Reprinted with permission from [30]. Copyright 2014 American Chemical Society

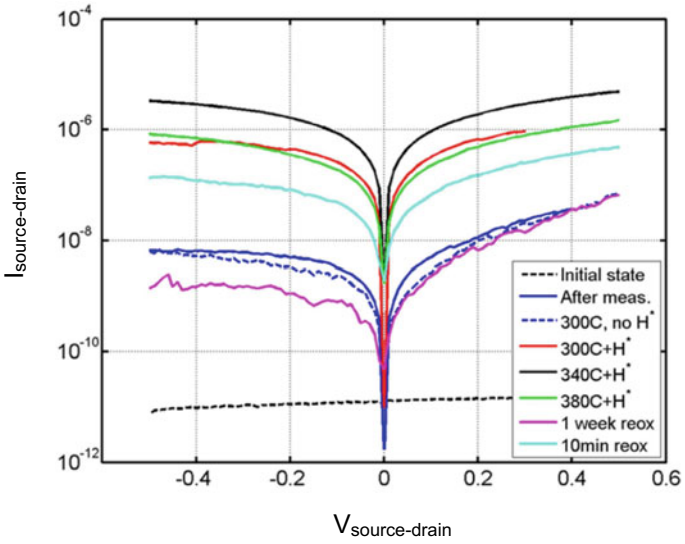

Fig. 12 Conductance of a single NW consisting of an axial InAs/InSb material stack, deposited on a Si/SiO_2 substrate and contacted at both ends with Ti/Au photolithographically defined electrodes. Continuous I-V measurements of the NW increased the initially very low conductance (dashed black and solid blue curves). Afterwards, the sample was treated as follows, while measuring the conductance after each step: Annealing to 300 °C (dashed blue curve), annealing to 300 °C under a flux of atomic Hydrogen (red curve), annealing to 340 °C with atomic Hydrogen (solid black curve), re-oxidation under ambient conditions for 1 week (pink curve), annealing again to 340 °C with atomic Hydrogen (not shown, similar as solid black curve), re-oxidation under ambient conditions for 10 min (bright blue curve), annealing to 380 °C with atomic Hydrogen (green curve). Reprinted with permission from [41]. Copyright 2015 American Chemical Society

In order to overcome the limitations of the native oxide on a semiconductor surface, even in industrial surroundings where the very clean, but also demanding and complex ultrahigh vacuum conditions cannot be fulfilled, semiconductor surfaces are typically passivated when they are going to be used in electronic, optoelectronic, or energy harvesting applications [13, 75, 76]. A very elegant way is the deposition of an ultrathin layer of an oxide with a high dielectric constant, also called high-k oxide, by atomic layer deposition (ALD). ALD of high-k layers such as HfO_2 or Al_2O_3 on III–V semiconductors comes along with the so-called self-cleaning effect, i.e., the removal of the native oxide along with the formation of the semiconductor/high-k interface [77, 78]. This self-cleaning effect has typically been explained by a ligand exchange model [79, 80], and only recently it was shown by ambient-pressure XPS that this model is not sufficient to describe the complex surface chemistry but needs to be enhanced by including a molecular adsorption step [81]. Also, more complex passivation schemes, combining steps of native oxide removal, formation of a controlled thermal oxide, and ALD of a high-k oxide, have been suggested to improve the performance of III–V semiconductor-based electronic devices [82], where a specific

stoichiometry of the thermal oxide layer has been found to improve the interface quality [57].

Also, the surfaces of III–V semiconductor NWs are typically passivated by ALD of high-k oxides as a standard procedure during device processing [14, 17, 40]. However, due to the geometry and the different surfaces involved, the ALD recipes cannot directly be transferred from planar samples, but need to be optimized and verified by thorough characterization. Figure 13 shows an XPS study of InAs NWs with about 2 nm thin ALD films of HfO_2 or Al_2O_3, in comparison with data from planar samples. The NWs had to be deposited on a suitable carrier substrate (see Fig. 13a), which leads to the experimentally challenging situation that only a small fraction of the XPS signal comes from the NWs themselves, compared to a large background from the substrate, but this can be overcome by using the high intensity of a synchrotron facility as an X-ray source. Qualitatively, the high-k deposition leads to the same self-cleaning effect as for planar samples, with a clear reduction of the As-oxide components in the As *3d* core-level spectra (see Fig. 13b–e), however, this oxide removal is far less effective for the NWs. A similar effect, though less dramatic, has been observed for In-oxides [40]. It should be mentioned that the NW geometry increases the apparent oxide component in the XPS data of the NWs by a factor of two due to attenuation effects in the oxide layer (see Fig. 5c and

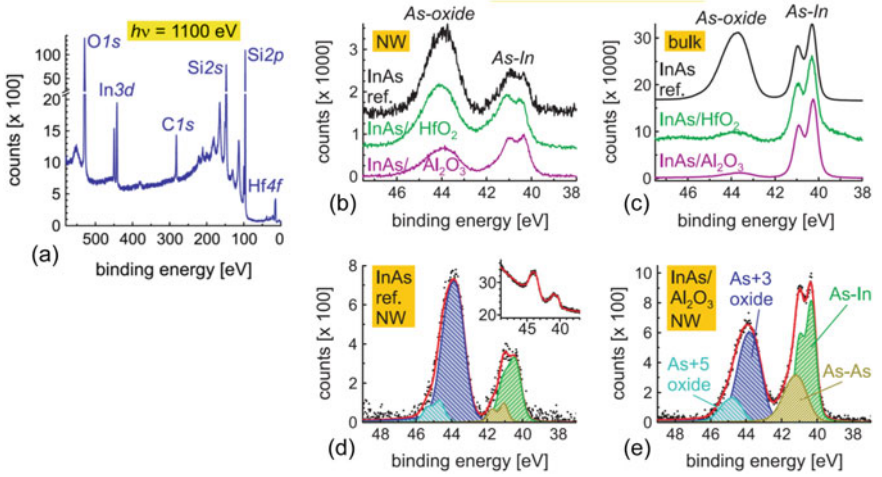

Fig. 13 XPS characterization of the semiconductor/high-k oxide interface of InAs NWs. **a** XPS overview spectrum of InAs NWs with a thin HfO_2 layer on a Si substrate. The substrate Si 2p, Si 2s, and O 1s contributions are dominating, but In 3d and Hf 4f core-level peaks from the NWs can clearly be seen. **b**–**e** As 3d core-level spectra acquired at a photon energy of 320 eV of **b** InAs NWs with native oxide (black), HfO_2 (green), and Al_2O_3 (purple) layers, **c** InAs(001) substrates with corresponding oxide layers, **d** InAs NWs with native oxide, and **e** InAs NWs with a thin Al_2O_3 layer. In **d** and **e**, experimental data are plotted as black dots and fitted results as red curves. Different fitted components are also indicated. The inset in **d** shows the spectrum prior to background subtraction. Reprinted from [40], with the permission of AIP Publishing

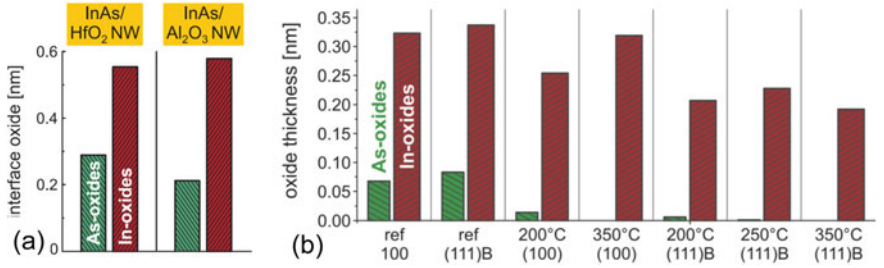

Fig. 14 Thickness of As- and In-interface oxides, as obtained from XPS data, **a** of the InAs NWs with thin HfO_2 or Al_2O_3 layers shown in Fig. 13, and **b** of InAs substrates with different surface orientation, as indicated in the figure, containing either a native oxide layer (ref) or a thin Al_2O_3 layer deposited by ALD at the indicated temperature. Reprinted from [40] (**a**) and [83] (**b**), with the permission of AIP Publishing

Ref. [40], for more details). Taking this into account, the thickness of the As- and In-oxides at the InAs/high-k oxide interface could be evaluated at about 0.2 nm and 0.6 nm, respectively. Figure 14 compares these values for NW samples with interface oxide thicknesses obtained from planar InAs/Al_2O_3 samples using different substrate orientations and ALD temperatures [83]. It was found that the self-cleaning efficiency varies for different substrate orientations, with the strongest oxide removal observed for InAs(111)B. These samples also showed a lower density of interface traps (D_{it}), underlining the relevance of a stoichiometrically clean interface for good electrical performance [83]. The NW geometry includes several different surface facets, which can partly explain the less efficient self-cleaning upon ALD of high-k oxides. In addition, the NW surface morphology typically contains more surface steps than a flat substrate, which might further limit the efficiency of native oxide removal.

The importance of NW surface roughness and morphology for device performance, especially for a low D_{it} in MOSFET application, has further been demonstrated by a correlated surface science and electrical transport experiment: InAs NWs, grown by MOCVD onto a thin InAs buffer layer on Si, were processed into wrap-gate MOS capacitors using an ALD bilayer Al_2O_3/HfO_2 high-k oxide, spacer layers, W finger gate contacts, and Ti/W/Au probing pads, as shown schematically in Fig. 15a, b and in the SEM image of Fig. 15c. More details can be found in Ref. [84]. A very low D_{it} was observed for these capacitors, varying between values of 2×10^{12} eV^{-1} cm^{-2} and 1×10^{13} eV^{-1} cm^{-2} at the conduction band edge depending on NW growth conditions and doping, with a minimum D_{it} in the conduction band of $<10^{12}$ eV^{-1} cm^{-2}, as shown in Fig. 15d. Reference InAs NWs, grown under the same growth conditions but without any further processing, were characterized by AFM (see Fig. 15e. Very smooth NW surface facets were observed, with a root mean square roughness of down to 0.1 nm [84], and only a few or even no atomic monolayer high surface steps, as shown in Fig. 15f. This example underlines how a high quality NW surface morphology, together with tailored and optimized processing conditions, is the key ingredient for improved NW device performance.

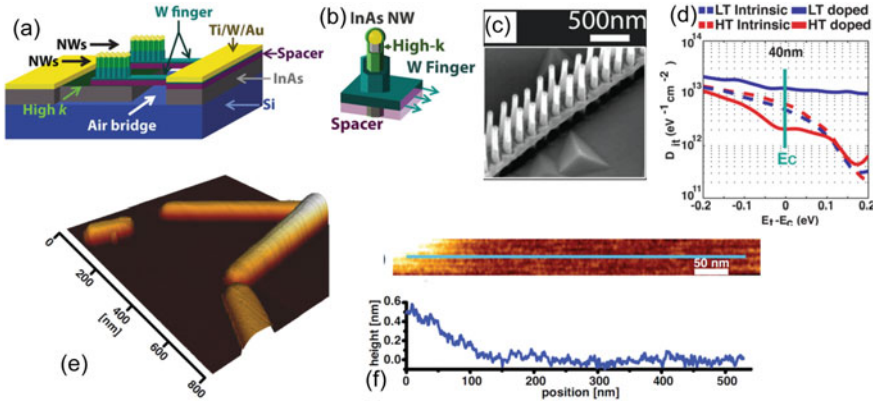

Fig. 15 Surface morphology of InAs NWs and electrical properties of processed NW MOSFETs. **a** Sketch of the MOSFET structure including InAs NWs, grown by MOCVD on an InAs buffer layer on Si substrates, as active channels, gate fingers, and top Ti/W/Au drain contacts. **b** Sketch and **c** SEM image of the InAs NW(s) with an Al_2O_3/HfO_2 high-k oxide layer and W gate metal. **d** Measured D_{it} in respect to the conduction band edge (E_C) and Fermi level (E_F) for intrinsic and doped NW samples grown at 420 °C with a V/III ratio of 69 (LT) and at 470 °C with a V/III ratio of 6 (HT), respectively. **e** AFM overview image of several NWs after transfer onto an InAs substrate and **f** AFM scan and height profile obtained at a NW side facet, showing minimal tapering at the end of the NW and an otherwise atomically flat surface. Reprinted with permission from [84]. Copyright 2016 American Chemical Society

6 Enhancing Nanowire Functionality via Surface Functionalization

As discussed above, NW surfaces need to be controlled if one wants to harness many of their generally excellent properties. A significant focus in the previous section was on removing the negative consequences of the presence of the surface, in particular, defects that lead to charge-recombination, surface pinning, and carrier scattering. However, the surface can also be actively used to enhance the properties of the NWs or give them completely new functionality. We will discuss some examples of what can be called active surface functionalization. Most importantly the use of the NW surface for sensing, the use of the surface for enhanced conductivity and finally the use of the crystal phase control of NW surfaces to potentially create new 2D materials and morphologies. A particular obvious case of the added functionality of the surface is for sensing [85], since the large surface to bulk ratio makes the wire electronic/optical properties highly sensitive to adsorption of even small amounts of material. The wire geometry also lends itself excellent to, for example, electrical measurements. InAs NWs have been demonstrated as excellent components for gas sensing [86, 87]. That InAs NWs are good low power FETs makes them also relevant for sensors as they can be directly incorporated with the Si CMOS platform and have low power expenditure, which for many sensing purposes can be an advantage. A further advantage is the electron accumulation layer that can form on InAs surfaces,

which makes them sensitive to charges and dipoles adsorbed on them. Several works have shown that the adsorption of molecules on the surface has led to a change in transport properties [87]. Interestingly, both charge transfer and change in carrier mobility occur by an order of magnitude or more. The charge transfer can be readily understood in that InAs surfaces can have a charge accumulation area which is heavily influenced by the surface oxide as described in Sect. 5. The presence of, for example, H_2O on the surface can then lead to charge transfer, which has been estimated to in average 0.2 elemental charges per H_2O molecule for a complexly covered InAs NW [87]. The question of enhanced mobility is a bit more intricate. However, again the change of free carriers in the surface region can influence surface-induced band bending. This will, in turn, result in a larger or smaller number of free carriers in the "bulk" of the NW vs its surface. Since these will have different mobility, it will result in a varying overall mobility. Beyond sensors, this can be used to design hybrid ion–electron circuitry [88], based on O/OH motion. Here a plastic is combined with InAs NWs so that ionic transport from bio-inspired systems can be combined with FET electronics. Interestingly, surface states of III–V NWs can also be manipulated by changing the wire strain [89]. It was found that 4 orders of magnitude differences in mobility could be induced by changing the strain of the wire, which in turn, changed the energy of the surface states. Strain in III–V NWs and NW devices has been studied extensively with X-rays by coherent diffraction imaging (CDI) as shown in a number of recent studies [90–94]. Straining the wire can easily be accomplished and thus opens up for manipulation properties using changes in surface states. A significant amount of surface states can result in the formation of specific currents at the surface, thus opening up an extra conduction channel that can have very different properties from the bulk. One may speculate that this can be used to introduce new transport properties along the III–V NWs creating a core shell structure with different currents radially.

An interesting further use of NW surfaces is as a template for constructing more complicated surface structures of varying dimensionality. The opportunity to tailor the crystal phase of the NWs and additional control of NW overgrowth allows for the design of wires with different surface structures radially along them. It is known that different surface structures of the same material might have very different adsorption properties, and the question came whether this would also be the case for surfaces of different crystal polytypes. In a recent paper [44], this was found to be the case for Sb adsorption and incorporation into GaAs NWs as can be seen in Fig. 16. It was found experimentally (using STM) that diffusion of Sb atoms at temperatures around 400 °C on NWs with both Zb and Wz crystal facets resulted in 4 times enhanced adsorption in the Zb (110) facet as compared to the Wz (11-20) facet. The incorporation happened by Sb-for-As exchange leading to a GaSbAs surface alloy formation. The preferential incorporation could be theoretically modeled using ab-initio calculations of each step in the Sb-for-As exchange. It was found that the preferential incorporation of Sb is a result of a higher energy barrier for the surface diffusion and exchange of As with Sb in its GaAs surface site. Interestingly, in both cases, the Sb incorporation is energetically less favorable than having Sb on the surface and As in its original site. However, as the surface has a surplus of free

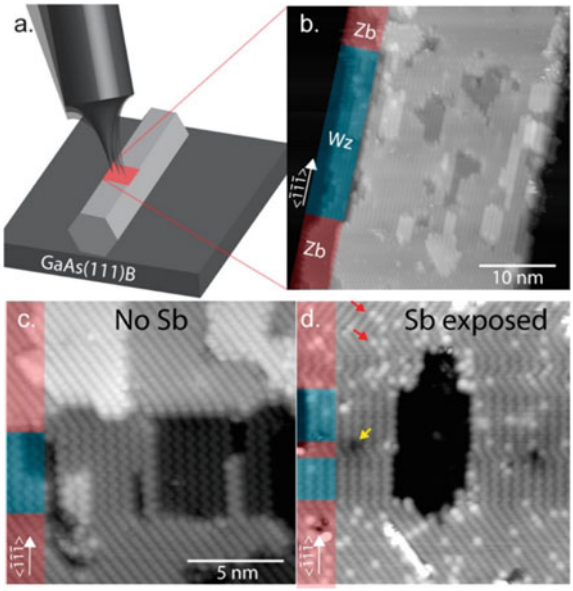

Fig. 16 Sb for As substitutional adsorption into the surface of a GaAs NW, exposing the factor of 4 difference in the incorporation of SB into the Zb crystal facet compared to the Wz. **a** Schematic of the STM imaging experiment showing the STM tip accessing a NW facet. **b** Overview image of a Wz segment in between two Zb segments. Zb and Wz are indicated by the red and blue overlay, respectively. **c** Image showing a Wz segment between two Zb segments on a GaAs NW that have been Hydrogen cleaned, but with no Sb adsorption. **d** Image similar to the one in panel (**c**) obtained from an Sb-exposed NW. Please note the existence of a small Zb segment in the middle of the image, as marked by the red overlay. Examples of single Sb atoms incorporated into As sites are shown by red arrows, and a single As vacancy is indicated by a yellow arrow. Scale bar in panel (**c**) is also valid for panel (**d**). Reprinted with permission from [44]. Copyright 2017 American Chemical Society

Sb and a lack of free As (As liberated by the Sb will quickly evaporate), one ends up with considerable incorporation of Sb. The alternative would then be much less favorable As vacancy sites. This would, however, indicate that forming such alloys is a kinetically driven process that needs controlled heating procedures to succeed. It can be speculated that low-temperature overgrowth of 2D GaSbAs alloys with GaAs would be possible, as that would not allow the Sb adsorbed in the As sites to be exchanged with a new supply of As. The reason would be that at low temperatures the barrier for As-for-Sb exchange would be too large to be overcome. As it is well known from surface metal alloys [95, 96], it is possible to form alloys on the surface that cannot exist in the bulk. This phenomena might also be exploitable at the NW surfaces and could be used to create completely new structures that are otherwise not achievable. Further, as the crystal facets can be confined both by crystal phase variation and by the diameter of the wire, it will be possible to create such surface alloys that can be confined into 1D or even 0D structures.

Extending on this preferential molecular adsorption might also be possible on the NWs by exploiting their morphology. Indeed molecular adsorption of a variety of proteins has been demonstrated on NWs [97], and it has been shown that besides from surface chemistry the actual morphology of the wire may lead to enhanced adsorption of proteins [98]. As the molecular size is comparable to the NW dimensions, this can potentially have even further peculiar adsorption possibilities at particular positions. Keeping in mind the opportunity to adsorb preferentially on certain crystal facets, it is interesting to note that these different crystal structures respond quite differently to polarization [99]. It was found that multiphoton excitation of hot electrons in NWs depends on crystal structure and facet, which in turn, could be used to influence the particular adsorbed chemical species. While not covered in detail here this leads us to the point of surface coating which can be used to enhance biomolecular adsorption while still allowing efficient light guiding by the NWs [100]. As a final future outlook, we note that the combination of 2D materials with the 1D NWs might lead to highly efficient devices that have the confined geometry of the wires and the interesting properties of van der Waals materials. Combining the interesting properties of 2D Van der Waals materials with the confined nature of the III–V NWs could also give qualitatively new behavior if atomically well-defined interfaces and wrapping of the 2D materials with the wires can be achieved. To conclude III–V NW surfaces is one of the key components for the exploitation of these structures, but there are still many open opportunities for a better understanding and control even after years of research and technology development—which could be central in realizing the many promises for NW technologies.

Acknowledgements The authors want to acknowledge Emelie Hilner, Martin Hjort, Johan Knutsson, Sahil Patel, Olof Persson, Andrea Troian, James Webb, Sofie Yngman, Magnus Borgström, Kimberly Dick Thelander, Lars-Erik Wernersson, Sepideh Gorji Ghalamestani, Sarah McKibbin, Sebastian Lehmann, Bernhard Mandl, Gustav Nylund, Chris Palmstrom, Jesper Wallentin, Edvin Lundgren and Lars Samuelson for experimental work, sample growth, processing and many valuable discussions. This work was performed within the NanoLund Center for Nanoscience.

References

1. P.Y. Huang, C.S. Ruiz-Vargas, A.M. van der Zande, W.S. Whitney, M.P. Levendorf, J.W. Kevek, S. Garg, J.S. Alden, C.J. Hustedt, Y. Zhu, J. Park, P.L. McEuen, D.A. Muller, Grains and grain boundaries in single-layer graphene atomic patchwork quilts. Nature **469**, 389–392 (2011)
2. F. Banharl, J. Kotakoski, A.V. Kraheninnikov, Structural defects in graphene. ACS Nano **5**(1), 26–41 (2011)
3. S.A. Jewett, J.A. Yoder, A. Ivanisevic, Surface modificaitons on InAs decrease indium and arsenic leaching under physiological conditions. Appl. Surf. Sci. **261**, 842–850 (2012)
4. O. Demichel, M. Heiss, J. Bleuse, H. Mariette, A. Fontcuberta i Morral, Impact of surfaces on the optical properties of GaAs nanowires. Appl. Phys. Lett. **97**, 201907 (2010)

5. L. Zhou, D.F. Swearer, C. Zhang, H. Robatjazi, H. Zhao, L. Henderson, L. Dong, P. Christopher, E.A. Carter, P. Nordlander, N.J. Halas, Quantifying hot carrier and thermal contributions in plasmonic photocatalysis. Science **362**(6410), 69–72 (2018)
6. J.G. Wang, W.X. Li, M. Borg, J. Gustafson, A. Mikkelsen, T.M. Pedersen, E. Lundgren, J. Weissenrieder, J. Klikovits, M. Schmid, B. Hammer, J.N. Andersen, One-dimensional PtO_2 at Pt steps: formation and reaction with CO. Phys. Rev. Lett. **95**(25), 256102 (2005)
7. H. Lee, Utilization of shape-controlled nanoparticles as catalysts with enhanced activity and selectivity. RSC Adv. **4**, 41017–41027 (2014)
8. J.F. Fennell Jr., S.F. Liu, J.M. Azzarelli, J.G. Weis, S. Rochat, K.A. Mirica, J.B. Ravnsbaek, T.M. Swager, Nanowire chemical/biological sensors: status and a roadmap for the future. Angew. Chem. Int. Ed. Engl. **55**(4), 1266–1281 (2016)
9. K. Tomioka, J. Motohisa, S. Hara, T. Fukui, Control of InAs nanowire growth directions on Si. Nano Lett. **8**(10), 3475–3480 (2008)
10. A. Mikkelsen, E. Lundgren, Surface science of free standing semiconductor nanowires. Surf. Sci. **607**, 97–105 (2013)
11. A. Mikkelsen, J. Eriksson, E. Lundgren, J.N. Andersen, J. Weissenrieder, W. Seifert, The influence of lysine on InP(001) surface ordering and nanowire growth. Nanotechnology **16**(10), 2354–2359 (2005)
12. I. Vurgaftman, J.R. Meyer, L.R. Ram-Mohan, Band parameters for III–V compound semiconductors and their alloys. J. Appl. Phys. **89**, 5815 (2001)
13. M.T. Borgström, J. Wallentin, M. Heurlin, S. Fält, P. Wickert, J. Leene, M.H. Magnusson, K. Deppert, L. Samuelson, Nanowires with promise for photovoltaics. IEEE J. Sel. Top. Quantum Electron. **17**, 1050 (2011)
14. J. Wallentin, N. Anttu, D. Asoli, M. Huffman, I. Åberg, M.H. Magnusson, G. Siefer, P. Fuss-Kailuweit, F. Dimroth, B. Witzigmann, H.Q. Xu, L. Samuelson, K. Deppert, M.T. Borgström, InP nanowire array solar cells achieving 13.8% efficiency by exceeding the ray optics limit. Science **339**, 1057 (2013)
15. I. Åberg, G. Vescovi, D. Asoli, U. Naseem, J.P. Gilboy, C. Sundvall, A. Dahlgren, K.E. Svensson, N. Anttu, M.T. Bjork, L. Samuelson, A GaAs nanowire array solar cell with 15.3% efficiency at 1 Sun. IEEE J. Photovolt. **6**(1), 185–190 (2016)
16. G. Otnes, E. Barrigón, Ch. Sundvall, K.E. Svensson, M. Heurlin, G. Siefer, L. Samuelson, I. Åberg, M.T. Borgström, Understanding InP nanowire array solar cell performance by nanoprobe-enabled single nanowire measurements. Nano Lett. **18**(5), 3038–3046 (2018)
17. E. Memisevic, J. Svensson, M. Hellenbrand, E. Lind, L.-E. Wernersson, Scaling of vertical InAs–GaSb nanowire tunneling field-effect transistors on Si. IEEE Electron Device Lett. **37**, 549–552 (2016)
18. E. Memisevic, J. Svensson, E. Lind, L.-E. Wernersson, Vertical nanowire TFETs with channel diameter down to 10 nm and point S-MIN of 35 mV/decade. IEEE Electron Device Lett. **39**(7), 1089–1091 (2018)
19. B. Monemar, B.J. Ohlsson, N.F. Gardner, L. Samuelson, Nanowire-based visible light emitters, present status and outlook. Semicond. Semimet. **94**, 227–271 (2016)
20. S. Lehmann, J. Wallentin, D. Jacobsson, K. Deppert, K.A. Dick, A General approach for sharp crystal phase switching in InAs, GaAs, InP, and GaP nanowires using only group V flow. Nano Lett. **13**, 4099 (2013)
21. D.L. Dheeraj, G. Patriarche, H. Zhou, T.B. Hoang, A.F. Moses, S. Gronsberg, A.T.J. van Helvoort, B.-O. Fimland, H. Weman, Growth and characterization of wurtzite GaAs nanowires with defect-free zinc blende GaAsSb inserts. Nano Lett. **8**(12), 4459–4463 (2008)
22. Ph. Ebert, Nano-scale properties of defects in compound semiconductor surfaces. Surf. Sci. Rep. **33**, 121–303 (1999)
23. A. Mikkelsen, N. Sköld, L. Ouattara, M. Borgström, J.N. Andersen, L. Samuelson, W. Seifert, E. Lundgren, Direct imaging of the atomic structure inside a nanowire by scanning tunneling microscopy. Nat. Mater. **3**, 519 (2004)
24. A. Mikkelsen, E. Lundgren, Cross-sectional scanning tunneling microscopy studies of novel III–V semiconductor structures. Prog. Surf. Sci. **80**, 1 (2005)

25. R. Timm, J. Grabowski, H. Eisele, A. Lenz, S.K. Becker, L. Müller-Kirsch, K. Pötschke, U.W. Pohl, D. Bimberg, M. Dähne, Formation and atomic structure of GaSb nanostructures in GaAs studied by cross-sectional scanning tunneling microscopy. Phys. E **26**, 231 (2005)
26. R. Timm, H. Eisele, A. Lenz, L. Ivanova, G. Balakrishnan, D.L. Huffaker, M. Dähne, Self-organized formation of GaSb/GaAs quantum rings. Phys. Rev. Lett. **101**, 256101 (2008)
27. J. Kawasaki, R. Timm, K.T. Delaney, E. Lundgren, A. Mikkelsen, C.J. Palmstrom, Local density of states and interface effects in semimetallic ErAs nanoparticles embedded in GaAs. Phys. Rev. Lett. **107**, 036806 (2011)
28. E. Hilner, U. Håkanson, L.E. Fröberg, M. Karlsson, P. Kratzer, E. Lundgren, L. Samuelson, A. Mikkelsen, Direct atomic scale imaging of III–V nanowire surfaces. Nano Lett. **8**, 3978 (2008)
29. M. Hjort, S. Lehmann, J. Knutsson, R. Timm, D. Jacobsson, E. Lundgren, K.A. Dick, A. Mikkelsen, Direct imaging of atomic scale structure and electronic properties of GaAs wurtzite and zinc blende nanowire surfaces. Nano Lett. **13**, 4492 (2013)
30. M. Hjort, S. Lehmann, J. Knutsson, A.A. Zakharov, Y.A. Du, S. Sakong, R. Timm, G. Nylund, E. Lundgren, P. Kratzer, K.A. Dick, A. Mikkelsen, Electronic and structural differences between wurtzite and zinc blende InAs nanowire surfaces: experiment and theory. ACS Nano **8**, 12346 (2014). https://pubs.acs.org/doi/10.1021/nn504795v
31. J.V. Knutsson, S. Lehmann, M. Hjort, E. Lundgren, K.A. Dick, R. Timm, A. Mikkelsen, Electronic structure cahnges due to crystal phase switching at the atomic scale limit. ACS Nano **11**, 10519–10528 (2017)
32. M. Hjort, J.V. Knutsson, B. Mandl, K. Deppert, E. Lundgren, R. Timm, A. Mikkelsen, Surface morphology of Au-free grown nanowires after native oxide removal. Nanoscale **7**, 9998 (2015)
33. M. Hjort, J. Wallentin, R. Timm, A.A. Zakharov, U. Håkanson, J.N. Andersen, E. Lundgren, L. Samuelson, M.T. Borgström, A. Mikkelsen, Surface chemistry, structure, and electronic properties from microns to the atomic scale of axially doped semiconductor nanowires. ACS Nano **6**(11), 9679 (2012)
34. P. Caroff, K.A. Dick, J. Johansson, M.E. Messing, K. Deppert, L. Samuelson, Controlled polytypic and twin-plane superlattices in III–V nanowires. Nat. Nanotechnol. **4**, 50–55 (2009)
35. J.V. Knutsson, S. Lehmann, M. Hjort, P. Reinke, E. Lundgren, K.A. Dick, R. Timm, A. Mikkelsen, Atomic scale surface structure and morphology of InAs nanowire crystal superlattices: the effect of epitaxial overgrowth. ACS Appl. Mater. Interfaces **7**, 5748–5755 (2015). https://pubs.acs.org/doi/10.1021/am507931z
36. L. Ouattara, A. Mikkelsen, N. Sköld, J. Eriksson, T. Knaapen, E. Cavar, W. Seifert, L. Samuelson, E. Lundgren, GaAs/AlGaAs nanowire heterostructures studied by scanning tunneling microscopy. Nano Lett. **7**(9), 2859–2864 (2007)
37. E. Uccelli, J. Arbiol, J.R. Morante, A. Fontcuberta i Morral, InAs quantum dot arrays decorating the facets of GaAs nanowires. ACS Nano **4**(10), 5985–5993 (2010)
38. M. Heiss, Y. Fontana, A. Gustafsson, G. Wüst, C. Magen, D.D. O'Regan, J.W. Luo, B. Ketterer, S. Conesa-Boj, A.V. Kuhlmann, J. Houel, E. Russo-Averchi, J.R. Morante, M. Cantoni, N. Marzari, J. Arbiol, A. Zunger, R.J. Warburton, A. Fontcuberta i Morral, Self-assembled quantum dots in a nanowire system for quantum photonics. Nat. Mater. **12**, 439–444 (2013)
39. A. Mikkelsen, N. Sköld, L. Ouattara, E. Lundgren, Nanowire growth and dopants studied by cross-sectional scanning tunnelling microscopy. Nanotechnology **17**, S362–S368 (2006)
40. R. Timm, M. Hjort, A. Fian, B.M. Borg, C. Thelander, J.N. Andersen, L.-E. Wernersson, A. Mikkelsen, Interface composition of InAs nanowires with Al_2O_3 and HfO_2 thin films. Appl. Phys. Lett. **99**, 222907 (2011)
41. J.L. Webb, J.V. Knutsson, M. Hjort, S.G. Ghalamestani, K.A. Dick, R. Timm, A. Mikkelsen, Electrical and surface properties of InAs/InSb nanowires cleaned by atomic hydrogen. Nano Lett. **15**, 4865 (2015)
42. A.A. Zakharov, A. Mikkelsen, J.N. Andersen, Recent advances in imaging of properties and growth of low dimensional structures for photonics and electronics by XPEEM. J. Electron Spectrosc. Relat. Phenom. **185**, 417 (2012)
43. E. Bauer, *Surface Microscopy with Low Energy Electrons* (Springer, New York, 2014)

44. M. Hjort, P. Kratzer, S. Lehmann, S.J. Patel, K.A. Dick, C.J. Palmstrom, R. Timm, A. Mikkelsen, Crystal structure induced preferential surface alloying of Sb on wurtzite/zinc blende GaAs nanowires. Nano Lett. **17**, 3634 (2017)
45. T. Xu, M.J. Wei, P. Capiod, A. Diaz Alvarez, X.L. Han, D. Troadec, J.P. Nys, M. Berthe, I. Lefebvre, G. Pariarche, S.R. Plissard, P. Caroff, Ph. Ebert, B. Grandidier, Type I band alignment in GaAs81Sb19/GaAs core-shell nanowires. Appl. Phys. Lett. **107**, 112102 (2015)
46. J. Knutsson, *Atomic Scale Characterization of III–V Nanowire Surfaces.* Lund University, Faculty of Science, Lund, Sweden (2017)
47. J.P. Ibe, P.P. Bey Jr., S.L. Brandow, R.A. Brizzolara, N.A. Burnham, D.P. DiLella, K.P. Lee, C.R.K. Marrian, R.J. Colton, On the electrochemical etching of tips for scanning tunneling microscopy. J. Vac. Sci. Technol. A **8**, 3570 (1990)
48. A. Fian, M. Lexholm, R. Timm, B. Mandl, U. Håkanson, D. Hessman, E. Lundgren, L. Samuelson, A. Mikkelsen, New flexible toolbox for nanomechanical measurements with extreme precision and at very high frequencies. Nano Lett. **10**, 3893 (2010)
49. R. Timm, O. Persson, D.L.J. Engberg, A. Fian, J.L. Webb, J. Wallentin, A. Jönsson, M.T. Borgström, L. Samuleons, A. Mikkelsen, Current-voltage characterization of individual as-grown nanowires using a scanning tunneling microscope. Nano Lett. **13**, 5182 (2013)
50. D.B. Suyatin, V. Jain, V.A. Nebol'sin, J. Trägårdh, M.E. Messing, J.B. Wagner, O. Persson, R. Timm, A. Mikkelsen, I. Maximov, L. Samuelson, H. Pettersson, Strong Schottky barrier reduction at Au-catalyst/GaAs-nanowire interfaces by electric dipole formation and Fermi level unpinning. To be published (2013)
51. O. Ueda, Reliability issues in III–V compound semiconductor devices: optical devices and GaAs-based HBTs. Microelectron. Reliab. **39**, 1839–1855 (1999)
52. J.J. Yang, J.J. Strukov, D.R. Stewart, Memristive devices for computing. Nat. Nanotechnol. **8**, 13–24 (2013)
53. J.L. Webb, J. Knutsson, M. Hjort, S.R. McKibbin, S. Lehmann, C. Thelander, K.A. Dick, R. Timm, A. Mikkelsen, Imaging atomic scale dynamics on III–V nanowire surfaces during electrical operation. Nat. Sci. Rep. **7**, 12790 (2017)
54. O. Persson, J.L. Webb, K.A. Dick, C. Thelander, A. Mikkelsen, R. Timm, Scanning tunneling spectroscopy on InAs–GaSb Esaki diode nanowire devices during operation. Nano Lett. **15**, 3684–3691 (2015)
55. J.L. Webb, O. Persson, K.A. Dick, C. Thelander, R. Timm, A. Mikkelsen, High resolution scanning gate microscopy measurements on InAs/GaSb nanowire Esaki diode devices. Nano Res. **7**, 877 (2014)
56. R. Timm, A. Fian, M. Hjort, C. Thelander, E. Lind, J.N. Andersen, L.-E. Wernersson, A. Mikkelsen, Reduction of native oxides on InAs by atomic layer deposited Al_2O_3 and HfO_2. Appl. Phys. Lett. **97**, 132904 (2010)
57. A. Troian, J.V. Knutsson, S.R. McKibbin, S. Yngman, A.S. Babadi, L.-E. Wernersson, A. Mikkelsen, R. Timm, InAs-oxide interface composition and stability upon thermal oxidation and high-k atomic layer deposition. AIP Adv. **8**, 125227 (2018)
58. A.A. Zakharov, E. Mårsell, E. Hilner, R. Timm, J.N. Andersen, E. Lundgren, A. Mikkelsen, Manipulating the dynamics of self-propelled gallium droplets by gold nanoparticles and nanoscale surface morphology. ACS Nano **9**, 5422 (2015)
59. E. Hilner, A.A. Zakharov, K. Schulte, P. Kratzer, J.N. Andersen, E. Lundgren, A. Mikkelsen, Ordering of the nanoscale step morphology as a mechanism for droplet self-propulsion. Nano Lett. **9**, 2710 (2009)
60. V. Martinelli, L. Siller, M.G. Betti, C. Mariani, U. del Pennino, Surface modification of InAs(110) surface by low energy ion sputtering. Surf. Sci. **391**(1–3), 73–80 (1997)
61. M. Schnedler, I. Lefebvre, T. Xu, V. Portz, G. Patriarche, J.-P. Nys, S.R. Plissard, P. Caroff, M. Berthe, H. Eisele, R.E. Dunin-Borkowski, Ph. Ebert, B. Grandidier, Lazarevicite-type short-range ordering in ternary III–V nanowires. Phys. Rev. B **94**, 195306 (2019)
62. J.K. Kawasaki, A. Sharan, L.I.M. Johansson, M. Hjort, R. Timm, B. Thiagarajan, B.D. Schultz, A. Mikkelsen, A. Janotti, C.J. Palmstrom, A simple electron counting model for half-Heusler surfaces. Sci. Adv. **4**, EEAR5832 (2018)

63. B. Mandl, J. Stangl, T. Mårtensson, A. Mikkelsen, J. Eriksson, L.S. Karlsson, G. Bauer, L. Samuelson, W. Seifert, Au-free epitaxial growth of InAs nanowires. Nano Lett. **6**, 1817–1821 (2006)
64. N. Anttu, A. Abrand, D. Asoli, M. Heurlin, I. Åberg, L. Samuelson, M. Borgström, Absorption of light in InP nanowire arrays. Nano Res. **7**(6), 816–823 (2014)
65. L.-E. Wernersson, Narrow gap nanowires: from nanotechnology to RF-circuits on Si. J. Appl. Phys. **117**(11), 112810 (2015)
66. H. Riel, L.-E. Wernersson, M. Hong, J.A. del Alamo, III–V compound semiconductor transistors—from planar to nanowire structures. MRS Bull. **39**(8), 668–677 (2014)
67. Y. Li, F. Qian, J. Xiang, Ch.M. Lieber, Nanowire electronic and optoelectronic devices. Mater. Today **9**(10), 18 (2006)
68. R.R. LaPierre, A.C.E. Chia, S.J. Gibson, C.M. Haapamaki, J. Boulanger, R. Yee, P. Kuyanov, J. Zhang, N. Tajik, N. Jewell, K.M.A. Rahman, III–V nanowire photovoltaics: review of design for high efficiency. Phys. Status Solidi (RRL) **7**(10), 815–830 (2013)
69. B. Khanbabaee, G. Bussone, J.V. Knutsson, I. Geijselaers, C.E. Pryor, T. Rieger, N. Demarina, D. Grützmacher, M.I. Lepsa, R. Timm, U. Pietsch, Band bending at the heterointerface of GaAs/InAs core/shell nanowires monitored by synchrotron X-ray photoelectron spectroscopy. J. Appl. Phys. **120**, 145703 (2016)
70. S.A. Dayeh, D. Susac, K.L. Kavanagh, E.T. Yu, D. Wang, Structural and room-temperature transport properties of zinc blende and wurtzite InAs nanowires. Adv. Funct. Mater. **19**(13), 2102 (2009)
71. J. Trägårdh, A.I. Persson, J.B. Wagner, D. Hessman, L. Samuelson, Measurements of the band gap of wurtzite InAs1-xPx nanowires using photocurrent spectroscopy. J. Appl. Phys. **101**(12), 123701 (2007)
72. A. De, C.E. Pryor, Predicted band structures of III–V semiconductors in the wurtzite phase. Phys. Rev. B **81**, 155210 (2010)
73. R.M. Feenstra, Tunneling spectroscopy of the (110)-surface of direct-gap III–V semiconductors. Phys. Rev. B **50**, 4561–1570 (1994)
74. O. Persson, L. Kral, S. Lehmann, C. Thelander, R. Timm, The effect of surface oxide removal on InAs nanowires of both wurtzite and zinc blende structure, to be published
75. R.M. Wallace, P.C. McIntyre, J. Kim, Y. Nishi, Atomic layer deposition of dielectrics on Ge and III–V materials for ultrahigh performance transistors. MRS Bull. **34**, 493 (2009)
76. T. Gougousi, Atomic layer deposition of high-k dielectrics on III–V semiconductor surfaces. Prog. Cryst. Growth Charact. Mater. **62**(4), 1–21 (2016)
77. C.L. Hinkle, A.M. Sonnet, E.M. Vogel, S. McDonnell, G.J. Hughes, M. Milojevic, B. Lee, F.S. Aguirre-Tostado, K.J. Choi, H.C. Kim, J. Kim, R.M. Wallace, GaAs interfacial self-cleaning by atomic layer deposition. Appl. Phys. Lett. **92**, 071901 (2008)
78. R. Timm, M. Hjort, A. Fian, C. Thelander, E. Lind, J.N. Andersen, L.-E. Wernersson, A. Mikkelsen, Interface composition of atomic layer deposited HfO_2 and Al_2O_3 thin films on InAs studied by X-ray photoemission spectroscopy. Microelectron. Eng. **88**, 1091 (2011)
79. S.M. George, Atomic layer deposition: an overview. Chem. Rev. **110**, 111 (2010)
80. S. Elliott, Atomic-scale simulation of ALD chemistry. Semicond. Sci. Technol. **27**, 074008 (2012)
81. R. Timm, A.R. Head, S. Yngman, J.V. Knutsson, M. Hjort, S.R. McKibbin, A. Troian, Ol. Persson, S. Urpelainen, J. Knudsen, J. Schnadt, A. Mikkelsen, Self-cleaning and surface chemical reactions during hafnium dioxide atomic layer deposition on indium arsenide. Nat. Commun. **9**, 1412 (2018)
82. H. Ko, K. Takei, R. Kapadia, S. Chuang, H. Fang, P.W. Leu, K. Ganapathi, E. Plis, H.S. Kim, S.-Y. Chen, M. Madsen, A.C. Ford, Y.-L. Chueh, S. Krishna, S. Salahuddin, A. Javey, Ultrathin compound semiconductor on insulator layers for high-performance nanoscale transistors. Nature **468**, 286 (2010)
83. J. Wu, E. Lind, R. Timm, M. Hjort, A. Mikkelsen, L.-E. Wernersson, Al2O3/InAs metal-oxide-semiconductor capacitors on (100) and (111)B substrates. Appl. Phys. Lett. **100**, 132905 (2012)

84. J. Wu, A.S. Babadi, D. Jacobsson, J. Colvin, S. Yngman, R. Timm, E. Lind, L.-E. Wernersson, Low trap density in InAs/High-k nanowire gate stacks with optimized growth and doping conditions. Nano Lett. **16**, 2418–2425 (2016)
85. F. Patolsky, C.M. Lieber, Nanowire nanosensors. Mater. Today **8**(4), 20–28 (2005)
86. P. Offermans, M. Crego-Calama, S.H. Brongersma, Gas detection with vertical InAs nanowire arrays. Nano Lett. **10**(7), 2412–2415 (2010)
87. J. Du, D. Liang, H. Tang, X.P.A. Gao, InAs nanowire transistors as gas sensor and the response mechanism. Nano Lett. **9**(12), 4348–4351 (2009)
88. D.J. Carrad, A.B. Mostert, A.R. Ullah, A.M. Burke, H.J. Joyce, H.H. Tan, C. Jagadish, P. Krogstrup, J. Nygård, P. Meredith, A.P. Micolich, Hybrid nanowire ion-to-electron transducers for integrated bioelectronic circuitry. Nano Lett. **17**(2), 827–833 (2017)
89. G. Signorello, S. Sant, N. Bologna, M. Schraff, U. Drechsler, H. Schmid, S. Wirths, M.D. Rossell, A. Schenk, H. Riel, Manipulating surface states of III–V nanowires with uniaxial stress. Nano Lett. **17**(5), 2816–2814 (2017)
90. D. Dzhigaev, A. Shabalin, T. Stankevic, U. Lorenz, R.P. Kurta, F. Seiboth, J. Wallentin, A. Singer, S. Lazarev, O.M. Yefanov, M. Borgström, M.N. Strikhanov, L. Samuelson, G. Falkenberg, C.G. Schroer, A. Mikkelsen, R. Feidenhans'l, I.A. Vartanyants, Bragg coherent X-ray diffractive imaging of a single indium phosphide nanowire. J. Opt. **18**, 064007 (2016)
91. D. Dzhigaev, T. Stankevic, Z. Bi, S. Lazarev, M. Rose, A. Shabalin, J. Reinhardt, A. Mikkelsen, L. Samuelson, G. Falkenberg, R. Feidenhans'l, I.A. Vartanyants, X-ray Bragg ptychography on a single InGaN/GaN core-shell nanowire. ACS Nano **11**(7), 6605–6611 (2017)
92. T. Stankevic, E. Hilner, F. Seiboth, R. Ciechonski, G. Vescovi, O. Kryliouk, U. Johansson, L. Samuelson, G. Wellenreuther, G. Falkenberg, R. Feidenhans'l, A. Mikkelsen, Fast strain mapping of nanowire light-emitting diodes using nanofocused X-ray beams. ACS Nano **9**, 6978 (2015)
93. A. Diaz, C. Mocuta, J. Stangl, B. Mandl, C. David, J. Vila-Comamala, V. Chamard, T.H. Metzger, G. Bauer, Coherent diffraction imaging of a single epitaxial InAs nanowire using a focused X-ray beam. Phys. Rev. B **79**, 125324 (2009)
94. V. Favre-Nicolin, F. Mastropietro, J. Eymery, D. Camacho, Y.M. Niquet, B.M. Borg, M.E. Messing, L.-E. Wernersson, R.E. Algra, E.P.A.M. Bakkers, Analysis of strain and stacking faults in single nanowires using Bragg coherent diffraction imaging. New J. Phys. **12**, 035013 (2010)
95. A. Mikkelsen, M. Borg, J.H. Petersen, J.N. Andersen, D.L. Adams, Unusual multilayer surface alloy: Al(100)-c(2x2)-2Li. Phys. Rev. Lett. **87**, 096102 (2001)
96. M. Borg, A. Mikkelsen, M. Birgersson, M. Smedh, E. Lundgren, D.L. Adams, C.-O. Almbladh, J.N. Andersen, Structure and formation of the Al(100)-(root 5 x root 5) R27 degrees-Na phase: a LEED, DFT and HRCLS study. Surf. Sci. **515**(2–3), 267–280 (2002)
97. M. Hjort, M. Bauer, S. Gunnarsson, E. Mårsell, A.A. Zakharov, G. Karlsson, E. Sanfins, Ch.N. Prinz, R. Wallenberg, T. Cedervall, A. Mikkelsen, Electron microscopy imaging of proteins on gallium phosphide semiconductor nanowires. Nanoscale **8**, 3936–3943 (2016)
98. G. Hammarin, H. Persson, A.P. Dabkowska, Ch.N. Prinz, Enhanced laminin adsorption on nanowires compared to flat surfaces. Colloids Surf. B **122**, 85–89 (2014)
99. E. Mårsell, E. Boström, A. Harth, A. Losquin, C. Guo, Y.-C. Cheng, E. Lorek, S. Lehmann, G. Nylund, M. Stankovski, C.L. Arnold, M. Miranda, K.A. Dick, J. Mauritsson, C. Verdozzi, A. L'Huillier, A. Mikkelsen, Spatial control of multiphoton electron excitations in InAs nanowires by varying crystal phase and light polarization. Nano Lett. **18**(2), 907–915 (2018)
100. D. Verardo, F.W. Lindberg, N. Anttu, C.S. Niman, M. Lard, A.P. Dabkowska, T. Nylander, A. Månsson, Ch.N. Prinz, H. Linke, Nanowires for biosensing: lightguiding of fluorescence as a function of diameter and wavelength. Nano Lett. **18**(8), 4796–4802 (2018)

Impurity Doping in Semiconductor Nanowires

Naoki Fukata

Abstract Due to their novel physical properties, semiconductor nanowires are of great research interest. To realize novel devices that feature them, however, they need to be modified. One of the most well-known, important and effective functionalization techniques is impurity doping: this will be the key to the application of nanowires to metal oxide field-effect transistors, solar cells, sensors, and similar devices. To control doping and obtain superior properties, it is important to fine-tune the impurity doping process to a high level of precision. In this chapter, several doping methods such as ex situ, in situ, and surface doping are described. Each method has its own advantages and disadvantages for impurity doping of nanowire structures. The characterization of dopant atoms is also important to understand the status and behaviors of dopant atoms in nanowire structures and to control their properties.

Keywords Nanowire · Doping · Silicon · Germanium

1 Introduction

Impurity doping is one of the most important and fundamental processes in functionalizing semiconductor nanowires for their application to various nanoscale devices such as next-generation field-effect transistors (FETs), solar cells, and sensors [1–7]. It has been thoroughly investigated in bulk semiconductor materials. Ion implantation techniques are now commonly used in semiconductor manufacturing. Many results have been reported for bulk materials and devices. The ion implantation method, which is an ex situ doping method, is increasingly being applied to semiconductor nanowires [8–13]. In situ doping methods are also important for nanostructures. The advantages of in situ doping are lack of damage and high controllability.

N. Fukata (✉)
International Center for Materials Nanoarchitectonics (MANA), National Institute for Materials Science (NIMS), 1-1 Namiki, Tsukuba 305-0044, Japan
e-mail: FUKATA.Naoki@nims.go.jp

© Springer Nature Singapore Pte Ltd. 2021

N. Fukata and R. Rurali (eds.), *Fundamental Properties of Semiconductor Nanowires*,
https://doi.org/10.1007/978-981-15-9050-4_3

To obtain the desired device properties by impurity doping, the states of dopant atoms, such as bonding structures, sites, and electrical activities, need to be characterized. Various characterization methods have so far been reported for semiconductor nanowires. These include Raman spectroscopy, infrared spectroscopy, electron energy loss spectroscopy (EELS), atom probe tomography, and electron spin resonance. Understanding the behaviors of dopant atoms in nanowire structures is also important for device applications.

This chapter focuses on the above-mentioned types of impurity doping in semiconductor nanowires and is organized into three sections: doping methods, the characterization of dopant atoms, and their behaviors.

2 Doping Methods

Several doping methods have been reported for semiconductor nanowires. Due to the structural properties of nanowires, such as their morphology and nanoscale size, the selection of doping methods is important. In this section, three kinds of doping methods: ex situ doping, in situ doping, and surface doping are described. Each doping method has its own merits and drawbacks.

2.1 Ex Situ Doping

2.1.1 Ion Implantation

The most well-known type of doping, ex situ doping, is an ion implantation technique. Controlling the acceleration voltage and ion dose makes it possible to control the depth profile of dopant ions in the device's active region. However, this process also causes defects in the implanted region. The recrystallization process to remove these defects in the implanted regions, and the subsequent reactivation and distribution process of dopant impurities, need to be understood to enable successful ion implantation. In this section, we describe some examples of ion implantation in silicon nanowires (SiNWs).

In the first example, ion implantation is used for fabricating semiconductor nanowire FETs [8, 9]. A vapor–liquid–solid (VLS) method is generally used to grow intrinsic SiNWs [14]. Phosphorus (P) implantation is performed at room temperature to form source and drain regions on the intrinsic SiNWs using shadow masks made of photoresist. The implantation energy and ion dose were 20 keV and 4×10^{12} cm^{-2}, respectively, in Ref 8. The authors fabricated n-type/intrinsic/n-type metal oxide semiconductors (nin-MOSFETs) that had strong and clear saturation currents. In Ref 9, p- and n-type FETs were fabricated and showed unipolar transport properties. Ion-implanted SiNWs are also used as channels in FETs. p- and n-type SiNW FET channels measuring 10–20 nm wide were fabricated using ion implantation at

room temperature in Ref 10. The implantation energies were 7 and 2.5 keV for B^+ and P^+ ions, respectively. The ion dose was 1×10^{15} cm^{-2} in both cases. Based on the results of Raman spectroscopy, the authors reported that a fully crystalline structure can be regained by thermal annealing at 800 °C [10]. However, the details of the crystal structure of SiNWs after thermal annealing have not been investigated.

Axial p–n junctions have also been realized by ion implantation [11–13]. Hoffmann et al. performed ion implantation at room temperature with ion energies varying from 1–400 keV and ion doses between 0.05–3 $\times$ 10^{14} cm^{-2} [11]. They used SiNWs with diameters of 150–400 nm and lengths of 250–500 nm. The authors used the electron beam-induced current (EBIC) method to investigate the activation of dopants in ion-implanted SiNWs [11]. The EBIC images reveal the expected doping and junctions and provide evidence that this is an effective technique for doping SiNWs. They also performed two-point current–voltage measurements and obtained well-defined rectifying behaviors [11]. Kanungo et al. performed ion implantation with B, P, and As ions, respectively, at room temperature to form p- and n-type SiNWs [12]. The diameter of the SiNWs was about 150 nm. To achieve a homogeneous doping profile along the length of the SiNWs, multi-energy implantations were performed in three to four steps using different implantation energies and doses. The intended doping levels of B, P, and As were 3×10^{18}, 1×10^{19}, and 1×10^{18} cm^{-3}, respectively. In their experiments, B-implanted SiNWs showed higher electrical conductivity than P- and As-implanted SiNWs. This is because the B^+ ion is lighter than P^+ and As^+, resulting in lower damage. Kanungo et al. also formed axial p–n junctions in SiNWs with a diameter of 120 nm by combining ion implantation and in situ doping [13]. They showed good diode properties.

To more clearly understand the damage caused by ion implantation and the recrystallization process that removes the defects in implanted regions by subsequent thermal annealing, structural observations need to be made. Some examples of transmission electron microscope (TEM) images of SiNWs before and after B^+ and P^+ ion implantation are shown in Fig. 1 [15]. SiNWs were synthesized at 1200 °C in flowing argon (Ar) gas at 50 sccm by catalytic laser ablation of an Si target, with Ni as the metal catalyst ($Si_{99}Ni_1$). SiNWs were then implanted with 30-keV $^{11}B^+$ ions or 80-keV P^+ ions at doses ranging from 1×10^{13} to 1×10^{16} cm^{-2} as shown in Fig. 1f. Figure 1g shows the B and P depth profiles estimated for bulk Si using TRIM simulation. Figure 1a clearly shows Si lattice fringes in SiNWs, indicating that the core comprises single-crystal Si sheathed with an amorphous SiO_x ($x \leq 2$) layer. Figure 1b shows that the crystalline Si core became amorphous after ion implantation at a dose of 1×10^{16} B^+/cm^2. To recrystallize SiNWs, thermal annealing was performed at 900 °C in an argon (Ar) gas atmosphere. After this process, the Si lattice fringes appeared again in the Si core region, as shown in Fig. 1c and d. The Si core showed a single-crystal structure for SiNWs implanted with a dose of 5×10^{15} B^+/cm^2 (Fig. 1c), while the Si core changed to a polycrystal state at doses exceeding 1×10^{16} cm^{-2} (Fig. 1d). With P implantation, polycrystal structures occur at doses above 1×10^{14} cm^{-2}, and surface roughness becomes significant. This is due to the greater damage caused by P implantation (Fig. 1e) since the mass of P is greater than that of B.

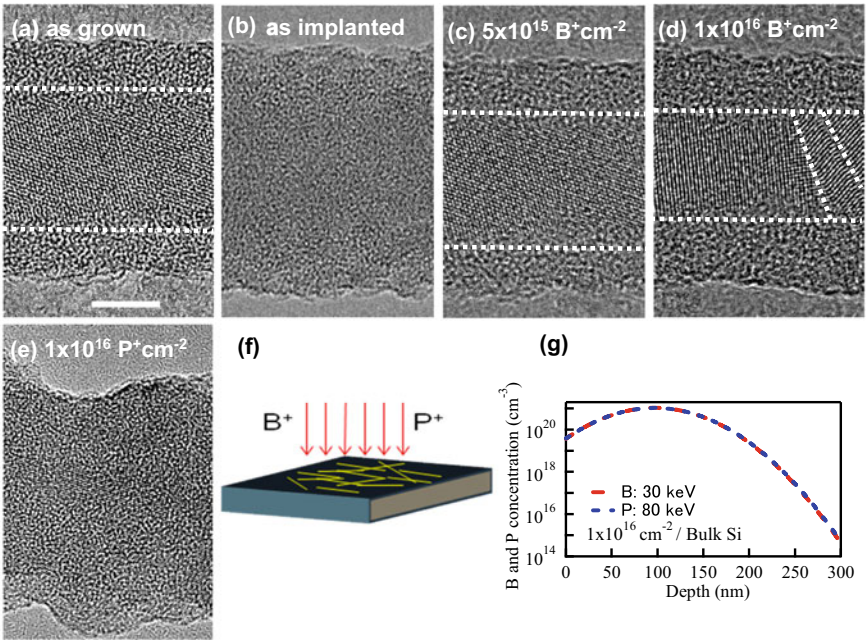

Fig. 1 Typical TEM images of SiNWs **a** as grown, **b** before ion implantation, and after ion implantation with a dose of **c** 5×10^{15} B^+/cm^2, **d** 1×10^{16} B^+/cm^2, and **e** 1×10^{16} P^+/cm^2. The scale bar is 5 nm. **f** Illustration of ion implantation for SiNWs. **g** The depth profiles of B and P as estimated by TRIM. Reproduced from Ref. [15]. Copyright 2012, with permission from American Chemical Society

Raman spectroscopy is one of several ways of clarifying both the recrystallization of SiNWs and the reactivation of B acceptors in SiNWs by thermal annealing. Figure 2 shows the dependence of Si optical phonon peaks on the annealing temperature. The Si optical phonon peak significantly decreased and a broad peak related to amorphous Si appeared at around 470 cm^{-1} after ^{11}B ion implantation, as shown in Fig. 2a. The Si optical phonon peak increased gradually on increasing the annealing temperature and had almost recovered after annealing at 900 °C. These results are in good agreement with the results of the TEM observations shown in Fig. 1. On increasing the annealing temperature, a peak appeared at about 618 cm^{-1} and the intensity increased (Fig. 2a and b). This peak is due to the ^{11}B local vibrational peak [1, 15], showing that the B acceptor atoms were doped in substitutional sites in the crystalline Si core of the SiNWs during the recrystallization process. The peak intensity of the ^{11}B local vibrational peak increases with increasing annealing temperature. The Si optical phonon peak showed a broadening with increasing annealing temperature (Fig. 2a and d). This is due to the Fano effect caused by the reactivation of B atoms. The characterization of dopant atoms is explained more fully in Sect. 3. These results clearly show the recrystallization of SiNWs and reactivation of B acceptor atoms.

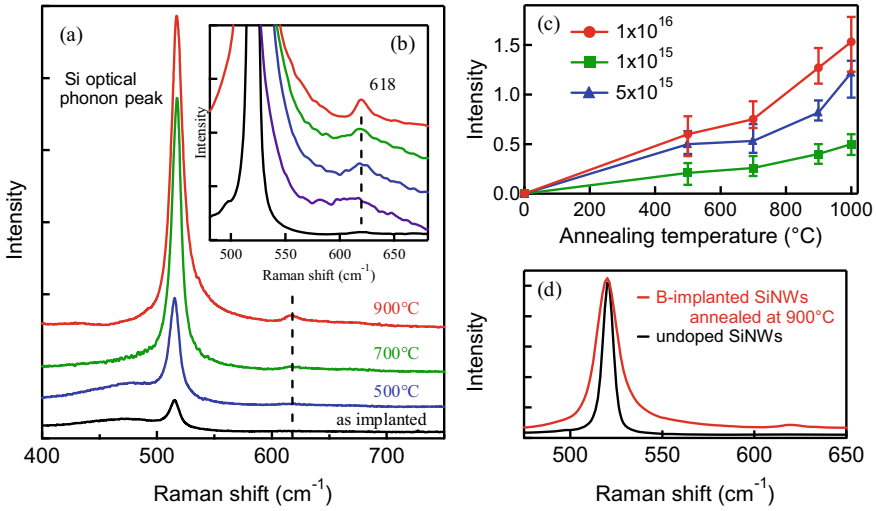

Fig. 2 **a** Si optical phonon peak and ^{11}B local vibrational peak observed for SiNWs after ^{11}B ion implantation and subsequent annealing. **b** Magnified image of (**a**). **c** Dependence of the intensity of the ^{11}B local vibrational peak on the annealing temperature. **d** Change in the Si optical phonon peak before and after implantation with a dose of 1×10^{16} $^{11}B^+/cm^2$. Reproduced from Ref. [15]. Copyright 2012, with permission from the American Chemical Society

This method is also applicable to P-implanted SiNWs. The results are summarized in Fig. 3. The Si optical phonon peak completely disappeared and a broad amorphous Si peak appeared after P^+ ion implantation at a dose of 1×10^{16} P^+/cm^2 (Fig. 3a), while B^+ implantation at the same dose resulted in a clear Si optical phonon peak, meaning that the damage caused by P ion implantation is much greater than that by B ion implantation. This is also in good agreement with the result shown in Fig. 1. Thermal annealing increases the intensity of the Si optical phonon peak due to recrystallization. The Si optical phonon peak showed a downshift after P^+ ion implantation and subsequent activation annealing compared to that before implantation (Fig. 3c). This can be explained by the phonon confinement effect due to the Si core structure being changed to a polycrystal structure and the phonon correlation length decreasing [16–18]. Electron spin resonance (ESR) is an effective characterization method of investigating defects in semiconductors. ESR measurements were carried out at 4.2 K with the microwave power set at 1 mW. Figure 3b shows ESR signals observed after P ion implantation followed by thermal annealing. The ESR signal observed for implanted SiNWs comprises at least three signals with g-values of 2.000, 2.003, and 2.005. The ESR signal with the g-value of 2.005 is assigned to defects in amorphous Si formed by P^+ ion implantation [19], while the ESR signals with g-values of 2.003 and 2.000 are probably, respectively, assigned to defects called *EX* centers [20] and oxide-deficient defects called *E'* centers in the oxide layer [21] in the SiNWs. The *EX* and *E'* centers were annihilated by thermal annealing at 500 °C. The intensity of the ESR signal with the g-value of 2.005 decreased at 500 °C and then increased.

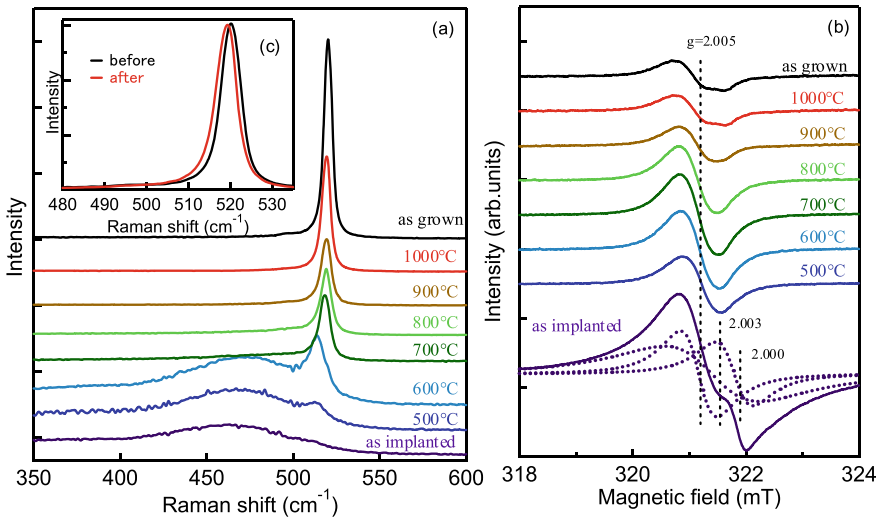

Fig. 3 Annealing behaviors of **a** Si optical phonon peak and **b** ESR spectra observed for SiNWs implanted with 1 x 10^{16} P^+/cm^2. **c** Change in the Si optical phonon peak before and after implantation with a dose of 1 x 10^{16} P^+/cm^2. Reproduced from Ref. [15]. Copyright 2012, with permission from the American Chemical Society

The initial decrease is due to the annihilation of defects in the amorphous Si induced by P^+ ion implantation, while the subsequent increase is due to the recrystallization of the Si core in the SiNWs. The interface between the crystal Si core and the surface oxide layer is formed again and, consequently, interfacial defects are again created at that location. The ESR signal for the interfacial defects again decreased on annealing at above 900 °C. This is due to the annihilation of excess interfacial defects by high-temperature annealing. The reactivation of P donors implanted into SiNWs was proved by observation of the ESR signal of the conduction electrons with a g-value of 1.998 [15]. The details of this characterization will be explained more fully in Sect. 3.

Defect annihilation in SiNWs is more of a challenge than in bulk Si. One strategy is to carry out ion implantation at higher temperatures to reduce defect production and to suppress the formation of polycrystals in SiNWs. This method is called hot implantation. Figure 4 shows the result of hot-implanting P^+ ions at 300 °C with a dose of 1 × $10^{15}/cm^2$. The result of RT implantation is also shown in Fig. 4a and b. The intensity of the Si optical phonon peak (Fig. 4a) and the ESR signal of conduction electrons (Fig. 4b) significantly increased for the hot-implanted sample. The electrically active P donor concentration increased up to about 2 × 10^{19} cm^{-3} as a result of hot implantation, which was two 100-folds greater than the value obtained for implantation at RT [15]. The TEM image of the hot-implanted sample shown in Fig. 4c shows clear lattice fringes and a single crystal structure. The hot implantation method is clearly a very effective way of suppressing the formation of polycrystals in SiNWs.

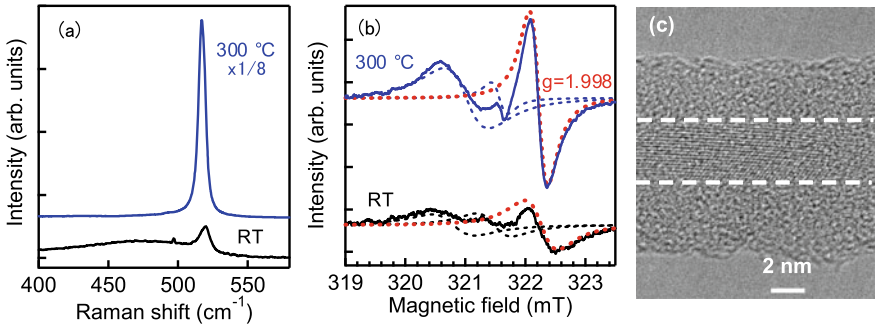

Fig. 4 **a** Raman spectra and **b** ESR signals observed for SiNWs implanted with 1×10^{15} P^+ cm^{-2} at RT and 300 ˚C, respectively. Activation annealing was performed at 900 ˚C. **c** TEM image of the SiNW after hot implantation at 300 ˚C.

Implantation dose and temperature affect the recrystallization process in the following ways. Figure 5 illustrates the defect introduction and recrystallization process during thermal annealing. High-dose ion implantation significantly damages the crystal Si core and converts it to an entirely amorphous state. This causes random nucleation because the initial crystal structure and orientation have been lost, and explains why polycrystal structures appear in SiNWs that have been implanted at high doses. However, the situation is different for low-dose ion implantation and hot

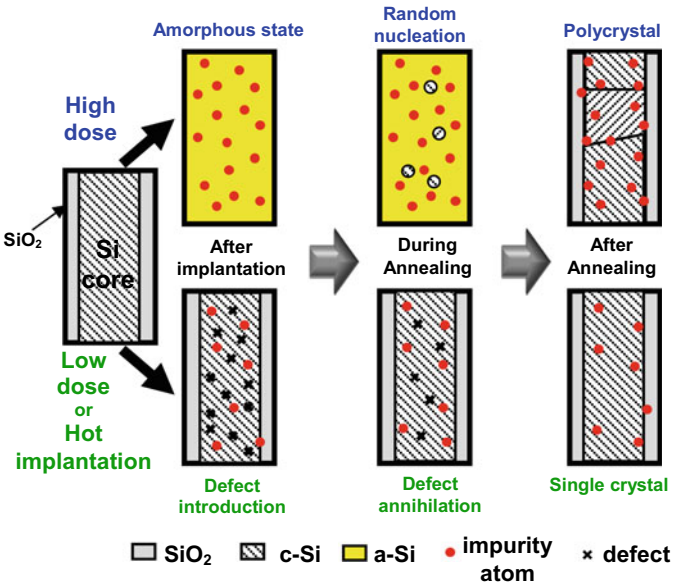

Fig. 5 Schematic of the recrystallization process of ion-implanted SiNWs by thermal annealing. Reproduced from Ref. [15]. Copyright 2012, with permission from the American Chemical Society

implantation. In these two latter cases, some of the crystal structures can be maintained, making it possible to cause nucleation from the remaining crystal regions, resulting in the re-appearance of single crystals in SiNWs.

2.1.2 Thermal Diffusion

Thermal diffusion is also an ex situ method. It is a technique based on solid-state diffusion. Spin-on-glass (SOG) or spin-on-dopant (SOD) techniques are generally used as impurity sources for the introduction of dopant atoms [22, 23]. Unlike with ion implantation, the thermal diffusion technique can introduce dopants without damage or significant changes in morphology. Several ways of introducing dopant atoms using SOG or SOD have been reported. Figure 6 is a schematic illustration of sample preparation for thermal diffusion. Beckman et al. applied the thermal diffusion method to SiNWs formed on silicon-on-insulator (SOI) [22]. They used phosphorosilica film (Emulsitone Co.) as the n-type dopant and borofilm (Emulsitone Co.) as the p-type dopant source and annealed at 800–1000 °C for 1–8 min. Their method is shown in Fig. 6a. They showed that the thermal diffusion of NW samples gave higher conductivity than ion-implanted NW samples at NW diameters of 10–25 nm. This is due to lattice damage caused by ion implantation. Ingole et al. also applied the thermal diffusion method using borofilm (Emulsitone Co.) as the p-type dopant source. They grew SiNWs with diameters of 120–180 nm using the VLS method and then annealed the samples at 800 and 900 °C for 5–10 min. Their method is shown in Fig. 6b. The electrically active B concentrations were estimated, using four-probe resistivity measurements, to be in the range of 10^{18}–10^{20} cm^{-3}. Hazut et al. formed p-i-n junctions in SiNWs by sandwiching them between two pretreated boron-containing and phosphorus-containing substrates (Fig. 6c) [24]. The advantage of thermal diffusion is that it is simple and causes no damage to nanostructures, while its disadvantages are lack of selectivity of the doping region and its reliance on a high-temperature process.

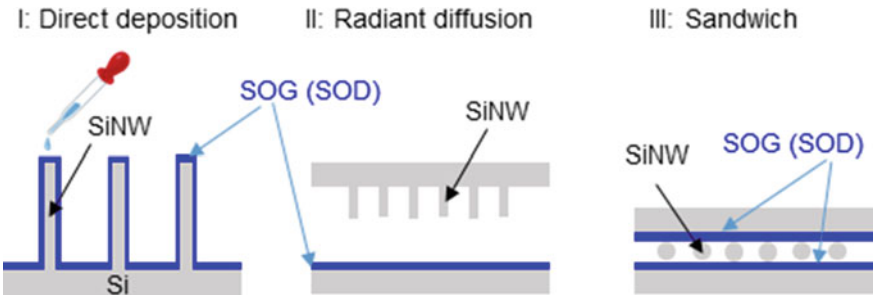

Fig. 6 Schematic illustration of sample preparation for thermal diffusion using SOG or SOD

2.2 *In Situ Doping*

In situ doping is a very important doping method for nanostructures. Its advantages are that it is a damage-free and highly controllable process. There are numerous reports on this process [25–33]. Impurity doping is performed during the VLS growth of semiconductor NWs. In the chemical vapor deposition (CVD) method, diborane (B_2H_6) gas and phosphine (PH_3) gas are generally used as the p-type and n-type dopant sources. The doping concentration can be controlled by adjusting the flux of the dopant gases. The dopant incorporation efficiency has been investigated by adjusting the flow rates of PH_3 gas and SiH_4 gas to vary the P-to-Si ratio in the inlet gas flow [31]. Four-point resistivity measurements clearly show a decrease in resistivity on increasing the P-to-Si ratio. On the other hand, radial surface deposition is enhanced in the case of B-doping by the reaction between B_2H_6 and silane (SiH_4) gases [28]. This effect has also been observed in germanium (Ge) NWs [34, 35]. Figure 7 shows the dependence of impurity doping on the morphology of GeNWs [35]. The scanning electron microscope (SEM) image of undoped GeNWs in Fig. 7a shows that the diameter is uniform along the length of the GeNWs. The TEM image of undoped GeNWs in Fig. 7i shows that the core comprises crystalline Ge and the surrounding layer is amorphous GeO_2 approximately 2 nm in thickness. The amorphous GeO_2 is a native oxide layer. The main growth direction is <110> for GeNWs with diameters smaller than about 20 nm, and <111> for GeNWs with diameters exceeding 20 nm. This is the same pattern as has been observed in SiNWs [36, 37]. The shape of the GeNWs closely depends on the flux of the B_2H_6 gas

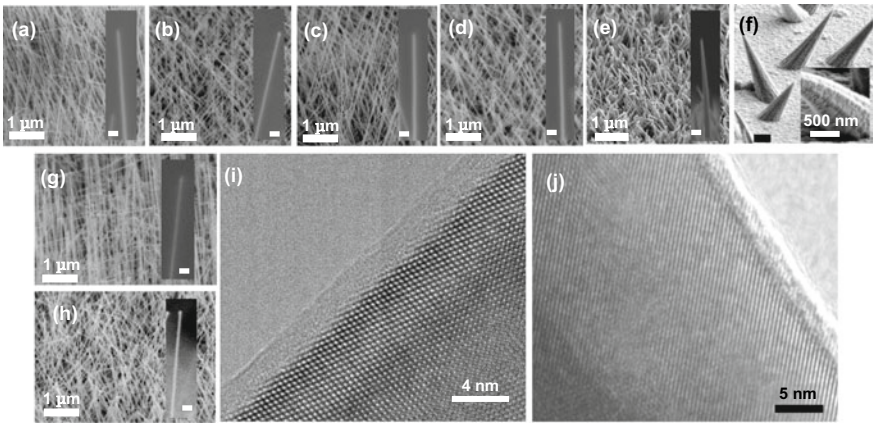

Fig. 7 SEM images of GeNWs synthesized by CVD with gas mixtures with ratios of GeH_4 to B_2H_6 of **a** 10:0, **b** 10:0.2, **c** 10:0.4, **d** 10:0.7, **e** 10:1.0, and **f** 10:2.2. The insets show the magnification of single NWs. The scale bar is 20 nm. SEM images of GeNWs synthesized by CVD with gas mixtures with ratios of GeH_4 to PH_3 of **g** 10:1.0 and **h** 10:7.0. The insets show the magnification of single NWs and the scale bars are 30 nm. **i** and **j** are the High-resolution TEM images of (**a**) and (**e**), respectively. Reproduced from Ref. [35]. Copyright 2010, with permission from American Chemical Society

during the growth stage (Fig. 7b-f). The B_2H_6 gas causes the deposition of a Ge layer with high B concentration. The shape of each GeNW finally changes to a tapered structure on increasing the flow of B_2H_6 gas. A high-resolution TEM image of the Ge extra shell layer is shown in Fig. 7j. This structure, called Ge microcones (GeMCs), has a hexagonal cross section with well-developed facets, corresponding to the low free energy {111} and {100} planes. The same result has also been observed in SiNWs [37, 38]. Unlike with B doping, the diameter of P-doped GeNWs does not significantly depend on the PH_3 gas ratio, resulting in a uniform diameter, as shown in Fig. 7g and h. This is a similar effect to that seen with SiNWs.

In situ doping can also be applied to selective doping in semiconductor NWs. One example is axial modulation doping in NWs [39, 40]. To achieve axial modulation doping in SiNWs, Yang et al. used a local substrate heater and added H_2 gas to suppress radial deposition [39]. Finally, they showed modulation-doped n^+–n–n^+ SiNWs by TEM analysis and scanning gate microscopy. Here, n^+ and n represent the heavy and light n-type regions. Eichfeld et al. also formed similar structures with periodic n^+ segments in n-type SiNWs.

Another example of selective doping is radial modulation doping in semiconductor NWs. The structure is called core–shell NWs. Core–shell structures are commonly used in solar cell applications [41–43]. In these structures, p–n junctions are radially formed in the NWs. By doing this, the light-trapping effect effectively increases and the carrier recombination rate is reduced due to the shorter carrier collection path. Figure 8 shows an example of a p–n homojunction formed using a core–shell NW structure. A metal-catalyzed electroless etching (MCEE) method [44, 45] was applied to form n-type SiNW structures on an n-type Si substrate. Figure 8a and b show a cross-sectional and top view of SEM images of SiNWs formed by MCEE. Impurity doping was performed during CVD shell formation. Figure 8c shows an SEM image of core–shell NWs after shell formation by CVD. The advantages of using CVD are that shell formation with impurity doping can be realized even for bundled NWs, and the doping concentration and doped regions can be controlled in the shell region [46–51].

Core–shell NWs using Si and Ge show potential for the suppression of impurity scattering and are considered to be high-speed transistor channels [52–60]. In situ selective doping is effective for functionalizing Si/Ge and Ge/Si core–shell hetero-NWs [58, 59]. This structure is similar to that in high electron mobility transistors (HEMTs) [61]. To construct an HEMT-type structure, it is important to form a sharp

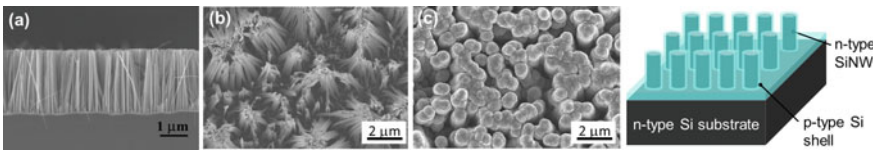

Fig. 8 **a** Cross-sectional and **b** top view of SEM images of SiNWs formed by MCEE. **c** SEM image of core–shell NWs after shell formation by CVD. **d** A schematic illustration of core–shell NW structures

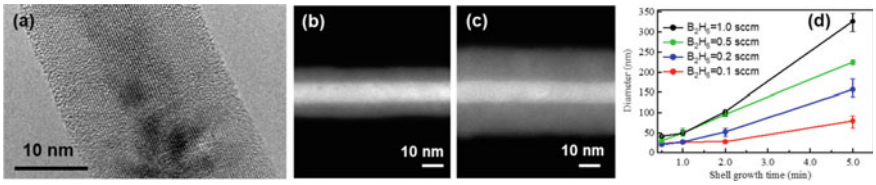

Fig. 9 **a** HRTEM image of i-Ge/p-Si core–shell NW. STEM images of i-Ge/p-Si core–shell NW with a shell growth time of **b** 30 s and **c** 1 min. **d** The B_2H_6 gas fluxes of p-Si layers was 0.5 sccm. Reproduced from Ref. [15]. Copyright 2012, with permission from the American Chemical Society

interface between Si and Ge by preventing any intermixing of the Si and Ge layers and realizing selective doping in the core and shell regions. An HRTEM image of i-Ge/p-Si core–shell NWs is shown in Fig. 9a. The thickness of the shell layer closely depends on the flux of the B_2H_6 gas (Fig. 9b). As explained above, the enhancement of radial shell formation is explained by the reaction between B_2H_6 and GeH_4 gases. The characterization of selective doping will be described in Sect. 3.

2.3 Molecular Doping (Surface Transfer Doping)

Impurity scattering becomes more significant as the diameter of NWs becomes smaller, resulting in a decrease in the carrier mobility of electronic devices using NWs. Adopting the HEMT-type structure described in the previous section is one way of preventing impurity scattering [59]. Here, molecular doping (surface transfer doping) is described as another way of introducing carriers into NWs [62–64]. Molecular doping can be used effectively in NWs with small diameters because of their high surface-to-volume ratio. Molecules terminated on NW surfaces transfer charge to NWs. There have been several studies on the molecular doping of SiNWs. Some results related to molecular doping are included below.

Hydrogen (H) is well known as a surface passivation element. Treatment with hydrofluoric acid (HF) solution causes the surface of Si to be terminated with H atoms. Partial electron transfer from Si to H takes place because the electronegativity of H is greater than that of Si. Guo et al. fabricated FETs from individual H–SiNWs etched from both n-type and intrinsic Si wafers and performed I–V measurements on them [62]. The I–V curves obtained from both samples showed the typical characteristic of a p-channel semiconductor FET, and the hole carrier concentrations of the H–SiNWs were estimated to be in the order of 10^{17} cm^{-3} [62]. This result clearly shows that electron transfer across the surface of SiNWs provides a majority of the carriers in H–SiNWs.

NH_3 and NO_2 are other candidates for molecular doping. The effects of n- and p-type conductivities caused by NH_3 and NO_2 gas exposures, respectively, have initially been observed for porous Si, prepared by anodic etching of highly B-doped Si wafers [63–67]. The same phenomena have also been observed in SiNWs exposed

to NH_3 [68]. First-principles electronic structure calculation has been done to clarify the mechanism of molecular doping in SiNW samples [69]. Termination with NH_3 molecules on the surface of SiNWs introduced a shallow donor state close to the conduction band edge [69]. On the other hand, NO_2 did not introduce a shallow acceptor level. This differs from what was reported in previous experiments on porous Si [63–67]. The authors theoretically elucidated that the role of NO_2 is to reactivate subsurface B atoms at dangling bond sites.

These molecular doping effects are potentially applicable to chemical gas sensors. The absorption of gas molecules modulates the transport properties of SiNWs, allowing changes in electrical conductivity to be detected. Due to the high surface-to-volume ratio of NW structures, they have major potential as high-sensitivity gas sensors, such as for NO_2 gas, which is emitted by internal combustion engines and damages the human respiratory system.

3 Characterization of Impurity Doping

The characterization of impurity doping is important to be able to functionalize NWs and control their properties. Various methods have been used for the characterization of impurity atoms in semiconducting NWs. There are three general categories of characterization methods: electrical, optical, and mass spectrometric methods.

3.1 Electrical Analysis

Electrical measurements are extensively used for doping characterization through carrier transport properties. One of the main applications is FETs. There have been many reports on the FET properties of NWs [2, 3]. Individual NW FETs can be fabricated on thermally oxidized Si substrates that have low resistivity. To form electrical contacts that act as source and drain electrodes, metals are deposited on both sides of NW surfaces by electron beam lithography. Metals are also deposited on the back surface of the Si substrate, and the gate bias is applied from there. This structure is termed a back-gate-type FET. A schematic illustration is shown in Fig. 10. Cui et al. reported doping and electrical transport in single-crystal n-type and p-type SiNWs in 2000 [25]. P and B doping were performed during the VLS growth of SiNWs. They measured gate-dependent measurements and showed n-type and p-type behaviors in n-type and p-type SiNWs, respectively. They also estimated carrier mobility by analyzing the data.

Figure 11 shows a result of gate-dependent current versus bias voltage (I–V) curves measured for p-type and n-type GeNWs. The I–V curves for n-type GeNWs showed increased conductance with increasingly positive gate voltage (Fig. 11a). This I–V behavior is similar to that of n-channel FETs. Figure 11b shows the opposite

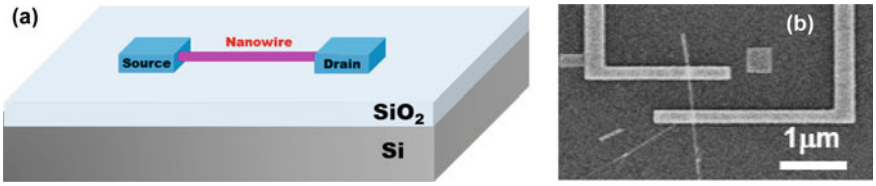

Fig. 10 **a** Schematic illustration and **b** SEM image of a back-gate-type single nanowire

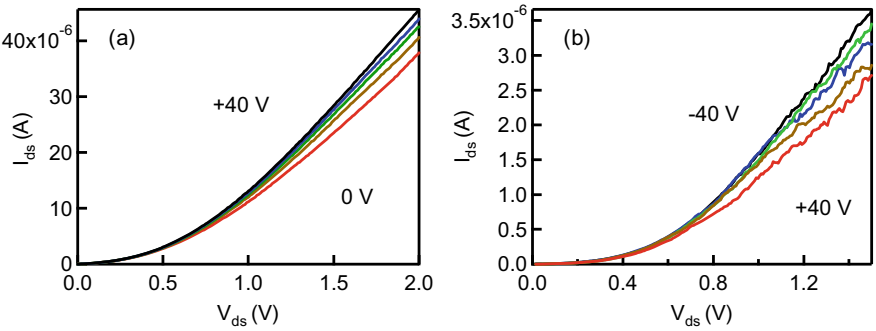

Fig. 11 Gate-dependency of I–V curves of **a** n-type and **b** p-type GeNWs

behavior, namely the conductance increasing as gate voltage becomes more negative, indicating a p-channel FET.

Scanning tunneling spectroscopy (STS) has also been used for making electrical measurements of semiconductor NWs [27]. In STS measurements, the surface morphology of NWs can be observed in the scanning tunneling microscopy (STM) mode. NWs have high surface-to-volume ratios, and the electrical properties of NWs strongly depend on their surface morphologies. Hence, simultaneous observations of surface morphology and electrical measurements are important to correctly understand the properties of NWs.

3.2 Optical Analysis

3.2.1 Raman Spectroscopy

The doping properties of NWs can also be analyzed by optical methods. Electrical properties depend on the device fabrication process because electrical contact with metal electrodes strongly affect them. Unlike, for electrical analysis, optical properties do not depend on sample preparation for analyses. Here, two optical analyses, Raman and infrared (IR) spectroscopies, will be described.

Raman spectroscopy can clarify the states of dopant atoms in NWs, specifically their bonding states and electrical activity [1]. Some results observed for ex situ doping by ion implantation have already been shown in Sect. 2.1.1. More detailed explanations and analyses will be shown for SiNWs, GeNWs, and Si/Ge (Ge/Si) core–shell NWs with in situ doping during NW growth. Figure 12 shows the results of Raman spectroscopy measurements obtained for B-doped SiNWs. These were synthesized using a catalytic laser ablation method employing a frequency-doubled NdYAG laser (532 nm, 7 ns pulse width, 10 Hz, 150 mJ/pulse). They were synthesized at 1200 °C in flowing argon (Ar) gas at 50 sccm by laser ablation of an Si target with nickel (Ni) as the metal catalyst and B as dopants. B-doped SiNWs were directly deposited on a SiO_2 substrate for the Raman spectroscopy measurements to avoid the effects of Si optical phonons from the Si substrate. The intense peak at about 519.0 cm^{-1} is due to the Si optical phonon peak from B-doped SiNWs. The peak position is lower than that for bulk Si (520.1 cm^{-1}). The peak also shows an asymmetric broadening toward lower wavenumbers. These can be effectively explained by the phonon confinement effect [16–18]. Two peaks at about 618 and 640 cm^{-1} are shown in Fig. 12b. The peak frequencies are in good agreement with the ^{11}B (620 cm^{-1}) and ^{10}B (643 cm^{-1}) local vibrational peaks in B-doped bulk Si [70]. The ratio of these peak intensities (I_{618}:I_{640}) is estimated as being roughly 4:1, which is also in good agreement with the natural abundance of the two isotopes of ^{11}B (80.2%) and ^{10}B (19.8%) [70]. Based on these results, the two peaks can be assigned to the local vibrational modes of B in SiNWs [1, 15, 30]. This demonstrates that B atoms have been doped in most of the sites in the SiNWs' crystalline Si core.

The optical phonon peak for B-doped SiNWs showed a larger broadening to higher wavenumbers than did undoped SiNWs, in addition to the asymmetric broadening toward lower wavenumber due to the phonon confinement effect. This can be attributed to the Fano effect, which is caused by the coupling between discrete optical phonons and the continuum of interband hole excitations in degenerately doped p-type Si [1, 15, 30, 71]. In this case, the Fano effect is caused by the presence of free

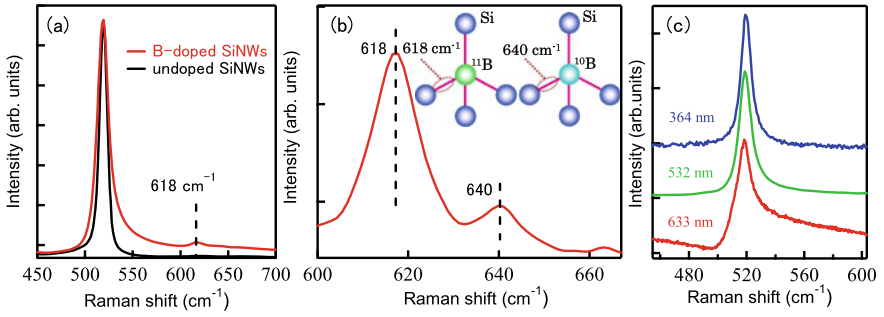

Fig. 12 **a** Optical phonon peaks of B-doped and undoped SiNWs measured by micro-Raman spectroscopy measurements. **b** Magnification of the Raman peak observed for B-doped SiNWs. **c** Dependence of the line shape of Si optical phonon peak on the excitation wavelength. Reproduced from Ref. [1]. Copyright 2009, with permission from Wiley VCH

holes in B-doped SiNWs, meaning that B atoms are electrically activated in SiNWs. The Fano effect can be confirmed by checking the dependence of the optical phonon peak on the excitation wavelength during Raman spectroscopy, as shown in Fig. 12c. The Si optical phonon peak showed a significant asymmetric broadening at higher wavenumbers with increasing excitation wavelength. The phonon peak observed at 633-nm excitation clearly showed antiresonance on the low wavenumber side. This dependence is characteristic of the Fano effect, indicating heavy B doping in the SiNWs.

To further confirm that this asymmetric broadening is due to the Fano effect, B acceptors in SiNWs were passivated by hydrogen (H) [30]. This process has been extensively studied for B- and P-doped bulk Si [72–81]. The H atoms become located at the bond-centered (BC) sites between B and neighboring host Si atoms, and B atoms are passivated by forming B–H–Si passivation centers when H atoms are introduced into B-doped Si. Hydrogen passivation readily occurs at temperatures ranging from 150–180 °C for B-doped Si. The results of H passivation by hydrogen atom treatment (HAT) [80, 81] at 180 °C are shown in Fig. 13a. The asymmetric broadening in the Si optical phonon peak significantly decreased. The Si optical phonon peak again showed broadening after annealing at 300 °C, indicating that the recovery of free holes results in the reappearance of asymmetric broadening. These results clearly demonstrate that the asymmetric broadening is due to the Fano effect. The formation of B–H–Si passivation centers causes a change in the local vibrational modes of B atoms in SiNWs [70]: it reduces the symmetry of B atoms in Si crystals from the tetrahedral symmetry of substitutional B atoms to axial symmetry with respect to the B–H–Si axis, causing splitting of the triply degenerate B vibrational mode with T_d point group symmetry into a doublet and a singlet with C_{3v} point group symmetry. This effect newly gives two Raman peaks at about 652 and 680 cm^{-1} in B-doped bulk Si after hydrogenation [70]. Figure 13b shows Raman spectra observed before and after HAT treatments at 150 and 180 °C for B-doped SiNWs. A broad peak was observed at around 650–680 cm^{-1} after HAT at 150 and 180 °C. The frequency of

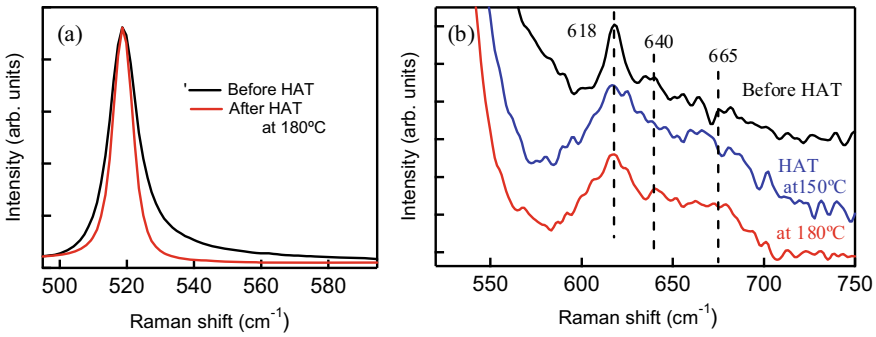

Fig. 13 **a** Si optical phonon peaks observed for B-doped and undoped SiNWs before and after HAT at 180 ˚C. **b** Raman spectra observed for B-doped SiNWs before and after HAT at 150 ˚C and 180 ˚C. Reproduced from Ref. [1]. Copyright 2009, with permission from Wiley VCH

the broad peak newly observed after HAT at 150 °C and 180 °C is in good agreement with that observed for B-doped bulk Si [70]. This result gives further confirmation of the assignment of B local vibrational peaks and the Fano effect observed in B-doped SiNWs.

The electrically active B concentration can be estimated by analyzing the peak shifts and asymmetric broadening due to the Fano effect in B-doped bulk Si. However, the Si optical phonon peak observed for B-doped SiNWs is also affected by the phonon confinement effect due to the nanoscale diameter, making it difficult to estimate the B active concentration. To estimate the B active concentration as accurately as possible, the intensity of the B local vibrational peak and the Fano broadening were considered, and finally, the B active concentration was estimated to range from 10^{19}–10^{20} cm^{-3}.

GeNWs have been intensively investigated by numerous researchers since both electron and hole mobilities in Ge are higher than those in Si [34, 83–90]. Raman spectroscopy is also applicable to the characterization of impurity doping in GeNWs [35, 91]. Figure 14a and b show the results for B-doped GeNWs. The B doping was performed by in situ doping during the CVD growth and the B doping concentration was controlled by changing the flux of B_2H_6 gas. The peak observed at around 300.2 cm^{-1} for bulk Ge is due to the Ge optical phonon peak. In addition to the Ge

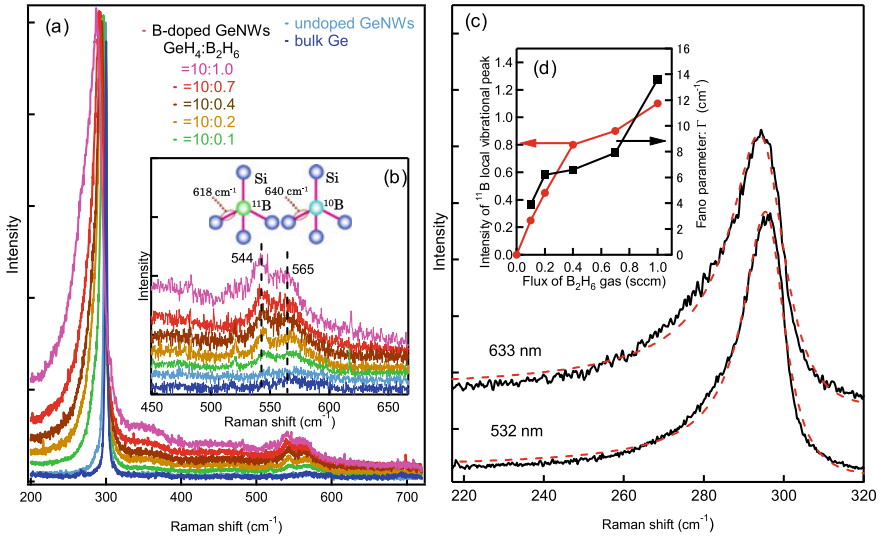

Fig. 14 **a** Raman spectra observed for B-doped GeNWs (B_2H_6 flux of 1.0, 0.7, 0.4, 0.2, and 0.1 sccm, starting from the top), undoped GeNWs (the second from the bottom), and bulk Ge (bottom). **b** Magnification of the Raman spectra. **c** Dependence of the line shapes of the Ge optical phonon peak on the excitation wavelength (GeH_4:B_2H_6 = 10:0.2). The dotted red lines are fitting curves generated by the Fano equation (Eq. 2). (**d**) Dependence of the intensity of ^{11}B local vibrational peak and the Fano fitting parameter (Γ) on the flux of B_2H_6 gas. B-doped GeNWs and undoped GeNWs were grown at 300 °C. Reproduced from Ref. [35]. Copyright 2010, with permission from the American Chemical Society

optical phonon peak, two peaks are observed at about 544 cm^{-1} and 565 cm^{-1} for B-doped GeNWs. The peak position of the latter peak is very close to that of the second-order Ge optical phonon peak that is observed for bulk Ge. However, the peak at 565 cm^{-1} is not the second-order Ge optical phonon peak, since there is no correlation between the intensity of the first-order Ge optical phonon peak and that of the second-order Ge optical phonon peak. The intensities of the peaks observed at about 544 and 565 cm^{-1} increase with increasing B_2H_6 gas ratio, showing a good correlation with B concentration. The B local vibrational peaks were observed at about 618 cm^{-1} and 640 cm^{-1} for ^{11}B and ^{10}B, respectively, for B-doped SiNWs. If Si atoms were completely replaced by Ge atoms, the B local vibrational peaks can be roughly estimated to be 540–580 cm^{-1} using the following relationship.

$$\frac{\omega(Ge-B)}{\omega(Si-B)} = \left(\frac{m_{Si}}{m_{Ge}}\right)^{1/2} \times \left(\frac{m_{Ge}+m_B}{m_{Si}+m_B}\right)^{1/2} \quad (1)$$

Here, *ω(Ge-B)* and *ω(Si-B)* are the frequencies of local vibrational modes of B in Ge and Si, respectively. m_{Si}, m_{Ge}, and m_B are the mass of Si, Ge, and B, respectively. The peaks observed at about 544 and 565 cm^{-1} are in the frequency range of 540–580 cm^{-1} estimated by Eq. 1. The peak shift of 544 and 565 cm^{-1} can be satisfactorily explained by the isotope shift of ^{11}B and ^{10}B. The intensity ratio of the peak at 544 cm^{-1} to that at 565 cm^{-1} is roughly estimated to be about 4:1 after removing the effects of the second-order Ge optical phonon peak. This ratio is in good agreement with the natural abundance of B isotopes (^{11}B:80.2%, $^{10}B = 19.8\%$). Based on these results, the peaks observed at about 544 and 565 cm^{-1} can be assigned to the local vibrational modes of ^{11}B and ^{10}B in GeNWs. This result shows B atoms to have been doped in most of the Ge atom sites in the crystalline Ge region of GeNWs.

The Ge optical phonon peak also shows a downshift and an asymmetric broadening toward lower wavenumbers as compared with bulk Ge. The downshift and asymmetric broadening becomes more pronounced if the B_2H_6 gas ratio is increased during the growth of GeNWs. This change in the phonon line shape can be explained by the Fano effect, which has been reported for degenerately doped p-type Ge [71, 92]. To demonstrate this, the dependence of the phonon line shapes on the excitation wavelength during Raman spectroscopy was investigated. The result is shown in Fig. 14c. The Ge optical phonon peak clearly showed major broadening at lower wavenumbers with increasing excitation wavelength, indicating that the downshift and asymmetric broadening are due to the Fano effect. This result demonstrates that B atoms are electrically activated in GeNWs. The Ge optical phonon peak can be analyzed by fitting with Eq. 2.

$$I(\omega) = I_0 \frac{(q+\varepsilon)^2}{(1+\varepsilon^2)} \quad (2)$$

where ω is the wavenumber, I_0 is the prefactor, q is the asymmetry parameter, and ε is given by $\varepsilon = (\omega-\omega_p)/\Gamma$, where ω_p is the phonon wavenumber and Γ is the line

width parameter. The dependence of the asymmetric broadening parameter of Γ and the peak intensity of ^{11}B shows a good correlation as shown in Fig. 14d. This result also gives evidence that the downshift and asymmetric broadening are due to the Fano effect. The fitting results of B-doped GeNWs excited with 532 and 633 nm lights are summarized in Table 1.

The results for P-doped GeNWs are shown in Fig. 15a and b. In addition to the Ge optical phonon peak, a peak is observed at around 342–345 cm^{-1}. The intensity of the peak increases on increasing the PH_3 gas flux. The peak position of the P local vibrational peak can be estimated in a similar way to that of the B local vibrational peaks using Eq. 1 but by replacing the B atom with a P atom. The estimated value is about 360 cm^{-1}, which is close to the experimental value of 342–345 cm^{-1}. Based on these observations, the peak at 342–345 cm^{-1} can be assigned to the P local vibrational peak in GeNWs. The P local vibrational peak shifts on increasing the PH_3 gas flux. This is probably due to the strain introduced by the incorporation of a high concentration of P atoms. The Ge optical phonon peak also shows a downshift and asymmetric broadening toward lower wavenumbers with on increasing the PH_3 gas flux. This trend becomes more pronounced if excitation wavelength is increased during Raman spectroscopy as shown in Fig. 15c. These results also demonstrate that the downshift and asymmetric broadening are due to the Fano effect. The Ge optical phonon peak can be analyzed by fitting with Eq. 2 as well as for B-doped GeNWs. The dependence of the asymmetric broadening parameter of Γ and the peak intensity of P also shows a good correlation, as shown in Fig. 15d. This result supports the contention that the downshift and asymmetric broadening is due to the Fano effect. The fitting results of P-doped GeNWs excited with 532- and 633-nm light are summarized in Table 2.

Selective doping is also an important technique for realizing high-speed transistor channels using Si/Ge and Ge/Si core–shell NW structures [58]. Figure 16 shows the results of selective doping in four different core–shell NWs measured by Raman spectroscopy. Figure 16a shows the result for n-Ge shells in i-Si/n-Ge core–shell NWs. The P local vibrational peak is clearly observed and the downshift and asymmetric broadening due to the Fano effect also appear in the Ge optical phonon peak, showing the formation of n-type Ge shells by selective doping of P atoms in the Ge shell layer. Figure 16b shows the result for n-Ge/i-Si core–shell NWs, which have the opposite structure of Fig. 16a. The P local vibrational peak and the Fano effect

Table 1 Fitting parameters (q and Γ) for the Fano line shapes of the Ge optical phonon peak observed for B-doped GeNWs with 532-nm and 633-nm excitation lights

B_2H_6 (sccm)	q: 532 nm	Γ(cm^{-1}): 532 nm	q: 633 nm	Γ(cm^{-1}): 633 nm
0.1	−7.2	3.9	−5.8	4.1
0.2	−6.4	6.2	−4.6	8.1
0.4	−4.8	6.6	−4.4	12.8
0.7	−3.9	7.9	−3.6	15.6
1.0	−3.6	13.6	−3.4	17.3

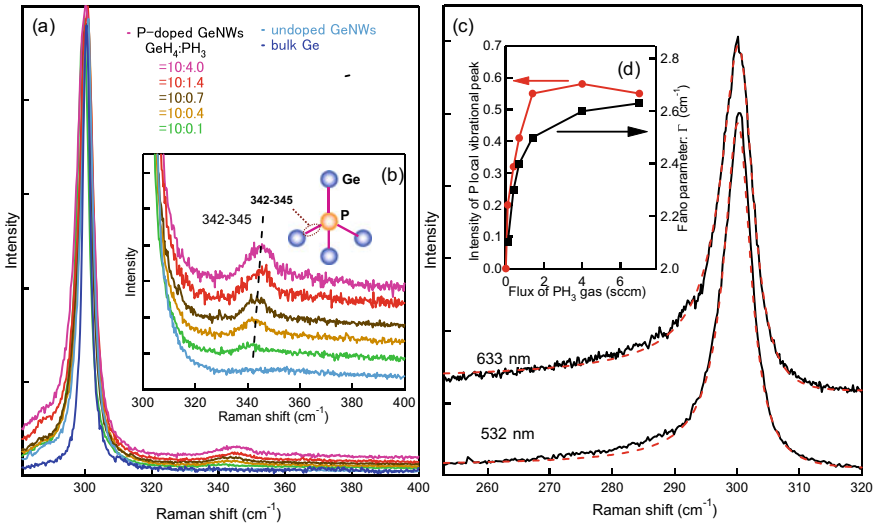

Fig. 15 **a** Raman spectra observed for P-doped GeNWs (PH_3 flux of 4.0, 1.4, 0.7, 0.4 and 0.1 sccm, starting from the top), undoped GeNWs (the second from the bottom), and bulk Ge (bottom). **b** Magnification of the Raman spectra. **c** Dependence of the line shapes of the Ge optical phonon peak on the excitation wavelength (GeH_4:PH_3 = 10:7.0). The dotted red lines are fitting curves generated by the Fano equation (Eq. 2). **d** Dependence of the intensity of P local vibrational peak and the Fano fitting parameter (Γ) on the flux of PH_3 gas. P-doped GeNWs and undoped GeNWs were grown at 350 and 300 ˚C, respectively. Reproduced from Ref. [35]. Copyright 2010, with permission from the American Chemical Society

are clearly observed as well as results for Fig. 16a, showing the formation of n-type Ge core NWs by selective doping of P atoms. Figure 16c and d show the results of B selective doping in the Si shell and Si core, respectively. The B local vibrational peaks and the Fano effect in the Si optical phonon peak are clearly observed, indicating the formation of p-type Si shells and core NWs by the selective doping of B atoms.

Table 2 Fitting parameters (q and Γ) for the Fano line shapes of the Ge optical phonon peak observed for P-doped GeNWs with 532-nm and 633-nm excitation lights

PH_3 (sccm)	q: 532 nm	Γ(cm^{-1}): 532 nm	q: 633 nm	Γ(cm^{-1}): 633 nm
0.1	−22.4	2.1	−16.1	2.2
0.4	−18.7	2.3	−12.6	2.4
0.7	−17.0	2.4	−11.0	2.5
1.4	−13.9	2.5	−7.7	2.8
4.0	−13.7	2.6	−6.7	3.0
7.0	−13.5	2.6	−6.3	3.1

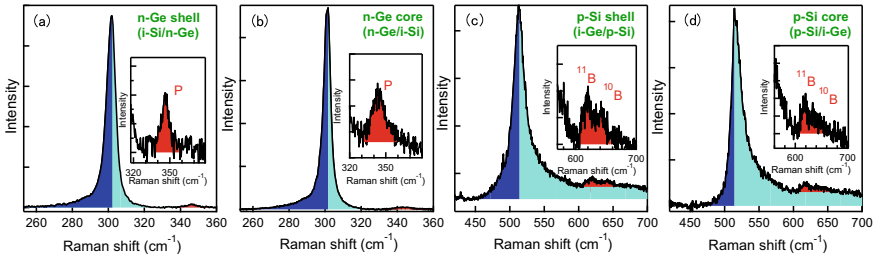

Fig. 16 Raman spectra observed for **a** i-Si/n-Ge, **b** n-Ge/i-Si, **c** i-Ge/p-Si, and **d** p-Si/i-Ge core–shell NWs. Insets are magnifications of the P and B local vibrational modes observed in each type of core–shell NW. Reproduced from Ref. [59]. Copyright 2015, with permission from the American Chemical Society

Impurity scattering can be mitigated by constructing radial core–shell nanowire heterojunction structures using Si and Ge. The sharp interface, band-offset between Si and Ge, and selective doping in the core and shell regions separate the carrier transport region from the impurity doped region, resulting in reduced impurity scattering. This structure can be used to realize high-electron mobility transistors (HEMTs): I term this NW-HEMT. Raman spectroscopy is also a powerful method to demonstrate hole gas accumulation in the i-Ge core NW region in i-Ge/p-Si core–shell NWs. The results are summarized in Fig. 17. The Ge optical phonon peak shows the downshift and asymmetric broadening that results from increasing the B_2H_6 gas flux during the formation of the p-Si shell layers, as shown in Fig. 17a and b. In i-Ge/p-Si core–shell NWs, the Ge optical phonon peak is influenced by three effects: the phonon confinement effect (nanoscale size effect) [16–18], the stress effect due to

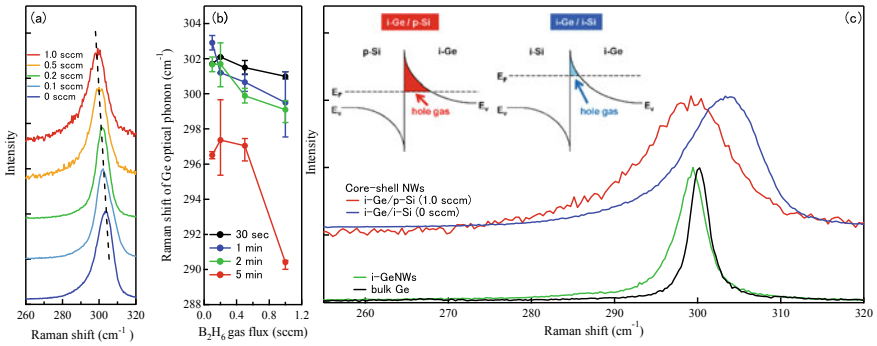

Fig. 17 **a** Ge optical phonon peak observed for i-Ge/p-Si core–shell NWs. **b** Raman shift of the Ge optical phonon peaks as a function of B_2H_6 gas flux. **c** Comparison of the Ge optical phonon peaks observed for i-Ge/p-Si (1.0 sccm) core–shell NWs, i-Ge/i-Si (0 sccm) core–shell NWs, i-GeNWs, and bulk Ge. The B_2H_6 gas fluxes of p-Si layers were varied from 0 to 1.0 sccm. The shell growth time is 2 min. Band diagrams around Si–Ge heterojunctions in Ge/Si core–shell NWs are shown in the inset of (**c**). E_v and E_f are the valence band edge and the Fermi energy, respectively. Reproduced from Ref. [59]. Copyright 2015, with permission from the American Chemical Society.

the heterostructures, and the Fano effect. To be able to demonstrate the creation of hole gases in the undoped regions of the i-Ge core in core–shell NWs, it is necessary to tease apart these three effects. A comparison of the Ge optical phonon peaks observed for i-Ge/p-Si (1.0 sccm) core–shell NWs, i-Ge/i-Si (0 sccm) core–shell NWs, i-GeNWs, and bulk Ge is shown in Fig. 17c. The Ge optical phonon peak for i-GeNWs shows a slight downshift and asymmetric broadening toward lower wavenumbers compared to bulk Ge. This can be explained by the phonon confinement effect because the diameter of GeNWs is about 10 nm [16–18, 35]. By forming the p-Si shell layers on the i-Ge core NWs, the Ge optical phonon peak shows an upshift and asymmetric broadening that is due to the compressive stress applied by the formation of i-Si shell layers because the lattice constant of Ge is larger than that of Si. The asymmetric broadening cannot be explained by the stress effect but is due to the Fano effect caused by the hole gas accumulation. To demonstrate this, the B concentration in p-Si shell layers was increased. The Ge optical phonon peak shows a downshift and further asymmetric broadening with increased B concentration in the Si shell layers, as shown in the spectrum of the i-Ge/p-Si (1.0 sccm) core–shell NWs as shown in Fig. 17c. The downshift and asymmetric broadening are decreased by HF etching of the p-Si layers. The thickness of B-doped p-Si shell layers decreases as a result of HF etching, and the number of holes introduced into the Ge core region is likely to be reduced. These results clearly demonstrate hole gas accumulation in undoped i-Ge layers by forming i-Ge/p-Si core–shell NW structures. By analyzing the Ge optical phonon peaks using the Fano equation (Eq. 2), the hole gas density is estimated to be 10^{17}–10^{18} cm^{-3}. Hole gas accumulation was also recently confirmed in p-Si/i-Ge core–shell NWs [93].

3.2.2 Infrared Spectroscopy

Fourier transform infrared (FT-IR) spectroscopy has often been used to characterize impurity atoms in semiconductor materials. However, it is generally difficult to apply FT-IR spectroscopy to characterize impurity atoms in nanostructures due to the difficulty of preparing sufficiently large samples. To overcome this difficulty, both sample preparation and the development of new characterization techniques are the keys. The laser ablation method can realize a relatively large amount of NW samples [94]. The thickness of the SiNW layers deposited on Si substrates can reach several tens of micrometers [94]. These samples make it possible to characterize nanostructure samples for FT-IR measurements. In addition to sample preparation, IR synchrotron radiation (IR-SR) is potentially a very effective new IR light source. A schematic illustration of a micro-IR synchrotron radiation system is shown in Fig. 18. The focus size of the IR-SR is 10 times smaller, and the light density 100 times greater, than black body light. This allows the optical spectrum, even in microscopic regions, to be measured up to lower frequency regions through the window of a cryostat.

The whole range of IR-SR absorption spectra observed for B-doped and undoped SiNWs is shown in Fig. 19a. The IR-SR absorption peaks were observed at 4.2 K using a continuous-flow liquid helium cryostat with KRS-5 windows. The spectral

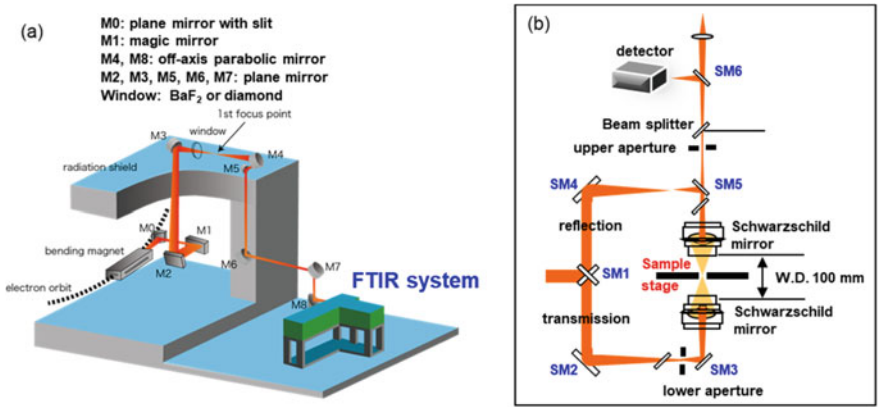

Fig. 18 Schematic illustrations of **a** a micro-FTIR system using the IR synchrotron radiation (IR-SR) beamline at SPring-8 and **b** the optics in the infrared microscope. Reproduced from Ref. [94] by permission of The Royal Society of Chemistry

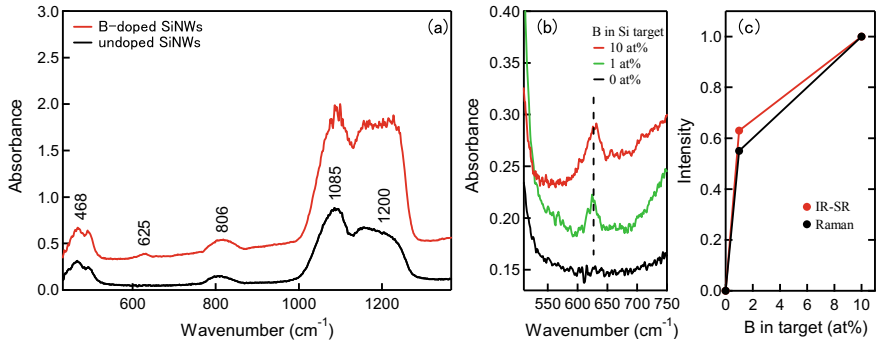

Fig. 19 **a** IR-SR absorption spectra observed for B-doped and undoped SiNWs. **b** Dependence of the B vibrational peak (625 cm^{-1}) observed by IR-SR measurements and ^{11}B local vibrational peak observed by Raman spectroscopy measurements on the content of B in the ablated targets. **c** Dependence of the peak intensity of the B vibrational peak on the content of B in the ablated targets. Reproduced from Ref. [94] by permission of The Royal Society of Chemistry

resolution was about 2 cm^{-1}. SiNWs were synthesized by laser ablation of an Si target with nickel (Ni) and B as the metal catalyst and dopant impurities, respectively. The clear peaks at 468, 806, 1085, and 1200 cm^{-1} are assigned to different oxygen-related vibrational modes [95]. The peaks at 468 and 806 cm^{-1} are due, respectively, to the rocking mode of the O atom about the axis through the two Si atoms and the symmetric stretching mode of the O atom along the line bisecting the axis formed by the two Si atoms. The peaks at 1085 and 1200 cm^{-1} are due to the asymmetrical stretching motion of the O atoms. Figure 19b shows the peak observed at 625 cm^{-1}. The peak intensity increased on raising the B doping concentration in the SiNWs. The result in Fig. 19c shows a good correlation between the intensity of the 625 cm^{-1} peak and

the B local vibrational peak observed by Raman spectroscopy. The ^{11}B and ^{10}B local vibrational peaks have been observed at about 618 and 643 cm^{-1}, respectively [1, 15, 30]. The peak frequency of 625 cm^{-1} is close to that of the B local vibrational peaks observed by Raman spectroscopy measurements, but it shows higher frequencies than those observed by Raman spectroscopy measurements. This shift to higher frequencies in IR-SR measurements can be explained mainly by the temperature effect. The Raman spectroscopy measurements were made at room temperature, while the IR-SR measurements were made at 4.2 K. Based on these results, the newly observed peak at 625 cm^{-1} can be assigned to the B vibrational peak in B-doped SiNWs [94]. Hence, the IR-SR measurements also clarify impurity doping in SiNWs.

Electronic transitions can also be detected by IR-SR measurements. In B-doped bulk Si, discrete electronic transitions of bound holes from the ground state of neutral B acceptor atoms to a series of hydrogen-like excited levels lying below the band edge have already been observed by several researchers [96–100]. The representative peaks, observed at about 278 and 320 cm^{-1}, were assigned to the 1s-2p and 1s-3p transitions of B in bulk Si. The results of IR-SR measurements are shown in Fig. 20a. Two peaks are newly observed at about 278 and 319 cm^{-1}. These peaks are not observed for undoped SiNWs, indicating that these peaks are related to B-doping. The peak frequencies are in good agreement with the 1s-2p and 1s-3p electronic transitions of B in bulk Si. These results show that the peaks newly observed at about 278 and 319 cm^{-1} by IR-SR measurements can be assigned to the 1s-2p and 1s-3p electronic transitions of B in SiNWs. Impurity levels in nanostructures are known to become deeper in decreasing their sizes [101]. The almost identical peak position for SiNWs and bulk Si means no significant change in impurity levels in SiNWs with an average diameter of 20 nm. The average diameter of B-doped SiNWs is about

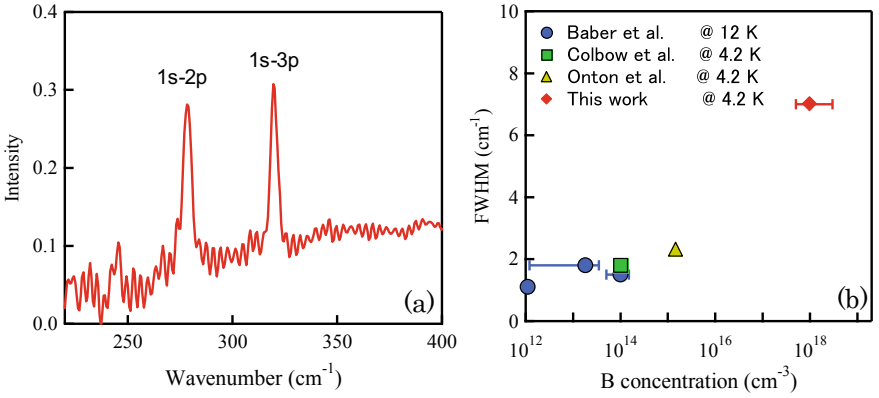

Fig. 20 **a** IR-SR absorption spectra related to the electronic transition of B in SiNWs. **b** Dependence of full width at half maximum (FWHM) on B concentration. Reproduced from Ref. [94] by permission of The Royal Society of Chemistry

20 nm. To observe the impurity level shift in SiNWs, their diameter has to be reduced to below 20 nm.

The electrical active B concentration in SiNWs can be estimated by the Fano effect observed for the Si optical phonon peak. The B concentration is used for the plotted data in Fig. 20b. The data previously reported for bulk Si are also plotted in Fig. 20b. The full width at half maximum of 1s–3p transition of B depends on the B concentration in Si. It is generally difficult to observe the electronic transition peaks for highly doped bulk Si; therefore, Si samples doped at less than 10^{15} cm^{-3} can be used for IR experiments, since IR light cannot penetrate the samples due to their strong absorption. The sample thickness for B-doped SiNWs is several tens of micrometers, which is much thinner than bulk Si samples. The use of thinned samples and a high-brilliance IR-SR beam has made it possible to evaluate the electronic transitions of neutral B acceptor atoms in highly B-doped NW samples: this is the first observation of the electronic transition of neutral B acceptor atoms in highly B-doped Si materials. This result shows that the IR-SR technique is applicable even to the characterization of Si nanostructures.

3.2.3 Other Methods

The electronic structures and chemical bonding of heavily P-doped SiNWs have been investigated by near edge X-ray absorption fine structure spectroscopy (NEXAFS) [102]. Tang et al. observed two sharp P K-edge NEXAFS peaks at around 2145 and 2153 eV. By analyzing the data, they showed that P atoms are present in the Si crystalline core as dopants and in the oxide layer. In the core region, P atoms locate at substitutional tetrahedral sites.

Ultrafast optical microscopy is also an effective method of characterizing NWs. This method makes it possible to detect the charge carrier transport through space and time in single semiconductor NWs without the influence of contacts [103, 104]. These experiments were carried out with undoped SiNWs, but are applicable for doped NWs and will clarify carrier diffusion depending on impurity dopants.

3.3 Spin Analysis

Doping in semiconductor NWs can be analyzed by electron spin resonance (ESR) [1, 32, 33]. This is a sensitive method for investigating P donors or conduction electrons in Si [81, 105, 106]. Typical results for P-doped SiNWs are shown in Fig. 21. ESR measurements were carried out at 4.2 K using an X-band ESR spectrometer with a magnetic field modulation of 100 kHz. P-doped SiNWs were synthesized at 1200 °C in flowing argon (Ar) gas at 50 sccm by catalytic laser ablation of an Si target with Ni_2P compounds: namely, Si_{100-x} $(Ni_2P)_x$, (x = 0.5, 5, and 10) targets. For comparison, an $Si_{99}Ni_1$ target was used for the synthesis of undoped SiNWs. Nickel in Si targets acts as a catalyst for the VLS growth of SiNWs. The ESR signal observed

for P-doped SiNWs is deconvoluted to at least two components, as shown in Fig. 21a. The origin of the ESR signals can be assigned by the signal position, namely the g-factor estimated using the following equation:

$$h\nu = g\beta H. \tag{3}$$

Here, h is the Planck constant, ν is microwave frequency, g is the g-factor, β is the Bohr magneton, and H is the magnetic field. The g-factors of the two components are 1.998 and 2.005–2.006, respectively. The latter component is also observed for undoped SiNWs. A similar ESR signal has also been observed for nanocrystalline Si embedded in SiO_2 [107]. These ESR signals are attributed to interfacial defects between the surface oxide and crystalline Si core region of SiNWs. These defects are termed P_b centers [108–112]. P_b centers are well-known Si dangling-bond-type defects ($Si_3 = Si\cdot$) formed at the Si/SiO_2 interface. The other component with a g-factor of 1.998 corresponds to that of the conduction electrons in Si, indicating that the ESR signal can be attributed to the conduction electrons in the crystalline Si core of the SiNWs and that P atoms were doped in the substitutional sites of the crystalline Si core region during the growth of SiNWs. The ESR linewidth of P donor/conduction electrons closely depends on the P concentration in Si [81, 105, 106]. The ESR linewidth obtained for P-doped SiNWs is plotted in Fig. 21b in addition to data reported for P-doped bulk Si. The electrically active P donor concentration can be roughly estimated by using this relationship. The P concentration in P-doped SiNWs can be roughly estimated to be in the range of 10^{19} cm^{-3} under the assumption that the relationship obtained for bulk Si is also true for SiNWs.

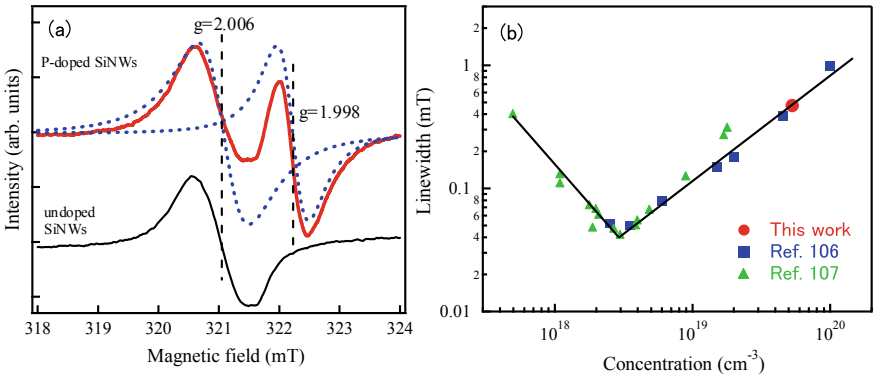

Fig. 21 **a** ESR spectra observed for undoped and P-doped SiNWs synthesized using $Si_{99}Ni_1$ and $Si_{90}(Ni_2P)_{10}$ targets, respectively. The ESR signal for P-doped SiNWs was deconvoluted into two components, shown as blue dotted lines. **b** Dependence of the ESR linewidth of conduction electrons on the P concentration in bulk Si (refs.[105, 106]) and P-doped SiNWs. Reproduced from Ref. [1]. Copyright 2009, with permission from Wiley VCH

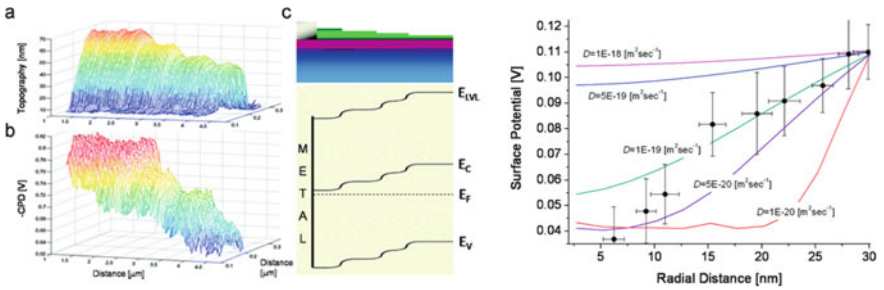

Fig. 22 **a** 3D AFM image showing four steps in topography: each step is ~7 nm. **b** 3D − CPD image showing four steps in − CPD. Each step is ~15 mV. **c** Schematic band diagram of the etched SiNW. **d** Simulated (solid lines) and measured (symbols) surface potential profiles. Simulation was carried out for different doping profiles, each profile was calculated for a different diffusion coefficient. The measured surface potential profile was averaged over three different samples. The results show a relatively good agreement with the calculated doping profile for D ~1 × 10^{-19} m^2s^{-1} (up to a radial distance of ~12 nm). The error bars in the measured profile represent the standard deviation in the KPFM measurement for all the three nanowires. Reproduced from Ref. [115]. Copyright 2010, with permission from the American Chemical Society

3.4 Probe Analysis

Scanning probe methods are also powerful techniques for characterizing doping in semiconductor NWs. Kelvin probe force microscopy (KPFM) has been proposed as a tool for measuring the local contact potential difference between a conducting atomic force microscopy (AFM) tip and a sample [113]. KFPM is a well-established method of determining surface potentials with nanometer spatial resolution [113]. Koren et al. applied the KPFM method to characterizing radial and axial P-dopant distributions in SiNWs [114–116]. The authors clarified that the radial distribution of P dopant atoms is inhomogeneous and that the P concentration decreases by about two orders of magnitude from the NW surface to its core region in as-grown P-doped SiNWs [115]. The results are shown in Fig. 22. The authors also obtained a nonlinear potential drop in the NW growth direction and clarified the nonuniform doping profile for P-doped SiNWs [114]. Axial nonuniformity occurs as a result of the exposure of NW surfaces to dopant gas throughout VLS growth. After these studies, the authors showed a way of obtaining uniform dopant distributions both radially and axially in SiNWs by thermal annealing [116].

3.5 Mass Analysis

Atom probe tomography (APT) is an increasingly important tool in nanoscale characterization. This method can reveal three-dimensional (3D) distributions of atoms in nanostructures with high spatial resolution and high sensitivity. Many studies of

semiconductor NWs have used APT [117–132]. It is especially useful for obtaining 3D profiles of dopant atoms, heterostructures and so on. For example, Perea et al. used APT to measure the P concentration in VLS-grown GeNWs [121]. These GeNWs showed a tapered morphology that is caused by dopant-enriched vapor–solid (VS) deposition layers on the VLS-grown core NWs. The authors confirmed, by the use of APT, that P concentration in the VS shell is higher than that in the VLS core region, as shown in Fig. 23.

By way of another example, the APT analysis of core–shell NWs is described next. Some results have already been reported for Si/Ge and Ge/Si core–shell NWs [122, 130]. Schlitz et al. used APT to measure B concentrations in VLS-grown core-SiNWs with Ge shell layers [122]. The B-doped core-SiNWs showed a tapered morphology caused by VS growth on the VLS-grown core NWs, showing a higher concentration of B at the NW surface as well as P-doped GeNWs. Figure 24 shows a comparison between i-Ge/p-Si and p-Si/i-Ge core–shell NWs. The results clearly show that the i-Ge core is covered with a p-Si shell (Fig. 24a) and that the p-Si core is covered with an i-Ge shell (Fig. 24c). The interfaces of the Si and Ge layers are clear, indicating no significant intermixing of Si and Ge. Shell doping in i-Ge/p-Si core–shell NWs shows that B atoms are randomly distributed in both radial and axial directions, with an almost constant B concentration (Fig. 24a and c). On the other hand, the result for p-Si/i-Ge core–shell NWs shows that B atoms preferentially locate at the surface region of the p-Si core NW. This is due to the same reason as described for P-doped GeNWs [121]. The B incorporation rate via the VS process is much higher than that via the VLS process, as reported previously [132], which causes a gradient in the B concentration in the radial direction. The average B concentration of the p-Si core in the p-Si/i-Ge core–shell NW increased gradually from the top to the bottom of the NW. This is also due to the tapered shape of the Si core caused by the VS process.

Secondary ion mass spectrometry (SIMS) is also used for the estimation of dopant concentration in NWs. Results obtained for B- and P-doped GeNWs are shown in Fig. 25. The GeNWs were grown on a Si substrate at high density to suppress the effects of the Si substrate. To estimate the concentration of dopant atoms, a standard sample has to be prepared for SIMS measurements. Unlike for the characterization of bulk materials, it is difficult to accurately estimate dopant concentrations in NW samples because there are many spaces among NWs, making it difficult to prepare standard samples. In Fig. 25, Ge wafers implanted with B and P were used for the calibration of B and P concentrations in GeNWs, respectively. The depth profiles of B and P show an abrupt decrease from 0.3 and 0.5 μm. Silicon atoms were not detected before the decrease, showing that the depth profiles before the decrease correspond to those in the GeNWs regions. The depth profiles before the decrease were used to estimate the concentration of B and P in the GeNWs. The estimated B and P concentrations are, respectively, about 2–3 $\times$ 10^{20} cm^{-3} for B- and P-doped GeNWs. Raman spectroscopy measurements were also performed to confirm these estimated values. By analyzing Ge optical phonon peaks using the Fano equation (Eq. 2), the concentrations of B and P atoms were estimated to be in the order of 10^{20} cm^{-3}. These values are in good agreement with those obtained by SIMS measurements.

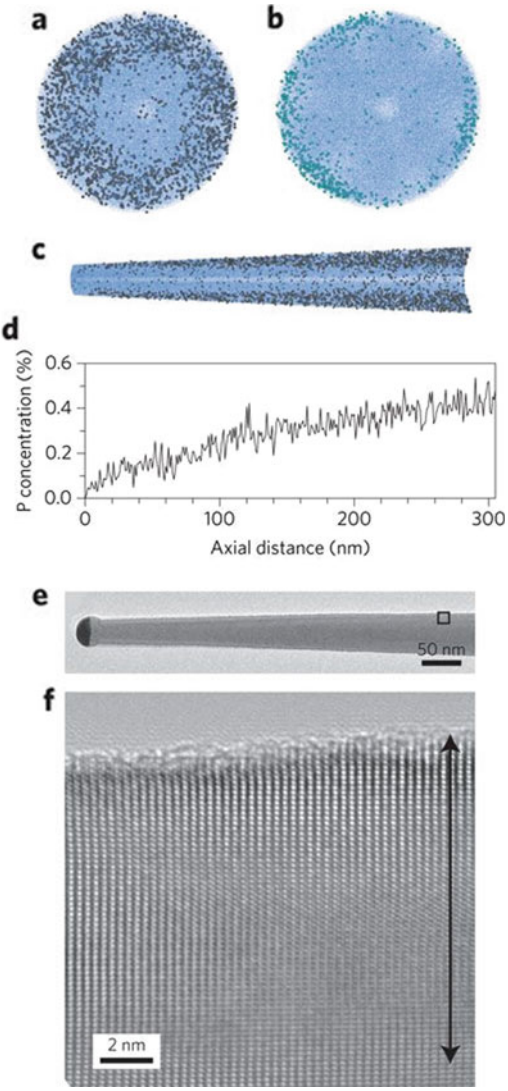

Fig. 23 Distribution of dopant atoms. **a**, **b** End-on view (43 nm in diameter) of nanowire highlighting the distribution of phosphorus (a, gray spheres) and oxygen (b, light blue spheres) in germanium (blue dots). The nanowire was grown under the same conditions as the one shown in 1. **c** Side view of nanowire cross section (2 nm thick) aligned with (**d**). **d** Average phosphorus concentration along the growth axis. **e** Bright-field TEM image of a phosphorus-doped germanium nanowire. **f** High-resolution bright-field TEM image of the phosphorus-doped shell region inside the box in e. The large black arrow (12 nm) illustrates the extent of the phosphorus-doped shell. Scale bar = 2 nm. Reproduced from Ref. [121]. Copyright 2009, with permission from Nature

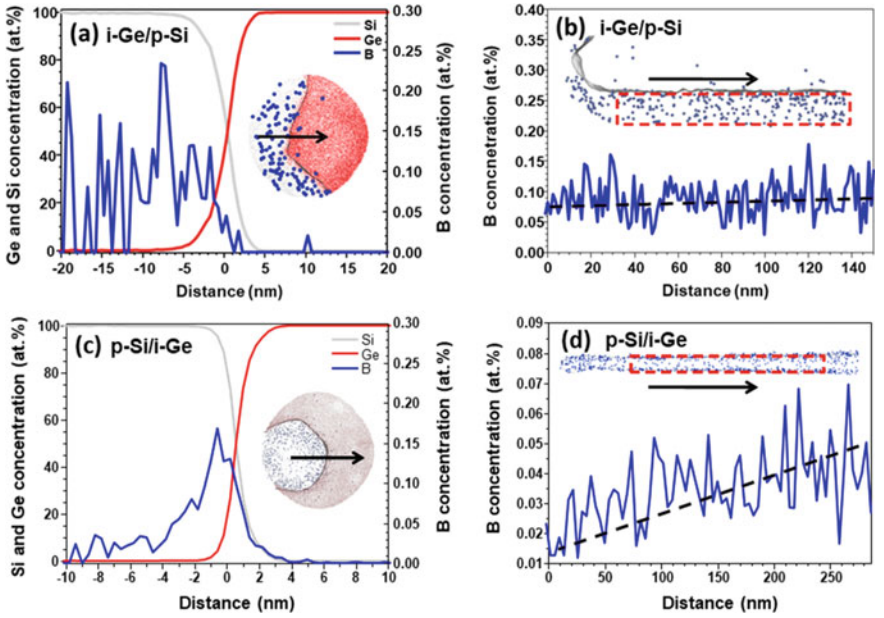

Fig. 24 B concentration along **a** the radial direction and **b** the growth axis of a Ge/Si core–shell NW. The black arrows indicate the directions along which the B concentrations were measured. B concentration along the **c** radial direction and **d** the growth axis of a Si/Ge core–shell NW. The black arrows also indicate the directions along which the B concentrations were measured. "Reprinted from [130] by The Author(s) licensed under CC BY 3.0, published by The Royal Society of Chemistry"

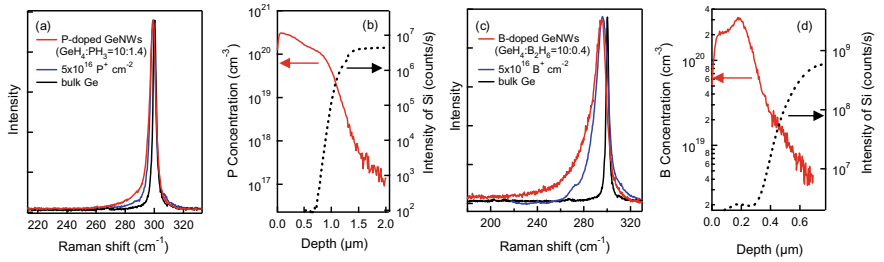

Fig. 25 **a** Raman spectra observed for B-doped GeNWs (GeH_4:B_2H_6 = 10:0.4), bulk Ge implanted with a dose of 5×10^{16} B^+ cm^{-2}, and bulk Ge without B implantation from the top. **b** B concentration profiles of B-doped GeNWs (GeH_4:B_2H_6 = 10:0.4). The Si concentration profile is also shown as a dotted line. **c** Raman spectra observed for P-doped GeNWs (GeH_4:PH_3 = 10:1.4), bulk Ge implanted with a dose of 5×10^{16} P^+ cm^{-2}, and bulk Ge without P implantation from the top. **d** P concentration profiles of P-doped GeNWs (GeH_4:PH_3 = 10:1.4). The Si concentration profile is also shown as a dotted line. Reproduced from Ref. [15]. Copyright 2012, with permission from the American Chemical Society

4 Behaviors of Dopant Atoms

Considering various device fabrication processes, an understanding of the behaviors of dopant atoms in NWs are also important. If NWs are thermally oxidized to form an oxide layer on their surface as an insulator, the segregation behaviors of dopant atoms in NWs during the thermal oxidation process need to be understood. Thermal oxidation thickens the surface oxide layer of nanowires, resulting in a decrease in the diameter of their crystalline core [17, 18, 133]. These SiNWs were synthesized using a laser ablation method. The diameter changes of SiNWs observed by TEM measurements are shown in Fig. 26c. The TEM images clearly show a distinct contrast inside the SiNW. The darker region in the center of the SiNW is the crystalline Si region, while the brighter region of the surrounding layer is an amorphous SiOx ($x \leq 2$) layer. Figure 26a shows the results of ESR measurements of P-doped SiNWs before and after annealing in oxygen, while the results of Ar annealing are shown in Fig. 26b. The ESR signal before oxygen annealing is deconvoluted at least to two components with g-factors of 1.998 and 2.006. As already explained in the section 3.3, the ESR signals with g-factors of 1.998 and 2.006 correspond to the conduction electrons and

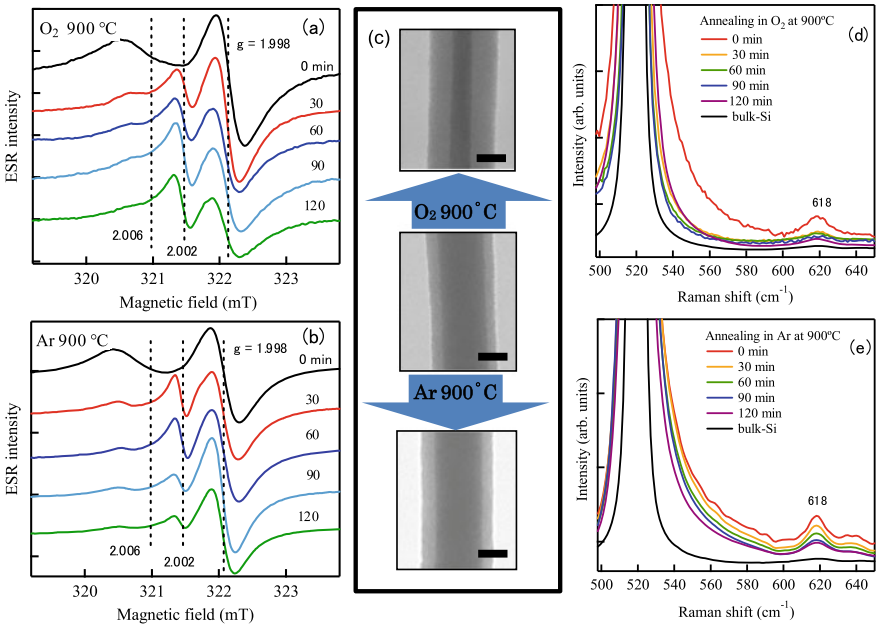

Fig. 26 ESR signals observed at 4.2 K for P-doped SiNWs annealed in **a** O_2 and **b** Ar. TEM images of P-doped SiNWs before and after annealing at 900 ˚C in O_2 and Ar. Annealing time was 120 min in each. The scale bars are 15 nm. Raman spectra observed for B-doped SiNWs annealed in **d** O_2 and **e** Ar. The $Si_{90}(Ni_2P)_{10}$ and $Si_{89}Ni_1B_{10}$ targets were used to synthesize the P- and B-doped SiNWs, respectively. Reproduced from Ref. [133]. Copyright 2011, with permission from the American Chemical Society

interfacial defects called P_b centers, respectively. The intensity of the conduction electron signal gradually decreased on increasing the annealing time in an oxygen atmosphere. This reduction can be explained by the segregation of P atoms from the Si core region to the surface oxide layer during annealing in oxygen. By segregation to surface oxide layers, P atoms lose electrical activity there, resulting in a decrease in the intensity of the conduction electron signal. To confirm the effect of heating at 900 °C, the thermal annealing experiments were also performed in an Ar gas atmosphere. The decrease in the ESR signal of conduction electrons becomes small in an Ar gas atmosphere (Fig. 26b). The TEM image of SiNWs after annealing in an Ar gas atmosphere shows no significant change in the NW structure. These results show that P segregation is caused mainly by thermal oxidation [133]. An ESR signal with a g-factor of 2.002 newly appears on thermal annealing in both oxygen and Ar. This ESR signal is assigned to defects in the surface oxide layer of SiNWs, called *EX* centers [20, 134].

The segregation behaviors of B atoms in SiNWs can be characterized by the asymmetric broadening of the optical phonon peak due to the Fano effect and B local vibrational peaks, which can be observed by Raman spectroscopy. The results are shown in Fig. 26d and e. The Si optical phonon peak for B-doped SiNWs is significantly broader than that for undoped SiNWs. This is due to the Fano effect. This Fano broadening significantly decreases on annealing in an oxygen atmosphere. The intensity of the B local vibrational peak observed at about 618 cm^{-1} also shows the same annealing behavior. This is due to the segregation of B atoms from the crystalline Si core region to the surface amorphous Si oxide layer during thermal oxidation. On the other hand, the Fano broadening and the intensity of the B local vibrational peak slightly decrease if annealing time in an Ar atmosphere is lengthened, indicating that thermal oxidation is the chief cause of the segregation of B atoms as well as in the case of P segregation.

The data on P-doped SiNWs and B-doped SiNWs obtained by ESR and Raman measurements are summarized in Fig. 27, which illustrates the segregation behaviors of dopant atoms in SiNWs. The ESR and Raman data show the dependence of the ESR signal intensity from the conduction electron signal and the peak intensity of the ^{11}B local vibrational mode, respectively, on annealing time in oxygen and Ar gas atmospheres. The results clearly show that B atoms segregate much faster than P atoms in SiNWs. The different segregation behaviors of B and P atoms in SiNWs can be explained in the following way. When a surface of crystalline Si is oxidized, an interface with two different solid phases, Si and SiO, is created. As the thermal oxidation proceeds, the interface advances into the crystalline Si region and redistributes the impurities that were originally contained within the Si. In bulk Si, the segregation behaviors of P and B atoms have already been investigated, showing the segregation coefficients of P and B to be about 10 and 0.3, respectively. As a result of these particular segregation coefficients, B atoms preferentially segregate in SiO_2, while P atoms pile up at the Si surface.[135, 136]. The segregation behaviors of P and B atoms in SiNWs summarized in Fig. 27, show the same pattern as those observed for bulk Si, indicating that the main difference between P and B segregation behaviors in SiNWs can be explained by the difference in their segregation coefficients.

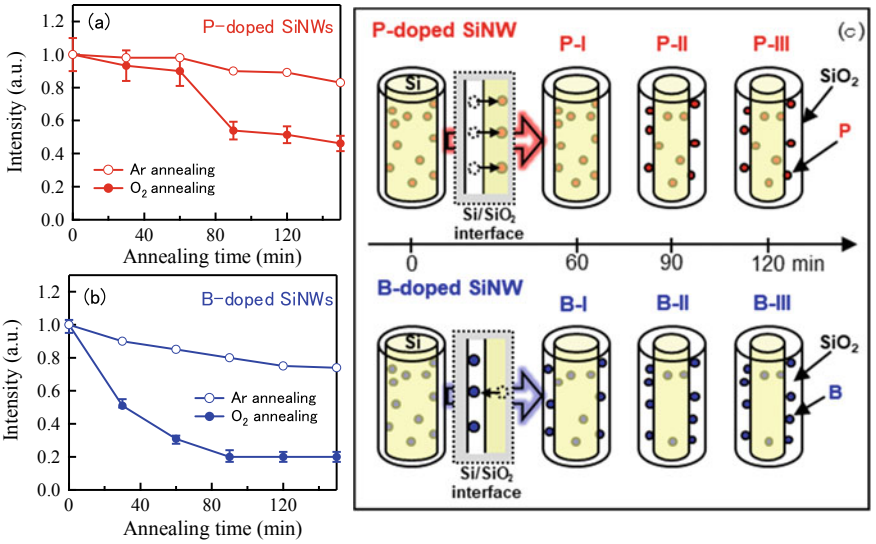

Fig. 27 Dependence of **a** the ESR signal from conduction electrons and **b** the peak intensity of the ^{11}B local vibrational speak on annealing time in O_2 and Ar. **c** Illustration of P and B segregation behaviors in SiNWs due to thermal oxidation. Reproduced from Ref. [133]. Copyright 2011, with permission from the American Chemical Society

The characteristic behaviors of P and B segregation during thermal oxidation are also observed in Fig. 27a and b. This can be attributed to the structural properties of SiNWs and can be explained as illustrated in Fig. 27c. The ESR signal intensity of conduction electrons appears almost constant during the first 60 min of annealing in an oxygen atmosphere (P-I in Fig. 27c); after annealing for 90 min, it then starts to decrease significantly (P-II in Fig. 27c). The former (P-I) clearly shows that P atoms tend to pile up in the crystalline Si region. The decrease in intensity (P-II) is a function of the solubility limit of P. The P concentration exceeds the solubility limit of P in Si with a decrease in the crystalline Si core diameter of SiNWs caused by thermal oxidation, resulting in the out-diffusion of P atoms to the surface oxide layer of SiNWs (P-II). In the surface oxide layer or at the interfaces between the crystal Si core and the surface oxide layer, P atoms are not electrically activated in their sites because these P atoms are not located at substitutional sites of Si atoms. This results in a decrease in ESR signal intensity from conduction electrons.

On the other hand, the rapid decrease in the intensity of the B local vibrational peak indicates the preferential segregation of B into the surface oxide layer (B-I and B-II in Fig. 27c), which can be fully accounted for by the segregation coefficient of B atoms in Si. The segregation of B atoms can also be enhanced by their characteristic diffusion during oxidation. Impurity diffusion is well known to be enhanced under an oxidizing ambient, which is called transient-enhanced diffusion (TED) or oxidation-enhanced diffusion (OED) [137–142]. Boron atoms diffuse in Si crystal predominantly via a kick-out mechanism that involves Si self-interstitials [143]. Silicon self-interstitials

can be generated at the Si/SiO_2 interface during oxidation [137–142, 144]. The Si self-interstitial kicks out the substitutional B atom to an interstitial position in Si crystal where it can easily diffuse. Another explanation has also been reported for the first diffusion of B atoms in Si. If Si self-interstitials and B atoms form pairs, they can be highly mobile pairs and act as high diffusing species [145]. The enhanced diffusion of P atoms in Si under an oxidizing ambient has also been observed, but the effect is much smaller than for B diffusion [138]. The difference in diffusivity between P and B during oxidation is also likely to be a reason for the observed difference in segregation behaviors.

To confirm the aforementioned explanation, it is necessary to eliminate the effect of the difference in diameter of P- and B-doped SiNWs, since the diameter of B-doped SiNWs synthesized by laser ablation is generally smaller than that of P-doped SiNWs. Figure 28 shows the results for thermal oxidation of B- and P-codoped SiNWs. Codoping of B and P atoms into the same SiNWs allows the effect of diameter difference to be completely eliminated. The Raman spectra observed before and after oxidation are shown in Fig. 28a. Asymmetric broadening due to the Fano effect was not observed for codoped SiNWs. This is due to the compensation by P donors. The intensity of B local vibrational peaks was decreased by thermal oxidation, which is due to the segregation of B to the surface oxide layer (Fig. 28a and c). The ESR signal intensity from conduction electrons was not observed for codoped SiNWs (Fig. 28b), due to compensation by B acceptors. After annealing at 900 °C in an oxygen atmosphere, the ESR signal from conduction electrons was observed with decreased intensity of the B local vibrational peaks (Fig. 28b and c). These inverse annealing behaviors of P and B atoms in codoped SiNWs can be explained by their different segregation behaviors as shown in Fig. 28d. These results clearly show that B atoms preferentially segregate in the surface oxide layer, whereas P atoms tend to accumulate in the Si region around the interface of SiNWs by thermal oxidation.

5 Summary and Conclusion

This chapter describes impurity doping in Group IV semiconductor NWs. Impurity doping functionalizes semiconductor NWs and is crucial for their application to metal oxide field-effect transistors, solar cells, sensors, and other devices. There are two chief ways of impurity doping, namely in situ (during growth) and ex situ (after growth) doping. The advantages of in situ doping are the lack of damage and high controllability. In situ doping is performed during the VLS growth of semiconductor NWs. For example, in chemical vapor deposition (CVD), diborane (B_2H_6) gas, and phosphine (PH_3) gas are generally used as p-type and n-type dopant sources, respectively. Ion implantation and thermal diffusion methods are well-known ex situ methods. In the former method, defects are introduced in the implanted region at the same time. The recrystallization process with defect annihilation in implanted regions and the subsequent reactivation and distribution process of dopant impurities need to be understood to enable successful ion implantation. Defect annihilation in NWs

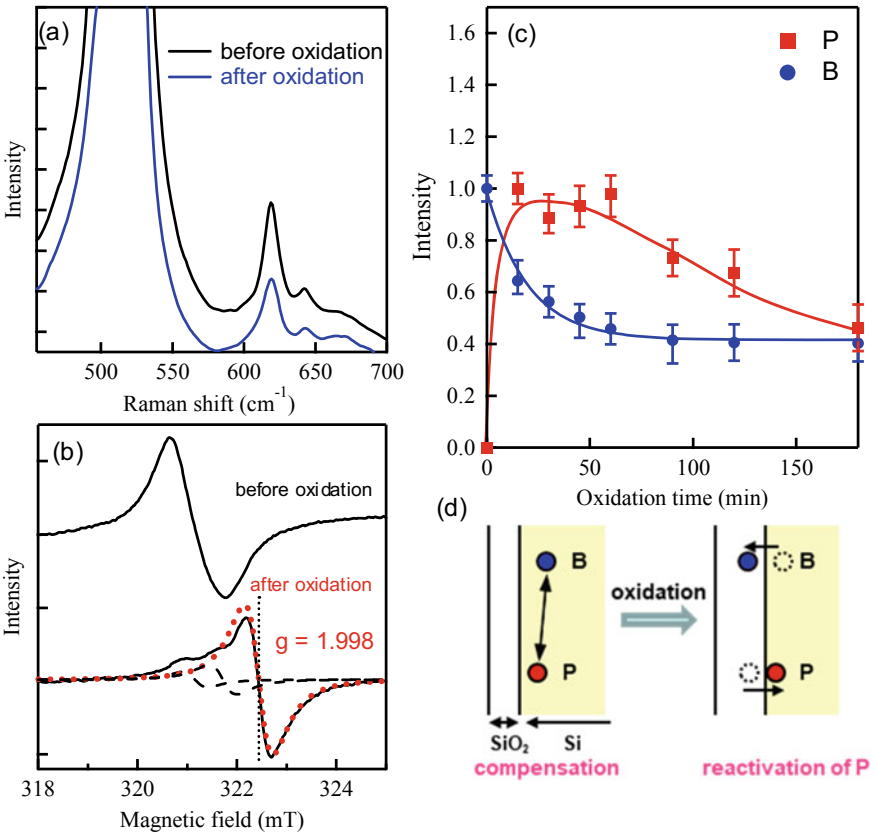

Fig. 28 **a** Thermal oxidation behaviors of the Si optical phonon peak and the B local vibrational peaks observed by Raman scattering measurements and **b** that of the ESR signal observed at 4.2 K for B- and P-codoped SiNWs. Oxidation time was 30 min. **c** Dependence of the peak intensity of the B local vibrational peak and the ESR signal from conduction electrons on thermal oxidation time for B- and P-codoped SiNWs. The $Si_{98}Ni_1B_1$ and $Si_{99}(Ni_2P)_1$ targets were used to synthesize the codoped SiNWs. **d** Illustration of the different segregation behaviors of B and P in SiNWs during thermal oxidation. Reproduced from Ref. [133]. Copyright 2011, with permission from the American Chemical Society

is more difficult than in bulk Si. Ion implantation is more effective at higher temperatures, which reduce defect production and suppress the formation of polycrystals in SiNWs. Unlike with ion implantation, thermal diffusion can introduce dopants without causing damage or significant morphology changes, while its disadvantages are a lack of selectivity of the doping region and the need for a high-temperature process.

Characterization of dopant atoms introduced by impurity doping is important to functionalize NWs and control their properties. In this chapter, various electrical,

optical, and mass spectrometric methods were described based on the results of experiments with NWs. Electrical measurements using individual NW FETs on thermally oxidized Si substrates with low resistivity are extensively used for doping characterization by examining carrier transport properties. However, their electrical properties depend on the device fabrication process because electrical contact with metal electrodes strongly affects them. Unlike with electrical analysis, optical properties do not depend on sample preparation for analyses. Raman spectroscopy and electron spin resonance can identify the states of dopant atoms in NWs, specifically their bonding states and electrical activity. IR spectroscopy can also clarify the bonding states and the electronic transitions of impurity atoms in NWs. Scanning probe methods such as KFPM are also powerful methods of characterizing doping in semiconductor NWs. KFPM is a well-established method of determining surface potentials at nanometer-scale spatial resolution. The radial and axial dopant distributions in NWs can be estimated using this method. Mass spectrometric methods are also used for the characterization of dopant distributions in NWs. Atom probe tomography (APT) is an increasingly important tool for nanoscale characterization. This method can clarify 3D distributions of atoms in nanostructures with high spatial resolution and high sensitivity.

An understanding of the behaviors of dopant atoms in NWs is also important. If NWs are thermally oxidized to form an insulating oxide layer on their surface, the segregation behaviors of dopant atoms in the NWs during the thermal oxidation process need to be understood. The segregation behaviors in SiNWs of B and P atoms are different. In response to thermal oxidation, boron atoms preferentially segregate in the surface oxide layer, whereas P atoms tend to accumulate in the Si region around the SiNW interface.

References

1. N. Fukata, Adv. Mater. **21**, 2829 (2009)
2. Y. Li, F. Qian, C.M. Lieber, Mater. Today **9**, 18 (2006)
3. C. Thelander, P. Agarwal, S. Brongersma, J. Eymery, L.F. Feiner, A. Forchel, M. Scheffler, W. Riess, B.J. Ohlsson, U. Gösele, L. Samuelson, Mater. Today **9**, 28 (2006)
4. P.J. Pauzauskie, P. Yang, Mater. Today **9**, 36 (2006)
5. H.J. Fan, P. Werner, M. Zacharias, Small **2**, 700 (2006)
6. Z.L. Wang, J. Song, Science **312**, 242 (2006)
7. R. Rurali, Rev. Mod. Phys. **82**, 427 (2010)
8. O. Hayden, M.T. Bjork, H. Schmid, H. Riel, U. Drechsler, S.F. Karg, E. Lortscher, W. Riess, Small **3**, 230 (2007)
9. G.M. Cohen, M.J. Rooks, J.O. Chu, S.E. Laux, P.M. Solomon, J.A. Ott, R.J. Miller, W. Haensch, Appl. Phys. Lett. **90**, 233110 (2007)
10. A. Colli, A. Fasoli, C. Ronning, S. Pisana, S. Piscanec, A.C. Ferrari, Nano Lett. **8**, 2188 (2008)
11. S. Hoffmann, J. Bauer, C. Ronning, Th. Stelzner, J. Michler, C. Ballif, V. Sivakov, S.H. Christiansen, Nano Lett. **9**, 1341 (2009)
12. P.D. Kanungo, R. Kögler, K. Nguyen-Duc, N. Zakharov, P. Werner, U. Gösele, Nanotechnology **20**, 165706 (2009)

13. P.D. Kanungo, R. Kögler, P. Werner, U. Gösele, W. Skorupa, Nanoscale Rec. Lett. **5**, 243 (2010)
14. R.S. Wagner, W.C. Ellis, Appl. Phys. Lett. **4**, 89 (1964)
15. N. Fukata, R. Takiguchi, S. Ishida, S. Yokono, S. Hishita, K. Murakami, ACS Nano **6**, 3278 (2012)
16. S. Piscanec, M. Cantoro, A.C. Ferrari, J.A. Zapien, Y. Lifshitz, S.T. Lee, S. Hofmann, J. Robertson, Phys. Rev. B **68**, 241312(R) (2003)
17. N. Fukata, T. Oshima, K. Murakami, T. Kizuka, T. Tsurui, S. Ito, Appl. Phys. Lett. **86**, 213112 (2005)
18. N. Fukata, T. Oshima, N. Okada, T. Kizuka, T. Tsurui, S. Ito, K. Murakami, J. Appl. Phys. **100**, 024311 (2006)
19. F.F. Morehead, B.L. Crowder, R.S. Title, J. Appl. Phys. **43**, 1112 (1972)
20. A. Baumer, M. Stutzmann, M.S. Brandt, F.C.K. Au, S.T. Lee, Appl. Phys. Lett. **85**, 943 (2004)
21. D.L. Griscom, Phys. Rev. B **22**, 4192 (1980)
22. R.E. Beckman, E. Johnston-Halperin, N.A. Melosh, Y. Luo, J.E. Green, J.R. Heath, J. Appl. Phys. **96**, 5921 (2004)
23. S. Ingole, P. Aella, P. Manandhar, S.B. Chikkannanavar, E.A. Akhadov, D.J. Smith, S.T. Picraux, J. Appl. Phys. **103**, 104302 (2008)
24. O. Hazut, B.C. Huang, A. Pantzer, I. Amit, Y. Rosenwaks, A. Kohn, C.S. Chang, Y.P. Chiu, R. Yerushalmi, ACS Nano **8**, 8357 (2014)
25. Y. Cui, X. Duan, J. Hu, C.M. Lieber, J. Phys. Chem. B **104**, 5213 (2000)
26. Y. Cui, C.M. Lieber, Science **291**, 851 (2001)
27. D.D.D. Ma, C.S. Lee, S.T. Lee, Appl. Phys. Lett. **79**, 2468 (2001)
28. K.K. Lew, L. Pan, T.E. Bogart, S.M. Dilts, E.C. Dickey, J.M. Redwing, Y. Wang, M. Cabassi, T.S. Mayer, S.W. Novak, Appl. Phys. Lett. **85**, 3101 (2004)
29. L. Pan, K.K. Lew, J.M. Redwing, E.C. Dickey, J. Crystal Growth **277**, 428 (2005)
30. N. Fukata, J. Chen, T. Sekiguchi, N. Okada, K. Murakami, T. Tsurui, S. Ito, Appl. Phys. Lett. **89**, 203109 (2006)
31. Y. Wang, K.K. Lew, T.T. Ho, L. Pan, S.W. Novak, E.C. Dickey, J.M. Redwing, T.S. Mayer, Nano Lett. **5**, 2139 (2005)
32. N. Fukata, J. Chen, T. Sekiguchi, S. Matsushita, N. Oshima, N. Uchida, K. Murakami, T. Tsurui, S. Ito, Appl. Phys. Lett. **90**, 153117 (2007)
33. N. Fukata, M. Mitome, Y. Bando, M. Seoka, S. Matsushita, K. Murakami, J. Chen, T. Sekiguchi, Appl. Phys. Lett. **93**, 203106 (2008)
34. E. Tutuc, S. Guha, J.O. Chu, Appl. Phys. Lett. **88**, 043113 (2006)
35. N. Fukata, K. Sato, M. Mitome, Y. Bando, T. Sekiguchi, M. Kirkham, J.I. Hong, Z.L. Wang, R.L. Snyder, ACS NANO, **4**, 3807 (2010)
36. Y. Cui, L.J. Lauhon, M.S. Gudiksen, J. Wang, C.M. Lieber, Appl. Phys. Lett. **78**, 2214 (2001)
37. Y. Wu, Y. Cui, L. Huynh, C.J. Barrelet, D.C. Bell, C.M. Lieber, Nano Lett. **4**, 433 (2004)
38. D.D.D. Ma, C.S. Lee, F.C.K. Au, S.Y. Tong, S.T. Lee, Science **299**, 2003 (1874)
39. C. Yang, Z. Zhong, C.M. Lieber, Science **310**, 1304 (2005)
40. C.M. Eichfeld, C. Wood, B. Liu, S.M. Eichfeld, J.M. Redwing, S.E. Mohney, Nano Lett **7**, 2642 (2007)
41. A.I. Hochbaum, P. Yang, Chem. Rev. **110**, 527 (2010)
42. K.Q. Peng, S.T. Lee, Adv. Mater. **23**, 198 (2011)
43. J. Li, H. Yu, Y. Li, Nanoscale **3**, 4888 (2011)
44. K. Peng, Y. Xu, Y. Wu, Y. Yan, S.T. Lee, J. Zhu, Small **1**, 1062 (2005)
45. Z. Huang, N. Geyer, P. Werner, J. de Boor, U. Gösele, Adv. Mater. **23**, 285 (2011)
46. M. Dutta, N. Fukata, Nano Energy **11**, 219 (2015)
47. M. Dutta, N. Fukata, J. Nanosci. Nanotech. **15**, 4339 (2015)
48. M. Dutta, L. Thirugnanam, P.M. Trinh, N. Fukata, ACS Nano **9**, 6891 (2015)
49. W. Jevasuwan, K. Nakajima, Y. Sugimoto, N. Fukata, Jpn J. Appl. Phys. **55**, 065001 (2016)
50. W. Jevasuwan, K.C. Pradel, T. Subramani, J. Chen, T. Takei, K. Nakajima, Y. Sugimoto, N. Fukata, Jpn. J. Appl. Phys. **56**, 04CP01, (2017)

51. W. Jevasuwan, J. Chen, T. Subramani, K.C. Pradel, T. Takei, K. Dai, K. Shinotsuka, Y. Hatta, N. Fukata, Jpn. J. Appl. Phys. **56**, 085201 (2017)
52. L.J. Lauhon, M.S. Gudiksen, D. Wang, C.M. Lieber, Nature **420**, 57 (2002)
53. J. Xiang, W. Lu, Y. Hu, Y. Wu, H. Yan, C.M. Lieber, Nature **441**, 489 (2006)
54. G. Liang, J. Xiang, N. Kharche, G. Klimeck, C.M. Lieber, M. Lundstrom, Nano Lett. **7**, 642 (2007)
55. J.-S. Park, B. Ryu, C.-Y. Moon, K.J. Chang, Nano Lett. **10**, 116 (2010)
56. L. Li, D.J. Smith, E. Dailey, P. Madras, J. Drucker, M.R. Mccartney, Nano Lett. **11**, 493 (2011)
57. Y. Zhao, J.T. Smith, J. Appenzeller, C. Yang, Nano Lett. **11**, 1406 (2011)
58. N. Fukata, M. Mitome, T. Sekiguchi, Y. Bando, M. Kirkham, J.-I. Hong, Z.L. Wang, R. Snyder, ACS Nano **6**, 8887 (2012)
59. N. Fukata, M. Yu, W. Jevasuwan, T. Takei, Y. Bando, W. Wu, Z.L. Wang, ACS NANO **9**, 12182 (2015)
60. B.-M. Nguyen, Y. Taur, S.T. Picraux, S.A. Dayeh, Nano Lett. **14**, 585 (2014)
61. T. Mimura, S. Hiyamizu, T. Fujii, K. Nanbu, Jpn. J. Appl. Phys. **19**, L225 (1980)
62. C.S. Guo, L.B. Luo, G.D. Yuan, X.B. Yang, R.Q. Zhang, W.J. Zhang, S.T. Lee, Angew. Chem. Int. Ed. **48**, 9896 (2009)
63. V.Y. Timoshenko, T. Dittrich, V. Lysenko, M.G. Lisachenko, F. Koch, Phys. Rev. B **64**, 085314 (2001)
64. L. Boarino, F. Geobaldo, S. Borini, A.M. Rossi, P. Rivolo, M. Rocchia, E. Garrone, G. Amato, Phys. Rev. B **64**, 205308 (2001)
65. M. Chiesa, G. Amato, L. Boarino, E. Garrone, F. Geobaldo, E. Giamello, Angew. Chem., Int. Ed. **42**, 5032 (2003)
66. Z. Gaburro, C.J. Oton, L. Pavesi, L. Pancheri, Appl. Phys. Lett. **84**, 4388 (2004)
67. E. Garrone, F. Geobaldo, P. Rivolo, G. Amato, L. Boarino, M. Chiesa, E. Giamello, R. Gobetto, P. Ugliengo, A. Viale, Adv. Mater. **17**, 528–531 (2005)
68. A. Miranda-Duran, X. Cartoixa, M.C. Irisson, R. Rurali, Nano Lett. **10**, 3590 (2010)
69. G.D. Yuan, Y.B. Zhou, C.S. Guo, W.J. Zhang, Y.B. Tang, Y.Q. Li, Z.H. Chen, Z.B. He, X.J. Zhang, P.F. Wang, I. Bello, R.Q. Zhang, C.S. Lee, S.T. Lee, ACS NANO **4**, 3045 (2010)
70. C.P. Herrero, M. Stutzmann, Phys. Rev. B **38**, 12668 (1988)
71. U. Fano, Phys. Rev. **124**, 1866 (1961)
72. J.I. Pankove, D.E. Carlson, J.E. Berkeyheiser, R.O. Wance, Phys. Rev. Lett. **51**, 2224 (1983)
73. K.J. Chang, D.J. Chadi, Phys. Rev. Lett. **60**, 1422 (1988)
74. M. Stavola, K. Bergman, S.J. Pearton, L. Lopata, Phys. Rev. Lett. **61**, 2786 (1988)
75. P.J.H. Denteneer, C.G. Van de Walle, S.T. Pantelides, Phys. Rev. B **39**, 10809 (1989)
76. M. Suezawa, N. Fukata, M. Saito, H. Yamada-Kaneta, Phys. Rev. B **65**, 075214 (2002)
77. N. Fukata, S. Fukuda, S. Sato, K. Ishioka, M. Kitajima, T. Hishita, K. Murakami, Phys. Rev. B **72**, 245209 (2005)
78. N.M. Johnson, C. Herring, D.J. Chadi, Phys. Rev. Lett. **56**, 769 (1986)
79. C.H. Seager, R.A. Anderson, D.K. Brice, J. Appl. Phys. **68**, 2268 (1990)
80. K. Murakami, H. Suhara, S. Fujita, K. Masuda, Phys. Rev. B **44**, 3409 (1991)
81. N. Fukata, S. Sasaki, S. Fujimura, H. Haneda, K. Murakami, Jpn. J. Appl. Phys. **35**, 3937 (1996)
82. J. Kikuchi, S. Fujimura, M. Suzuki, H. Yano, Jpn. J. Appl. Phys. **32**, 3120 (1993)
83. H. Adhikari, A.F. Marshall, C.D.E. Chidsey, P.C. Mclntyre, Nano Lett. **6**, 318 (2006)
84. C.B. Jin, J.E. Yang, M.H. Jo, Appl. Phys. Lett. **88**, 193105 (2006)
85. H. Jagannathan, M. Deal, Y. Nishi, J. Woodruff, C. Chidsey, P.C. Mclntyre, J. Appl. Phys. **100**, 024318 (2006)
86. A.B. Greytak, L.J. Lauhon, M.S. Gudliksen, C.M. Lieber, Appl. Phys. Lett. **84**, 4176 (2004)
87. T. Hanrath, B.A. Korgel, Nano Lett. **4**, 1455 (2004)
88. E. Tutuc, J. Appenzeller, M.C. Reuter, S. Guha, Nano Lett. **6**, 2070 (2006)
89. E. Tutuc, J.O. Chu, J.A. Ott, S. Guha, Appl. Phys. Lett. **89**, 263101 (2006)
90. J.H. Woodruff, J.B. Ratchford, I.A. Goldthorpe, P.C. Mclntyre, C.E.D. Chidsey, Nano Lett. **7**, 1637 (2007)

91. N. Fukata, Phys. Stat. Solid. C **11**, 320 (2014)
92. D. Olego, M. Cardona, Phys. Rev. B **23**, 6592 (1981)
93. X. Zhang, W. Jevasuwan, K.C. Pradel, T. Subramani, T. Takei, N. Fukata, Nanoscale **10**, 21062 (2018)
94. N. Fukata, W. Jevasuwan, Y. Ikemoto, T. Moriwaki, Nanoscale **7**, 7246 (2015)
95. C.T. Kirk, Phys. Rev. B Condens. Mater. **38**, 1255 (1988)
96. E. Burstein, G. Picus, B. Henvis, R. Wallis, J. Phys. Chem. Solids **1**, 65 (1956)
97. H.J. Hrostowski, R.H.J. Kaiser, J. Phys. Chem. Solids **4**, 148 (1958)
98. B. Pajot, J. Phys. Chem. Solids **25**, 613 (1964)
99. B.O. Kolbesen, Appl. Phys. Lett. **27**, 353 (1975)
100. S.C. Baber, Thin Solid Films **72**, 201 (1980)
101. T.-L. Chan, M.L. Tiago, E. Kaxiras, J.R. Chelikowsky, Nano Lett. **8**, 596 (2008)
102. Y.H. Tang, T.K. Sham, A. Jürgensen, Y.F. Hu, C.S. Lee, S.T. Lee, Appl. Phys. Lett. **80**, 3709 (2002)
103. M.A. Seo, S.A. Dayeh, P.C. Upadhya, J. Martinez, B.S. Swartzentruber, S.T. Picraux, A.J. Taylor, R.P. Prasankumar, Appl. Phys. Lett. **100**, 071104 (2012)
104. M.A. Seo, J. Yoo, S.A. Dayeh, S.T. Picraux, A.J. Taylor, R.P. Prasankumar, Nano Lett. **12**, 6334 (2012)
105. S. Maekawa, N. Kinoshita, J. Phys. Soc. Jpn. **20**, 1447 (1965)
106. J.D. Quirt, J.R. Marko, Phys. Rev. B **5**, 1716 (1972)
107. N. Fukata, C. Li, H. Morihiro, K. Murakami, M. Mitome, Y. Bando, Appl. Phys. A **84**, 395 (2006)
108. Y. Nishi, Jpn. J. Appl. Phys. **10**, 52 (1972)
109. E.H. Poindexter, P.J. Caplan, B.E. Deal, R. Razouk, J. Appl. Phys. **52**, 879 (1981)
110. A. Stesmans, J. Braet, J. Witters, R.F. Dekeersmaecker, Surf. Sci. **141**, 255 (1984)
111. K.L. Brower, Semicond. Sci. Technol. **4**, 970 (1989)
112. J.L. Cantin, M. Schoisswohl, H.J. von Bardeleben, N.H. Zoubir, M. Vergnat, Phys. Rev. B **52**, R11599 (1995)
113. M. Nonnenmacher, M.P. O'Boyle, H.K. Wickramasinghe, Appl. Phys. Lett. **58**, 2921 (1991)
114. E. Koren, Y. Rosenwaks, J.E. Allen, E.R. Hemesath, L.J. Lauhon, Appl. Phys. Lett. **95**, 092105 (2009)
115. E. Koren, N. Berkovitch, Y. Rosenwaks, Nano Lett. **10**, 1163 (2010)
116. E. Koren, J.K. Hyun, U. Givan, E.R. Hemesath, L.J. Lauhon, Y. Rosenwaks, Nano Lett. **11**, 183 (2011)
117. D.E. Perea, J.E. Allen, S.J. May, B.W. Wessels, D.N. Seidman, L.J. Lauhon, Nano Lett. **6**, 181 (2006)
118. D.E. Perea, J.L. Lensch, S.J. May, B.W. Wessels, L.J. Lauhon, Appl. Phys. A **85**, 271 (2006)
119. J.E. Allen, E.R. Hemesath, D.E. Perea, J.L. Lensch-Falk, Z.Y. Li, F. Yin, M.H. Gass, P. Wang, A.L. Bleloch, R.E. Palmer, L.J. Lincoln, Nat. Nanotechnol. **3**, 168 (2008)
120. T. Xu, J.P. Nys, B. Grandidier, D. Stievenard, Y. Coffinier, R. Boukherroub, R. Larde, E. Cadel, P. Pareige, J. Vac. Sci. Technol. B **26**, 1960 (2008)
121. D.E. Perea, E.R. Hemesath, E.J. Schwalbach, J.L. Lensch-Falk, P.W. Voorhees, L.J. Lauhon, Nature Nanotech. **4**, 315 (2009)
122. R.A. Schlitz, D.E. Perea, J.L. Lensch-Falk, E.R. Hemesath, L.J. Lauhon, Appl. Phys. Lett. **95**, 162101 (2009)
123. S. Zhang, E.R. Hemesath, D.E. Perea, E. Wijaya, J.L. Lensch-Falk, L.J. Lauhon, Nano Lett. **9**, 3268 (2009)
124. J.G. Connell, K.H. Yoon, D.E. Perea, E.J. Schwalbach, P.W. Voorhees, L.J. Lauhon, Nano Lett. **12**, 199 (2012)
125. J.R. Riley, R.A. Bernal, Q. Li, H.D. Espinosa, G.T. Wang, L.J. Lauhon, ACS Nano **6**, 3898 (2012)
126. O. Moutanabbir, D. Isheim, H. Blumtritt, S. Senz, E. Pippel, D. Seidman, Nature **496**, 78 (2013)

127. N. Jeon, B. Loitsch, S. Morkoetter, G. Abstreiter, J. Finley, H.J. Krenner, G. Koblumueller, L.J. Lauhon, ACS Nano **9**, 8335 (2015)
128. Z. Gan, D.E. Perea, J. Yoo, Y. He, R.J. Colby, J.E. Barker, M. Gu, S.X. Mao, C. Wang, S.T. Picraux, D.J. Smith, M.R. Mccartney, J. Appl. Phys. **120**, 104301 (2016)
129. Z. Sun, O. Hazut, B.-C. Huang, Y.-P. Chiu, C.-S. Chang, R. Yerushalmi, L.J. Lauhon, D.N. Seidman, Nano Lett. **16**, 4490 (2016)
130. B. Han, Y. Shimizu, J. Wipakorn, K. Nishibe, Y. Tu, K. Inoue, N. Fukata, Y. Nagai, Nanoscale **8**, 19811 (2016)
131. S. Assali, A. Dijkstra, A. Li, S. Koelling, M.A. Verheijen, L. Gagliano, N. von den Driesch, D. Buca, P.M. Koenraad, J.E.M. Haverkort, E.P.A.M. Bakkers, Nano Lett. **17**, 1538 (2017)
132. W. Chen, V.G. Dubrovskii, X. Liu, T. Xu, R. Lardé, J. Philippe Nys, B. Grandidier, D. Stiévenard, G. Patriarche, P. Pareige, J. Appl. Phys. **111**, 094909 (2012)
133. N. Fukata, S. Ishida, S. Yokono, R. Takiguchi, J. Chen, T. Sekiguchi, K. Murakami, Nano Lett. **11**, 651 (2011)
134. R.P. Wang, Appl. Phys. Lett. **88**, 142104 (2006)
135. K. Sakamoto, K. Nishi, F. Ichikawa, F. Ushio, J. Appl. Phys. **61**, 1553 (1987)
136. A.S. Grove, O. Leistiko, C.T. Sah, J. Appl. Phys. **35**, 2695 (1964)
137. G. Masetti, S. Solmi, G. Soncini, Philos. Mag. **33**, 613 (1976)
138. S.M. Hu, J. Appl. Phys. **45**, 1567 (1974)
139. S. Matsumoto, Y. Ishikawa, T. Niimi, J. Appl. Phys. **54**, 5049 (1983)
140. H.J. Gossmann, C.S. Rafferty, H.S. Luftman, F.C. Unterwald, T. Boone, J.M. Poate, Appl. Phys. Lett. **63**, 639 (1993)
141. P.A. Stolk, H.J. Gossmann, D.J. Eaglesham, J.M. Poate, Nucl. Instrum. Methods Phys. Res. B **96**, 187 (1995)
142. S.C. Jain, W. Schoenmaker, R. Lindsay, P.A. Stolk, S. Decouter, M. Willander, H.E. Maes, J. Appl. Phys. **91**, 8919 (2002)
143. P.M. Fahey, P.B. Griffin, J.D. Plummer, Rev. Mod. Phys. **61**, 289 (1989)
144. H. Kageshima, M. Uematsu, K. Akagi, S. Tsuneyuki, T. Akiyama, K. Shiraishi, Jpn. J. Appl. Phys. **43**, 8223 (2004)
145. B. Sadigh, T.J. Lenosky, S.K. Theiss, M.J. Caturla, T.D. de la Rubia, M.A. Foad, Phys. Rev. Lett. **83**, 4341 (1999)

Characterization

X-ray Methods for Structural Characterization of III-V Nanowires: From an *ex-situ* Ensemble Average to Time-resolved Nano-diffraction

Ludwig Feigl and Philipp Schroth

Abstract Understanding and controlling the highly dynamical self-catalyzed vapor–liquid–solid growth of GaAs nanowires remains being a challenge. In order to gain deeper insight into these processes, our approach is the analysis by *in-situ* synchrotron X-ray diffraction during MBE-growth. This allows recording time-resolved information about crystal structure and shape of the nanowires. Within this chapter, we give a detailed overview of how this goal can be achieved. Starting from crucial basics about the crystal structure of GaAs nanowires and the signal obtained by X-ray diffraction, we describe how an asymmetric three-dimensional mapping of the reciprocal space is possible using a fixed angle of incidence—a geometry that is highly advantageous for time-resolved in-situ characterization. Additionally, the experimental setup is introduced and accompanying challenges are discussed. Applying the described methods, we were able to directly observe and distinguish several different effects during the growth of GaAs nanowires as well as of (In,Ga)As core-shell heterostructures. Firstly, an increasing transition probability from wurtzite to zinc-blende is observed during the course of growth, which is converted into the corresponding energy difference of the nucleation barriers of both phases. Secondly, analyzing the shape of the nanowires during growth, the evolution of the Ga-droplet on top of the nanowire was derived and the contributions of facet growth and tapering to the total radial growth were distinguished. Additionally, the effect of interfacial strain during the epitaxial growth of an (In,Ga)As shell layer around GaAs nanowires is monitored by X-ray diffraction and described by applying basic model representations. Finally, most recent results on nanowire arrays grown on Si substrates patterned by electron beam lithography are discussed.

L. Feigl (✉) · P. Schroth
Institute for Photon Science and Synchrotron Radiation (IPS), Karlsruhe Institute of Technology Campus North, Hermann-von-Helmholtz-Platz 1, 76344 Eggenstein-Leopoldshafen, Germany
e-mail: ludwig.feigl@kit.edu

P. Schroth
e-mail: philipp.schroth@kit.edu

P. Schroth
Solid State Physics, Department of Physics, University of Siegen, Walter-Flex Straße 3, 57068 Siegen, Germany

© Springer Nature Singapore Pte Ltd. 2021

N. Fukata and R. Rurali (eds.), *Fundamental Properties of Semiconductor Nanowires*,
https://doi.org/10.1007/978-981-15-9050-4_4

Keywords III–V Semiconductor;Nanowire · Polytypism · GaAs · (In,Ga)As · Si · Self-catalyzed · Epitaxial growth · Molecular beam epitaxy · Tapering · Diameter · Wurtzite; Zinc-blende · Core-shell · Bending · Interfacial strain · *in-situ* XRD · Synchrotron radiation · Vapor–liquid–solid · X-ray diffraction · Nano-beam · Nano-focus · Selective area growth

1 Introduction

1.1 Motivation

1.1.1 Applications of Semiconductor Nanowires

Semiconductor nanowires are in continuous focus of intense research due to their highly promising potential to cause a breakthrough in current microtechnology [1–5]. Their small contact area with the supporting substrate is in the range of a few tens of nanometers, which on the one hand allows fabrication of very small structures with a high density and on the other hand also allows the combination of materials with very dissimilar lattice parameters. Additionally, their high aspect ratio with a length of several micrometers creates a very large surface area. Depending on the field of application, different properties are of importance, as will be discussed in detail below.

Firstly, the long-sought epitaxial integration of III–V semiconductor materials on Si becomes possible by the growth of III–V nanowires, because the large lattice mismatch ($f = -4.1\,\%$ in case of GaAs on Si) is released elastically—without the introduction of misfit dislocations—due to the small footprint of the nanowires. This integration enables the fabrication of a high density of nano-sized structures for high-speed transistors [6–10], on-chip electro-optical conversion for low heat dissipation computing, LEDs, or integrated LASERs [11–17]. Secondly, structures of vertical nanowires exhibit a strongly enhanced light absorption, resulting from the large absorption cross section caused by their small diameter and from the reduced reflection caused by their geometrical arrangement, which makes them highly suitable for solar cells [18–22]. On top of that, nanowires are also investigated as components for quantum computing [23–25], thermoelectrics [26] and sensors [27–29].

The properties of such nanowire devices are determined by their microstructural properties. These comprise crystal phase, strain, stacking faults, misfit dislocations, impurities, point defects, or other deformations. In most cases, the crystal structure should be as perfect as possible, with only a minimum of the mentioned defects. Such high demands on the microstructure require a very high degree of control during the fabrication of the nanowires. In order to achieve this, a thorough understanding of the complex processes during their self-organized growth is a must.

1.1.2 X-Ray Diffraction as Versatile Non-destructive Probe

X-ray diffraction (XRD) is able to probe the crystal structure and their distortions caused by lattice mismatch, composition, or defects, as well as the outer shape of nanostructures. These properties make XRD a highly suitable tool to characterize structural properties of crystalline nanostructures such as nanowires. Additionally, using X-rays as a probe offers several further advantages, which provides XRD an essential role within the pool of complementary investigation methods.

Firstly, it is a scalable approach. For laboratory-based X-ray diffractometers, the size of the X-ray beam spot is in the order of millimeters. In this way, a large ensemble of nanowires can be probed to provide statistical information regarding their structural properties. The sample doesn't need any special preparation and the nanowires can be investigated in the as-grown state, i.e., still standing on substrate. Additionally, due to the possibility of focusing highly brilliant and coherent synchrotron radiation, the size of the X-ray beam spot can be continuously varied all the way down to a few nanometers. This simultaneously reduces the number of illuminated nanowires, until only a single nanowire is probed which could even be scanned with the X-ray beam.

Furthermore, X-rays are non-destructive and not affected by harsh environmental conditions of the sample, such as different gases, ultra-high-vacuum (UHV) or a high temperature. This allows applying them for *in-situ* studies in order to monitor processes while they are happening under realistic conditions, instead of creating artificial environments for investigations or resorting to post-growth *ex-situ* studies.

In order to effectively analyze III–V semiconductor nanowires by XRD, it is necessary to be familiar with the particular crystal structure of the material system as well as with the effect of crystal structure and outer shape of nanostructures on the diffraction pattern. Therefore, a brief introduction to these topics is given in the following sections. In particular, we are focusing on the III–V compound GaAs as the material system used for nanowire growth.

1.2 GaAs Crystal Structure

In this section (reprinted from Ref. [30] with the author's permission), we will describe the crystalline structure of GaAs nanowires, their epitaxial relation to the Si(111) substrate, and the polytypism between wurtzite and zinc-blende. This polytypism, the coexistence of different crystal phases in the same nanowire, is not exclusive for GaAs nanowires, but has also been observed for nanowires grown by other III–V materials, e.g., InAs [31, 32], GaP [33], or InP [34]. GaAs nanowires grow along the [111]–direction, which in our case is the same principle direction as the substrate-orientation. Ideally, the wires grow free-standing and vertical to the substrate surface and are truncated by (110)-type facets in case of Ga-catalyzed GaAs nanowires, or (112)-type facets if Gold is chosen as a catalyst material instead (see Ref. [35], and references therein).

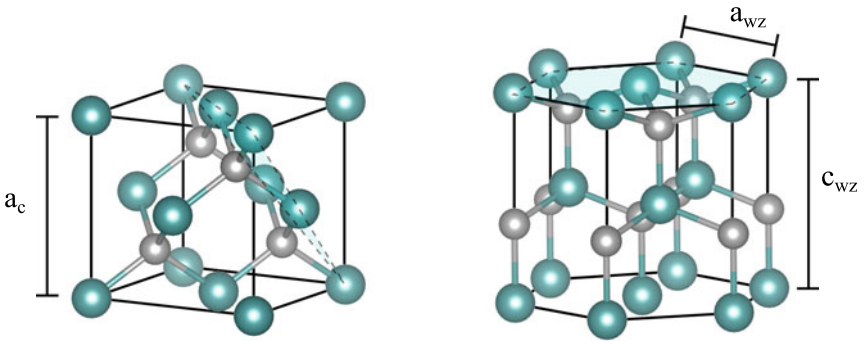

(a) Zinc-blende unit cell composed of As atoms at the corners, and Ga atoms. An atomic layer of As atoms perpendicular to the $[111]_c$ direction is depicted.

(b) Wurtzite structure of GaAs. An atomic layer of As atoms perpendicular to $[111]_c = [00.2]_{h,wz}$ is depicted.

Fig. 1 Zinc-blende and wurtzite structures of GaAs. Image reprinted from Ref. [30] with the author's permission

The stable crystalline phase of bulk GaAs and bulk Si crystals at ambient conditions is the cubic zinc-blende and the cubic diamond structure, respectively. For both structures, the atoms within the cubic unit cell can be found at positions defined by two superposed face-centered cubic (fcc) unit cells with lattice parameter a_c shifted by $(1/4, 1/4, 1/4)\ a_c$. Whereas for Si in the diamond structure, the positions $(0, 0, 0)\ a_c$ and $(1/4, 1/4, 1/4)\ a_c$ are both occupied by Si atoms, they are occupied only by As or Ga ions in case of the zinc-blende structure.

A cubic zinc-blende crystal such as GaAs can be decomposed into hexagonal close-packed atomic sub-layers stacked in a certain sequence along the [111]-direction. These sub-layers are perpendicular to the [111]-direction and contain either only Ga or only As atoms, for which the atomic species is alternating for each neighboring layer. For illustration, these atomic sub-layers are depicted within the unit cells of cubic and hexagonal GaAs in Fig. 1. For the following discussion, we will refer to a "layer" to be composed by two neighboring atomic sub-layers of Ga and As atoms, so that the stacking of the GaAs nanowire can be described as a periodic repetition of a certain stacking sequence of these (bi-atomic) GaAs layers along the [111]-direction.

Polytypism in GaAs nanowires refers to the observation of extended segments with cubic (zinc-blende) or hexagonal (wurtzite) stacking of the GaAs layers—even within the same wire. For a cubic zinc-blende crystal the stacking along $[111]_c$ can be described as a periodic repetition of three layers 'ABC' as depicted in Fig. 2a. Since the growth on nanowires occurs in a layer-by-layer mode, stacking faults are the most often observed defect structure causing an interruption of the 'ABCABCABC'-type sequence of zinc-blende. The crystal structure of the zinc-blende twin corresponds

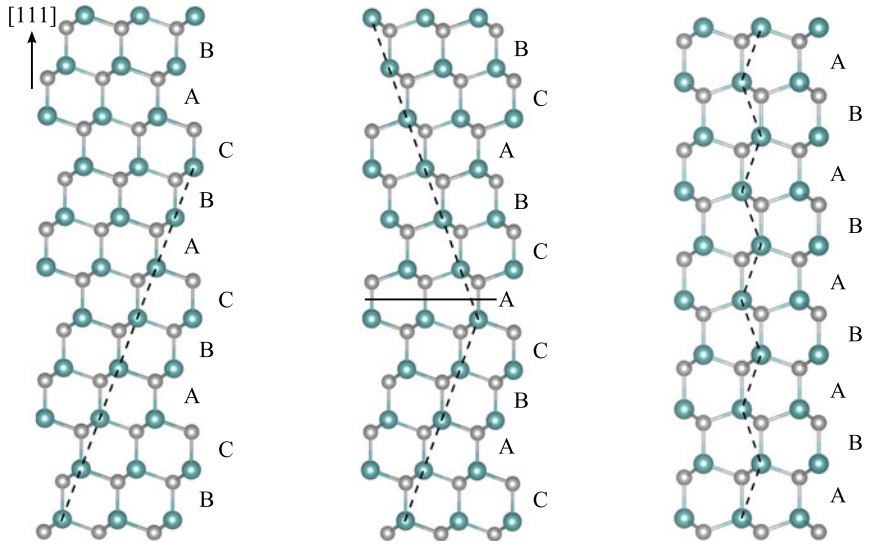

(a) zinc-blende stacking

(b) mixed zinc-blende and twinned zinc-blende stacking

(c) wurtzite stacking

Fig. 2 Stacking sequences of atomic bi-layers along the $[111]_c$ direction viewed along $[10\bar{1}]_c$. The zinc-blende stacking is a periodic repetition of the '...ABC...' sequence. The twinned zinc-blende structure is described by an inversion of this sequence into '...CBA...'. The twin-boundary is marked by a horizontal line. The wurtzite stacking is a sequence of alternating layers, e.g., '...ABAB...' that can be created by successive nucleation of twin-boundaries. Image reprinted from [30] with the author's permission

to a 180° rotation of the non-twinned structure around the $[111]_c$-growth axis, which causes an inversion of the 'ABCABC'-type stacking sequence to 'CBACBA'-type one. Therefore, a stacking fault in the layer sequence needs to be generated, the twin-boundary, e.g., 'ABCA|CBACBA' where the twin-boundary is indicated by the vertical line (compare also Fig. 2b). This single stacking fault generates a local 'ABA'- type (or like 'BCB', or 'CAC') layer sequence. Atoms arranged in a stacking sequence of two alternating layers '...ABABABA...' are hexagonally close-packed (hcp) and constitute the wurtzite poltytype of GaAs. Consequently, repeated twin-boundaries cause formation of extended segments of wurtzite (as shown in Fig. 1b and Fig. 2c).

In analogy to Refs. [36, 37], we now introduce a surface coordinate system that accounts for the hexagonal symmetry of the (111)-planes in which the cubic $[111]_c$ direction corresponds to the $[00.2]_{h,wz}$ direction of wurtzite. The hexagonal basis for zinc-blende structures and for wurtzite structures are given by the following convention.

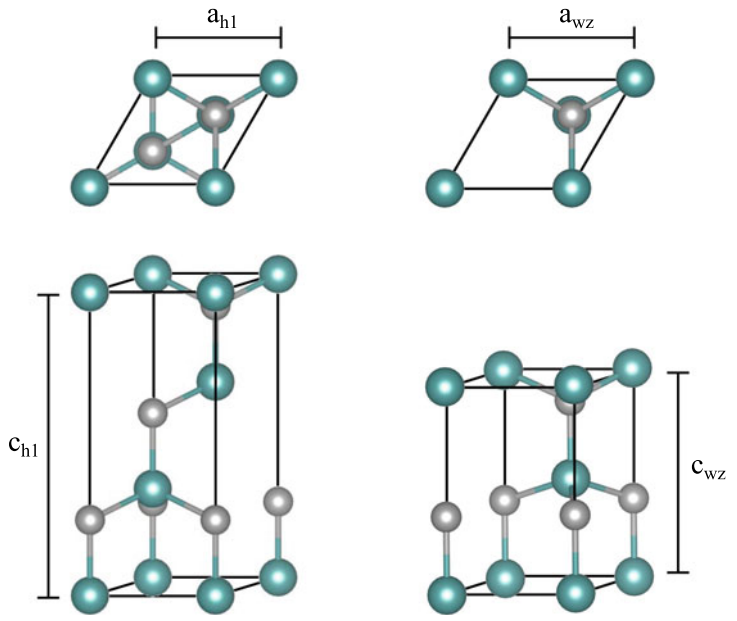

(a) zinc-blende unit cell in hexagonal basis

(b) wurtzite unit cell in hexagonal basis

Fig. 3 Unit cell of zinc-blende (**a**) and wurtzite (**b**) in hexagonal basis. On top, the unit cells are displayed with view along the [111]-direction. The lattice constants $a_{h,zb} = a_{wz} = a_c/\sqrt{2}$, and $c_{h,zb} = \sqrt{6}a_{h,zb} = \sqrt{3}a_c$. The c-lattice constant for wurtzite is $c_{wz} = a_{wz}\sqrt{\frac{8}{3}}(1 + \frac{d_{wz}}{d_{zb}})$. Image reprinted from Ref. [30] with the author's permission

Where a_c is the lattice constant of the cubic lattice, $a_{wz} = a_c/\sqrt{2}$ is the lattice constant for the hexagonal lattice. The ratio of the layer-distance between wurtzite and zinc-blende GaAs in $[111]_c$ direction is d_{wz}/d_{zb}. The distance d_{hkl} between two crystallographic planes can be calculated by

$$d_{[hkl]_c} = \frac{a_c}{\sqrt{h^2 + k^2 + l^2}}; \quad \text{and } d_{[hkl]_{h,wz}} = \frac{a_{wz}}{\sqrt{\frac{4}{3}(h^2 + k^2 + hk) + \left(\frac{a_{wz}}{c_{wz}}\right)^2 l^2}} \tag{1}$$

for the cubic and hexagonal structure, respectively, [36–39].

For illustration, we depict the unit cells for the GaAs zinc-blende and wurtzite structure in the hexagonal basis in Fig. 3.

Another important difference between wurtzite and zinc-blende GaAs is a slight variation in the vertical spacing of the atomic layers in $[111]_c$ direction. However, different values for the ratio $(d_{wz} - d_{zb})/d_{zb}$ have been reported in literature which span a wide range: In 1992, Yeh et al. [40] predict the ratio to be -1.3%, whereas 2011 Panse et al. [41] obtain a value of 0.55%. In experimental reports, the values

range from 0.52% to 1.49% ([35, 36, 42–45]). Interestingly, values reported for bulk GaAs (0.554%) by McMahon and Nelmes [44] are close to the theoretical values from Panse et al. [41] (0.55%). For wurtzite in GaAs nanowires only one the value obtained by Tchernycheva et al. [42] is with 0.52% close to these reports. All other values for wurtzite in GaAs nanowires are larger than for bulk GaAs: 0.62% [35], 0.65% [46], 0.7% [36], and 1.49% [43].

In this section, we described the geometrical properties of the two polytypes zinc-blende and wurtzite GaAs. In the following, we will briefly discuss the occurrence of polytypism in GaAs nanowires from a thermodynamic and a kinetic point of view, analogous to [47].

Usually III–V materials in bulk adopt the cubic zinc-blende crystal structure. An exception are nitrides, e.g., GaN which exhibit the hexagonal wurtzite structure in their bulk form. In case of GaAs the reported differences in the cohesive binding energies between wurtzite and zinc-blende are about $\delta E = E_{wz} - E_{zb} = 24\,\mathrm{meV/pair}$ [40] which makes zinc-blende the energetically favorable structure. This difference for GaN, $\delta E = -36.8\,\mathrm{meV/pair}$ is negative [40] and consequently GaN should obtain the hexagonal wurtzite structure. However, for $[111]_c$ oriented nanowires with hexagonal cross section, wurtzite phase has been observed for various III–V materials (e.g., GaAs [32, 48, 49], InAs [32, 49–51], InP [49] and GaP [49]).

Early explanations for the existence of wurtzite in III–V nanowires were based on the lower surface energies of the side-wall facets of wurtzite nanowires caused by the lower number of dangling bonds as compared to the facets of zinc-blende. Depending in the nanowires' composition (i.e., the inonicity of the III–V compound), Akiyama et al. [52] estimate a critical radius ranging from 1–22 nm for which wurtzite nanowires are energetically preferred. Moreover the authors report on an intermediate regime ranging from 12 to 32 nm for which both polytypes, zinc-blende as well as wurtzite can coexist in the same structure. Similarly, Magri and Rosini [53, 54] find a critical diameter for the wurtzite-zinc-blende transition in GaAs nanowire of 6.3 3 nm below which the cost to create a solid wurtzite volume is overcompensated by the gain in surface energy of the respective wurtzite facets. However, these values are too small to explain experimental observations of polytypism in GaAs nanowires with diameters up to 285 nm [36].

Consequently, solely thermodynamic considerations might be insufficient for a description of the wurtzite-zinc-blende polytypism. Therefore, we now consider polytypism by kinetic aspects of nanowire growth.

For GaAs nanowires, wurtzite segments are often observed at the very bottom of the wire close to the substrate, and at the tip, just below the droplet [35, 36]. Accordingly, these segments were formed at the beginning and at the end of growth. As observed for self-catalyzed GaAs nanowires by Rieger et al. [55] wurtzite controllably formed during the consumption of the liquid Ga-droplet. This means that the growth parameters such as the substrate temperature or the V/III ratio and therefore the supersaturation and the shape of the catalyst are important parameters for describing and understanding polytypism. Consequently, a kinetic approach to polytypism which is able to describe the above observations needs to take into account

important values like the supersaturation [56], the shape of the droplet [57] and the geometry of the nucleation site [58] (and thereby the surface energies of the involved facets [59]) defining the energy barrier E for creating critical nucleus [47].

1.3 X-Ray Diffraction of GaAs Nanostructures

Here, we give a brief introduction to scattering from surface nanostructures such as nanowires (NWs). In the following description (based on previously published material Ref. [30]) we restrict to elastic scattering. Since nanowires are comparably small (several μm in length and 10 to few 100 100 nm in diameter), we discuss scattering within the kinematic approximation (1. order Born approximation). Thereby, we neglect multiple scattering which has to be considered in case of large, defect-free crystals or X-ray experiments under grazing incidence conditions [60, 61]. As typical sample-detector distances R are in the range of meters and the size of our inspected sample r is in the range of several μm we consider to be in the far-field limit, $r \ll R$ so that the Fraunhofer approximation is valid. The size of the X-ray beam is sufficiently large, to illuminate a large number N_{NW} of nanostructures. We consider the coherence volume of the X-ray beam to be sufficient for complete coherent illumination of a single nanostructure, but to be smaller than the size of the X-ray beam.

For elastic scattering processes, energy is conserved: $|\mathbf{k}_i| = |\mathbf{k}_f| = \frac{2\pi}{\lambda}$ and the scattering vector writes $\mathbf{q} = \mathbf{k}_f - \mathbf{k}_i$. Here, λ is the wavelength, and $\mathbf{k}_{i,f}$ are the wavevectors of incident and outgoing waves. With the above assumptions, the amplitude of the scattering amplitude is given by [61]

$$S(\mathbf{q}) \propto \int \rho(\mathbf{r}) e^{i\mathbf{q}\mathbf{r}} d\mathbf{r} \tag{2}$$

and is proportional to the Fourier transform of the electron density $\rho(\mathbf{r})$ of the nanostructure. For an infinite, defect-free crystal, $S(\mathbf{q})$ is zero (within the 1. order Born approximation) unless the scattering vector is equal to a reciprocal lattice vector $\mathbf{G}_{hkl}$, with $\mathbf{G}_{hkl} \cdot \mathbf{r} = 2\pi m$, $m \in \mathbb{Z}$. The diffraction condition $\mathbf{q} = \mathbf{G}_{hkl}$ is equivalent to Bragg's law.

For X-rays the location of the scattering center $\mathbf{r}$ is given by the location of the electrons in the solid crystal (the X-ray photons also interact with the atomic cores, however to a much lesser extent, which we will therefore neglect). For crystals with finite size composed of N_{uc} unit cells, the integral 2 reduces to a sum over all electron contributions contained therein. For a certain scattering center, $\mathbf{r}$ can then be expressed by the location of the unit cell in the crystal $\mathbf{r}_{uc}$, the location of an atom in the unit cell $\mathbf{r}_\alpha$, and the electron-distribution around this atom $\mathbf{r'}_\alpha$ as

$$\mathbf{r} = \mathbf{r}_{uc} + \mathbf{r}_\alpha + \mathbf{r'}_\alpha \tag{3}$$

and

$$S(\mathbf{q}) \propto \sum_{N_{\text{cell}}} e^{i\mathbf{q}\mathbf{r}_{uc}} \sum_{\alpha} \left(\int \rho(\mathbf{r'}_{\alpha}) e^{i\mathbf{q}\mathbf{r'}_{\alpha}} d\mathbf{r'}_{\alpha} \right) e^{i\mathbf{q}\mathbf{r}_{\alpha}} = \sum_{N_{\text{cell}}} e^{i\mathbf{q}\mathbf{r}_{uc}} \sum_{\alpha} f_{\alpha}(\mathbf{q}) e^{i\mathbf{q}\mathbf{r}_{\alpha}}. \quad (4)$$

Here, $f_{\alpha}(\mathbf{q})$ is the atomic form factor. We write the structure factor

$$F_{hkl}(\mathbf{q}) = \sum_{\alpha} f_{\alpha}(\mathbf{q}) e^{i\mathbf{q}\mathbf{r}_{\alpha}} \quad (5)$$

and the geometrical factor

$$L(\mathbf{r}_{uc}) = \sum_{N_{\text{cell}}} e^{i\mathbf{q}\mathbf{r}_{uc}}. \quad (6)$$

The structure factor $F_{hkl}(\mathbf{q})$ expresses the strength of a Bragg reflection, and the geometrical factor $L(\mathbf{r}_{uc})$ defines possible locations of allowed Bragg reflections in the reciprocal space.

Following [36, 37], we will now derive the scattering from a single nanostructure, e.g., a single nanowire for a symmetric Bragg reflection $\mathbf{Q}_B$. Accounting for the finite size and the shape of the nanowire, we introduce the shape function $\Omega(\mathbf{r})$ which is unity inside the nanowire, and zero elsewhere. We split the nanowire into N_l bi-atomic layers consisting of Ga and As atoms perpendicular to the $[111]_{\text{c}}$ growth direction. The electron density of a nanowire writes then

$$\rho(\mathbf{r})_{NW} = \sum_{l}^{N_l} \Omega_l(\mathbf{r}_{||}) \sum_{\alpha \in \{Ga,As\}} \rho_{l\alpha}(\mathbf{r}_{||}, z_{l\alpha}). \quad (7)$$

$\Omega_l(\mathbf{r}_{||})$ corresponds to the cross section of the wire in the $(111)_{\text{c}}$-plane and is defined by the diameter of the nanowire at layer l. The electron density of a single atomic sub-layer $l\alpha$ at height $z_{l\alpha}$ is $\rho_{l\alpha}$. The height $z_{l\alpha}$ depends on the atomic species and can be expressed as

$$z_{l\alpha} = z_l + \delta z_{\alpha} = \sum_{l=0}^{l-1} d_l + \delta z_{\alpha}, \quad (8)$$

where z_l is the beginning of bi-layer l and δz_{α} is a vertical shift of the sub-layer, depending on the atomic species. For Ga-atoms $\delta z_{\alpha} = 3/4 d_l$, whereas $\delta z_{\alpha} = 0$ for As atoms. d_l is the thickness of layer l and depends on the local polytype

$$3/4\ d_l = \begin{cases} 1/4\ c_{h1} & \text{for zinc} - \text{blende} \\ 3/8\ c_{wz} & \text{for wurtzite.} \end{cases} \quad (9)$$

We now restrict to q_z-profiles ($\mathbf{q}_{||} = 0$) in the close vicinity of a symmetric reflection $\mathbf{Q}_B$ and consequently approximate the atomic form factor with its value at the

Bragg reflection $f_\alpha(\mathbf{q}) \approx f_\alpha(\mathbf{Q}_B)$. The scattering amplitude of a single nanowire then only depends on q_z

$$S_{NW}(\mathbf{q}) = S_{NW}(\mathbf{q}_{||} = 0, q_z) \propto \sum_{l}^{N_l} \tilde{\Omega}_l(\mathbf{q}_{||} = 0, q_z)\, e^{-iq_z z_l} \sum_{\alpha \in \{Ga,As\}} f_\alpha(\mathbf{Q}_B)\, e^{-iq_z \delta z_\alpha} \tag{10}$$

with the two-dimensional Fourier transform of the shape function $\tilde{\Omega}_l$. Here, we assume constant diameter over the whole length, therefore the shape function is layer independent and becomes a constant pre-factor. If the NW exhibit tapering however (non-constant diameter over the NW length), the shape function is not layer independent.

Finally we sum up all N_{NW} illuminated nanowires incoherently and obtain the intensity distribution along q_z in the vicinity of a symmetric Bragg reflection $\mathbf{Q}_B$

$$I(q_z) \propto \sum_{N_{NW}} |S_{NW}(q_z)|^2. \tag{11}$$

As we can see from Eq. 5, the magnitude of the structure factor depends on the relative atomic positions in the respective unit cell. In Sect. 1.2 we have discussed the geometric differences between the GaAs polytypes zinc-blende, twinned-zinc-blende and wurtzite. Due to their different symmetry, the structure factors of wurtzite and zinc-blende GaAs differ. Here we approximate the atomic form factors by their atomic number and give the structure factor of a certain cubic reflection $(h, k, l)_c$ for cubic zinc-blende GaAs F^c_{hkl}:

$$F_{(hkl)_c} = (1 + e^{i\pi(h+k)} + e^{i\pi(h+l)} + e^{i\pi(k+l)}) \cdot (f_{As} + f_{Ga}\, e^{i\frac{\pi}{2}(h+k+l)}) \tag{12}$$

$$F_{(hkl)_c} = 4 \cdot \begin{cases} f_{As} + f_{Ga} \text{ if } h,k,l \text{ even and } h+k+l = 4n;\, n \in \mathbb{Z} \\ f_{As} - f_{Ga} \text{ if } h,k,l \text{ even and } h+k+l \neq 4n;\, n \in \mathbb{Z} \\ f_{As} \pm i f_{Ga} \text{ if } h,k,l \text{ odd} \\ 0 \text{ else} \end{cases} \tag{13}$$

and the structure factor of a wurtzite reflection $(hk.l)_{h,wz}$ for hexagonal wurtzite GaAs $F^{h,wz}_{hk.l}$

$$F_{(hk.l)_{h,wz}} = (f_{As} \cdot (1 + e^{-2\pi i(\frac{h+2k}{3} + \frac{1}{2}l)}) + f_{Ga} \cdot (e^{-2\pi i(\frac{3}{8}l)} + e^{-2\pi i(\frac{h+2k}{3} + \frac{7}{8}l)}). \tag{14}$$

If we restrict to symmetric reflections, $(00.l)_{h,wz}$, Eq. 14 becomes

$$F_{(00.l)_{h,wz}} = \begin{cases} 2 \cdot (f_{As} + f_{Ga}\, e^{-i\frac{3}{4}\pi l}) \text{ if } l \text{ even} \\ 0 \text{ else.} \end{cases} \tag{15}$$

The structure factors of zinc-blende and wurtzite allow us to calculate the strength and the position in reciprocal space of Bragg reflections suitable for studying polytypism in GaAs nanowires. Further discussions and detailed lists of allowed $(h, k, l)_c$ and $(hk.l)_{h,wz}$ reflections can be found in [36, 37].

1.4 X-Ray Diffraction Geometry for in-situ 3D reciprocal space mapping

This section is based on previously published material (Refs. [30] and [62]).

X-ray structure analysis [61, 63] is sensitive to the atomic structure of crystalline materials and nanostructures. By evaluating the X-ray diffraction intensity patterns, crystal symmetry, atomic arrangements, size, faceting, chemical, and strain distribution of the nano-objects as well as the statistical structure correlation properties, e.g., of surface and interface roughness can be determined. Consequently, the structural properties of crystalline nanostructures can be reconstructed by evaluating the 3-dimensional distribution of the scattered intensity in reciprocal space in the vicinity of suitable Bragg reflections.

The scattered intensity can be expressed as function of the scattering vector **Q**, whereas the components of the scattering vector are given by [61]

$$Q_x = K(\cos\alpha_f \sin\theta_f + \cos\alpha_i \sin\theta_i) \tag{16}$$

$$Q_y = -K(\cos\alpha_f \cos\theta_f - \cos\alpha_i \cos\theta_i) \tag{17}$$

$$Q_z = K(\sin\alpha_f + \sin\alpha_i). \tag{18}$$

The in-plane component of **Q** is given by $Q_{||} = \sqrt{Q_x^2 + Q_y^2}$.

Modern epitaxial semiconductor nanostructures are complex 3-dimensional nano-objects, which, according to their morphology, produce composite reciprocal space intensity patterns, and their extremely small size (and coherent scattering volume) creates a number of challenges for X-ray studies.

X-ray diffraction (XRD) is sensitive to the atomic lattice and displacement fields therein via the scalar product of the displacement and diffraction vectors and thus insensitive to the components of the displacement vector perpendicular to the diffraction vector. Therefore, a set of non-collinear reflections is required to reconstruct the orthogonal and lateral strain components. In standard *coplanar Bragg diffraction* geometry (the surface normal being in the plane of scattering) the variety of accessible reflections is limited to the so-called Bragg-geometry ($\alpha_{i,f} > 0°$, see Fig. 4).

Moreover—in case of *in-situ* experiments, the accessible range for the out-of-plane angles α_i and α_f may be bound by the experimental setup and limit the accessible Bragg reflections in coplanar geometry further. For the symmetric case, the Bragg planes are parallel to the surface and $\alpha_i = \alpha_f$ and are equal to the Bragg angle Θ_B if the Bragg condition is fulfilled. For symmetric reflections with $Q_{\|} = 0\,\text{Å}^{-1}$,

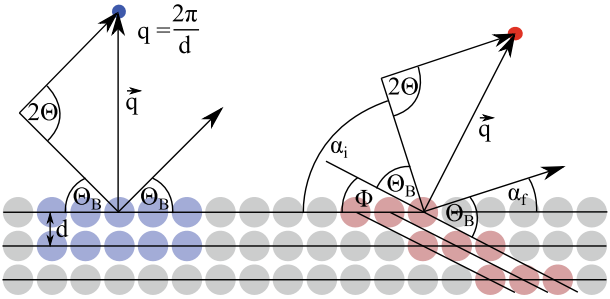

Fig. 4 Illustration of symmetric and asymmetric coplanar scattering geometry. In asymmetric coplanar geometry, the inclination angle Φ of the Bragg planes toward the surface additionally increase or decrease incidence angle $\alpha_i = \Theta_B \pm \Phi$ or outgoing angle $\alpha_f = \Theta_B \mp \Phi$. Image reprinted from Ref. [30] with the author's permission

signals of wurtzite and zinc-blende GaAs can only be distinguished by the small difference in their vertical lattice constants. Since zinc-blende and its twin have the same lattice constants, they cannot be distinguished in a symmetric reflection.

If we however consider asymmetric reflections in coplanar geometry we additionally have to account for the inclination angle Φ of the Bragg planes toward the surface (and thereby increasing or decreasing incidence angle $\alpha_i = \Theta_B \pm \Phi$ or outgoing angle $\alpha_f = \Theta_B \mp \Phi$). For the asymmetric case ($Q_\parallel \neq 0\,\text{Å}^{-1}$), polytype *specific* reflections are located at different, well-separated positions in reciprocal space which allows obtaining information on each polytype (including twinned zinc-blende) separately.

For [001] zinc-blende semiconductor systems, for instance, the most popular coplanar reflections belong to the span of symmetric (004) and asymmetric (224) reflections [64–68]. Whereas (within the range of commonly used X-ray energies) polar Bragg reflections of the {111} series are out of reach in coplanar geometry, but—if accessible—would allow to be material sensitive in case of ternary systems such as InAs/GaAs compounds.

In general, the available reflections measured in non-grazing geometries are characterized by high information depth Z_{inf}, which, according to the expression

$$\frac{1}{Z_{\text{inf}}} = \frac{1}{Z_{\text{inc}}} + \frac{1}{Z_{\text{scatt}}},$$

depends on the values of the absorption depths of the incident (Z_{inc}) and scattered (Z_{scatt}) beams. Z_{inf} reaches the value of tens of microns in the case of coplanar reflections, and significantly exceeds the thicknesses of the nanostructures (usually up to hundreds of nanometers).

Bragg diffraction in the *skew geometry* is widely used in its non-coplanar-*symmetric* form for investigations of GaN films [69–71]. It also provides access to reflections of the {111} series for [001] grown III–V semiconductor systems, which

are not accessible within the methodology of the coplanar geometry. But usually, the information depth for the symmetric skew geometry remains high.

In order to remedy the shortcoming of high penetration depth, an extremely asymmetric skew geometry in grazing incidence conditions has been developed [72–75]. Here, a sample rotation around the diffraction vector **Q** is performed in order to create the extremely asymmetric skew geometry, where the angle of incidence is small (grazing incidence) and the exit angle is steep. Usual θ or $\theta - 2\theta$ scans in this configuration change the angle of incidence during the scan with θ and, consequently change the information depth too [76, 77].

We provide an approach which combines surface sensitivity with the advantages of the conventional coplanar and skew geometry, in particular it facilitates the access to polar reflections and vertical strain components. By this approach we are capable of measuring the 3D reciprocal space intensity distribution in extremely asymmetric skew geometry, realized by a *single azimuthal rotation* of the sample at *fixed incident angle* and therefore at constant information depth.

In the following sections, we first develop the technique of X-ray diffraction at fixed incidence angle (FIXD) [62] and describe its technical realization - performing scans and transformation of the measured data into the reciprocal space. This approach is later applied to GaAs NW.

1.4.1 Accessing the Bragg Reflection in the Basic FIXD Setup

The following considerations are based on a six circle diffractometer layout (see Fig. 5). In this layout, the sample scan can be organized in the most effective way, if two circles are used for the detector positioning, three circles for the sample orientation, and the last (free) motor is dedicated to the scan itself. Let us define the lab coordinate system **x**, **y**, **z** and diffractometer rotation-axes φ, χ, θ, ν, δ, μ. The axes of the lab coordinate system are oriented as follows: the **x**-axis is parallel to the incident beam, the **z**-axis points in vertical direction, and the **y**-axis is defined as the vector product $\mathbf{z} \times \mathbf{x}$. In the initial conditions (all angular values of the diffractometer are set to 0) we assume all rotation-axes of the diffractometer except χ-axis to be perpendicular to the incident beam and the incident beam hits the center of the detector. The χ-axis is parallel to the incident beam and the **x**-axis.

The sample coordinate system is defined as following: the lateral component of the reciprocal node under investigation $Q_{||}$ defines the axis x_s. At this point, the axes x_s, y_s, z_s coincide with the corresponding axes of the lab system. This arrangement corresponds to the state of a well-adjusted sample at the beginning of the experiment. The Bragg condition for a given reciprocal vector Q is achieved in two simple but important steps.

First, we set the incident angle α_i to the chosen value by rotating the sample around the **y**-axis in negative direction.

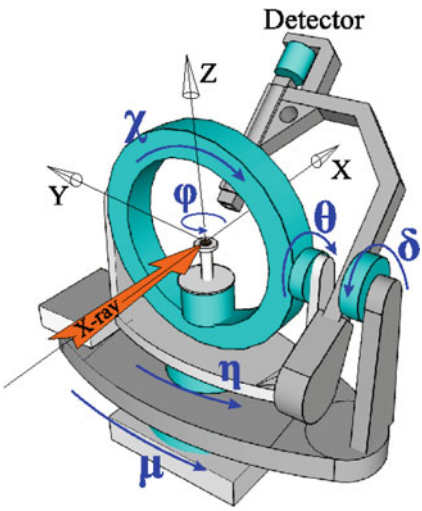

Fig. 5 Six circle diffractometer, its rotational axes and lab coordinate system. Image reprinted from Ref. [62] with the permission of IUCr

Second, the Bragg condition has to be fullfilled. This happens for two azimuthal (rotation by the motor φ about the $\mathbf{z}_s$ sample axis) positions $\varphi^\star = \pm(180 - \psi)$ of the sample, where ψ is the angle between the axis $\mathbf{x}_s$ and the projection of the incident beam onto the sample surface. Here and further the asterisk sign is used to denote the actual angular positions of given goniometer motors. With the wavevector $\mathrm{k} = 2\pi/\lambda$, we can express ψ as

$$\psi = \arccos\left(\frac{\mathrm{Q}_{||}^2 + \mathrm{Q}_z^2 - 2\mathrm{k}\cdot\sin\alpha_i\cdot\mathrm{Q}_z}{2\mathrm{k}\cdot\cos\alpha_i\cdot\mathrm{Q}_{||}}\right). \tag{19}$$

The angle ψ is a complex number if the desired reflection could be achieved in a coplanar geometry and the chosen angle α_i is smaller than the incident angle for the coplanar diffraction.

We implement a *single rotation scan* to probe the volume around the reciprocal node **Q**. As we see from Fig. 6, during the scan by the sample rotation round the $\mathbf{z}_s$-axis (φ-scan) the reciprocal node (shown as the rose sphere) moves along the arc from the beginning point (b) to the end point (e). It crosses the Ewald sphere (marked in green) at the exact Bragg position. It is very important to mention that a φ-scan does not alter the angle of incidence α_i. At each step of the scan the absolute position of the reciprocal node in the lab coordinate system can be evaluated [62]:

$$\begin{pmatrix} \mathrm{Q}_x^{\mathrm{Exp}} \\ \mathrm{Q}_y^{\mathrm{Exp}} \\ \mathrm{Q}_z^{\mathrm{Exp}} \end{pmatrix} = R^{\mathrm{Exp}}(\alpha_i, \varphi^\star) \begin{pmatrix} \mathrm{Q}_{||} \\ 0 \\ \mathrm{Q}_z. \end{pmatrix}$$

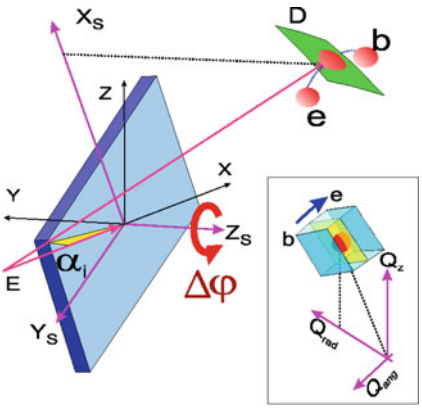

Fig. 6 FIXD scan with vertical sample position. A scheme of the scan in the lab coordinate system is shown. The green surface marked with D corresponds to the segment of the Ewald sphere covered by the detector window. The scan is executed by the rotation about the axis z_S ($\Delta\varphi$). The reciprocal node (rose sphere) passes along the trace between the points b (beginning of the scan) and e (end of the scan). The inset demonstrates the reciprocal volume in the vicinity of the main reflection (red sphere) covered by the detector window during the scan from b to e in the sample reciprocal coordinates. Image reprinted from Ref. [62] with the permission of IUCr

A rotation matrix $R^{\mathrm{smp}} = R^{\mathrm{Exp}}(\alpha_i, \varphi^{\star})^{-1}$ projects the node coordinates in the lab system back to the initial position. This matrix, being applied to the coordinates of the detector in the lab system

$$\left(\mathrm{Q}^{\mathrm{D}}_{\mathrm{x(i,j)}}(\mu,\delta),\ \mathrm{Q}^{\mathrm{D}}_{\mathrm{y(i,j)}}(\mu,\delta),\ \mathrm{Q}^{\mathrm{D}}_{\mathrm{z(i,j)}}(\mu,\delta)\right) \tag{20}$$

transforms them to the sample coordinate system, keeping their relative positions in respect to the reciprocal node constant.

The sequence of the "back-transformed" detector frames, taken at each step of the scan, fills the 3D volume around the reciprocal node (blue box on the Fig. 6, inset).

The described approach, based on rotation matrices, facilitates the non-trivial geometrical calculations for 3D reciprocal space mapping in skew geometry. However, it is not restricted to this single problem and can be *universally* applied for any other geometry (coplanar, non-coplanar, grazing incidence diffraction) and any trajectory of the reciprocal node and detector. The only requirement is the access to the motor positions, which are usually available through the log-files of the scan or (preferable) recorded in the file header of each frame. The practical advantages of the rotation matrix algorithm have been demonstrated and analyzed comprehensively in [78–80], for instance. For further details on the FIXD approach, we refer the reader to [62].

2 *in-situ* X-ray Diffraction of Nanowire Ensembles During Growth

2.1 Experimental Requirements

2.1.1 Sample Environment Chambers for *in-situ* X-ray investigations at synchrotron beamlines

The past years have seen a rapid development in X-ray optics and synchrotron radiation sources, providing the scientific community with X-ray beams of high brilliance having focal spots in the micro- and nanometer range being the ideal characterization tool for surface science. To this end, sample environment chambers are frequently employed at synchrotron radiation facilities, in order to investigate surface phenomena, nanostructures, and thin films and their behavior during thermal treatment under controlled (oftentimes UHV) conditions [81, 82]. Such compact chambers usually provide sample positioning and heating, Be-windows and a pumping system, and are installed at suitable synchrotron beamlines supporting heavy-duty goniometers and providing room for bulky instrumentation.

In response to challenges encountered in epitaxy of lattice-mismatched thin films and multilayers, as well as nanostructures—ranging from 0D quantum dots to 1D nanowires, various multifuctional vacuum systems have been designed, allowing for time-resolved in-situ X-ray experiments during the deposition process [83–86].

Among other deposition methods, Molecular Beam Expitaxy (MBE) is a versatile technique allowing precise control over the deposition environment in a wide range of growth conditions [87], at the same time being a pure technique without resorting to foreign compounds. In the past there have been several approaches to combine UHV equipment and MBE systems with synchrotron diffractometers [81, 86, 88–96].

In principle, these concepts can be separated to two general philosophies.

The first approach integrates a large stationary UHV system in an X-ray diffractometer. This is usually advantageous in terms of vacuum quality and growth conditions, because the overall weight of the MBE components is not limited by additional constraints such as mobility of the system. This holds as well for the vacuum system, and surface analysis equipment. However, a complete beamline has to be dedicated to this single purpose in this case.

The second approach utilizes small lightweight UHV chambers installed at a suitable diffractometer at a synchrotron beamline on demand. The latter approach often lacks adequate control over the growth parameters and scanning motions of the diffractometer. Yet, it gives versatile possibilities in choosing the appropriate beamline suitable for the particular X-ray experiment. We chose the latter philosophy in order, to have a standalone MBE system which, nevertheless is portable and suitable to be mounted on a diffractometer at a synchrotron beamline of our choice.

The following section is reprinted from Ref. [30] with the author's permission and Ref. [97] with the permission of AIP publishing.

2.1.2 A Portable MBE System for *in-situ* X-Ray investigations at synchrotron beamlines

In this section, we describe a portable UHV system for molecular beam epitaxy (MBE) which can be used at various synchrotron beamlines but without compromising on quality of epitaxial nanostructures. The growth chamber is equipped with all the standard MBE components such as effusion cells with shutters, main shutter, cooling shroud, manipulator, reflection high-energy electron diffraction (RHEED) setup, and pressure gauges. The characteristic feature of the system is the beryllium-windows which are used for *in-situ* X-ray measurements.

2.1.3 System Layout and Technical Design

Together with "Createc Fischer and Co. GmbH" it was our aim to design a portable MBE system which should be able to transport and process samples grown at the MBE clusters of our collaboration partners under UHV conditions. In addition, growth of nanostructures should be possible within this chamber during X-ray experiments. The system should offer a possibility for X-rays to enter, hit the sample and leave the chamber in a widest angular range possible, to allow for investigations of Bragg reflections with large momentum transfer, or simultaneous combination of scattering geometries such as grazing incidence diffraction (GID) and grazing incidence small-angle scattering (GISAXS) [97].

The portable MBE system (see Fig. 7) comprises three main parts, a unit for sample UHV transfer and loading called transfer case (TC), a unit for sample storage called storage chamber (SC), and a chamber for MBE-growth. This growth chamber (GC) features two beryllium-windows for the X-rays as it depicted in Fig. 8. To make this system as versatile and mobile as possible, these three parts are located on a steel frame supported by wheels. The wheel mounting renders the system mobile for fast transfer to the experimental hutch at the synchrotron facility. Also, long range transportation by trucking company is possible and has been realized several times.

The SC and GC can be decoupled from the TC and relocated from the frame onto the diffractometer for X-ray measurements. To maintain the vacuum during each step of the experiment, each separate chamber is individually pumped by an ion getter pump.

Despite the fact, that specialized equipment and parts could yield a considerable decrease in the weight of the UHV system, we resort to standard CF components where it is possible. Therefore, the UHV system comprising of GC, SC, and TC has a total weight of 350kg. Standard components, however, reduce delays in the case of component failure and decrease operational costs. Consider that the combined GC and SC weight is about 155 155 kg only.

Experimental layouts have been realized at the NANO beamline at the lightsource of the Karlsruhe Institute of Technology (KIT), at the surface diffraction beamline ID03 at the European Synchrotron Radiation Facility (ESRF), where the first *in-situ* measurements with this instrument have been performed, and the resonant scattering beamline P09 at Petra III.

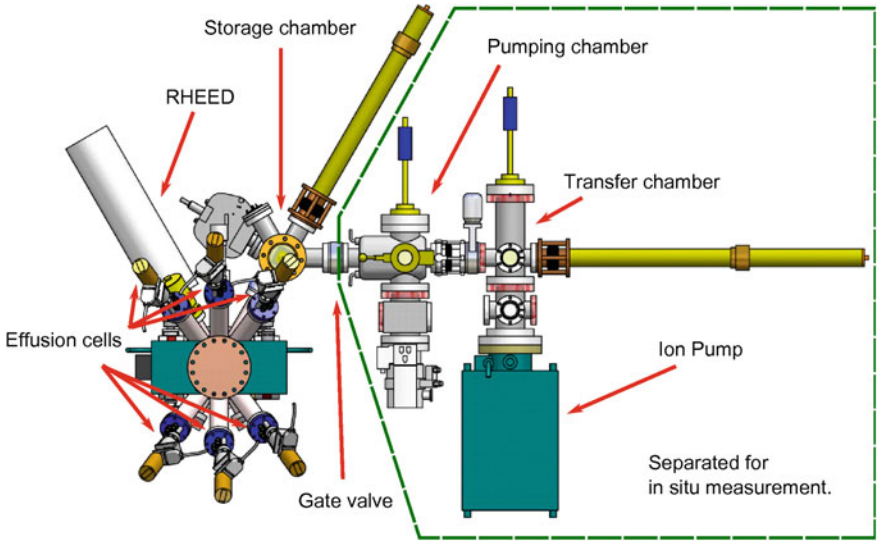

Fig. 7 Scheme of the portable MBE system. The green box indicates the transfer case which is separated during X-ray experiments. Image reprinted from Ref. [97] with the permission of AIP publishing

2.1.4 Growth Chamber

The manipulator allows sample positioning featuring translation and endless-rotation required to align the sample for X-ray investigations. A pneumatically actuated stabilization stamp can fix the sample position during X-ray measurements if required. It is possible to position the sample in such a way that RHEED and X-ray measurements can be performed at the same time. In this configuration the sample is located in the center between the beryllium window ports. Tungsten heating wires provide sample heating. The sample heater supports heating up to $T = 900$ °C. The temperature at the sample is measured by a thermocouple located in the substrate heater near to the substrate.

The standard samples used in our system have the size of a quarter of a 2" wafer. This provides a sufficiently large opening at the back of the sample holder to achieve a homogeneous temperature distribution over the sample. A second advantage of the sample size is the fact, that the large beam-footprint resulting of the grazing incidence geometry will completely be projected on the sample surface. Thus unfavorable edge effects of the scattered and reflected beam can be avoided [86].

The two beryllium-windows, located on the opposite sides of the deposition chamber (see Fig. 8), allow *in-situ* X-ray measurements. Motorized shutters in front of the beryllium-windows prevent the contamination of the beryllium-windows during growth when no X-ray experiments are performed. The same shutters can be used as in-vacuum X-ray beam stop to decrease the effect of parasitic scattering on the

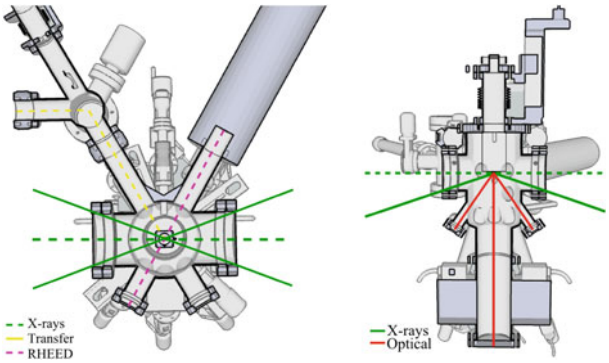

Fig. 8 **a** Vertical cut through growth chamber. The sample position is in the crossing points of the lines. Pink: RHEED, Green: X-rays, Yellow: Sample transfer. **b** Horizontal cut through growth chamber. Green: X-rays, Orange: Optical. Image reprinted from Ref. [97] with the permission of AIP publishing

exit Be-windows when it is needed. X-ray diffraction experiments can be performed in various geometries, such as symmetric, asymmetric, GID, and GISAXS. Characteristic XRD patterns of GaAs nanowires on (111) plane Si wafers are presented in Fig. 9a for the symmetric (111) Bragg peaks and in Fig. 9b for a asymmetric set of Bragg peaks using the FIXD approach described in Sect. 1.4.

A 30 keV RHEED gun "SPECS RHD30" is operated for monitoring the growth process. The RHEED pattern is projected to an opposing fluorescence screen on a CF40 flange (pink line Fig. 8, left). Besides RHEED being an effective tool to investigate the surface quality and growth speed, it is commonly used to monitor the growth of nanostructures, especially to determine the 2D-3D transition during quantum dot growth, for example. Utilizing the motorized manipulator for sample rotation various surface reconstructions can be investigated.

In between synchrotron experiments, RHEED is routinely used to monitor crystal phase evolution of the nanowires during their growth. The CF40 RHEED view port of our growth chamber is located at the distance of 300 mm from the center of the substrate. This provides sufficient angular range to capture the electron diffraction pattern at an acceleration energy of 24 keV. In order to allow for simultaneous *in-situ* XRD and RHEED under suitable diffraction geometry, the RHEED interlock system is coupled to the interlock system of the synchrotron beamline.

2.2 Evolution of Polytypism in GaAs Nanowires

This section is reprinted from Ref. [30] with the author's permission and Reprinted excerpt with permission from [98]. Copyright (2015) by the American Physical Society.

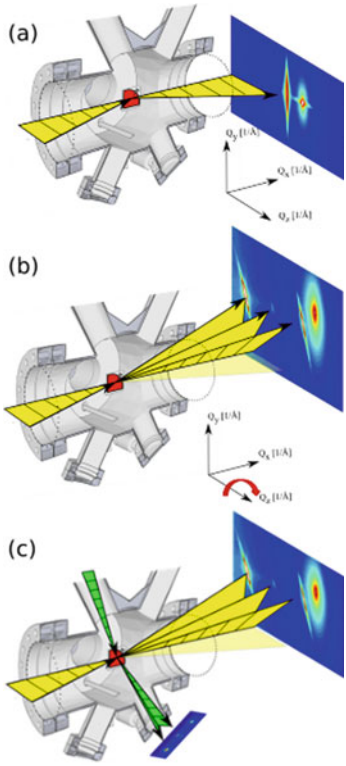

Fig. 9 **a** Symmetric and **b** asymmetric X-ray diffraction geometries realizable with the pMBE setup. The internal sample rotation can be used for sample pre-alignment. **c** If compatible with the X-ray geometry, RHEED can be used simultaneously

2.2.1 Monitoring the Evolution of Polytypism During Growth of GaAs Nanowires

In III–V nanowires the energetic barriers for nucleation in zinc blende or wurtzite arrangement are typically of similar order of magnitude. As a result, both arrangements can occur in a single wire. Here, we investigate the evolution of this polytypism in self-catalyzed GaAs nanowires on Si(111) grown by molecular beam epitaxy with time-resolved *in-situ* X-ray diffraction. We interpret our data in the framework of a height-dependent Markov model for the stacking in the nanowires. This way, we extract the mean sizes of faultless wurtzite and zinc-blende segments—a key parameter of polytypic nanowires—and their temporal evolution during growth. Thereby, we infer quantitative information on the differences of the nucleation barriers including their evolution without requiring a model of the nucleus.

Although lateral strain relaxation in a NW facilitates a strongly reduced dislocation density compared to conventional 2D layer growth in lattice-mismatched heteroepitaxy [99–101], the wurtzite zinc-blende polytypism [49] deteriorates electronic and optical properties of III–V NWs [102–104].

Growing a NW often involves a liquid droplet at its tip which induces uniaxial growth and serves as material reservoir during the growth process [105]. The properties of the droplet during the growth—such as its shape, composition, and dynamics [106–109]—have strong impact on the growing NW. Further, the morphology [110–112] of the growing NW, the involved crystallographic surfaces and their energies [113, 114] are of importance, in particular for the currently growing phase. As a result, a complicated interplay of the crystalline wire and the droplet determines the energetic nucleation barriers $E_{\mathrm{P}|\mathrm{P}}$ and $E_{\bar{\mathrm{P}}|\mathrm{P}}$ for continuing the growth of phase $\mathrm{P} \in \{\mathrm{ZB}, \mathrm{WZ}\}$ or for beginning a segment of the complementary phase $\bar{\mathrm{P}}$ on top of the current phase P [56, 58, 113, 115]. The nucleation barrier differences $\delta E_{\bar{\mathrm{P}}|\mathrm{P}} = E_{\bar{\mathrm{P}}|\mathrm{P}} - E_{\mathrm{P}|\mathrm{P}}$ determine the polytypic behavior: if $\delta E_{\bar{\mathrm{P}}|\mathrm{P}}$ significantly exceed the energy scale $\mathrm{k_B}T_{\mathrm{Growth}}$ responsible for thermal fluctuations ($\mathrm{k_B}$ is the Boltzmann constant and T_{Growth} the growth temperature in Kelvin), phase transitions are highly unlikely and very pure wires emerge. In contrast, the frequent observation of polytypism implies that $\delta E_{\bar{\mathrm{P}}|\mathrm{P}}$ is only slightly larger than $\mathrm{k_B}T_{\mathrm{Growth}}$ for typical growth conditions. Moreover, experimental access to that quantity is of crucial importance for phase engineering in NWs. Consequently, considerable theoretical [57, 58, 108, 116, 117] and experimental [115, 118] efforts aim at understanding and controlling [49, 110] polytypism.

As a result of the different lattice constants of ZB and WZ in NWs [40, 41, 45, 119], these polytypes can be well resolved by XRD [120–123]. In this section, we infer the differences of the nucleation barriers $\delta E_{\bar{\mathrm{P}}|\mathrm{P}}$ and the evolution thereof from time-resolved *in-situ* X-ray diffraction data which has been obtained during growth of NWs. The changes in the shape of the scattered intensity over time (beyond simple rescaling due to increased scattering volume or effects from changes in the geometry of the NWs) reveal the gradient of the properties of the NWs with increasing growth time. For interpretion of the time-resolved experimental data, we employ a model for the length distribution of faultless segments of each polytype with mean value L_{P} ("phase purity"). As an advantage of this approach, the derived nucleation barrier differences $\delta E_{\bar{\mathrm{P}}|\mathrm{P}}$ neither rely on assumptions on the geometry of the nucleus, nor on the exact mechanisms of nucleation or the catalyst dynamics [56–58, 105, 107, 109, 113, 114, 116, 118, 124].

We monitored the growth of self-catalyzed GaAs NWs in a MBE system [97] suitable for *in-situ* X-ray measurements at NANO beamline at the synchrotron ANKA, KIT, with highly monochromatic ($\Delta E/E \approx 10^{-4}$) X-ray radiation at an energy of $E = 14\mathrm{keV}$.

During $t_{\mathrm{Max}} = 60\,\mathrm{min}$ of growth after opening the Ga shutter, the intensity near the (111) Bragg reflection was recorded with a 2D PILATUS 100k detector located at a fixed spatial position (distance to sample $\approx$ 1m). During these time-resolved measurements, incidence, and exit angle α_i and α_f of the X-ray beam were kept constant and chosen such that the Ewald sphere intersects the crystal truncation rod (CTR) of Si close to the (111) GaAs signal. As a consequence, the plane in reciprocal space recorded by such a single frame of the 2D detector is essentially parallel to q_z and thus obtained detector frames contain all essential information for our q_z

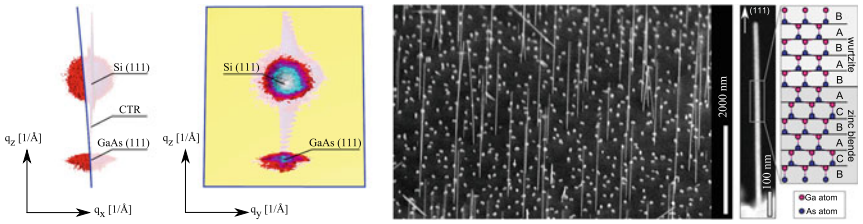

(a) Isosurfaces of the intensity distribution $\mathcal{I}(\mathbf{q})$ near the (111) Bragg reflections of Si and GaAs. The plane (blue box) is the domain measured during *in-situ* growth by the 2D detector. (left: q_x-q_z; right: q_y-q_z)

(b) Left: Long, thin, vertical NWs with low number density. The depicted area is representative for the central region where the X-ray beam hit the sample. Due to charging effects, some NWs appear to be bended. Parasitic growth is also observed. Right: Magnified image of a single NW.

Fig. 10 Post-growth characterization of the sample grown during time-resolved *in-situ* X-ray diffraction by means of X-ray diffraction in (**a**) and SEM in (**b**)

intensity profiles $\mathcal{I}(q_z, t_i)$. The position of this plane in three dimensional reciprocal space and the intensity distribution in this plane for our geometry during the *in-situ* growth measurements are illustrated in Fig. 10a.

As substrate, we used p-doped Si(111) covered by a thin native oxide layer. Before growth, the substrate was heated to $T_{\text{Sub}} = 750°\text{C}$. At a temperature of $T_{\text{Sub}} = 590°\text{C}$ and a background pressure of $2.9 \cdot 10^{-7}$mbar, NW growth was initiated by opening the Ga shutter 5min after opening the As shutter. The V/III ratio was 4.9 at a Ga-flux which is equivalent to a nominal 2D GaAs layer growth–rate of 30nm/h on GaAs(001). The calibration of the V/III ratio done at T_{Sub} by the transition from the (2×4) to the (4×2) surface reconstruction in the reflection high-energy electron diffraction (RHEED) pattern using a GaAs (001) substrate. At these growth conditions, the NWs grow with a rate of approx. 40nm/min. This growth rate is constant for NW lengths up to 5 μm as confirmed by NW growth calibrations.

After $t_{\text{Max}} = 60$min the Ga and As shutters were closed simultaneously with ending the X-ray measurements. Substrate heating was stopped, and its temperature was ramped down to $T_{\text{Final}} = 100°\text{C}$ in 8min.

In addition to the time-resolved X-ray data of the (111) reflection of GaAs recorded during growth, a three-dimensional post-growth scan of this reflection in reciprocal space was performed *in-situ* after the growth was stopped: Apart from the silicon Bragg peak, its diffuse scattering and the crystal truncation rod (CTR) of the substrate, an extended diffuse cloud of intensity close to the GaAs Bragg peak is observed. Additional post-growth *ex-situ* scanning electron microscopy (SEM) reveals low-density NWs (around 2 NWs per μm^2) with approximately 17 ± 5nm in diameter and a height of $2.2 \pm 0.25\mu$m (Fig. 10b).

During growth, the arrangement of beam, sample and detector has been kept constant. The information recorded by the 2D X-ray detector essentially corresponds to the q_y-q_z plane in reciprocal space as illustrated in Fig. 10a. The recorded frames

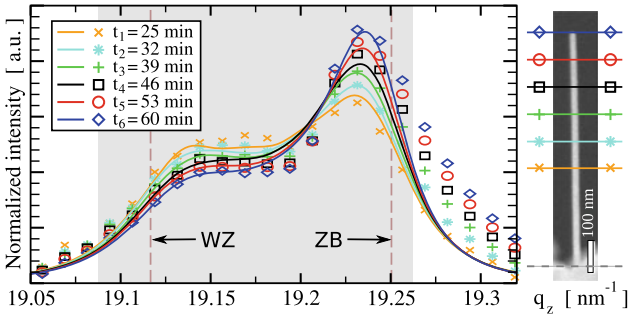

Fig. 11 Measured *in-situ* X-ray diffraction intensity profiles $\mathcal{I}(q_z, t_i)$ after various growth times t_i (symbols) and the best fit of the simulated profiles based on Eq. 23 (solid lines) in the gray region. Each profile has been normalized to an equal area in the gray region. Reprinted figure with permission from [98]. Copyright (2015) by the American Physical Society

have been corrected for background and integrated in q_y direction. Thereby we obtain time-resolved q_z profiles, which are sensitive to the arrangement of the crystalline layers in the NWs which are parallel to the (111) surface of the substrate.

Fig. 11 contains these profiles $\mathcal{I}(q_z, t_i)$ after various growth times t_i (symbols): Although the external growth parameters have been kept constant during growth, we observe a monotonous drift of the scattered intensity $\mathcal{I}(q_z, t_i)$ toward zinc-blende (smaller vertical lattice constant [45]) with advancing growth time t_i which indicates a gradient of the properties of the NWs with increasing height.

2.2.2 Markov Model for the Statistical Generation of Stacking Sequences

We now relate these profiles of the scattered X-ray intensity to time-resolved information on the purities L_P of both phases and the differences $\delta E_{\bar{P}|P}$ of the nucleation barriers.

For that purpose, we generate stacking sequences of a large set of wires based on a time-dependent Markov chain—motivated, e.g., by the results in [115, 117]. Then, we calculate the respective q_z profile of this set of NWs. Finally, we compare the set of profiles $\{\mathcal{I}(q_z, t_i)\}$ resulting from different parameters of the Markov chain to the experimentally measured intensity distribution. The solid lines in Fig. 11 correspond to our best fit in the framework of the time-dependent Markov model.

We now discuss this model in more detail. First, we relate the stacking sequence to the wurtzite and zinc-blende phase: the vertical stacking of each wire is constituted by a sequence of layers of either type A, B, or C. Zinc-blende phase is composed by three adjacent layers of different type (e.g., ABC). In particular, the type of the first and last layer is different. The wurtzite phase is defined by three adjacent layers where the first and last layer are of the same type (e.g., ABA). Direct repetitions of the same type in the sequence (e.g., ABBC) are not allowed.

In our simulations, we initialize the first three layers of each wire in wurtzite stacking with probability $p_{\mathrm{WZ}}^{(0)}$ and, consequently, zinc-blende with probability $1 - p_{\mathrm{WZ}}^{(0)}$. After this, we append a new layer n to the wire's stacking sequence according to a Markov chain: First, the current phase P is determined by comparison of layer $n-1$ and $n-3$. Layer n continues the sequence of the current phase P with probability $p_{\mathrm{P}\to\mathrm{P}}(n)$ and switches to the stacking of the complementary phase $\bar{\mathrm{P}}$ with probability $p_{\mathrm{P}\to\bar{\mathrm{P}}}(n) = 1 - p_{\mathrm{P}\to\mathrm{P}}(n)$. This Markov chain is repeated until n reaches the total number of layers n_l corresponding to a particular growth time ($n_l \approx 6700$ after $t_{\mathrm{Max}} = 60\mathrm{min}$, equivalent to $2.1\mu\mathrm{m}$ in height). For growth times $t_{\mathrm{Max}} < 60\mathrm{min}$, we assume a linear relation between the NW height n_l and the growth time t.

The parameters $p_{\mathrm{P}\to\bar{\mathrm{P}}}(n)$ in the stacking model determine the phase distribution of the grown wires. In case of probabilities, $p_{\mathrm{P}\to\bar{\mathrm{P}}}$ independent of the layer n the phase fractions for long wires (stationary limit for $n_l \to \infty$) are $p_{\mathrm{P}}^{(\mathrm{S})} = p_{\bar{\mathrm{P}}\to\mathrm{P}}/(p_{\bar{\mathrm{P}}\to\mathrm{P}} + p_{\mathrm{P}\to\bar{\mathrm{P}}})$, and the thicknesses of the phase segments are exponentially distributed with mean $L_{\mathrm{P}} = p_{\mathrm{P}\to\mathrm{P}}/p_{\mathrm{P}\to\bar{\mathrm{P}}}$. Such exponential behavior has, for example, been observed with high-resolution transmission electron microscopy (HRTEM) by Johansson et al. [56, 115] for values in the order of $L_{\mathrm{P}} \approx 3 - 9$ layers.

However, the longer the mean phase segment, the large fluctuations of the thickness of each individual phase segment make the detection of the mean value L_{P}—and in particular a possible change along the wire—more and more difficult by means of HRTEM. On the contrary, the high statistical significance of X-ray ensemble measurements will facilitate the detection of a gradient in L_{P} in growth direction of the NWs in a range that is currently not accessible by other methods and despite the huge fluctuations of the length of the phase segments.

Consequently, we now discuss the relation between the stacking sequences of the nanowires and the q_z profiles close to the (111) GaAs reflection. Then, we illustrate the influence of the phase fractions $p_{\mathrm{P}}^{(\mathrm{S})}$ and purities L_{P} on such profiles for probabilities $p_{\mathrm{P}\to\bar{\mathrm{P}}}$ independent of the layer n (see Fig. 12). Finally, we introduce layer dependent transition probabilities $p_{\mathrm{P}\to\bar{\mathrm{P}}}(n)$ in order to unterstand the time-dependent experimental X-ray data.

A single NW contributes to the scattered intensity $\mathcal{I}(q_z)$ near the symmetric (111) Bragg reflection as the absolute square of the single wire scattering factor

$$\mathcal{F}(q_z, \mathbf{q}_{||}) \propto \sum_{n=1}^{n_l} \Omega_n(\mathbf{q}_{||}) \sum_{\substack{\alpha\in \\ \{\mathrm{Ga,As}\}}} f_{\mathbf{Q}_{\mathrm{B}}}^{(\alpha)} \cdot \mathrm{e}^{-iq_z(z_n + z_{\alpha n})} \,, \tag{21}$$

where $f_{\mathbf{Q}_{\mathrm{B}}}^{(\alpha)}$ is the atomic form factor of Ga and As atoms approximated by the value at the (111) Bragg peak $\mathbf{Q}_{\mathrm{B}}$. z_n refers to the beginning of layer n and $z_{\alpha n}$ is the distance of the As sub-layer to the Ga sub-layer within the same layer n. $\Omega_n(\mathbf{q}_{||})$ is the two-dimensional Fourier transform of the the cross section of layer n. For our NWs we observe no pronounced tapering and, therefore, simplify $\Omega_n(\mathbf{q}_{||}) = \Omega(\mathbf{q}_{||})$. However, geometrical information on tapering of NWs (e.g., from post-growth SEM) can be incorporated easily through $\Omega_n(\mathbf{q}_{||})$. The dependence of $\mathbf{q}_{||}$ is irrelevant for the subsequent discussions.

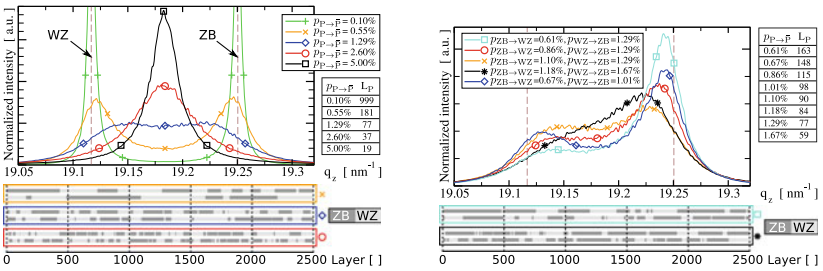

(a) $p_{P\to\bar{P}} = p_{WZ\to ZB} = p_{ZB\to WZ}$ (b) $p_{WZ\to ZB} \neq p_{ZB\to WZ}$

Fig. 12 Intensity profiles near the (111) GaAs Bragg peak for ensembles of NWs with stacking sequences obtained by a Markov chain with layer independent transition probabilities $p_{P\to\bar{P}}$. The area below all profiles is equal. For some parameters (indicated by the color of the box enclosing the NW realizations), we added two examples for the phase distributions generated according to the Markov model. In **a**, the parameters $p_{WZ\to ZB}$ and $p_{ZB\to WZ}$ are equal, whereas **b** illustrates the result for $p_{WZ\to ZB} \neq p_{ZB\to WZ}$. Reprinted figure with permission from [98]. Copyright (2015) by the American Physical Society

For the determination of z_n and $z_{\alpha n}$, we attribute the thickness of layer n according to the native value of the local phase (determined from layer $n-1$ and $n+1$ in the stacking sequence of this wire). For the difference in vertical lattice constant of wurtzite and zinc-blende polytypes, we employ $d_{WZ}/d_{ZB} = 1.007$ [45], where $d_P = z_n - z_{n-1}$. Finally, the contributions from 2500 different wires are summed up incoherently in our simulated data.

In Fig. 12 we depict simulated q_z intensity profiles close to the (111) GaAs Bragg reflection for layer independent transition probabilities $p_{P\to\bar{P}}$. These examples provide an overview how the characteristic features of the X-ray profile change with either the phase fraction or with the phase purity at constant phase fraction and, thereby, facilitate a qualitative understanding of the experimental profiles in Fig. 11.

Although the fraction of wurtzite and zinc-blende are equal to 50% in all curves of Fig. 12a, the X-ray signal strongly differs in shape depending on the wires' phase purity: Starting from NWs with high phase purity (low transition probability), the diffraction signal shows sharp maxima at either wurtzite or zinc-blende position (dashed lines), respectively. For increasing transition probability, peak broadening is observed ($p_{P\to\bar{P}} \approx 0.55\%$) which results in a pronounced plateau at $p_{P\to\bar{P}} = 1.29\%$. For even higher transition probabilities ($p_{P\to\bar{P}} \in \{2.60\%, 5.00\%\}$), only a single peak centered at the mean q_z value of the pure wurtzite peak and the pure zinc blende peak remains. In Fig. 12b, we consider an ensemble of wires with $p_P^{(S)} \neq 0.5$ which implies $p_{WZ\to ZB} \neq p_{ZB\to WZ}$. On the one hand, the three cases with $p_{WZ\to ZB} = 1.29\%$ illustrate the change in the X-ray signal as a function of the phase fraction $p_P^{(S)}$, where $p_P^{(S)}$ increases from $p_P^{(S)} = 0.32$ ($p_{ZB\to WZ} = 0.61\%$) over $p_P^{(S)} = 0.4$ ($p_{ZB\to WZ} = 0.86\%$) to $p_P^{(S)} = 0.46$ ($p_{ZB\to WZ} = 1.10\%$). On the other hand, the wurtzite fraction of the three cases $p_{ZB\to WZ} \in \{0.67\%, 0.86\%, 1.18\%\}$ is equal ($p_{WZ}^{(S)} = 0.4$). As well as for $p_P^{(S)} = 0.5$ in Fig. 12a, the X-ray profile changes significantly as a function of the

phase purities L_P for $p_P^{(S)} \neq 0.5$. Thus, the q_z intensity profile near the (111) Bragg reflection is highly sensitive to the transition probabilities and, thereby, reveals the average segment thickness of each polytype in the NW ensemble.

If no time-resolved experimental data is available, i.e., if only a single experimental profile $\mathcal{I}(q_z, t_i)$ after a particular time t_i in Fig. 11 is considered, it can be explained by *static* transition probabilities $p_{P\to\bar{P}}$ as its features are very similar to the profiles depicted in Fig. 12b (e.g., $p_{ZB\to WZ} = 1.10\%$ for $t_1 = 25$min and $p_{ZB\to WZ} = 0.86\%$ for $t_5 = 53$ min).

For layer independent probabilities $p_{P\to\bar{P}}$, the average fraction of wurtzite $\bar{p}_{WZ}$ up to layer n can be expressed as a weighted average

$$\bar{p}_{WZ}(n) = w_I(n, \bar{p}_{12})\, p_{WZ}^{(0)} + w_S(n, \bar{p}_{12})\, p_{WZ}^{(S)}\,, \tag{22}$$

of the initial growth $p_{WZ}^{(0)}$ and the stationary limit $p_{WZ}^{(S)}$ where $\bar{p}_{12} = 1 - (p_{WZ\to ZB} + p_{ZB\to WZ})$. The stationary limit is given by $p_{WZ}^{(S)} = p_{ZB\to WZ}/(p_{WZ\to ZB} + p_{ZB\to WZ})$ and observed for $n \to \infty$ in case $\bar{p}_{12} < 1$.

2.2.3 Simulation of Time-Resolved In-Situ X-Ray Intensity Profiles

However, the change in the experimental profile with increasing growth time t_i is *in*compatible with static transition probabilities $p_{P\to\bar{P}}$. We attribute these changes to a non-vanishing gradient of the structural properties of the grown NWs with increasing height.

Thus, we consider layer-dependent transition probabilities

$$p_{P\to\bar{P}}(n) = u_{P\to\bar{P}} + v_{P\to\bar{P}} \cdot n \tag{23}$$

and generated a data base of intensity profiles $\mathcal{I}(q_z, t_i)$ for $N = 6000$ sets of random parameters $u_{P\to\bar{P}}$ and $v_{P\to\bar{P}}$.

Equation (23) is motivated by a Taylor-expansion of the layer-dependent transition probabilities $p_{P\to\bar{P}}(n)$ which we truncate after the first order. Consequently, we approximate the layer-dependent transition probabilities by $p_{P\to\bar{P}}(n) = u_{P\to\bar{P}} + v_{P\to\bar{P}} \cdot n$ and thereby obtain the mean gradient $v_{P\to\bar{P}}$ from our experimental data.

For the extraction of the parameters $u_{P\to\bar{P}}$ and $v_{P\to\bar{P}}$ of Eq. (23), we pursued the following approach: Based on the assumption of a linear relation of NW height n_l versus growth time t and an experimental resolution of $\approx 0.03\text{nm}^{-1}$, a data base of intensity profiles $\mathcal{I}(q_z, t_i)$ for $N_1 = 3000$ sets of random parameters $u_{P\to\bar{P}}$ and $v_{P\to\bar{P}}$ with bounds $-2.5 \cdot 10^{-6} \leq v_{WZ\to ZB} \leq 2.5 \cdot 10^{-6}$, $-5.0 \cdot 10^{-6} \leq v_{ZB\to WZ} \leq 2.5 \cdot 10^{-6}$, and $0.25\% \leq u_{P\to\bar{P}} \leq 5.00\%$ has been generated. From the best $N_F = 60$ fits (2%) for $\mathcal{I}(q_z, t_i)$ in the central region (gray background in Fig. 11), a reduced phase space limited by $-1.8 \cdot 10^{-6} \leq v_{WZ\to ZB} \leq 2.0 \cdot 10^{-6}$, $-3.8 \cdot 10^{-6} \leq v_{ZB\to WZ} \leq 1.2 \cdot 10^{-6}$, $9.3‰ \leq u_{WZ\to ZB} \leq 2.1\%$, and $7.4‰ \leq u_{ZB\to WZ} \leq 2.4\%$ has been defined by the 10% and 90% quantiles of each of the four parameters. Another

$N_2 = 3000$ simulations with uniform random sampling of this reduced phase space have been added to the data base. Thus, the data base contained $N = N_1 + N_2 = 6000$ data sets in total.

For the evaluation of our experimental data, we determine the local polytype of layer n and its thickness by the neighboring layers $n-1$ and $n+1$. This way, we neglect strain in (111) growth direction at the interfaces between wurtzite and zinc blende segments. For comparison: Such strain at atomically sharp hetero-interfaces of InAs/InP (lattice mismatch of 3.1%) in InAs nanowires influences the local lattice constants only up to approx. 2nm from the interface (approximately 6 layers) [125]. Given that (i) our mean segment sizes (50–400 layers) are significantly larger than these 2nm or 6 layers and (ii) the in-plane strain at the interface of the polytypes in GaAs nanowires is approximately one order of magnitude smaller (0.3%) [126] and thus even smaller than the lattice contrast in (111) growth direction, we assume that such strain has only minor influence on the evaluation of our experimental data. Yet we emphasize that it is possible to incorporate strain at the interface of the polytypes (or other extensions of the Markov model for the stacking such as the ANNNI model [117]) in our approach.

Based on the linear approximation for the wire height versus growth time, the NWs exceed $n \approx 2800$ layers after the growth time $t_1 = 25$ min (see Fig. 11). We point out that the strain induced by the mismatch of 4, 1% between GaAs and the Si substrate is already relaxed close to the substrate [126–128] at layers $n \ll 2800$. Consequently, the influence thereof is neglected.

Since the shape of the experimental X-ray profile at $t_1 = 25$min in Fig. 11 shows no traces of two separated peaks, which would indicate small transition probabilities $p_{\mathrm{P}\to\bar{\mathrm{P}}} \lesssim 1.0\%$ (see Fig. 12a), we assume $p_{\mathrm{WZ}\to\mathrm{ZB}} + p_{\mathrm{ZB}\to\mathrm{WZ}} \geq \max(p_{\mathrm{P}\to\bar{\mathrm{P}}}) \gtrsim 0.01$ during growth of the first $n = 2800$ layers and restrict to $n > 2800$. For these assumptions $w_{\mathrm{I}}(n > 2800, \bar{p}_{12} < 0.99)$ is bound from above by 3.7% in the Markov model. Thus, the influence of the initial growth parameter $p_{\mathrm{WZ}}^{(0)}$ on the scattering signal for wires longer than $n \approx 2800$ layers (i.e., after the growth time t_1) is negligible and cannot be reliably estimated from our experimental data.

Therefore, we limited our treatment of the intensity profiles to the two-parameter space $\{p_{\mathrm{WZ}\to\mathrm{ZB}}(n), p_{\mathrm{ZB}\to\mathrm{WZ}}(n)\}$ (see Figs. 11 and 12). Moreover, it is valid to approximate the average wurtzite fraction $\bar{p}_{\mathrm{WZ}}$ by its stationary limit $p_{\mathrm{WZ}}^{(\mathrm{S})}$ for layer independent probabilities (see Fig. 12).

2.2.4 Transition Probabilities and Nucleation Energy Barrier Differences

From the comparison to the experimental data, we obtain estimates for the layer-dependent transition probabilities $p_{\mathrm{P}\to\bar{\mathrm{P}}}(n)$ which are depicted in Fig. 13: Whereas newly grown zinc blende and wurtzite segments are approximately equally thick (with $L_{\mathrm{P}} \approx 80$) at early growth times $t \approx 20$ min, the average segment thickness of zinc-blende $L_{\mathrm{ZB}} \approx 200$ becomes about 3.5 times larger than the one of wurtzite after $t_{\mathrm{Max}} = 60$ min.

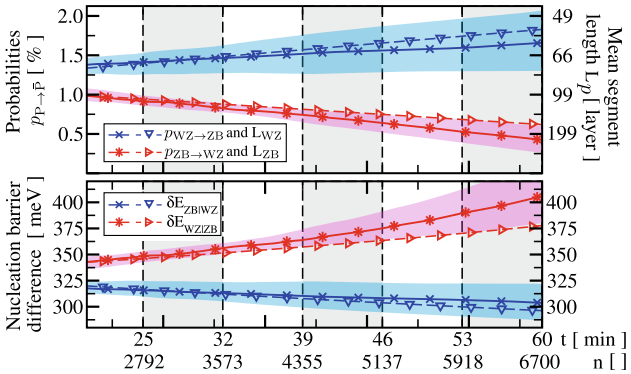

Fig. 13 Extracted transition probabilities $p_{P\to\bar{P}}(n)$ according to Eq. 23, mean segment lengths $L_P(n) \approx p_{P\to P}/p_{P\to\bar{P}}$ of newly grown segments (phase purity), and differences of the nucleation barriers $\delta E_{\bar{P}|P}(n)$ as given in Eq. 26 as function of the layer n (or the growth time t). The triangular symbols represent the best fit of the simulated data to $\mathcal{I}(q_z, t_i)$ in the gray region in Fig. 11. The values depicted by cross, circle, and star symbols are the median at each layer n of the best $N_F = 60$ fits. The errors are estimated by the 25% and 75% quantiles thereof and marked as color shaded background. The negative (positive) slope in case of $p_{ZB\to WZ}$ ($p_{WZ\to ZB}$) implies increasing (decreasing) phase purity for zinc-blende (wurtzite) with advancing time. Reprinted figure with permission from [98]. Copyright (2015) by the American Physical Society

We assume that the nucleation process is close to thermodynamic equilibrium. Then, the differences in the nucleation barriers are linked to the transition probabilities as [56, 58]

$$p_{P\to P} = \frac{c_{P|P}\cdot \mathrm{e}^{-\beta E_{P|P}}}{c_{P|P}\cdot \mathrm{e}^{-\beta E_{P|P}} + c_{\bar{P}|P}\cdot \mathrm{e}^{-\beta E_{\bar{P}|P}}}, \tag{24}$$

with $\beta = 1/k_B T_{Sub}$. The parameters $c_{P|P}$ and $c_{\bar{P}|P}$ describe the degeneracy which is given by the number of nuclei that can be formed with nucleation barrier $E_{P|P}$ and $E_{\bar{P}|P}$, respectively. Determination of these degeneracy parameters requires a sophisticated microscopic modeling of the nucleation process which involves growth temperature, concentration of group V element in the droplet, and the difference in chemical potential of III–V pair between liquid and solid phase [124]. For our estimation of the differences of the nucleation barriers, we assume that these degeneracy parameters are similar ($c_{\bar{P}|P} \approx c_{P|P}$) as compared to the variations of the Boltzmann factors $\mathrm{e}^{-\beta E_{P|P}}$ and $\mathrm{e}^{-\beta E_{\bar{P}|P}}$, and, therefore, have negligible influence in Eq. (24). Consequently, the difference of the nucleation barriers is approximated by

$$\delta E_{\bar{P}|P} = k_B T_{Sub}\cdot \ln\left(\frac{1-p_{P\to\bar{P}}}{p_{P\to\bar{P}}}\right). \tag{25}$$

Finally, we exploit the probabilities $p_{P\to\bar{P}}(n)$ for concluding on the differences of the nucleation barriers [56, 58]

$$\delta E_{\bar{\mathrm{P}}|\mathrm{P}}(n) = \mathrm{k_B}\, T_{\mathrm{Sub}}\, \ln\left(\frac{1 - p_{\mathrm{P}\to\bar{\mathrm{P}}}(n)}{p_{\mathrm{P}\to\bar{\mathrm{P}}}(n)}\right), \tag{26}$$

which are also depicted in Fig. 13 for our particular growth conditions. We obtain values in the range from 315 meV (after $t \approx 25$ min) to 300 meV (after $t_{\mathrm{Max}} = 60$ min) for $\delta E_{\mathrm{ZB|WZ}}(n)$. For $\delta E_{\mathrm{WZ|ZB}}(n)$, we extracted 350meV (after $t \approx 25$ min) to approximately 400meV (after $t_{\mathrm{Max}} = 60$ min). In contrast to experiments with varying growth conditions [120], we observe a trend toward higher phase purity of zinc-blende despite constant growth parameters. This behavior can be attributed to the dynamics of the droplet at the NW tip, in particular its shape and its composition. Firstly, the supersaturation of As in the liquid droplet might increase during growth, which would lead to a higher probability for the nucleation of zinc-blende [129]. Secondly, the volume of the liquid droplet, which is mainly constituted by Ga, might decrease [57]. This could result from a reduction in the Ga-flux toward the droplet via the NW side-walls as the NW grows longer [130–132]. Since there is no evidence for an onset of pronounced tapering [133] (which would indicate a reduction of the diameter of the droplet), the reduced volume likely induces a decrease of the wetting angle of the droplet rather than a reduction of its diameter [57].

In conclusion, we demonstrated that the temporal evolution of the intensity $\mathcal{I}(q_z, t)$ obtained by *in-situ* X-ray diffraction provides quantitative access to the nucleation barrier differences which determine the phase distribution of the grown NWs. Based on a layer-dependent Markov chain in order to model polytypism, height-dependent estimates for the phase purity for the ensemble of NWs have been extracted. For our particular growth conditions, a gradient of the phase purity toward larger zinc blende segments has been observed with advancing growth time. From the transition probabilities $p_{\mathrm{P}\to\bar{\mathrm{P}}}(n)$ in the Markov model we inferred layer-dependent differences of the nucleation barriers $\delta E_{\bar{\mathrm{P}}|\mathrm{P}}(n)$. For our example of self-catalyzed GaAs NWs, the values of $\delta E_{\bar{\mathrm{P}}|\mathrm{P}}(n)$ evolved in the range from 300 meV to 400 meV. We emphasize that the determined values neither rely on a particular geometrical model for the nucleus, nor on the exact mechanisms of nucleation or the catalyst dynamics.

Providing such access to the nucleation energy barriers, our approach opens a way for systematic studies of the evolution of polytypism during the growth of NWs to gain further understanding and developing theoretical and practical aspects of NW growth. Higher order polytypism such as 4H can also be implemented in the Markov approach if required [134, 135].

2.3 *Radial Growth of GaAs Nanowires and Shape Evolution of Liquid Ga-Droplet*

This section is reprinted from [30] with the author's permission and Reprinted (adapted) with permission from [136]. Copyright (2018) American Chemical Society.

2.3.1 Monitoring the Evolution of the Liquid Ga-Droplet During Growth of GaAs Nanowires

This section reports on a growth study of self-catalyzed GaAs nanowires based on time-resolved *in-situ* X-ray structure characterization during MBE in combination with *ex-situ* SEM. The evolution of nanowire radius and polytypism is monitored by asymmetric X-ray diffraction which allows distinguishing radial growth processes responsible for tapering and side-wall growth. The results are interpreted using a model for diameter self-stabilization processes during growth of self-catalyzed GaAs nanowires including the shape of the liquid Ga-droplet, and its evolution during growth.

GaAs nanowires can be grown by the self-catalyzed method [137] via the vapor-liquid–solid (VLS) mode [138]. In this process their morphology is strongly influenced by the liquid Ga-droplet at the NW tip [131, 139]. This droplet acts as a catalyst for the uniaxial NW growth and at the same time as material reservoir. The size of the droplet correlates with the actual NW diameter [140–145]. Composition, [116, 146] and shape [55, 57, 140] of the droplet, and therefore its wetting conditions at the liquid–solid interface and the facets involved, determine the microstructure of the growing NW [31, 34, 57, 108, 147]. Regarding the wetting conditions, two different regimes can be identified: The zinc-blende (ZB) phase is favored for large wetting angles $\beta \approx 130°$, whereas the wurtzite (WZ) phase is typically favored for wetting angles $\beta \approx 90°$[57, 108, 120, 147–149]. Usually, the transition of β between these two regimes is causing highly faulted segments [149]. Altough good control over the crystal structure has been achieved for Au-catalyzed GaAs NWs [150], controlling the droplet shape and crystal structure in self-catalyzed VLS-grown NWs is more challenging, but could ultimately be performed at CMOS compatible temperatures [151]. However, not only the crystalline phase is affected by the droplet. For large wetting angles, radial growth can be strongly enhanced [34] resulting in a variation of the NW diameter along its length, so-called tapering. On the one hand, tapering was first regarded as unintended side-effect [131] due to, e.g., an inflation of the droplet during growth, as a consequence of unbalanced material fluxes [116], and its minimization was desired [152]. On the other hand, by harnessing radial growth processes, tapered NWs geometries could be exploited, for example, axial NW heterostructures [153], and for advanced device applications [154–156]. Hence, current efforts aim at the control [140, 142, 157–159], and understanding [124, 143, 144, 160–168] of radial growth processes responsible for tapering. Of particular interest here are self-stabilizing growth processes that are closely linked to the liquid Ga-droplet [169, 170].

In addition to the radial growth processes involving the droplet (VLS), growth at the NW side-walls via the vapor–solid (VS) mode further influences the final shape of the NW [144, 152, 163, 164, 167] and impedes the direct observation of the aforementioned self-stabilization processes.

In the following we show for self-catalyzed GaAs NW that tapering and subsequent side-wall growth can be distinguished by a combination of time-resolved *in-situ* X-ray diffraction (XRD) during growth and post-growth *ex-situ* characteriza-

tion by scanning electron microscopy (SEM). Our results allow for a refinement of recently presented growth models [169, 170] and give insight into the evolution of the shape of the liquid Ga-droplet during growth.

We use molecular beam epitaxy (MBE) for the growth of self-catalyzed GaAs NWs on Si(111) substrates covered by native oxide. In order to monitor the growth process non-destructively, we apply time-resolved *in-situ* XRD which has recently gained appeal in the field of NW structure characterization [31, 98, 120, 172], and from which we infer information on the evolution of crystal structure and the shape of the NWs during growth. The XRD experiments for this study have been performed at the beamline P09 [173] at the synchrotron facility PETRA III, using a specially designed portable MBE chamber [97].

2.3.2 MBE Growth Conditions

The growth of the GaAs nanowires was performed on n-doped Si(111) wafers covered by native oxide at a substrate temperature of $T_{\text{sub}} = 600°\text{C}$ and a comparably low V/III ratio in order to achieve low axial growth rates and to obtain nanowires with a pronounced droplet and a large diameter. Prior to the growth the substrate was annealed for 30 min at $T_{\text{sub}} = 660°\text{C}$. Subsequently, Ga-droplets were deposited on the substrate. The nanowire growth was then initiated by applying As_4-flux and Ga-flux.

The calibration of $F_{V/III}$ has been performed by RHEED on GaAs(001) substrates at T_{sub} by monitoring the transition between the 2×4 and 4×2 surface reconstructions when switching from As-rich to Ga-rich growth conditions.

SEM images of the NWs grown for this study are shown in Fig. 14. After a final growth time of $t_f = 255$ min at a substrate temperature of $T_{\text{sub}} = 600°\text{C}$ and a V/III ratio of $F_{V/III} \approx 2.6 \pm 0.1$, and Ga-limited 2D GaAs growth rate $R_{GaAs} = 4545\, nm/h$, the GaAs NWs are inversely tapered with a length of approximately $l(t_f) \approx 4\,\mu$m, a base diameter $d_e(0) = 79\,\text{nm} \pm 10\,\text{nm}$ (measured from edge to edge, compare inset in Fig. 14b), and a tip diameter below the droplet $d_e(4\mu m) = 157\,\text{nm} \pm 8\,\text{nm}$, resulting in a tapering angle $\delta \approx 0.5° \pm 0.1°$. The SEM image in the top left panel of Fig. 14a illustrates the homogeneity of the grown NW ensemble. The inverse tapering of the NWs becomes evident in the panel at the bottom left. On the high-resolution image at the right panel of Fig. 14a, (110)-type side-facets [59] and the pronounced Ga-droplet are visible. The contact angle between droplet and NW top-facet is $\beta_{\text{SEM}} \approx 135° \pm 2°$. In Fig. 14b, the mean radius after growth $r_{NW}(z, t_f)$ is shown as a function of height z above the substrate. Further, $r_{NW}(z, t_f)$ is well characterized by a third-order polynomial fit given by the red solid line. Hence, describing tapering by a constant tapering angle δ along the NW length is insufficient. For the remainder of the chapter we will refer to the distance between opposite side-facets when using the terms "diameter" or "radius". In this case, the distance measured in the SEM image (see the inset of Fig. 14b) has to be multiplied by a factor of $\sqrt{3}/2$.

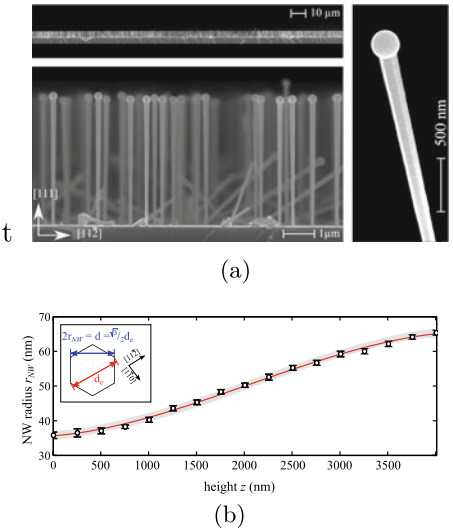

Fig. 14 Representative scanning electron images of the grown NW ensemble. The large field of view at the upper left gives an impression on the homogeneity of the NW ensemble. At the lower left, the inverse tapering of the wires is visible. In both images, the view-direction is parallel to the normals of one pair of (110) side-facets which allows us to calculate the facet distance. The high magnification image at the right [171] shows a single NW from a tilted view. The (110)-type side-facets and a pronounced Ga-droplet at its tip are visible. In the bottom panel, the height-resolved mean NW radius is depicted, as well as a fit using a third-order polynomial (red). Reprinted (adapted) with permission from [136]. Copyright (2018) American Chemical Society

2.3.3 *in-situ* X-ray diffraction experiment

For *in-situ* structure characterization of the growing ensemble of self-catalyzed GaAs NW, we monitor the evolution of the phase-selective Bragg reflections (311) of GaAs zinc-blende (ZB), (220) of GaAs twinned zinc-blende (TZB) and (10.3) of GaAs wurtzite (WZ) [37, 62]. Here, we used the asymmetric geometry with fixed incidence angle. The X-rays enter and leave the chamber via circular Be-windows. After impinging upon the specimen, the diffracted X-rays leave the chamber and are recorded at the detector as a two-dimensional intensity distribution. By rotation of the sample about its surface normal, Bragg reflections for ZB, TZB, and WZ GaAs, and Si can be excited without changing the incidence angle [37, 62].

For this set of reflections, scattering from ZB, TZB, and WZ is well separated in reciprocal space, in contrast to the symmetric (111) reflection where the signals of WZ and ZB can overlap [37, 134].

The X-ray experiment was performed at the beamline P09 at PETRA III. We used a highly monochromatic X-ray beam with an energy of 15keV and a size of 145 μm x 50 μm. The incidence angle was $\alpha_i = 15.5°$ and has been kept constant during the measurement. The undulator insertion device provided a photon flux of $\approx 10^{13}\, ph/s$. Employing a Pilatus 300K detector, we measured the scattered intensity

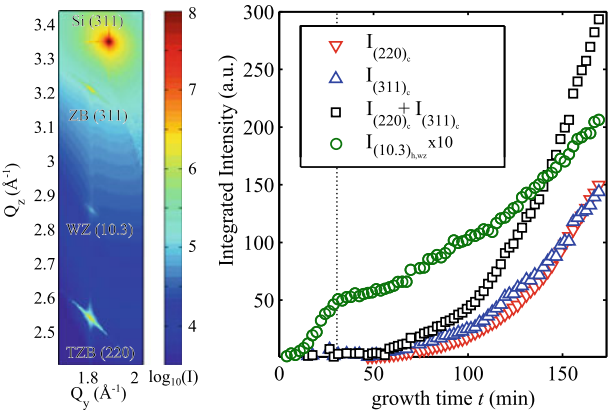

Fig. 15 Time-evolution of the integrated intensity of phase-selective Bragg reflections of GaAs as a measure of the growing material in the NW ensemble. Initially GaAs nucleates in WZ phase. After 30 min a transition toward ZB and TZB takes place. For better visibility, the intensity of WZ $I_{(10.3)}$ is multiplied by a factor of 10. Reprinted (adapted) with permission from [136]. Copyright (2018) American Chemical Society

in the vicinity of the cubic $(311)_c$ reflection of zinc-blende, the wurtzite $(10.3)_{h,wz}$ reflection, and the $(220)_c$ reflection of twinned zinc-blende GaAs in a time-resolved manner during the growth. After 170 min of growth we changed the measurement geometry and investigated another reflection (not shown here). After the growth, full 3D reciprocal space maps of the asymmetric reflections have been measured at growth temperature by a rotation around the sample-normal.

In the right panel of Fig. 15, the time-evolution of the integrated intensities $\mathcal{I}_p(t)$ of 2D-cuts through the centers of those three phase-selective Bragg reflections (illustrated in the reciprocal space map (RSM) in the left panel) are shown after renormalization to correct their structure-factor differences, and subtraction of the contribution from parasitic GaAs islands to the scattering signal [98, 174]. We take the integrated scattered intensity of a phase-selective Bragg reflection as a measure for the volume of the respective phase in the crystal. During the nucleation, we observe that the (10.3) WZ reflection emerges first, providing evidence that the NW base consists mainly of WZ GaAs. Until t = 30 min (dotted vertical line in Fig. 15), WZ GaAs is almost exclusively formed, until the nucleation probabilities [57, 98] start to change in favor of the formation of GaAs ZB and TZB phases. This may be caused by a transition of the wetting angle [57, 147, 149] to values favoring ZB over WZ. In our case this transition could be related to the abrupt change in the slope of the integrated intensity of the GaAs (10.3) WZ reflection, and the concomitant emergence of the GaAs ZB and TZB reflections. Subsequently, the majority of growing GaAs is of ZB or TZB type. In fact, post-growth transmission-electron microscopy (TEM) did not reveal any extended WZ segments in the NWs at heights corresponding to growth times $t > 30$ min. Consequently, the remaining intensity increase observed

in the WZ reflection after the distinct change is an indication for radial VS side-wall growth, increasing the radius of already existing WZ segments at the NW base.

In the kinematical approximation, and in absence of non-homogenous strain, the distribution of scattered X-ray intensity around a Bragg peak reflects the square modulus of the Fourier transform of the NW shape [175]. From suitable key interference features of the (10.3) WZ and (220) TZB reflections we can therefore infer information on the evolution of the mean radius of segments of WZ and TZB GaAs in the growing NW ensemble. Since the scattering vector Q_z is defined to be parallel to the [111] growth direction, the intensity distribution $I(\mathbf{q}, t)$, with scattering vector $\mathbf{q}$ in the Q_x/Q_y-plane, around these reflections contains direct information on the cross-sectional shape Ω_{NW} of the [111]-oriented NW, and therefore its radius (see Fig. 16a, in absence of tapering). The full-width-half-maximum (FWHM) of the Bragg reflection $q_{FWHM}(t)$ and the distance of the first-order size-oscillation $q_{\max}(t)$ are inversely proportional to the radius of the NW. In the absence of tapering the radius can be directly determined by a sinc-squared function via $r(t) \approx 2.78/q_{FWHM}(t)$, and $r(t) \approx 4.49/q_{\max}(t)$. If tapering is present, an additional weight-function has to be applied in order to consider the effect of height-dependent radius variation, providing a weighted mean radius $\bar{r}_w(t)$, averaged over the NW length.

The intensity distribution around the (220) TZB Bragg reflection in the Q_x/Q_y-plane crossing the Q_z-axis at $Q_z = 2.542$ Å^{-1} at the final growth time t_f is shown in Fig. 16b. We observe a characteristic scattering feature with sixfold symmetry, originating from the (110) side-facets of TZB segments with hexagonal cross section. From the intensity profiles $I(q, t)$, essentially along a so-called facet truncation rod, as indicated by the dotted line in Fig. 16b, we estimate $q_{FWHM}(t)$ and the position of the first-order side maximum $q_{max}(t)$. The measured intensity profiles $I(q, t)$ are shown in Fig. 16b for several different times during growth.

In our case, $q_{FWHM}(t)$ and $q_{\max}(t)$ of the intensity profiles from the (220) reflection decrease for increasing growth time t, which is indicative for radial growth as result of both inverse tapering (as newly grown TZB-type layers at the NW top have larger radii than the segments below), as well as subsequent side-wall growth. As a consequence of this superposition, the interpretation of the results from the (220) TZB reflection needs further modeling. Before we discuss a model that is capable of describing both aspects of radial growth, we now focus on the WZ reflection. The (10.3) WZ Bragg reflection is an ideal starting point for our evaluation, since the corresponding WZ segments are present only at the NW base ($t < 30$ min) and tapering is negligible. The first-order side-maxima are not detectable (compare Fig. 16b), and the (10.3) Bragg reflection is weak but yet sufficiently strong in order to estimate the mean radius of WZ segments $\bar{r}_{WZ}(t)$ from the the FWHM of the reflection, as we discussed earlier. In this way, direct information on the side-wall growth is accessible. In the following discussion, we correlate the *in-situ* results for $\bar{r}_{WZ}(t)$ with the NW radius $r_{NW}(z, t_f)$ along the NW growth axis z obtained by SEM after the growth.

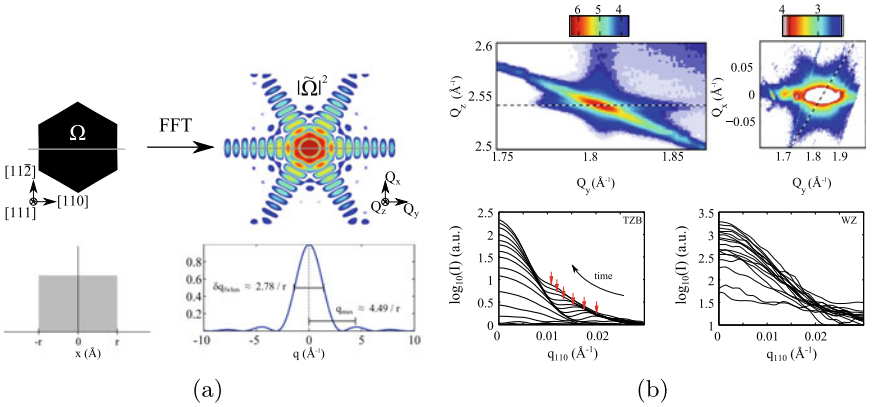

Fig. 16 **a** Top panel—Schematic illustration of NW cross-sectional geometry and resulting scattering signal in reciprocal space. Bottom panel shows the corresponding cross sections indicated by the gray lines. **b** Measured intensity distribution around the (220) TZB reflection after growth. Upper left panel: Q_y/Q_z-RSM of the (220) TZB reflection. Tilted structures (mainly crystallites) scatter along a Debye-Scherrer ring causing the oblique feature passing through the reflection. The NW side-facets cause the scattering streaks perpendicular to Q_z. Upper right panel: Q_x/Q_y-RSM at the Q_z-level depicted by the dotted line left. The line on the right corresponds to the direction along which the intensity profiles $I(q, t)$ of the facet-streaks were evaluated during growth. The bottom left panel shows the facet-streaks extracted from the TZB reflection, the bottom right panel shows the corresponding profiles of the (10.3) WZ reflection. In both cases, the FWHM decreases with time. Reprinted (adapted) with permission from [136]. Copyright (2018) American Chemical Society

2.3.4 Model for Radial Growth

We model the evolution of NW length and radius, where we allow radial growth processes containing contributions of tapering *and* side-wall growth. We associate $\bar{r}_{WZ}(t)$ with the time-evolution of the NW base radius $r_{NW}(0, t)$. Supposing the initial NW radius is $r(0, 0)$ at growth time $t = 0$ min and $l = 0$ nm, we express the height- and time-dependent NW radius $r_{NW}(z, t)$ as

$$r_{NW}(z, t) = r(0, 0) + \Delta r_{\text{radial}}(z, t) \tag{27}$$

$$= r(0, 0) + \Delta r_T(z, t) + \Delta r_F(z, t) \tag{28}$$

assuming that the radius of the NW can be described by two independent quantities constituted by tapering $\Delta r_T(z, t)$, and subsequent side-wall growth at the NW facets $\Delta r_F(z, t)$, both depend on z and growth time t in general [176]. $\Delta r_T(z, t)$ describes the radial VLS-growth of the top-facet due to tapering [169, 170] at $z = l(t)$ and can thus be expressed by $\Delta r_T(l(t)) = \Delta r_T(t)$. The term $\Delta r_F(z, t)$ accounts for subsequent VS side-wall growth along the NW. Although $\Delta r_F(z, t)$ can in general be a function of NW length and growth time, we here first assume that the side-wall growth rate $m_{\text{facet}} = dr_F/dt$ is constant and homogeneous along the NW

growth axis ($dr_F/dz = \text{const.}$), and $\Delta r_F(l,t) = 0$ at the tip of the NW. Moreover, we assume that the NW grows with a constant axial growth rate v_a, resulting in the NW length $l(t) = v_a \cdot t$ at time t. At our growth conditions the axial growth rate is $v_a = 15.68\,\text{nm/min} \pm 0.19\,\text{nm/min}$, and side-wall growth at height $z = l(t_0) \leq l(t)$ in the interval $\delta t = t - t_0$, and $t \geq t_0$ can be expressed as

$$\Delta r_F(z,t) = \frac{\mathrm{d}r_F}{\mathrm{d}t}(t - t_0) \tag{29}$$

$$= \frac{m_{\text{facet}}}{v_a}\,(v_a\, t - z). \tag{30}$$

Due to VS side-wall growth, the mean radius $\bar{r}_{WZ}(t)$ increases with time as shown in Fig. 17a. The side-wall growth rate $m_{\text{facet}} = 0.094\,\text{nm/min} \pm 0.009\,\text{nm/min}$ follows from the slope of $\bar{r}_{WZ}(t)$, and defines the time-evolution of the NW base radius $r_{NW}(0,t)$. In addition we estimate the initial radius $r(0,0) = 11.1\,\text{nm} \pm 1.0\,\text{nm}$ from linear extrapolation of $\bar{r}_{WZ}(t)$ at $t = 0$. The values $r_{SEM}(z)$ measured by SEM can then be expressed by

$$r_{SEM}(z) = r_{NW}(z,t_f) = r(0,0) + \Delta r_T(l(t)) + \Delta r_F(l(t),t_f), \tag{31}$$

where we have to keep in mind that z at the left hand of the equation is the height above the substrate after growth, and $l(t)$ on the right hand is the corresponding NW length during growth. The initial radius $r(0,0)$, as well as the facet growth rate m_{facet} have been extracted from the X-ray experiment. With Eq. 30, and $r_{SEM}(z)$, and assuming homogeneous facet growth, this allows us to conclude the NW shape during growth. More precisely, we obtain $\Delta r_T(l(t))$ empirically by

$$\Delta r_T(l(t)) = r_{NW}(l(t),t_f) - \Delta r_F(l(t),t_f) - r(0,0). \tag{32}$$

Knowing $\Delta r_T(l(t))$, the NW shape $r_{NW}(z,t)$ at any time during growth can be determined according to Eq. 28, based on the *in-situ* XRD and *ex-situ* SEM results. No further model for Δr_T is required for calculation of the NW shape evolution during growth. The results are summarized in Fig. 17a. The broken black curve, $r_{NW}(z,t_f)$ is a fit to $r_{SEM}(z)$ given by the black circles. The red circles show the evolution of the top-facet radius $r_{top}(t) = \Delta r_T(t) + r(0,0)$ as calculated from r_{SEM} and Δr_F. The linear fit $r_{NW}(0,t)$ to $\bar{r}_{WZ}(t)$ is given by the green broken line. We now briefly check the values so obtained at the beginning and the end of growth for consistency. The initial radii $r(0,0)$ and $r_{top}(0)$ (using Eq. 32) are consistent within the errors as shown in Fig. 17a. Moreover, the value of the WZ base radius at the end of growth is consistent with the measured value by SEM at the NW base.

In order to verify our assumptions, we use the results from Fig. 17a to simulate the temporal evolution of the diffraction pattern and compare these simulations with the experimental results from the (220) TZB reflection. In other words, we simulate the X-ray scattering from a NW during growth, based on the NW shape evolution shown in Fig. 17a. Therefore, we calculate the two-dimensional scattered intensity

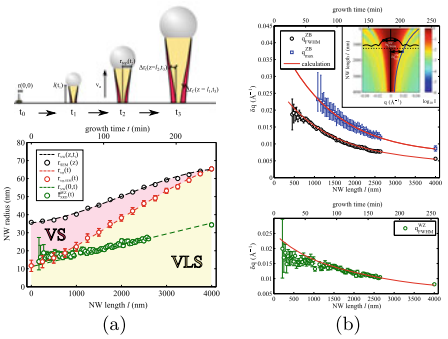

Fig. 17 **a** Top: Illustration of the NW shape at several exemplary growth times t shown for our growth parameters. The contribution of VS facet growth Δr_F is depicted by the red area. The inner yellow shape corresponds to $r_{top}(t)$ (VLS-growth). Bottom: Mean NW radius obtained by SEM and fit (black), mean radius of WZ segments $\bar{r}_{WZ}(t)$ (green circles), interpreted as mean radius of the NW base $r_{NW}(0,t)$ (linear fit for $\bar{r}_{WZ}(t > 50\,\text{min})$, green broken line). The resulting top-radius $r_{top}(t)$ below the Ga-droplet from Eq. 32 is given by the red circles and the broken red line shows the corresponding fit. **b** Comparison of key features extracted from experiment (symbols) and simulation (red solid lines). The calculated values are obtained from the simulated intensity profiles shown in the inset. Each profile $I^{NW}(q, l(t))$ corresponds to scattering along a facet streak from a NW with length $l(t)$ and shape defined by $r_{NW}(z,t)$ at growth time t. For completeness, also the FWHM corresponding only to the NW base is compared to the FWHM of the WZ reflection. Reprinted (adapted) with permission from [136]. Copyright (2018) American Chemical Society

distribution $I(\mathbf{q}, t)$ for a single NW with non-uniform radius $r_{NW}(z,t)$ as given by Eq. 28, at a certain time t. We build the incoherent sum over the squared absolute values of the two-dimensional Fourier transforms

$$I(\mathbf{q}, t) = \sum_{z=0}^{z=l(t)} |\tilde{\Omega}(z,t)|^2 \tag{33}$$

of the hexagonal cross sections $\Omega(z,t)$ of the NW with radius $r_{NW}(z,t)$ from the base at $z = 0$ to the NW tip at $z = l(t)$ with a step size of $\Delta z = 1\,\text{nm}$. In this approximation, we neglect interference related to the vertical stacking in the NW.

From the simulated two-dimensional intensity distribution $I(\mathbf{q}, t)$, we extract the line-profiles $I^{NW}(q,t)$ along a NW facet streak in analogy to the procedure shown in Fig. 16a. The inset in the top of Fig. 17b shows those line-profiles $I^{NW}(q,t)$ normalized to the maximum intensity at each time t (or equivalent NW length $l(t)$). With increasing growth time t, both $q^{NW}_{fwhm}(t)$ and $q^{NW}_{max}(t)$ decrease. The values of these key features (red solid line) are compared to the experimental results given in Fig. 17b. Although we cannot fully exclude contributions of parasitic GaAs islands to the FWHM of the (220) TZB Bragg reflection, the agreement of simulation and experiment is remarkable. Further, this agreement confirms that the shape evolution based on the results from the WZ reflection and SEM shown in Fig. 17a is consistent with our X-ray data extracted from the (220) TZB Bragg reflection. In the bottom

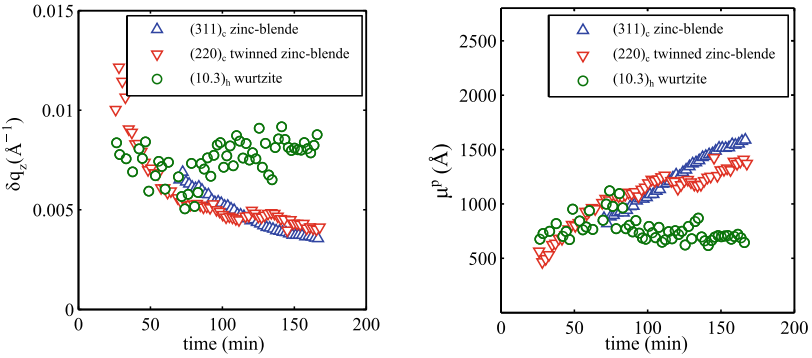

(a) FWHM in q_z - direction of the phase selective Bragg reflections during growth.

(b) Correlation length $\mu^p = 2 * \pi / \delta q_z$ which is indicative for the mean segment length in <111>-direction.

Fig. 18 Width of the phase-selective Bragg reflections and their behavior during growth, and corresponding correlation length

panel of Fig. 17b the corresponding values $q^{WZ}_{fwhm}(t)$ obtained from the (10.3) WZ reflection are compared to the calculated FWHM values obtained from $r_{NW}(0, t)$, showing reasonable agreement as well. An independent study based on *ex-situ* SEM investigations on a whole series of nanowire samples grown on patterned substrates came up with a similar model for the contributions to radial growth [177]. This agreement evidences the validity of the developed model for different nanowire growth environments.

Our analysis is based on the assumption that after a certain growth time the NW elongates mainly by nucleation of new layers in TZB and ZB stacking, and extended WZ growth is essentially located at the base of the NW. Under this assumption, information on radial side-wall growth can be directly obtained from the evolution of the (10.3) WZ Bragg peak during growth. Both, the course of the integrated intensities of the phase-selective reflections (Fig. 15) and also the FWHM in q_z-direction of the respective reflections are in agreement and even a strong indication for such an assumption. The FWHM in q_z-direction behaves inversely proportional to the mean segment length, the precise proportionality additionally depends on the actual distribution of the segment length along the z-axis [52]. That, in principle, allows as to empirically define a correlation length $\mu^p = 2 * \pi / \delta q_z$, which, in case of a Gaussian distribution would even directly correspond to the mean segmentation length. As we show in Fig. 18, FWHM and the related correlation length of WZ stay constant after 30 min of growth. If the mean length of newly growing WZ segments would change along the NW height, most probably also the FWHM should change, which was not observed. The remaining hypothetical case the WZ segments would grow with the same mean length as in the beginning of growth seems to be highly unlikely regarding the evolution of the integrated intensities, and FWHMs of the ZB and TZB reflections, and the observed droplet dynamics.

Until now, we distinguished tapering and side-wall growth and gained insight into the evolution of the top-facet radius $r_{\mathrm{top}}(t)$. This is of particular interest since $r_{\mathrm{top}}(t)$ is in contact with the liquid Ga-droplet which acts as the catalyst for axial NW growth. The growth model suggested in Ref. [170] links the radial growth of the top-facet radius $r_{\mathrm{top}}(t)$ to the shape η of the Ga-droplet. Here, we employ Eq. 11 in Ref. [170] in order to model the evolution of the NW radius due to tapering, expressing $r_{\mathrm{top}}(t)$ using

$$\frac{\mathrm{d}r_{\mathrm{top}}(t)}{\mathrm{d}t} = \frac{2\Omega_{Ga}/\Omega_{GaAs}}{\eta_{eq}(3+\eta_{eq}^2)}\left[F_{V/III}^{-1}\left(1+\frac{\lambda_{Ga}}{(1+\eta_{eq}^2)r_{top}(t)}\right)-1\right], \tag{34}$$

where Ω_{Ga} is the volume of Ga in liquid and Ω_{GaAs} is the volume of a GaAs pair in the solid, and $\Omega_{Ga}/\Omega_{GaAs} = 0.42$ [170]. The diffusion length of Ga-atoms at (110)-facets is given by λ_{Ga}. $F_{V/III}$ is the V/III ratio, and η_{eq} is the equilibrium droplet shape factor, which relates the height of a spherical droplet to the radius of the NW top-facet.

The discussions in Ref. [170] focus on a constant value for the Ga-droplet shape η_{eq} independent of its volume and the top-facet radius $r_{top}(t)$ during growth. This requires a mechanism for easy tapering, e.g., when the side-walls are not oriented along stable surface facets [170, 178]. Then the NW radius below the droplet can be readily adjusted in order to maintain η_{eq}. In our case of self-catalyzed GaAs NWs however, the side-facets are composed of (110)-type surfaces. Therefore the actual droplet shape factor $\eta(t)$ may differ from its equilibrium value and may also change during growth in order to approximate the equilibrium value η_{eq} [170, 179]. Since the exact functional behavior of $\eta(t)$ during growth is unknown, a Fermi-function has been chosen in order to empirically describe the behavior of $\eta(t)$ with growth time t. In this way we can express $\eta(t)$ as function of initial η_i and equilibrium value η_{eq}, whereas the transition between both limits is described by the width f_w of the Fermi-function and the transition time t_0

$$\eta(t) = \eta_i - \frac{\eta_i - \eta_{eq}}{e^{-(t-t_0)/f_w}+1}. \tag{35}$$

We point out, that we obtain the original model for $\eta_i = \eta_{eq}$. We further substitute η_{eq} in Eq. 34 by $\eta(t)$ from Eq. 35, which allows us to model $r_{NW}(z,t)$. Now we determine a set of parameters which yields $r_{NW}(z,t)$, which describes simultaneously both SEM and XRD data. Therefore sampling of the parameter space given by λ, $r(0,0)$, $\mathrm{F_{V/III}}$, and η_i, η_{eq}, t_0 and f_w is required. From our growth calibrations we obtained $\mathrm{F_{V/III}} = 2.6$. Also $\mathrm{r}(0,0) = 11.1$ nm is known from the X-ray experiment. From SEM we obtain the wetting angle $\beta_{SEM} = 135° \pm 2°$ which allows us to limit a probable range of $\eta_{eq} \in \{2.1, 5.7\}$ with a certain safety margin to higher values, accounting for a possible shrinkage of the droplet wetting angle after growth [55]. In the remaining parameter space bounded by $\lambda \in \{550, 4500\}$, $\eta_i \in \{4.5, 11.4\}$, $f_w \in \{20, 60\}$ and $t_0 \in \{0, 32\}$.

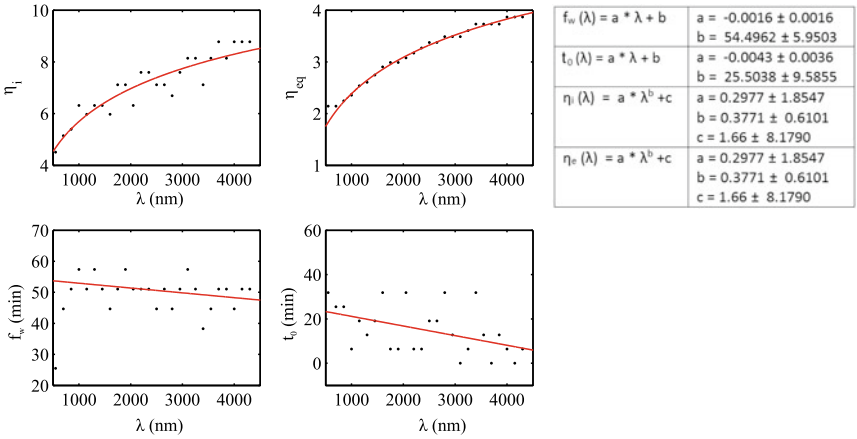

Fig. 19 Sets of parameters resulting in $r_{NW}(l, t_f)$ according to Eq. 31, with the minimum least-squared value in comparison to the $r_{top}(t)$ shown by the black symbols. The red solid line is a fit. Especially, η_{eq} shows a clear correlation with λ which is well described empirically by a power-law $\eta_{eq}(\lambda) = a\ \lambda^b + c$. The obtained values for the droplet shape factor provide reasonable wetting angles during growth. Also, the values of f_w provide a smooth evolution of the droplet shape. For our growth experiment under constant conditions, we would not expect abrupt changes for $\eta(t)$, for example, resulting from $f_w \approx 11$ min

The model allows us to describe our experimental data $r_{SEM}(l)$ and $r_{\text{top}}(t)$. However, for each value λ there exists a $\eta(t)$ which results in $r_{NW}(l, t_f)$ compatible with the experiment. Interestingly, the solutions can be parametrized via the diffusion length λ. Meaning, by selecting a value λ defines the remaining parameters η_i, η_{eq}, f_w and t_0 which in turn define $\eta(t)$. This parameterization is shown in Fig. 19.

As a result we are able to calculate the time-dependent droplet shape $\eta_\lambda(t)$ for a given value of λ, which is illustrated in Fig. 20. Here exemplary $\eta_\lambda(t)$ for $\lambda = 1000$, 2000, 3000, and 4000 nm are depicted by the gray lines. From these solutions for $\eta_\lambda(t)$, we select the ones that provide values $\eta(t_f)$ that are compatible with SEM observations. This is possible since $\eta(t_f)$ increases monotonously with λ.

In fact, solutions within this parameter space are found which describe the experiment to a very high degree. We note, however, that the solutions are not unique for $\eta(t)$ and λ, but can be parameterized via the diffusion length λ. Thus, by choosing values of $\eta(t_f)$ compatible to the wetting angle β_{SEM} obtained from SEM, a range of possible solutions can be identified. Figure 21a depicts the radii measured by SEM and the calculated values $r_{NW}(z, t_f)$, which show good agreement. Also, the radii obtained by *in-situ* XRD $\bar{r}_{ZB}$ and $\bar{r}_{WZ}$ are well reproduced by the calculated values for the weighted mean radius $\bar{r}_w(t)$ and the radius at the NW base $r_{NW}(0, t)$.

For interpretation of the X-ray diffraction data, and in the presence of tapering and facet growth, we use a weight function in order to account for the scattering strength of layers with different area A_{layer} within the same NW. Therefore, we introduce a weighted mean radius

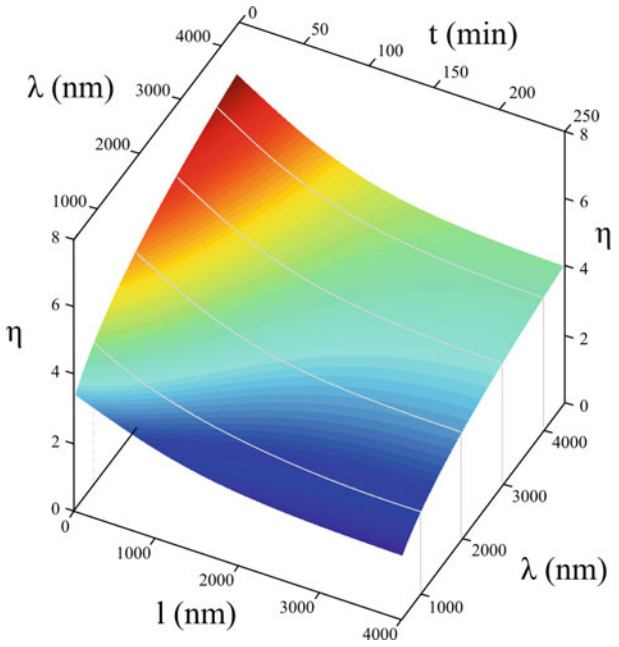

Fig. 20 Droplet shape η as function of growth time t, or NW length $l(t)$, and the diffusion length λ

$$\bar{r}_w(t) = \int_0^{l(t)} w(z,t)\, r_{NW}^p(z,t)\, dz \tag{36}$$

with the weight

$$w(z,t) = \frac{A_{layer}(z,t)}{\int_0^{l(t)} A_{layer}(z,t)dz}. \tag{37}$$

in order to relate the XRD results for FWHM q_{fwhm} and first-order maximum position $q_{\max}$ with the mean weighted radius $\bar{r}_w$ obtained by the shape evolution of the growing NW from our calculations. This choice of $w(z,t)$ allows us to illustrate the relation of the XRD key features with the growing NW structure in our case. We point out that the actual choice of the weight function does not influence the evaluation of our data and the findings presented within this chapter. Therefore a general form of the weight function is not further discussed.

In addition, the final value $\eta(t_f) = 2.41$, equivalent to a wetting angle $\beta(t_f) = 135.0°$, is consistent with the measured wetting angle by SEM $\beta_{SEM} \approx 135° \pm 2°$ as observed after growth. With the limits for β_{SEM}, we obtain values for the Ga-diffusion length $\lambda = 991^{+134}_{-111}$ nm. Compared to literature, Dubrovskii et al. [169] obtained similar values $\lambda = 750$ nm obtained from site-selective grown self-catalyzed GaAs NWs. This value is close to ours, and differences may be caused by different growth parame-

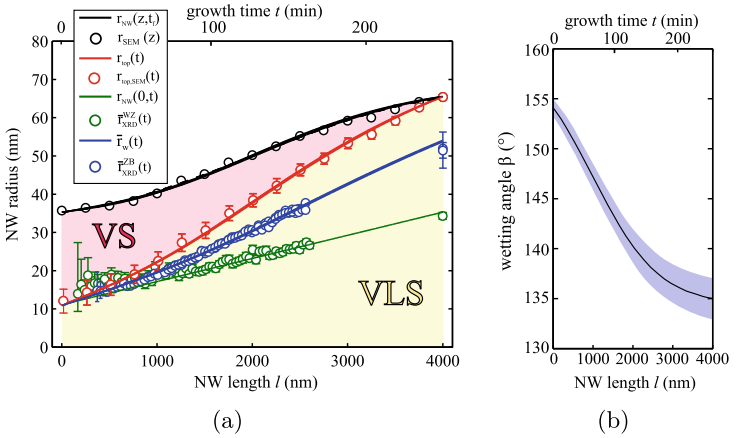

Fig. 21 **a** Evolution of the NW radius measured after growth $r_{SEM}(z)$, and measured mean weighted radius during growth $\bar{r}_{TZB}(t)$ from XRD in comparison with the calculations of $r_{NW}(z, t_f)$ according to Eq. 31 and the calculated mean NW radius $\bar{r}_w(t)$. The calculated curves correspond to the set of the best parameters for $\eta(t_f) = 2.41^{+0.13}_{-0.11}$ which is compatible with SEM. In addition, $r_{top}(t)$ and the contribution of facet growth to the NW bottom $r_{NW}(0, t)$ in comparison with the mean radius of WZ segments $\bar{r}_{WZ}(t)$ is given. **b** Evolution of the droplet wetting angle. Starting below $\beta(0) \approx 155°$ the wetting angle decreases over time, approaching the final value $\beta(t_f) \approx 135°$. Reprinted figure with permission from Ref. [136]. Copyright 2018 American Chemical Society.

ters used and the different mean distances of neighboring NWs. In contrast, our values are lower than Ga-diffusion length $\lambda > 2\,\mu$m on GaAs (110)-facets reported, e.g., by Lopez et al. [180]. Such high values for λ would, in our case, require large $\eta(t_f)$ which are incompatible with our observations. This implies that either the diffusion length on Ga-adatoms at NW (110)-type side-walls is different compared to extended plain GaAs(110)-surfaces, or the growth conditions are not directly comparable to 2D layer growth. This may be caused by As re-evaporation effects in the case of NW growth [181, 182] or a lower effective Ga-diffusion length, reduced by the number density and mean distance of neighboring NWs [169].

The evolution of the wetting angle $\beta(t)$ during growth (calculated from the droplet shape factor $\eta(t)$) for our case is depicted in Fig. 21b. Within the model the wetting angle decreases monotonously with growth time and approaches its equilibrium value $\beta_{eq} = 134.34°$ ($\eta_{eq} = 2.38$). We note that the wetting angle during WZ growth ($t < 30$ min) may differ from the values obtained by the model. In order to investigate the nucleation and early growth-stage, further dedicated experiments, e.g., taking advantage of grazing incidence X-ray geometry are required, which is out of the scope of this study.

In conclusion, we have determined the evolution of crystal structure and shape of inversely tapered self-catalyzed GaAs NWs by time-resolved *in-situ* XRD. Combined with post-growth electron microscopy analysis, we gain insight into the processes of radial growth which are responsible for tapering and side-wall growth. We have

refined a theoretical model for diameter self-stabilization processes, enabling its application to growth experiments and allowing the extraction of Ga-diffusion length and evolution of the Ga-droplet shape during growth. The proposed experimental approach opens the way for further fundamental studies aimed at validating and refining existing NW growth models. Furthermore, the approach allows correlation of the wetting properties of the liquid droplet directly to the evolution of polytypism in VLS-grown semiconductor NWs, which is an essential for crystal phase control and an important step toward the synthesis of phase pure self-catalyzed nanowires.

2.4 in-situ X-ray diffraction of GaAs-(In,Ga)As core-shell nanowires during growth

The processing of nanowires toward a device typically requires the fabrication of one or multiple shell layers to create the desired heterostructure [2, 3, 7, 16, 183]. The possible types of heterostructures are analogous to the ones in case of thin films present in current semiconductor technology. If junctions between regions with different types of majority carriers are required (intrinsic, n-type, p-type), as, e.g., in transistor devices, a suitable type of dopant has to be added at a specific point, whereas the growth of the actual shell material simply proceeds. If quantum wells should be created, e.g., to tune electro-optical properties, this is mostly realized by an epitaxial combination of different compounds, often leading to the creation of misfit strain. Additionally, a passivation layer is sometimes needed in order to suppress either a further reaction of the material or surface electronic states [184, 185]. The structure of such passivation layer strongly depends on its function, it spans all the range from an epitaxial layer to amorphous material. While doping only slightly changes the lattice parameter of the matrix material, far-reaching structural changes are possible in case of deposition of heteroepitaxial layers, which therefore is going to be in the focus of our XRD investigations.

2.4.1 Heteroepitaxial Shell Growth on Semiconductor Nanowires

The deposition of the epitaxial shell layer after VLS-growth of the nanowire core is done in the vapor-solid mode, e.g., by regular epitaxial 2D growth, similar to the fabrication of epitaxial thin films. For a schematic representation of the processing steps, see Fig. 22a. Depending on material combination, the lattice parameter, the crystal phase, or both of them change between heteroepitaxial shell layer and the nanowire core. If the lattice parameters are different, core and shell will be strained to an equilibrium value which changes with increasing shell thickness [186–188]. As soon as the critical thickness is exceeded, misfit dislocations are introduced [189]. So far, this is analogous to the behavior of epitaxial thin films. Additionally, in case of nanowires, the formation of misfit dislocations during shell growth can be

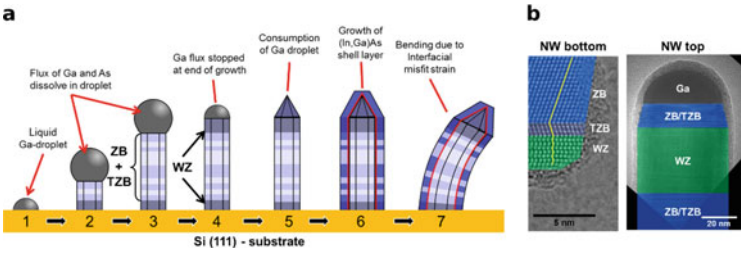

Fig. 22 **a** Schematic of the growth process required to achieve epitaxial core-shell NW heterostructure using VLS-growth on Si. (1) Liquid Ga is deposited on the Si surface. (2)-(3) Ga and As dissolve in the Ga droplet causing the NW to grow below the Ga-droplet. During the first stage of growth, WZ is often formed [126, 136], followed by a stacking of ZB and TZB segments. (4) VLS-growth is stopped by shutting of Ga-flux. Residual As background partially consumes Ga-droplet leading to formation of WZ. (5) Ga-droplet is fully consumed by providing more As. (6) A heterointerface (red line) is formed during the deposition of the heteroepitaxial shell. The stacking sequence may be continued in the shell layer. (7) An inhomogeneous strain distribution causes bending of the nanowire heterostructure **b** HRTEM images from the bottom and the top of a GaAs NW, showing the presence of the WZ phase

completely avoided if the nanowire diameter is smaller than the critical thickness. An interesting situation arises, if the crystal phase of the shell is different from the core. It is frequently observed, that the shell layer adopts the crystal structure of the nanowire core, which already has been used to force the material of the shell layer into the desired crystal structure [190, 191] and even realize a crystal structure not observed in bulk or thin film materials [192]. Complimentary, specific boundary conditions are also able to change the crystal structure of the nanowire itself [46, 193, 194].

2.4.2 X-Ray Diffraction of Core-Shell Nanowire Heterostructures

During MBE-growth, highly directional material fluxes are used. This has the consequence for shell growth, that due to the 3D geometry of the nanowires, only the side facing the material source is reached by the material flux. Even though the diffusion length required to reach the backside of the nanowire is small, a substrate rotation is often employed to increase homogeneity of the shell. Furthermore, the growth conditions need to be carefully tuned to avoid asymmetric band structures or bending of the nanowires [195–197]. On the other hand, controlled bending is an alternative method to modify optical properties or to create interconnects [198]. Another example where inhomogeneities can be advantageous is elemental segregation observed in (Al,Ga)As core-shell heterostructures [199], which can be employed to create self-assembled quantum dot structures [183].

XRD is highly suitable to investigate the structural changes of such core-shell nanowire heterostructures. However, the resulting diffraction pattern is rather complex, being composed of contributions from the nanowire core and from each of the

epitaxial shell layers which are deposited on six different nanowire side facets, all of them affected by misfit strain induced at facets and corners. Therefore a careful analysis is required to derive the structural properties of the nanowires. Using a nanosized X-ray beam to investigate isolated single core-shell nanowire heterostructures, the bending [195] as well as the rich microstructure can be determined [200, 201]. The microstructure can be correlated with complementary investigations on the same nanowire in order to derive structure-property relationships or to reveal growth mechanisms of individual nanowires.

Such analysis of individual nanowires showed a significant fluctuation of their structural and resulting electro-optical properties. This spread of properties prohibits linking the microstructure to specific thermodynamic boundary conditions set by the growth parameters. In order to deduce this relation instead of separately looking at individual cases, it is necessary to investigate statistical meaningful ensembles of nanowires which can be done using a larger X-ray beam spot size. During various *ex-situ* investigations, a gradual shift of the lattice parameters of both core and shell material with increasing shell thickness could be verified for the GaAs/InAs core-shell system [186] by doing symmetrical RSMs around the (111) Bragg reflections. Measuring the RSMs around an asymmetric set of Bragg reflections, the structure of the InP-(In,Ga)As core-shell system with varying shell composition was investigated [202]. Here, a phase separation of GaAs and (In,Ga)As was observed from the position of the Bragg peaks, together with the formation of a second set of facet orientations as seen from the facet-streaks.

Summarizing, several effects induced by the deposition of a heteroepitaxial shell were successfully be observed and distinguished by the high sensitivity of XRD both to the lattice and to the shape of the nanowires. These analyses already allowed gaining a better understanding of the resulting electro-optical properties of such core-shell structures and corresponding consequences to improve their fabrication. This understanding can now be even further improved by *in-situ* XRD investigations, which are capable of directly monitoring the temporal evolution of the structural changes during growth in order to derive the kinetics and dynamics of these processes.

2.4.3 *in-situ* X-ray diffraction of GaAs-(In,Ga)As core-shell nanowires

This section is partially based on results, which are going to be published as Ref. [203].

The preparation of the nanowire core sample for a subsequent *in-situ* XRD investigation of shell growth could be done in two different ways: Either by growing the nanowires in advance and re-loading them into the growth chamber or by directly growing them on a bare substrate during the experiment. Re-loading the nanowire sample has the advantage that the nanowire structure can be investigated by complementary methods like SEM, before it is covered by the shell layer. However, this bears the risk that the properties of the nanowires might change due to oxidation or other surface contamination. In contrast, if the whole process is done in one *in-situ* run, there is no risk of contamination but a residual uncertainty about the preceding

state of the core. In the end, it may depend on the reproducibility of the nanowire growth process, if an intermediate control by SEM is required.

If the whole process is done *in-situ* (ideally accompanied by an *in-situ* XRD measurement as described in Chap. 2), the growth conditions have to be adjusted after the nanowire core growth has been finished to enable epitaxial shell growth. In case of Ga-assisted VLS-growth, the Ga droplet located at the tip of the NW has to be consumed to suppress any further axial growth (see Fig. 22a for schematic representation). In case of GaAs nanowires, this is simply done by continuous As-supply at growth temperature after the Ga-flux has been stopped. The consumption can be closely observed by *in-situ* XRD or RHEED since the shrinkage of the droplet effectively means a change of growth conditions leading to highly faulted segments or a WZ segment on top of a GaAs nanowire which is mainly composed of ZB/TZB segments [55, 135, 149] (for HRTEM see 22b). Afterward, the growth conditions have to be adjusted to favor nucleation at the nanowire facets with respect to nucleation on the substrate. This is achieved by reducing the Ga-diffusion length via a lower substrate temperature and a higher V/III ratio compared to the preceding VLS growth of the NWs [16, 187].

During the fabrication of the heteroepitaxial shell, both a change of existing Bragg peaks (shift, broadening, shape change, etc.) and the appearance of new Bragg reflections may occur, depending on the material system. If all these changes in the diffraction pattern should be recorded, a relatively large range of angles needs to be covered. Because of this larger angular range, the time resolution of *in-situ* XRD during shell growth is not as high as during NW growth. However, since the shell growth takes place in vapor–solid mode without involving a liquid phase, it is possible to pause the growth process by interrupting the flux of the group III element. During that pause, both wide range scans and a re-aligning of short range scans can be realized. In this way, 3D RSMs around the Bragg peaks of interest can be recorded and subsequently be analyzed by selecting specific sections of this 3D reciprocal volume.

Here, the nanowire core growth is done as described in Sect. 2.3. Two different sets of nanowires are fabricated, having an average diameter of 50 nm (thin nanowires) and 120 nm (thick nanowires). For the shell growth, a V/III ratio $F_{V/III} \approx 4-7$, a substrate temperature $T_{\mathrm{Sub}} \approx 390-470°\mathrm{C}$ and fluxes corresponding to a Ga-limited 2D GaAs growth rate $R_{GaAs} \approx 90$ nm/h are set. As a shell material, different (In,Ga)As compositions are used. The lattice parameter varies continuously with the composition according to Vegard's law [204] from 0.5653 nm for pure GaAs to 0.6058 nm for pure InAs [205], introducing a tensile strain on GaAs. The substrate is not rotated during shell growth in order to investigate the effect of the resulting inhomogeneity on the microstructure in dependence on the nanowire core diameter.

Figure 23 shows sections along the $Q_y - Q_z$ plane at $Q_x = 0\,\mathrm{Å}^{-1}$ of 3D reciprocal space maps around the (111) and (311) Si Bragg peaks of GaAs nanowires and GaAs-(In,Ga)As core-shell structures on Si, respectively. The symmetric (111) RSM is easily measurable and suitable to derive the diameter and any tilt of the nanowire, i.e., properties of the shape. From the line profile (Fig. 23c), it can be seen that the GaAs ZB Bragg peak is shifted to lower Q_z after shell growth, corresponding to a strained core lattice parameter. However, the crystal phases cannot be fully sepa-

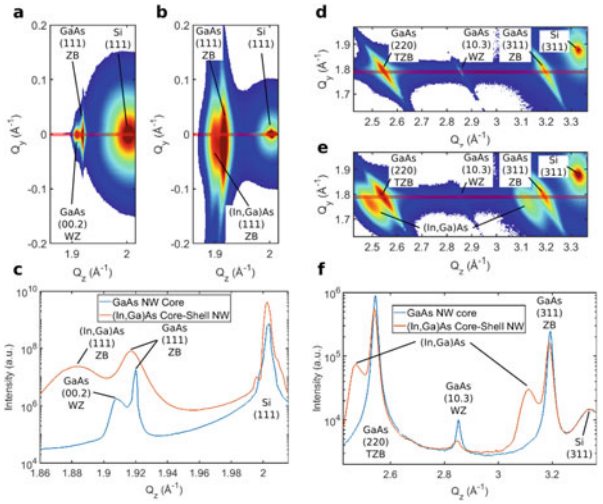

Fig. 23 Symmetric (a, b) and asymmetric (d, e) $Q_y - Q_z$ XRD reciprocal space maps recorded *in-situ* after growth of the nanowire core and the subsequent heteroepitaxial shell. The position of the corresponding line profiles (c, f) are indicated by the red lines in the RSMs

rated. Firstly, ZB and TZB are at the same position. Secondly, the (In,Ga)As peak is overlapping with the GaAs WZ peak which doesn't allow to draw conclusions regarding the behavior of the WZ phase. In contrast, the asymmetric set of Bragg peaks comprising the (311) Si, (311) ZB, (10.3) WZ, and (220) TZB provides a good separation of the occurring GaAs and (In,Ga)As crystal phases. As can be seen from Fig. 23d–f, additional (In,Ga)As peaks appear at the ZB and TZB positions after shell growth, while no (In,Ga)As peak forms at the position of the WZ phase. In order to derive more detailed results from the symmetric and asymmetric RSMs, the different peaks have to be treated individually by selecting corresponding regions of interest from the 3D RSM. Here, we will focus on the symmetric RSMs in order to analyze the effect of bending on the XRD pattern of core-shell nanowires.

The impact of the shell on the shape and crystal structure of the resulting heterostructure depends strongly on the diameter of the NW core. NWs with a small diameter are very sensitive to the properties of the shell. In Fig. 24, RSMs of the (111) Bragg reflections and corresponding SEM images of GaAs-$In_{0.15}Ga_{0.85}As$ core-shell NWs with different core diameters are shown. In case of the core-shell structure with a core diameter of 120 nm, the Bragg peak extends symmetrically along with both Q_y-directions.

In contrast, the Bragg peak of a core-shell structure with a core diameter of 50 nm is strongly distorted, in this particular case toward negative Q_y-values, which is attributed to a bending of the nanowires, caused by inhomogeneities during shell growth. Interestingly, the Bragg peaks of the different phases don't shift homogeneously. Instead, the WZ peak splits into two peaks with different magnitudes of shift whereas the ZB peak shifts as a whole without any splitting, while the amount of shift

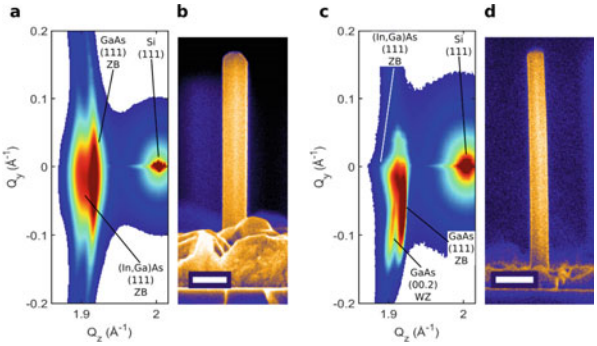

Fig. 24 Symmetric $Q_y - Q_z$ XRD reciprocal space maps (a,c) and SEM images (b,d) of thick, straight nanowire (left) and thin, bent GaAs-$In_{0.15}Ga_{0.85}As$ core-shell nanowire (right), respectively. Scale bar is 200 nm

lies in between the two WZ peaks. This is attributed to the particular arrangements of WZ and ZB segments (schematically shown at step 4 in Fig. 22a and evidenced by TEM as shown in Fig. 22b): WZ is located mainly at the bottom and at the top of the NW, whereas the middle section is composed of ZB/TZB segments. If now a circular bending of the NWs is assumed, this will generate two WZ peaks at different angles and one ZB peak at an intermediate angle. Simultaneously, epitaxial strain is shifting the position of the Bragg peak along Q_z. In order to separate the effects of strain and bending, and to derive the magnitude of bending on both perpendicular directions, the intensity distribution of the Bragg peak is analyzed on a sphere with a constant radius Q_r of

$$Q_r = \sqrt{Q_x^2 + Q_y^2 + Q_z^2}. \tag{38}$$

The evolution of the peak positions during growth is monitored, using scans with a smaller range and a larger step size to reach a time resolution of about 8 min/scan. This time-series of RSMs recorded during growth are used to follow the movement of the individual Bragg peaks (Fig. 25a–c, approximate peak positions marked by circles). All Bragg peaks shift to smaller values of Q_r, a signature of tensile strain caused by the (In,Ga)As shell growth. The strain ε is increasing for all segments along the NW similarly, up to a maximum value of approximately 0.03%.

In addition to the lattice parameter, the evolution of bending can be derived from the time-resolved *in-situ* XRD measurements. The tilt angle β follows the relation

$$\tan\beta = \frac{Q_y}{Q_z}. \tag{39}$$

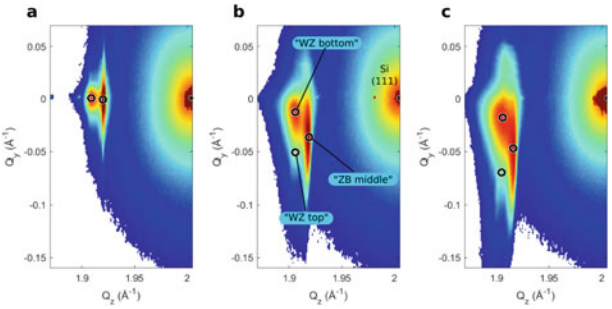

Fig. 25 Time-resolved *in-situ* XRD during shell growth. The evolution of the Bragg peak positions (marked by circles) evidences strain and bending of the nanowire core

If a constant curvature κ is assumed for the bending of the NW, this case described by a specific bending radius $r_0 = \kappa^{-1}$ and a bending angle α which are related by

$$\alpha = \kappa \cdot l, \tag{40}$$

where l is the final length of the NW as measured by SEM. The bending angle α is determined from the WZ Bragg peak attributed to the WZ segment at the top of the NW. Knowing the bending curvature κ, the tilt angle β measured by XRD can be used in order to calculate the approximate height h_i at which the segment is located which is giving rise to the Bragg peak. Example calculations are shown in Fig. 26a whereas the appearance of the nanowire at different stages of bending is visualized in Fig. 26b.

When looking only at the $Q_y - Q_z$ RSMs, it has to be taken into account that this plane actually represents a *projection* of the Bragg peak which can be shifted in both Q_x and Q_y. Figure 27a shows the symmetric $Q_y - Q_z$ RSM of GaAs-$In_{0.30}Ga_{0.70}As$ core-shell NWs with a core diameter of 50 nm, which are strongly bent. In this case, it is not possible to distinguish well separated Bragg peaks of different phases, but instead a broad intensity distribution spanning a wide angular range toward negative Q_y is observed. The intensity of this feature after integration over a range of $Q_r = 1.909 \pm 0.003\,\text{Å}^{-1}$ (indicated by white circular line in Fig. 27a) is displayed in Fig. 27b. The elongation of the peak is attributed to (I) a continuous change of β along the height of each NW and (II) an additional variation of angles in between different NWs of the probed ensemble. The peak spans a range of $\Delta Q_y \approx 0.1\,\text{Å}^{-1}$ and $\Delta Q_x \approx 0.15\,\text{Å}^{-1}$, which corresponds to a tilt of more than 5°. In order to exclude that the distortion of the peak is caused or affected by the experimental setup, the sample is manually rotated to four additional, approximately perpendicular directions (see inset of Fig. 27b). It is clear that the direction of the elongation is rotated as well. This is in agreement with the assumption that the distortion is a signature of the bending seen in SEM (see Fig. 24d). The elongation of the Bragg peak toward a specific direction evidences a preferred direction of bending determined by the setup of the growth chamber. In contrast, if we had the case of bending in random directions,

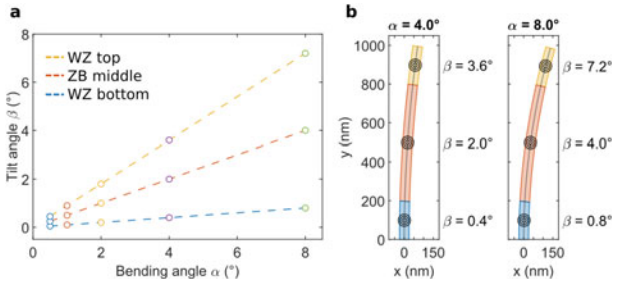

Fig. 26 Model calculations for circular bending of a nanowire with 1000 nm length and 50 nm diameter. **a** Behavior of tilt angles β on the bending angle α, stemming from segments at different heights along a polytypic nanowire. **b** Visualization of nanowire appearance for different bending angles

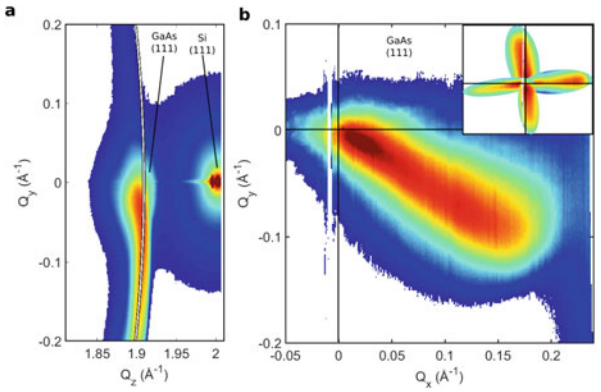

Fig. 27 **a** Symmetric $Q_y - Q_z$ RSM of bent GaAs-$In_{0.30}Ga_{0.70}As$ core-shell NWs showing a preferred direction of bending. The curved line indicates values with a constant Q_r which are used to create the $Q_x - Q_y$ RSM. **b** $Q_x - Q_y$ RSM obtained by integrating along the circle indicated in 27a. The correlation of the orientation of the Bragg peak with the NWs is evidenced by the rotation of the RSM (inset) when turning the sample

the width of the Bragg peak would increase concentrically around the peak, whose center would stay at the same position.

Finally, the amount of inhomogeneity required to cause the observed bending can be modeled. Since inhomogeneities in composition as well as in shell thickness cause similar bending behavior, it is not possible to distinguish between these two effects. However, it is possible to estimate the limits of these two contributions. We apply a simple 1D model as described in Ref. [198]. Within this model, the strain ε is described as

$$\varepsilon = \frac{a_0 - a}{a_0} + \frac{x}{r_0}, \tag{41}$$

where a is the actual lattice parameter, a_0 the unstrained lattice parameter, x the distance from the interface and r_0 the bending radius. As model dimensions, $d_{\text{core}} = 50\,\text{nm}$ and $d_{\text{core-shell}} = 70\,\text{nm}$ are set as determined by SEM. Now the In-content and the shell thickness are modified separately. In order to achieve the observed curvature, this 1D model estimates an In-excess of 9% if the shell thickness is considered to be homogeneous. If reversely the In-content is kept constant for the whole shell, a difference in shell thickness of 4 nm would be required. Even though the ratio of inhomogeneities in composition and thickness of the shell cannot be determined, these values represent the limits for each of these contributions.

In summary, both strain and bending of the nanowires can be derived from a shift of the Bragg peaks along all three dimensions. Additionally, the height-dependent tilt angle of the lattice planes allows analyzing the height distribution of different polytypic crystal phases. The time-resolved shift of individual Bragg peaks during the growth of core-shell nanowires could be monitored due to the high angular resolution of *in-situ* XRD. The X-ray spot size was chosen to be in the range of a few μm in order to probe the structural evolution of an ensemble of some 10^4 NWs which allows correlating growth conditions and average properties of the resulting heterostructure. For further reading, we refer to Ref. [203].

3 Outlook

3.1 in-situ X-ray diffraction of individual nanowires

The size of X-ray beams provided by synchrotron light sources is typically in the order of 10 to 1000 μm. This size is convenient if large ensembles of nanostructures are to be investigated, or even small, well-defined regular groups of nanostructures. Focusing optics such as Kirkpatrick-Baez (KB)-mirrors, Fresnel-Zone-Plates and compound-refractive-lenses allow to focus the X-ray beam down to sizes below 100 100 nm facilitating X-ray measurements of indiviudal nanowires [123, 174, 206].

The small beam size, together with piezo-stages allowing for sample alignment at nm precision, enable scanning X-ray diffraction (SXD) of nanostructures. In order to locate the nanowire, complementary techniques such as optical microscopy or X-ray fluorescence are typically implemented at the same beamline in order to be able to locate the nanowire of interest on the required nanometer scale. This way, structural information encoded in the Bragg peaks can be correlated to real-space information of the nanowires on the sample. The origin of the scattering signal can be attributed to individual nanowires, or even to different parts of the same wire, depending on beam size and positioning.

Further, the coherence properties of the X-ray beam allow for total coherent illumination of a nanowire, or parts of it. Coherent X-ray diffraction imaging (CDI) is requirement for phase-retrieval [207] and Bragg ptychograpy [208] aiming on solving the so-called phase problem in X-ray crystallography CDI revealed information on

structure, polytypism and stacking faults in single nanowires [128, 209–212], strain in core-shell NW [201, 213], bending [195, 214], and even allowed for a correlation of electrical and structural properties [214, 215]. The potential of ptychography for the structural investigation of individual nanowires is currently becoming apparent [216–218].

In contrast, applying these techniques to *in-situ* investigations during growth of individual nanowires is still very challenging and time consuming. This starts with the difficulty to locate the nanowire (which is located on a substrate inside a UHV system) with the X-ray beam spot, because commonly used complementary techniques like optical microscopy or X-ray fluorescence cannot be applied. Alternatively, the nanowire could be found by scanning the sample until a characteristic XRD pattern is observed. Tiny vibrations during this kind of scan, which is moving the whole UHV chamber, can already be sufficient to miss the nanowire. Changes in the substrate temperature will cause a drift in the micrometer range which makes it necessary to frequently verify the position of the nanowire until the drift has come to an end. During growth, the microstructure of the nanowire keeps evolving, which makes the use of ptychography effectively impossible if the sample changes during the scan duration, since this technique requires overlapping patterns from the *identical* sample state.

While the recent studies demonstrated the applicability and power of these methods for the analysis of individual nanowires, they showed at the same time that these nanowires often are true individuals, meaning they do not exhibit identical properties. Consequently, even though *in-situ* X-ray investigations of single nanowires are (like TEM) perfectly suited to observe physical effects and processes [219] or to correlate structural properties with complimentary electrical or elastic investigations, they provide only very limited insight into the average properties of larger ensembles, which would be required for a control of the growth conditions, since the neighboring nanowire could already exhibit a different behavior under nominally identical conditions. Additionally, in order to freely access an individual nanowire for investigation, it has to be located at an isolated position, without any nanowires in the close environment. This means the nanowire experiences growth conditions which are vastly different from the conditions inside a dense array of nanowires [135, 220–222].

In the future, the advent of fourth generation synchrotron sources and advances of scanning and imaging optics (enabling, e.g., *in-situ* full-field diffraction X-ray microscopy in combination with growth equipment) may prove to reduce the current technical limitations, but the fundamental limitations of the significance of results obtained on individual nanowires for larger ensembles of nanowires will remain.

3.2 *in-situ X-ray diffraction of small ensembles defined by substrate patterning*

An alternative approach, representing an intermediate path between individual nanowires and randomly distributed large ensembles is the investigation of regular arrays of nanowires on patterned substrates. In this case, regular hole patterns are prepared into a thick silicon oxide layer to reach the crystalline silicon. Due to the low sticking coefficient of Ga on such thick oxide, the nanowires will grow only inside these holes [222–225].

Such pattern provides the advantage of a well defined and realistic environment, identical to the conditions which will be used to prepare nanowires for further processing toward applications. Additionally, a systematic variation of the characteristic properties of the pattern (such as hole size and distance) allows comparing the effect of the growth conditions on all these different types of patterns without having to fabricate the corresponding number of samples. Additionally, it is assured that the nominal growth conditions like material flux and substrate temperature are identical for the different patterns, which excludes uncertainties which occur when comparing results obtained from growth experiments on different substrates.

The typical array size in the range of $100 \times 100\,\mu m^2$ strongly relaxes the constraints of a nanobeam and single nanowire preparation. In fact, the currently available beam spot size and scanning resolution of the heavy load goniometers already provide a good resolution for such experiments.

In order to locate the nanowire pattern for XRD, the sample is brought to a position where the X-ray beam spot approximately hits the center of the sample. The scan range needs to cover the whole sample size to scan for the sample edges. In the next step, the position of the individual patterns has to be found using markers on the sample at different length scales. However, since the nanowire growth takes place in a UHV environment at high temperature, typical markers made from organic precursors or metal cannot be used, since these would interfere with the growth or even cause contamination of the UHV environment. One possibility which avoids these risks is to etc.h additional regions as markers into the SiO_x during the preparation of the hole patterns. If the *in-situ* experiment is going to be done on pre-grown nanowire samples (compare Sect. 2.4), nanowire structures will have grown in the marker regions as well so that their characteristic Bragg peaks provide a guidance (see Fig. 28). When starting with a bare substrate, the absorption of X-rays in the thick SiO_x layer causes discernible *intensity* variations of the Si Bragg peaks between patterned and non-patterned regions allowing to identify them, eve without any GaAs signal.

Currently, *in-situ* investigations on nanowire arrays are indeed possible, but the temporal resolution is still very limited. Scanning the UHV chamber using the motors of the heavy load goniometer causes vibrations which have to decay before the XRD measurement can be started. Additionally, the movement of the motors is relatively slow. Under these conditions, *in-situ* experiments require a very long time. There are different possibilities to overcome these limitations.

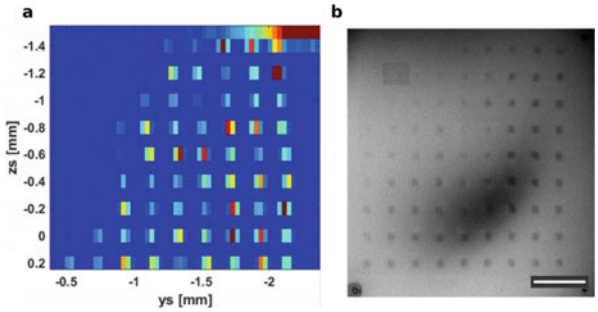

Fig. 28 Reprinted figure from Ref. [226] with the author's permission. **a** x-y mapping using the GaAs Bragg peak in order to locate patterned regions. **b** SEM image of patterned regions, scale bar is 400 μm

Firstly, suitable X-ray optics could be implemented at a synchrotron beamline in combination with an *in-situ* MBE, which allows scanning the X-ray beam spot across the sample surface instead of having to move the whole UHV system. This will reduce the time required for the location of the patterns from hours to minutes and increase the time resolution during *in-situ* scans from minutes to seconds.

Secondly, the upgrade to fourth generation synchrotron sources will improve the temporal and spatial resolution. They are much smaller X-ray beam spot will make additional focusing optics dispensable which both reduces the beam divergence and increases the X-ray photon flux.

With these technical improvements, time-resolved *in-situ* high-resolution XRD investigations will become feasible and allow monitoring growth processes of statistical meaningful ensembles of nanowire arrays growing under application-relevant conditions, thereby leading to a better understanding of these complex mechanisms.

References

1. J. Xiang, L. Wei, H. Yongjie, W. Yue, H. Yan, C.M. Lieber, Ge/Si nanowire heterostructures as high-performance field-effect transistors. Nature **441**(7092), 489–493 (2006). May
2. O. Hayden, R. Agarwal, W. Lu, Semiconductor nanowire devices. Nano Today, **3**(5–6), 12–22 (2008)
3. C.M. Lieber, Semiconductor nanowires: a platform for nanoscience and nanotechnology. MRS Bull. **36**(12), 1052–1063 (2011)
4. N.P. Dasgupta, J. Sun, C. Liu, S. Brittman, S.C. Andrews, J. Lim, H. Gao, R. Yan, P. Yang, 25th anniversary article: semiconductor nanowires synthesis, characterization, and applications. Adv. Mater. **26**(14), 2137–2184 (2014)
5. T.E. Kazior, Beyond CMOS: heterogeneous integration of III-V devices, RF MEMS and other dissimilar materials/devices with Si CMOS to create intelligent microsystems. Philos. Trans. Roy. Soc. A—Math. Phys. Eng. Sci. **372**(2012), (2014)
6. T. Bryllert. L.E. Wernersson, L.E. Froberg, L. Samuelson, Vertical high-mobility wrap-gated InAs nanowire transistor. IEEE Electron Device Lett. **27**(5), 323–325 (2006)

7. K. Tomioka, T. Tanaka, S. Hara, K. Hiruma, T. Fukui, III–V nanowires on Si substrate: selective-area growth and device applications. IEEE J. Sel. Top. Quantum Electron. **17**(4), 1112–1129 (2011)
8. K. Tomioka, M. Yoshimura, T. Fukui, A III–V nanowire channel on silicon for high-performance vertical transistors. Nature **488**(7410), 189–192 (2012). August
9. K. Tomioka, T. Fukui, Recent progress in integration of III–V nanowire transistors on Si substrate by selective-area growth. J. Phys. D-Appl. Phys. **47**(39, SI), (2014)
10. X. Miao, K. Chabak, C. Zhang, P.K. Mohseni, D. Walker, Jr., X. Li, High-speed planar GaAs nanowire arrays with f(max) > 75 GHz by wafer-scale bottom-up growth. Nano Lett. **15**(5), 2780–2786 (2015)
11. Y. Xiangfeng Duan, R.A. Huang, C.M. Lieber, Single-nanowire electrically driven lasers. Nature **421**(6920), 241–245 (2003). January
12. K. Tomioka, J. Motohisa, S. Hara, K. Hiruma, T. Fukui, GaAs/AlGaAs core multishell nanowire-based light-emitting diodes on Si. Nano Lett. **10**(5), 1639–1644 (2010)
13. R. Chen, T.-T.D. Tran, K.W. Ng, W.S. Ko, L.C. Chuang, F.G. Sedgwick, C. Chang-Hasnain, Nanolasers grown on silicon. Nat. Photonics **5**(3), 170–175 (2011)
14. M.E. Reimer, G. Bulgarini, N. Akopian, M. Hocevar, M.B. Bavinck, M.A. Verheijen, E.P.A.M. Bakkers, L.P. Kouwenhoven, V. Zwiller, Bright single-photon sources in bottom-up tailored nanowires. Nat. Commun. **3**, 737 (2012)
15. D. Saxena, S. Mokkapati, P. Parkinson, N. Jiang, Q. Gao, H.H. Tan, C. Jagadish, Optically pumped room-temperature GaAs nanowire lasers. Nat. Photonics **7**(12), 963–968 (2013)
16. E. Dimakis, U. Jahn, M. Ramsteiner, A. Tahraoui, J. Grandal, X. Kong, O. Marquardt, A. Trampert, H. Riechert, L. Geelhaar, Coaxial multishell (In,Ga)As/GaAs nanowires for near-infrared emission on Si substrates. Nano Lett. **14**(5), 2604–2609 (2014)
17. R. Chen, K.W. Ng, W.S. Ko, D. Parekh, F. Lu, T.-T.D. Tran, K. Li, C. Chang-Hasnain, Nanophotonic integrated circuits from nanoresonators grown on silicon. Nat. Commun. **5** (2014)
18. B. Tian, X. Zheng, T.J. Kempa, Y. Fang, Yu. Nanfang, Yu. Guihua, J. Huang, C.M. Lieber, Coaxial silicon nanowires as solar cells and nanoelectronic power sources. Nature **449**(7164), 885–889 (2007). October
19. C. Colombo, M. Heiss, M. Graetzel, A. Fontcuberta i Morral. Gallium arsenide p-i-n radial structures for photovoltaic applications. Appl. Phys. Lett. **94**(17) (2009)
20. P. Krogstrup, H.I. Jorgensen, M. Heiss, O. Demichel, J.V. Holm, M. Aagesen, J. Nygard, A. Fontcuberta i Morral, Single-nanowire solar cells beyond the Shockley-Queisser limit. Nat. Photonics **7**(4), 306–310 (2013)
21. M. Heiss, E. Russo-Averchi, A. Dalmau-Mallorqui, G. Tuetuencueoglu, F. Matteini, D. Rueffer, S. Conesa-Boj, O. Demichel, E. Alarcon-Llado, A. Fontcuberta i Morral, III–V nanowire arrays: growth and light interaction. Nanotechnology **25**(1, SI) (2014)
22. G. Otnes, M.T. Borgstrom, Towards high efficiency nanowire solar cells. Nano Today **12**, 31–45 (2017)
23. J. Cartwright, Qubit in a nanowire. Nat. News (2010)
24. V. Mourik, K. Zuo, S.M. Frolov, S.R. Plissard, E.P.A.M. Bakkers, L.P. Kouwenhoven, Signatures of majorana fermions in hybrid superconductor-semiconductor nanowire devices. Science **336**(6084), 1003–1007 (2012)
25. S. Gazibegovic, D. Car, H. Zhang, S.C. Balk, J.A. Logan, M.W.A. de Moor, M.C. Cassidy, R. Schmits, D. Xu, G. Wang, P. Krogstrup, R.L.M. Op het Veld, K. Zuo, Y. Vos, J. Shen, D. Bouman, B.S. Hojaei, D. Pennachio, J.S. Lee, P.J. van Veldhoven, S. Koelling, M.A. Verheijen, L.P. Kouwenhoven, C.J. Palmstrom, E.P.A.M. Bakkers, Epitaxy of advanced nanowire quantum devices. Nature **548**(7668), 434+ (2017)
26. A.I. Hochbaum, R. Chen, R.D. Delgado, W. Liang, E.C. Garnett, M. Najarian, A. Majumdar, P. Yang, Enhanced thermoelectric performance of rough silicon nanowires. Nature **451**(7175), 163–167 (2008)
27. Y. Cui, Q. Wei, H. Park, C.M. Lieber, Nanowire nanosensors for highly sensitive and selective detection of biological and chemical species. Science **293**(5533), 1289–1292 (2001). August

28. E. Stern, J.F. Klemic, D.A. Routenberg, P.N. Wyrembak, D.B. Turner-Evans, A.D. Hamilton, D.A. LaVan, T.M. Fahmy, M.A. Reed, Label-free immunodetection with CMOS-compatible semiconducting nanowires. Nature **445**(7127), 519–522 (2007). February
29. P.K. Sahoo, R. Janissen, M.P. Monteiro, A. Cavalli, D.M. Murillo, M.V. Merfa, C.L. Cesar, H.F. Carvalho, A.A. de Souza, E.P.A.M. Bakkers, M.A. Cotta, Nanowire arrays as cell force sensors to investigate adhesin-enhanced holdfast of single cell bacteria and biofilm stability. Nano Lett. **16**(7), 4656–4664 (2016)
30. P. Schroth. Growth of self-catalyzed GaAs nanowires using molecular-beam-epitaxy and structural characterization by in-situ X-ray diffraction. Dissertation, Universität Siegen, 2016
31. A. Biermanns, E. Dimakis, A. Davydok, T. Sasaki, L. Geelhaar, M. Takahasi, U. Pietsch, Role of liquid indium in the structural purity of wurtzite inas nanowires that grow on si(111). Nano Letters **14**(12), 6878–6883 (2014)
32. M. Koguchi, H. Kakibayashi, M. Yazawa, K. Hiruma, T. Katsuyama, Crystal structure change of GaAs and InAs whiskers from zinc-blende to wurtzite type. Jpn. J. Appl. Phys. **31**(7R), 2061 (1992). July
33. G.E. Cirlin, V.G. Dubrovskii, I.P. Soshnikov, N.V. Sibirev, Y.B. Samsonenko, A.D. Bouravleuv, J.C. Harmand, F. Glas, Critical diameters and temperature domains for mbe growth of iii–v nanowires on lattice mismatched substrates. Physica Status Solidi (RRL)—Rapid Research Letters **3**(4), 112–114 (2009)
34. D.S. Oliveira, L.H.G. Tizei, D. Ugarte, M.A. Cotta, Spontaneous periodic diameter oscillations in inp nanowires: the role of interface instabilities. Nano Lett. **13**(1), 9–13 (2013). PMID: 23205668
35. S. Breuer, Molecular beam epitaxy of GaAs nanowires and their suitability for optoelectronic applications. Dissertation, Humboldt-Universität zu Berlin, 2011
36. A. Biermanns. X-ray diffraction from single GaAs nanowires. Dissertation, Universität Siegen, 2012
37. M. Köhl. Analysis of nanostructures based on diffraction of X-ray radiation. Dissertation, Karlsruhe Institute of Technology, 2014
38. N.W. Ashcroft, N.D. Mermin. Festkörperphysik. Oldenbourg Wissenschaftsverlag, 2007
39. C. Kittel, S. Hunklinger, Einführung in die Festkörperphysik. Oldenbourg Wissenschaftsverlag, 2013
40. C.-Yu Yeh, Z.W. Lu, S. Froyen, A. Zunger, Zinc-blende-wurtzite polytypism in semiconductors. Phys. Rev. B **46**, 10086–10097 (1992)
41. C. Panse, D. Kriegner, F. Bechstedt, Polytypism of GaAs, InP, InAs, and InSb: an ab initio study. Phys. Rev. B **84**(7), 075217 (2011). August
42. M. Tchernycheva, J.C. Harmand, G. Patriarche, L. Travers, G.E. Cirlin, Temperature conditions for gaas nanowire formation by au-assisted molecular beam epitaxy. Nanotechnology **17**(16), 4025 (2006)
43. S.O. Mariager, S.L. Lauridsen, C.B. Sörensen, A. Dohn, P.R. Willmott, J. Nygård, R. Feidenhansl, Stages in molecular beam epitaxy growth of gaas nanowires studied by x-ray diffraction. Nanotechnology **21**(11), 115603 (2010)
44. M.I. McMahon, R.J. Nelmes, Observation of a wurtzite form of gallium arsenide. Phys. Rev. Lett. **95**, 215505 (2005). Nov
45. A. Biermanns, S. Breuer, A. Davydok, L. Geelhaar, U. Pietsch, Structural evolution of self-assisted gaas nanowires grown on si(111). Physica Status Solidi (RRL)—Rapid Research Letters **5**(4), 156–158 (2011)
46. D. Jacobsson, F. Yang, K. Hillerich, F. Lenrick, S. Lehmann, D. Kriegner, J. Stangl, L.R. Wallenberg, K.A. Dick, J. Johansson. Phase transformation in radially merged wurtzite GaAs nanowires. Cryst. Growth Des. **15**(10), 4795–4803 (2015)
47. V.G. Dubrovskii, *Nucleation Theory and Growth of Nanostructures* (NanoScience and Technology. Berlin, Heidelberg, 2014)
48. A.I. Persson, M.W. Larsson, S. Stenström, B.J. Ohlsson, L. Samuelson, L.R. Wallenberg, Solid-phase diffusion mechanism for GaAs nanowire growth. Nat. Mater. **3**(10), 677–681 (2004)

49. K.A. Dick, P. Caroff, J. Bolinsson, M.E. Messing, J. Johansson, K. Deppert, L.R. Wallenberg, L. Samuelson, Control of III–V nanowire crystal structure by growth parameter tuning. Semicond. Sci. Technol. **25**(2), 024009 (2010)
50. E. Dimakis, J. Lahnemann, U. Jahn, S. Breuer, M. Hilse, L. Geelhaar, H. Riechert, Self-assisted nucleation and Vapor-Solid growth of InAs nanowires on bare si(111). Cryst. Growth Des. **11**(9), 4001–4008 (2011). September
51. K.A. Dick, J. Bolinsson, M.E. Messing, S. Lehmann, J. Johansson, P. Caroff, Parameter space mapping of InAs nanowire crystal structure. J. Vac. Sci. Technol. B **29**(4), 04D103 (2011). July
52. T. Akiyama, K. Sano, K. Nakamura, T. Ito, An empirical potential approach to wurtzite-zinc-blende polytypism in group III–V semiconductor nanowires. Jpn. J. Appl. Phys. **45**(9), L275–L278 (2006)
53. R. Magri, M. Rosini, F. Casetta, Structural stability of clean GaAs nanowires grown along the [111] direction. Physica Status Solidi C **7**(2), 374–377 (2010)
54. M. Rosini, R. Magri, Surface effects on the atomic and electronic structure of unpassivated GaAs nanowires. ACS Nano **4**(10), 6021–6031 (2010). October
55. T. Rieger, M.I. Lepsa, T. Schäpers, D. Grützmacher, Controlled wurtzite inclusions in self-catalyzed zinc blende III–V semiconductor nanowires. J. Cryst. Growth **378**, 506–510 (2013)
56. J. Johansson, L.S. Karlsson, K.A. Dick, J. Bolinsson, B.A. Wacaser, K. Deppert, L. Samuelson, Effects of supersaturation on the crystal structure of gold seeded III–V nanowires. Cryst. Growth Des. **9**(2), 766–773 (2009). February
57. P. Krogstrup, S. Curiotto, E. Johnson, M. Aagesen, J. Nygård, D. Chatain, Impact of the liquid phase shape on the structure of III–V nanowires. Phys. Rev. Lett. **106**, 125505 (2011). Mar
58. F. Glas, J.-C. Harmand, G. Patriarche, Why does wurtzite form in nanowires of III–V zinc blende semiconductors? Phys. Rev. Lett. **99**(14), 146101 (2007). October
59. S. Breuer, L.-F. Feiner, L. Geelhaar, Droplet bulge effect on the formation of nanowire side facets. Cryst. Growth Des. **13**(7), 2749–2755 (2013)
60. M. Schmidbauer, *X-Ray Diffuse Scattering from Self-Organized Mesoscopic Semiconductor Structures* (Springer Tracts in Modern Physics. Springer, Berlin Heidelberg, Berlin, Heidelberg, 2004)
61. U. Pietsch, V. Holy, T. Baumbach, *High-Resolution X-Ray Scattering: From Thin Films to Lateral Nanostructures* (Advanced Texts in Physics. Springer, New York, 2004)
62. D. Grigoriev, S. Lazarev, P. Schroth, A.A. Minkevich, M. Köhl, T. Slobodskyy, M. Helfrich, D.M. Schaadt, T. Aschenbrenner, D. Hommel, T. Baumbach, Asymmetric skew X-ray diffraction at fixed incidence angle: application to semiconductor nano-objects. J. Appl. Crystallogr. **49**(3), 961–967 (2016). Jun
63. J.M. Cowley, *Diffraction Physics* (Elsevier Science B.V., 1995)
64. V. Holý, J. Stangl, S. Zerlauth, G. Bauer, N. Darowski, D. Luebbert, U. Pietsch, Lateral arrangement of self-assembled quantum dots in an sige/si superlattice. J. Phys. D: Appl. Phys. **32**(10A), A234 (1999)
65. T. Baumbach, D. Luebbert, M. Gailhanou, Strain relaxation in surface nano-structures studied by x-ray diffraction methods. Jpn. J. Appl. Phys. **38**(12R), 6591 (1999)
66. M. Schmidbauer, S. Seydmohamadi, D. Grigoriev, Z.M. Wang, Y.I. Mazur, P. Schaefer, M. Hanke, R. Köhler, G.J. Salamo, Controlling planar and vertical ordering in three-dimensional (in, ga)as quantum dot lattices by gaas surface orientation. Phys. Rev. Lett. **96**, 066108 (2006)
67. M. Schmidbauer, P. Schaefer, S. Besedin, D. Grigoriev, R. Köhler, M. Hanke, A novel multi-detection technique for 3d reciprocal space mapping in grazing incidence x-ray diffraction. J. Synchrotron Rad. **15**(6), 549–57 (2008)
68. V. Holý, K. Mundboth, C. Mokuta, T.H. Metzger, J. Stangl, G. Bauer, T. Boeck, M. Schmidbauer, Structural characterization of self-assembled semiconductor islands by three-dimensional x-ray diffraction mapping in reciprocal space. Thin Solid Films **516**(22), 8022–8028 (2008). Sep
69. H. Heinke, V. Kirchner, S. Einfeldt, D. Hommel, X-ray diffraction analysis of the defect structure in epitaxial gan. Appl. Phys. Lett **77**(14), 2145–2149 (2000)

70. M.A. Moram, C.F. Johnston, J.L. Hollander, M.J. Kappers, C.J. Humphreys, Understanding x-ray diffraction of nonpolar gallium nitride films. J. Appl. Phys. **105**, 113501 (2009)
71. V.M. Kaganer, O. Brandt, A. Trampert, K.H. Ploog, X-ray diffraction peak profiles from threading dislocations in gan epitaxial films. Phys. Rev. B **72**, 264 (2005)
72. J. Haertwig. X-ray diffraction in the extremely asymmetric laue case with a small angle between the crystal surface and the incident beam. Physica Status Solidi A **42**, 495 (1977)
73. H.R. Hoche, O. Brummer, J. Nieber, Extremely skew x-ray diffraction. Acta Crystallographica Section A: Foundations of Crystallogr. **42**(6), 585–587 (1986)
74. S. Stepanov, R. Kohler, A dynamical theory of extremely asymmetric x-ray diffraction taking account of normal lattice strain. J. Phys. D: Appl. Phys. **27**(9), 1922 (1994)
75. V. Bushuev, A. Oreshko, X-ray specular reflection under conditions of extremely asymmetric noncoplanar diffraction from a bicrystal. Crystallogr. Rep. **48**, 180–186 (2003)
76. H.-G. Bruel, T. Baumbach, V. Gottschlach, U. Pietsch, Extreme asymmetric x-ray bragg reflection of semiconductor heterostructures near the edge of total external reflection. J. Appl. Cryst **23**, 228–233 (1990)
77. H.R. Ress, W. Faschinger, G. Landwehr, Depth-dependent x-ray diffraction using extremely asymmetric reflections. J. Phys. D: Appl. Phys. **31**, 3272 (1998)
78. E. Vlieg, Integrated intensities using a six-circle surface X-ray diffractometer. J. Appl. Crystallogr. **30**(5 Part 1), 532–543 (1997)
79. E. Vlieg, A (2+3)-type surface diffractometer: mergence of the z-axis and (2+2)-type geometries. J. Appl. Crystallogr. **31**(2), 198–203 (1998). Apr
80. C.M. Schleputz, S.O. Mariager, S.A. Pauli, R. Feidenhans'l, P.R. Willmott, Angle calculations for a (2+ 3)-type diffractometer: focus on area detectors. J. Appl. Crystallogr. **44**(1), 73–83 (2010)
81. P.H. Fuoss, I.K. Robinson, Apparatus for x-ray diffraction in ultrahigh vacuum. Nucl. Instrum. Methods Phys. Res. **222**(1), 171–176 (1984)
82. S. Ibrahimkutty, A. Seiler, T. Prüßmann, T. Vitova, R. Pradip, O. Bauder, P. Wochner, A. Plech, T. Baumbach, S. Stankov, A portable ultrahigh-vacuum system for advanced synchrotron radiation studies of thin films and nanostructures: $EuSi_2$ nano-islands. J. Synchrotron Radiat. **22**(1), 91–98 (2015). Jan
83. T. Tsuchiya, T. Taniwatari, K. Uomi, T. Kawano, Y. Ono. In-situ x-ray monitoring in movpe and feedback growth of strained ingaas, in *LEOS 1992 Summer Topical Meeting Digest on Broadband Analog and Digital Optoelectronics, Optical Multiple Access Networks, Integrated Optoelectronics, and Smart Pixels* (1992), pp. 646–649
84. R. Döhrmann, S. Botta, A. Buffet, G. Santoro, K. Schlage, M. Schwartzkopf, S. Bommel, J.F.H. Risch, R. Mannweiler, S. Brunner, E. Metwalli, P. Müller-Buschbaum, S.V. Roth, A new highly automated sputter equipment for in situ investigation of deposition processes with synchrotron radiation. Rev. Sci. Instrum. **84**(4), 043901 (2013)
85. B. Krause, S. Darma, M. Kaufholz, H.-H. Gräfe, S. Ulrich, M. Mantilla, R. Weigel, S. Rembold, T. Baumbach, Modular deposition chamber for in situ X-ray experiments during RF and DC magnetron sputtering. J. Synchrotron Radiat. **19**(2), 216–222 (2012). Mar
86. S. Couet, T. Diederich, K. Schlage, R. Roehlsberger, A compact UHV deposition system for in situ study of ultrathin films via hard x-ray scattering and spectroscopy. Rev. Sci. Instrum. **79**(9) (2008)
87. J.R. Arthur, Molecular beam epitaxy. Surf. Sci. **500**(1–3), 189–217 (2002)
88. M. Albrecht, H. Antesberger, W. Moritz, H. Plockl, M. Sieber, D. Wolf, Six-circle diffractometer for surface diffraction using an in-vacuum x-ray detector. Rev. Sci. Instrum. **70**(8), 3239–3243 (1999)
89. R. Baudoing-Savois, M. De Santis, M.C. Saint-Lager, P. Dolle, O. Geaymond, P. Taunier, P. Jeantet, J.P. Roux, G. Renaud, A. Barbier, O. Robach, O. Ulrich, A. Mougin, G. Berard, A new UHV diffractometer for surface structure and real time molecular beam deposition studies with synchrotron radiations at ESRF. Nucl. Instrum. Methods Phys. Res. Section B-Beam Interact. Mater. Atoms **149**(1–2), 213–227 (1999)

90. P. Bernard, K. Peters, J. Alvarez, S. Ferrer, Ultrahigh vacuum high pressure chamber for surface x-ray diffraction experiments. Rev. Sci. Instrum. **70**(2), 1478–1480 (1999)
91. M. Takahasi, Y. Yoneda, H. Inoue, N. Yamamoto, J. Mizuki, X-ray diffractometer for studies on molecular-beam-epitaxy growth of III–V semiconductors. Jpn. J. Appl. Phys. **41**(10R), 6247 (2002)
92. B. Jenichen, W. Braun, V.M. Kaganer, A.G. Shtukenberg, L. Daweritz, C.G. Schulz, K.H. Ploog, A. Erko, Combined molecular beam epitaxy and diffractometer system for in situ X-ray studies of crystal growth. Rev. Sci. Instrum. **74**(3, 1), 1267–1273 (2003)
93. S. Stankov, R. Rüffer, M. Sladecek, M. Rennhofer, B. Sepiol, G. Vogl, N. Spiridis, T. Slezak, J. Korecki, An ultrahigh vacuum system for in situ studies of thin films and nanostructures by nuclear resonance scattering of synchrotron radiation. Rev. Sci. Instrum. **79**(4), 045108 (2008)
94. H. Tajiri, K. Sumitani, S. Nakatani, T. Takahashi, K. Akimoto, H. Sugiyama, X. Zhang, H. Kawata. Sample holder assembly covering a wide range of temperatures for surface X-ray diffraction. Appl. Surf. Sci. **237**(1–4), 645–648 (2004); *7th International Symposium on Atomically Controlled Surfaces, Interfaces and Nanostructures* (Nara, JAPAN, 16–20 Nov, 2003)
95. E. Vlieg, A. Van't Ent, A.P. De Jongh, H. Neerings, J.F. Van Der Veen. An ultrahigh-vacuum chamber for surface X-ray diffraction combined with MBE. Nucl. Instrum. Methods Phys. Res. Section A-Accelerators Spectrometers Detectors and Associated Equipment **262**(2–3), 522–527 (1987)
96. P.M.J. Marée, A.P. De Jongh, J.W. Derks, J.F. Van Der Veen, A system for MBE growth and high-resolution RBS analysis. Nucl. Instrum. Methods Phys. Res. Section B-Beam Interact. Mater. Atoms **28**(1), 76–81 (1987)
97. T. Slobodskyy, P. Schroth, D. Grigoriev, A.A. Minkevich, D.Z. Hu, D.M. Schaadt, T. Baumbach, A portable molecular beam epitaxy system for in situ x-ray investigations at synchrotron beamlines. Rev. Sci. Instrum. **83**(10) (2012)
98. P. Schroth, M. Köhl, J.-W. Hornung, E. Dimakis, C. Somaschini, L. Geelhaar, A. Biermanns, S. Bauer, S. Lazarev, U. Pietsch, T. Baumbach, Evolution of polytypism in gaas nanowires during growth revealed by time-resolved in situ x-ray diffraction. Phys. Rev. Lett. **114**, 055504 (2015). Feb
99. F. Glas, Critical dimensions for the plastic relaxation of strained axial heterostructures in free-standing nanowires. Phys. Rev. B **74**, 121302 (2006). Sep
100. K.L. Kavanagh, Misfit dislocations in nanowire heterostructures. Semicond. Sci. Technol. **25**(2), 024006 (2010). February
101. X. Zhang, V.G. Dubrovskii, N.V. Sibirev, X. Ren, Analytical study of elastic relaxation and plastic deformation in nanostructures on lattice mismatched substrates. Cryst. Growth Des. **11**(12), 5441–5448 (2011). December
102. J. Bao, D.C. Bell, F. Capasso, J.B. Wagner, T. Mårtensson, J. Trägårdh, L. Samuelson, Optical properties of rotationally twinned InP nanowire heterostructures. Nano Lett. **8**(3), 836–841 (2008). March
103. D. Spirkoska, J. Arbiol, A. Gustafsson, S. Conesa-Boj, F. Glas, I. Zardo, M. Heigoldt, M.H. Gass, A.L. Bleloch, S. Estrade, M. Kaniber, J. Rossler, F. Peiro, J.R. Morante, G. Abstreiter, L. Samuelson, A. Fontcuberta i Morral, Structural and optical properties of high quality zinc-blende/wurtzite GaAs nanowire heterostructures. Phys. Rev. B **80**(24), 245325 (2009)
104. M. Hjort, S. Lehmann, J. Knutsson, R. Timm, D. Jacobsson, E. Lundgren, K.A. Dick, A. Mikkelsen, Direct imaging of atomic scale structure and electronic properties of GaAs wurtzite and zinc blende nanowire surfaces. Nano Lett. **13**(9), 4492–4498 (2013). September
105. R.S. Wagner, W.C. Ellis, Vapor-liquid-solid mechanism of single crystal growth. Appl. Phys. Lett. **4**(5), 89–90 (1964)
106. M. Moseler, F. Cervantes-Sodi, S. Hofmann, G. Csányi, A.C. Ferrari, Dynamic catalyst restructuring during carbon nanotube growth. ACS Nano **4**(12), 7587–7595 (2010)
107. A.D. Gamalski, C. Ducati, S. Hofmann, Cyclic supersaturation and triple phase boundary dynamics in germanium nanowire growth. The J. Phys. Chem. C **115**(11), 4413–4417 (2011)

108. V.G. Dubrovskii, G.E. Cirlin, N.V. Sibirev, F. Jabeen, J.C. Harmand, P. Werner, New mode of vapor-liquid-solid nanowire growth. Nano Lett. **11**(3), 1247–1253 (2011). PMID: 21344916
109. A.D. Gamalski, J. Tersoff, R. Sharma, C. Ducati, S. Hofmann, Metastable crystalline auge catalysts formed during isothermal germanium nanowire growth. Phys. Rev. Lett. **108**, 255702 (2012). Jun
110. P. Caroff, K.A. Dick, J. Johansson, M.E. Messing, K. Deppert, L. Samuelson, Controlled polytypic and twin-plane superlattices in III–V nanowires. Nat. Nanotechnol. **4**(1), 50–55 (2009). January
111. J. Johansson, K.A. Dick, P. Caroff, M.E. Messing, J. Bolinsson, K. Deppert, L. Samuelson, Diameter dependence of the Wurtzite-Zinc blende transition in InAs nanowires. The J. Phys. Chem. C **114**(9), 3837–3842 (2010). March
112. C.-Y. Wen, J. Tersoff, K. Hillerich, M.C. Reuter, J.H. Park, S. Kodambaka, E.A. Stach, F.M. Ross, Periodically changing morphology of the growth interface in si, ge, and GaP nanowires. Phys. Rev. Lett. **107**(2), 025503 (2011). July
113. R.E. Algra, M.A. Verheijen, M.T. Borgström, L. Feiner, G. Immink, W.J.P. van Enckevort, E. Vlieg, E.P.A.M. Bakkers, Twinning superlattices in indium phosphide nanowires. Nature **456**(7220), 369–372 (2008)
114. H.J. Joyce, J. Wong-Leung, Q. Gao, H. Hoe Tan, C. Jagadish. Phase perfection in zinc blende and wurtzite III-V nanowires using basic growth parameters. Nano Lett. **10**(3), 908–915 (2010)
115. J. Johansson, L.S. Karlsson, C. Patrik, T. Svensson, T. Mårtensson, B.A. Wacaser, K. Deppert, L. Samuelson, W. Seifert, Structural properties of 111 111, b-oriented III–V nanowires. Nat. Mater. **5**(7), 574–580 (2006)
116. V.G. Dubrovskii, N.V. Sibirev, J.C. Harmand, F. Glas, Growth kinetics and crystal structure of semiconductor nanowires. Phys. Rev. B **78**, 235301 (2008). Dec
117. J. Johansson, J. Bolinsson, M. Ek, P. Caroff, K.A. Dick, Combinatorial approaches to understanding polytypism in III–V nanowires. ACS Nano **6**(7), 6142–6149 (2012)
118. P. Caroff, J. Bolinsson, J. Johansson, Crystal phases in III–V nanowires: from random toward engineered polytypism. IEEE J. Select. Top. Quantum Electron. **17**(4), 829–846 (2011)
119. D. Kriegner, C. Panse, B. Mandl, K.A. Dick, M. Keplinger, J.M. Persson, P. Caroff, D. Ercolani, L. Sorba, F. Bechstedt, J. Stangl, G. Bauer, Unit cell structure of crystal polytypes in InAs and InSb nanowires. Nano Lett. **11**(4), 1483–1489 (2011). April
120. P. Krogstrup, M. Hannibal Madsen, W. Hu, M. Kozu, Y. Nakata, J. Nygård, M. Takahasi, R. Feidenhans'l. In-situ x-ray characterization of wurtzite formation in gaas nanowires. Appl. Phys. Lett. **100**(9) (2012)
121. D. Kriegner, J.M. Persson, T. Etzelstorfer, D. Jacobsson, J. Wallentin, J.B. Wagner, K. Deppert, M.T. Borgström, J. Stangl. Structural investigation of GaInP nanowires using X-ray diffraction. Thin Solid Films **543**(0), 100–105 (2013); *International Conference NanoSEA* (NANOstructures SElf Assembly, 2012)
122. S.T. Haag, M.-I. Richard, V. Favre-Nicolin, U. Welzel, L.P.H. Jeurgens, S. Ravy, G. Richter, E.J. Mittemeijer, O. Thomas. In situ coherent x-ray diffraction of isolated core-shell nanowires. Thin Solid Films **530**, 113–119 (2013); *6th Size-Strain International Conference Diffraction Analysis of the Microstructure of Materials*
123. J. Gulden, S.O. Mariager, A.P. Mancuso, O.M. Yefanov, J. Baltser, P. Krogstrup, J. Patommel, M. Burghammer, R. Feidenhans'l, I.A. Vartanyants, Coherent x-ray nanodiffraction on single gaas nanowires. Physica Status Solidi A **208**(11), 2495–2498 (2011)
124. F. Glas, M.R. Ramdani, G. Patriarche, J.-C. Harmand, Predictive modeling of self-catalyzed iii-v nanowire growth. Phys. Rev. B **88**, 195304 (2013)
125. M.W. Larsson, J.B. Wagner, M. Wallin, P. Håkansson, L.E. Fröberg, L. Samuelson, L.R. Wallenberg, Strain mapping in free-standing heterostructured wurtzite inas/inp nanowires. Nanotechnology **18**(1), 015504 (2007)
126. A. Biermanns, S. Breuer, A. Trampert, A. Davydok, L. Geelhaar, U. Pietsch, Strain accommodation in ga-assisted gaas nanowires grown on silicon (111). Nanotechnology **23**(30), 305703 (2012)

127. A. Davydok, S. Breuer, A. Biermanns, L. Geelhaar, U. Pietsch, Lattice parameter accommodation between gaas(111) nanowires and si(111) substrate after growth via au-assisted molecular beam epitaxy. Nanoscale Res. Lett. **7**(1), 109 (2012)
128. A. Biermanns, S. Breuer, A. Davydok, L. Geelhaar, U. Pietsch, Structural polytypism and residual strain in GaAs nanowires grown on Si(111) probed by single-nanowire X-ray diffraction. J. Appl. Crystallogr. **45**(2), 239–244 (2012). Apr
129. M. Yamaguchi, J.-H. Paek, H. Amano, Probability of twin formation on self-catalyzed GaAs nanowires on Si substrate. Nanoscale Res. Lett. **7**(1), 558 (2012). October
130. V. Dubrovskii, N. Sibirev, G. Cirlin, J. Harmand, V. Ustinov, Theoretical analysis of the vapor-liquid-solid mechanism of nanowire growth during molecular beam epitaxy. Phys. Rev. E **73**(2) (2006)
131. C. Colombo, D. Spirkoska, M. Frimmer, G. Abstreiter, A. Fontcuberta i Morral. Ga-assisted catalyst-free growth mechanism of gaas nanowires by molecular beam epitaxy. Phys. Rev. B **77**, 155326 (2008)
132. V. Pankoke, S. Sakong, P. Kratzer, Role of sidewall diffusion in GaAs nanowire growth: a first-principles study. Phys. Rev. B **86**(8), 085425 (2012). August
133. J.C. Harmand, G. Patriarche, N. Péré-Laperne, M.-N. Mérat-Combes, L. Travers, F. Glas, Analysis of vapor-liquid-solid mechanism in au-assisted GaAs nanowire growth. Appl. Phys. Lett. **87**(20), 203101 (2005). November
134. M. Köhl, P. Schroth, T. Baumbach, Perspectives and limitations of symmetric X-ray bragg reflections for inspecting polytypism in nanowires. J. Synchrotron Radiat. **23**(2), 487–500 (2016). Mar
135. P. Schroth, J. Jakob, L. Feigl, S.M.M. Kashani, U. Pietsch, T. Baumbach, Lithography-free variation of the number density of self-catalyzed GaAs nanowires and its impact on polytypism. MRS Commun. **8**(3), 871–877 (2018)
136. P. Schroth, J. Jakob, L. Feigl, S.M.M. Kashani, J. Vogel, J. Strempfer, T.F. Keller, U. Pietsch, T. Baumbach, Radial growth of self-catalyzed GaAs nanowires and the evolution of the liquid Ga-droplet studied by time-resolved in situ X-ray diffraction. Nano Lett. **18**(1), 101–108 (2018)
137. A. Fontcuberta i Morral, C. Colombo, G. Abstreiter, J. Arbiol, J.R. Morante, Nucleation mechanism of gallium-assisted molecular beam epitaxy growth of gallium arsenide nanowires. Appl. Phys. Lett. **92**(6) (2008)
138. R.S. Wagner, W.C. Ellis, *Vapor-Liquid-Solid Mechanism of Crystal Growth and its Application to Silicon* (Bell Telephone Laboratories, 1965)
139. P. Krogstrup, R. Popovitz-Biro, E. Johnson, M.H.Madsen, J. Nygård, H. Shtrikman, Structural phase control in self-catalyzed growth of gaas nanowires on silicon (111). Nano Lett. **10**(11), 4475–4482 (2010) (PMID: 20932012)
140. B.J. O'Dowd, T. Wojtowicz, S. Rouvimov, X. Liu, R. Pimpinella, V. Kolkovsky, T. Wojciechowski, M. Zgirski, M. Dobrowolska, I.V. Shvets, J. Furdyna, Effect of catalyst diameter on vapour-liquid-solid growth of gaas nanowires. J. Appl. Phys. **116**(6) (2014)
141. S. Crawford, S.K. Lim, S. Gradečak, Fundamental insights into nanowire diameter modulation and the liquid/solid interface. Nano Lett. **13**(1), 226–232 (2013) (PMID: 23256571)
142. H. Wang, Z. Xie, W. Yang, J. Fang, L. An, Morphology control in the vapor-liquid-solid growth of sic nanowires. Cryst. Growth Des. **8**(11), 3893–3896 (2008)
143. G. Priante, S. Ambrosini, V.G. Dubrovskii, A. Franciosi, S. Rubini, Stopping and resuming at will the growth of gaas nanowires. Cryst. Growth Des. **13**(9), 3976–3984 (2013)
144. Y. Greenberg, A. Kelrich, Y. Calahorra, S. Cohen, D. Ritter, Tapering and crystal structure of indium phosphide nanowires grown by selective area vapor liquid solid epitaxy. J. Cryst. Growth **389**, 103–107 (2014)
145. Y. Zhang, A.M. Sanchez, Y. Sun, W. Jiang, M. Aagesen, S. Huo, D. Kim, P. Jurczak, X. Xiulai, H. Liu, Influence of droplet size on the growth of self-catalyzed ternary gaasp nanowires. Nano Lett. **16**(2), 1237–1243 (2016). PMID: 26708002
146. V.G. Dubrovskii, The theory of nucleation and polytypism of III–V semiconductor nanowires. Tech. Phys. Lett. **41**(2), 203–207 (2015)

147. Yu. Xuezhe, H. Wang, L. Jun, J. Zhao, J. Misuraca, P. Xiong, S. von Molnár, Evidence for structural phase transitions induced by the triple phase line shift in self-catalyzed gaas nanowires. Nano Lett. **12**(10), 5436–5442 (2012). PMID: 22984828
148. C. García Núñez, A.F. Braña, J.L. Pau, D. Ghita, B.J. García, G. Shen, D.S. Wilbert, S.M. Kim, P. Kung. Pure zincblende GaAs nanowires grown by Ga-assisted chemical beam epitaxy. J. Cryst. Growth **372**, 205–212 (2013)
149. D. Jacobsson, F. Panciera, J. Tersoff, M.C. Reuter, S. Lehmann, S. Hofmann, K.A. Dick, F.M. Ross, Interface dynamics and crystal phase switching in GaAs nanowires. Nature **531**(7594), 317+ (2016)
150. S. Lehmann, D. Jacobsson, K.A. Dick, Crystal phase control in GaAs nanowires: opposing trends in the Ga- and As-limited growth regimes. Nanotechnology **26**(30) (2015)
151. L. Balaghi, T. Tauchnitz, R. Huebner, L. Bischoff, H. Schneider, M. Helm, E. Dimakis, Droplet-confined alternate pulsed epitaxy of GaAs nanowires on Si substrates down to CMOS-compatible temperatures. Nano Lett. **16**(7), 4032–4039 (2016)
152. X. Hongyi, Y. Wang, Y. Guo, Z. Liao, Q. Gao, N. Jiang, H.H. Tan, C. Jagadish, J. Zou, High-density, defect-free, and taper-restrained epitaxial gaas nanowires induced from annealed au thin films. Cryst. Growth Des. **12**(4), 2018–2022 (2012)
153. G. Priante, F. Glas, G. Patriarche, K. Pantzas, F. Oehler, J.-C. Harmand, Sharpening the interfaces of axial heterostructures in self-catalyzed AlGaAs nanowires: experiment and theory. Nano Lett. **16**(3), 1917–1924 (2016)
154. Vijay Kris Narasimhan and Yi Cui, Nanostructures for photon management in solar cells. Nanophotonics **2**(3), 187–210 (2013)
155. K.H. Li, X. Liu, Q. Wang, S. Zhao, Z. Mi, Ultralow-threshold electrically injected AlGaN nanowire ultraviolet lasers on Si operating at low temperature. Nat. Nanotechnol. **10**(2), 140–144 (2015). February
156. S. Zhao, S.Y. Woo, M. Bugnet, X. Liu, J. Kang, G.A. Botton, Z. Mi, Three-dimensional quantum confinement of charge carriers in self-organized algan nanowires: a viable route to electrically injected deep ultraviolet lasers. Nano Lett. **15**(12), 7801–7807 (2015). PMID: 26539880
157. P. Periwal, T. Baron, P. Gentile, B. Salem, F. Bassani. Growth strategies to control tapering in ge nanowires. APL Mater. **2**(4) (2014)
158. S. Krylyuk, A.V. Davydov, I. Levin, Tapering control of si nanowires grown from sicl4 at reduced pressure. ACS Nano **5**(1), 656–664 (2011). PMID: 21158417
159. S.K. Lim, S. Crawford, G. Haberfehlner, S. Gradečak, Controlled modulation of diameter and composition along individual III–V nitride nanowires. Nano Lett. **13**(2), 331–336 (2013) (PMID: 22313231)
160. P. Krogstrup, H.I. Jørgensen, E. Johnson, M.H. Madsen, C.B. Sørensen, A. Fontcuberta i Morral, M. Aagesen, J. Nygård, F. Glas. Advances in the theory of III–V nanowire growth dynamics. J. Phys. D: Appl. Phys. **46**(31), 313001 (2013)
161. K.W. Schwarz, J. Tersoff, S. Kodambaka, Y.-C. Chou, F.M. Ross, Geometrical frustration in nanowire growth. Phys. Rev. Lett. **107**, 265502 (2011). Dec
162. V.G. Dubrovskii, V. Consonni, L. Geelhaar, A. Trampert, H. Riechert, Scaling growth kinetics of self-induced GaN nanowires. Appl. Phys. Lett. **100**(15), 153101 (2012)
163. N. Jiang, J. Wong-Leung, H.J. Joyce, Q. Gao, H.H. Tan, C. Jagadish. Understanding the true shape of au-catalyzed gaas nanowires. Nano Lett. **14**(10), 5865–5872 (2014) (PMID: 25244584)
164. P. Rueda-Fonseca, E. Bellet-Amalric, R. Vigliaturo, M. den Hertog, Y. Genuist, R. André, E. Robin, A. Artioli, P. Stepanov, D. Ferrand, K. Kheng, S. Tatarenko, J. Cibert, Structure and morphology in diffusion-driven growth of nanowires: the case of znte. Nano Lett. **14**(4), 1877–1883 (2014). PMID: 24564275
165. S.N. Filimonov, Y.Y. Hervieu, Model of step propagation and step bunching at the sidewalls of nanowires. J. Cryst. Growth **427**, 60–66 (2015)
166. C.-Y. Wen, J. Tersoff, M.C. Reuter, E.A. Stach, F.M. Ross, Step-flow kinetics in nanowire growth. Phys. Rev. Lett. **105**, 195502 (2010). Nov

167. C. Chen, M.C. Plante, C. Fradin, R.R. LaPierre, Layer-by-layer and step-flow growth mechanisms in gaasp/gap nanowire heterostructures. J. Mater. Res. **21**, 2801–2809 (2006)
168. V.G. Dubrovskii, Y. Berdnikov, N.V. Sibirev, Regimes of radial growth for ga-catalyzed gaas nanowires. Appl. Phys. A **122**(7), 671 (2016)
169. V.G. Dubrovskii, T. Xu, A. Díaz Álvarez, S.R. Plissard, P. Caroff, F. Glas, B. Grandidier. Self-equilibration of the diameter of ga-catalyzed gaas nanowires. Nano Lett. **15**(8), 5580–5584 (2015) (PMID: 26189571)
170. J. Tersoff, Stable self-catalyzed growth of III–V nanowires. Nano Lett. **15**(10), 6609–6613 (2015). PMID: 26389697
171. A. Stierle, T.F. Keller, H. Noei, V. Vonk, R. Roehlsberger, DESY NanoLab. J. large-scale Res. Facil. JLSRF **2**, 76 (2016). June
172. M. Takahasi, M. Kozu, T. Sasaki, H. Wen, Mechanisms determining the structure of gold-catalyzed gaas nanowires studied by in situ x-ray diffraction. Cryst. Growth Des. **15**(10), 4979–4985 (2015)
173. J. Strempfer, S. Francoual, D. Reuther, D.K. Shukla, A. Skaugen, H. Schulte-Schrepping, T. Kracht, H. Franz, Resonant scattering and diffraction beamline P09 at PETRA III. J. Synchrotron Radiat. **20**(4), 541–549 (2013). Jul
174. M. Köhl, P. Schroth, A.A. Minkevich, J.-W. Hornung, E. Dimakis, C. Somaschini, L. Geelhaar, T. Aschenbrenner, S. Lazarev, D. Grigoriev, U. Pietsch, T. Baumbach, Polytypism in GaAs nanowires: determination of the interplanar spacing of wurtzite GaAs by X-ray diffraction. J. Synchrotron Radiat. **22**(1), 67–75 (2015). Jan
175. A. Biermanns, A. Davydok, H. Paetzelt, A. Diaz, V. Gottschalch, T.H. Metzger, U. Pietsch, Individual GaAs nanorods imaged by coherent X-ray diffraction. J. Synchrotron Radiat. **16**(6), 796–802 (2009)
176. M. Köhl, Suggested to include both time- and heigth-dependence in the general expression of the contributions to radial growth. Private Communication (2017)
177. H. Kuepers, R.B. Lewis, A. Tahraoui, M. Matalla, O. Krueger, F. Bastiman, H. Riechert, L. Geelhaar, Diameter evolution of selective area grown Ga-assisted GaAs nanowires. Nano Res. **11**(5), 2885–2893 (2018)
178. K.W. Schwarz, J. Tersoff, From droplets to nanowires: dynamics of vapor-liquid-solid growth. Phys. Rev. Lett. **102**, 206101 (2009). May
179. M. Köhl, Proposed to express the droplet shape time-dependently introducing a fermi-function. Private Communication (2017)
180. M. López, Y. Nomura, Surface diffusion length of Ga adatoms in molecular-beam epitaxy on GaAs (100)—(110) facet structures. J. Cryst. Growth **150**(Part 1), 68–72 (1995)
181. M.R. Ramdani, J.C. Harmand, F. Glas, G. Patriarche, L. Travers, Arsenic pathways in self-catalyzed growth of GaAs nanowires. Cryst. Growth Des. **13**(1), 91–96 (2013)
182. T. Rieger, S. Heiderich, S. Lenk, M.I. Lepsa, D. Grützmacher, Ga-assisted MBE growth of GaAs nanowires using thin HSQ layer. J. Cryst. Growth **353**(1), 39–46 (2012)
183. M. Heiss, Y. Fontana, A. Gustafsson, G. Wuest, C. Magen, D.D. O'Regan, J.W. Luo, B. Ketterer, S. Conesa-Boj, A.V. Kuhlmann, J. Houel, E. Russo-Averchi, J.R. Morante, M. Cantoni, N. Marzari, J. Arbiol, A. Zunger, R.J. Warburton, A. Fontcuberta i Morral, Self-assembled quantum dots in a nanowire system for quantum photonics. Nat. Mater. **12**(5), 439–444 (2013)
184. C.-C. Chang, C.-Y. Chi, M. Yao, N. Huang, C.-C. Chen, J. Theiss, A.W. Bushmaker, S. LaLumondiere, T.-W. Yeh, M.L. Povinelli, C. Zhou, P.D. Dapkus, S.B. Cronin, Electrical and optical characterization of surface passivation in GaAs nanowires. Nano Lett. **12**(9), 4484–4489 (2012)
185. N. Jiang, Q. Gao, P. Parkinson, J. Wong-Leung, S. Mokkapati, S. Breuer, H.H. Tan, C.L. Zheng, J. Etheridge, C. Jagadish, Enhanced minority carrier lifetimes in GaAs/AlGaAs core-shell nanowires through shell growth optimization. Nano Lett. **13**(11), 5135–5140 (2013)
186. A. Biermanns, T. Rieger, G. Bussone, U. Pietsch, D. Gruetzmacher, M.I. Lepsa, Axial strain in gaas/inas core-shell nanowires. Appl. Phys. Lett. **102**(4) (2013)
187. R.B. Lewis, L. Nicolai, H. Kuepers, M. Ramsteiner, A. Trampert, L. Geelhaar, Anomalous strain relaxation in core-shell nanowire heterostructures via simultaneous coherent and incoherent growth. Nano Lett. **17**(1), 136–142 (2017)

188. T. Rieger, P. Zellekens, N. Demarina, A. Al Hassan, F.J. Hackemueller, H. Lueth, U. Pietsch, T. Schaepers, D. Gruetzmacher, M.I. Lepsa, Strain relaxation and ambipolar electrical transport in GaAs/InSb core-shell nanowires. Nanoscale **9**(46), 18392–18401 (2017)
189. F. Glas, G. Patriarche, J.C. Harmand, Growth, structure and phase transitions of epitaxial nanowires of III–V semiconductors. J. Phys.: Conf. Ser. **209**, 012002 (2010)
190. M. Paladugu, J. Zou, Y.N. Guo, X. Zhang, H.J. Joyce, Q. Gao, H.H. Tan, C. Jagadish, Y. Kim, Evolution of wurtzite structured GaAs shells around InAs nanowire cores. Nanoscale Res. Lett. **4**(8), 846–849 (2009)
191. L. Namazi, L. Gren, M. Nilsson, M. Garbrecht, C. Thelander, R.R. Zamani, K.A. Dick, Realization of wurtzite GaSb using InAs nanowire templates. Adv. Funct. Mater. **28**(28) (2018)
192. R.E. Algra, M. Hocevar, M.A. Verheijen, I. Zardo, G.G.W. Immink, W.J.P. van Enckevort, G. Abstreiter, L.P. Kouwenhoven, E. Vlieg, E.P.A.M. Bakkers, Crystal structure transfer in core/shell nanowires. Nano Lett. **11**(4), 1690–1694 (2011)
193. G. Patriarche, F. Glas, M. Tchernycheva, C. Sartel, L. Largeau, J.-C. Harmand, G.E. Cirlin, Wurtzite to zinc blende phase transition in GaAs nanowires induced by epitaxial burying. Nano Lett. **8**(6), 1638–1643 (2008)
194. K.W. Ng, W.S. Ko, F. Lu, C.J. Chang-Hasnain, Metastable growth of pure wurtzite InGaAs microstructures. Nano Lett. **14**(8), 4757–4762 (2014)
195. J. Wallentin, D. Jacobsson, M. Osterhoff, M.T. Borgström, T. Salditt, Bending and twisting lattice tilt in strained core-shell nanowires revealed by nanofocused X-ray diffraction. Nano Lett. **17**(7), 4143–4150 (2017)
196. P. Mohan, J. Motohisa, T. Fukui, Realization of conductive InAs nanotubes based on lattice-mismatched InP/InAs core-shell nanowires. Appl. Phys. Lett. **88**(1) (2006)
197. H. Küpers, Growth and properties of GaAs/(In,Ga)As core-shell nanowire arrays on Si. Dissertation, Humboldt-Universität zu Berlin, Mathematisch-Naturwissenschaftliche Fakultät, 2018
198. R.B. Lewis, P. Corfdir, H. Kuepers, T. Flissikowski, O. Brandt, L. Geelhaar, Nanowires bending over backward from strain partitioning in asymmetric core-shell heterostructures. Nano Lett. **18**(4), 2343–2350 (2018)
199. N. Skold, J.B. Wagner, G. Karlsson, T. Hernan, W. Seifert, M.-E. Pistol, L. Samuelson, Phase segregation in AlInP shells on GaAs nanowires. Nano Lett. **6**(12), 2743–2747 (2006)
200. A. Al Hassan, R.B. Lewis, H. Küpers, W.-H. Lin, D. Bahrami, T. Krause, D. Salomon, A. Tahraoui, M. Hanke, L. Geelhaar, U. Pietsch, Determination of indium content of gaas/(in,ga)as/(gaas) core-shell(-shell) nanowires by x-ray diffraction and nano x-ray fluorescence. Phys. Rev. Mater. **2**, 014604 (2018)
201. A. Davtyan, T. Krause, D. Kriegner, A. Al Hassan, D. Bahrami, S.M.M. Kashani, R.B. Lewis, H. Küpers, A. Tahraoui, L. Geelhaar, M. Hanke, S.J. Leake, O. Loffeld, U. Pietsch, Threefold rotational symmetry in hexagonally shaped core—shell (In,Ga)As/GaAs nanowires revealed by coherent X-ray diffraction imaging. J. Appl. Crystallogr. **50**(3), 673–680 (2017)
202. M. Heurlin, T. Stankevic, S. Mickevicius, S. Yngman, D. Lindgren, A. Mikkelsen, R. Feidenhans'l, M.T. Borgstrom, L. Samuelson, Structural properties of wurtzite InP-InGaAs nanowire core-shell heterostructures. Nano Lett. **15**(4), 2462–2467 (2015)
203. L. Feigl, M. Al Humaidi, J. Jakob, P. Schroth, S.M.M. Kashani, A. Davtyan, A. Al Hassan, D. Bahrami, U. Pietsch, T. Baumbach, *in-situ* X-ray analysis of misfit strain and curvature of bent polytypic (In,Ga)As core-shell nanowires. Manuscript in preparation. Expected publishing year 2021
204. L. Vegard, Die konstitution der mischkristalle und die raumfüllung der atome. Zeitschrift für Physik **5**(1), 17–26 (1921). Jan
205. Semiconductors on nsm. http://www.ioffe.ru/SVA/NSM/Semicond/. Accessed 29 Nov 2018
206. B. Andreas, D. Anton, P. Hendrik, D. Ana, G. Volker, M.T. Hartmut, P. Ullrich, Individual gaas nanorods imaged by coherent x-ray diffraction. J. Synchrotron Radiat. **16**(6), 796–802 (2009)

207. J.R. Fienup, Phase retrieval algorithms: a comparison. Appl. Opt. **21**(15), 2758–2769 (1982). Aug
208. S.O. Hruszkewycz, M. Allain, M.V. Holt, C.E. Murray, J.R. Holt, P.H. Fuoss, V. Chamard. High-resolution three-dimensional structural microscopy by single-angle bragg ptychography. Nat. Mater. **16**, 244 (2016)
209. A. Davtyan, A. Biermanns, O. Loffeld, U. Pietsch, Determination of the stacking fault density in highly defective single gaas nanowires by means of coherent diffraction imaging. New J. Phys. **18**(6), 063021 (2016)
210. A. Diaz, C. Mocuta, J. Stangl, B. Mandl, C. David, J. Vila-Comamala, V. Chamard, T.H. Metzger, G. Bauer, Coherent diffraction imaging of a single epitaxial inas nanowire using a focused x-ray beam. Phys. Rev. B **79**, 125324 (2009). Mar
211. S. Labat, M.-I. Richard, M. Dupraz, M. Gailhanou, G. Beutier, M. Verdier, F. Mastropietro, T.W. Cornelius, T.U. Schülli, J. Eymery, O. Thomas, Inversion domain boundaries in gan wires revealed by coherent bragg imaging. ACS Nano **9**(9), 9210–9216 (2015)
212. D. Dzhigaev, A. Shabalin, T. Stankevič, U. Lorenz, R.P. Kurta, F. Seiboth, J. Wallentin, A. Singer, S. Lazarev, O.M. Yefanov, M. Borgström, M.N. Strikhanov, L. Samuelson, G. Falkenberg, C.G. Schroer, A. Mikkelsen, R. Feidenhans'l, I.A. Vartanyants, Bragg coherent x-ray diffractive imaging of a single indium phosphide nanowire. J. Optics **18**(6), 064007 (2016)
213. T. Stankevič, D. Dzhigaev, Z. Bi, M. Rose, A. Shabalin, J. Reinhardt, A. Mikkelsen, L. Samuelson, G. Falkenberg, I.A. Vartanyants, R. Feidenhans'l, Strain mapping in an InGaN/GaN nanowire using a nano-focused x-ray beam. Appl. Phys. Lett. **107**(10), 103101 (2015)
214. S. Lazarev, D. Dzhigaev, Z. Bi, A. Nowzari, Y.Y. Kim, M. Rose, I.A. Zaluzhnyy, O.Y. Gorobtsov, A.V. Zozulya, F. Lenrick, A. Gustafsson, A. Mikkelsen, M. Sprung, L. Samuelson, I.A. Vartanyants, Structural changes in a single gan nanowire under applied voltage bias. Nano Lett. **18**(9), 5446–5452 (2018) (PMID: 30033733)
215. G. Bussone, H. Schäfer-Eberwein, E. Dimakis, A. Biermanns, D. Carbone, A. Tahraoui, L. Geelhaar, P.H. Bolívar, T.U. Schülli, U. Pietsch, Correlation of electrical and structural properties of single as-grown gaas nanowires on si (111) substrates. Nano Lett. **15**(2), 981–989 (2015)
216. D. Dzhigaev, T. Stankevič, Z. Bi, S. Lazarev, M. Rose, A. Shabalin, J. Reinhardt, A. Mikkelsen, L. Samuelson, G. Falkenberg, R. Feidenhans'l, I.A. Vartanyants, X-ray bragg ptychography on a single InGaN/GaN core-shell nanowire. ACS Nano **11**(7), 6605–6611 (2017). PMID: 28264155
217. M.O. Hill, I. Calvo-Almazan, M. Allain, M.V. Holt, A. Ulvestad, J. Treu, G. Koblmüller, C. Huang, X. Huang, H. Yan, E. Nazaretski, Y.S. Chu, G.B. Stephenson, V. Chamard, L.J. Lauhon, S.O. Hruszkewycz, Measuring three-dimensional strain and structural defects in a single InGaAs nanowire using coherent X-ray multiangle Bragg projection ptychography. Nano Lett. **18**(2), 811–819 (2018)
218. A. Davtyan, V. Favre-Nicolin, R.B. Lewis, H. Küpers, L. Geelhaar, D. Kriegner, D. Bahrami, A. Al-Hassan, G. Chahine, O. Loffeld, U. Pietsch, Coherent X-ray diffraction imaging meets ptychography to study core-shell-shell nanowires. MRS Adv. **3**(39), 2317–2322 (2018)
219. S.M.M. Kashani, D. Kriegner, D. Bahrami, J. Vogel, A. Davtyan, L. Feigl, P. Schroth, J. Jakob, T. Baumbach, U. Pietsch, X-ray diffraction analysis of the angular stability of self-catalyzed GaAs nanowires for future applications in solar-light-harvesting and light-emitting devices. Appl. Nano Mater. **2**, 689–699 (2019)
220. S.J. Gibson, R.R. LaPierre, Model of patterned self-assisted nanowire growth. Nanotechnology **25**(41), 415304 (2014)
221. D. Rudolph, L. Schweickert, S. Morkötter, B. Loitsch, S. Hertenberger, J. Becker, M. Bichler, G. Abstreiter, J.J. Finley, G. Koblmüller, Effect of interwire separation on growth kinetics and properties of site-selective gaas nanowires. Appl. Phys. Lett. **105**(3), 033111 (2014)
222. P. Schroth, M. Al Humaidi, L. Feigl, J. Jakob, A. Al Hassan, A. Davtyan, H. Küpers, A. Tahraoui, L. Geelhaar, U. Pietsch, T. Baumbach, Impact of the shadowing effect on the crystal structure of patterned self-catalyzed GaAs nanowires. Nano Lett. **19**, 4263–4271 (2019)

223. B. Bauer, A. Rudolph, M. Soda, A. Fontcuberta i Morral, J. Zweck, D. Schuh, E. Reiger, Position controlled self-catalyzed growth of GaAs nanowires by molecular beam epitaxy. Nanotechnology **21**(43) (2010)
224. S. Plissard, K.A. Dick, G. Larrieu, S. Godey, A. Addad, X. Wallart, P. Caroff, Gold-free growth of GaAs nanowires on silicon: arrays and polytypism. Nanotechnology **21**(38) (2010)
225. H. Küpers, Manuscript in preparation. Expected publishing year 2019
226. J. Vogel, Limits for x-ray nanowire diffraction with synchrotron radiation. Master's thesis, Universität Siegen, 2016

Characterisation of Semiconductor Nanowires by Electron Beam Induced Microscopy and Cathodoluminescence

Maria Tchernycheva, Gwénolé Jacopin, and Valerio Piazza

Abstract Nowadays the realization of market-competitive devices based on nanomaterials is a major challenge. Optimization of the device performance requires a deep understanding of the physical phenomena at the nanoscale. In this context, electron beam-based techniques become indispensable. Several instruments have been developed in the past decades to provide versatile diagnostic solutions for improving materials, designs, and device fabrication. These characterization techniques applied to nanostructured semiconductors can help filling the gap between material science and engineering by bringing in light important physical parameters. In this Chapter, the family of electron beam-based techniques is briefly introduced. First, the electron beam/matter interaction is described both in physical and operational terms. In particular, different phenomena occurring when a flux of electron collides with a semiconductor material are discussed. Then, two main electron beam scanning techniques are discussed in the following sections: electron beam induced current microscopy and cathodoluminescence. After a short description of the fundamentals, for each technique, a bibliographic review is presented to illustrate its applications to analyses of semiconductor nanowires.

Keywords Electron beam · Scanning techniques · Electron beam induced current · Cathodoluminescence · Semiconductor nanowires

The use of scanning beam probe microscopy techniques is fundamental in the development of novel devices. Indeed, thanks to the advances in the epitaxial growth and nanofabrication, almost all electronic and optical components are based on materials having a sub-micron size in one or several dimensions. The optimization of the device performance requires careful design and control of the active semiconductor materials. The assessment of the properties of nanometric sized materials is still an open

M. Tchernycheva · V. Piazza (✉)
Centre de Nanosciences Et de Nanotechnologies, UMR 9001, CNRS, Université Paris Sud, Université Paris-Saclay, 10 Boulevard Thomas Gobert, 91120 Palaiseau, France
e-mail: v.piazza@live.com

G. Jacopin
Institut Néel, Université Grenoble Alpes, CNRS, Grenoble INP, 38000 Grenoble, France

© Springer Nature Singapore Pte Ltd. 2021

N. Fukata and R. Rurali (eds.), *Fundamental Properties of Semiconductor Nanowires*,
https://doi.org/10.1007/978-981-15-9050-4_5

task. For this reason, a comprehensive characterization at the nanoscale is necessary to determine their advantages and drawbacks for different applications.

Among the characterization techniques suited for this purpose, electron beam-based techniques have gained a lot of interest in the last years due to the strong and highly localized interaction of the electron beam with the matter. By coupling the high resolution of the electron probe with the typical scanning mode of the electron microscopes, it is possible to analyze large surfaces with high accuracy and in a short time. Besides the classical structural and compositional characterization methods (such as scanning electron microscopy SEM, transmission electron microscopy TEM, scanning transmission electron microscopy STEM, Energy-dispersive X-ray spectroscopy EDS, etc.), other types of electron beam-based techniques have been developed specifically for the investigation of semiconductor materials. Due to the physical phenomena occurring upon electron exposure, the electron beam is able to excite excess carriers in semiconductors, which can probe the electrical and the optical properties of the sample. For this reason, dedicated techniques and setups have been developed, aiming to access the electronic properties of semiconductor materials. These techniques already gave interesting insights for the analysis of bulk and layered materials, but they become indispensable for the investigation of nanostructures. Besides the analysis of the material properties, electron beam-based techniques have been largely used to assess the physical phenomena in a wide variety of optoelectronic devices such as light-emitting diodes (LEDs), solar cells, and photodetectors. These techniques are particularly useful for the investigation of nanostructured devices (e.g., nanowire-based LEDs and solar cells that will be discussed in this chapter).

This chapter starts with a brief section which describes the electron beam/semiconductor interaction, defining the spatial resolution and carrier injection and focusing on the variation of these quantities by tuning the electron beam excitation. This introduction provides an understanding of the basic operation principles of two electron probe techniques discussed in this chapter, namely the electron beam induced current microscopy (EBIC) and the cathodoluminescence (CL). Both EBIC and CL have gained the interest of the semiconductor nanomaterial community in the last years due to their versatility and the large amount of information that they can provide about the investigated specimen. These techniques will be described in this chapter by giving the working principles and the main technical aspects. In each Section, a large bibliographic review is reported to give an overview of the different applications of these techniques for the characterization of different types of nanowires currently under investigation for the development of novel optoelectronic devices.

1 Electron Beam/Matter Interaction

When a solid material is exposed to a high-energy electron beam (3–30 kV), a high number of interactions occurs due to elastic and inelastic scattering of the

injected electrons. The scattering events lead to a transfer of energy from the beam to the material which can induce a large number of phenomena, such as emission of secondary electrons (SE), backscattered electrons (BSE), Auger electrons (AE), and X-rays. The peculiarity of each interaction and the ability to detect the emitted particles is generally used to develop characterization techniques which allow to get access to specific material properties. Classical examples are given by the detection of secondary electrons, which is used to perform morphological analysis (SE images), and by the analysis of the X-ray emissions, used for compositional analysis of the investigated material (XEDS).

In semiconductor materials, the inelastic scattering of the injected electrons induces the generation of e^-/h^+ pairs, analogously to the photon excitation. Thanks to this phenomenon and to the small volume affected by the beam exposure, the electron beam techniques offer the possibility to investigate locally the properties related to the electronic bands of the material. The main differences with respect to the case of the excitation of carriers by light exposure depend on characteristic features of the electron beam/samples interaction, i.e., on the electron scattering and on the carrier generation.

(a) ***Electron scattering and interaction volume***

Due to the high-energy of the injected electrons, multiple scattering events occur in the material and therefore, this process affects a certain region. This region is called *interaction volume* and it is the volume of semiconductor material where the generation of excess carriers occurs under electron beam exposure. The interaction volume can extend from a few tens of nanometers up to a few hundreds of microns depending on the nature of the investigated materials and on the operational conditions. As it is intuitive, the interaction volume is intimately related to the spatial resolution achievable by a scanning probe technique. For this reason, the interaction volume is a key element to be taken into consideration for all the scanning beam techniques and its peculiarities must be carefully evaluated.

The spatial resolution is defined by the shape and size of the interaction volume, which, being related to the electron scattering, depends on the primary electron energy and on the material (chemical composition, density, scattering crosssection). Pear, spherical, and hemispherical shapes are obtained for increasing atomic numbers [1, 2]. Although it concerns few electron probe techniques, it is to be noticed that the shape of the interaction volume affects also the sensitivity to the surface properties, since the volume involved as a function of the penetration depth can strongly change in the different cases. For instance, this is important for the morphological analysis by SEM microscopy where the emission of a large ratio of secondary electrons from the surface is desirable.

Concerning the techniques which probe the bulk properties of the material, the importance of the shape is related to the ratio between the penetration depth of the beam into the material and the lateral size of the interaction volume which strongly affects the spatial resolution of the scanning techniques. These parameters can be tuned by varying the energy of the injected electron, i.e., the acceleration voltage

of the beam (V_{acc}). Indeed, the energy of the injected electrons increases with the acceleration voltage. As a consequence, in bulk materials the number of sequential scattering events per injected electrons increases, resulting in deeper penetration of the interaction volume. For this reason, high voltage beams are generally used to probe structures or insertion buried into the material [3, 4]. However, contextually to the penetration depth, the lateral size of the interaction volume increases, leading to a reduction of the spatial resolution. Depending on the systems under investigation, a thorough optimization could be required to achieve a fine resolution when investigating buried elements.

To estimate the interaction volume in a material with a given geometry and for given experimental conditions, Monte Carlo simulations can be used. This stochastic simulation forecasts the electron scattering phenomena by calculating the trajectories considering random scattering events in a stepwise manner. The energy lost by the injected electrons can be evaluated with this method as well. The loss of energy is a fundamental parameter since the electrons need a threshold energy value to be able to induce the physical phenomenon used to probe the sample (such as X-rays emission, secondary electron emission). For this reason, the boundaries of the interaction volume cannot be considered abrupt. Depending on the physical phenomenon used to probe the properties of the material, the dimensions of the interaction volume have to be properly defined. In the case of the generation of e^-/h^+ pairs in semiconductor materials, several models have been developed to define this threshold value, called *cut-off energy*. The cut-off energy, in fact, affects the dimensions of the interaction volume, when estimating the resolution of a scanning probe techniques on a given sample. This is illustrated in Fig. 1a, which shows an example of a Monte Carlo simulation of the electron energy loss in a GaAs layer for a beam with an acceleration voltage of 10 kV. The lines represent the iso-energetic distribution of the scattered electrons and the numbers indicate the percentage of energy lost outside the given iso-energy line. As a general rule in bulk materials, the interaction volume increases with increasing beam acceleration voltage.

Another factor that strongly affects the spatial resolution of the electron probe techniques is the carrier diffusion length in the material [5], which can be influenced by bandgap gradients, charge barriers, heterostructures or passivated surfaces. For the sake of simplicity, let's consider the case of an optical emission upon carrier recombination. Indeed, if the carrier diffusion length is much larger than the lateral size of the interaction volume, the generated carriers can travel over large distances before recombining. In this case, the recombination occurs further from the injection point and outside the interaction volume, and therefore, the spatial resolution is not related to its dimensions. In other terms, the spatial resolution is limited by the carrier diffusion length in the material. This is typically the case of III-V thin films or Si structures (independently on its geometry), which are characterized by diffusion length from 1 to 100 μm [6, 7]. On the contrary, if the carrier diffusion length is comparable with the lateral size of the interaction volume, the charges excited in the interaction volume poorly diffuse before recombining and the spatial resolution is mostly given by the geometry of the interaction volume. This is mostly the case of

III-V NWs which are characterized by low values of diffusion length (50–150 nm) [8, 9].

When probing nanostructured materials, it has to be taken into account that the penetration depth can be as large as, or even larger than the thickness of the investigated sample. In this case, the shape and size of the interaction volume is strongly modified due to the partial transmission of the beam and the presence of backscattered electrons (BSEs) from the substrate, if there is any (Fig. 1b). The transmission of the electrons causes a narrowing of the interaction volume when increasing the acceleration voltage (contrary to the bulk case), and therefore, an increase of the resolution, similarly to the case of transmission scanning techniques (such as TEM, STEM) [10]. However, if a substrate is present on the beam path, the effect of BSEs, which lead to an enlargement of the interaction volume, can be dominant and no improvement in resolution is obtained.

(b) ***Carrier generation: theoretical models and operational aspects***

The generation of excess carriers in the interaction volume is fundamental for probing the properties of the investigated samples. Different models were proposed to describe the carrier generation in semiconductor materials under an electron beam irradiation. The main works were produced by Donolato [11–13], who developed a model assuming that, at a fixed depth, the ionization density follows a radial Gaussian distribution. Under this assumption, it is possible to describe the local carrier generation induced by the electron beam as a function $g(z, r; R)$, where z, r represent the geometrical variables (respectively, the depth and the radius) and R = R(E) is the electron energy distribution (as bi-dimensionally illustrated in Fig. 1). In other terms, this function allows to determine the number of carriers generated per unit time at a certain point within the interaction volume, depending on the energy of the

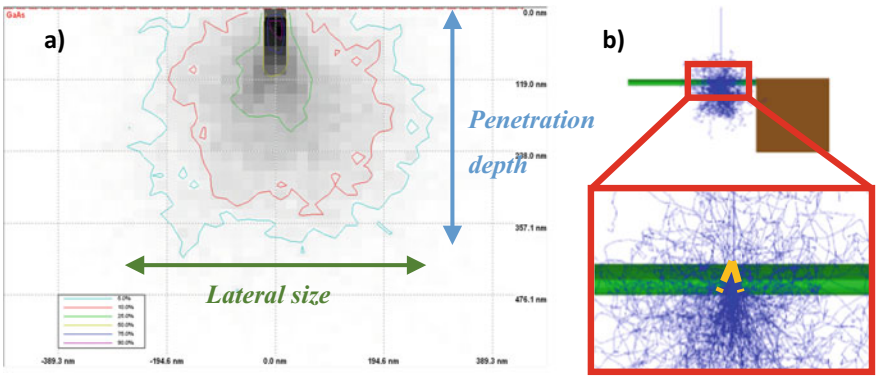

Fig. 1 Example **a** of a Monte Carlo simulation and definition of the penetration depth and of the lateral size of the interaction volume considering a 5% cut-off. Different cut-off energies are shown by the colored lines representing the iso-energetic distribution of the scattered electrons. **b** Simulation of the electron trajectory after the interaction with a suspended GaAs NW. In the red-framed inset, the partial transmission of the electron beam can be observed

electrons scattered in this point. The local generation function can be expressed as

$$g(z, r; R) = \frac{A(z, R)}{2\pi\sigma^2(z, R)} \exp\left[-\frac{r^2}{2\sigma^2(z, R)}\right], \tag{1}$$

where A and σ represent the amplitude and the width of the ionization density. The great advantage of this model is that the properties of the material which affect the carrier generation are fully embedded in two independent functions, i.e., the ionization density approximated with a Gaussian function and the electron energy distribution R(E). Providing these functions, the proposed model gives a universal mathematical description of the number of carriers generated per unit time by an electron beam injected in a semiconductor material.

On the other hand, the mentioned functions which take into account the nature of the material (in particular the ionization density) have to be considered case by case since they depend on both material properties and electron beam parameters. For this reason, the model has been further developed in the following works [14, 15]. In particular, Leamy described the local carrier generation with a function which splits the geometrical and the intensive factors, expressed in the form

$$g(z, r) = \langle g \rangle \frac{V_{acc} I_b (1 - f)}{q E_{eh}}, \tag{2}$$

where $\langle g \rangle$ is the normalized energy distribution of the electrons within the interaction volume, V_{acc} and I_b are the main beam parameters, i.e., the acceleration voltage and the beam current impinging the surface, f is the energy fraction of the incident electron beam that is reflected from the sample surface, q is the electron charge and E_{eh} is the energy fraction spent by the electrons to excite the electron–hole pairs, which is a constant for a given material and independent on the electron beam. To be noticed that the model from Leamy requires the same information as in Eq. 1: the electron energy distribution and the ionization energy. The latter is here considered through the factor E_{eh}, which is roughly equal to three times the material bandgap energy ($3E_g$), if the losses due to the interaction with phonons are neglected (for more details, please refer to Ref. [16]).

This simplified expression allows to determine the variation of the local generation rate with the operation parameters and thus it has a more practical application for the description of experimental cases. In fact, by integrating Eq. 2, it is possible to define the overall generation rate G_0 (Eq. 3), which enables the calculation of the carrier concentration (Δp) under beam exposure (Eq. 4) [17]

$$G_0 \approx \frac{1}{3q E_g} \frac{V_{acc}}{V} I_b \tag{3}$$

$$\Delta p = G_0 \tau \approx \frac{1}{3q E_g} \frac{V_{acc}}{V} I_b \tau, \tag{4}$$

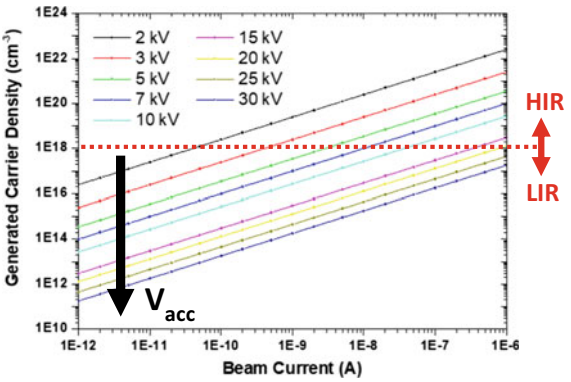

Fig. 2 Generated carrier concentration in bulk n-doped GaN as a function of the beam current: the colored straight lines are calculated at a fixed acceleration voltage which is increasing as indicated by the black arrow. The horizontal dotted red line indicates the high injection regime limit, assuming a background doping of 10^{18} cm^{-3}: above this line, the excitation occurs in a high injection regime (HIR), while below it occurs in a low injection regime (LIR)

where V is the total interaction volume and τ is the carrier lifetime in the medium. Equation 1.4 indicates that the excess carrier density in the interaction volume changes linearly with the beam current, i.e., the flux of injected electrons, and therefore, it is possible to control the excitation in the material by tuning I_b. An example is shown in Fig. 2, which displays the dependence of the generated carrier concentration in bulk n-doped GaN as a function of the beam current. The lines in the plot are calculated at a fixed acceleration voltage following the model by Leamy expressed by Eqs. 2, 3, and 4. To perform the calculations, the parameter f is considered as half of the backscattered coefficient for the material,[1] as suggested in the work of Leamy [14]. The lifetime of both electrons and holes is assumed to be 1 ns, in agreement with values reported in the literature for GaN (Refs. [18, 19] and references therein). Moreover, the diffusion of the induced carriers out of the interaction volume is neglected for the sake of simplicity. For more details, please refer to Ref. [20].

Looking at this relation one could naively think that the same effect can be achieved by varying the acceleration voltage, however, this isn't true. As previously discussed, the acceleration voltage affects the shape and the dimensions of the interaction volume, and therefore, by tuning V_{acc}, the total interaction volume V is also changed. In bulk materials (or more generally, in specimen thick enough to prevent the electron beam transmission), the interaction volume scales with the acceleration voltage faster than the generation rate [20]. In other terms, the overall effect is that, at a fixed beam current, the generated carrier density decreases when V_{acc} is increased (Fig. 2).

[1]The f values determined for beam voltages of 2 keV, 3 keV, 5 keV, 7 keV, 10 keV, 15 keV, 20 keV, 25 keV, and 30 keV were 0.135, 0.135, 0.131, 0.125, 0.124, 0.121, 0.118, 0.118, and 0.117, respectively.

The control of the excess carrier concentration is fundamental for the analysis of the material, since the relation between the generated carrier density and the free carrier concentration can affect the transport phenomena in the materials [21]. If the excess carrier density is comparable or higher than the equilibrium carrier concentration (either the intrinsic concentration—n_0—or the intentional doping level in doped semiconductors—N_a or N_d), the induced current is ruled by ambipolar diffusion. In this regime, both electrons and holes contribute to the current and the definition of minority and majority carriers becomes meaningless. This situation is referred to as high injection regime (HIR). On the contrary, if the generated carrier density is much lower than the equilibrium concentration, a so-called low injection regime (LIR) is established and the collected current is given by minority carrier diffusion. As it will be discussed in the following sections, the latter regime is highly desirable to investigate material parameters such as the minority carrier diffusion length.

2 Electron Beam Induced Current Mapping

Electron Beam Induced Current microscopy (EBIC) is a probe scanning technique which enables the investigation of internal electric fields in semiconductor materials. EBIC microscopy has been widely used in optoelectronics, and in particular solar cells, for more than thirty years [22]. In 2D solar cells, EBIC was used to probe the electrical activity of the devices with a high resolution, to extract material parameters and to detect failures induced by material defects. Thanks to the development of nano- and micro-fabrication of electrical contacts, more recently EBIC mapping has been applied to the investigation of the physical properties of nanostructured materials. Concerning nanowires, its use has ranged from the estimation of material parameters such as minority carrier diffusion length and active dopants concentration to the investigation of complex heterostructures embedded in the nano-objects.

2.1 Measurement Configurations

The working principle of EBIC microscopy is based on the ability to collect in an electrical circuit the generated carriers drifted by an internal field present in the investigated specimen. The drift of excess carriers generated by the electron beam and their diffusion towards the internal field offers the possibility to extract a so-called "*induced current*" in the external circuit (Fig. 3a). By scanning the electron beam on a line or on a surface, an EBIC profile or map can be built where each pixel indicates the induced current measured when the electron beam was injected in that position. Due to the nanometric extension of the interaction volume (as previously mentioned), EBIC allows to visualize and to analyze internal fields at the nanoscale, and therefore, the electrical properties of the material can be locally investigated.

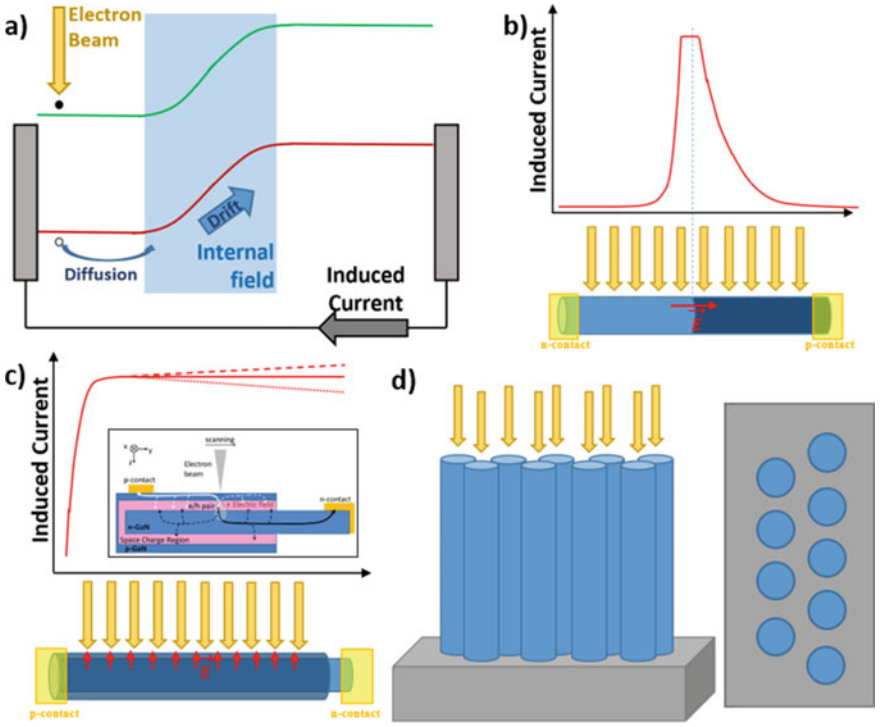

Fig. 3 **a** Schematic of EBIC working principle; **b** Qualitative EBIC profile obtained by scanning the axis of a NW containing an axial junction; **c** Qualitative EBIC profile obtained by scanning the axis of a NW containing a radial junction. Solid, dashed, and dotted lines represent the induced current profile depending on the ratio between core and shell resistances. In the inset, the charge collection mechanism in core/shell NWs is schematically reported. In both panels (**b**) and (**c**), the current profile is considered positive if it flows through the junction from the n-side to the p-side. **d** Schematic of a top-view EBIC measurement on a NW array and the corresponding top-view image. In all the panels, the electron beam injection direction is indicated by yellow arrows. [Inset in panel c is reproduced with permission from P Lavenus, A Messanvi, L Rigutti, A De Luna Bugallo, H Zhang,F Bayle, F H Julien, J Eymery, C Durand and M Tchernycheva, 2014, "Experimental and theoretical analysis of transport properties of core–shell wire light emitting diodes probed by electron beam induced current microscopy", Nanotech. 25(25), 255,201, DOI:https://doi.org/10.1088/0957-4484/25/25/255201. Copyright (2014) IOP Publishing]

Generally, different configurations can be used to perform EBIC measurements depending on the geometry and the internal structure of the investigated material. Both factors, in fact, play a key role in the interpretation of the maps and profiles, especially in the case of individual NWs since EBIC mapping is sensitive to the direction of the internal electric fields with respect to the direction of the electron beam. For the sake of clarity, in the following, the case of an EBIC scan along the axis of a NW containing a p–n junction is considered: this configuration is called *cross-sectional*.

If the NW contains an axial junction, the built-in field ($\overrightarrow{E}$) is oriented perpendicularly to the electron beam, i.e., the active region is confined in the scan direction. Therefore, a non-negligible induced current is recorded only in the vicinity of the junction during cross-sectional measurements and both diffusive and drift transport regimes can be analyzed [23]. A schematic of this configuration is shown in Fig. 3b, where an example of current profile (i.e., the current recorded in each position along the scanned axis) is shown for the case of a NW containing an axial junction. This configuration also enables the analysis of the carrier diffusion, which manifests as an exponential variation of the induced current along the scan direction. Several models have been proposed to describe the induced current profile as a function of the minority carrier diffusion length (L_{diff}) [5, 24, 25], hence allowing to estimate this material parameter from EBIC measurements. Charge drift is characterized by a sub-exponential variation of the induced current (assuming an infinitesimally small interaction volume, induced current would be constant, as shown in Fig. 3b). The localization of the region where carriers are drifted enables the estimate of the extension of the depletion region (W_{dep}) which depends on doping levels in the p- and n- parts of the NW [4]. It is worthy to notice that in the case of NWs containing a core/shell junction L_{diff} and W_{dep} can be investigated by cleaving the wire: the cleavage edge allows to obtain a junction directly exposed and perpendicular to the electron beam. The analysis of L_{diff} and W_{dep} through cross-sectional EBIC measurements can be used also for the optimization of NW devices, since they both contribute to define the charge collection volume, i.e., the active volume where the generated carriers can be collected in an external circuit. This is of great interest for NW solar cells [23, 26] and for NW light-emitting diodes (LEDs) [4, 27], since it can be used as a feedback measurement to optimize the extension of the active region.

The EBIC analysis of a NW containing a radial p–n junction by scanning the central axis is more complex since the built-in field is parallel to the electron beam. In this case, the EBIC profile is not sensitive to the charge transport regimes, since charges move in the direction of the electron beam (in Fig. 3c, the red arrows indicating the electric field are parallel to the electron beam). In other terms, the extension of the depletion region and the charge diffusion cannot be addressed in this configuration. However, the profile along the axis can be analyzed by taking into account the exact geometry of the junction.

In fact, the geometry of a real NW containing a radial junction deviates from an ideal cylinder and is not trivial: on top, the capping of the internal core typically gives rise to an axial junction (i.e., to a presence of a non-radial electric field component). Away from the extremities along the axis, the electric field is purely radial in the ideal case of a defect-free structure. A schematic representation is displayed in Fig. 3c. Due to this geometry, the current profile is expected to be nonlinear on top of the NW and to become constant if a homogenous $\overrightarrow{E}$ is present along the length of the wire [28]. Therefore, in this configuration EBIC mapping can be used to assess the variation of the built-in field within the nano-object (*intra-wire homogeneity*). Several phenomena can lead to an inhomogeneous field, such as 1D defects [29], inhomogeneous doping concentration or alloy composition along the length of the wire [30].

In addition to the built-in field, also the local carrier collection properties can influence the EBIC profile in this configuration. Being differently doped, core and shell conduct different type of majority carriers to the external circuit (in the inset of Fig. 3c, illustrating a core/shell nitride nanowire LED [31], holes are transported in the shell and electrons are transported in the core). It means that the resistances of the core and the shell play a role for the carrier collection [31]. If the shell is more resistive than the core, it limits the current collection and the EBIC profile decreases from top to the bottom, since the carriers collected in the bottom part of the shell have to overcome a higher resistance than the carriers collected in the top part of the core (dotted line in Fig. 3c). Vice versa, if the core is more resistive than the shell, the EBIC profile increases from the top to the bottom (dashed line in Fig. 3c). Therefore, comparable core and shell resistance is necessary to maximize the current extraction. In this case, the EBIC profile is flat (solid line in Fig. 3c).

Another possible configuration for the EBIC analysis of NWs is the *top-view configuration*, i.e., the electron beam and the NW axis are parallel (Fig. 3d). Top-view configuration can be interesting for analyses of radial junction nanowires: similarly to the case of cross-sectional mapping, by cleaving the top part of the wire, top-view measurements enable the analysis of the internal electric field since the junction field is perpendicular to the electron beam, as was mentioned before. For axial junction NWs, instead, the junction is buried deep from the surface, and therefore, the lateral resolution is lower than in cross-sectional measurements. The extraction of the junction parameters is more complex since an analysis at different beam acceleration voltages (and thus at different beam penetration depth) needs to be carried out. As a consequence, the accuracy of this analysis is strongly dependent on the precision of the model used to describe the electron beam/wire interaction volume. For this reason, top-view analyses are usually used to get information on the wire-to-wire homogeneity of the electrical properties within an array: the top-view visualization (schematically represented in Fig. 3d) allows to compare the collection properties of several tens or hundreds of wires under the same excitation conditions [32], which is of great interest for NW devices.

To be noticed that performing EBIC measurements on arrays or on single NWs requires a different preparation of the samples and in particular different types of electrical contacts. For NW arrays, a top contact is required on a large area. Since the top contact is influencing the shape of the interaction volume and the energy of electrons penetrating into the semiconductor sample, the contact material, and thickness should be adjusted to find a compromise between a low electrical resistance and a low attenuation of the electron beam. In NW array optoelectronic devices, the top contact is usually made of transparent conductive oxides (typically ITO), which has a good optical transparency over a large spectral range, although it strongly attenuates the electron beam [33, 34].

On the other side, the investigation of single NWs requires nanometric contacts to connect the individual nano-objects to an external electrical circuit where the induced current can be detected. This step usually involves destructive processes, since the NWs need to be detached from the substrate; in addition time- and energy-consuming fabrication steps are required to realize nano-contacts by means of electron beam

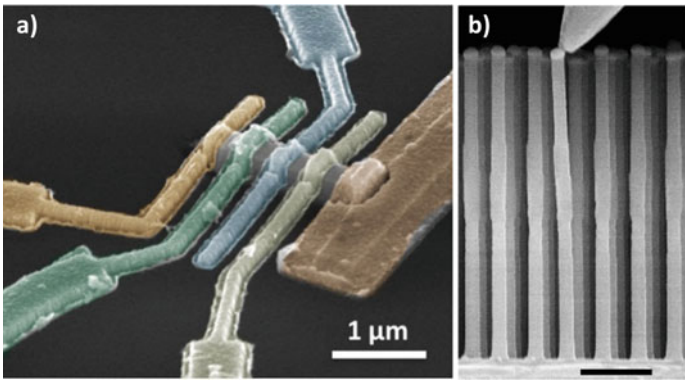

Fig. 4 Examples of electrical contacts on single NWs by metal deposition (**a**) and by in-situ nano-manipulators (**b**). The scale bar in panel b corresponds to 0.5 µm

lithography [31, 35]. Although the resulting contacts are highly reliable, the contact resistance can be low and their fabrication can be very accurate (an example is given in Fig. 4a), this method limits the number of NWs that can be investigated. In this context, in the last years, many works have been reported in the literature concerning the use of metallic nano-tips to collect electrical outputs from individual NWs, as in the case of c-AFM analysis and KPFM microscopy [36–39]. This is a high throughput method which allows to analyze a large number of individual NWs. The use of the nano-manipulators results in faster and more flexible measurements, since the contact points can be easily changed (Fig. 4b). However, it is challenging to control the contact area and the contact resistance, which depends on the mechanical pressure applied by the tip, on the chemistry of the surface and on the work-functions of the semiconductor and of the metallic tip. This approach often results in the formation of a Schottky barrier between the tip and the NW, which can perturb the measurement.

2.2 EBIC Applied to the Analysis of NW Properties

In this Section, the use of EBIC microscopy for NW analyses is discussed through a bibliographic review. As previously discussed, EBIC can be used in a versatile way to investigate several physical phenomena and material properties depending on the internal structure of the wires and the measurement configuration. For the sake of clarity, this section is divided into 3 parts concerning (i) the investigation of the depletion region, (ii) the analysis of the minority carrier diffusion length, and (iii) the assessment of the intra-wire and wire-to-wire homogeneity.

(a) Analysis of the Space Charge Region

The visualization and the analysis of the space charge region (or depletion region) across a junction by EBIC mapping can provide information on the phenomena occurring in a nanostructure in its working conditions. This is particularly interesting for the development of high efficiency solar cells and LEDs where the extension of the depleted region in the active material is strongly correlated to the overall efficiency of the device.

An example is given by Zhong and coworkers who used EBIC mapping on InP NWs containing an axial p-i-n junction. In order to prove the effective charge collection of these structures at the nanoscale, the authors performed EBIC mapping and profiling on individual NWs, demonstrating the extraction of a high EBIC current in a large portion of the nano-object (Fig. 5a, b). Similarly, Tchoulfian et al. used EBIC to investigate the properties of GaN NWs containing a radial p–n junction in view of their application as light emitters [4]. By probing cleaved NWs, EBIC maps showed the collection of the current in correspondence of the junction position (Fig. 5c), allowing to localize the field region and to estimate the doping.

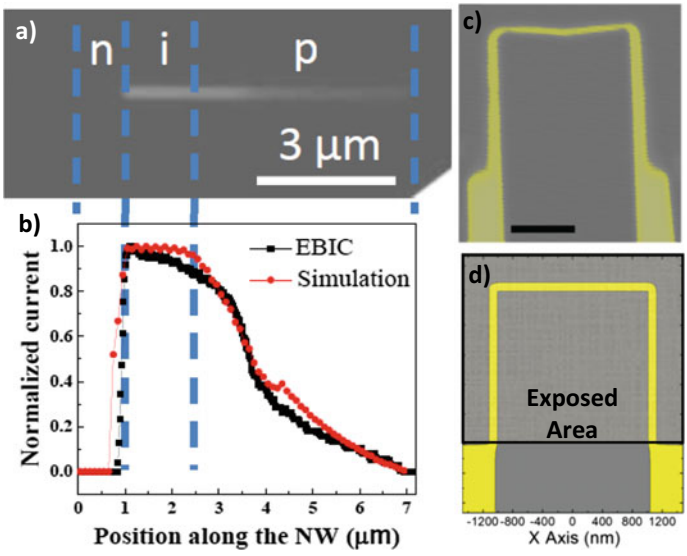

Fig. 5 EBIC map (**a**) and profile along the longitudinal axis (**b**) of a single InP NW; **c** EBIC map of a GaN/InGaN core/shell NW and (**d**) its schematics with respect to the beam exposure. The scale bar represents 1 µm. [Panels a and b are reproduced with permission from Z. Zhong, Z. Li, Q. Gao, Z. Li, K. Peng, L. Li, S. Mokkapati, K. Vora, J. Wu, G. Zhang, Z. Wang, L. Fu, H. H. Tan, and C. Jagadish, 2016, "Efficiency Enhancement of Axial Junction InP Single Nanowire Solar Cells by Dielectric Coating", Nano energy, 28, 106–114, https://doi.org/10.1016/j.nanoen.2016.08.032. Copyright (2016) Elsevier. Panels c and d are reproduced and re-adapted with permission from P. Tchoulfian, F. Donatini, F. Levy, A. Dussaigne, P. Ferret, J. Pernot, 2014, "Direct imaging of p–n junction in core–shell GaN wires", Nano Lett. 14, 3491–3498. Copyright (2014) American Chemical Society.]

In addition, EBIC maps allowed to observe dopant activation phenomena upon exposure of the inner part of the wire to the electron beam. In particular, the areas exposed to an intense electron beam showed a narrower space charge region, as schematized in Fig. 5d.

To understand the relation between the depletion region extension and the doping level, it should be recalled that the depleted volume across a p–n junction reduces as the doping level in the semi-junctions gets higher, due to the larger carrier density. Generally, those quantities are related as

$$V_{dep}\alpha\sqrt{\frac{1}{N_d}+\frac{1}{N_a}}=\sqrt{\frac{1}{N_{eff}}}, \tag{5}$$

where V_{dep} is the space charge region volume, N_d and N_a represent, respectively, the donor and acceptor doping levels across the junction and N_{eff} is the effective doping level. Considering a 1D model for an abrupt p–n junction, the relation between the depletion region width (W) and N_{eff} can be expressed as

$$W=\sqrt{\frac{2\varepsilon(V_{bi}-V)}{q}\mathrm{x}\left(\frac{1}{N_{eff}}\right)}, \tag{6}$$

where ε is the permittivity of the material, V_{bi} is the built-in field arising across the abrupt junction, V is the applied bias and q is the electron charge.

Referring to the work of Tchoulfian and coauthors, they used these equations to estimate the effective doping level in the material at the nanoscale by analyzing quantitatively the EBIC maps and profiles, as shown in Fig. 6a where W is experimentally estimated.

Since the model, described by Eq. 5 and 6, takes into consideration also the effect of an external bias, several measurements can be performed at a different voltage on a single wire (Fig. 6b). By plotting W(V) it is possible to obtain an estimation of N_{eff}, as shown in Fig. 6c. This approach has been used also to estimate separately the active acceptor and donor concentrations in a p–n junction [40]. This was achieved using the aforementioned EBIC analysis method in combination with voltage-induced SE contrast imaging which can be used to localize the position of an abrupt junction due to the different contrast given by p- and n- dopants [41, 42]. An example of this phenomenon can be observed in the SEM images of Fig. 6d, where the secondary electron contrast allows to localize the position of the axial p–n junction. In this work, the authors investigated the possibility to obtain an Esaki diode, i.e., an abrupt heavily doped p^{++}/n^{++} junction where a tunneling current could flow under voltage [43, 44]. Since the depletion region width is a critical parameter for the design of an Esaki diode, EBIC mapping has been used to measure the extension of the space charge region in different wires (Fig. 6d) [45]. The quantitative analysis of those maps by tracing the profile along the axis (reported in Fig. 6e), allowed to correlate the

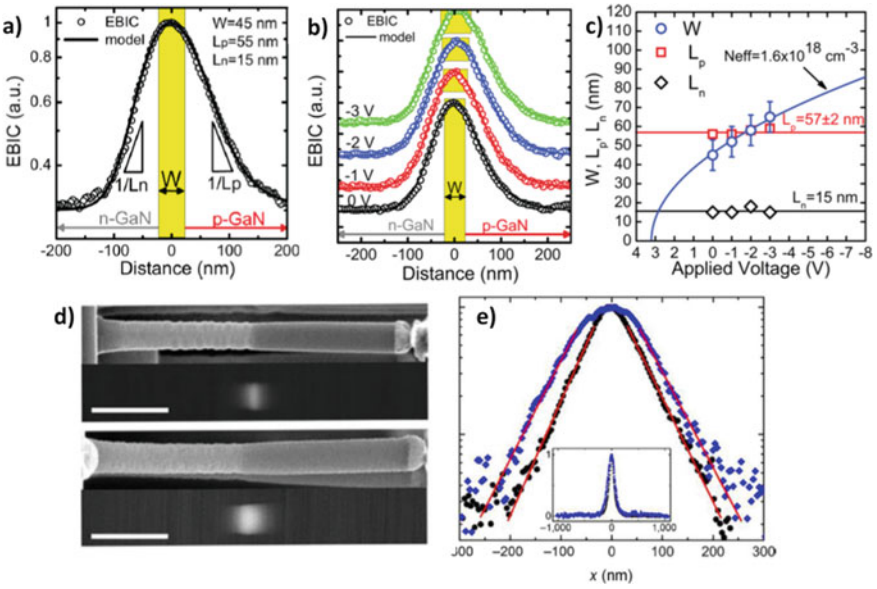

Fig. 6 Estimation of the minority carrier diffusion lengths (L_n, L_p) and depleted region extension (W) in an EBIC profile (**a**) and in several profiles acquired under several external biases (**b**); **c** W, L_n and L_p as a function of the applied voltage. The plot enables the estimation of the effective doping level across the junction (N_{eff}) by fitting of W(V). **d** SEM images and corresponding EBIC maps of two InGaP/InP NWs containing a tunnel diode; **e** Axial EBIC profiles corresponding to the maps in panel d. [Panels a-c are reproduced with permission from P. Tchoulfian, F. Donatini, F. Levy, A. Dussaigne, P. Ferret, J. Pernot, 2014, "Direct imaging of p–n junction in core–shell GaN wires", Nano Lett. 14, 3491–3498, https://doi.org/10.1021/nl5010493. Copyright (2014) American Chemical Society. Panels d-e are reproduced with permission from X. Zeng, G. Otnes, M. Heurlin, R. T Mourão, and M. T. Borgström, 2018, "InP/GaInP nanowire tunnel diodes", Nano Resear., 11(5), 2523–2531. Copyright (2018) Springer Nature]

I(V) characteristic curves of the Esaki diode with the presence of a narrow depletion region in individual nanowires.

(b) Estimation of the Minority Carrier Diffusion Length

While the extension of the space charge region depends on the design of the junction, the minority carrier diffusion length (L_{diff}) can be considered as a material parameter which measures the mean free path of the minority carriers in a doped semiconductor. Generally, L_{diff} can be influenced by a number of factors as defect density, impurities concentration, doping level, and in nanowires, surface-to-volume ratio [46–48]. For these reasons, it is a parameter of great interest for the analysis of the materials in view of their application.

In order to estimate L_{diff} in NWs by EBIC mapping, a rectifying interface is required to obtain a localized charge collection region where the carrier diffusion can be analyzed. To study homogeneous materials, a Schottky contact is intentionally

induced at the interface with a metal contact for this purpose. This is the case of Solanki et al. [49], who performed several EBIC line scans under different external bias on p-doped Si NWs to evaluate their suitability for photovoltaic applications (Fig. 7a). An estimated average L_{diff} value was around 700 nm, which is much lower than what typical values observed in high quality bulk Si ($L_{diff} > 100$ μm [6, 50]). A reduction of the minority carrier diffusion length is observed in NWs with respect to the bulk material also in other materials such as GaAs, GaN, InP [8, 17, 51].

On the other hand, an electrical junction is naturally present in active structures like solar cells, LEDs, and transistors, and the analysis of L_{diff} is useful to describe both material properties and the architecture of the whole devices. For example, in the case of a NW containing an axial junction, the minority carrier diffusion length is related to the ability of the structure to collect the generated carriers, and therefore, the L_{diff} value is important to determine the material quality for specific applications. For instance, high L_{diff} values are desirable for NW solar cells, where a large collection region needs to be achieved. On the contrary, low values are expected for an Esaki diode, where very high doping levels are necessary to maximize the tunneling properties. An example is given by Wallentin et al. who performed EBIC microscopy on InP NWs which exploited tunneling properties to prove the existence of a sharp and highly doped axial junction (Fig. 7b) [8].

As previously mentioned, it has been experimentally observed that the minority carrier diffusion is lower in NWs than in bulk materials. The reason for this can be addressed to the high surface-to-volume ratio of these nano-objects. In this case, surface recombination rate becomes predominant and thus the minority carriers recombine faster in NWs than in bulk. The relationship between the minority carrier diffusion length and the surface in NWs has been widely investigated experimentally [17]. As shown in Fig. 7c, d, Chang et al. [9], reported the EBIC analysis of L_{diff} in GaAs NWs with and without surface passivation, proving a sixfold increase when saturating the surface dangling bonds.

The variation of L_{diff} with the surface recombination rate can be better appreciated through the equations describing the variation of the carrier lifetime in high aspect ratio structures [52] (Eq. 7), and the definition of L_{diff} for a NW (Eq. 8)

$$\frac{1}{\tau_{NW}} = \frac{1}{\tau_B} + \frac{4S}{d} \tag{7}$$

$$L_{diff} = \sqrt{D * \tau_{NW}} \tag{8}$$

where τ_{NW} and τ_B are, respectively, the minority carrier lifetimes in the NW and in bulk, S is the surface recombination rate, d is the NW diameter, and D is the diffusion coefficient defined by the Einstein–Smoluchowski relationship.

Gutsche et al. [17] measured the L_{diff} of GaAs NWs containing a p–n junction with and without passivation, testing also the stability in time of the ammonium sulfide passivating action (Fig. 7e). By using these equations, the surface recombination rate in p- and n-doped GaAs NWs is estimated (Fig. 7f), and values comparable to

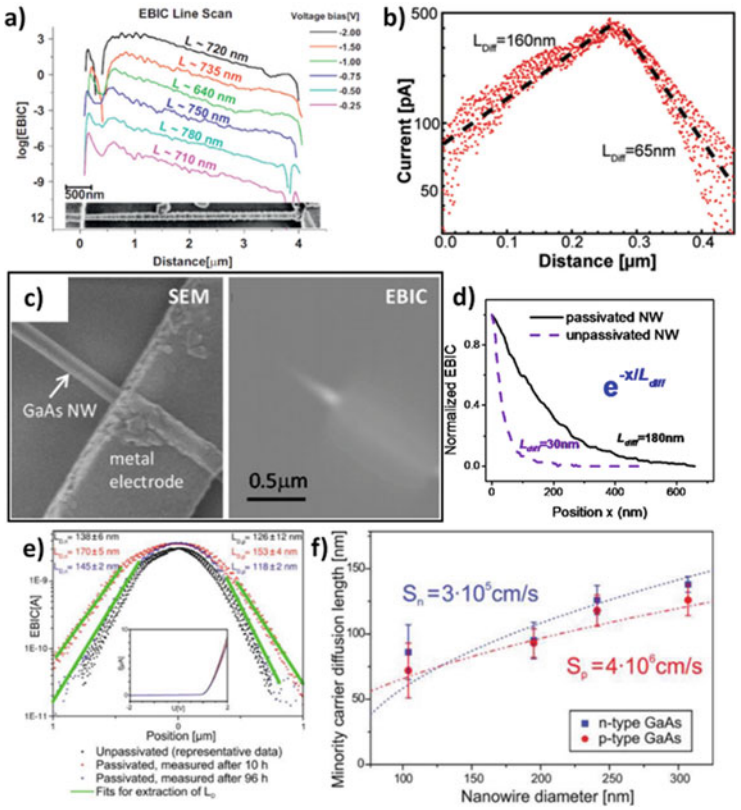

Fig. 7 **a** EBIC profile lines of a p-Si NW under different external bias (L_{diff} is estimated for each profile); **b** EBIC profile of an InP NW containing an axial junction (L_{diff} is estimated on both p- and n- segments); **c** SEM and corresponding EBIC map of a GaAs NW under a metal pad forming a Schottky contact; **d** EBIC profile of the GaAs NWs with and without surface passivation; **e** EBIC profiles of a GaAs NW containing a p–n junction with and without ammonium sulfide passivation; **f** L_{diff} versus NW diameter corresponding to panel e and corresponding estimation of the surface recombination rate in p- and n-doped GaAs NWs. [Panel a is reproduced with permission from A. Solanki, P. Gentile, V. Calvo, G. Rosaz, B. Salem, V. Aimez, D. Drouin, N. Pauc, 2012, "Geometrical control of photocurrent in active Si nanowire devices", Nano Energy 1(5), 714–722, https://doi.org/10.1016/j.nanoen.2012.05.010. Copyright (2012) Elsevier. Panel b is reproduced with permission from J. Wallentin, P. Wickert, M. Ek, A. Gustafsson, L. R. Wallenberg, M. H. Magnusson, L. Samuelson, K. Deppert, and M. T. Borgström, 2011, "Degenerate p-doping of InP nanowires for large area tunnel diodes", App. Phys. Lett.., 99(25), 253,105, https://doi.org/10.1063/1.3669697. Copyright (2018) AIP Publishing. Panels c and d are reproduced with permission from C.-C. Chang, C.-Y. Chi, M. Yao, N. Huang, C.-C. Chen, J. Theiss, A. W. Bushmaker, S. LaLumondiere, T.-W. Yeh, M. L. Povinelli, C. Zhou, P. D. Dapkus, S. Cronin, 2012, "Electrical and Optical Characterization of Surface Passivation in GaAs Nanowires", Nano Lett., 12 (9), 4484–4489, https://doi.org/10.1021/nl301391h. Copyright (2012) American Chemical Society. Panels e and f are reproduced with permission from C. Gutsche, R. Niepelt, M. Gnauck, A. Lysov, W. Prost, C. Ronning, F.-J. Tegude, 2012, "Direct Determination of Minority Carrier Diffusion Lengths at Axial GaAs Nanowire p − n Junctions", Nano Lett., 12 (3), 1453 − 1458, https://doi.org/10.1021/nl301391h. Copyright (2012) American Chemical Society]

the bulk materials are found. This work proved that the lower carrier lifetime and therefore lower minority carrier diffusion length is related to the large extension of the lateral surface and its recombination action. This negative effect can be alleviated by a dedicated surface passivation.

(c) **Homogeneity Assessment by EBIC Mapping**

The analysis of the space charge region and the estimation of the diffusion length can also be used to assess the homogeneity of the electrical properties in individual wires. This approach is particularly useful in the case of NWs consisting of several materials (hetero-structured NWs) or having a complex internal structure (such as wires containing quantum insertions). While the first case is typical for photovoltaic structures, the second one represents a common case for LED NWs.

A comprehensive example of intra-wire homogeneity analysis is given by the work of Tchernycheva et al. on GaN/InGaN NWs [30]. The SEM image of the core/shell NW and the corresponding EBIC map is shown in Fig. 8a, b. In this work, the EBIC current is measured in a cross-sectional configuration upon cleavage of the NWs, in order to expose the inner ternary alloy quantum well. The authors used the current collected from the active region to describe the intra-wire variation of the electrical properties of the GaN core/shell structure. For instance, by tracing the profile at different height along the wire (Fig. 8c), and by estimating the L_{diff} values, the homogeneity of the charge transporting layers (n-GaN in the core and p-GaN in the shell) is assessed. In fact, by overlapping the normalized radial EBIC profiles acquired at different position, it was possible to prove that a homogeneous charge transport is achieved within individual NWs, which is a necessary condition to obtain high performing nanostructured LEDs.

In addition to the radial analysis, the variation of the EBIC current along the axial direction can provide useful information on the properties of the LED. As shown in Fig. 8d, a higher current is collected at the bottom of the wire and a lower current is collected at the top. Several factors could affect the axial collection properties of a core/shell wire, such as inhomogeneous properties of the core/shell junction along the axis, increased defect density on top, and different core and shell resistance [31, 53]. However, the radial analysis of the EBIC profile revealed a highly homogeneous junction while an increased defect density would have resulted in a sharper variation of the signal, as for bulk materials [54]. On the contrary, a higher core resistance is expected to induce a gradually decreasing EBIC signal from the bottom to the top in agreement with the observations [31].

This qualitative analysis is very important for the core/shell structure where the characterization of the electrical properties of the inner core is usually a challenging task. With this respect, EBIC microscopy can be used as a powerful characterization tool for fast analysis of NW devices. This was done by Piazza et al. [28], who investigated GaAs NWs containing a radial p–n junction. By contacting a GaAs NW with a micromanipulator, as shown in the SEM image in Fig. 8e, the authors observed highly constant EBIC current along the length of the wire (from both the map and

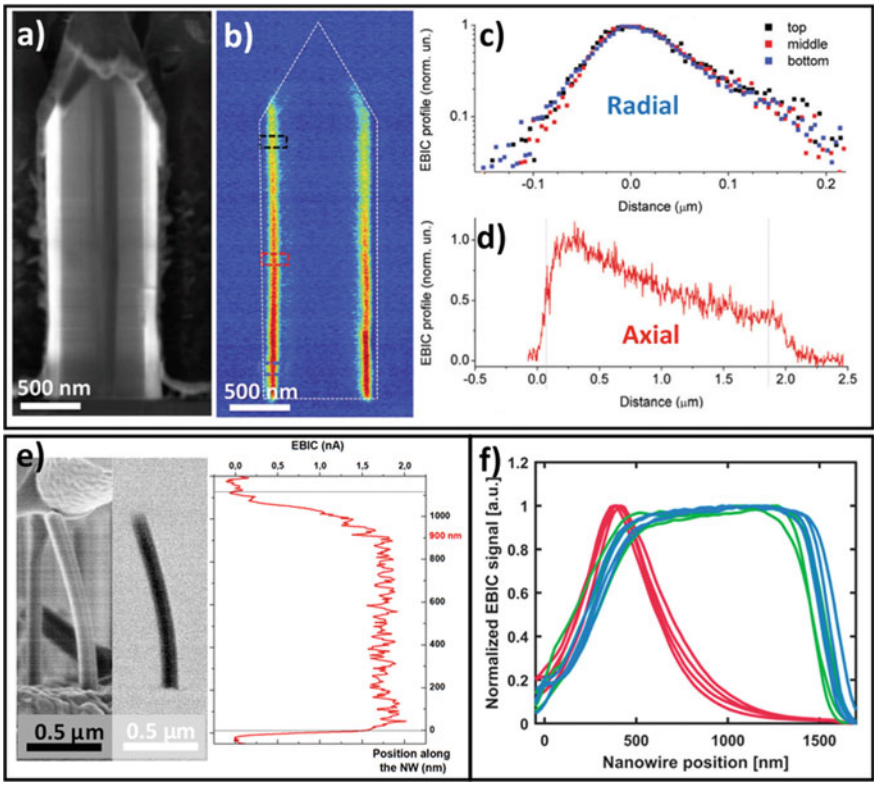

Fig. 8 SEM image (**a**) and corresponding EBIC map (**b**) of a core/shell InGaN/GaN NW; **c** Normalized radial EBIC profile (the origin of the horizontal axis corresponds to the maximum EBIC current value); **d** Normalized axial EBIC profile (the origin of the horizontal axis corresponds to the NW/substrate interface); **e** SEM image, EBIC map and corresponding axial EBIC profile of a core/shell GaAs NW; **f** EBIC profiles of several InP NWs containing a nominal p-i-n structure with different level of compensation used in the middle segment, respectively equal to $^{\chi}{}_{DEZn} = 0$ (red), $^{\chi}{}_{DEZn} = 0.5\ 10^{-7}$ (green) and $^{\chi}{}_{DEZn} = 2.1\ 10^{-7}$ (blue). [Panels a-d are reproduced with permission from M. Tchernycheva, V. Neplokh, H. Zhang, P. Lavenus, L. Rigutti, F. Bayle, F. H. Julien, A. Babichev, G. Jacopin, L. Largeau, R. Ciechonski, G. Vescovi, O. Kryliouk, 2015, "Core–shell InGaN/GaN nanowire light emitting diodes analyzed by electron beam induced current microscopy and cathodoluminescence mapping", Nanoscale 7, 11,692–11,701, https://doi.org/10.1039/C5NR00623F. Copyright (2012) The Royale Society of Chemistry. Panel e is reproduced with permission from V. Piazza, M. Vettori, A. A. Ahmed, P. Lavenus, F. Bayle, N. Chauvin, F. H. Julien, P. Regreny,G. Patriarche, A. Fave, M.l Gendry, M. Tchernycheva, 2018, "Nanoscale investigation of a radial p–n junction in self-catalyzed GaAs nanowires grown on Si (111)", Nanoscale 10, 20,207–20,217, https://doi.org/10.1039/c8nr03827a. Copyright (2012) The Royale Society of Chemistry. Panel f is reproduced with permission from G. Otnes, E. Barrigón, C. Sundvall, K. E. Svensson, M. Heurlin, G. Siefer, L. Samuelson, I. Åberg, M. T. Borgström, 2018, "Understanding InP Nanowire Array Solar Cell Performance by Nanoprobe-Enabled Single Nanowire Measurements", Nano Lett. 18, 3038 − 3046, . Copyright (2018) American Chemical Society]

the axial profile), demonstrating that the doping concentrations induce a comparable series resistance in the core and in the shell.

As intuitive, this approach can be very useful also for axial structures where EBIC mapping and profiling can be used to optimize the growth parameters in order to achieve optimal junction properties. For instance, Otnes et al. [26], used this approach to optimize the MOCVD growth of InP NWs containing an axial p-i-n junction for photovoltaic devices. In particular, the authors faced the challenge given by the n-type background doping of InP due to P-vacancies, which induced a fairly abrupt p-n^--n junction instead of the desired p-i-n architecture, as pointed out by the red EBIC curve in Fig. 8f. By using a dimethyl-zinc (DMZn) flow, a compensating p-doping was added to the middle segment to restore its intrinsic behavior. The authors were able to obtain a wide space charge region, as necessary for photovoltaic devices and to define the optimal dopant flow to be used to overcome the problem (green and blue curves).

Besides the analysis of the intra-wire properties, EBIC mapping also can be used to assess the wire-to-wire homogeneity of the electrical properties. For this purpose, the measurement can be performed in a top-view or in a cross-sectional configuration. Tchoulfian et al. [4], for instance, acquired an EBIC map on a tilted array to prove the homogeneity of the GaN core/shell NWs (Fig. 9a, b). Thanks to the cleavage of one NW row, they proved that the depleted region, which produces the EBIC current, is reasonably homogeneous in all the observed wires. Togonal and coauthors, instead, combined different measurement configurations in order to perform a more systematic analysis of the array homogeneity [55]. They analyzed Si/a-Si NW radial junction solar cells obtained by a combination of a top-down etching with subsequent a-Si shell overgrowth. The authors observed the presence of few non-active Si wires (labeled as "dead wires" in Fig. 9c) by cross-sectional EBIC measurements where a clear difference with the active wires could be observed. The impact of the "dead wires" on the overall activity of the array can be appreciated by the top-view measurement (reported in the inset of Fig. 9c).

A particularly interesting case is the analysis of non-vertical NWs. In this case, the EBIC map can provide a feedback on the phenomena occurring at the points of contact between NWs, which can potentially induce leakage paths, and therefore, an electrical loss. Misra et al. [56] analyzed solar cells based on self-assembled Si/a-Si NWs grown by PECVD, which present a highly irregular morphology. EBIC mapping on these non-vertical NWs was performed to visualize eventual current loss at morphological defects (Fig. 9d). Surprisingly, EBIC map revealed that the array is electrically robust in particular at the NW crossings (highlighted with yellow arrows) where no decrease in the collected current is observed.

3 Cathodololuminescence

Cathodoluminescence (CL) is a spectroscopic technique which combines the analysis of the radiative recombination phenomena, typical of luminescence methods such as photoluminescence, and the spatial resolution of electron probe microscopy. With

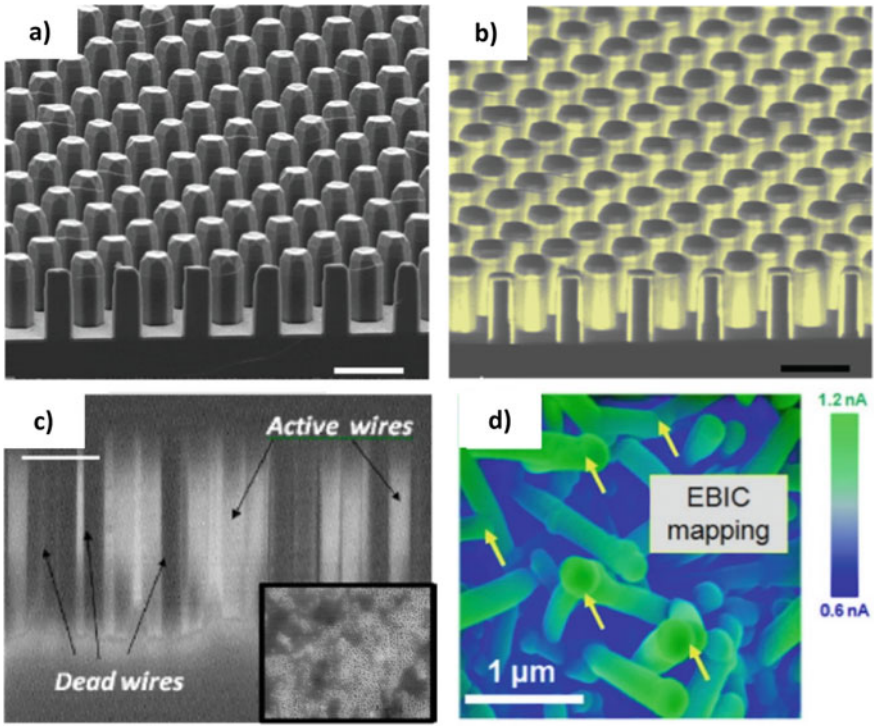

Fig. 9 SEM image (**a**) and corresponding EBIC map (**b**) of a GaN/InGaN NWs array; **c** Cross-section EBIC mapping of samples with "dead" and electrically active Si NWs. The scale bar represents 1 µm. The inset shows the EBIC top-view EBIC mapping confirming that only few nanowires are active. **d** EBIC map of non-vertical Si NWs containing a radial structure. [Panels a and b are reproduced with permission from P. Tchoulfian, F. Donatini, F. Levy, A. Dussaigne, P. Ferret, J. Pernot, 2014, "Direct imaging of p–n junction in core–shell GaN wires", Nano Lett. 14, 3491–3498, https://doi.org/10.1021/nl5010493. Copyright (2014) American Chemical Society. Panel c is reproduced with permission from A. S. Togonal, M. Foldyna, W. Chen, J. X. Wang, V. Neplokh, M. Tchernycheva, J. Nassar, P. Roca i Cabarrocas, Rusli, 2016, "Core – Shell Heterojunction Solar Cells Based on Disordered Silicon Nanowire Arrays", J. Phys. Chem. C, 120, 2962 – 2972, . Copyright (2016) American Chemical Society. Panel d is reproduced with permission from S. Misra, L. Yu, W. Chen, M. Foldyna, P. Roca i Cabarrocas, 2014, "A review on plasma-assisted VLS synthesis of silicon nanowires and radial junction solar cells", J. Phys. D: Appl. Phys. 47 393,001-, . Copyright (2016) IOP Publishing]

this regard, the main advantages of CL with respect to the photoluminescence are the ability of visualizing the morphology of the investigated sample and the nanoscale excitation which allows to achieve a very high resolution for the investigation of the optical properties. As discussed in Sect. 1, the spatial resolution depends on the interaction volume, the geometry of the sample, and the diffusion of the excited carriers (free carriers and/or excitons).

CL working principle can be schematized as in Fig. 10a: the e^-/h^+ pairs, locally excited by the electron beam, induce the emission of photons due to the radiative

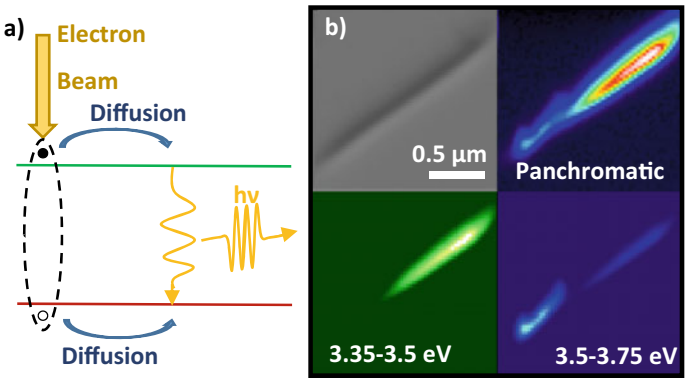

Fig. 10 **a** Schematic of the working principle of CL mapping of semiconductor materials; **b** SEM image of a GaN NWs containing AlN/GaN MQDs and corresponding panchromatic, 3.35–3.5 eV and 3.5–3.75 eV filtered CL maps

recombinations in the material. By associating the position of the scanning beam, with the SE image and the detected luminescence spectra in each point a so-called spectrum-image is acquired. In particular, it provides a 2D optical map of the investigated sample. We note that this is an excitation map. Indeed, while the excitation position is precisely defined, the exact recombination position is not known since the excited carriers (eventually bound by excitonic interaction) can move over a non-negligible distance. For instance, carrier diffusion towards a low-bandgap region results in a redshift in the photon emission [57].

In order to extract, from the spectrum-image, useful information about the emitted luminescence, CL maps show the integrated intensity for each pixel. If the luminescence intensity is integrated over the whole detected spectrum, a spectrally integrated map (or panchromatic map) is obtained. Often the integration is done in a narrow wavelength range of interest to display the properties of a specific material or structure. In fact, the energy of the emitted photons reflects the local band structure which may depend on a large number of factors, such as the crystal structure, local composition and strain state [58–60]. An example is given in Fig. 10b, where the SEM image of a GaN NW containing AlN/GaN multiple quantum discs and corresponding CL maps built by integrating the luminescence in different spectral ranges are shown. In this case, due to the strain arising from the heterostructure, photons with higher energy are emitted from the bottom part of the wire. This phenomenon cannot be observed in panchromatic maps since a spectral analysis of the emission is needed. For more details on this work, refer to Ref. [59].

The main application of CL mapping is the visualization of the optical transition energies and intensities [61]. Indeed, the variations of these quantities can be related to the presence of quantum confining heterostructures [62–67] or to inhomogeneous composition and alloy fluctuations [60, 68, 69]. Another wide application of CL mapping is the assessment of material defects, which can be sites for both non-radiative and radiative recombination phenomena. In the first case, the presence of

defects can be revealed by a local quenching of the CL emission [70, 71]. The analysis of radiative defects, instead, relies on the knowledge of their emission wavelength, since specific types of defects are characterized by radiative recombination of carriers at determined energy levels. Indeed, point defects, stacking faults or dislocations create levels within the bandgap which capture the charge carriers by allowing them to recombine at lower energies [47, 72, 73].

In some cases (e.g., for materials containing closely packed nano-emitters [62, 63]), even higher resolution is desirable. For this reasons, several variations of the CL setup have been developed in the last years [61, 62]: for instance, STEM-CL was demonstrated to be able to characterize the optical properties of closely packed quantum discs [62, 63] or of 2D and 1D radiative and non-radiative defects with unmatched spatial resolution [74, 75].

Another important application of CL mapping, which has gained a strong interest in the recent years, is the analysis of the luminescence lifetime with nanometric spatial resolution, which can be applied to investigate the properties of quantum emitters or to assess the impact of localized defects [57, 76, 77] (e.g., grain boundaries in solar cells [78]). This can be obtained by time-resolved CL measurements (TR-CL).

A schematic of a complete SEM-CL/TR-CL tool equipped with time-resolved capabilities is shown in Fig. 11. Different existing approaches providing temporal resolution of CL will be discussed in detail later in Sect. 3.2. The electron probe is generated by the electron source (Schottky/Field-emission gun – FEG) and focused on the sample by means of a diaphragm characterized by the illumination aperture and by the magnetic lenses. The electron beam current injected into the sample is usually in the nA range. However, it can be tuned from a few tens of pA up to a few tens of nA, depending on the radiative efficiency and the high/low injection regime targeted. The CL emission generated in the far-field by the probe/sample interaction (represented by the dashed yellow lines in Fig. 11), is collected by a parabolic mirror,

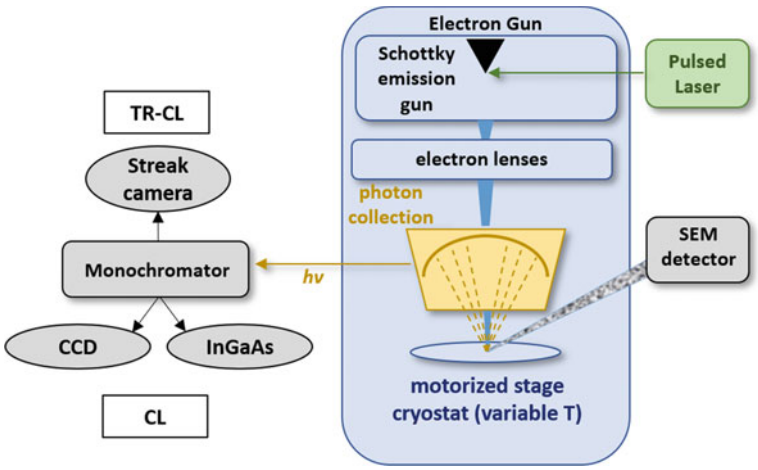

Fig. 11 Simplified schematic of a SEM-CL/TR-CL setup

directed out of the microscope, and analyzed by a monochromator and a detector array. To be noticed that using detectors made of different materials it is possible to be sensitive to different photon energy: for instance, a silicon CCD is used for visible and near-infrared wavelengths up to 1.1 μm, while an InGaAs detector array can be used for wavelengths up to 1.7 μm. The stability of the sample stage is a key factor for high-resolution CL maps: the drift can reach values as low as 200 nm/hour, allowing high-resolution mapping of single NWs with low radiative efficiencies with total integration times up to several tens of minutes. In addition, CL setups usually allow low-temperature measurements (5 K–10 K) thanks to a He cryostat, enabling the analysis of the optical properties as a function of the temperature.

3.1 SEM-CL Mapping Applied to Nanowires

CL mapping is sensitive to the variation of the bandgap in the investigated sample since the energy of the photons emitted upon a band-to-band transition changes; therefore, it can be used to assess the homogeneity of individual NWs. As already mentioned, one of the most common uses of CL mapping is related to the analysis of the defects. In fact, the presence of defects can induce a quenching of the band edge transition (if non-radiative recombination phenomena occur in the defect) and/or the emission of less energetic photons, i.e., a redshift of the emission (if radiative recombination phenomena occur in the defect). For instance, Bolinsson et al. investigated the variation of the optical properties of GaAs/AlGaAs core/shell NWs characterized by a high stacking fault density [79]. In this work, the authors proved that due to the high defect densities the NWs exhibit a luminescence peak below the material bandgap at 1.48 eV. In addition, the expected 1.52 eV emission (zinc-blende GaAs) has been observed only in NWs containing large single crystal segments; in the other cases, the near band edge luminescence was strongly quenched (Fig. 12a).

The possibility to have a high spatial resolution when mapping individual wires allow to study the origin of specific emissions. This advantage has several applications not only for the analysis of the defects, but in general for the investigation of elements which induce an intra-wire inhomogeneity, such as the crystal phase in materials which exhibit polytypism. Indeed, the luminescence emission is characteristic of the chemical nature of the material and its crystal phase. With this respect, an interesting study was carried out by Spirkoska et al. [80], on GaAs NWs containing periods of wurtzite (WZ) and zinc-blende (ZB) phases (Fig. 12b). By scanning NWs dispersed on a substrate, the CL maps revealed optical emissions at different energies (by several tens of meV) in the same nanostructures. The authors attribute this peculiar behavior to the presence of different crystal phases with nanometric dimensions and short diffusion lengths, which therefore act as a sequence of quantum heterostructures as schematically represented in Fig. 12c. By the use of luminescence techniques, also the bandgap of these phases in NWs and their band alignment has been determined [81].

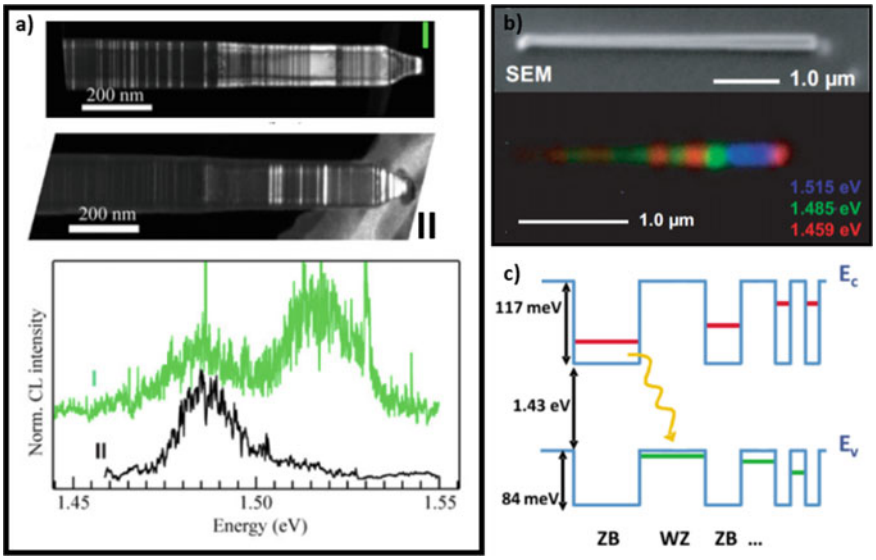

Fig. 12 **a** A combined CL and TEM study of two different single GaAs nanowires with a high stacking fault density and with/without a long zinc-blende GaAs segment (respectively labeled as "I" and "II"). In the CL spectra, the low energy emission of the defect (1.48 eV) is visible in both NWs, while the band edge transition is visible only in the NW I. **b** SEM image and corresponding CL map of a single GaAs NW containing wurtzite and zinc-blende insertions (the color legend is displayed); **c** Schematic of the band alignment of ZB and WZ insertions characterized by quantum confinement. [Panel a is reproduced with permission from J. Bolinsson, M. Ek, J. Trägårdh, K. Mergenthaler, D. Jacobsson, M.-E. Pistol, L. Samuelson, A. Gustafsson, 2014, "GaAs/AlGaAs heterostructure nanowires studied by cathodoluminescence", Nano Res. 7(4), 473–490, https://doi.org/10.1007/s12274-014-0414-2. Copyright (2014) Springer-Nature. Panels b and c are reproduced with permission from D. Spirkoska, J. Arbiol, A. Gustafsson, S. Conesa-Boj, F. Glas, I. Zardo, M. Heigoldt, M. H. Gass, A. L. Bleloch, S. Estrade, M. Kaniber, J. Rossler, F. Peiro, J. R. Morante, G. Abstreiter, L. Samuelson, A. Fontcuberta i Morral, 2009, "Structural and optical properties of high quality zinc-blende/wurtzite GaAs nanowire heterostructures", Phys. Rev. B 80, 245,325. Copyright (2009) American Physical Society]

In the last years, the control on the growth of nanometer-sized insertions in nanowires has been improved also thanks to the use of CL imaging for the analysis of quantum structures. For example, CL mapping enables the investigation of the optical properties of heterostructures containing quantum dots, wells, and disks [27, 59, 82]. This research branch is particularly interesting for the development of new generation devices (single photons emitters and detectors, and other direction of quantum photonics). As an example, Heiss and coworkers studied GaAs/AlGaAs core/shell NWs where low Al ternary alloy quantum dots form with a self-assembly mechanism [83]. The properties of these quantum dots are hardly predictable due to the complexity of the system which involves a core/shell structure, several ternary alloy compositions, and different crystal phases. However, the peculiar composition of the dots allows their characterization by means of CL mapping. As shown in

Fig. 13a, the optical map proves the presence of discontinuous structures within the wire exhibiting emission of photons at ~1.8 eV, consistently with the expected energy levels of the quantum dots.

The use of CL mapping has led also to the improvement of NW based LEDs and solar cells, where the optical properties can be finely tuned by inserting quantum structures. For instance, Tchernycheva et al. extensively investigated the fabrication of GaN NWs containing InGaN quantum wells for light-emitting diode applications [3, 27, 30, 84]. They found that one of the limiting factors of this technology was the spectrally broad electroluminescence of the final device. For this reason, the authors used CL mapping to probe the homogeneity of the composition of the ternary alloy along the length of single wires (Fig. 13b) [30]. This analysis revealed an In gradient from the bottom (estimated around 10%) to the top (estimated around 20%).

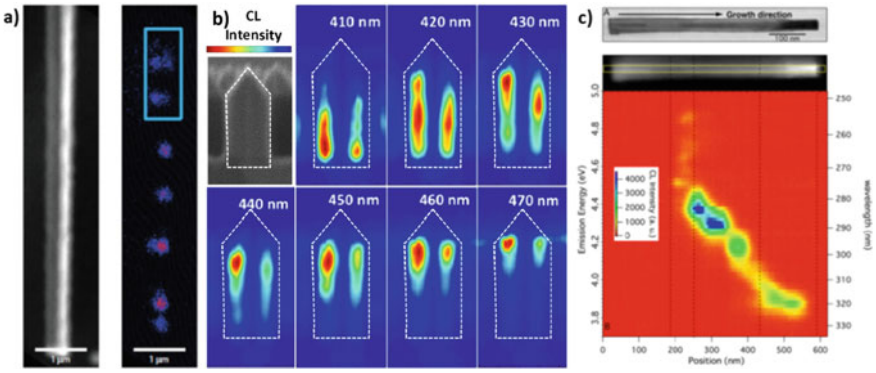

Fig. 13 **a** SEM image and corresponding CL map (filtered between 1.8 and 1.9 eV) of an individual GaAs/AlGaAs core/shell NW containing low Al quantum dots; **b** SEM image of the inner cross-section of a GaN NWs containing radial InGaN insertions and corresponding CL maps at different emission wavelengths. The dashed white lines define the outer borders of the wire. CL relative intensity is represented by a color bar displayed in the inset. The maps show that the luminescence from the ternary alloy is redshifted from the bottom to the top; **c** SEM image, panchromatic CL map and spectrally resolved CL map of an individual AlGaN wire. [Panel a is reproduced with permission M. Heiss, Y. Fontana, A. Gustafsson, G. Wüst, C. Magen, D. D. O'Regan, J.W. Luo, B. Ketterer, S. Conesa-Boj, A. V. Kuhlmann, J. Houel, E. Russo-Averchi, J. R. Morante, M. Cantoni, N. Marzari, J. Arbiol, A. Zunger, R. J.Warburton and A. Fontcuberta i Morral, 2013, "Self-assembled quantum dots in a nanowire system for quantum photonics", Nat. Mat. 12(5), 439–444, https://doi.org/10.1038/NMAT3557. Copyright (2012) Springer Nature. Panel b is reproduced with permission from M. Tchernycheva, V. Neplokh, H. Zhang, P. Lavenus, L. Rigutti, F. Bayle, F. H. Julien, A. Babichev, G. Jacopin, L. Largeau, R. Ciechonski, G. Vescovi, O. Kryliouk, 2015, "Core–shell InGaN/GaN nanowire light-emitting diodes analyzed by electron beam induced current microscopy and cathodoluminescence mapping", Nanoscale 7, 11,692–11,701, https://doi.org/10.1039/C5NR00623F. Copyright (2012) The Royale Society of Chemistry. Panel c is reproduced with permission from A. Pierret, C. Bougerol, B. Gayral, M. Kociak, B. Daudin, 2013, "Probing alloy composition gradient and nanometer-scale carrier localization in single AlGaN nanowires by nanocathodoluminescence", Nanotech. 24, 305,703, https://doi.org/10.1088/0957-4484/24/30/305703. Copyrigth (2013) IOP Publishing]

Generally, the presence of alloy fluctuations is one of the most common limiting factors for optoelectronic devices, where a strict control over the optical properties is required, and therefore, a homogeneous composition is desirable. Indeed, a variation of the composition of III-V alloys induces a variation of the electronic bandgap and, thus, of the optical emission [68]. For this reason, this phenomenon is largely studied by CL, especially in III-N NWs [3, 30]. This the case of Pierret et al. [60], who investigated the growth of AlGaN NWs for ultraviolet LEDs. In Fig. 13c, the CL spectral map of a single NW is shown, indicating the energy (and the corresponding wavelength) of the photons emitted along the axis of the wire. The map shows that the emission wavelength shifts to higher values moving from the bottom to the top, indicating a Ga-poor composition on the bottom and a Ga-rich composition on the top. This analysis gave the possibility to investigate the growth regimes for the wires under observation. Moreover, CL allowed to investigate other growth-related phenomena such as the presence of alloy fluctuation in the order of 20–30 nm and the formation of a parasitic AlN shell around the wire [85].

Due to the complex growth kinetics, the composition of III-V alloy NWs can be influenced by doping incorporation [86, 87]. This is an important issue since many applications require doped ternary alloy materials (a common example is the use of InGaN for LEDs and InGaP and AlGaAs for tandem solar cells). In this scenario, the use of CL is fundamental for the design of nanowires containing electrical junctions. A representative example is given by the work of Bologna and coauthors [86], who optimized the growth of InGaP NWs via template-assisted selective epitaxy (TASE). While a homogeneous composition was achieved in undoped wires, CL maps revealed a strong compositional variation in NWs containing an axial p–n junction (Fig. 14a, b). In particular, they observed a blue-shift of the emission in a single NW containing a p–n junction (Fig. 14c), associated to an increase of the Ga content in the p-doped segment, which is expected to have a negative effect on the spectral absorption of the light. To be noticed that the effect of the doping type on the alloy composition was already known for InGaP NWs grown by different methods [87].

Beside the doping type, also the doping level can have an influence on the optical emission of III-V materials. This is commonly related to effects of bandgap narrowing (leading to a redshift of the luminescence wavelength) [88, 89] or to the increase of the optical bandgap due to the population of some conductive states which increases the absorption edge of the material (Burstein−Moss shift) [90]. These shifts from the band edge transition can be locally observed and measured by CL analysis, which inspired Chen et al. [91], to develop a CL map analysis method for the estimation of the doping level in single NWs (Fig. 14d, e). In their work, the authors studied GaAs NWs with different doping levels and considered the energy peak shift and broadening as critical parameters. This approach paves the way to the use of CL as a non-destructive tool to estimate the doping level in individual nanowires, which is still a challenge in the development of NW based device.

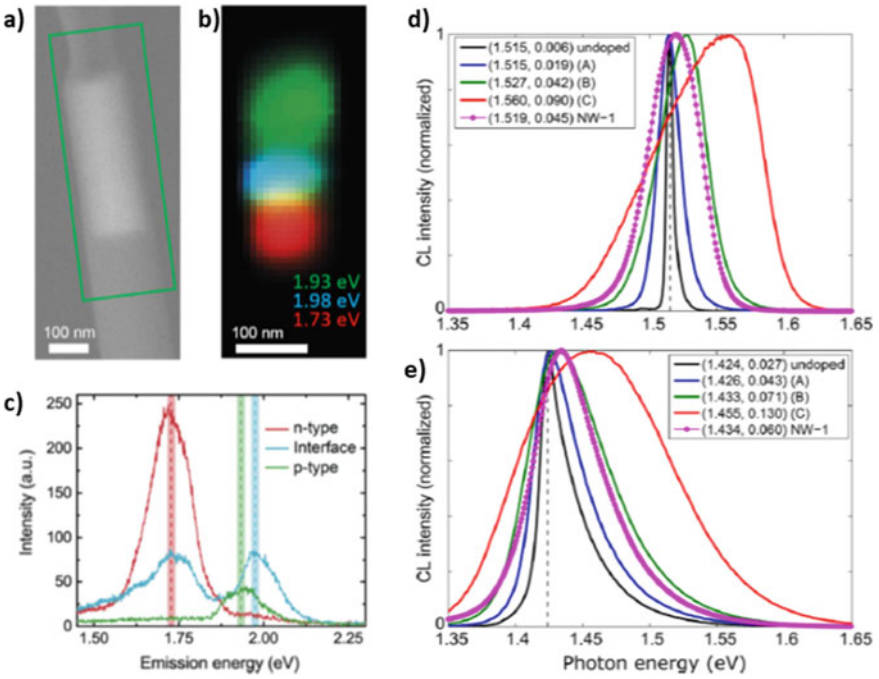

Fig. 14 SEM image (**a**) and corresponding CL map (**b**) of an individual InGaP NW containing an axial p–n junction; **c** CL spectra acquired along the axis of the NW from the CL map in panel b (the color legend is reported in panel b); CL spectra acquired at low temperature (**d**) and at room temperature (**e**) of n-doped GaAs thin films with different doping levels compared to the spectra obtained from a single homogeneously doped GaAs NW. [Panels a-c are reproduced with permission from N. Bologna, S. Wirths, L. Francaviglia, M. Campanini, H. Schmid, V. Theofylaktopoulos, K. E Moselund, A. Fontcuberta i Morral, R. Erni, H. Riel, M. D. Rossell, 2018, "Dopant-induced modifications of $Ga_xIn_{(1-x)}P$ nanowire-based p-n junctions monolithically integrated on Si (111)", ACS Applied Materials & Interfaces. 10(38), 32,588–32,596, https://doi.org/10.1021/acsami.8b10770. Copyright (2012) American Chemical Society. Panels d and e are reproduced with permission from H.-C. Chen, C. Himwas, A. Scaccabarozzi, P. Rale, F.Oehler, A. Lemaître, L. Lombez, J.-F. Guillemoles, M. Tchernycheva, J.-C. Harmand, A. Cattoni, S. Collin, 2017, "Determination of n-type doping level in single GaAs nanowires by cathodoluminescence. Nano Lett. 17, 6667–6675. . 7b02620. Copyright (2017) American Chemical Society]

3.2 TR-CL Analysis Applied to Nanowires

While CL spectroscopy provides important and direct information on the optical properties of materials at the nanoscale, time-resolved CL (TR-CL) can be used to characterize the temporal evolution of the CL emission of a material after an excitation pulse. This technique measures the carrier dynamics at the nanoscale and can be used to determine material quality, carrier transfer or to identify CL emissions characterized by different carrier dynamics. To add temporal resolution to standard

CL spectroscopy, three main techniques can be used and will be presented in the following sections.

(a) **Beam blanking techniques**

Historically, the first TR-CL experiments were performed using a beam blanking technique [92–94]. In such a configuration, the beam is deflected by applying a polarization to electrostatic deflection plates in the SEM column. In its standard configuration, the electron beam is swept out by applying a fast voltage pulse on the deflection plate. The temporal resolution of such a system is, therefore, limited by the rise time of the pulse generator, the spacing between the two deflection plates and the speed of the photodetector. Typically, such systems can achieve temporal resolutions of up to 100–200 ps [94, 95]. However, this technique can reach a temporal resolution up to 30 ps when the beam blanker is used in a conjugated mode in combination with two small apertures in the SEM column [96]. The main advantages of this technique are its relative ease of installation and its flexibility in pulse duration and repetition rate. On the other hand, this technique suffers from its relatively low temporal and spatial resolution since the electron beam is generally swept on the sample when it is deflected.

Such beam blanking TR-CL have often been used to characterize semiconductor nanostructures. In this respect, Metzner et al. carried out pioneering work in 2011 [97]. They investigate the optical properties of InGaN/GaN quantum wells grown on inverted pyramid surface thanks to spatially, spectrally, and time-resolved CL microscopy. By recording on the same spatial region, the CL spectra and decay traces, the authors were able to determine for each pixel of the SEM image, the peak wavelength, integrated intensity, initial lifetime, and radiative lifetime (Fig. 15c–f). This allowed them to correlate the emission properties (wavelength, lifetime) directly with the change in structural properties (indium content and quantum well thickness) from the center to the ridge of the inverted pyramids.

Since then, beam blanking TR-CL has been successfully applied to other nanostructures. Fisher et al. correlated the structural, electronic, and optical properties of AlN/GaN multiple quantum discs in GaN NWs grown on Si(111). In their study, the authors benefit from the use of TR-CL to determine the confinement regime in the heterostructure. In their experiments, they observed an increase of the CL lifetime when the temperature increases, which thus suggests that the quantum discs do not behave as quantum dots but rather as quantum wells [98]. As another example, Gačević et al. studied the influence of the composition, strain, and anisotropy of electric fields on the recombination dynamics of InGaN nanodisks in pencil-like GaN NWs. Thanks to beam blanking TR-CL experiments at low- temperature, the authors observed the CL decay time at different positions of the NW to probe the local electric field. In particular, the fast recombination in the semipolar InGaN ($\sim$0.5 ns) revealed by TR-CL allowed them to demonstrate that the electric field across this section was low, which was associated with a near-unity electron–hole overlap [99].

Beam blanking TR-CL was also used to characterize the coupling of excitons to surface plasmon polaritons (SPPs) [100]. As an illustration, Estrin et al. characterized

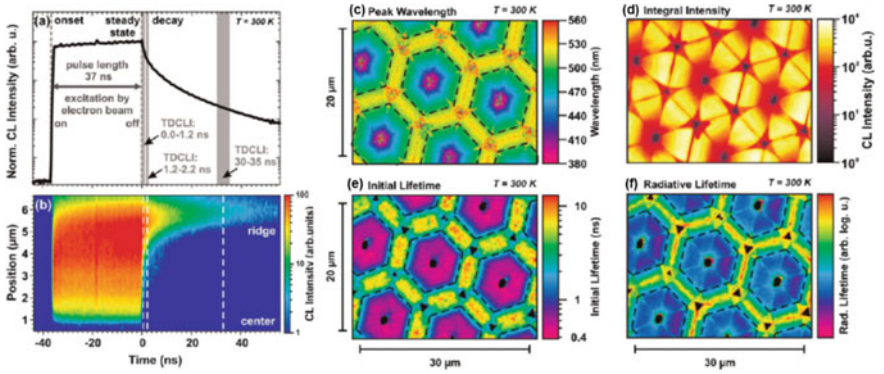

Fig. 15 Transients recorded along a {1122} facet of an inverted pyramid via time-resolved CL. **a** Example of transient showing the establishment of steady state, as well as the decay characteristics; **b** Transient linescan over one facet from center to ridge; **c** Mapping of the CL peak wavelength from spectrally resolved measurements; **d** Spectrally integrated intensity distribution gained from spectral mapping; **e** Mapping of the initial lifetime of inverse pyramids evaluated from a mapping of local transients; **f**) Mapping of the qualitative radiative lifetime achieved by normalizing the initial lifetime distribution (**e**) to the steady state intensity distribution. The dashed hexagons mark the position of the SiO_2 masking pads relative to the inverted pyramids. [Panels a-f are reproduced with permission from S. Metzner, F. Bertram, C. Karbaum, T. Hempel, T. Wunderer, S. Schwaiger, F. Lipski, F. Scholz, C. Wächter, M. Jetter, P. Michler, J. Christen, 2011, "Spectrally and time-resolved cathodoluminescence microscopy of semipolar InGaN SQW on $(11\bar{2}2)$ and $(10\bar{1}1)$ pyramid facets", PSSB. 248(3), 632–637, https://doi.org/10.1002/pssb.201046500. Copyright (2011) John Wiley and Sons.]

the influence of the deposited metal on the exciton-SPP coupling in GaAs/AlAs core − shell NWs (Fig. 16a). By measuring the CL decay of bare NWs as a function of temperature (Fig. 16b) and comparing with the CL decays of Au- and Al- coated NWs (Fig. 16c), the authors were able to deduce the Purcell enhancement factor that describes the improvement in the radiative recombination rate through the coupling of the exciton to SPP. In particular, they showed that Au-coated NWs may have a Purcell enhancement factor of more than two while Al-coated NWs do not exhibit significant changes.

Finally, Donatini et al. recently used beam blanking TR-CL to quantify the influence of the electron beam dose on excitonic diffusion in ZnO NWs [95]. Using the TR-CL, the authors measured the CL decay time for different exposures. From these measurements, they deduced the surface recombination velocity, as well as the exciton diffusion length, and their dependence on the electron irradiation.

(b) **Laser-driven electron beam**

In order to avoid the limitation of the electronics of the beam blanking unit and to achieve a temporal resolution of a few picoseconds, a team led by J.-D. Ganière at EPFL developed in 2005, an optically driven electron gun [57]. This electron gun consists of a 20-nm-thick gold photocathode deposited on a quartz plate. By

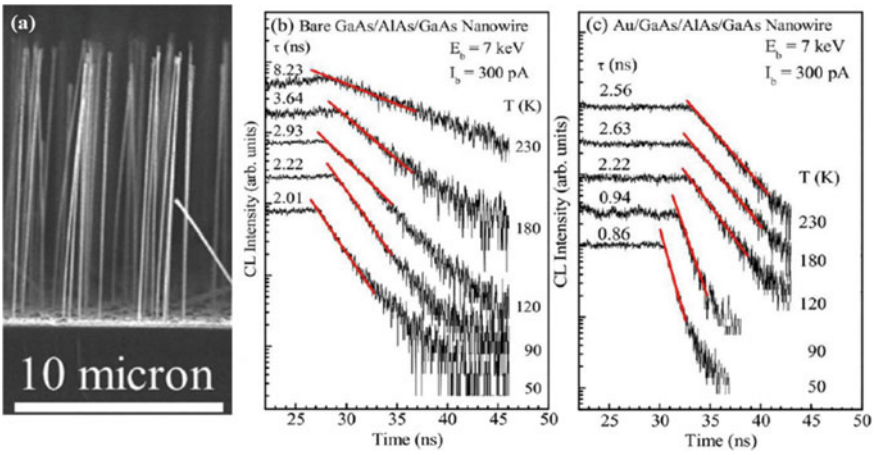

Fig. 16 **a** Side-view SEM image of the as-grown GaAs/AlAs/GaAs core − shell NWs. Local CL decay transients for the bare (**b**) and Au-covered (**c**) NWs, respectively, at various temperatures from 50 to 230 K. Such a comparison reveals faster recombination when NWs are coated with gold suggesting an enhancement of radiative rate, thanks to the Purcell effect through exciton-plasmon coupling. [Panels a-c are reproduced with permission from Y. Estrin, D. H. Rich, A. V. Kretinin, H. Shtrikman, 2013, "Influence of Metal Deposition on Exciton–Surface Plasmon Polariton Coupling in GaAs/AlAs/GaAs Core–Shell Nanowires Studied with Time-Resolved Cathodoluminescence", Nano Lett.13(4) 1602–1610 https://doi.org/10.1021/nl400015a. Copyright (2013) American Chemical Society.]

illuminating the photocathode with a 200 fs pulsed laser emitting at 266 nm, the photoelectric effect converts the photon pulse into an electron pulse. Thanks to this technique, the temporal resolution is limited only by the speed of the photodetector, which can be less than two picoseconds if a streak camera is used. For this reason, this technique is often referred to as picosecond TR-CL in the literature. Since then, other laser-driven electron guns have been designed, to increase both the brightness and flexibility of use (Fig. 17a) [96].

Picosecond TR-CL was first applied to NWs in the investigation of the optical properties of ZnO NWs by Corfdir and coworkers [101]. In this paper, the authors benefit from the use of TR-CL to identify the biexcitonic emission in these nanostructures. The TR-CL technique helps them to confirm that excitons can be efficiently trapped by non-radiative defects closing basal stacking faults.

Moreover, picosecond TR-CL has also been used to directly observe the motion of excitons in ZnO microwires [77]. As described in Fig. 17b, to put carriers in motion, the ZnO wires were bent. This bending creates a strain gradient along the cross section of the ZnO wire (Fig. 17c). Then, thanks to the pulsed electron beam, excitons were created on the high-energy side (inner region of the bent wire) and their motion has been monitored directly on the streak camera detector (Fig. 17d). This motion is characterized by the shift in energy with time delay. Indeed, by converting the change in energy into a change in position along the strain gradient, the

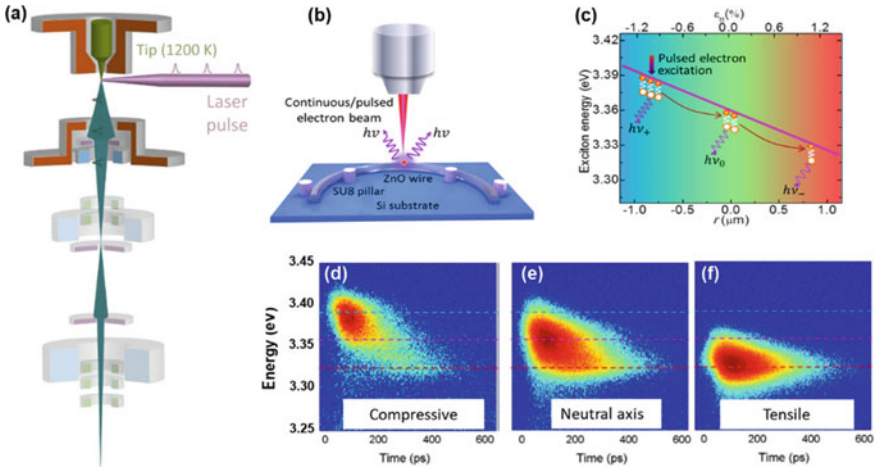

Fig. 17 **a** Schematics of the SEM column of a TR-CL setup in the pulsed laser-driven configuration. **b** Schematic diagram of TR-CL measurements on the bending region of a bent ZnO microwire in a four-point bending configuration. **c** Schematic diagram of exciton drift in a cross section of the bent ZnO microwire after pulsed electron excitation at the inner side (high-energy region). **d**–**f**) Streak camera images showing emission energy as a function of bent section (**d**, **e**, **f**). The maps show a drift of exciton from compressive to tensile part, characterized by an overall redshift with time. [Panel a is reproduced with permission from S.Meuret,, T.Coenen, E.Kieft, H.Zeijlemaker, M.Lätzel, S.Christiansen, S.Y.Woo, Y.H.Ra, Z.Mi, A.Polman, 2019, "Complementary cathodoluminescence lifetime imaging configurations in a scanning electron microscope", Ultramicroscopy 197, 28–38, https://doi.org/10.1016/j.ultramic.2018.11.006. Copyright (2019) Elsevier. Panels b-f are reproduced with permission from X. Fu, G. Jacopin, M. Shahmohammadi, R. Liu, M. Benameur, J.-D. Ganière, J. Feng, W. Guo, Z.-M. Liao, B. Deveaud, D. Yu,, 2014, "Exciton Drift in Semiconductors under Uniform Strain Gradients: Application to Bent ZnO Microwires", ACS Nano 8(4) 3412–3420 https://doi.org/10.1021/nn4062353. Copyright (2014) American Chemical Society]

authors derived an exciton velocity of about 7 nm/ps, corresponding to an excitonic mobility of 1400 ± 100 cm^2 eV^{-1} s^{-1}. In the same vein, similar measurements were performed on an energy gradient in InGaN/GaN core–shell NWs, where the picosecond TR-CL helps to characterize the hopping process between localized states [102]. As a final example, by probing the carrier dynamics with a nanometer spatial and picosecond time resolution, picosecond TR-CL has been used to characterize the internal quantum efficiency of NW LEDs [103].

(c) Hanbury Brown and Twiss measurements

More recently, a different technique has been developed to access carrier dynamics at the nanoscale by taking advantage of the specificity of the excitation by an energetic electron beam.

Indeed, in the case of such excitation of a material, the electron–hole pair generation statistics differs from the one obtained with an optical stimulus. In the case of optical excitation, when a photon is absorbed into a material, it creates at best one electron–hole pair. In an electron microscope, the electron beam is very energetic

(>3 keV) and each incident electron can generate a large number of electron–hole pairs (>1,000). Since these pairs are created simultaneously, there is a high probability that they will de-excite at the same time by emitting a photon. In such a case, this results in a strong bunching of photons. Moreover, by studying the autocorrelation function of the CL signal (g^2 (τ)) as a function of the delay, it is possible to characterize the carrier dynamics. Indeed, it has been shown that the g^2 (τ) evolves as the CL decay time [104].

In order to benefit from this unique property, Meuret and colleagues [105], used a Hanbury Brown and Twiss intensity interferometer placed in the collection line to analyze the photon statistic of the CL emission (Fig. 18a).

The main advantage of this technique is that it allows to access carrier dynamics at the nanoscale without modifying the SEM column. Indeed, it only relies on the specificity of the unique electron–hole pair generation statistics by an electron beam, and thus can be easily applied to any SEM [96, 105], or transmission electron microscope (TEM) [104, 106].

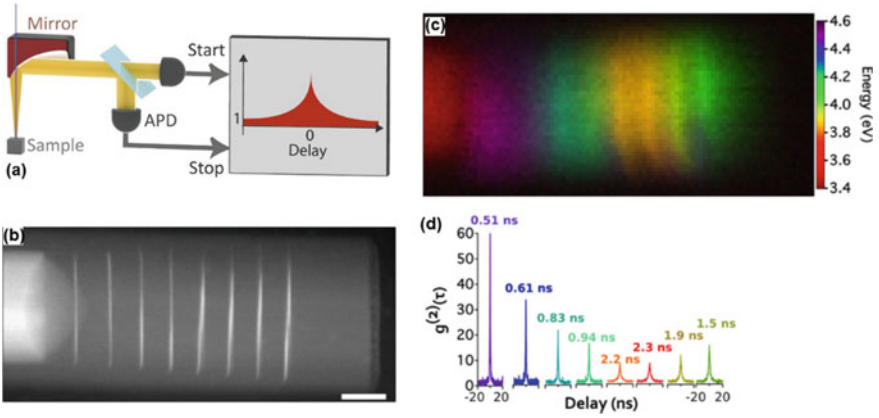

Fig. 18 **a** Schematic diagram of the CL setup in autocorrelation mode where the light is collected by the parabolic mirror and sent to a Hanbury Brown and Twiss intensity interferometer. **b** HAADF image of an AlN NW containing 8 GaN quantum discs with different thicknesses. Scale bar is 20 nm; **c** Compression of a spectral image acquired on an AlN NW containing 8 GaN quantum discs and (**d**) series of $g^2(\tau)$ measured at each quantum disc position. These have been shifted on the abscissa to align with the corresponding quantum disc for clarity. The deduced lifetime is printed close to each bunching peak. The color change represents the evolution of emission wavelength from disc to disc. [Panel a is reproduced with permission from S.Meuret,, T.Coenen, E.Kieft, H.Zeijlemaker, M.Lätzel, S.Christiansen, S.Y.Woo, Y.H.Ra, Z.Mi, A.Polman, 2019, "Complementary cathodoluminescence lifetime imaging configurations in a scanning electron microscope", Ultramicroscopy 197, 28–38, https://doi.org/10.1016/j.ultramic.2018.11.006. Copyright (2019) Elsevier. Panels b-d are reproduced with permission from Sophie Meuret, Luiz H. G. Tizei, Thomas Auzelle, Rudee Songmuang, Bruno Daudin, Bruno Gayral, Mathieu Kociak, 2016, "Lifetime Measurements Well below the Optical Diffraction Limit", ACS Photonics 3(7), 1157–1163, https://doi.org/10.1021/acsphotonics.6b00212. Copyright (2016) American Chemical Society]

With this type of setup in a TEM, the lifetime of several quantum discs embedded in an AlN NW (Fig. 18b), has been quantified with a spatial resolution well below the diffraction limit [106]. In these NWs, because of the growth conditions, the thickness is changing from disc to disc. Therefore, both the quantum confinement and the influence of the internal electric field is varying, leading to different emission energies for the eight quantum discs (Fig. 18c). Due to the strong internal electric field in the GaN quantum discs, the change in thickness of a quantum disc induces a strong modification of the electron–hole overlap, and therefore, of the recombination probability and wavelength. By evaluating the $g^2(\tau)$ measured at each quantum disc position, the authors were able to correlate the quantum disc thickness and the CL emission energy to the radiative recombination rate. Using a similar configuration in a SEM, Meuret et al. used autocorrelation CL measurements to characterize the emission properties of GaN/InGaN quantum discs in NWs [107].

4 Conclusions

Today the use of nanomaterials in electronic and optoelectronic applications witnesses a substantial growth. However, the complexity of their nanostructured three-dimensional morphology brings new conceptual and technological challenges. Understanding the processes taking place at the nanoscale in individual nano-objects has become indispensable for their successful integration in functional devices. However, a reliable measurement of electrical and optical properties of nano-objects represents a big challenge. Electron beam induced current microscopy and cathodoluminescence can respond to this need. This is illustrated in the present chapter with the example of semiconductor nanowires. We have shown how these electron beam-based techniques provide access to the key physical parameters, which govern the nanowire device efficiency, namely, to the material homogeneity, the bandgap, the radiative and non-radiative recombinations, the doping, the minority carrier diffusion lengths, etc. These parameters guide the optimization of the nanostructured devices and provide input for their advanced modeling.

Acknowledgements This work has been partially financially supported by the French National Research Agency in the framework of the "Investissements d'avenir" program (ANR-15-IDEX-02), by EU ERC project 'NanoHarvest' (grant no. 639052) and by H2020 ITN Marie Curie project 'INDEED' (grant no. 722176).

References

1. L. Reimer, *Scanning Electron Microscopy: Physics of Image Formation and Microanalysis* (Springer, 2013)
2. B.G. Yacobi, D.B. Holt, *Cathodoluminescence Microscopy of Inorganic Solids* (Springer Science & Business Media, 2013)

3. M. Tchernycheva, P. Lavenus, H. Zhang, A.V. Babichev, G. Jacopin, M. Shahmohammadi, F.H. Julien, R. Ciechonski, G. Vescovi, O. Kryliouk, Nano Lett. **14**, 2456 (2014)
4. P. Tchoulfian, F. Donatini, F. Levy, A. Dussaigne, P. Ferret, J. Pernot, Nano Lett. **14**, 3491 (2014)
5. E.B. Yakimov, S.S. Borisov, S.I. Zaitsev, Phys. Tech. Poluprovodiekov **41**, 426 (2007)
6. P. Würfel, T. Trupke, T. Puzzer, E. Schäffer, W. Warta, S.W. Glunz, J. Appl. Phys. **101**, 123110 (2007)
7. F.J. Schultes, T. Christian, R. Jones-Albertus, E. Pickett, K. Alberi, B. Fluegel, T. Liu, P. Misra, A. Sukiasyan, H. Yuen, N.M. Haegel, Appl. Phys. Lett. **103**, 242106 (2013)
8. J. Wallentin, P. Wickert, M. Ek, A. Gustafsson, L. Reine Wallenberg, M.H. Magnusson, L. Samuelson, K. Deppert, and M.T. Borgström, Appl. Phys. Lett. **99**, 253105 (2011)
9. C.-C. Chang, C.-Y. Chi, M. Yao, N. Huang, C.-C. Chen, J. Theiss, A.W. Bushmaker, S. LaLumondiere, T.-W. Yeh, M.L. Povinelli, C. Zhou, P.D. Dapkus, S.B. Cronin, Nano Lett. **12**, 4484 (2012)
10. Y. Arroyo Rojas Dasilva, R. Kozak, R. Erni, M.D. Rossell, Ultramicroscopy **176**, 11 (2017).
11. C. Donolato, Phys. Status Solidi A **65**, 649 (1981)
12. C. Donolato, J. Appl. Phys. **54**, 1314 (1983)
13. C. Donolato, Appl. Phys. Lett. **43**, 120 (1983)
14. H.J. Leamy, J. Appl. Phys. **53**, R51 (1982)
15. L. Pasemann, Ultramicroscopy **6**, 237 (1981)
16. C.A. Klein, J. Appl. Phys. **39**, 2029 (1968)
17. C. Gutsche, R. Niepelt, M. Gnauck, A. Lysov, W. Prost, C. Ronning, F.-J. Tegude, Nano Lett. **12**, 1453 (2012)
18. Z.Z. Bandić, P.M. Bridger, E.C. Piquette, T.C. McGill, Appl. Phys. Lett. **72**, 3166 (1998)
19. Z.Z. Bandić, P.M. Bridger, E.C. Piquette, T.C. McGill 8 (2000)
20. K.L. Bunker, Development and Application of Electron Beam Induced Current and Cathodoluminescence Analytical Techniques for Characterization of Gallium Nitride-Based Devices, North Carolina State University (2004)
21. D. Cavalcoli, A. Cavallini. Mater. Sci. Eng. **98** (1994)
22. K. Durose, P.R. Edwards, D.P. Halliday, J. Cryst. Growth **197**, 733 (1999)
23. I. Aberg, G. Vescovi, D. Asoli, U. Naseem, J.P. Gilboy, C. Sundvall, A. Dahlgren, K.E. Svensson, N. Anttu, M.T. Bjork, L. Samuelson, IEEE J. Photovolt. **6**, 185 (2016)
24. W. Van Roosbroeck, J. Appl. Phys. **26**, 380 (1955)
25. D.E. Ioannou, C.A. Dimitriadis, IEEE Trans. Electron Devices **29**, 445 (1982)
26. G. Otnes, E. Barrigón, C. Sundvall, K.E. Svensson, M. Heurlin, G. Siefer, L. Samuelson, I. Åberg, M.T. Borgström, Nano Lett. **18**, 3038 (2018)
27. H. Zhang, G. Jacopin, V. Neplokh, L. Largeau, F.H. Julien, O. Kryliouk, M. Tchernycheva, Nanotechnology **26**, 465203 (2015)
28. V. Piazza, M. Vettori, A.A. Ahmed, P. Lavenus, F. Bayle, N. Chauvin, F.H. Julien, P. Regreny, G. Patriarche, A. Fave, M. Gendry, M. Tchernycheva, Nanoscale **10**, 20207 (2018)
29. Y.L. Shabel'nikova, E.B. Yakimov, J. Surf. Investig. X-Ray Synchrotron Neutron Tech. **6**, 894 (2012)
30. M. Tchernycheva, V. Neplokh, H. Zhang, P. Lavenus, L. Rigutti, F. Bayle, F.H. Julien, A. Babichev, G. Jacopin, L. Largeau, R. Ciechonski, G. Vescovi, O. Kryliouk, Nanoscale **7**, 11692 (2015)
31. P. Lavenus, A. Messanvi, L. Rigutti, A. De Luna Bugallo, H. Zhang, F. Bayle, F.H. Julien, J. Eymery, C. Durand, M. Tchernycheva, Nanotechnology **25**, 255201 (2014)
32. H. Zhang, X. Dai, N. Guan, A. Messanvi, V. Neplokh, V. Piazza, M. Vallo, C. Bougerol, F.H. Julien, A. Babichev, A.C.S. Appl, Mater. Interfaces **8**, 26198 (2016)
33. C.I. Bright, 50 Years Vac. Coat. Technol. Growth Soc. Vac. Coaters (2007)
34. T.J. Coutts, T.O. Mason, J.D. Perkins, D.S. Ginley, Proc Electrochem Soc **99**, 274 (1999)
35. O. Hultin, G. Otnes, M.T. Borgström, M. Björk, L. Samuelson, K. Storm, Nano Lett. **16**, 205 (2016)

36. J. Alvarez, I. Ngo, M.-E. Gueunier-Farret, J.-P. Kleider, L. Yu, P.R. Cabarrocas, S. Perraud, E. Rouvière, C. Celle, C. Mouchet, Nanoscale Res. Lett. **6**, 110 (2011)
37. J.-S. Hwang, M.-C. Kao, J.-M. Shiu, C.-N. Fan, S.-C. Ye, W.-S. Yu, H.-M. Lin, T.-Y. Lin, S. Chattopadhyay, L.-C. Chen, K.-H. Chen, J. Phys. Chem. C **115**, 21981 (2011)
38. D. Mikulik, M. Ricci, G. Tutuncuoglu, F. Matteini, J. Vukajlovic, N. Vulic, E. Alarcon-Llado, and A. Fontcuberta i Morral, Nano Energy **41**, 566 (2017)
39. E. Halpern, G. Elias, A.V. Kretinin, H. Shtrikman, Y. Rosenwaks, Appl. Phys. Lett. **100**, 262105 (2012)
40. V. Piazza, S. Wirths, N. Bologna, A.A. Ahmed, F. Bayle, H. Schmid, F. Julien, M. Tchernycheva, Appl. Phys. Lett. **114**, 103101 (2019)
41. P. Narchi, V. Neplokh, V. Piazza, T. Bearda, F. Bayle, M. Foldyna, C. Toccafondi, P. Prod'homme, M. Tchernycheva, P.R. i Cabarrocas, Sol. Energy Mater. Sol. Cells **161**, 263 (2017)
42. I. Volotsenko, M. Molotskii, Z. Barkay, J. Marczewski, P. Grabiec, B. Jaroszewicz, G. Meshulam, E. Grunbaum, Y. Rosenwaks, J. Appl. Phys. **107**, 014510 (2010)
43. L. Esaki, Phys. Rev. **109**, 603 (1958)
44. W. Guter, A.W. Bett, IEEE Trans. Electron Devices **53**, 2216 (2006)
45. X. Zeng, G. Otnes, M. Heurlin, R.T. Mourão, M.T. Borgström, Nano Res. **11**, 2523 (2018)
46. H.C. Casey, B.I. Miller, E. Pinkas, J. Appl. Phys. **44**, 1281 (1973)
47. G. Nogues, T. Auzelle, M. Den Hertog, B. Gayral, B. Daudin, Appl. Phys. Lett. **104**, 102102 (2014)
48. O. Demichel, M. Heiss, J. Bleuse, H. Mariette, Appl Phys Lett 3 (n.d.).
49. A. Solanki, P. Gentile, V. Calvo, G. Rosaz, B. Salem, V. Aimez, D. Drouin, N. Pauc, Nano Energy **1**, 714 (2012)
50. D. Baek, J. Lee, B. Choi, Mater. Res. Bull. **58**, 157 (2014)
51. L. Baird, C.P. Ong, R.A. Cole, N.M. Haegel, A.A. Talin, Q. Li, G.T. Wang, Appl. Phys. Lett. **98**, 132104 (2011)
52. Y. Dan, K. Seo, K. Takei, J.H. Meza, A. Javey, K.B. Crozier, Nano Lett. **11**, 2527 (2011)
53. M. Yang, D. Dvorak, K. Leistner, C. Damm, S.P. Watkins, K.L. Kavanagh, Nanotechnology **30**, 025701 (2019)
54. S. Kono, T. Teraji, H. Kodama, A. Sawabe, Diam. Relat. Mater. **63**, 30 (2016)
55. A.S. Togonal, M. Foldyna, W. Chen, J.X. Wang, V. Neplokh, M. Tchernycheva, J. Nassar, P. Roca i Cabarrocas, Rusli, J. Phys. Chem. C **120**, 2962 (2015)
56. S. Misra, L. Yu, W. Chen, M. Foldyna, P.R. i Cabarrocas, J. Phys. Appl. Phys. **47**, 393001 (2014)
57. M. Merano, S. Sonderegger, A. Crottini, S. Collin, P. Renucci, E. Pelucchi, A. Malko, M.H. Baier, E. Kapon, B. Deveaud, J.-D. Ganière, Nature **438**, 479 (2005)
58. M. Mattila, T. Hakkarainen, M. Mulot, H. Lipsanen, Nanotechnology **17**, 1580 (2006)
59. V. Piazza, A. Babichev, L. Mancini, M. Morassi, P. Quach, F. Bayle, ludovic largeau, F.H. Julien, P. Rale, S. Collin, J.-C. Harmand, N. Gogneau, M. Tchernycheva, Nanotechnology (2019)
60. A. Pierret, C. Bougerol, B. Gayral, M. Kociak, B. Daudin, Nanotechnology **24**, 305703 (2013)
61. M. Kociak, L.F. Zagonel, Ultramicroscopy **176**, 112 (2017)
62. L.F. Zagonel, S. Mazzucco, M. Tencé, K. March, R. Bernard, B. Laslier, G. Jacopin, M. Tchernycheva, L. Rigutti, F.H. Julien, R. Songmuang, M. Kociak, Nano Lett. **11**, 568 (2011)
63. L.F. Zagonel, L. Rigutti, M. Tchernycheva, G. Jacopin, R. Songmuang, M. Kociak, Nanotechnology **23**, 455205 (2012)
64. J.T. Griffiths, S. Zhang, B. Rouet-Leduc, W.Y. Fu, A. Bao, D. Zhu, D.J. Wallis, A. Howkins, I. Boyd, D. Stowe, M.J. Kappers, C.J. Humphreys, R.A. Oliver, Nano Lett. (2015)
65. L.H.G. Tizei, S. Meuret, K. March, K. Hestroffer, T. Auzelle, B. Daudin, M. Kociak, Appl. Phys. Lett. **105**, 143106 (2014)
66. S.K. Lim, M. Brewster, F. Qian, Y. Li, C.M. Lieber, S. Gradečak, Nano Lett. **9**, 3940 (2009)
67. G. Tourbot, C. Bougerol, F. Glas, L.F. Zagonel, Z. Mahfoud, S. Meuret, P. Gilet, M. Kociak, B. Gayral, B. Daudin, Nanotechnology **23**, 135703 (2012)

68. K. Pantzas, G. Patriarche, D. Troadec, M. Kociak, N. Cherkashin, M. Hÿtch, J. Barjon, C. Tanguy, T. Rivera, S. Suresh, A. Ougazzaden, J. Appl. Phys. **117**, 055705 (2015)
69. A. Pierret, C. Bougerol, M. den Hertog, B. Gayral, M. Kociak, H. Renevier, B. Daudin, Phys. Status Solidi RRL – Rapid Res. Lett. **7**, 868 (2013)
70. S.F. Chichibu, A. Uedono, T. Onuma, B.A. Haskell, A. Chakraborty, T. Koyama, P.T. Fini, S. Keller, S.P. DenBaars, J.S. Speck, U.K. Mishra, S. Nakamura, S. Yamaguchi, S. Kamiyama, H. Amano, I. Akasaki, J. Han, T. Sota, Nat. Mater. **5**, 810 (2006)
71. S.F. Chichibu, A. Uedono, T. Onuma, T. Sota, B.A. Haskell, S.P. DenBaars, J.S. Speck, S. Nakamura, Appl. Phys. Lett. **86**, 021914 (2005)
72. H. Lei, H.S. Leipner, V. Bondarenko, J. Schreiber, J. Phys. Condens. Matter **16**, S279 (2004)
73. R. Liu, A. Bell, F.A. Ponce, C.Q. Chen, J.W. Yang, M.A. Khan, Appl. Phys. Lett. **86**, 021908 (2005)
74. M. Müller, G. Schmidt, S. Metzner, P. Veit, F. Bertram, S. Krylyuk, R. Debnath, J.-Y. Ha, B. Wen, P. Blanchard, A. Motayed, M.R. King, A.V. Davydov, J. Christen, Jpn. J. Appl. Phys. **55**, 05FF02 (2016)
75. A. Urban, M. Müller, C. Karbaum, G. Schmidt, P. Veit, J. Malindretos, F. Bertram, J. Christen, A. Rizzi, Nano Lett. **15**, 5105 (2015)
76. M. Grundmann, J. Christen, D. Bimberg, A. Fischer-Colbrie, R. Hull, J. Appl. Phys. **66**, 2214 (1989)
77. X. Fu, G. Jacopin, M. Shahmohammadi, R. Liu, M. Benameur, J.-D. Ganière, J. Feng, W. Guo, Z.-M. Liao, B. Deveaud, D. Yu, ACS Nano **8**, 3412 (2014)
78. B.G. Mendis, D. Gachet, J.D. Major, K. Durose, Phys. Rev. Lett. **115** (2015)
79. J. Bolinsson, M. Ek, J. Trägårdh, K. Mergenthaler, D. Jacobsson, M.-E. Pistol, L. Samuelson, A. Gustafsson, Nano Res. **7**, 473 (2014)
80. D. Spirkoska, J. Arbiol, A. Gustafsson, S. Conesa-Boj, F. Glas, I. Zardo, M. Heigoldt, M.H. Gass, A.L. Bleloch, S. Estrade, M. Kaniber, J. Rossler, F. Peiro, J.R. Morante, G. Abstreiter, L. Samuelson, A. Fontcuberta i Morral, Phys. Rev. B **80** (2009)
81. M. Heiss, S. Conesa-Boj, J. Ren, H.-H. Tseng, A. Gali, A. Rudolph, E. Uccelli, F. Peiró, J.R. Morante, D. Schuh, E. Reiger, E. Kaxiras, J. Arbiol, A. Fontcuberta i Morral, Phys. Rev. B **83** (2011)
82. B. Loitsch, M. Müller, J. Winnerl, P. Veit, D. Rudolph, G. Abstreiter, J.J. Finley, F. Bertram, J. Christen, G. Koblmüller, New J. Phys. **18**, 063009 (2016)
83. M. Heiss, Y. Fontana, A. Gustafsson, G. Wüst, C. Magen, D.D. O'Regan, J.W. Luo, B. Ketterer, S. Conesa-Boj, A.V. Kuhlmann, J. Houel, E. Russo-Averchi, J.R. Morante, M. Cantoni, N. Marzari, J. Arbiol, A. Zunger, R.J. Warburton, A. Fontcuberta i Morral, Nat. Mater. **12**, 439 (2013)
84. H. Zhang, N. Guan, V. Piazza, A. Kapoor, C. Bougerol, F.H. Julien, A.V. Babichev, N. Cavassilas, M. Bescond, F. Michelini, M. Foldyna, E. Gautier, C. Durand, J. Eymery, M. Tchernycheva, J. Phys. Appl. Phys. **50**, 484001 (2017)
85. A. Pierret, C. Bougerol, S. Murcia-Mascaros, A. Cros, H. Renevier, B. Gayral, B. Daudin, Nanotechnology **24**, 115704 (2013)
86. N. Bologna, S. Wirths, L. Francaviglia, M. Campanini, H. Schmid, V. Theofylaktopoulos, K.E. Moselund, A. Fontcuberta i Morral, R. Erni, H. Riel, M.D. Rossell, ACS Appl. Mater. Interfaces **10** (2018)
87. G. Otnes, M. Heurlin, X. Zeng, M.T. Borgström, Nano Lett. **17**, 702 (2017)
88. R.A. Abram, G.N. Childs, P.A. Saunderson, J. Phys. C Solid State Phys. **17**, 6105 (1984)
89. G. Borghs, K. Bhattacharyya, K. Deneffe, P. Van Mieghem, R. Mertens, J. Appl. Phys. **66**, 4381 (1989)
90. D.M. Szmyd, P. Porro, A. Majerfeld, S. Lagomarsino, J. Appl. Phys. **68**, 2367 (1990)
91. H.-L. Chen, C. Himwas, A. Scaccabarozzi, P. Rale, F. Oehler, A. Lemaître, L. Lombez, J.-F. Guillemoles, M. Tchernycheva, J.-C. Harmand, A. Cattoni, S. Collin, Nano Lett. **17**, 6667 (2017)
92. S.M. Davidson, J. Microsc. **110**, 177 (1977)
93. A. Steckenborn, J. Microsc. **118**, 297 (1980)

94. D. Bimberg, J. Christen, A. Steckenborn, G. Weimann, W. Schlapp, J. Lumin. **30**, 562 (1985)
95. F. Donatini, J. Pernot, Nanotechnology **29** (2018)
96. S. Meuret, M. Solà Garcia, T. Coenen, E. Kieft, H. Zeijlemaker, M. Lätzel, S. Christiansen, S.Y. Woo, Y.-H. Ra, Z. Mi, A. Polman, Ultramicroscopy **197**, 28 (2019)
97. S. Metzner, F. Bertram, C. Karbaum, T. Hempel, T. Wunderer, S. Schwaiger, F. Lipski, F. Scholz, C. Wächter, M. Jetter, P. Michler, J. Christen, Phys. Status Solidi B Basic Res. **248**, 632 (2011)
98. A.M. Fischer, K.W. Sun, F.A. Ponce, R. Songmuang, E. Monroy, Appl. Phys. Express **5**, 1 (2012)
99. Gačević, N. Vukmirović, N. García-Lepetit, A. Torres-Pardo, M. Müller, S. Metzner, S. Albert, A. Bengoechea-Encabo, F. Bertram, P. Veit, J. Christen, J.M. González-Calbet, E. Calleja, Phys. Rev. B **93**, 1 (2016)
100. Y. Estrin, D.H. Rich, A.V. Kretinin, H. Shtrikman, Nano Lett. **13**, 1602 (2013)
101. P. Corfdir, M. Abid, A. Mouti, P.A. Stadelmann, E. Papa, J.P. Ansermet, J.D. Ganiére, B. Deveaud-Plédran, Nanotechnology **22** (2011)
102. M. Shahmohammadi, J.D. Ganière, H. Zhang, R. Ciechonski, G. Vescovi, O. Kryliouk, M. Tchernycheva, G. Jacopin, Nano Lett. **16**, 243 (2016)
103. W. Liu, C. Mounir, G. Rossbach, T. Schimpke, A. Avramescu, H.-J. Lugauer, M. Strassburg, U. Schwarz, B. Deveaud, G. Jacopin, Appl. Phys. Lett. **112**, 052106 (2018)
104. S. Meuret, L.H.G. Tizei, T. Cazimajou, R. Bourrellier, H.C. Chang, F. Treussart, M. Kociak, Phys. Rev. Lett. **114**, 1 (2015)
105. S. Meuret, T. Coenen, H. Zeijlemaker, M. Latzel, S. Christiansen, S. Conesa-Boj, A. Polman, Phys. Rev. B **96**, 035308 (2017)
106. S. Meuret, L.H.G. Tizei, T. Auzelle, R. Songmuang, B. Daudin, B. Gayral, M. Kociak, ACS Photonics **3**, 1157 (2016)
107. S. Meuret, T. Coenen, S.Y. Woo, Y.H. Ra, Z. Mi, A. Polman, Nano Lett. **18**, 2288 (2018)

Photoluminescence Spectroscopy Applied to Semiconducting Nanowires: A Valuable Probe for Assessing Lattice Defects, Crystal Structures, and Carriers' Temperature

Davide Tedeschi, Marta De Luca, and Antonio Polimeni

Abstract Photoluminescence (PL) spectroscopy is a reliable, non-invasive tool widely employed to investigate the electronic properties of semiconductors and their nanostructures near the band-gap edge states. PL is particularly relevant for determining the energy and symmetry properties of excitons as well as the nature and relative abundances of defects in a semiconductor material. In this chapter, we will present PL measurements on InP nanowires (NWs), a notable material system for NW structures. We address the electronic and defect properties of wurtzite NWs, and provide a comparison with the zincblende counterpart. PL as a function of various external parameters, such as photoexcited carrier density and temperature, allows us to assign the origin of various recombination bands typically observed in InP NWs grown by selective area epitaxy or by vapor–liquid–solid method. The possibility to explore the density of states of NWs is implemented by PL-excitation measurements as a function of polarization, which unveil the optical selection rules pertinent to the wurtzite crystal phase. Finally, a careful analysis of the PL lineshape provides also access to carriers' temperature and thus precious insight on carrier relaxation phenomena that occur in thin NWs.

Keywords III-V nanowires · Wurtzite InP · Photoluminescence · Band structure · Hot carriers

D. Tedeschi · A. Polimeni (✉)
Dipartimento di Fisica, Sapienza Università di Roma, Rome 00185, Italy
e-mail: antonio.polimeni@roma1.infn.it

D. Tedeschi
e-mail: davide.tedeschi@uniroma1.it

M. De Luca
Departement Physik, Universität Basel, 4056 Basel, Switzerland
e-mail: marta.deluca@unibas.ch

© Springer Nature Singapore Pte Ltd. 2021

N. Fukata and R. Rurali (eds.), *Fundamental Properties of Semiconductor Nanowires*,
https://doi.org/10.1007/978-981-15-9050-4_6

1 Introduction

In semiconductors, PL and absorption can be considered as complementary techniques. While the latter is dominated by transitions involving the intrinsic energy levels related to the crystal density of states, the former is mainly ruled by fast relaxation processes of carriers that favor recombination from low-energy levels near the band gap. In particular, at low temperature, transitions from the lowest excited state or from states with the shortest radiative lifetime are usually observed. PL is therefore most suited to investigate transitions at, or just below, the energy gap, or deeper states in heavily defected materials. In particular, the PL linewidth, peak energy, and lineshape may provide information about impurity concentration and type [1] and size/composition fluctuations in low-dimensional systems. Moreover, PL measurements as a function of temperature allow investigating the role of non-radiative centers and their thermal activation energy. Secondly, nanostructures like nanowires (NWs), whose density of states can be hardly probed by direct optical absorption, can be investigated by PL or by PL-excitation spectroscopy, a technique that mimics optical absorption [2].

NWs feature typically few μm lengths and diameters ranging from few nm to several hundreds of nm. The resulting largely anisotropic shape and high surface-to-volume ratio make NWs suitable in diverse applicative fields comprising gas sensing, photovoltaics, and optoelectronics. Due to the direct band-gap matching with the solar spectrum and the low surface recombination velocity [3], InP NWs are the favorite building blocks among the III-V compounds for high-efficiency solar cells [4–6]. InP is also interesting for optical telecommunications [7] and high-speed electronics [8]. Clearly, all these applications require knowledge of both the intrinsic electronic properties of NWs, such as those related to the NW lattice and hence band structure (e.g., carrier effective mass and characteristics of light absorption) and of the extrinsic modifications of the electronic states induced by the presence of defects, especially impurities. Insights into these aspects can be gained by absorption and emission techniques.

As in the case of GaAs and InAs (two prominent cases of III-V NWs), one of the most exciting properties of InP NWs is their capability to grow with different crystal structures, known as polytypism [9], which has provided a platform for fundamental studies and technological applications. Indeed, non-nitrides III-V materials, which are stable only in the zincblende (ZB) phase in bulk, can crystallize in the wurtzite (WZ) structure when grown in the NW form under suitable growth conditions [9, 10]. Also, NW crystal growth techniques have progressed enormously over the past years leading to the possibility to switch between different crystal phases during the NW accretion. Nowadays, continuous switch from WZ to ZB phases within a same wire can be obtained on demand [11], and therefore band-gap modulation along the NW growth axis can be controllably realized with no compositional disorder. Indeed, promising devices based on crystal-phase homostructures can be realized owing to the high degree of control reached in the abruptness of the WZ/ZB interfaces [12].

In this chapter, we review the results we obtained by means of PL spectroscopy on the fundamental properties of free carriers and excitons in InP NWs with WZ crystal phase. In the following session, we present the general properties of PL spectra recorded on WZ InP NWs at low temperature showing a number of different recombination bands ascribable to the presence of both acceptors and donors in the lattice. The polarization properties of the NW emission and absorption (this latter determined by PL-excitation, PLE) are discussed in relation to the WZ phase symmetry. The last section reports on the evolution of the PL and PLE spectra with temperature and on the observation of thermal unbalance between the carrier and lattice temperatures in NWs. The conclusive session summarizes the results reported.

2 Low-temperature Photoluminescence

2.1 Samples

We will present results obtained on NWs formed by both the vapor–liquid–solid (VLS) mechanism [13] and the selective area epitaxy (SAE) catalyst-free growth [14]. VLS and SAE methods provide WZ InP NWs with high crystal and optical quality [15, 16]. These two approaches, though, present different characteristics. SAE occurs with a slow growth rate, which impedes to fabricate high aspect ratio NWs, and thus VLS remains the best method to grow NWs with small diameter. On the other hand, up-scaling diameters in VLS often lead to the formation of defects, including twinning and polytypism, and therefore SAE is preferred for large diameter NWs. In addition, SAE-grown NWs are usually tapering-free and have a smaller variety of impurity species due to high growth temperature [17].

Here, we consider two exemplificative sets of WZ InP NWs. Both sets were grown in a horizontal flow MOVPE reactor with phosphine and trimethylindium as precursors. VLS NWs were Au-catalyzed and their formation took 20 min at the temperature of 480 °C with a V/III ratio of 350 on a semi-insulated InP (111)B oriented substrate. The scanning electron microscope (SEM) image of VLS NWs is displayed in Fig. 1a. The wires are randomly spaced, perpendicular to the substrate, parallel each other, and are ~1–2 μm-long. They have an irregular hexagonal cross-sectional arising from growth along the <111> direction and feature a staggered structure with about three regions having different diameters. We point out that marked tapering in NWs is not associated with low optical and structural quality. The tapered NWs used here have good optical quality and feature a very pure WZ phase (with the $\hat{c}$ axis aligned to the NW long symmetry axis), as demonstrated by the high-resolution transmission electron microscope (HR-TEM) micrograph shown in Fig. 1b. The NWs do not contain any ZB insertion and very few stacking faults are seen along the NWs, except at the NW tips that are formed during the cooling down after growth and feature some more stacking faults. The good crystalline quality of the WZ lattice is confirmed by the selected-area diffraction pattern shown in the

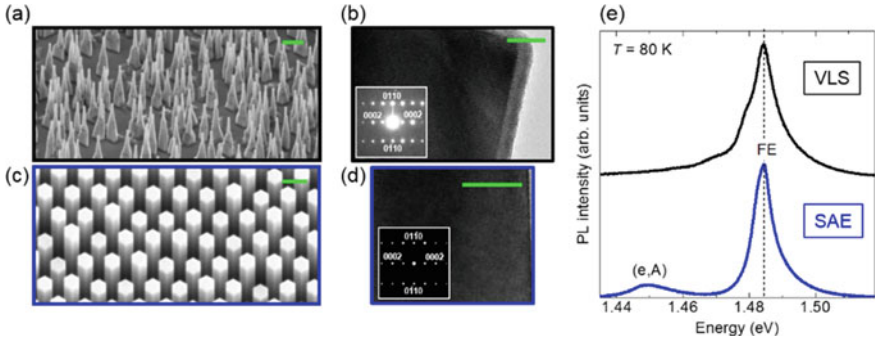

Fig. 1 **a** SEM images of VLS InP NWs. Scale bar is 500 nm. **b** HRTEM image of a VLS NW with the selected-area diffraction pattern in the left-bottom corner confirming the WZ phase. Scale bars are 10 nm. **c** SEM images of SAE NWs (NW diameter = 310 nm). Scale bar is 500 nm. **d** HRTEM image of a SAE NW with the selected-area diffraction pattern in the left-bottom corner confirming the WZ phase. Scale bar is 10 nm (**e**) PL spectra collected at $T = 80$ K on WZ InP NWs grown by VLS (top part) or SAE (bottom part). The SAE NWs have diameter of 310 nm. All spectra were taken on NWs' ensembles (spot size ~200 μm) in backscattering geometry with laser and NW long axis directions parallel to each other. FE indicates the band-gap free-exciton band and (e,A) the free-electron to neutral-acceptor recombination. Data are normalized to the maximum intensity. The area of the FE peak in the PL spectrum of the SAE sample is about three times bigger than that of the VLS sample in similar experimental conditions

inset of Fig. 1b. The second set of samples was grown by SAE on a (111)A InP substrate. Before NW growth, the substrate was patterned by a SiO_2 mask as to leave a regular arrays of round openings in which the NW vertical growth took place. The NWs were grown at 730 °C for 20 min with V/III ratio of 80. Their SEM image is displayed in Fig. 1c. These NWs with diameter $d = 310$ nm are untapered, ~5 μm long, perfectly vertical on the substrate, equally spaced, and have a regular hexagonal cross section. They have a defect-free WZ crystal structure, as demonstrated by HR-TEM image and the selected-area diffraction pattern in panel (d). Details on the growth characteristics can be found in Refs. [17] and [18].

Typical photoluminescence (PL) spectra of VLS and SAE InP WZ NWs are displayed in Fig. 1e. The measurement temperature is 80 K to avoid major contributions from impurity states and thus to highlight the similar lineshape of intrinsic states directly related to the crystal phase of the samples. FE indicates the band associated with the band-gap free-exciton, centered at ~1.484 eV and (e,A) indicates the free-electron to neutral-acceptor recombination at ~1.45 eV. This latter can be observed in the SAE NWs, only. In the FE region, the SAE and VLS NW spectra are very similar indicating the same band-gap energy. While this quantity is clearly determined in WZ InP, this is not the case of other III-V materials, such as GaAs and InAs, where NWs grown in different ways/groups result to have different band-gap energies [19–23]. We notice that the linewidth of the FE band is about 10 meV at 80 K, with VLS NWs having a slightly broader lineshape than SAE NWs. This indicates an overall good optical quality of the two samples, the SAE NWs being slightly

better likely due to their better crystalline quality. A further proof of this is that the integrated area of the PL spectra of the VLS samples is typically about a factor three smaller than that of the SAE samples under similar experimental conditions. In the VLS NWs, the bands between 1.460 and 1.480 eV are likely defect related.

2.2 *Impurity States*

Information about impurity states can be obtained at low temperature. We focus first on SAE NWs. Figure 2a shows the PL at 10 K of NWs having different diameter d = 120, 310, and 650 nm. The measurements were performed on an array of NWs by exciting the samples with a frequency-doubled Nd:YVO_4 laser (532 nm) with a spot diameter of ~200 μm resulting in the excitation of >10^4 NWs. The same power density 3.2 W/cm^2 was used for all ds'. The spectra are displayed on a logarithmic scale to highlight the contribution of impurity states to the spectra. We can notice several differences with varying d. The integrated intensity of the NWs decreases with increasing the surface-to-volume ratio and this cannot be accounted for only

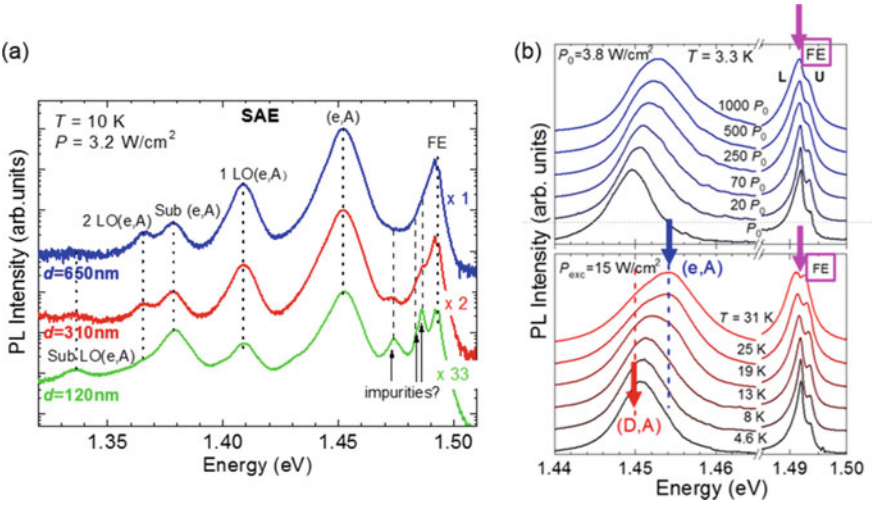

Fig. 2 **a** PL spectra acquired on arrays of InP WZ NWs grown by SAE and having different diameters. Spectra are stacked for clarity and multiplication factors for intensities are given. The transitions highlighted by vertical lines are described in the text. **b** PL spectra on SAE NWs with d = 310 nm. Upper panel: PL spectra at 3.3 K for different values of the laser power density. Note the blue-shift of the PL peak energy as the power density increases. Lower panel: PL spectra recorded for different temperatures. The presence of two different spectral components is apparent and highlighted by arrows. (D,A) indicates a donor-to-acceptor recombination and (e,A) a free-electron to neutral-acceptor recombination. The splitting of the FE peak is discussed in the description of Fig. 3. Figure 2b is reprinted (readapted) with permission from Ref. [18], American Chemical Society, Copyright (2016)

by the smaller volume giving rise to the PL signal. Instead, this is likely due to a relatively larger influence of non-radiative recombination centers at the surface termination of the thinnest NWs and to charge-separating electric fields therein located. In addition, the NWs with $d = 120$ nm feature a larger density of impurities with respect to $d = 310$ and 650 nm. This finding suggests that impurities are incorporated more effectively close to the NW surface, with a correspondingly larger spectral weight in NWs with larger surface-to-volume ratio. Despite these important differences, all NWs exhibit a number of common spectral features, but for $d = 120$ nm, where a series of bound exciton states between 1.47 and 1.49 eV are clearly visible (with decreasing importance in the larger NWs). As shown in Fig. 2b, at 1.452 eV, a band labeled (e,A)/(D,A) dominates the spectra: (e,A) indicates a free-electron to neutral-acceptor recombination and (D,A) indicates a neutral-donor to neutral-acceptor recombination. This band comprises indeed two contributions as apparent in the studies displayed in Fig. 2b. The lower and upper panels show, respectively, temperature (T)- and laser power (P_{exc})-dependent PL of an array of NWs with $d =$ 650 nm. With increasing temperature and laser power, the centre of mass of the band moves at higher energy, thus pointing to the existence of two spectral components. As a matter of fact, with increasing temperature, the progressive ionization of the low-energy component causes a blue-shift of the band. Likewise, for increasing laser power density, the saturation of the same low-energy component leads to a skewing of the band toward higher energy. Therefore, we assign these two spectral contributions, highlighted with arrows, to a (D,A) pair recombination (at ~1.451 eV) and to a (e,A) recombination (at 1.454 eV). This assignment is supported by the larger binding energy of holes to acceptors (~40 meV) [24] with respect to that of electrons to donors (~3 meV) [25] that leads to a rapid quenching of the (D,A) transition with increasing T, while the (e,A) band can be observed up to $T = 80$ K (see Fig. 1e). Similar trends were previously found in bulk zincblende InP [26]. At 1.409 and 1.3661 eV, two progressively weaker bands can be observed in Fig. 2a. We assign these bands to the longitudinal-optical (LO) phonon replica of the (e,A) band with one and two phonons involved. The resulting LO energy, equal to about 43 meV, is in very good agreement with previously reported experimental [27] and theoretical [28] results in WZ InP. In addition, the (e,A) transition and its phonon replica of the ZB InP substrate are also present in the spectra of Fig. 2a. The LO energy is also close to 43 meV, consistently with the very similar phonon dispersion curves of InP WZ and ZB crystals [28].

The series of bound exciton states between 1.47 and 1.49 eV observable in Fig. 2a is better highlighted in Fig. 3, where the $T = 10$ K PL spectra of an ensemble of VLS (lower panel) and SAE (upper panel) NWs with similar diameter are compared. In the VLS NWs, the 1.493 eV is due to the FE recombination. Bands labeled Z, Y, and V share common behaviors: their relative spectral weight decreases with respect to that of the FE peak when the laser power increases and they quench completely at $T > 80$ K (they are indeed almost absent in Fig. 1e). This indicates that the energy levels associated with those bands are characterized by a limited volume density. Furthermore, the energy position of Z, Y, and V are not compatible with type-II transitions occurring at the interface between alternate thick layers made of

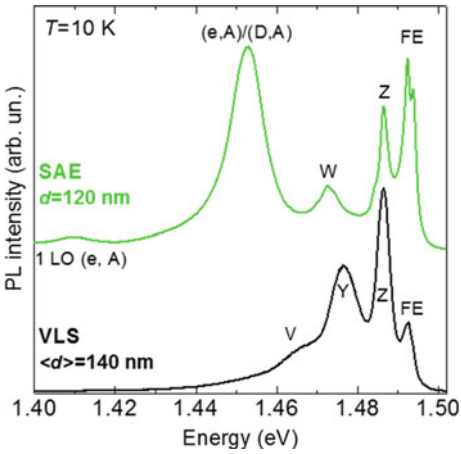

Fig. 3 PL spectra at $T =$ 10 K of arrays of InP WZ NWs grown by different techniques (VLS vs. SAE) and having similar diameter d. The bottom spectrum refers to VLS NWs. The top spectrum was recorded on SAE NWs. Different letters refer to different transitions discussed in the text

WZ and ZB phases (additionally, these bands do not show a sizable blue-shift with increasing laser power characteristic of those transitions) [15, 29–31]. Band Z is 7 meV distant from the FE peak. This energy is compatible with excitons bound to neutral acceptors (A,X) [32]. Bands Y and V can be hardly assigned to conventional transitions associated with impurities (either neutral or charged). These bands could be ascribed instead to line defects, such as stacking faults that in high-purity bulk ZB GaAs were found to lie about 20 meV far from the FE line [33].

In the SAE NWs, the PL spectrum displays a few similarities with the VLS NW one. The same band Z is noticed, while band W, which is close to band Y in the VLS NWs, can be tentatively assigned to staking faults as before. The band at about 1.453 eV was previously discussed, see Fig. 2b, and attributed to the overlap of (e,A) with (D,A) transitions. In addition, the SAE NW spectrum shows a clear splitting of the FE peak [18]. This splitting (amounting to 1.5 meV) is due to the elastic-scattering between polaritons (i.e., exciton–photon mixed quasi-particles carrying the optical excitation through the crystal) and neutral donors. The cross section of the polariton-donor scattering has a maximum at a specific energy, corresponding to the dip recorded in the PL spectra. Similar findings were reported in high-purity ZB bulk InP [34] and GaAs [35].

3 Optical Selection Rules in Wurtzite Crystals

As discussed in the previous section, PL spectroscopy provides information on band-gap states and impurity/defect levels, but in general no hint can be achieved about higher energy points of the electronic band structure. In this regard, absorption spectroscopy is the most suitable technique to address the full density of states. However, standard absorption measurements are quite challenging in NWs, due to the small volume of the nanostructures that are typically grown on a substrate and the prevailing

absorption from this latter. In ordered arrays of NWs with constant diameter and pitch, reflection measurements coupled to multiple scattering analysis provided a good approximation of the amount of the adsorbed light [36]. On the other hand, PLE has proved to be a powerful approach to perform absorption-like measurements in NWs (single wires or ensembles) [37–39]. PLE is a technique complementary to conventional PL. Conversely to the PL case, in PLE the excitation energy E_{ex} is varied, while detection energy E_{det} is kept fixed at the energy of one of the resonances in the PL spectrum of the sample. The relationship between the intensity of the PL signal, I_{PL}, at energy E_{det} and that of the exciting radiation, I_{ex}, can be written explicitly as [2]

$$I_{PL}(E_{ex}, E_{det}) = P_{abs}(E_{ex}) \cdot P_{rel}(E_{ex}, E_{det}) \cdot P_{em}(E_{det}) \cdot I_{ex}(E_{ex}) \quad (1)$$

The probability that a photon of energy E_{ex} is absorbed by the sample, $P_{abs}(E_{ex})$, is proportional to the absorption coefficient $\alpha_{abs}(E_{ex})$. $P_{rel}(E_{ex}, E_{det})$ is the probability that photogenerated e-h pairs will relax toward the states giving rise to the emission of photons of energy E_{det}. Finally, $P_{em}(E_{det})$ is the probability that photons of energy E_{det} will actually be emitted after relaxation. In a PLE experiment, $P_{em}(E_{det})$ is constant with E_{ex}. Then, I_{PL}/I_{ex} is proportional to $\alpha_{abs}(E_{ex})$ only if $P_{rel}(E_{ex}, E_{det})$ is independent of the excitation energy.

Figure 4a sketches the experimental configuration that was employed to measure the absorption spectrum of ensembles of WZ NWs and to assess the optical selection rules related to different interband transitions. These latter are especially dependent on the linear polarization of the absorbed photons with respect to the WZ $\hat{c}$ axis (corresponding to the vertical growth direction of the NWs). To exploit such dependence, the NWs were excited in a side-scattering geometry that allowed us to rotate the exciting laser linear polarization with respect to the NW axis as depicted in Fig. 4a. The resulting luminescence was collected along the NW axis. The band structure of non-nitride III-V WZ materials was reported in several works, see *e.g.* Refs [40–42]. Briefly, from the lowest CB, Γ_{7C}, three optical direct transitions are possible in a relatively narrow energy range close to the band gap: they are named as A ($\Gamma_{7C} \leftrightarrow \Gamma_{9V}$), B ($\Gamma_{7C} \leftrightarrow \Gamma^{u}_{7V}$), and C ($\Gamma_{7C} \leftrightarrow \Gamma^{l}_{7V}$). Figure 4b depicts the optical selection rules according to which the lowest energy transition A should be allowed only for absorbed light polarized perpendicular to $\hat{c}$. The same applies to transition B. Transition C would be instead forbidden for exciting photons polarized perpendicular to the NW axis. However, spin–orbit interaction makes C be observable, though still weak [40]. In the opposite polarization direction, transition A is forbidden and B is partially forbidden thanks to the spin–orbit interaction (like C in the previous case), while transition C is permitted. Of course, many factors concur to affect these selection rules. Deviations from the pure crystalline structure may relax considerably the rules sketched in Fig. 4b. In addition, the dielectric constant mismatch between a NW and its surroundings results in image forces that tend to reduce sizably the amplitude of the electric field inside the NW. This effect depends on the relative direction between the field and the NW long axis. In most cases, the amplitude of the field component polarized perpendicular to the NW symmetry axis is lowered with

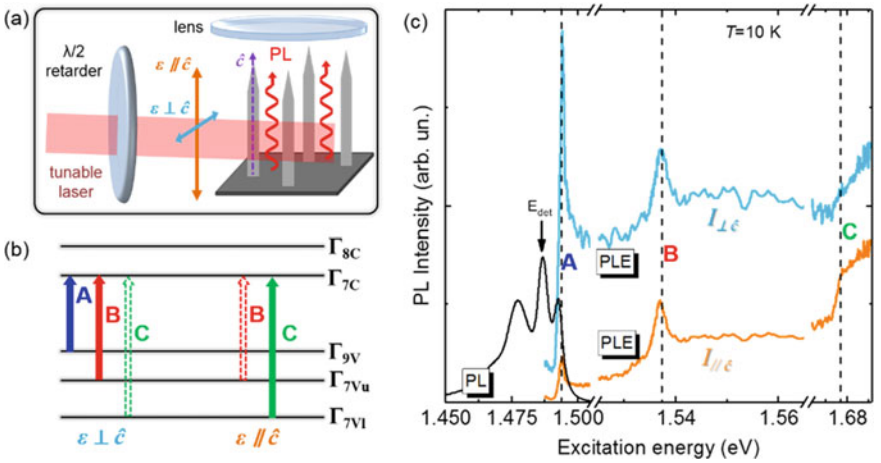

Fig. 4 **a** Sketch of the geometry used for polarization-resolved PLE measurements: NWs are vertical on their growth substrate, the wavevector of a Ti:sapphire laser is perpendicular to the NWs $\hat{c}$ axis (in a grazing incidence configuration), laser polarization vector is controlled by rotating the optical axis of a λ/2 retarder. PL emission for each laser polarization is collected along the NWs axis by a lens system. **b** Optical selection rules for interband A, B, and C transitions (the symmetry of the conduction and valence bands are indicated) of the WZ band structure as derived by PLE measurements and confirmed by theoretical calculations. ε is the versor of the polarization direction of absorbed light. Empty, dashed arrows indicate transitions allowed only by spin–orbit interaction. **c** PLE spectra recorded at $T = 10$ K on ensembles of WZ InP NWs grown by VLS with laser polarization vector parallel (orange line) or perpendicular (light blue line) to the NW $\hat{c}$ axis. The PL spectrum (normalized for clarity reasons) and the detection energy (1.486 eV) are also shown. The relative intensities of the two spectra are given as recorded, namely, they were not changed by data analysis or normalized. A, B, and C transitions are indicated by dashed lines

respect to the component, which is parallel polarized [43]. As a result, this may alter the measured ratios of the different polarization absorption signals. A model able to take this effect into account is described in Ref.[44].

Figure 4c shows the PLE spectra recorded on VLS NWs in a grazing incidence configuration using a Ti:Sa tunable laser. The PL spectrum is also shown and the detection energy indicated. For each excitation wavelength, the PL signal was collected for two different polarizations of the laser: parallel ($\varepsilon \parallel \hat{c}$) and perpendicular ($\varepsilon \perp \hat{c}$) to the NW symmetry axis $\hat{c}$ resulting in the PLE spectra displayed by an orange line and cyan line, respectively. For $\varepsilon \perp \hat{c}$, the A and B exciton transitions are intense and well contrasted with respect to the background absorption related to $k \neq 0$ (or continuum) transitions. On the contrary, the resonance due to the excitonic transition C is rather weak. For $\varepsilon \parallel \hat{c}$, the overall PLE intensity is lower as compared to $\varepsilon \perp \hat{c}$, but for transition C, which is much more evident than in the opposite polarization case. The very high polarization anisotropy of peak A intensity agrees with the A transition selection rule. The sizably smaller anisotropy of peak B suggests a considerable perturbation by the spin–orbit effect, as parallel polarized light absorption at and beyond transition B is allowed only by this effect. The even

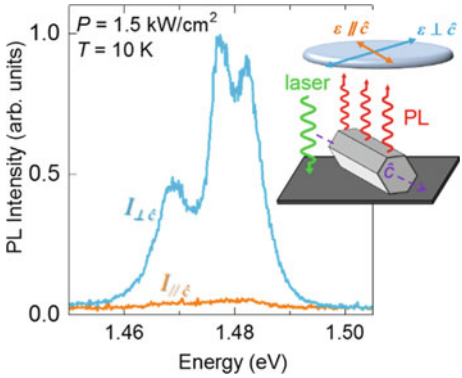

Fig. 5 Polarization-resolved measurements of the light emitted by a single VLS InP wire. The experimental geometry is sketched in the top-right part. PL spectra with polarization vector perpendicular ($I_{\perp}$, blue line) and parallel ($I_{//}$ orange line) to the NW axis have been obtained by setting the retarder's delay to λ/2 and zero, respectively. The emission degree of polarization is about 0.95

lower anisotropy found for transition C is due to the fact that this transition is favored for $\varepsilon \parallel \hat{c}$ with respect $\varepsilon \perp \hat{c}$. We can conclude that the measured polarized absorption spectra confirm the WZ selection rules indicated in panel (b) [44].

The high crystal-phase purity featured by the exciton states (see Fig. 4) is also apparent in the impurity states. Figure 5a shows the low-temperature PL spectra of a single VLS NW similar to those of the preceding figure. The low power density allows highlighting the impurity states, whose attribution was discussed in Fig. 3. The inset depicts the experimental configuration employed, where the light emitted by the single wire is filtered by a combination of a half-wave plate and a linear polarizer. An exceptionally high degree of polarization (nearly 100%), with the luminescence polarized perpendicular to the NW $\hat{c}$ axis, is observed. We stress this is a feature of the band-gap FE (and nearby impurity states) of the WZ phase and as such it can be detected also in large ensembles of NWs, provided that they are not randomly oriented. Indeed, similar polarization-dependent measurements, performed on ensembles of the same VLS InP NWs, show that the PL of the FE is polarized perpendicular to the NW axis, though with a lower degree of polarization (56%) [45].

4 Temperature-Dependent Studies

The emission efficiency in a PL experiment at a given lattice temperature depends on the presence of thermally activated non-radiative recombination centers and to the perturbation induced by lattice vibrations.

Temperature-dependent PL and PLE studies provide also important information on the electronic properties of the critical points and on the interaction between

photogenerated carriers and the lattice. Furthermore, the detailed analysis of the PL lineshape upon varying temperature is relevant for addressing heat management mechanisms. These play a pivotal role in driving the design of NW-based devices. In particular, the rate at which charge carriers cool down after an external excitation [46] is crucial for the efficiency of solar cells [47, 48] and optoelectronic devices [49, 50].

4.1 Temperature Dependence of Optical Transitions in Wurtzite Nanowires

Figure 6a shows the PLE spectra (magenta thick lines) of an ensemble of VLS InP NWs recorded at different temperatures. The excitonic resonances corresponding to the transitions A, B, and C are progressively smeared with increasing T and

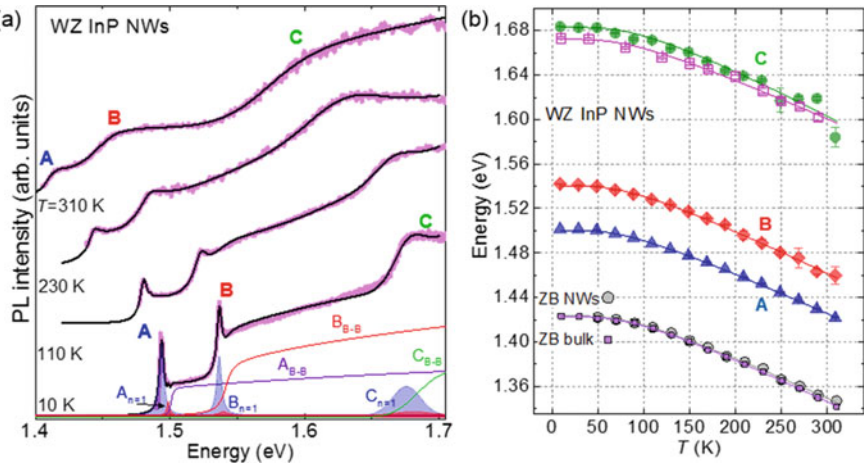

Fig. 6 **a** PL-excitation (thick magenta lines) spectra recorded at different temperatures on an ensemble of VLS WZ InP NWs. The detection energies were set on the low-energy side of the fundamental band-gap free-exciton A. Thin black lines are fits to the data by Elliot's theory, see Eq. (2). A, B, and C indicate the three lowest energy transitions pertinent to the WZ band structure. For the $T = 10$ K PLE spectrum, the various contribution to the spectrum according to Eq. (2) are indicated by filled areas for excitons E_i^n (with i = A, B, and C, and n = 1 and 2; for clarity purposes, labels $E_{\mathrm{A}}^{n=2}$, $E_{\mathrm{B}}^{n=2}$, and $E_{\mathrm{C}}^{n=2}$ indicating the red-colored areas are not shown) and by colored lines for continuum states E_i^{B-B} (with i = A, B, and C). We find $E_{g,\mathrm{A}} = 1.492$ eV, $E_{g,\mathrm{B}} = 1.532$ eV, and $E_{g,\mathrm{C}} = 1.673$ eV. **b** Temperature dependence of the band-gap energies associated with transitions A, B, and C. A and B data are determined by the PLE measurements shown in (**a**). For transition C, full circles refer to data extracted using a best fit to PLE spectra, and open squares refer to data extracted by employing the degree of polarization, as detailed in Ref. [39]. The solid lines through the data are fittings to the data via Eq. 2 in Ref. [39]. Figure 6b is reprinted (readapted) with permission from Ref. 3918, American Chemical Society, Copyright (2015)

red-shift accordingly to the band-gap thermal shrinkage due to the lattice expansion and carrier–phonon interactions [51]. The thin black lines are a fit to the PLE spectra by a model of the absorption coefficient in which the excitonic and continuum contributions are included [39, 52, 53]:

$$\alpha(\hbar\omega) = C \sum_{i=\mathrm{A,B,C}} |M_i|^2 \left\{ \frac{1}{r_{\mathrm{exc},i}^3} \left[\sum_{n\geq 1} \frac{1}{n^3} B\left(E_{g,i} - \frac{R_i}{n^2} - \hbar\omega \right) \right] + \left(\frac{2\mu_{\mathrm{exc},i}}{\hbar^2} \right)^{\frac{3}{2}} \frac{\sqrt{R_i}}{2} \int_{E_{g,i}}^{\infty} \frac{B(E-\hbar\omega)}{1-\exp\left[-2\pi\sqrt{R_i/(E-E_{g,i})} \right]} \mathrm{d}E \right\} \quad (2)$$

where C is a constant, M_i is the matrix element of transition i (with i = A, B and C), $r_{\mathrm{exc},i}$, R_i and $\mu_{\mathrm{exc},i}$ are respectively the exciton Bohr radius, Rydberg and reduced mass related to transition i, $B(x)$ is a suitable broadening function. The first addendum in braces represents the sum over the excitonic resonances with principal quantum number n and the second term represents the Sommerfel factor [52] taking into account the continuum states and their interaction with the bound Coloumb states. These different contributions are explicitly shown in the 10 K spectrum. The resulting values of the A, B, and C band gaps as a function of temperature are displayed in Fig. 6b. They all follow the same thermal shift as observed in other WZ crystals, such as ZnO [54], GaN [55], CdS [56], and CdSe [57], thus indicating that this is a general characteristic of WZ materials, in NW or bulk forms. In addition, we notice that the band-gap thermal shrinkage of WZ NWs is very close to that observed in the ZB crystal phase. This is likely a consequence of the similarity of the WZ and ZB lattices that leads to similar phonon dispersion curves [27, 28] and thermal expansion coefficients [58].

4.2 Thermal Budget Management in NWs

Figure 7 shows the evolution of the PL spectra with increasing temperature of SAE NWs with diameter equal to 650 nm. It can be clearly seen that, as $T > 100$ K, the contribution from impurity states quenches and a long Boltzmann-like tail develops on the high-energy side of the spectra. At the highest temperatures, high-energy states start being populated and the B transition can be observed.

This is more apparent in Fig. 8a, b that shows micro-PL spectra performed on single SAE NWs with diameter $d = 120$ and 650 nm, respectively. The spectra were recorded at different lattice temperature T_L. Notably, the lineshape is strongly dependent on the NW diameter. In particular, the weight of the B transition appears much more prominent in the thinner NW. Indeed, at $T_\mathrm{L} = 310$ K the weight of band B in the $d = 120$ nm NW exceeds that of band A. This finding points to a higher

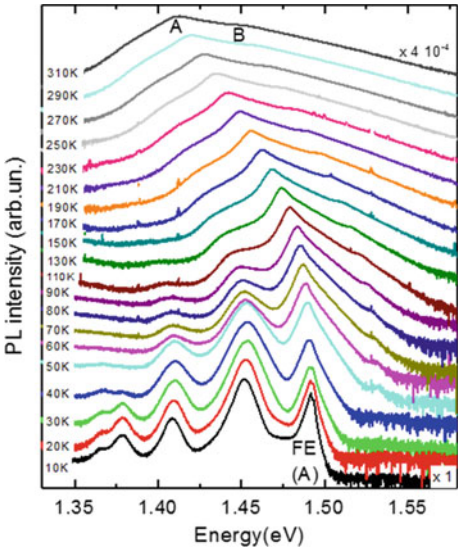

Fig. 7 Temperature-dependent PL spectra on semi-logarithmic scale acquired on arrays of InP WZ NWs grown by SAE with diameters of 650 nm in a backscattering geometry. Spectra are stacked for clarity and multiplication factors for intensities are given for 10 and 310 K. The A and B transitions are labeled, while low-energy peaks are not (see Fig. 2 for their identification)

carrier temperature T_C in the thinner NWs, possibly exceeding that of the lattice reservoir. T_C can be derived by fitting the PL lineshape through:

$$I_{PL}(\hbar\omega) = \alpha(\hbar\omega)e^{-\frac{\hbar\omega}{k_B T_C}} \tag{3}$$

where $\alpha(\hbar\omega)$ is given by Eq. (2). The PL lineshape is very well reproduced by Eq. (3), see dashed lines in panels (a) and (b), and provides us with a robust determination of the carrier temperature [59]. For $T_L = 310$ K, we show the various contributions to the PL lineshape using the same notation of Fig. 6a.

The temperature mismatch between carriers and lattice is shown as a function of T_L in Fig. 8c. A dramatic difference is observed: while in the larger diameter NW the photogenerated carriers are in thermal equilibrium with the lattice bath, in the thinner NW the temperature of electrons and holes increasingly deviates from that of the lattice as soon as $T_L > 100$ K. Similar behaviors were observed in NWs grown by VLS and independently of the crystal phase (WZ vs. ZB) [58] with the NW diameter being the only physical parameter that matters in the phenomenology presented in Fig. 8c. These findings are particularly relevant in photovoltaic devices and may lead to overall enhanced performances [60, 61] provided the origin of the inability of photogenerated carriers to dissipate heat efficiently is better understood. By different experiments, we found that hot phonons are negligible and carriers have enough time to dissipate the excess energy provided by the laser excitation [58]. On the other hand,

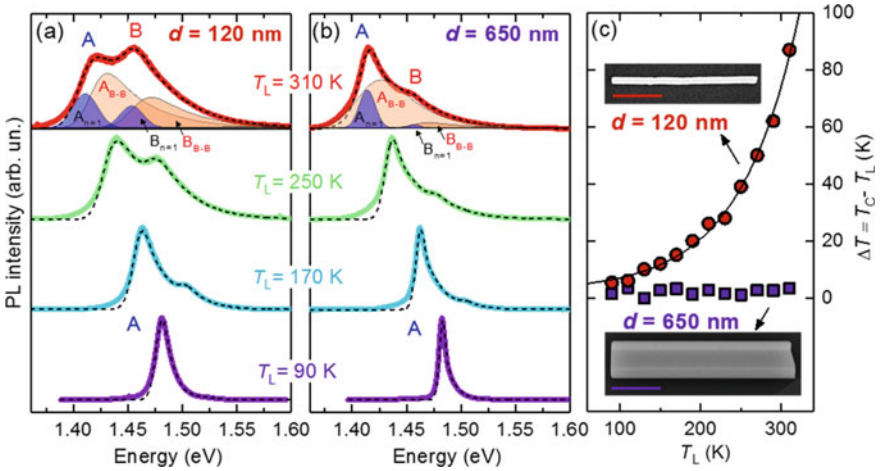

Fig. 8 **a**, **b** PL spectra (thick colored lines) recorded at the indicated lattice temperature T_L on single WZ InP NWs in backscattering geometry. The NWs were grown by SAE and then transferred on Si substrates. Dashed lines are fits to the spectra to extract the carrier temperature. For $T_L = 310$ K, the various contributions to the PL lineshape are shown: filled blue areas for excitons E_i^n (with i = A, B, and C and n = 1) and filled orange areas for continuum states E_i^{B-B} (with i = A, B, and C). The contributions to the C band are not labeled as they are only slightly visible (see grey areas). The small mismatch between data and fits in the low-energy side is due to contribution from defect states not taken into account in the fits. The spectra in (**a**) were recorded on a NW singled out form the array with $d = 120$ nm (at power density $P = 1.1$ kW/cm^2); the spectra in (**b**) were recorded on a NW singled out from the array with $d = 650$ nm ($P = 0.5$ kW/cm^2). SEM images of both NWs are in (**c**), where scale bars are 1 μm. **c** Difference between carriers and lattice temperatures, $\Delta T = T_C - T_L$, as a function of T_L for the NW with $d = 120$ nm (circles) and the NW with $d = 650$ nm (squares). Solid line is an exponential fit to the data

the reduced heat dissipation we observed in small NWs could be ascribed either to a reduced carrier–phonon interaction or to an inhibited phonon emission. Thermal conductivity, κ, measurements in several NW systems, such as ZnO NWs [62] and InAs NWs [63], evidenced that κ decreases with decreasing NW diameter, thus prompting an experimental phenomenology that resembles the diameter dependence of T_C discussed so far. In NWs, the reduced thermal conductivity as compared to bulk is usually ascribed to a suppression of available phonon modes due to the modified phonon density of states in 1D and phonon scattering by various elements [64, 65]. Therefore, we suggest that the mechanisms that impede heat flow (i.e., dissipation) in NWs play a major role also in preventing photogenerated carriers from releasing their excess energy by phonons. Among these mechanisms there are temperature-dependent phonon–phonon and Umklapp processes, and temperature-independent interaction with impurities, line defects, roughness, and boundaries [61, 66].

5 Conclusions

In this chapter, we reviewed the PL properties of InP NWs. We described the low-temperature spectra with particular regard to the presence of impurity-related transitions. By temperature- and photogenerated carrier density-dependent PL studies we addressed the origin of various recombination lines in NWs in the WZ crystal phase. This is especially relevant considering that WZ does not exist in the bulk form and that WZ sections and their doping are pivotal in crystal-phase NW homostructures. By PLE, we investigated the absorption properties of WZ NWs in energy regions at and beyond the three main band gaps (A, B, and C) involving the top most valence band maxima. Specifically, we discussed the role played by the polarization of absorbed light on the efficiency of the absorption process in NWs. The dielectric mismatch with the environment and the optical selection rules of WZ combine non-trivially. The effect of lattice temperature on the absorption and emission processes was investigated. We found a common trend in the temperature-induced reduction of the A, B, and C band gaps like that found in hexagonal GaN, ZnO, CdS, and CdSe bulk materials thus highlighting a general properties holding regardless of the bond polarity and energy gap of the crystal. Finally, we reported on the effect of NW size on the thermal energy retained by photogenerated carriers. Indeed, in steady-state conditions, carriers in small NWs do not reach a full thermal equilibrium with the lattice and their temperature can be in excess of up to 100 K with respect to that of the lattice. This finding points to inhibited phonon emission primarily caused by the large surface-to-volume ratio of small diameter NWs.

References

1. J.I. Pankove, Cathodoluminescence of n-Type GaAs. J. Appl. Phys. **39**(12), 5368–5371 (1968)
2. P.Y. Yu, M. Cardona, *Fundamentals of Semiconductors—Physics and Materials Properties* (Springer, Heidelberg, 2005)
3. H.J. Joyce, J. Wong-Leung, C.K. Yong, C.J. Docherty, S. Paiman, Q. Gao, H.H. Tan, C. Jagadish, J. Lloyd-Hughes, L.M. Herz, M.B. Johnston, Ultralow surface recombination velocity in InP nanowires probed by terahertz spectroscopy. Nano Lett. **12**(10), 5325–5230 (2012)
4. J. Wallentin, N. Anttu, D. Asoli, M. Huffman, I. Aberg, M.H. Magnusson, G. Siefer, P. Fuss-Kailuweit, F. Dimroth, B. Witzigmann, H.Q. Xu, L. Samuelson, K. Deppert, M.T. Borgström, InP nanowire array solar cells achieving 13.8% efficiency by exceeding the ray optics limit. Science **339**(6), 1057–1060 (2013)
5. M. Yoshimura, E. Nakai, K. Tomioka, T. Fukui, Indium tin oxide and indium phosphide heterojunction nanowire array solar cells. Appl. Phys. Lett. **103**(24), 243111 (2013)
6. S.A. Mann, S.Z. Oener, A. Cavalli, J.E.M. Haverkort, E.P.A.M. Bakkers, E.C. Garnett, Quantifying losses and thermodynamic limits in nanophotonic solar cells. Nat. Nanotech. **11**(12), 1071–1075 (2016)
7. Y. Bai, N. Bandyopadhyay, S. Tsao, S. Slivken, M. Razeghi, Room temperature quantum cascade lasers with 27% wall plug efficiency. Appl. Phys. Lett. **98**(18), 181102 (2011)
8. R. Flückiger, R. Lövblom, M. Alexandrova, O. Ostinelli, C.R. Bolognesi, Type-II InP/GaAsSb double-heterojunction bipolar transistors with f_{MAX}> 700 GHz. Appl. Phys. Express **7**(3), 034105 (2014)

9. P. Caroff, J. Bolinsson, J. Johansson, Crystal phases in III–V nanowires: from random toward engineered polytypism. IEEE J. Sel. Top. Quant. Electron. **17**(4), 829–846 (2011)
10. J. Johansson, Z. Zanolli, K.A. Dick, Polytype attainability in III–V semiconductor nanowires. Cryst. Growth Des. **16**(1), 371–379 (2016)
11. S. Assali, L. Gagliano, D.S. Oliveira, M.A. Verheijen, S.R. Plissard, L.F. Feiner, E.P.A.M. Bakkers, Exploring crystal phase switching in GaP nanowires. Nano Lett. **15**(12), 8062–8069 (2015)
12. N. Akopian, G. Patriarche, L. Liu, J.-C. Harmand, V. Zwiller, Crystal phase quantum dots. Nano Lett. **10**(4), 1198–1201 (2010)
13. R.S. Wagner, W.C. Ellis, Vapor-liquid-solid mechanism of single crystal growth. Appl. Phys. Lett. **4**(5), 89–90 (1964)
14. Q. Gao, V.G. Dubrovskii, P. Caroff, J. Wong-Leung, L. Li, Y. Guo, L. Fu, H.H. Tan, C. Jagadish, Simultaneous selective-area and vapor–liquid–solid growth of InP Nanowire Arrays. Nano Lett. **16**(7), 4361–4367 (2016)
15. M.H. Hadj Alouane, N. Chauvin, H. Khmissi, K. Naji, B. Ilahi, H. Maaref, G. Patriarche, M. Gendry, C. Bru-Chevallier, Excitonic properties of wurtzite InP nanowires grown on silicon substrate. Nanotechnology **24**(3), 035704 (2012)
16. Q. Gao, D. Saxena, F. Wang, L. Fu, S. Mokkapati, Y. Guo, L. Li, J. Wong-Leung, P. Caroff, H.H. Tan, C. Jagadish, Selective-area epitaxy of pure wurtzite InP nanowires: high quantum efficiency and room-temperature lasing. Nano Lett. **14**(9), 5206–5211 (2014)
17. M. De Luca, A. Polimeni, H.A. Fonseka, A.J. Meaney, P.C.M. Christianen, J.C. Maan, S. Paiman, H.H. Tan, F. Mura, C. Jagadish, M. Capizzi, Magneto-optical properties of wurtzite-phase InP nanowires. Nano Lett. **14**(8), 4250–4256 (2014)
18. D. Tedeschi, M. De Luca, A. Granados del Águila, Q. Gao, G. Ambrosio, M. Capizzi, H.H. Tan, P.C.M. Christianen, C. Jagadish, A. Polimeni, Value and anisotropy of the electron and hole mass in pure wurtzite InP nanowires. Nano Lett. **16**(10), 6213–6221 (2016)
19. M. De Luca, G. Lavenuta, A. Polimeni, S. Rubini, V. Grillo, F. Mura, A. Miriametro, M. Capizzi, F. Martelli, Excitonic recombination and absorption in $In_xGa_{1-x}As$/GaAs heterostructure nanowires Phys. Rev. B **87**(23), 235304 (2013)
20. F. Martelli, G. Priante, S. Rubini, Photoluminescence of GaAs nanowires at an energy larger than the zincblende band-gap: dependence on growth parameters. Semicond. Sci. And Tech. **30**(5), 055020 (2015)
21. J. Greil, S. Assali, Y. Isono, A. Belabbes, F. Bechstedt, F.O. Valega Mackenzie, A.Y. Silov, E.P.A.M.Bakkers,, J. E. M. Haverkort, Optical properties of strained Wurtzite gallium phosphide nanowires. Nano Lett. **16**(6), 3703–3709 (2016)
22. M.B. Rota, A.S. Ameruddin, H.A. Fonseka, Q. Gao, F. Mura, A. Polimeni, A. Miriametro, H.H. Tan, C. Jagadish, M. Capizzi, Bandgap energy of Wurtzite InAs nanowires. Nano Lett. **16**(8), 5197–5203 (2016)
23. A. Senichev, P. Corfdir, O. Brandt, M. Ramsteiner, S. Breuer, J. Schilling, L. Geelhaar, P. Werner, Electronic properties of wurtzite GaAs: a correlated structural, optical, and theoretical analysis of the same polytypic GaAs nanowire. Nano Res. **11**(9), 4708 (2018)
24. R.A. Lewis, Y.-J. Wang, Magneto-optical far-infrared absorption spectroscopy of the hole states of indium phosphide. Phys. Rev. B **71**(11), 115211 (2005)
25. S. Charbonneau, L.B. Allard, A.P. Roth, T. Sudersena Rao, Time-resolved photoluminescence studies of biexcitons in InP. Phys. Rev. B **47**(20), 13918–13921 (1993)
26. E. Kubota, Y. Ohmori, K. Sugii, Electrical and optical properties of Mg-, Ca-, and Zn-doped InP crystals grown by the synthesis, solute diffusion technique. J. Appl. Phys. **55**(10), 3779–3784 (1984)
27. E.G. Gadret, M.M. de Lima, J.R. Madureira, T. Chiaramonte, M.A. Cotta, F. Iikawa, A. Cantarero, Optical phonon modes of wurtzite InP. Appl. Phys. Lett. **102**(12), 122101 (2013)
28. S. Mukhopadhyay, D.A. Stewart, First-principles study of the phonon dispersion and dielectric properties of wurtzite InP: role of In 4d electrons. Phys. Rev. B **89**(5), 054302 (2014)
29. K. Li, H. Sun, K.W. Hg, T.-T.D. Tran, R. Chen, C.J. Chang-Hasnain, Tailoring the optical characteristics of microsized InP Nanoneedles directly grown on silicon. Nano Lett. **14**(1), 183–190 (2014)

30. J. Bao, D.C. Bell, F. Capasso, J.B. Wagner, T. Mårtensson, J. Trägårdh, L. Samuelson, Optical properties of rotationally twinned InP nanowire heterostructures. Nano Lett. **8**(3), 836–841 (2008)
31. K. Pemasiri, M. Montazeri, R. Gass, L.M. Smith, H.E. Jackson, J. Yarrison-Rice, S. Paiman, Q. Gao, H.H. Tan, C. Jagadish, X. Zhang, J. Zou, Carrier dynamics and quantum confinement in type II ZB-WZ InP nanowire homostructures. Nano Lett. **9**(2), 648–654 (2009)
32. L. Pavesi, F. Piazza, A. Rudra, J.F. Carlin, M. Ilegems, Temperature dependence of the InP band gap from a photoluminescence study Phys. Rev. B **44**(16), 9052 (1991)
33. T. Karin, X. Linpeng, M.M. Glazov, M.V. Durnev, E.L. Ivchenko, S. Harvey, A. Rai, A. Ludwig, A.D. Wieck,, K.-M.C. Fu, Giant permanent dipole moment of two-dimensional excitons bound to a single stacking fault. Phys. Rev. B **94**(4) 041201(R) (2016)
34. R. Benzaquen, R. Leonelli, S. Charbonneau, Exciton-impurity interactions in high-purity InP. Phys. Rev. B **59**(3), 1973–1985 (1999)
35. E.S. Koteles, J. Lee, J.P. Salerno, M.O. Vassell, Elastic scattering of exciton polaritons by neutral impurities. Phys. Rev. Lett. **55**(8), 867–870 (1985)
36. M. Aghaeipour, N. Anttu, G. Nylund, L. Samuelson, S. Lehmann, M.-E. Pistol, Tunable absorption resonances in the ultraviolet for InP nanowire arrays. Opt. Express **22**(23), 29204 (2014)
37. E.G. Gadret, G.O. Dias, L.C.O. Dacal, M.M. de Lima, C.V.R.S. Ruffo, F. Iikawa, M.J.S.P. Brasil, T. Chiaramonte, M.A. Cotta, L.H.G. Tizei, D. Ugarte, A. Cantarero, Valence-band splitting energies in wurtzite InP nanowires: Photoluminescence spectroscopy andab initiocalculations. Phys. Rev. B **82**(12), 125327 (2010)
38. S. Perera, K. Pemasiri, M.A. Fickenscher, H.E. Jackson, L.M. Smith, J. Yarrison-Rice, S. Paiman, Q. Gao, H.H. Tan, C. Jagadish, Probing valence band structure in wurtzite InP nanowires using excitation spectroscopy. Appli. Phys. Lett. **97**(2), 023106 (2010)
39. A. Zilli, M. De Luca, D. Tedeschi, H.A. Fonseka, A. Miriametro, H.H. Tan, C. Jagadish, M. Capizzi, A. Polimeni, Temperature dependence of interband transitions in Wurtzite InP nanowires. ACS Nano **9**(4), 4277–4287 (2015)
40. F. Bechstedt, J. Belabbes, Structure, energetics, and electronic states of III–V compound polytypes. J. Phys. Cond. Matter **25**(27), 273201 (2013)
41. J.L. Birman, Some selection rules for band-band transitions in Wurtzite structure. Phys Rev. **114**(6), 1490–1492 (1959)
42. P. Tronc, Y.E. Kitaev, G. Wang, M.F. Limonov, A.G. Panfilov,, G. Neu, Optical selection rules for hexagonal GaN. Phys. Stat. Sol. (b) **216**(1), 599–603 (1999)
43. H.E. Ruda, A. Shik, Polarization-sensitive optical phenomena in semiconducting and metallic nanowires Phys. Rev. B **72**(15), 115308 (2005)
44. M. De Luca, A. Zilli, A. Fonseka, S. Mokkapati, A. Miriametro, H. Tan, L. Smith, C. Jagadish, M. Capizzi, A. Polimeni, Polarized light absorption in Wurtzite InP nanowire ensembles. Nano Lett. **15**(2), 998–1005 (2015)
45. M. De Luca, A. Polimeni, Electronic properties of wurtzite-phase InP nanowires determined by optical and magneto-optical spectroscopy. Appl. Phys. Rev. **4**(4), 041102 (2017)
46. A.J. Nozik, Spectroscopy and hot electron relaxation dynamics in semiconductor quantum wells and quantum dots. Annu. Rev. Phys. Chem. **52**, 193–231 (2001)
47. R.T. Ross, A.J. Nozik, Efficiency of hot-carrier solar energy converters. J. Appl. Phys. **53**(5), 3813–3818 (1982)
48. G. Conibeer, S. Shrestha, S. Huang, R. Patterson, H. Xia, Y. Feng, P. Zhang, N. Gupta, M. Tayebjee, S. Smyth, Y. Liao, S. Lin, P. Wang, X. Dai, S. Chung, Hot carrier solar cell absorber prerequisites and candidate material systems. Sol. Energy Mater. Sol. Cells **135**, 124–129 (2015)
49. K. Yoon, J.K. Hyun, J.G. Connell, I. Amit, Y. Rosenwaks, L.J. Lauhon, Barrier height measurement of metal contacts to Si nanowires using internal photoemission of hot carriers. Nano Lett. **13**(12), 6183–6188 (2013)
50. Y. Yang, X. Peng, H.-S. Kim, T. Kim, S. Jeon, H.K. Kang, W. Choi, J. Song, Y.-J. Doh, D. Yu, Hot carrier trapping induced negative photoconductance in InAs nanowires toward novel nonvolatile memory. Nano Lett. **15**(9), 5875–5882 (2015)

51. P. Lautenschlager, M. Garriga, M. Cardona, Temperature dependence of the interband critical-point parameters of InP. Phys. Rev. B **36**(9), 4813–4820 (1987)
52. E. Grilli, M. Guzzi, R. Zamboni, L. Pavesi, High-precision determination of the temperature dependence of the fundamental energy gap in gallium arsenide. Phys. Rev. B **45**(4), 1638–1644 (1992)
53. R.J. Elliot, Intensity of optical absorption by excitons. Phys. Rev. **108**(6), 1384–1389 (1957)
54. H. Alawadhi, S. Tsoi, X. Lu, A.K. Ramdas, M. Grimsditch, M. Cardona, R. Lauck, Effect of temperature on isotopic mass dependence of excitonic band gaps in semiconductors: ZnO. Phys. Rev. B **75**(20), 205207 (2007)
55. W. Shan, T.J. Schmidt, X.H. Yang, S.J. Hwang, J.J. Song, B. Goldenberg, Temperature dependence of interband transitions in GaN grown by metalorganic chemical vapor deposition. Appl. Phys. Lett. **66**(8), 985–987 (1995)
56. A. Imada, S. Ozaki, S. Adachi, Photoreflectance spectroscopy of Wurtzite CdS. J. Appl. Phys. **92**(4), 1793–1798 (2002)
57. S. Logothetidis, M. Cardona, P. Lautenschlager, M. Garriga, Temperature dependence of the dielectric function and the interband critical points of CdSe. Phys. Rev. B **34**(4), 2458–2469 (1986)
58. F. Benkabou, P. Becker, M. Certier, H. Aourag, Structural and dynamical properties of zincblende GaN. Phys. Stat. Sol. (b) **209**(2), 223–233 (1998)
59. D. Tedeschi, M. De Luca, H.A. Fonseka, Q. Gao, F. Mura, H.H. Tan, S. Rubini, F. Martelli, C. Jagadish, M. Capizzi, A. Polimeni, Long-lived hot carriers in III–V Nanowires. Nano Lett. **16**(5), 3085–3093 (2016)
60. M. Li, J. Fu, Q. Xu, T.C. Sum, Slow hot-carrier cooling in halide perovskites: prospects for hot-carrier solar cells. Adv. Mat. **31**(47), 1802486 (2019)
61. S. Limpert, A. Burke, I.-J. Chen, N. Anttu, S. Lehmann, S. Fahlvik, S. Bremner, G. Conibeer, C. Thelander, M.-E. Pistol, H. Linke, Bipolar Photothermoelectric effect across energy filters in single nanowires. Nano Lett. **17**(7), 4055–4060 (2017)
62. C.T. Bui, R. Xie, M. Zheng, Q. Zhang, C.H. Sow, B. Li, J.T.L. Thong, Diameter-dependent thermal transport in individual ZnO nanowires and its correlation with surface coating and defects. Small **8**(5), 738–745 (2012)
63. M.Y. Swinkels, M.R. van Delft, D.S. Oliveira, A. Cavalli, I. Zardo, R.W. van der Heijden, E.P.A.M. Bakkers, Diameter dependence of the thermal conductivity of InAs nanowires. Nanotechnology **26**(38), 385401 (2015)
64. A.I. Hochbaum, P. Yang, Semiconductor nanowires for energy conversion. Chem. Rev. **110**(1), 527–546 (2010)
65. X. Lü, J.H. Chu, W.Z. Shen, Modification of the lattice thermal conductivity in semiconductor rectangular nanowires. J. Appl. Phys. **93**(2), 1219–1229 (2003)
66. P. Martin, Z. Aksamija, E. Pop, U. Ravaioli, Impact of phonon-surface roughness scattering on thermal conductivity of thin Si nanowires. Phys. Rev. Lett. **102**(12), 125503 (2009)

Addressing Crystal Structure in Semiconductor Nanowires by Polarized Raman Spectroscopy

Claudia Fasolato, Ilaria Zardo, and Marta De Luca

Abstract Raman scattering is a powerful inelastic light scattering technique able to probe the vibrational properties of materials. This technique has been successfully employed in semiconductor nanowires to provide information on their fundamental properties, such as the phononic properties, the crystal composition, and the electronic band structure. When performed in a polarization-resolved manner on a single nanowire, Raman spectroscopy can even allow addressing the nanowire's crystal structure. This is a fact of pivotal importance, as crystal phase is emerging as a novel degree of freedom in the bandgap engineering and phonon engineering of materials, and the control of the crystal phase is a possibility uniquely offered by nanowires. Indeed, recent advances in the synthetic growth of nanowires have given access to crystal phases (*e.g.,* hexagonal phase in Si and Ge) that in the bulk can only be obtained under extreme pressure conditions, and it is possible to controllably switch between different crystal phases during the growth of nanowires. The realization and, even more, the interpretation of polarized Raman experiments on nanowires can be non-trivial, as several issues have to be considered. Therefore, in this chapter, we provide the basic theoretical background necessary to calculate Raman selection rules and interpret polarization-resolved Raman spectra of semiconductor nanowires. We also discuss the main ingredients of a Raman setup, with a focus on the scattering geometries typically used for nanowires. We highlight the main differences in the Raman spectra of nanowires with cubic and hexagonal crystal symmetries, and we treat also the case of the most challenging type of heterostructure: a nanoscale crystal-phase homostructure. Finally, we discuss resonant Raman experiments that allow the determination of the energy of some electronic transitions in nanowires. We focus mostly on a very new material system, namely Ge nanowires with controlled crystal phase, but the general procedure that we establish can be applied to several types of nanostructures.

C. Fasolato
Dipartimento di Fisica e Geologia, Università degli Studi di Perugia, 06123 Perugia, Italy

C. Fasolato · I. Zardo · M. De Luca (✉)
Departement Physik, Universität Basel, Klingelbergstrasse 82, CH4056 Basel, Switzerland
e-mail: marta.deluca@unibas.ch

© Springer Nature Singapore Pte Ltd. 2021

N. Fukata and R. Rurali (eds.), *Fundamental Properties of Semiconductor Nanowires*,
https://doi.org/10.1007/978-981-15-9050-4_7

Keywords Semiconductor nanowires · Raman spectroscopy · Phonon dispersion · Crystal phases · Heterostructures · Electronic properties

1 Introduction

Semiconductor III–V materials crystallize either in the cubic zincblende (ZB) phase or in the hexagonal wurtzite (WZ) phase. Apart from the nitrides, which can grow in WZ phase, the most conventional III–V materials such as phosphides, arsenides, and antimonides of Al, Ga, and In in the bulk form crystallize in the ZB structure under ambient conditions. However, it was soon realized that this was not the case for nanowires (NWs) [1]. Indeed, as first demonstrated for InAs NWs [2], non-nitrides III–V compounds with WZ crystal structure can be stable when grown in the NW form. After several years of investigation, recently great progress has been achieved in the general understanding of the intrinsic causes of the WZ formation in III–V nanowires [3, 4]. In parallel, many successful strategies have been developed for controlling experimentally the crystal phase of NWs [5], as also discussed in the first chapter of this book. This opened the way to crystal-phase engineering, where not only unconventional crystal phases like WZ can be controllably obtained but also they can be juxtaposed to the most common phases like ZB to obtain crystal-phase homostructures. In some cases, the juxtaposition can occur in an ordered fashion for few periods, enabling the formation of crystal-phase superlattices [6, 7]. Crystal-phase engineering is becoming a relevant degree of freedom in the engineering of NW properties for specific technological applications, as typical issues that degrade the quality of conventional heterostructures, such as lattice mismatch and atomic interdiffusion, are absent in crystal-phase homostructures, where only the crystal structure changes, while the atomic species and the nature of chemical bonding stays the same.

Besides III–V compounds, a "crystal-phase revolution" has concerned also group-IV semiconductors. Indeed, Si and Ge, which in nature are ubiquitous in the cubic phase, can be grown in the hexagonal phase in the NW geometry [8, 9]. The advent of these novel polymorphs holds the promise to overcome the main limitation that has kept these materials out of the "photonic arena" so far, namely their indirect bandgap. Indeed, the bandgap of hexagonal Ge and hexagonal SiGe alloys is predicted to be direct [10], a fact that could finally enable to reach the long-standing goal of designing cost-effective light-emitting materials that can be easily integrated on Si chips. Very recently, the direct bandgap nature of hexagonal SiGe has been experimentally demonstrated [11].

A full understanding of the NWs' physical properties and of their dependence on crystal structure is the first step toward the realization of devices based on NWs, and thus it has been the focus of several experimental and theoretical studies in the last decade. Raman spectroscopy is a valuable and non-destructive tool to investigate the structural, phononic, and electronic properties of NWs. In particular, it provides information on the phonon modes near the Brillouin zone center (first-order Raman

scattering) as well as on the electronic transitions (resonant Raman scattering). As a consequence, Raman has soon become one of the most powerful and diffused techniques to assess the crystal phase of NWs. While it has been largely employed on pure-phase NWs, studies of crystal-phase homostructured NWs are scarce and sometimes limited by the crystal quality of the sample and/or by the difficult interpretation of the data. In this work, the reader is guided into the world of Raman spectroscopy in NWs composed by a same or different crystal phases, both concerning data acquisition and interpretation. Besides the crystal phase, Raman experiments can provide precious information on the structural quality, crystal composition, and strain level of NWs. However, in this book chapter, we focus mainly on the Raman studies of the crystal structure of NWs, as it is the NW property which is most different from the bulk, and thus the methods to address it and its effects on the physical behavior of the system are the less known. The reader is referred to Ref. [12] for an overview of Raman studies aimed at addressing phonon confinement, crystal composition, and strain level of NWs.

We start the description of the use of Raman spectroscopy to address the properties of the two most common crystal phases in NWs (cubic and hexagonal) by discussing differences and similarities between the crystal structures (Sect. 1.1). In Sect. 1.2, we show the impact of the crystal structure on the phonon dispersion.

1.1 Crystal Structures of Nanowires

The description of the structural similarities and differences between ZB and WZ crystals has the aim to stress that the similarities between the two crystal structures are large enough to allow to deduce the electronic and phononic properties of the WZ starting from the ZB ones, while the differences between WZ and ZB properties are large enough to allow electrons and phonons to see a different electronic and phononic landscape when they are in the different types of structures, rendering the WZ/ZB interface effective despite the constant composition of the NW. As an example, we mention that a same semiconductor in WZ and ZB structures has different bandgap energies; therefore, in crystal-phase homostructures, the bandgap varies along the wire axis over tailored nanometer length scales. Such changes in bandgap and confinement potentials have allowed the realization of crystal-phase quantum dots in III–V NWs [13, 14].

The ZB lattice (as well as the diamond lattice) belongs to the cubic crystal system. Indeed, the two atoms of the basis form two interpenetrating face-centered cubic (fcc) lattices. The differences between ZB and WZ are best understood by viewing them along the [111] direction, along which both look like stacked hexagonal layers [5]. Along the ZB [111] direction, ZB compounds possess a fixed stacking ABCABC…, as displayed in Fig. 1a (left). Each bilayer labeled by a capital letter consists of a cation and an anion layer in III–V compounds with the ZB structures, or by the same type of atoms in group-IV semiconductors with the diamond structure. The WZ lattice (lonsdaleite lattice if the two atoms are equal) belongs to the hexagonal crystal

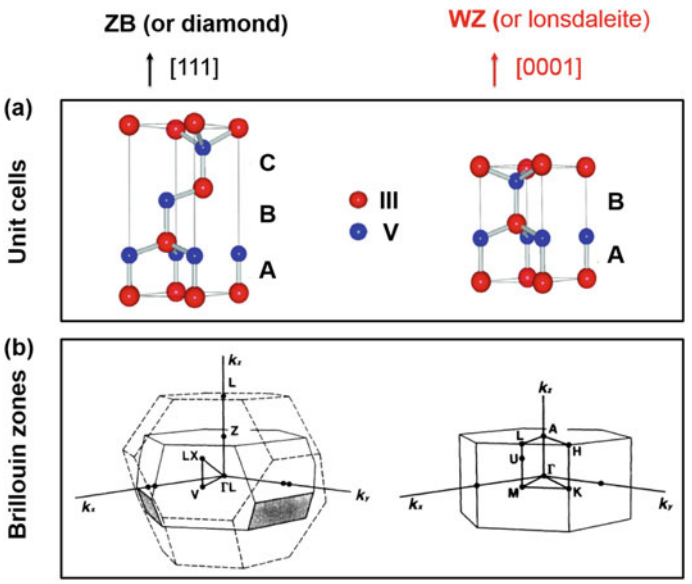

Fig. 1 **a** Stick and ball models of the unit cells of ZB (left) and WZ (right) lattices for a III–V compound (if group-III and group-V atoms are the same, we represent diamond and lonsdaleite lattices). The atomic bilayers are indicated by the symbols A, B, or C. The unit cell of the WZ is primitive, while a non-primitive hexagonal cell is considered to illustrate the ZB, in order to highlight the similarities between ZB and WZ. The bonding chains in the (–1–120) plane are indicated by thick gray lines. **b** Brillouin zones for ZB (left) and WZ (right) structures drawn in the same scale. The k_z axis is parallel to the ZB [111] direction. In the left panel, the dashed line indicates the usual ZB fcc Brillouin zone, the solid line that of the half-size Brillouin zone very similar to the WZ Brillouin zone in the right panel. Shaded planes indicate the surfaces common to full size and half-size ZB Brillouin zones

system. Indeed, the two atoms form two interpenetrating hexagonal close-packed (hcp) lattices. Similar to the ZB, the WZ structure displays tetrahedral coordination: the nearest neighbors of each atom are four atoms of the opposite type, positioned at the four vertices of a regular tetrahedron. However, because of bond tetrahedra rotation by 60°, it results in a stacking sequence ABABAB… along with the WZ [0001] direction,[1] as shown in Fig. 1a (right). An element or compound is polytypic if it occurs in several crystal phases, each of which differs from the other ones for the layer stacking sequence, while the layer structure and composition is the same in all the polytypic forms. Therefore, ZB and WZ (as well as diamond and lonsdaleite) are very good examples of polytypism, and crystal-phase homostructures are commonly named polytypic homostructures.

[1] In hexagonal lattices, the four index Bravais–Miller scheme is often used for indicating crystal directions, with [0001] labeling the c-axis direction.

1.2 Crystal Symmetry and Phonon Dispersion

In ZB and WZ crystals, all the nearest neighbors and 9 out of the 12 second-nearest neighbors are in the same positions [15, 16]. Due to the several similarities of the two crystal structures, many of the high symmetry points in the first Brillouin zone of ZB and WZ are related to each other, and establishing correspondences is useful for understanding trends in the band structures and phonon dispersions of the two polytypes [17]. In particular, ZB crystals have two atoms per unit cell, whereas WZ crystals have four atoms per unit cell. Therefore, the Brillouin zone (BZ) of ZB along the [111] direction is twice as large as that of the WZ along with the [0001] direction, as depicted in Fig. 1b, where the dashed line on the left side represents the usual BZ of the ZB, and the solid line on the right side represents the BZ of the WZ. A correspondence between ZB and WZ Brillouin zones is easily established if for the ZB a half-size BZ is considered (solid line on the left side). In this way, the half-size ZB BZ has the same volume as the WZ BZ and many of the high-symmetry points of the ZB and WZ Brillouin zones are related to each other [16, 17]. Hence, it is possible to derive the phonon dispersions for the WZ structures along Γ-A by simply folding the ones for the ZB structures along Γ-L [18], as pictured in Fig. 2a

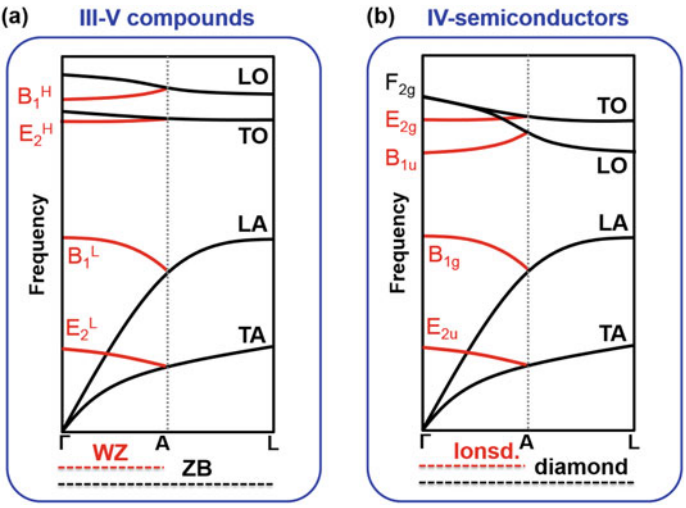

Fig. 2 Folding of the phonon dispersion along the cubic ΓL (corresponding to [111]) direction to obtain the phonon dispersion of the hexagonal crystals along the hexagonal ΓA (corresponding to [0001]) direction. Cubic crystals have only the phonon branches along the cubic ΓL depicted with black lines, hexagonal crystals have the phonon branches along ΓA depicted by both the black and red lines. The folding operation is represented in (**a**) for III–V semiconductor and in (**b**) for a group-IV semiconductor. The symmetries of the modes at the Γ point are indicated. The symmetry of the optical modes at Γ in the hexagonal materials is not indicated, as it can be either A_1-like or E_1-like depending on the material and on the scattering geometry

for a III–V compound. In doing this operation, we are neglecting perturbations due to the difference in the layer stacking order.

Let us first focus on the phonon dispersion of the ZB (black lines in Fig. 2a). In a three-dimensional crystal with N atoms per primitive unit cell, there are 3 N phonon branches, among which three are acoustic and the remaining 3 N–3 are optical. Along the high-symmetry directions, the phonons can be classified as transverse or longitudinal according to whether the atomic displacements are perpendicular or parallel to the direction of the phonon wave vector. In the diamond and ZB lattices, there are two atoms per cell, therefore, six phonon branches: two transverse and one longitudinal acoustic branches (TA and LA, respectively), two transverse and one longitudinal optical branches (TO and LO, respectively). In the WZ materials, the total number of phonon branches doubles (due to the double number of atoms in the unit cell). Indeed, there are all the branches of the ZB plus the branches arising from the folding operation (red lines in Fig. 2). In the ZB materials, only the transverse TO and longitudinal LO optical phonons modes have a non-zero frequency at Γ point and are both detectable by first-order Raman spectroscopy. In WZ, at Γ point there are also the two non-polar modes with E_2 symmetry (arising from the TO(L) and TA(L) modes in the ZB) and the two non-polar modes with B_1 symmetry (arising from the LO(L) and LA(L) modes in the ZB) [18, 19]. In addition to the modes arising from the folding, in WZ, there are also modes originating from broken degeneracies due to the lower degree of symmetry of WZ compared to ZB. Indeed, in the hexagonal structures, polar phonons induce an anisotropy in the macroscopic electric fields within the material. Therefore, the TO modes at the zone center in ZB split into A_1(TO) and E_1(TO) modes in the WZ structure and the same occurs to LO modes. The frequency order of the A_1(TO), E_1(TO), $E_2{}^H$, A_1(LO), E_1(LO) modes in a Raman spectrum depends on the material [20]. Therefore, in Fig. 2, the symmetry of TO and LO modes is not specified.

The A_1 and B_1 modes are associated with atomic displacements along the c-axis, while E_1 and E_2 modes are associated with atomic displacements perpendicular to the c-axis. The A_1 and E_1 modes are both Raman and infrared active, the two E_2 modes are only Raman active, and the two B_1 modes are neither Raman nor IR active (silent modes) [21]. The scattering configurations in which each mode can be observed are discussed in Sect. 2.2.

Figure 2b depicts a similar folding operation for a group-IV semiconductor. Notice that in nonpolar semiconductors, like Si or Ge, the TO and LO optical phonons are degenerate at Γ point, and the degenerate TO-LO mode is labeled as F_{2g} mode. Instead, in polar semiconductors like III–V crystals, there is a TO–LO splitting arising from the difference between the low- and high-frequency dielectric permittivities (or the effective charges), and such splitting is a measure of the polarity of the semiconductor. Similar to the ZB/WZ case, also in group-IV semiconductors, the zone center mode in the diamond structure (F_{2g}) splits into A_{1g} and E_{1g} modes in the lonsdaleite structure [22]. The A_{1g} is the longitudinal optical mode and the E_{1g} and E_{2g} are the transverse optical modes. The A_{1g}, E_{1g}, and E_{2g} are Raman active modes. The B_{1g}, B_{1u}, and E_{2u} are optically inactive modes. Both diamond and lonsdaleite have no infrared active modes [22]. It has been shown by first-principles density

functional calculations that the existence of additional mid-frequency optical modes in the lonsdaleite structure of Si has a huge impact on the thermal conductivity, which is indeed significantly lower than in diamond Si, a fact that could be of interest for phonon manipulations and thermoelectric applications [23].

In a more specialized treatment, we can say that the phonon modes in cubic and hexagonal crystals have different symmetries (reflected by a different capital letter to indicate the phonon modes) because the different atomic arrangements, described in Sect. 1.1, result in different point and space groups. Specifically, the point groups of the crystals with a basis of two equal atoms, like group-IV semiconductors, is O_h for the diamond and D_{6h} for the lonsdaleite, and the point groups of crystals with a basis of two different atoms, like III–V semiconductors, is T_d for the ZB and C_{6v} for the WZ. The symmetry of the crystal not only has implication on the symmetry of the phonon modes but also on the electronic band structures, as deeply explained in [1, 15, 24] and in Sect. 4 of this chapter.

In this section, we have learnt that in Raman spectra of NWs the crystal structure is reflected by the number, symmetry, and frequency of the observed phonon modes. In particular, we stress that the presence of the $E_2{}^H$ mode in III–V crystals (or of the E_{2g} mode in group-IV crystals) has been recognized as one of the first experimental proofs of the existence of the WZ (or lonsdaleite) phase in NWs [8, 25].

2 Polarized Raman Scattering: Fundamental Aspects and Selection Rules

When impinging on a sample, electromagnetic radiation can be transmitted, reflected, absorbed, or scattered. Raman spectroscopy relies on the inelastic scattering of the radiation by a physical system: monochromatic light is usually delivered to a sample, and the scattered light is analyzed. Scattered radiation features not only an elastically scattered component, at the same frequency of the incident field (Rayleigh band), but also light at frequencies lower (Stokes) or higher (anti-Stokes Raman band) than the incident radiation. Due to quantum mechanical reasons, Stokes peaks have intensity higher than the anti-Stokes peaks. This is why most of the Raman experiments on NWs deal with Stokes Raman. The inelastic peaks appear at frequencies that differ from the incident one by a quantity called Raman shift, namely the frequency of the phonon mode. This is independent from the excitation frequency and is characteristic of the material system. Therefore, it is a very significant information in a Raman experiment. Another important information is the intensity of each phonon mode, which is usually dependent on the scattering geometry. In particular, its dependence on the relative angle between light polarization and specific sample's crystallographic directions can be compared to theoretical calculations and unveil precious information of the symmetry of phonon modes, thus on the symmetry of the crystal (*e.g.,* crystal structure). In the following, after providing the fundamental concepts for the

theoretical treatment of inelastic light scattering (Sect. 2.1), we explain how to calculate the intensity of phonon modes and derive selection rules to be compared with the experimental intensity of phonon modes (Sect. 2.2).

2.1 Theoretical Description of Inelastic Light Scattering

Raman scattering is a manifestation of the interaction between the electromagnetic radiation and vibrational excitations within a material. Raman spectroscopy reveals the lattice dynamics of a solid and gives insight into the physical properties that are linked to the lattice vibrations, like crystal structure and symmetry, composition, lattice compression and expansion, and phonon density of states (second-order Raman scattering) through the measurements of the phonon frequencies ω_q.

The scattering process involves two energy quanta simultaneously, though it is usually schematized in two steps:

1. A photon with energy $\hbar\omega_i$ and wave vector $\overrightarrow{k}_i$ is absorbed, exciting the system from an initial state $|i\rangle$ to a state $|n\rangle$
2. The system emits a photon with energy $\hbar\omega_s$ and wave vector $\overrightarrow{k}_s$ and relaxes from the state $|n\rangle$ to a final state $|f\rangle$.

In the case where the final state is identical to the initial one, the incident and scattered light have the same frequency ($\hbar\omega_s = \hbar\omega_i$). This process is called elastic or Rayleigh scattering. When the final state is different from the initial one, the scattering process is inelastic. In this case, the creation or the annihilation of an excited state of the system occurs and the emitted photon has lost or gained energy. These processes are called respectively Stokes scattering and anti-Stokes Raman scattering. For the conservation of energy, the frequency of the scattered radiation is given by

$$\omega_s = \omega_i \pm \frac{E_i - E_f}{\nu} = \omega_i \pm \omega_q$$

with E_i and E_f the energies of the initial and final state of the system. The difference between the Raman scattering frequency ω_s and the excitation frequency ω_i is independent of ω_i and it is equal to ω_q. Conservation of momentum gives:

$$\vec{k}_s = \vec{k}_i \pm \vec{q}$$

The probability of the Stokes scattering and the anti-Stokes scattering is different because of the different population of the two initial energy levels at a temperature T. Indeed, for an anti-Stokes process to take place, the initial state needs to be an excited state of the system, while Stokes process can occur starting from the system ground state. Since the intensity of the Raman lines is proportional to the transition

probability, and the probability of transitions from the more populated ground state to the excited state (Stokes transitions) is higher than in the opposite direction (anti-Stokes transitions), the Stokes lines are more intense than the anti-Stokes lines.

The quantum mechanical description of the Raman effect presented in this section is necessary for a thorough description of the process. However, it is not needed for discussing Raman selection rules and, specifically, the dependence of the Raman intensity on the incident/scattered photon polarizations. Therefore, for sake of simplicity, in the following section, we will discuss Raman in classical terms, by deriving it from the macroscopic electric susceptibility.

2.2 Raman Cross Section and Raman Tensors: Selection Rules

Quasi-particle excitations like phonons, plasmons, magnons, excitons, etc., modify the electric susceptibility $\overleftrightarrow{\chi}$ of a solid, which is, in general, a second rank tensor defined as the response of the polarization P of a material to an external electric field E modulated at frequency ω_i.

When an external electric field E modulated at frequency ω_i excites a lattice vibration (phonon) with energy $\hbar\omega_q$, this induces a dependence on ω_q in the electric susceptibility $\overleftrightarrow{\chi}(\omega_i, \omega_q)$. The Raman scattering cross section depends on $\left|\overleftrightarrow{\chi}(s)\right|^2$. Namely, the polarization oscillates with the same frequency of the external field ω_i, and it emits radiation with intensity $I \propto \left|\ddot{P}(r,t)\right|^2 = \omega^4 \chi(k_i, \omega_i)^2 |E(r,t)|^2$. The atomic vibration will modulate the electric susceptibility, which can be written as $\chi(k_i, \omega_i, Q) = \chi_0(k_i, \omega_i) + \chi(Q)e^{i(q\cdot r - \omega_q t)}$, where $\chi_0(k_i, \omega_i)$ is the electric susceptibility unaffected by the phonons, Q are the vibration normal coordinates, and $\chi(Q)$ is the term modulated by the lattice vibrations.

The scattering efficiency S is given by the scattered power P_s over the power P_i incident on an area A per unit time:

$$S = \frac{\omega_s^4}{c^4} VL|\varepsilon_i \cdot \chi(Q) \cdot \varepsilon_s|^2,$$

where $V = AL$ is the scattering volume, L is the scattering length, $\varepsilon_{i(s)}$ is the polarization vector of the incident (scattered) light.

If we consider only one-phonon Raman scattering, keeping only the first term in the Taylor expansion of $\chi(k_i, \omega_i, Q)$, we obtain:

$$S = \frac{\omega_s^4}{c^4} VL|\varepsilon_i \cdot \left(\frac{\partial \chi}{\partial Q}\right)_0 Q(\omega_0) \cdot \varepsilon_s|^2. \quad (1)$$

Table 1 Raman selection rules for backscattering geometries in zinc blende-type crystals. The axis coordinates are $x = [111]$, $y = \left[1\ \bar{1}\ 0\right]$, $z = \left[11\ \bar{2}\right]$, $y' = [011]$, and $z' = \left[0\ \bar{1}\ 1\right]$. $|d_{TO}|$ and $|d_{LO}|$ denote the non-zero Raman tensor elements for the TO and LO phonons, respectively [21]

Scattering geometry	Selection rules	
	TO phonon mode	LO phonon mode
$\bar{x}\ (z, z)x$	$\frac{2}{3}\|d_{TO}\|^2$	$\frac{1}{3}\|d_{LO}\|^2$
$\bar{x}\ (z, y)x$	$\frac{2}{3}\|d_{TO}\|^2$	0
$\bar{y}\ '(z', z')y'$	$\|d_{TO}\|^2$	0

The intensity of the scattered radiation I_s can be calculated from the time-averaged power radiated by the induced polarization P_{ind} into a unit solid angle and is proportional to the scattering cross section:

$$I \propto \left|\varepsilon_i \cdot \left(\frac{\partial \chi}{\partial Q}\right)_0 Q(\omega_0) \cdot \varepsilon_s\right|^2.$$

The intensity vanishes or is maximized choosing appropriate directions of the polarization of the incident and scattered light, according to the symmetry of the second rank tensor $\frac{\partial \chi}{\partial Q} Q$,which is called Raman tensor R.Therefore, we can write:

$$I \propto |\varepsilon_i \cdot R \cdot \varepsilon_s|^2 \tag{2}$$

and polarization-dependent Raman spectroscopy allows the determination of both the frequency and the symmetry of a phonon at the Γ point, according to Raman selection rules. In polarization-dependent Raman measurements the scattering configuration, defined indicating the wavevector and polarization of the excitation and scattered radiation, is represented in the so-called Porto notation as $\overrightarrow{k}_i(\varepsilon_i, \varepsilon_s)\overrightarrow{k}_s$: the outer terms, from left to right, refer to the excitation and scattering direction of the light, respectively, and the inner bracket refers to the excitation and detection polarizations.

The Raman selection rules for backscattering geometries in zinc-blende- and wurtzite-type crystals, for the most common scattering geometries, are summarized in Tables 1 and 2, respectively.

2.3 Experimental Setup and Scattering Geometry

A typical Raman setup is sketched in Fig. 3. The excitation energy is provided by a monochromatic laser source. As shown in Eq. (1), the Raman scattering efficiency increases with increasing photon energy, *i.e.,* with decreasing wavelength. Therefore,

Table 2 Raman selection rules for backscattering geometries in wurtzite-type crystals. The axis coordinates are $x = \left[0\ \bar{1}\ 1\right]$, $y = [211]$, and $z = \left[\bar{1}\ 11\right]$ [25]

Scattering geometry	Selection rules			
	E_2^L TO mode	E_2^H TO mode	(A_1/E_1) TO mode	(A_1/E_1) LO mode
$\bar{x}\ (z, z)x$	No	No	Yes	No
$\bar{x}\ (y, y)x$	Yes	Yes	Yes	No
$\bar{x}\ (z, y)x$	No	No	Yes	No

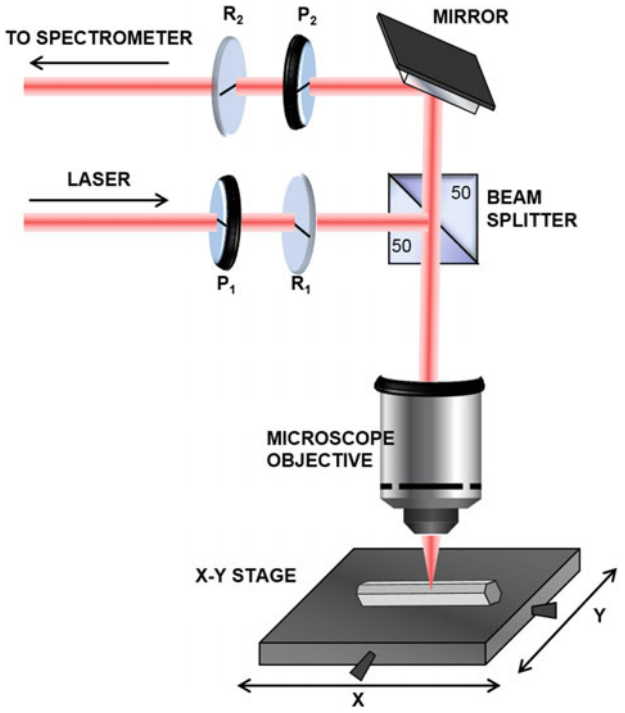

Fig. 3 Sketch of a typical micro-Raman setup for polarization-resolved measurements in backscattering. Laser sources and spectrometers are not depicted. The sketch is focused on the experimental tools to control the polarization of laser beam and scattered signal. Polarizers are indicated by P_i and retarders by R_i

excitation wavelengths in the 400–700 nm range are widely used. Before reaching the sample, the laser light can be filtered by a narrow bandpass filter and/or a small monochromator (not shown) to eliminate possible sidebands. To control the polarization of the laser beam and perform polarized Raman experiments, the beam passes through a polarizer (P_1 in the figure) to clean the already polarized laser emission

from possible, small depolarizing effects (due to the laser itself or to optical elements in the beam path), and through a lambda half-plate (R_1 in the figure) whose optical axis can be rotated. By rotating it by $\theta/2$ with respect to the optical axis of P_1, the polarization of the laser beam coming out from R_1 will form an angle θ with the optical axis of P_1. The beam is then guided towards the sample with a polarization conserving beam splitter (50:50). To study nanostructures, it is convenient to focus the laser light via a microscope objective (micro-Raman setups). As the diffraction-limited spot size is approximately given by the excitation wavelength divided by the numerical aperture (NA) of the objective [26], a short wavelength and a high NA (>0.8) objective are ideal to measure nanostructures with sub-micrometric resolution. As sketched in Fig. 3, the nanostructure is typically positioned on an X–Y piezoelectric stage, in such a way that it can be automatically scanned with high precision.

In a backscattering geometry, the scattered Raman signal is collected by the same objective, passes through the same beam splitter of the excitation, and is guided by a set of mirrors to a spectrometer. Before entering into the spectrometer, the polarization of the scattered light has to be analyzed. Therefore, a polarizer (P_2) is used to select the scattered radiation with components of the polarization typically either parallel or perpendicular to the polarization of the excitation beam. Since the efficiency of a spectrometer depends on the polarization of the entering light, a lambda half-plate (R_2) before the spectrometer is used to flip the polarization of the light into the most efficient direction.

Raman spectrometers are equipped with high-resolution diffraction gratings (>1200 lines/mm). The signal dispersed by the grating is then sent to a detector (usually a Si multichannel charge-coupled device (CCD) detector if the excitation wavelength is in the 400–700 nm range). When using single-stage spectrometers, a notch (or edge) filter (different for different excitation wavelengths) before the spectrometer is necessary to reject the intense elastic component, while in triple stages spectrometers the first two gratings work as a tunable bandpass filter and enable the rejection of the elastic contribution (in the so-called "subtractive mode"), and the third grating disperses the light and determines the spectral resolution. In a triple spectrometer in "additive mode," instead, the three gratings disperse the light, so the signal is lower but the resolution is higher [27]. Nowadays, with both single and triple spectrometers, it is possible to detect signal frequencies very close to the elastic component and measure Raman shifts below ~20 cm^{-1}. While in triple spectrometers this is enabled by the action of three gratings, in single spectrometers it is possible only by adding to the conventional notch filters special Bragg filters placed before the entrance slit [28]. To provide an idea of the spectral resolution of a single-stage spectrometer or of a triple spectrometer used in subtractive mode, an 1800 lines/mm grating mounted on a spectrometer with 0.65 m focal length gives a resolution of ~ 0.4 cm^{-1} at 630 nm and of ~ 0.8 cm^{-1} at 480 nm.

Regardless of the resolution of the spectrometer, several factors (e.g., the temperature stability of the laboratory) can contribute to a small miscalibration of the spectrometer. Therefore, after the measurements, an accurate frequency calibration of the

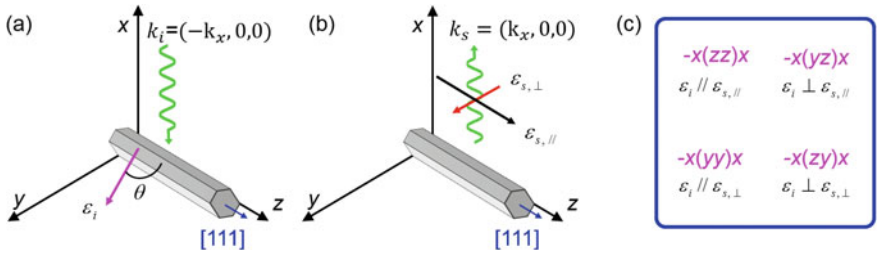

Fig. 4 Sketch of typical polarization-resolved Raman experiments on a single NW. **a** k_i is parallel to the x-axis and during polar plots its polarization vector ε_i varies, forming an angle θ with z. **b** The scattered light wavevector (k_s) is along x and the components of its polarization vector either parallel or perpendicular to z can be selected. **c** Four common scattering geometries for NWs, indicated in the Porto notation: $k_i(\varepsilon_i,\varepsilon_s)k_s$

Raman spectra is usually performed exploiting the well-known frequencies of the emission lines of a Neon (or Xenon, etc.) lamp [29].

Figure 4 depicts a typical back-scattering geometry for performing polarization-resolved Raman measurements on a single NW. For clarity, excitation and detection paths are represented in two different panels ((a) and (b), respectively). As an example, we are considering a ZB NW grown along the [111] direction (which is parallel to the z-axis of our reference system) and with a hexagonal cross section and facets of the {110} family. It is reasonable to assume that, after transferring the NW on a substrate, the flat facet of the family {110} is perpendicular to the incident light wavevector ($\vec{k}_i$), which is parallel to the x-axis. The scattered light wavevector ($\vec{k}_s$) is opposite to it. All light polarization vectors of the incident and scattered light are in the yz plane. Some examples of the four most common scattering configurations for polarized Raman indicated in Porto notation are given in panel (c). However, to completely characterize the symmetry of a phonon mode, it is more appropriate to perform a more complete polarized Raman study, a so-called "polar plot," as those discussed in sessions 7.3.1, 7.3.2, and 7.3.3. During the measurements, the polarization of the excitation (ε_i) is rotated by an angle θ with respect to the nanowire growth axis (see panel (a)). The scattered radiation is analyzed by selecting the component of the polarization either parallel to the NW growth direction ($\varepsilon_{s,//}$) or perpendicular to it ($\varepsilon_{s,\perp}$), as depicted in panel (b). The roles of excitation and detection can be exchanged, as intuitive from equation $I \propto |\varepsilon_i \cdot R \cdot \varepsilon_s|^2$ by considering that the Raman tensors are symmetric for phonon frequencies negligible to the frequency of the exciting light [30].

2.4 Relaxation of Selection Rules

In Sect. 2.2, we have summarized the main selection rules determining the observation of phonon modes in first-order Raman scattering experiments. However, real-life

polarized Raman experiments can provide results that are quite different from the calculated ones, as there are some effects responsible for relaxation of selection rules. In Sect. 2.4.1, we discuss the effect of the NA of microscope objectives, which is typical of any Raman experiment performed with high NA objective, even on bulk samples, while in Sect. 2.4.2, we discuss size effects which scramble selection rules only in nanostructures, such as NWs.

2.4.1 Effect of Microscope objective's Numerical Aperture

Using a high NA objective is very convenient to enhance the Raman signal and to obtain a very good spatial resolution. However, high NA objectives can allow forbidden Raman modes to appear. In order to discuss the influence of the microscope objective on optical selection rules, we have investigated a bulk sample, where the absence of tilted facets and size effects typical of NWs allows for a clean and reliable evaluation of this purely optical effect. Figure 5a displays the Raman spectra collected on the cleaved (011) GaP surface lying on the *yz* plane with a 100 × objective (NA = 0.95), a 50 × objective (NA = 0.6), and a 20 × objective (NA = 0.4) with the same power in a same $\bar{x}$ $(z, z)x$ scattering geometry (power density is different due to different spot sizes, and thus the signals are normalized to the TO mode). In the spectrum acquired with the 20 × objective the intensity of the LO mode is almost zero, which renders the spectrum very similar to the calculated one displayed in panel (b), where the LO mode is absent because LO phonon contribution from (011)-type surfaces is always forbidden in backscattering configuration (i.e., exciting and scattered photon with *k* vector // [011]), as summarized in the third line in Table 1. Details about methods to calculate Raman spectra are given in Sect. 3.1.1. The LO mode would be instead theoretically fully allowed for photon wavevectors in the *yz* plane and polarization vectors out of the plane. In the experiment, the forbidden LO mode becomes relatively more and more visible as the NA of the objective increases. This happens because a higher NA implies a higher density of photons with wavevector more tilted with respect to the normal direction to the plane. In the top parts of Fig. 5a, we report a sketch of this effect: the red light cones represent the ensemble of all wavevectors impinging on (and collected after the scattering by) the sample. The angle between the *x*-axis (dashed line) defined in Fig. 4 and the most tilted wavevector in the cone is given. In the 100 × case, the angle is very big and thus the Raman spectrum displays a quite intense LO mode.

2.4.2 Size Effects in Nanowires

Unlike most bulk materials, NWs exhibit strong sensitivities in their optical absorption, emission, and scattering efficiency to light polarization. This can be due to electronic properties related to the symmetry of the band structure (*e.g.*, in WZ NWs, light absorption and emission close to the bandgap energy are strongly polarized

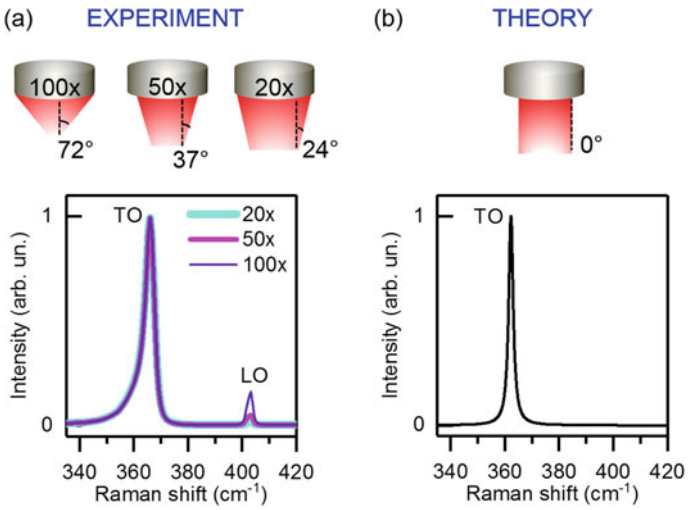

Fig. 5 **a** Normalized experimental Raman spectra (bottom) collected on GaP bulk in $\bar{x}\ (z, z)x$ scattering geometry with three different objectives (20x, 50x, 100x) and sketch (top) of the effect of their NA on the tilting of the photon wavevectors: the angle α between the vertical x direction (dashed line) and the most tilted wavevector in the light cone is given in degrees (calculated by NA $= n \sin \alpha$, where $n = 1$ is the air refractive index). Notice that the spot size increases for decreasing NA. **b** Calculated Raman spectrum in $\bar{x}\ (z, z)x$ configuration (bottom) in the ideal case (sketched on top) of objective with NA $= 0$ and thus all wavevectors directed along x

perpendicular to the NW axis [1, 15, 24, 31]), or to optical properties related to the geometry of the NWs (size effects) [32, 33], or to a combination of both [34]. In a Raman scattering experiment performed with excitation energy far from electronic resonances, band structure-related selection rules do not have a considerable impact on Raman intensity. Therefore, here we discuss the impact of size effects, and in the Sect. 4 on resonant Raman, we discuss the coupling of Raman selection rules with electronic transitions.

NWs are filamentary crystals with length much larger than the NW diameter and diameter smaller or comparable to the laser excitation wavelength. Moreover, there is a sizable dielectric mismatch between NWs and their local surrounding environment, stemming from the fact that the refractive index of NWs is about one order of magnitude bigger than the one of air/vacuum. In these conditions, electromagnetic resonances strongly modulate the absorption/emission/scattering of polarized light in the NW. In other words, the magnitude of the electric field of an electromagnetic wave inside an NW depends on the orientation of the light polarization vector with respect to the NW axis due to the effects of electrostatic mismatch (image forces) [33].

Let us consider an external electric field (E_0) surrounding the NW. When the field impinges at normal incidence on an NW with a given diameter, the parallel and perpendicular components of the electric field inside the NW ($E_{\parallel, \mathrm{NW}}$, $E_{\perp, \mathrm{NW}}$) as a

function of E_0 are [35]

$$E_{NW,\parallel} = E_{0,\parallel}$$

$$E_{NW,\perp} = \frac{2\varepsilon_0}{\varepsilon_{NW,\perp}(\omega) + \varepsilon_0} E_{0,\perp} \tag{3}$$

where ε_{NW} is the dielectric constant of the NW at the frequency of the electromagnetic field wave. Clearly, the component of the field parallel to the NW axis stays the same, while the one perpendicularly polarized with respect to the NW axis is strongly depleted. For the same reason, external non-polarized light ($E_{0,\parallel} = E_{0,\perp}$) becomes strongly polarized inside an NW due to its high refractive index ($E_{NW,\parallel} \neq E_{NW,\perp}$). This happens because at normal incidence on a dielectric medium the boundary conditions for the electromagnetic field have to be satisfied: optical modes of the field that are purely transverse magnetic (TM: electric field polarization parallel to the wire) are transmitted across the boundary unimpeded, while transverse electric (TE: electric field polarization perpendicular to the wire) modes are strongly reflected.

Any electromagnetic field interacting with NWs is affected by this effect. In a Raman scattering experiment, both the exciting field and scattered field are thus affected by the dielectric mismatch. As a consequence, the dielectric mismatch depletes the intensity associated to the phonon modes in all scattering geometries where there is at least one polarization vector (of the exciting photons and/or of the detected photons) perpendicular to the NW axis. Dielectric mismatch effects occur regardless of the crystal phase of the NWs, being them caused by the geometry of the NW and not by the crystal phase. However, to clearly discuss this effect, it is convenient to consider cubic NWs, as the selection rules are very well known both theoretically and experimentally and deviations from them are easy to estimate. Moreover, it is convenient to consider NWs whose diameters are larger than those for which other size effects (quantum confinement of phonons and charge carriers) may become dominant. Figure 6a shows the Raman spectra calculated for a cubic Ge crystal with < 111 > axis directed along the z-axis of the reference system depicted in Fig. 4 by using Eq. (2) and tensor forms appropriate to the diamond crystal phase [30]. As expected from diamond-type crystals (see Fig. 2b), the main feature of the spectrum is a single peak ascribed to the F_{2g} optical mode. Figure 6b shows the experimental spectra collected on a cubic Ge NW (with NW < 111 > growth axis oriented along the z-axis and diameter of about 50 nm) in the same scattering configurations considered in the computed spectra [36]. The F_{2g} mode is centered at about 301 cm^{-1} and has a full width at half maximum (FWHM) of about 3 cm^{-1}. For comparing theory and experiment, we have normalized to the maximum intensity the F_{2g} mode in $\bar{x}\ (z, z)x$ the calculated and experimental spectra, so that possible effects of the NA of the objective (and of other experimental effects) are negligible. The lower intensity of the F_{2g} mode in the $\bar{x}\ (y, y)x$ experimental spectrum compared to the theoretical one where Raman selection rules have been taken into account can

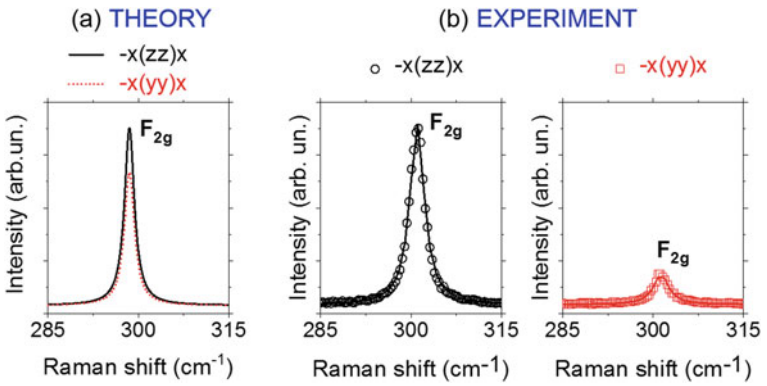

Fig. 6 Raman spectra of cubic Ge. **a** Theoretical Raman spectra computed on bulk Ge in the $\bar{x}$ $(z, z)x$ (black solid line) and $\bar{x}$ $(y, y)x$ (red dashed line) scattering geometry. Lorentzian lineshapes with FWHM = 2 cm^{-1} are adopted for the peak ascribed to the F_{2g} mode for a realistic comparison with experiments. **b** Experimental spectra of a cubic Ge NW collected in the $\bar{x}$ $(z, z)x$ (open circles) and $\bar{x}$ $(y, y)x$ (open squares) scattering geometry, with superimposed Lorentzian fits (solid lines). Polarized Raman experiments were performed exciting the system with the 633 nm line of a HeNe laser. Experimental spectra are plotted with the same intensity scale

be attributed only to the dielectric mismatch, which is quite strong in the $\bar{x}$ $(y, y)x$ geometry according to Eq. (3).

Dielectric mismatch effects have to be carefully considered when using polarized Raman experiments to address the crystal phases of NWs. As anticipated, for the differentiation between ZB and WZ GaAs, the detection of the $E_2{}^H$ phonon mode can be used as a fingerprint for the WZ phase. However, the $E_2{}^H$ mode can only be observed for incoming laser light polarized perpendicular to the NW axis (see Table 2). At the same time, exactly this kind of linearly polarized light suffers from a vanishing optical transmission in the direction perpendicular to the NW axis when the radius-to-wavelength ratio decreases below a certain value. As a result, the $E_2{}^H$ mode can become undetectable. In order to understand if the lack of $E_2{}^H$ mode has to be ascribed to the absence of WZ phase or to the dielectric mismatch effect, it is very important to perform wavelength-dependent polarized Raman experiments on the same NW (or to vary NW diameter for a fixed excitation wavelength). Indeed, if the dielectric mismatch is responsible, by varying the excitation wavelength and/or the NW diameter (in a controlled fashion), it will be possible to detect the $E_2{}^H$ mode, while in a ZB NW, its observation is fundamentally impossible. For example, in WZ GaAs NWs with radii in the range of 25 nm, because of the dielectric contrast in the coupling of polarized light into NWs, an almost complete quenching of the $E_2{}^H$ mode was observed for excitation wavelengths larger than 600 nm [37].

If the contribution of the dielectric mismatch in a Raman experiment is particularly relevant, it may be convenient to estimate it quantitatively by computational simulations [38, 39]. Emission from a given phonon mode, see can be constructed

from the incoherent superposition of radiating dipoles distributed inside the NW. The orientation of each dipole is given by the transformation of the local internal electric field by the Raman tensors (as a consequence, the NW crystal structure can have an impact on the dielectric mismatch effect). The starting point of any effort to model Raman scattering is therefore the solution for the electric field in the NW at the exciting frequency. This can be obtained by analytical solutions for a plane wave incident on a freely suspended infinitely long cylinder or by numerical calculations if the effects of a substrate and focused beam have to be considered [38]. Convergence of a full numerical calculation and integration of the incoherent radiation fields from induced dipoles may take long time. Therefore, approximate models of Raman scattering that match experiments for useful ranges of experimental conditions have been developed [38]. In all cases, even when the tensorial nature of Raman scattering is not fully considered, it is typical to obtain an oscillating behavior of the Raman intensity as a function of diameter due to electromagnetic resonances arising when the size of the nanostructure is commensurate with the optical path. The same happens to the intensity of the absorbed and emitted light as a function of the diameter [33, 40]. The presence of metallic substrates may shift the resonances to larger diameters or modify their magnitudes, but the oscillating behavior stays [38]. At resonance condition, the electromagnetic field can be enhanced. In conclusion, we can say that the dielectric mismatch effect not only inhibits transmission of light for transverse polarizations, suppressing Raman signals, but can even enhance them if certain combinations of diameter/wavelength/dielectric constant are satisfied. Since the dielectric mismatch effect strongly depends on conditions that are often not known, particular care has to be taken in analyzing Raman spectra acquired with polarization transverse to the NW axis.

3 Polarized Raman Scattering: Phononic and Crystalline Properties of Nanowires

3.1 Cubic Monoatomic Crystals

As discussed in the previous Sect. 2, group IV semiconductors are naturally found in the cubic crystal phase, arranged in an FCC structure with a two-atom basis. The basis is typically described as a couple of atoms positioned at (0,0,0) and at (a/4, a/4, a/4), with a lattice parameter (see Fig. 1a). This type of systems supports only three optical phonon modes, which are found to be degenerate at the Γ point of the Brillouin zone (see Fig. 2b). This implies that the Raman spectrum of cubic germanium or silicon mainly consists of a single, intense band, ascribed to the F_{2g} symmetry, degenerate TO–LO phonon modes (see Fig. 6). In cubic Ge, this band is found at 301 cm^{-1} [41]. This band is often accompanied by broader, less intense features associated with overtone, two-phonon or electronic scattering processes [30].

Given the degeneracy of the phonon modes, the intensity of the F_{2g} Raman band comes from photons inelastically scattered by both the TO and LO modes, preventing the discrimination of the transverse and longitudinal phonon contributions. Nevertheless, the effect of Raman selection rules is quite evident despite the degeneracy. To each of the three individual phonon modes, indeed, a Raman tensor with a different form is associated. The Raman scattering by each phonon mode will independently be subject to different selection rules, in some cases resulting in a depletion of the inelastically scattered intensity.

3.1.1 Calculations of Selection Rules in Bulk and in Nanowires: A Tutorial

In the previous Sect. 2.1, we have derived the expression of the Raman intensity by a given phonon mode, see Eq. (2). In this section, we illustrate how the predicted Raman intensity is calculated for a crystal with arbitrary orientation. A standard calculation estimating which modes are allowed/forbidden depending on the scattering geometry can be performed for a given crystal system based on the general tensor forms provided by Loudon [30]. With these tensors, one can calculate the polarization-dependent response of a phonon mode featuring a specific symmetry in the $k \rightarrow 0$ limit, i.e., at the Γ point of the ZB. This is indeed the limit explored by Raman spectroscopy, as the maximum exchanged momentum in a typical light scattering experiment is of the order of $2k_{inc} \sim 10^5\ \mathrm{cm}^{-1}$, while the edge of the first BZ in typical crystal systems is of the order of $k_{(max)} \sim 3 \cdot 10^8\ \mathrm{cm}^{-1}$.

For a quantitative, sample dependent prediction, one can rely on calculated Raman tensors calculated, e.g., within DFPT. In this framework, Raman tensors can be derived from the third derivative of the total energy, twice with respect to the application of an electric field and once with respect to the phonon displacement coordinates [42]. Calculated tensors can account for the small (but finite) value of the transferred momentum by modifying the $k \rightarrow 0$ extrapolation with the so-called non-analytical corrections (NAC) along a given direction in the reciprocal space. For a correct calculation, it is important to select the proper NAC, depending on the scattering geometry. In experiments performed in backscattering geometry, the transferred momentum is parallel to the wave vector of the exciting photon, therefore the NAC to be selected is the one corresponding to that physical direction, given the orientation of the sample. In isotropic crystal systems as the cubic lattice, the values of the NAC are the same for all directions, but in anisotropic system, the selection has a critical impact on the predicted Raman response. We also stress that, in order to fairly compare the computed and experimental Raman intensities, a scaling of the theoretical data to the real experimental conditions (finite scattering volume, limited detection efficiency, etc.) has to be implemented.

Whether generic or calculated tensor expressions are used for the calculation of Raman intensity, the tensors are expressed in a crystal-related reference system, that is typically composed by the system principal axes as described by Nye [43] or by the reference frames employed for the calculations, respectively. When describing the

experimental scattering configuration, on the other hand, we refer to axes selected based on the macroscopic orientation of the system under investigation with respect to the laboratory setup (see Fig. 4). In lucky cases, these two reference frames coincide, but most commonly a transformation of the Raman tensor is needed in order to express it in a reference frame that is experimentally convenient.

Let us first analyze the case of a bulk, cubic germanium crystal, and calculate its Raman selection rules. As discussed in previous sections, cubic Ge features a point group symmetry O_h and its principal axes reference frame is the usual: $x = [100]$, $y = [010]$, $z = [001]$ (Fig. 7). When probing a Ge wafer with $\langle 100 \rangle$ orientation, one falls in the case in which the reference frame of the system and the one of the laboratory coincide, as depicted in Fig. 8.

Once the reference frame for the calculation is specified, for calculating the predicted Raman intensity the following procedure needs to be implemented:

(1) Determine the direction of the k vector of the incident and outcoming photon: in the case depicted in Fig. 8, given the orientation of the sample and the backscattering geometry, k_i and k_s are antiparallel to each other and both oriented along the $x = [100]$ axis. This is also the facet/plane type under direct illumination.
(2) Define the direction of the light polarization: since the photon k vectors are directed along x, the polarization vectors lie in the yz plane. It is possible to consider a generic tilting angle φ of the polarization with respect to the z-axis. Hence, the general expression for the polarization vector becomes:

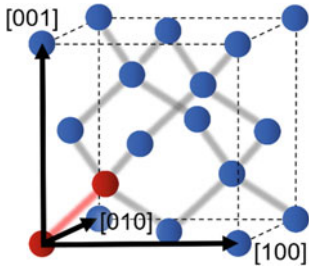

Fig. 7 Atomic arrangement in a Bravais cell of a cubic group IV semiconductor. The two-atom basis is highlighted in red. The black arrows indicate the most common reference frame adopted to describe the lattice

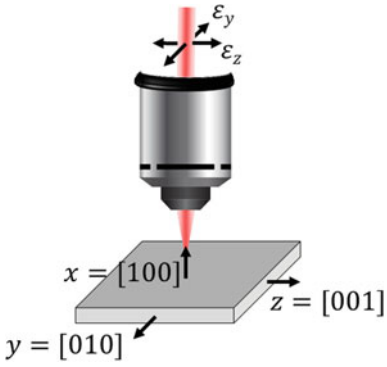

Fig. 8 Sketch of a Raman scattering experiment performed in backscattering configuration on a cubic crystal sample. In this case, the most intuitive frame for expressing the light polarization (laboratory reference frame) coincides with the principal axis frame of the crystal

$$\varepsilon_i = (0\ \sin\varphi\ \cos\varphi) \tag{4}$$

(3) Identify the Raman tensor of the mode under examination. In our case, the generic tensor forms for the three components of the F_{2g} mode, polarized along the three axes, are the following:

$$R_{F2g}(x) = \begin{pmatrix} 0 & 0 & 0 \\ 0 & 0 & d \\ 0 & d & 0 \end{pmatrix}$$

$$R_{F2g}(y) = \begin{pmatrix} 0 & 0 & d \\ 0 & 0 & 0 \\ d & 0 & 0 \end{pmatrix}$$

$$R_{F2g}(z) = \begin{pmatrix} 0 & d & 0 \\ d & 0 & 0 \\ 0 & 0 & 0 \end{pmatrix}$$

It is worth noting that the definition of longitudinal and transverse phonon modes depends on the direction of the phonon wavevector, that can be calculated according to the arguments discussed above. In the present case (backscattering along x), the phonon wavevector is directed along x; therefore, the LO phonon mode is represented by the $R_{F2g}(x)$ tensor, while $R_{F2g}(y)$ and $R_{F2g}(z)$ are associated with the TO phonons.

(4) According to Eq. (2), the Raman scattered intensity can be calculated from

$$I_{F2g}(LO) \propto |\varepsilon_i \cdot R_{F2g}(x) \cdot \varepsilon_s|^2$$

$$I_{F2g}(TO) \propto |\varepsilon_i \cdot R_{F2g}(y) \cdot \varepsilon_s|^2 + |\varepsilon_i \cdot R_{F2g}(z) \cdot \varepsilon_s|^2$$

as thoroughly discussed in the pioneering work by Loudon [30].

It is important to remember that individual degrees of freedom contribute to the scattered intensity independently. Therefore, the square product of the matrix elements has to be calculated separately for distinct tensors, and finally summed up to account for the independent contributions of the degenerate modes. In this case, for example, the total intensity of the $I_{F_{2g}}$ optical phonon is obtained by the sum of the LO and TO contributions: $I_{F_{2g}} = I_{F_{2g}}(LO) + I_{F_{2g}}(TO)$.

The contribution of the TO modes to the Raman scattered intensity from facets of the type ⟨100⟩ is zero. These modes are indeed forbidden in the given geometry for any scattered polarization in the yz plane, as easily derived by the calculation:

$$I_{F_{2g}}(TO) \propto \left| (0\ \sin\varphi\ \cos\varphi) \cdot \begin{pmatrix} 0 & 0 & d \\ 0 & 0 & 0 \\ d & 0 & 0 \end{pmatrix} \cdot \varepsilon_s \right|^2 + \left| (0\ \sin\varphi\ \cos\varphi) \cdot \begin{pmatrix} 0 & d & 0 \\ d & 0 & 0 \\ 0 & 0 & 0 \end{pmatrix} \cdot \varepsilon_s \right|^2$$
$$= |(d\cos\varphi\ \ 0\ \ 0) \cdot \varepsilon_s|^2 + |(d\sin\varphi\ \ 0\ \ 0) \cdot \varepsilon_s|^2 = 0$$

because in ε_s only the second and third terms can be nonzero. Selection rules of the same kind also forbid Raman scattering by the LO phonon from facets of type ⟨1 1 0⟩, as anticipated in Sect. 2.2).

The calculation of the Raman selection rules from crystals with a different orientation, i.e., for which the principal axes reference does not coincide with the laboratory reference, requires a preliminary step. This is a coordinate transformation, allowing the expression of the Raman tensor in the same reference system used for describing the scattering geometry. Calculating the intensity of the Raman scattering from a nanowire requires the same preliminary step as, for what concerns the Raman selection rules, nanowires behave like bulk fragments with appropriate orientation [25, 36].

It is known that ZB/diamond NWs can be grown along the ⟨1 1 1⟩ direction, usually displaying a hexagonal cross section with facets of type ⟨1 1 0⟩ [44]. A good choice of the reference system for expressing the direction of the light polarization is the one depicted in Fig. 9. For what discussed above, the calculation illustrated in the following for a NW can be applied as well to the calculation of the Raman scattering from a bulk crystal exposing facets of type ⟨1 1 0⟩ to the microscope. Let us now proceed and express the Raman tensors in the reference frame $x' = [\bar{1}\ 10]$, $y' = [112]$, $z' = [11\ \bar{1}]$. The choice of the basis vectors can be driven by TEM studies or can be arbitrarily based on the consideration that the NW axis is of the type ⟨1 1 1⟩, while the facets are of the type ⟨1 1 0⟩. It is important to remember that x', y', z' need to be an orthonormal triad.

As discussed above, the Raman tensors are typically expressed in the preferential reference

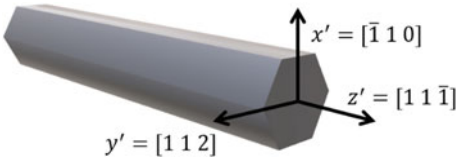

Fig. 9 Sketch of a cubic NW with the common hexagonal cross section, in which the orientation of the reference system used for the calculation is highlighted. The three crystallographic axes of a NW are typically derived by transmission electron microscopy (TEM) investigation

$$x = [1\ 0\ 0],\ y = [0\ 1\ 0],\ z = [0\ 0\ 1]$$

To transform them into the new NW basis, we need to construct the transformation matrix that leads from the *old* reference x, y, z to the *new* reference x', y', z'. The normalized expression of the new basis vectors x', y', z', with respect to the old cubic reference x, y, z is the following:

$$x'_{old} = \frac{1}{\sqrt{2}}\left[\bar{1}\ \ 1\ 0\right];\ y'_{old} = \frac{1}{\sqrt{6}}[1\ 1\ 2];\ z'_{old} = \frac{1}{\sqrt{3}}[1\ 1\ \ \bar{1}]$$

where we have indicated in the pedix the reference system in which the vectors are expressed. The transformation matrix M is defined as such if we apply it to a vector of the new basis (expressed itself in the *new* basis as $x'_{new} = [1\ 0\ 0]$), we obtain its expression in the old reference system:

$$Mx'_{i,new} = x'_{i,old}$$

where $x'_{i,old}$ is the i-th vector of the new basis, expressed in the old reference frame (e.g., $x'_{1,old} = x'_{old} = \frac{1}{\sqrt{2}}[\bar{1}\ \ 1\ 0]$), while $x'_{i,new}$ is the same physical vector, but expressed in the new basis (e.g.,$x'_{1,new} = x'_{new} = [1\ 0\ 0]$). This means that the application of M yields:

$$M[1\ 0\ 0] = \frac{1}{\sqrt{2}}[\bar{1}\ \ 1\ 0]$$

It follows that the transformation matrix has the form

$$M = \begin{pmatrix} -\frac{1}{\sqrt{2}} & \frac{1}{\sqrt{6}} & \frac{1}{\sqrt{3}} \\ \frac{1}{\sqrt{2}} & \frac{1}{\sqrt{6}} & \frac{1}{\sqrt{3}} \\ 0 & \frac{2}{\sqrt{6}} & -\frac{1}{\sqrt{3}} \end{pmatrix}$$

easily obtainable setting as columns the new basis vectors, expressed in the old basis. By definition, as the columns of the matrix form an orthonormal triad, the matrix is orthogonal, and $M^{-1} = M^T$. Accordingly, the transformation of the Raman tensor for a mode polarized along the x_i-axis results:

$$R'_{F2g}(x_i) = M^T R_{F2g}(x_i) M$$

We can now reconstruct the expression of the tensor for a mode polarized along the new x'_i-axis, from the rotated $R'(x)$, $R'(y)$, $R'(z)$ as follows:

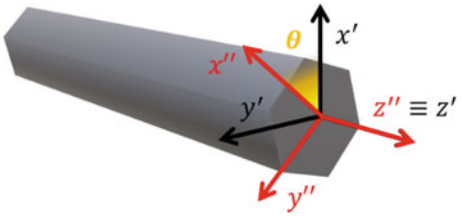

Fig. 10 Reciprocal orientation of the $x'y'z'$ and $x''y''z''$ reference systems, where the second is the rotation of the first about the z'-axis of a given angle θ

$$R'_{F2g}\left(x'_{i,new}\right) = x'_{i,old} \cdot \begin{pmatrix} R'_{F2g}(x) \\ R'_{F2g}(y) \\ R'_{F2g}(z) \end{pmatrix}$$

With this transformation, we can express the Raman tensors in the NW reference system, in which the polarization vectors can be intuitively expressed by referring to the NW geometry. We can further consider the possible rotation of the nanowire about its axis of an angle θ. The situation is sketched in Fig. 10.

To implement in the calculation the effect of the rotation, the transformation of the Raman tensor can to be composed of two steps, resulting, therefore in

$$R'_{F2g}(x_i) = S^T M^T R_{F2g} M S$$

where S is the rotation matrix

$$S = \begin{pmatrix} \cos\theta & -\sin\theta & 0 \\ \sin\theta & \cos\theta & 0 \\ 0 & 0 & 1 \end{pmatrix}$$

We stress that the procedure illustrated in this section is very general and can be applied to an arbitrary choice of orthonormal basis vectors, enabling the calculation of Raman selection rules for any crystal orientation, both in the bulk and in nanostructured samples.

3.1.2 Experimental Polarized Raman Spectra

When experimentally investigating a sample of doubtful crystal phase or orientation, measuring the Raman spectra in the main scattering configurations (Tables 1 and 2) might not be sufficient to derive structural information on the system, or even impossible if the crystal orientation is completely unknown. In these cases, a complete study requires the variation of either the incident or the scattered photon polarization, while the second polarization is kept fixed along selected axes of the system. The plot of the Raman intensity of a given phonon mode as a function of the angle of

rotation of the incident/scattered photon polarization is called polar plot. In the study of NWs, polar plots with polarization vector along and across the NW growth axis are typically performed, as sketched in Fig. 4. The results of the polar plots can be easily predicted theoretically by choosing for the varying polarization the generic form as a function of the rotation angle. The scattered intensity will have the form of a $\cos^2$ function, with an orientation to be determined.

We have already discussed how the dielectric mismatch can cause a strong mismatch of the Raman intensities detected on an NW. In Fig. 11, we report the theoretical prediction and the experimental results of a polar study on a cubic germanium NW. The spectra in the main scattering configurations are reported in Fig. 6. The theoretical polar plots were obtained by applying Eq. (2) to tensors transformed by both the usual cubic to NW reference system transformation and by considering the additional rotation of the NW about its axis of an angle $\theta = 33°$. The detected polarization was set along y'' and z'', defined as the axes obtained after the NW rotation. The experimental data were obtained by measuring the Raman spectra while varying the incident photon polarization over 360°. The fitted intensity of the Raman band (see Fig. 6) was then plotted as a function of the angle of rotation. In both cases, we have reported the results for the detected polarization along and across the NW axis. The theoretical and experimental plots are in remarkable agreement if we avoid considering the intensity drop observed experimentally for the y'' detection polar plot which, as discussed, can be ascribed to dielectric mismatch effect.

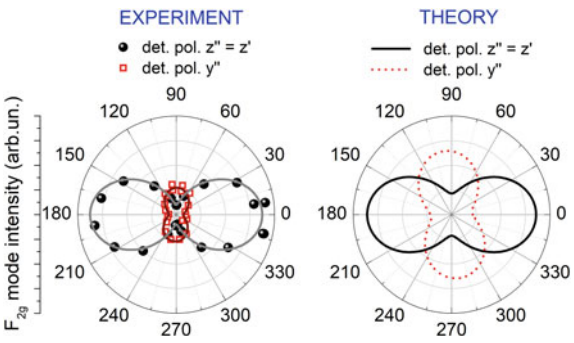

Fig. 11 Left panel: experimental polar plots on a cubic germanium NW obtained by setting the detected photon polarization along (black) or across (red) the NW axis. The dots and the squares are experimental data, while the lines are $\cos^2$ fitting of the data. Right panel: theoretical polar plots calculated by transforming the Raman tensors of the F_{2g} mode according to the description in Sect. 3.3.1, and by setting an angle of rotation of 33° about the z'-axis (the NW axis)

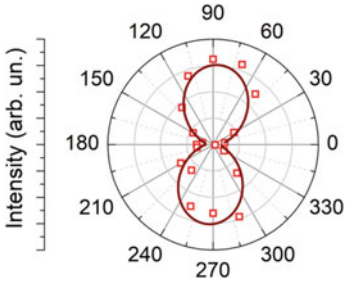

Fig. 12 Experimental polar plot of the E_{2g} mode measured on the hexagonal germanium shell within a core–shell NW. The dots are experimental data, the solid line is a $\cos^2$ fitting. The orientation of the plot along the *b*-axis (90° tilting with the *c*-axis, set as 0°, in the *bc* plane) is evident. *Courtesy of Diego De Matteis*

3.2 Hexagonal Monoatomic Crystals

As thoroughly discussed in Sect. 1.2, the phonon dispersion in hexagonal crystal structures can be intuitively inferred by backfolding the phonon dispersion of the corresponding cubic crystal. In group IV hexagonal crystals, the F_{2g} mode splits into A_{1g} and the doubly degenerate E_{1g} modes, while the E_{2g} mode (again, doubly degenerate) arises from backfolding of the TO mode at L.

3.2.1 Calculations of Selection Rules in Bulk and in Nanowires: A Tutorial

In the case of a hexagonal crystal, the principal axes system for the expression of the Raman tensors is composed of the c-axis and of two orthogonal vectors on the plane orthogonal to it. Since the c-axis is also the growth axis for hexagonal NWs, the calculation of the Raman intensity from a hexagonal NW typically does not require the rotation of the reference system from the principal axes system to the laboratory one.

Tensors are usually expressed in a basis of the type:

$$a = \left[2\,\bar{1}\,\bar{1}\,0\right]; b = \left[01\,\bar{1}\,0\right]; c = [0001]$$

where the vectors are identified using the four index Bravais–Miller notation. Moving from the structural similarities between diamond/ZB and hexagonal/WZ crystals, one can establish an important equivalence not only between axes *c* and z' as defined for the diamond structure (see Sect. 3.1.1) but also between *a* and x', *b* and y'. Indeed, the similarities in the stacking sequences mentioned in Sect. 1.1 can be appreciated along the *c*-axis (z') if the crystal is observed from the *a* (x') direction.

The calculation of Raman selection rules is now easily performed as in the cubic case.

The generic forms of the Raman tensors are the following:

$$R_{A1g} = \begin{pmatrix} a & 0 & 0 \\ 0 & a & 0 \\ 0 & 0 & b \end{pmatrix}$$

$$R_{E1g} = \begin{pmatrix} 0 & 0 & 0 \\ 0 & 0 & c \\ 0 & c & 0 \end{pmatrix} R_{E1g} = \begin{pmatrix} 0 & 0 & -c \\ 0 & 0 & 0 \\ -c & 0 & 0 \end{pmatrix}$$

$$R_{E2g} = \begin{pmatrix} 0 & d & 0 \\ d & 0 & 0 \\ 0 & 0 & 0 \end{pmatrix} R_{E1g} = \begin{pmatrix} d & 0 & 0 \\ 0 & -d & 0 \\ 0 & 0 & 0 \end{pmatrix}$$

and the Raman intensity can be calculated independently for each phonon mode by applying Eq. (2).

Due to its form, the A_{1g} mode will always yield the maximum intensity when the incident and scattered polarizations are aligned, as the tensor form partially hinders the information on the crystal orientation. Interestingly, on the other hand, having incident/scattered light purely polarized along the c-axis of the crystal prevents the visibility of the E_{2g} phonon mode, as is easily derived:

$$I_{E2g} \propto \left| (0 \;\; 0 \;\; 1) \cdot \begin{pmatrix} 0 & d & 0 \\ d & 0 & 0 \\ 0 & 0 & 0 \end{pmatrix} \cdot \varepsilon_s \right|^2 + \left| (0 \;\; 0 \;\; 1) \cdot \begin{pmatrix} d & 0 & 0 \\ 0 & -d & 0 \\ 0 & 0 & 0 \end{pmatrix} \cdot \varepsilon_s \right|^2$$
$$= |(0 \;\; 0 \;\; 0) \cdot \varepsilon_s|^2 + |(0 \;\; 0 \;\; 0) \cdot \varepsilon_s|^2 = 0$$

Thus, in order to be observed, the E_{2g} phonon mode requires a polarization with a nonzero component along an axis different to the c-axis of the crystal for both the incident and the scattered photons. This is the reason why the E_{2g} mode is in general more subject to intensity depletion due to the dielectric mismatch phenomenon described in Sect. 2.4.2. If one assumes a NW orientation as in Fig. 9, with photons wave vectors along the a-axis, it follows that the only detectable polar plot of the E_{2g} mode is obtained by setting the detected polarization across the NW axis, parallel to b. The intensity becomes then

$$I_{E2g} \propto \left| (0 \quad \sin\varphi \quad \cos\varphi) \cdot \begin{pmatrix} 0 & d & 0 \\ d & 0 & 0 \\ 0 & 0 & 0 \end{pmatrix} \cdot \begin{pmatrix} 0 \\ 1 \\ 0 \end{pmatrix} \right|^2 + \left| (0 \quad \sin\varphi \quad \cos\varphi) \cdot \begin{pmatrix} d & 0 & 0 \\ 0 & -d & 0 \\ 0 & 0 & 0 \end{pmatrix} \cdot \begin{pmatrix} 0 \\ 1 \\ 0 \end{pmatrix} \right|^2$$
$$= \left| (d\sin\varphi \ 0 \ 0) \cdot \begin{pmatrix} 0 \\ 1 \\ 0 \end{pmatrix} \right|^2 + \left| (0 \ -d\sin\varphi \ 0) \cdot \begin{pmatrix} 0 \\ 1 \\ 0 \end{pmatrix} \right|^2 = d^2\sin^2\varphi$$

which means that the maximum of the scattered intensity is expected for y'-polarized incident and scattered photons.

3.2.2 Experimental Polarized Raman Spectra

Hexagonal group IV NWs are hardly obtained by standard growth procedures, but recently they have been obtained within radial or axial heterostructures, during the growth (radial, namely core–shell heterostructures) [8, 45] or with post-growth transformations (axial heterostructures) [9]. In Sect. 3.3.1, we will present the results obtained on the polarized Raman study of a crystal phase axial homostructure obtained by martensitic transformation of diamond Ge NWs.

In Fig. 12, instead, we report the result of a polar plot of the E_{2g} mode measured on a hexagonal germanium shell in a GaAs-Ge core–shell NW. Due to the growth conditions, the orientation of hexagonal germanium (and of hexagonal GaAs) is the one usually found in WZ NWs, with the c-axis aligned along the NW axis. As argued before based on selection rules (Sect. 3.2.1), one finds experimentally that the intensity of the E_{2g} mode is nonzero only when the detected photon is polarized across the NW axis [45]. In this case, the maximum of the scattering intensity is retrieved when the incident and detected light polarization is directed along b.

3.3 Polytypic Homostructures in Nanowires

In nanowires, we can also push forward the realization of heterostructures, by playing with the crystal phase or even with the crystal orientation. All these constructs strongly affect the phonon spectrum, therefore Raman can be employed as a non-invasive characterization/diagnostic tool to verify the presence of the heterostructures and to localize it within a nanowire.

3.3.1 Crystal-Phase Homostructures

In the following, we discuss the Raman study on a crystal phase homostructure obtained by post-growth transformation of cubic germanium NWs. The strain-induced transformation produces hexagonal inclusions (~20 nm) alternating with the original cubic segments within a part of the NW length [9]. It is known from analogous experiments in the bulk [46] and from TEM studies [9] that the transformation causes a relative alignment of the domains such that the $[\bar{1}\ 10]$ direction of the cubic segment is parallel to the $[2\ \bar{1}\bar{1}\ 0]$ of the hexagonal, and that the plane (1 1 0) of the cubic is parallel to the (0 0 0 1) of the hexagonal domain. Keeping these relations in mind, the polarization-resolved Raman study of the crystal phase homostructure is aimed at (i) verifying the presence of a homostructure within an NW and localizing it; (ii) determining whether on such small segments Raman selection rules can still be validly applied; and (iii) verifying the orientation of the hexagonal inclusion (and, overall, the orientation of the system).

The presence of the hexagonal inclusions is witnessed by the number and relative intensity of the peaks composing the Raman spectrum on one end of the NW (Fig. 13a). The spectrum detected on the other end is the one presented in Fig. 6 exclusively featuring the peak characteristic of the cubic phase. Here, instead, a peak is observed on the low-frequency side of the main Ge phonon band (at 287 cm^{-1}, while the main peak is centered at 301 cm^{-1}) and is compatible with the peculiar E_{2g} selection rules (i.e., higher when the detection is orthogonal to the NW axis) [36]. As the argument was strongly in favor of the presence of some hexagonal inclusions, we performed full polarized Raman studies on this end of the NW. In the left panels of Fig. 13b, we report the polar plots obtained by monitoring independently the two peaks of panel (a). Of these, the low-frequency one can be ascribed to the E_{2g} mode of the hexagonal inclusions, while the high-frequency peak is expected to include the contribution of the A_{1g} and E_{1g} modes, as well as of the F_{2g} mode of the cubic. It is important to stress that, since we expect the relative orientation of the domains contributing to the Raman signal to be nontrivial, a calculation is necessary for the correct interpretation of the experimental data. The results of the calculations are reported in the right panels of Fig. 13b, and the procedure is discussed in the following.

As discussed in the previous sections, the generic form of the Raman tensors is often sufficient to calculate and predict the Raman selection rules. If the aim of the investigation is to infer quantitative information from the Raman spectra, e.g., in terms of relative intensity of the peaks, a system-dependent, calculated tensor form is necessary. In our case, the tensors calculated by DFPT were expressed in the usual reference system for hexagonal crystals:

$$a = \left[2\ \bar{1}\bar{1}\ 0\right]; b = \left[01\ \bar{1}\ 0\right]; c = [0001]$$

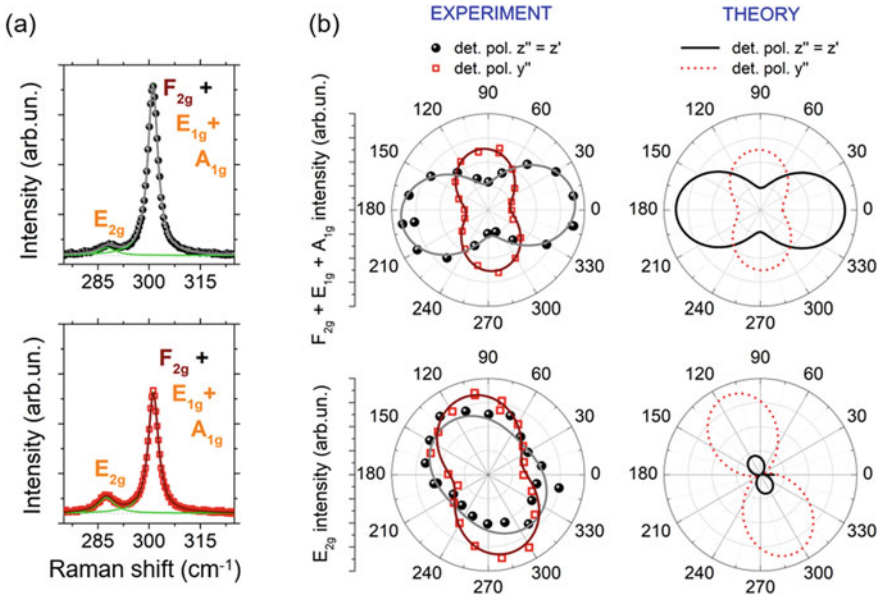

Fig. 13 **a** Raman spectra collected on the transformed end of a cubic Ge NW. Top and bottom panels are spectra acquired selecting z' (top panel) and y' polarized (bottom panel) scattered light in the detection. In both cases, witnessing the presence of the hexagonal inclusions, the peak ascribed to the E_{2g} mode is evident at a lower frequency (287 cm^{-1}) with respect to the usual Ge band at 301 cm^{-1}. The latter is ascribed to both the F_{2g} mode of the cubic segments, and to the almost degenerate A_{1g} and E_{1g} modes of the hexagonal segment. Dots are experimental points, solid lines are fitting, green lines are Lorentzian fit components. **b** Left panels, experimental polar plots acquired on the same end of the transformed NW, reporting the Raman intensity of the degenerate $F_{2g} + A_{1g} + E_{1g}$ peak (top panel) and of the E_{2g} mode (bottom panel). Dots are experimental data, solid lines are $\cos^2\theta$ fittings. Right panels, theoretical polar plots calculated taking into account the finite relative orientation of cubic and hexagonal domains in the homostructure

In order to reliably predict the Raman scattered intensity from the hexagonal inclusions, one needs to transform such tensors so that they are expressed in an NW-related reference, as the x', z', y' introduced for the cubic crystal in Sect. 3.1.1. This indeed will be used for the cubic segments of the crystal homostructure. In order to identify the transformation matrix, we need to express the vectors x', z', y' as a function of the hexagonal (old) basis. As discussed, we know that $a//x'$ and that $c//v'$ where $v' = \frac{1}{\sqrt{3}}(y' + 2z')$, which is the vector [110] in the old cubic reference x, y, z. The expression of the (old) hexagonal basis in the x', z', y' basis can be easily calculated by the relations above, and by remembering that the third basis vector can be derived from the vector product of a and c:

$$a_{new} = [100]\, c_{new} = \frac{1}{\sqrt{3}}[012]$$

$$b_{new} = -a_{new} \times c_{new} = \frac{1}{\sqrt{5}}[02\ \bar{1}]$$

In order to derive the transformation matrix, though, one needs to express the new basis vectors in the old basis. These expressions will be the columns of the transformation matrix N. Above is the expression of the old basis vectors a, b, c expressed in the new basis, that are the physical vectors forming the NW preferential reference, so $a^{'} = x^{'}, b^{'} = y^{'}, c^{'} = z^{'}$. This means that

$$a = a^{'}$$

$$b = \frac{1}{\sqrt{5}}\left(2b^{'} - c^{'}\right)$$

$$c = \frac{1}{\sqrt{5}}\left(b' + 2c'\right)$$

and by easily inverting the system

$$a^{'} = a$$

$$b^{'} = \frac{1}{\sqrt{5}}(2b + c)$$

$$c' = \frac{1}{\sqrt{5}}(-b + 2c)$$

The transformation matrix N that can be used to translate the hexagonal crystal tensors into the NW basis is, therefore:

$$N = \begin{pmatrix} 1 & 0 & 0 \\ 0 & \frac{2}{\sqrt{5}} & -\frac{1}{\sqrt{5}} \\ 0 & \frac{1}{\sqrt{5}} & \frac{2}{\sqrt{5}} \end{pmatrix}$$

and as discussed in the case of the cubic system, the transformation matrix can now be composed with an arbitrary rotation of the NW about its axis, by making wise use of the rotation matrix S:

$$R^{'} = S^T N^T R N S$$

At this point, the cubic and hexagonal tensors are expressed in the same basis. In order to calculate the predicted Raman intensity scattered by the homostructure, one has to consider the two contributions separately, calculate the Raman scattering

by each of them, and then sum them up with a weight reflecting how much of each crystal phase is expected to fall within the scattering volume.

To summarize, for addressing the crystal orientation of the homostructure with the characteristics described, these steps need to be followed:

(1) Start from the calculated Raman tensors of the two phases, expressed in the crystal principal axes;
(2) Transform the Raman tensors of the cubic phase with the aim of expressing them in the x', y', z' NW basis (Fig. 9);
(3) Transform, as well, the Raman tensors of the hexagonal phase, so that the basis respected the geometrical relations with the cubic basis, as suggested by TEM investigation;
(4) Implement a rotation of the tensors of the two structures about the z'-axis of the diamond phase of a variable angle θ (see Fig. 10) to get to the x'', y'', z'' reference system that best fits the experimental data.

The free parameters of the fitting are the percentual amount of hexagonal phase within the scattering volume α, which can be determined by TEM studies or by knowing and controlling the growth conditions, and the rotation angle about the NW axis z', θ. For the results in Fig. 13, we considered the 35% of hexagonal phase based on TEM study and spectroscopic considerations [36].

The fitting of the data yielded a rotation angle about the NW axis of 33°, nicely reproducing the polar plots both on the transformed part (Fig. 13b) and the untransformed part (Fig. 11). In order to bring further support to our interpretation, we also performed measurements by tilting the NW in such a way that the laser could impinge on the sample with an orientation orthogonal to the hexagonal *c*-axis, and so that the light polarized across the NW was orthogonal to the *c*-axis. This was realized by rotating the wire about its axis of −33°, and by rotating the sample about the microscope axis of −35°, that is the angle between z' and c. In Fig. 14, these new measurements are compared with the ones presented in Fig. 13a. As it is evident, the tilting enhances the low-frequency E_{2g} mode visibility for light polarized across the NW axis and brings it to zero for the orthogonal configuration.

3.3.2 Twinning Superlattices

Twinning superlattices (TSL) are a limiting case of crystal phase superstructures, where the crystal composition and crystal phase do not change along the NW axis, but the only crystal phase present (namely, the ZB) exhibits a periodic 60° rotation of the crystal lattice about the NW axis. This is a unique metamaterial that in III–V compounds has been obtained only with NWs [5]. Here, we focus on GaP TSL NWs. Figure 15a shows a TEM image of a TSL NW, in which the distance between two consecutive twin planes increases when going from the NW base to the NW tip. As displayed in Fig. 15b, NW tip and base (extended about 0.5 μm each) are characterized by a nearly constant spacing between twin planes (equal to ~4 nm at the NW base and to ~13 nm at the NW tip), while in the central part of the NW the spacing

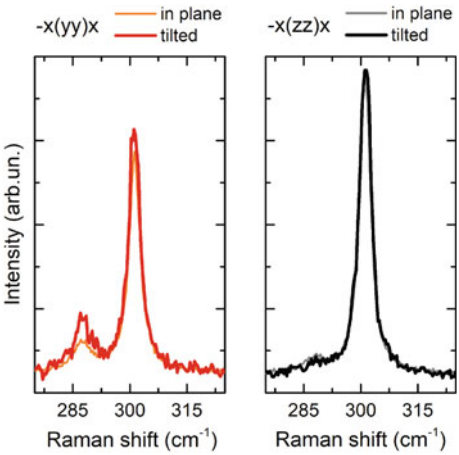

Fig. 14 Measurements acquired by tilting the NW so that the $\bar{x}\ (zz)x$ and $\bar{x}\ (yy)x$ configurations refer to a reference where the z is the [0001], c-axis of the wurtzite (red/black line) are compared to the measurements shown in Fig. 13 (orange/gray line). Specifically, the NW axis was tilted of -35° after rotating the substrate of −33° about the NW axis. The red/black spectra are multiplied by the same constant scale factor to account for the less efficient signal acquisition in the tilted configuration (mainly due to the lower reflection of the substrate, that is not horizontal below the microscope, and the different filling of the accessible scattering volume). Despite the cumbersome procedure, it is evident that the visibility of the E_{2g} mode results increased in the $\bar{x}\ (yy)x$ configuration and decreased in the $\bar{x}\ (zz)x$, as expected by selection rules

gradually increases from 4 to 13 nm. The constant twin spacing at the NW tips and bases characteristic of our NWs enabled us to investigate the phononic properties of TSL NWs for different TSL periods under otherwise identical conditions [47]. We stress that although the twin planes themselves can be considered as the shortest possible WZ inclusion [5], these NWs are made exclusively of segments of ZB GaP.

Following the procedure described for the Ge polytypic homostructure, we have combined DFPT calculations and Raman measurements to determine the phononic properties on the GaP TSL NWs. Experiments and calculations were performed in the $\bar{x}\ (yy)x$ scattering geometry depicted in Fig. 4. Figure 15c shows the calculated Raman spectrum of a GaP TSL with 4.5 nm twin spacing and Fig. 15d shows the calculated reference spectra of bulk ZB and WZ GaP. Panels (e) and (f) display the experimental spectra corresponding to the theory in panels (c) and (d), respectively. In the experimental spectra of TSL, WZ, and ZB crystals we observe the peak corresponding to the TO mode, similarly to the computed spectra, and the peak corresponding to the theoretically forbidden LO mode (the reasons for this latter observation are discussed in Sect. 2.4). Moreover, the spectrum of the TSL features a quite pronounced $E_2{}^H$ mode, similar to the WZ sample but much less intense. The presence of the $E_2{}^H$ mode in the TSL NW is a clear indication that the overall symmetry of a TSL is hexagonal. Indeed, we found that its corresponding

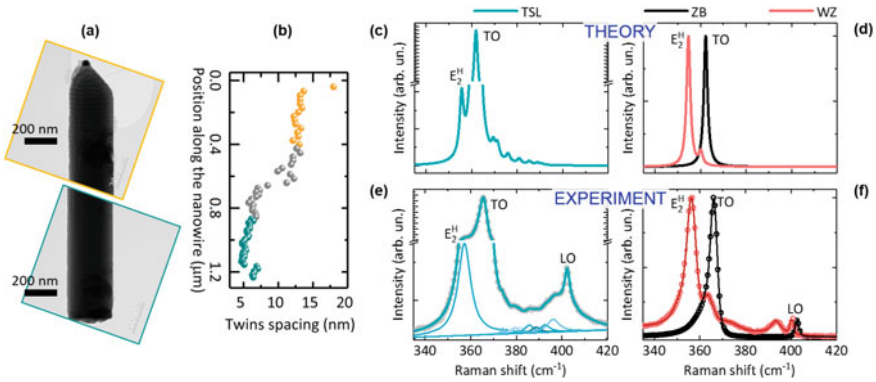

Fig. 15 **a** Bright-field TEM image of a typical GaP TSL nanowire. *Courtesy of M. A. Verheijen.* **b** Spacing between consecutive twin planes as a function of the position along the axis of the NW displayed in **a**. **c** Calculated Raman spectrum of a GaP TSL with twin spacing of 4.5 nm, which is the typical TSL spacing at the NW base. **d** Calculated reference spectra of bulk GaP in the ZB (black solid line) and WZ (red solid line) crystal structures. **e** Raman spectrum (gray circles) measured on the base of a single GaP TSL NW (with 4.5 nm twin spacing). Solid thin lines are deconvoluted Lorentzian components of the data (only phonon modes arising from the superlattice are displayed); the solid thick line display the fit result. **f** Measured spectra of GaP on a bulk ZB substrate (black circles) and a single WZ NW (red circles) with superimposed fit results (solid lines). All the experimental spectra of NW samples feature a peak on the low-frequency side of the LO mode, ascribed to a surface optical mode due to the finite size of the NW. All theoretical and experimental spectra in panels (**c**)–(**f**) were obtained in the $\bar{x}\ (yy)x$ configuration depicted in Fig. 4 and were normalized to their most intense peak

space group is $P6_3mc$ (#186), the same as the WZ structure [47]. The computed and experimental Raman spectra of the TSL also consist of few phonon modes on the high-frequency side of the TO mode, which are neither observed in the ZB nor in the WZ phase as they arise from the backfolding of the phonon dispersion in a very small region of the Brillouin zone, due to the long lattice parameter typical of the superlattice. The experimentally found number of the TSL modes as well as their frequencies closely compare to the theoretical ones. The presence of the $E_2{}^H$ mode and of the other backfolded peaks in the TSL NWs suggests that the mean free path of the corresponding phonons is longer than the twin spacing and that the phonons actually perceive the presence of the superlattice.

Our study also demonstrates the tunability of the phononic spectrum of TSL. Indeed, we found that TSL crystals with twin spacing smaller than 4.5 nm display a lower number of TSL modes (due to a smaller unit cell) and both the $E_2{}^H$ mode and the TSL modes are more intense [47]. In the limiting case of an almost null TSL spacing, we retrieve the WZ case, where there is only one very intense folded mode ($E_2{}^H$). Since the spacing between the twin planes determines the number, frequency, and intensity of the phonon modes, we envision the possibility to use material engineering at the nanoscale for a rational manipulation of the heat transport properties of materials based on coherent phonon transport.

4 Electronic Properties of Nanowires: Resonant Raman

4.1 Resonant Raman Studies as a Probe of Electronic Transitions

Since the energy of the external field $\hbar\omega_i$ lies in the visible range, in the case of semiconductors, the electronic transitions can play a relevant role in the expression of $\left|\chi\left(\omega_i, \omega_q\right)\right|^2$ because the energy gaps s, $E_0 + \Delta_0$, E_1, and $E_1 + \Delta_1$ can lie in the same energy range as the excitation. Raman scattering cross section has a strong dependence on ω_i, from which electronic properties of the system can be deduced. This is the case of resonant Raman scattering process, that can be described as follows.

The incident photons are coupled to the electrons of the system by the electron radiation Hamiltonian H_{eR}. The system is excited into an intermediate state by creating an electron–hole pair. This electron–hole pair is scattered into another state by emitting/destroying a phonon via the electron–phonon interaction Hamiltonian H_{e-ion}. Finally, the electron–hole pair recombines radiatively with the emission of the scattered photon. In the initial state $|i\rangle$ (before scattering occurs) there are, respectively, $N(\omega_i)$ and $N(\omega_s)$ photons with the frequencies ω_i and ω_s. Assuming $T \neq 0$, there are also N_q phonons present in the system. The electrons are all in their ground states. In the final state $|f\rangle$, after Stokes (anti-Stokes) Raman scattering, $N(\omega_i)$ has decreased (increased) by one while $N(\omega_s)$ and N_q have both increased (decreased) by one. The electrons remain unchanged. The Fermi Golden Rule gives the probability for scattering a system from the initial state $|i\rangle$ to the final state $|f\rangle$. The probability per unit time for a one-phonon (Stokes) Raman scattering can be calculated with third-order perturbation theory and is given by

$$
\begin{aligned}
P_{ph}(\omega_i) \approx \left(\frac{2\pi}{\hbar}\right) \Bigg| \sum_{n,n'} & \frac{\langle i|H_{eR}(\omega_i)|n\rangle\langle n|H_{e-ion}|n'\rangle\langle n'|H_{eR}(\omega_s)|i\rangle}{[\hbar\omega_i-(E_n-E_i)]\left[\hbar\omega_i-\hbar\omega_0-\left(E_{n'}-E_i\right)\right]} \\
&+ \frac{\langle i|H_{eR}(\omega_i)|n\rangle\langle n|H_{eR}(\omega_s)|n'\rangle\langle n'|H_{e-ion}|i\rangle}{[\hbar\omega_i-(E_n-E_i)]\left[\hbar\omega_i-\hbar\omega_s-\left(E_{n'}-E_i\right)\right]} \\
&+ \frac{\langle i|H_{eR}(\omega_s)|n\rangle\langle n|H_{e-ion}|n'\rangle\langle n'|H_{eR}(\omega_s)|i\rangle}{[-\hbar\omega_s-(E_n-E_i)]\left[-\hbar\omega_s-\hbar\omega_0-\left(E_{n'}-E_i\right)\right]} \\
&+ \frac{\langle i|H_{eR}(\omega_s)|n\rangle\langle n|H_{eR}(\omega_i)|n'\rangle\langle n'|H_{e-ion}|i\rangle}{[-\hbar\omega_s-(E_n-E_i)]\left[-\hbar\omega_s+\hbar\omega_i-\left(E_{n'}-E_i\right)\right]} \\
&+ \frac{\langle i|H_{e-ion}|n\rangle\langle n|H_{eR}(\omega_i)|n'\rangle\langle n'|H_{eR}(\omega_s)|i\rangle}{[-\hbar\omega_0-(E_n-E_i)]\left[-\hbar\omega_0+\hbar\omega_i-\left(E_{n'}-E_i\right)\right]} \\
&+ \frac{\langle i|H_{e-ion}|n\rangle\langle n|H_{eR}(\omega_s)|n'\rangle\langle n'|H_{eR}(\omega_i)|i\rangle}{[-\hbar\omega_0-(E_n-E_i)]\left[-\hbar\omega_0-\hbar\omega_s-\left(E_{n'}-E_i\right)\right]} \times \delta(\hbar\omega_i - \hbar\omega_s - \hbar\omega_0)\Bigg|^2
\end{aligned}
\tag{5}
$$

where $|n\rangle$ and $|n'\rangle$ are intermediate electronic states with energies E_n and $E_{n'}$, respectively. In Eq. (5) each matrix element represents an interaction during the process, the denominators express the energy conservation after the interactions and the delta function expresses the overall energy conservation conditions.

Since the scattering cross section, which is proportional to the probability per unit time for one-phonon Raman scattering given by Eq. (5), contains the electron-phonon and the electron–radiation interaction Hamiltonians via the matrix elements $\langle j|H_{e-ion}|l\rangle$ and $\langle j|H_{eR}(\omega_i)|l\rangle$, respectively, as well as electronic states for electron–hole pair, Raman spectroscopy can be used to investigate the electron band structure and the electron–phonon interaction in semiconductors. Nevertheless, it is experimentally very improbable to access this information, due to summation over all the intermediate states, unless resonant conditions are used. In resonant conditions the excitation energy is tuned to be equal to electronic interband transitions, leading to resonant Raman scattering. In terms of scattering cross section, this is equivalent to selecting few intermediate states which reset the denominator of Eq. (5) to zero making the contribution of those terms predominant. The other terms can then be neglected. Furthermore, the first term of the scattering cross section is predominant and the Raman scattering probability can be approximated to

$$P_{ph}(\omega_i) \approx \left(\frac{2\pi}{\hbar}\right)\left|\frac{\langle 0|H_{eR}(\omega_i)|r\rangle\langle r|H_{e-ion}|r\rangle\langle r|H_{eR}(\omega_s)|0\rangle}{(E_r-\hbar\omega_i)(E_r-\hbar\omega_s)}\right|^2 \tag{6}$$

where $|r\rangle$ is the resonant intermediate state with energy E_r. Here, the initial electronic state was supposed to be the ground state $|0\rangle$ and the delta function was already applied. Considering that $(\hbar\omega_i - \hbar\omega_s)$ is the phonon energy, it is small compared to the electronic energies and it can be considered $(E_r - \hbar\omega_i) \approx (E_r - \hbar\omega_s)$. Therefore, Eq. (6) contains a "double resonance". The so-called incoming resonance occurs whenever $E_r \approx \hbar\omega_i$ and the outgoing resonance when $E_r \approx \hbar\omega_s$.

4.2 Probing Critical Points of Electronic Bands

In the case of a cubic germanium NW, we can refer to the pivotal work by Cerdeira, et al. who studied the resonant Raman scattering (RRS) response in bulk Ge and identified an optical transition at the M point of the BZ as responsible for the resonant behavior [48]. The result of the resonant Raman study of a cubic Ge NW is reported in Fig. 16a. In an RRS study, the data are acquired by keeping fixed the exciting laser power and by further normalizing the Raman intensities to the Raman intensity detected under the same conditions on a reference, nonresonant sample as a CaF_2 crystal. This normalization removes the ω^4 dependence of the scattered intensity on the exciting photon energy, as well as the influence of the experimental setup efficiency. A peak in the trend of the Raman intensity as a function of the exciting photon energy can therefore identify an optically allowed electronic transition that enhances the Raman cross section.

Indeed, along with the experimental data, we report in Fig. 16b the band structure of cubic Ge as calculated by density functional theory (DFT). The experimental data show a trend that peaks around exciting photon energy of about 2.2 eV, which is in

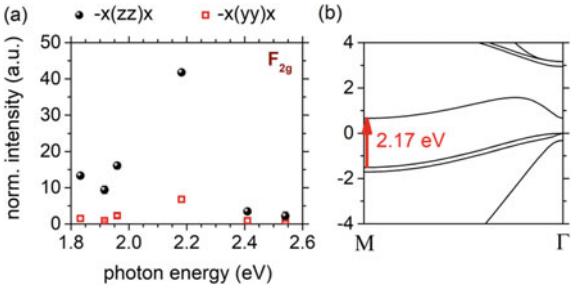

Fig. 16 **a** Resonant Raman study on the cubic part of the Ge NW, oriented as discussed above. We report the intensity of the F_{2g} mode as a function of the excitation energy. The different laser energies used for the study are distributed in the whole visible spectrum. The Raman intensity is clearly peaked around 2.2 eV. **b** Bandstructure diagram for 3C-Ge calculated within HSE06-DFT and including spin–orbit coupling [36]. Energies are referred to the top of the valence band. The experimental result is in good agreement with the calculation if one considers the transition marked by the red arrow, that is the one responsible for the resonant Raman behavior in Ge, as reported by Cerdeira et al. [48]

agreement with the calculated energy value of the transition responsible for resonant Raman in cubic Ge, i.e., 2.17 eV (ascribed to E_1, $E_1 + \Delta_1$ according to ref.[48]). This result thus demonstrates the feasibility of an indirect investigation on the critical points of electronic bands by RRS even in nanowires and other nanostructured systems.

4.3 Unveiling Band Alignment in Heterostructures

We have just demonstrated that resonant Raman can be used to probe the electronic band structure in semiconductors, including NWs. Here, we want to show that this kind of investigation can even provide information on the type of band alignment in heterostructures. We will consider once again the most challenging type of heterostructure: a nanoscale polytypic homostructure, namely the transformed Ge NWs described in Sect. 3.3.1. Indeed, if crystal-phase homostructures have to be used for bandgap engineering, it is crucial to determine how the energy barriers for electrons and holes, *i.e.*, the conduction and valence band offsets, are formed. The electronic band structure of cubic and hexagonal group-IV crystals, as well as the band-alignment of their polytypic homostructure, was calculated at Γ point in Ref.[49] by hybrid-DFT with the VASP code. The exchange–correlation functional was approximated using a hybrid Heyd–Scuseria–Ernzerhof (HSE06) functional. Spin–orbit interaction, which is important in Ge, was also included. Very similar calculations, performed at Γ and L/M points for Ge, are reported in Ref. [36]. While Si homostructures are characterized by a type-II band alignment (namely, the valence-band edge is localized on the hexagonal phase and the conduction-band edge is localized on the cubic phase), Ge homostructures exhibit a type-I band alignment

(where the valence- and the conduction-band edges are both located in the hexagonal region). The results for the Ge case are displayed in Fig. 17a in the top panel [36]. Clearly, the Ge homojunctions present a direct bandgap whose value is smaller if compared to the one of the cubic phases. In the bottom panel, also the calculated band structure and band alignment at L/M points are displayed. In hexagonal Ge, the direct transition has an energy of 2.61 eV at the M point, quite larger than the energy of the direct transition (2.17 eV) in the cubic phase at the L point (that is equivalent to the M point of the hexagonal BZ). Moreover, while the band alignment between the cubic and the hexagonal bands at the Γ point is of type I, at the L/M point it is of type II, resulting in an allowed optical transition of 2.12 eV (dashed arrow), which is energetically more favorable than the direct transitions at the L/M point.

While the predicted transitions at Γ point cannot be probed by resonant Raman and by conventional photoluminescence spectroscopies as they are in the IR range

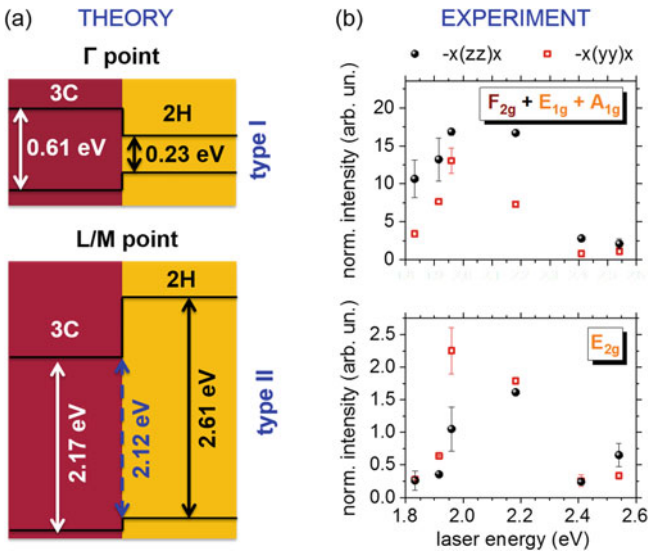

Fig. 17 **a** Band structure alignment calculated within HSE06-DFT including spin–orbit coupling for a crystal-phase homostructure made by cubic (3C) and hexagonal (2H) Ge. The top panel refers to the Γ point, where the alignment is predicted to be of type I. The bottom panel refers to the L/M points (the M point of the hexagonal BZ is equivalent to the L point of the cubic BZ [17]), where the alignment is predicted to be of type II. Solid arrows highlight spatially direct transitions taking place either in the cubic or in the hexagonal sections, while the dashed arrow highlights the spatially indirect type-II transition taking place across the homostructure. **b** Experimental resonant Raman study performed by monitoring the Raman intensity as the homostructured part of the NW is excited with different laser energies in the visible range. Spectra were collected in the $\bar{x}\ (z, z)x$ (full circles) and $\bar{x}\ (y, y)x$ (open squares) scattering geometry. The top panel refers to the degenerate phonon modes of the cubic (F_{2g}) and hexagonal ($E_{1g} + A_{1g}$) segments, while the bottom panel refers to the E_{2g} mode of the hexagonal segment. For all the modes, the intensity is peaked at energies between 2.0 and 2.2 eV (lower than in the cubic case in Fig. 16), in agreement with the calculated energy of the type-II transition at the L/M point (dashed arrow in **a**)

(and indeed the bandgap of hexagonal Ge has been measured only very recently [11]), the spectral range of the transitions at L/M points can be probed by resonant Raman. Figure 17b shows an RRS study performed as described in Sect. 4.2 on the transformed regions of the Ge NW [36]. While cubic Ge has a quite strong resonance at about 2.2 eV (see Fig. 16), when moving to the heterostructured part we observe a different behavior: even if the scale of the enhancement is smaller, the trend is here peaked at lower energies, between 2.0 and 2.2 eV. This can be explained with the new electronic resonant transition arising from band alignment in the heterostructured part of the NW. Indeed, as our DFT calculations of the electronic band structure of hexagonal Ge provide a value of the direct transition at the M point of 2.61 eV, the mere presence of the hexagonal phase in our NW is not sufficient to explain our experimental observation. We have to consider that when we study the transformed region, our scattering volume includes both the cubic and the hexagonal phases, and therefore, we can probe not only the direct transitions in each segment but also the spatially indirect transitions across them. In the case of Ge, the spatially indirect transition is energetically favourable, that is why our RRS study clear unveils its presence.

5 Conclusions

In conclusion, we have discussed the theoretical foundation of Raman scattering focusing on its dependence on the incident/scattered photon polarization. We have highlighted how the crystal structure of NWs is reflected in Raman spectra not only by the number and frequency of the observed phonon modes but also by their symmetry, which is unveiled by their selective observation under polarized light.

More specifically, for the differentiation between cubic and hexagonal group-IV semiconductors, we have shown that the detection of the E_{2g} phonon mode can be used as a fingerprint for the hexagonal phase. However, it is important to keep in mind that, for optical excitation through the side facets of hexagonal NWs grown along the c direction, the E_{2g} phonon mode can only be observed for incoming laser light polarized perpendicular to the NW axis and that exactly this kind of linearly polarized light can suffer from a vanishing optical transmission through NW side facets when the radius-to-wavelength ratio decreases below a certain value due to dielectric mismatch effects. Therefore, retrieval of crystal symmetry information encoded in the anisotropic nature of Raman scattering intensities, though well established in bulk crystals, might become complicated at crystal sizes of the order of the excitation wavelength. In order to fully exploit the potential of Raman microscopy to investigate the crystal structure, a model that accounts for both crystallographic and small particle polarization-dependent selection rules can be needed. It is worth stressing that despite the intensity of the E_{2g} mode can be dependent on NW size and excitation wavelengths and therefore not always easily measured, the frequency and polarization dependence of this mode are instead independent on these factors and therefore they provide unambiguous proof of the presence of the hexagonal phase.

We have shown that this fact not only can be exploited to study the crystal phase but also to finely determine its orientation in NWs, as well as to discriminate between oriented polytypic inclusions from defects in complex hetero- and homostructures in NWs.

Acknowledgments C.F. acknowledges financial support from The Sapienza University scholarship "Borsa di Perfezionamento all'Estero 2017-2018." I.Z. acknowledges financial support from the Swiss National Science Foundation research grant (Project Grant No. 200021_165784) and from the European Research Council (ERC) under the European Union's Horizon 2020 research and innovation program (grant agreement No 756365). M.D.L. acknowledges support from the Swiss National Science Foundation Ambizione grant (Grant No. PZ00P2_179801). We thank Laetitia Vincent and Erik P.A.M. Bakkers for providing us with samples, Riccardo Rurali and Michele Amato for theoretical calculations, Diego De Matteis for the measurements in Figure 12, and Marcel A. Verheijen for the TEM in Figure 15. C.F. is thankful to professor Paolo Piccinni from Sapienza University for the fruitful discussion.

References

1. F. Bechstedt, A. Belabbes, Structure, energetics, and electronic states of III–V compound polytypes. J. Phys. Condens. Matter **25**, 273201 (2013)
2. K. Takahashi, T. Morizumi, Growth of InAs whiskers in wurtzite structure. Japan. J. Appl. Phys. **5**, 657 (1966)
3. D. Jacobsson, F. Panciera, J. Tersoff, M.C. Reuter, S. Lehmann, S. Hofmann, K.A. Dick, F.M. Ross, Interface dynamics and crystal phase switching in GaAs nanowires. Nature **531**, 317–322 (2016)
4. P. Krogstrup, H.I. Jorgensen, E. Johnson, M.H. Madsen, C.B. Sorensen, A. Fontcuberta i Morral, M. Aagesen, J. Nygard, F. Glas, Advances in the theory of III–V nanowire growth dynamics. J. Phys. D Appl. Phys. **46**, 313001 (2013)
5. P. Caroff, J. Bolinsson, J. Johansson, Crystal phases in III–V nanowires: from random toward engineered polytypism. IEEE J. Sel. Top. Quant. Electron. **17**, 829 (2011)
6. P. Caroff, K.A. Dick, J. Johansson, M.E. Messing, K. Deppert, L. Samuelson, Controlled polytypic and twin-plane superlattices in III–V nanowires. Nat. Nanotech. **4**, 50 (2009)
7. K.A. Dick, C. Thelander, L. Samuelson, P. Caroff, Crystal phase engineering in single InAs nanowires. Nano Lett. **10**, 3494 (2010)
8. H.I.T. Hauge, M.A. Verheijen, S. Conesa-Boj, T. Etzelstorfer, M. Watzinger, D. Kriegner, I. Zardo, C. Fasolato, F. Capitani, P. Postorino et al., Hexagonal silicon realized. Nano Lett. **15**, 5855–5860 (2015)
9. L. Vincent, G. Patriarche, G. Hallais, C. Renard, C. Gardes, D. Troadec, D. Bouchier, Novel heterostructured Ge nanowires based on polytype transformation. Nano Lett. **14**, 4828–4836 (2014)
10. X. Cartoixà, M. Palummo, H.I.T. Hauge, E.P.A.M. Bakkers, R. Rurali, Optical emission in hexagonal SiGe nanowires. Nano Lett. **17**, 4753–4758 (2017)
11. E.M.T. Fadaly, A. Dijkstra, J. R. Suckert, et al., Direct-bandgap emission from hexagonal Ge and SiGe alloys. Nature **580**, 205–209 (2020)
12. M. De Luca, I. Zardo, *Semiconductor Nanowires: Raman Spectroscopy Studies, in Raman Spectroscopy and Applications*, ed. by K. Maaz (InTech, 2017)
13. B. Loitsch, J. Winnerl, G. Grimaldi, J. Wierzbowski, D. Rudolph, Crystal phase quantum dots in the ultrathin core of GaAs-AlGaAs Core-shell nanowires. Nano Lett. **15**, 7544 (2015)
14. MB. Bavinck, KD. Jöns, M. Zieliński, G. Patriarche, JC. Harmand, N. Akopian, V. Zwiller, Photon cascade from a single crystal phase nanowire quantum dot. Nano Lett. **16**, 1081 (2016)

15. A. De, C.E. Pryor, Predicted band structures of III–V semiconductors in the wurtzite phase. Phys. Rev. B **81**, 155210 (2010)
16. J.L. Birman, Simplified LCAO method for zincblende, wurtzite, and mixed crystal structures. Phys. Rev. B **115**, 1493 (1959)
17. M. Murayama, T. Nakayama, Chemical trend of band offsets at wurtzite/zinc-blende heterocrystalline semiconductor interfaces. Phys. Rev. B **49**, 4710 (1994)
18. J. Ziy, X. Wan, G. Wei, K. Zhang, X. Xie, Lattice dynamics of zinc-blende GaN and AlN: I. Bulk phonons. J. Phys. Condens. Matter **8**, 6323 (1996)
19. Harima, H, Properties of GaN and related compounds studied by means of Raman scattering. J. Phys. Condens. Matter **14**, R967–R993 (2002)
20. C.A. Arguello, D.L. Rousseau, S.P.S. Porto, First-order raman effect in wurtzite-type crystals. Phys. Rev. **181**, 1351 (1969)
21. M. Cardona, *Light Scattering in Solids II (Springer Topics in Applied Physics)*, ed. by M. Cardona, G. Güntherodt, vol. 50 (Berlin: Springer, 1982), pp. 5019–178
22. B.R. Wu, First-principles study on the high-pressure behavior of the zone-center modes of lonsdaleite silicon. Phys. Rev. B **61**, 5–8 (2000)
23. M. Raya-Moreno, H. Aramberri, J.A. Seijas-Bellido, X. Cartoixà, R. Rurali, Thermal conductivity of hexagonal Si and hexagonal Si nanowires from first-principles. Appl. Phys. Lett. **111**, 032107 (2017)
24. M. De Luca, A. Polimeni, Electronic properties of wurtzite-phase InP nanowires determined by optical and magneto-optical spectroscopy. Appl. Phys. Rev. **4**, 041102 (2017)
25. I. Zardo, S. Conesa-Boj, F, Peiro, J.R. Morante, J. Arbiol, E. Uccelli, G. Abstreiter, A. Fontcuberta i Morral, Raman spectroscopy of wurtzite and zinc-blende GaAs nanowires: Polarization dependence, selection rules, and strain effects. Phys. Rev. B **80**, 245324 (2009)
26. G. Turrel, J. Corset (ed.), *Raman Microscopy Developments and Applications*, 1st edn. (Malta: Academic Press, 1996). https://www.horiba.com/us/en/scientific/products/raman-spectroscopy/raman-academy/raman-faqs/what-analysis-spot-or-laser-spot-size-is-used-for-a-raman-microscope/
27. Spectroscopy and Imaging GmbH. S&I Spectroscopy & Imaging GmbH, Warstein (Germany). (2015). https://www.s-and-i.eu/index.php/products/triple. Accessed 31 Mar 2019
28. A. Glebov et al., *Novel Volume Bragg Grating Notch Filters for Ultralow-Frequency Raman Measurements.* The 3rd Scientific EOS Annual Meeting (EOSAM 2010), paper, vol. 4007. (2010)
29. NIST, *Atomic Spectra Database Lines Form.* (National Institute of Standards and Technology, US Department of Commerce, Gaithersburg, 1995). https://physics.nist.gov/PhysRefData/ASD/lines_form.html. Accessed 31 Mar 2019
30. R. Loudon, The Raman effect in crystals. Adv. Phys. **13**, 423–482 (1964)
31. M. De Luca, Addressing the electronic properties of III–V nanowires by photoluminescence excitation spectroscopy. J. Phys. D Appl. Phys. **50**, 054001 (2017)
32. J. Wang, M.S. Gudiksen, X. Duan, Y. Cui, C.M. Lieber, Highly polarized photoluminescence and photodetection from single indium phosphide nanowires. Science **293**, 1455 (2001)
33. H.E. Ruda, A. Shik, Polarization-sensitive optical phenomena in semiconducting and metallic nanowires. Phys. Rev. B **72**, 115308 (2005)
34. M. De Luca, A. Zilli, A. Fonseka, S. Mokkapati, A. Miriametro, H. Tan, L. Smith, C. Jagadish, M. Capizzi, A. Polimeni, Polarized light absorption in wurtzite InP nanowire ensembles. Nano Lett. **15**, 998 (2015)
35. L.D. Landau, E.M. Lifshitz, L.P. Pitaevskii, *In Electrodynamics of Continuous Media.* (Pergamon, Oxford, UK, 1984), p. 3442
36. C. Fasolato, M. De Luca, D. Djomani, L. Vincent, C. Renard, G. Di Iorio, V. Paillard, M. Amato, R. Rurali, I. Zardo, Crystalline, phononic, and electronic properties of heterostructured polytypic Ge nanowires by Raman spectroscopy. Nano Lett. **18**, 7075 (2018)
37. M. Ramsteiner, O. Brandt, P. Kusch, S. Breuer, S. Reich, L. Geelhaar, Quenching of the E_2 phonon line in the Raman spectra of wurtzite GaAs nanowires caused by the dielectric polarization contrast. Appl. Phys. Lett. **103**, 043121 (2013)

38. F.J. Lopez, J.K. Hyun, U. Givan, I.S. Kim, A.L. Holsteen, L.J. Lauhon, Diameter and polarization-dependent raman scattering intensities of semiconductor nanowires. Nano Lett. **12**, 2266 (2012)
39. J. Fréchette, C. Carraro, Diameter-dependent modulation and polarization anisotropy in Raman scattering from individual nanowires. Phys. Rev. B **74**, 161404 (2006)
40. M.Y. Swinkels, A. Campo, D. Vakulov, K. Wonjong, L. Gagliano, S. Escobar Steinvall, H. Detz, M. De Luca, A. Lugstein, E. Bakkers, A. Fontcuberta i Morral, I. Zardo, Measuring the optical absorption of single nanowires. Phys. Rev. Appl. **14**, 024045 (2020)
41. J.H. Parker Jr., D.W. Feldman, M. Ashkin, Raman scattering by silicon and germanium. Phys. Rev. **155**, 712 (1967)
42. X. Gonze, J.-P. Vigneron, Density-functional approach to nonlinear-response coefficients of solids. Phys. Rev. B **39**, 13120 (1989)
43. J.F. Nye, *Physical Properties of Crystals* (Clarendon Press, Oxford, 1957)
44. S.A. Fortuna, X. Li, Metal-catalyzed semiconductor nanowires: a review on the control of growth directions. Semicond. Sci. Technol. **25**, 024005 (2010)
45. D. de Matteis, M. De Luca, E.M.T. Fadaly, M.A. Verheijen, M. López-Suárez, R. Rurali, E.P.A.M. Bakkers, I. Zardo, Probing lattice dynamics and electronic resonances in hexagonal Ge and SixGe1-x alloys in nanowires by Raman spectroscopy. ACS Nano. **14**(6), 6845–6856 (2020)
46. A.A. Kelly, K.M. Knowles, *Crystallography and Crystal Defects*, 2nd edn. (Wiley, Weinheim, Germany, 2012)
47. M. De Luca, C. Fasolato, M.A. Verheijen, Y. Ren, M.Y. Swinkels, S. Kölling, E.P.A.M. Bakkers, R. Rurali, I. Zardo, Phonon engineering in twinning superlattice nanowires. Nano Lett. **19**, 4702 (2019)
48. F. Cerdeira, W. Dreybrodt, M. Cardona, Resonant Raman scattering in germanium. Solid State Comm. **10**, 591 (1972)
49. T. Kaewmaraya, L. Vincent, M. Amato, Accurate estimation of band offsets in group IV polytype junctions: a first-principles study. J. Phys. Chem. C **121**, 5820 (2017)

Theoretical Aspects of Point Defects in Semiconductor Nanowires

Riccardo Rurali, Maurizia Palummo, and Xavier Cartoixà

Abstract We review several fundamental and practical aspects of the theoretical treatment of neutral and charged point defects—i.e., vacancies, interstitials, substitutional impurities, and complexes—in bulk and nanowires (NWs). In particular, we show how a few of the issues preventing the straightforward application of bulk methods to NWs can be partially remedied. With this, we show how standard substitutional doping yields too high activation energies for ultrathin NWs, and that substrate bias should also be an important parameter to control impurity incorporation into the NW during growth.

Keywords Nanowires · DFT · Defects · Dopants

1 Introduction

It is hard to overestimate the technological importance of the study of defects in materials. Although the term defect carries a negative connotation, intentionally placed substitutional defects in trace concentrations—dopants—lie at the heart of semiconductor devices enabling information society. These same devices can be adversely affected by the presence of other kinds of impurities; it is well known that Au can kill the conduction efficiency in silicon [1], yet it can be used to build infrared detectors [2]. In another example, the nitrogen–vacancy (NV) complex in diamond has gained a lot of attention in the last decade due to it being perceived

R. Rurali
Institut de Ciència de Materials de Barcelona (ICMAB-CSIC), Campus de Bellaterra, 08193 Bellaterra, Barcelona, Spain

M. Palummo
Dipartimento di Fisica, European Theoretical Spectroscopy Facility (INFN), Università di Roma, "Tor Vergata", Via della Ricerca Scientifica 1, 00133 Roma, Italy

X. Cartoixà (✉)
Departament d'Enginyeria Electrònica, Universitat Autònoma de Barcelona, 08193 Bellaterra, Spain
e-mail: Xavier.Cartoixa@uab.es

© Springer Nature Singapore Pte Ltd. 2021

N. Fukata and R. Rurali (eds.), *Fundamental Properties of Semiconductor Nanowires*,
https://doi.org/10.1007/978-981-15-9050-4_8

as an important component for quantum information as well as various nanoscale technologies [3].

On the other hand, nanowires have long been a preeminent system where to study fundamental aspects of one-dimensional (1D) physics, as well as having strong technological importance. Much of their interest stems from the quasi-1D structure, which confers nanowires with a coexisting nature of interconnections and active devices. Additionally, compared to classical planar device technology, nanowires can better accommodate surrounding gates, which provide a more effective electrostatic control of the charge carriers in the channel and thus higher field-effect efficiency, device performance and mobilities. Finally, yet importantly, their electronic character is always semiconducting, at variance with nanotubes, the obvious competitors as 1D systems are concerned.

In this chapter, we will address several aspects that must be taken into account when addressing the computational study of the structural and electronic properties of neutral and point defects in nanowires. Some of these aspects, such as the definition of formation energy or the interpretation of the transition energy between impurity states with a different charge, are common to bulk materials, while others, such as the appropriate electrostatic correction to subtract the effect of the periodic boundary conditions, are particular to nanowires. Although aspects concerning bulk materials have been covered in the excellent and more extensive review by Freysoldt et al. [4], we will include them here for completeness while discussing some of the particularities specific to nanowires.

2 Fundamentals

In this section, we review a few basic concepts necessary for the discussion that follows.

2.1 Excitation Energies Versus Transition Levels

Consider the band profile customary in semiconductor physics, shown in Fig. 1, and compare it to the band diagram for Si with a single vacancy in Fig. 2. Figure 1 indicates the position of two forbidden gap levels, 0.09 and 0.71 eV above the valence band edge, and the $(+2/0)$ notation indicates that, when the Fermi energy is below the impurity level, the level has a double positive charge, i.e., it has released two electrons, whereas when the Fermi energy is above the impurity level the level is charged neutral. This is an example of a *transition level*, which can be computed from theory by considering the energy of two ground states, one with N electrons and the other one with $N - 2$ electrons. The key point is that, being obtained from ground-state calculations, the transition level takes into account the structural relaxations that may go along with different charge states.

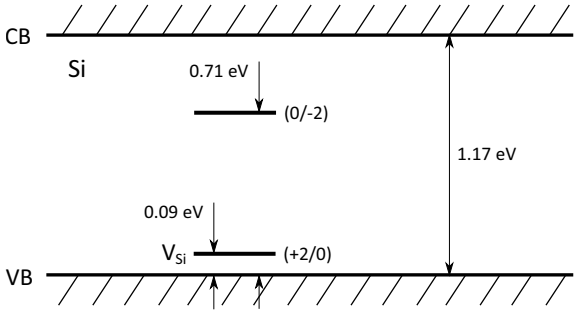

Fig. 1 Band profile of Si with a single vacancy, showing a double donor level (negative-U [5]) close to the valence band (VB) edge and a double acceptor level 0.46 eV below the conduction band (CB). The value given for the bandgap are experimentally determined for low temperature [6], while the positions of the levels correspond to maximum likelihood values provided in page 137 of Ref. [7]

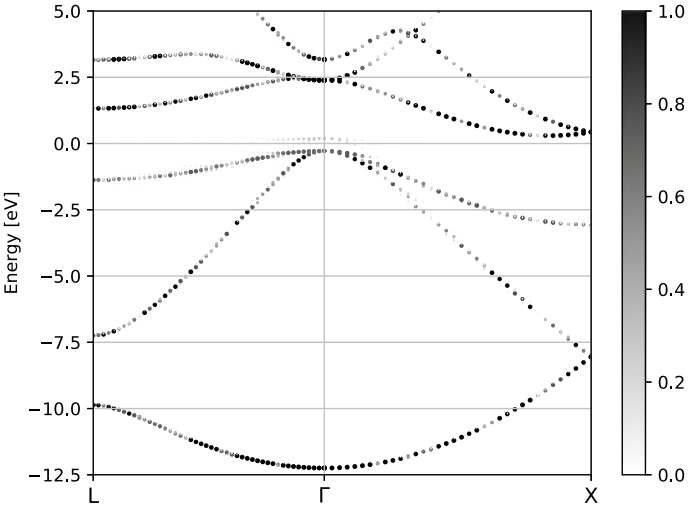

Fig. 2 Unfolded band structure of Si with a single vacancy. The deep level is the nondispersive band close to the VB edge

On the other hand, Fig. 2 has been obtained from a single calculation in a reference configuration, and the position of the impurity level does not take into account the possible structural relaxations that may stem from occupancy of that impurity level different from the one used in the reference configuration. In this case, this is called an *excitation energy*.

In general, transition levels and excitation energies need not coincide, but both have physical meaning. Excitation energies are experimentally meaningful when dealing with fast electronic transitions such as those occurring in optical experiments

of absorption and photoemission, while transition levels, corresponding to thermal ionization energies [4], will manifest in dopant-induced carrier concentrations or in deep-level transient spectroscopy (DLTS) [8].

2.2 Formation Energy

The energetics of the formation of a defect in a solid can be studied analogously to that of a chemical reaction: some atoms/electrons in an initial (reactants) configuration will transition to a final (product) state. Therefore, the formation energy E_{form} of a defect will be given by

$$E_{\text{form}} = E_{\text{final}} - E_{\text{init}} = E_{\text{prod}} - E_{\text{react}}, \tag{1}$$

where $E_{\text{final}}/E_{\text{prod}}$ ($E_{\text{init}}/E_{\text{react}}$) corresponds to the total energy of the final/product (initial/reactants) state.

For example, the reaction associated with the formation of a vacancy in silicon will be

$$\text{Si}_{\text{N}} \rightarrow \text{Si}_{\text{N}-1} + \text{Si}, \tag{2}$$

to which there will correspond a formation energy $E_{\text{prod}} - E_{\text{react}}$

$$E_{\text{form}}^{\text{vac}} = \left(E_{\text{Si}_{\text{N}-1}} + \mu_{\text{Si}}\right) - \left(E_{\text{Si}_{\text{N}}}\right), \tag{3}$$

where $E_{\text{Si}_{\text{N}-1}}$ is the energy of the (structurally relaxed) system with the vacancy, $E_{\text{Si}_{\text{N}}}$ is the energy of the pristine system, and μ_{Si} is the energy/chemical potential of the Si atom that has been removed. This leads us naturally to the question of what happens to the removed atom when a vacancy is formed. We will discuss in more detail in the next section the role of the source and destination of the atoms participating in the constitution of the defect.

Similarly, the reaction associated with the formation of a silicon self-interstitial will be

$$\text{Si}_{\text{N}} + \text{Si} \rightarrow \text{Si}_{\text{N+int}}, \tag{4}$$

and we will have

$$E_{\text{form}}^{\text{int}} = \left(E_{\text{Si}_{\text{N+int}}}\right) - \left(E_{\text{Si}_{\text{N}}} + \mu_{\text{Si}}\right), \tag{5}$$

where $E_{\text{Si}_{\text{N+int}}}$ is the energy of the system with the self-interstitial.

Finally, unless otherwise noted, in this chapter we will deal with formation energies, as opposed to formation enthalpies or Gibbs energies [9].

2.3 Chemical Potential

We already hinted in the previous section that, when atoms must be added to or removed from the system in order to build the defect, we have to make assumptions about where these atoms have gone to or are coming from in order to maintain the same number of particles at both sides of the reaction. It is customary to assume that the removed/added atoms are exchanged with a reservoir of the same element in some elementary or compound phase, temperature and pressure conditions, and thus their energy will be given by the chemical potential μ of the corresponding element in that elementary or compound phase.

In the self-interstitial/vacancy processes of Sect. 2.2, all the energies involved were well defined because, in the real growth conditions, Si atoms were really exchanged with the diamond lattice Si host, and the contribution from a single Si atom to the total energy can be computed in an internally consistent manner from first principles.

On the other hand, the formation energies of native defects in a binary compound, such as GaAs, require a less straightforward treatment [10]. Consider, similarly to the previous section, the formation of a Ga vacancy in GaAs. The associated reaction will be, now with a more conventional notation,

$$(\mathrm{GaAs})_\mathrm{N} \rightarrow (\mathrm{GaAs})_\mathrm{N} + \mathrm{V_{Ga}} + \mathrm{Ga}, \tag{6}$$

where $\mathrm{V_{Ga}}$ denotes the Ga vacancy, to which there will correspond formation energy

$$E_\mathrm{form}^{\mathrm{V_{Ga}}} = \left(E_{\mathrm{GaAs}+\mathrm{V_{Ga}}} + \mu_\mathrm{Ga}\right) - \left(E_\mathrm{GaAs}\right), \tag{7}$$

where $E_{\mathrm{GaAs}+\mathrm{V_{Ga}}}$ is the total energy of the bulk GaAs with a single vacancy, E_GaAs is the energy of the pristine GaAs with the same number of primitive cells, and μ_Ga is the chemical potential of the released Ga atom, i.e., the energy of that atom in the phase or compound where it has incorporated. During vapor–liquid–solid (VLS) or vapor-solid-solid (VSS) nanowire (NW) growth, this Ga atom that has not incorporated—leaving a vacancy behind—will eventually occupy a different site inside the NW lattice. Then, μ_Ga would be the energy contribution of a single Ga atom to the total energy of the GaAs NW (or bulk, if the NW is thick enough that surface effects are unimportant).

It is not immediate how to assign a value to μ_Ga, as it is determined from experimental conditions [4]. Even from a computational standpoint, first-principles calculations only provide the total energy of a GaAs primitive cell, but not the individual contribution of one of the constituents of the compound. Thus, μ_Ga is to be regarded as an externally imposed quantity. Nevertheless, sensible bounds are set on μ_Ga as the common—and desired—situation is that Ga does not form precipitates in the grown material. Thus, we have $\mu_\mathrm{Ga} < \mu_{\mathrm{Ga,elem}}$, where $\mu_{\mathrm{Ga,elem}}$ is the chemical potential of a Ga atom in the most stable form of elementary gallium at the chosen temperature and pressure conditions. Similarly, we will have for As that $\mu_\mathrm{As} < \mu_{\mathrm{As,elem}}$; and finally, we also have that, if growth is proceeding not very far from equilibrium, the

individual chemical potentials must add up to the known energy of a primitive cell, μ_{GaAs}:

$$\mu_{\mathrm{Ga}} + \mu_{\mathrm{As}} = \mu_{\mathrm{GaAs}} \tag{8}$$

The upper bound on μ_{As} becomes, when combined with Eq. (8), a lower bound for μ_{Ga}:

$$\mu_{\mathrm{Ga,elem}} + \left(\mu_{\mathrm{GaAs}} - \mu_{\mathrm{Ga,elem}} - \mu_{\mathrm{As,elem}}\right) = \mu_{\mathrm{Ga,elem}} + \Delta H_f^{\mathrm{GaAs}} < \mu_{\mathrm{Ga}}, \tag{9}$$

which introduces the formation enthalpy defined as follows:

$$\Delta H_f^{\mathrm{GaAs}} \equiv \mu_{\mathrm{GaAs}} - \left(\mu_{\mathrm{Ga,elem}} + \mu_{\mathrm{As,elem}}\right), \tag{10}$$

which, of course, will be negative for a stable compound. In summary, we have that μ_{Ga} will take some value in the range $\mu_{\mathrm{Ga,elem}} + \Delta H_f^{\mathrm{GaAs}} \leq \mu_{\mathrm{Ga}} \leq \mu_{\mathrm{Ga,elem}}$ under experimental conditions, with the upper (lower) bound corresponding to Ga-rich (Ga-poor) conditions.

2.4 Charged Defects

A point defect may have a natural tendency to release or take electrons from the host material. The most prominent example of this is, of course, dopants in semiconductors. Other technologically important instances of charged defects are the positively charged oxygen vacancies at the core of the resistive switching mechanism in resistive random access memories (RRAMs) [11, 12].

The formation of a charged defect involves, in addition to the exchange of an atomic species with a suitable reservoir, an exchange of a number of electrons with an electron reservoir. The sample under growth will typically act as the electron reservoir, which will be characterized by its corresponding Fermi level μ_e, which in turn can be externally controlled by placing the substrate under some bias.

From these considerations, we would be able to immediately write, for example, the process for the creation of a negatively charged $\mathrm{Si_{As}}$ substitutional defect in GaAs:

$$(\mathrm{GaAs})_{\mathrm{N}} + \mathrm{Si} + \mathrm{e}^- \rightarrow \mathrm{Ga_N As_{N-1} Si^-} + \mathrm{As}, \tag{11}$$

where e^- is the electron taken from the Fermi level μ_e, and the corresponding formation energy

$$E_{\mathrm{form}}^{\mathrm{Si}_{\mathrm{As}}^-} = \left(E_{\mathrm{Si}_{\mathrm{As}}^-} + \mu_{\mathrm{As}}\right) - \left(E_{\mathrm{GaAs}} + \mu_{\mathrm{Si}} + \mu_{\mathrm{e}}\right),$$

and for an arbitrary charge state q

$$E_{\text{form}}^{\text{Si}_{\text{As}}^{\text{q}}} = \left(E_{\text{Si}_{\text{As}}^{\text{q}}} + \mu_{\text{As}}\right) - (E_{\text{GaAs}} + \mu_{\text{Si}}) + q\mu_{\text{e}}. \tag{12}$$

Given that in this case, we have a removal of one constituent atom in a non-elemental host, an addition of an external impurity and a change in the charge of the localized defect/impurity, this is a comprehensive example including all types of processes that can take place in the formation of a charged defect. This example is not only academic, as Si is an amphoteric dopant in GaAs acting as a donor when it substitutes a Ga atom and as an acceptor when substituting an As atom [13].

When all the needed calculations are done—see Sect. 2.5 for technical details that need to be taken into account—results are typically presented as in Fig. 3. There we see the formation energy Eq. (12) plotted for the neutral, $q = 0$, and $q = -1$ charge states, as a function of μ_{e}, ranging from 0 [i.e., the valence band maximum (VBM)] to the energy gap E_{gap} [i.e. the conduction band minimum (CBM)].[1] The thermodynamically stable charge state will be the one with the lowest formation energy at any given μ_{e} (solid line in Fig. 3). The plot has been generated taking μ_{Si} as the total energy of a single Si atom in the gas phase, and the negative value of the formation energy of the Si_{As} substitutional reflects that the Si atom prefers to occupy a substitutional site as opposed to remaining isolated in the gas phase. On the other hand, since it is very reasonable to presume that the displaced As atom will end up at another anion site in the GaAs lattice, the figure is generated with μ_{As} obtained from the energy of an unrelaxed single As vacancy in a 216-atom GaAs supercell. When absolute values of the formation energy are wanted, μ_{Si} and μ_{As} will need to be reevaluated, from knowledge of the precursor molecules in growth and As-rich or As-poor conditions.

Figure 3 provides two important pieces of information. First, the values of the formation energy can be used to calculate the concentration of Si donors that will be incorporated into the GaAs host, with the preferred charge state being the one with the lowest value. From this, it can be deduced that the amount of Si incorporation can be controlled by biasing the substrate, with positive voltages leading to an increased Si@Ga incorporation and, though not shown here, a decreased amount Si@As. So, proper substrate bias is a parameter that can complement precursor concentration when growing structures, a line that has received little attention in the literature. The other important value that can be extracted from Fig. 3 is the Fermi level of the $(+1/0)$ crossover, which will determine the position of the donor level, paramount for predicting the electronic behavior of the structure. The energy at which this crossover takes place is the transition level discussed in Sect. 2.1.

[1] It is common to provide μ_{e} as a fraction of the gap because of the well-known inability of LDA and GGA to provide accurate gaps for semiconductors, see the part about the electronic gap in Sect. 2.5.

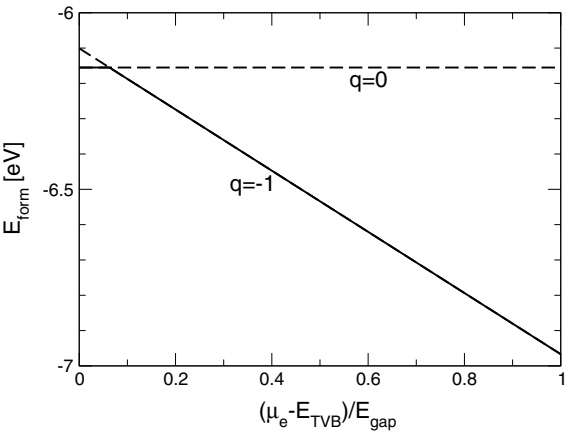

Fig. 3 Formation energy of the $q = 0$ and $q = -1$ states of a Si_{As} substitutional in GaAs, showing its shallow acceptor character. The $(0/-1)$ transition level is found to be at 0.05 eV, to be compared to the experimental value of 0.03 eV [13]

2.5 Computational Aspects

Formation energies of (charged) point defects can be computed, in principle, within any atomistic framework. Commonly, due to the limited system size achievable—a few hundreds of atoms—first-principles calculations are used to provide reference values against which force fields are parametrized in order to tackle larger problems. Here, we focus on first-principles calculations, but many of the issues we will review are also of application to classical interatomic potentials and force fields. We discuss below several of the issues that need to be considered.

Periodic Boundary Conditions

A possible way to classify first-principles codes is according to the underlying basis set, which can be comprised of extended (e.g., plane waves, muffin tin orbitals) or localized (e.g., Gaussians, wavelets, pseudo-atomic orbitals) states. Codes based on plane waves are intrinsically tied to periodic boundary conditions (PBCs), as they make extensive use of discrete Fourier transforms when evaluating Hamiltonian matrix elements. In addition, the basic Poisson solver implemented in most codes, including those using localized basis functions, also works in reciprocal space, again effective imposing PBCs.

Thus, when studying point defects one should make sure that there is no structural nor electrostatic coupling between the defect instances imposed by the PBCs. For the structural part, this is accomplished by the use of a large computational cell and monitoring convergence of the atomic coordinates and dispersion of the impurity bands as the cell size increases. For example, a 128–216 atomic site cell is needed to converge the properties of a single vacancy in bulk Si [14]. The effects of the spurious overlap between the defect wavefunction replicas can be partially corrected by application of model tight-binding (hydrogenic) Hamiltonians for deep (shallow) levels [15–17].

Electrostatic coupling is even harder because of the long-range character of the Coulomb interaction. The general idea is to take a large enough cell so that the high-order multipole moments of the charge perturbation due to the defect do not interact, and then analytically compute the Coulomb energy due to the interactions of the lower order moments—i.e., monopole–monopole and monopole–dipole for charged defects, dipole–dipole for neutral and charged states—and remove it from the energy provided by the first-principles code [18].

Since, for a charged cell, the monopole–monopole contribution to the total energy is divergent, a compensating homogeneous background charge is introduced [18, 19]. Then the different interactions of the point charges are calculated, obtaining a Madelung factor γ [20]. For a simple cubic computational cell, the correction to the total energy becomes [18]

$$E_{\text{aper}} = E_{\text{per}} - \frac{q^2\gamma}{2L\varepsilon} - \frac{2\pi q Q}{3L^3\varepsilon} + O(L^{-5}), \tag{13}$$

where E_{aper} is the sought energy (in Ha) of the system with the single defect, E_{per} is the output of the code including the spurious Coulomb interactions of the defect with its replicas, L is the size of the computational cell, ε is the relative macroscopic static dielectric constant of the material, Q is the quadrupole (second radial) moment of the charge density neutralized with a point charged placed so to have a zero dipole moment and for an arrangement of point charges q in a simple cubic lattice plus a neutralizing jellium [21], $\gamma = 2.837297$.

Potential Alignment

Another issue that must be taken into account is that the zero of the nuclear potentials should be aligned when subtracting the total energies of the defected and the pristine systems. For neutral defects, taking no action should introduce a small error, of the order of the inverse of the number of atoms in the calculation supercell, since many first-principles codes implicitly set the zero of potential to the average of the atomic potentials by setting $V(q = 0) = 0$ when solving the Poisson equation in reciprocal space. On the other hand, the charge associated to charged defects will carry a long Coulomb tail that might significantly alter the average of the total potential over the computational cell.

Freysoldt et al. have introduced a scheme [22, 23] that takes care of both the potential alignment and the closely related spurious interaction between the image charges described in the previous subsection. By modeling the real defect charge distribution with a simple Gaussian or decaying exponential, solving the associated electrostatic problem and then comparing the potential of the model charge distribution to an average of the real potential, they are able to provide a simple scheme with the added benefit that it is easy to verify whether the underlying assumptions—basically the higher order multipoles having decayed and applicability of the bulk dielectric constant—are met.

The Electronic Gap

It is widely known that the local density (LDA) or the generalized gradient (GGA) approximations to the exact—and unknown—density breakfunctional theory (DFT) exchange–correlation functional consistently underpredict the energies of excited states, most notably the gaps of semiconducting and insulating materials [24]. This poses a serious problem when trying to accurately predict the position of transition levels. Is the accuracy different if the level is close to the valence band, or close to the conduction band? Is there a fundamental difference in the accuracy of the first-principles energy of, say, a filled neutral defect state versus its empty positively charged counterpart? Also, the localized character of defect-associated states increases self-interaction effects, which are not corrected in LDA or GGA.

For this reason, quantitative computations should aim to make use of more advanced techniques including some measure of self-interaction correction (SIC). These can be, for example, hybrid functionals, the GW approximation for excited states, or diffusion Monte Carlo (DMC). The Heyd–Scuseria–Ernzerhof (HSE) hybrid functional [25] was found to yield formation energies of Si self-interstitials within 0.25 eV of the DMC value, while GGA underestimated it by $\sim$1 eV and LDA by $\sim$1.5 eV [26]. Also, the performance of HSE and other hybrid functionals and the many-body GW approximation has been thoroughly reviewed in Ref. [27].

Zero-Point Energies

Vibrational degrees of freedom are, of course, important when computing enthalpies of formation and possibly in the determination of the chemical potential of participating species at high temperatures. On the other hand, and for point defects, the only vibrational effects that have an influence in the formation energy are the zero-point energies of each mode of the host material. The common underlying assumption is that the presence of the defect does not significantly alter the energy distribution of the vibrational modes, and thus zero-point energies mostly cancel when carrying out the subtraction in the equation analogous to Eq. (12) for the specific problem.

3 Defects in Nanowires

One of the main attractions of NWs is, of course, the capability they offer to tailor the electronic and optical properties. When the properties of a defect in an NW are of interest, two factors significantly change with respect to the bulk counterpart. One is the reservoir used to define the chemical potential, which should have an effect in systems with a high surface-to-volume ratio; and the other is the altered screening environment, which is important even for NWs with diameters of a few hundreds of nm [28].

3.1 Chemical Potentials

The general expression for the formation energy, $E_{\text{form}}^{D^q}$, of a charged defect D^q in a semiconductor is given by [10]

$$E_{\text{form}}^{D^q} = E_{D^q} - E_{\text{prist}} - \sum n_i \mu_i + q(\varepsilon_v + \mu_e), \tag{14}$$

where E_{D^q} (E_{prist}) is the total energy of the defective (pristine) system, n_i is positive (negative) for atoms of species i added to (removed from) the clean system, μ_i is the chemical potential of species i, and now the chemical potential for electrons μ_e is referred to the energy of the top of the valence band of the clean host, ε_v.

Extending the use of this formalism to 1D nanostructures involves some subtleties related to the definitions of the chemical potential of intrinsic species. For example, when a vacancy is formed in bulk, the removed atom is implicitly assumed to be added to another crystal site; thus, the use of the bulk chemical potential is justified. For a NW, the details of the microscopic process must be carefully observed in order to write a sensible expression for the vacancy (or substitutional) formation energy. We consider a nanoparticle-catalyzed VLS growth mechanism for a SiNW [29]. As the Si atoms are epitaxially added to the NW, very few of them do not occupy their lattice positions, forming a vacancy. However, it is clear from the growth process that the misplaced atoms do not precipitate into a bulk phase, but they rather stay within the NW. Thus, the NW acts as the forming species reservoir for both vacancy/substitutional and, analogously, self-interstitial formation, rendering the use of the bulk chemical potential inadequate.

Having established this, we should now overcome the difficulty that the displaced atom can be added into multiple nonequivalent positions as opposed to bulk, where all lattice sites are equivalent. This induces an ambiguity with respect to the choice of the chemical potential; but even if somehow a preferred site for the displaced atom were selected, the calculation of its contribution to the total energy would be computationally intractable. In addition, if the NW is passivated, it is not clear how many passivating atoms or fraction thereof should be assigned to the displaced atom. Clearly, any attempt to use Eq. (14) directly will not be able to deal with the possibility that the NWs may be surface passivated. We must therefore give up any use of chemical potentials regarding the host system and go to a microscopic treatment.

These issues can be circumvented by considering the formation of n_{Si}^{PC} defects instead of a single defect (see Fig. 4), where n_{Si}^{PC} is the number of silicon atoms in an NW primitive cell (PC). These displaced atoms are then added at the end of the NW to form an extra primitive cell with the needed passivating agents. Thus, for the vacancy/substitutional, we will be studying the energetics of following two final states:

$$n_{Si}^{PC}(Si_n H_m) + n_{Si}^{PC} X + \frac{n_H^{PC}}{2} H_2 \leftrightarrow n_{Si}^{PC}(Si_{n-1} H_m X) + Si_{n_{Si}^{PC}} H_{n_H^{PC}}, \tag{15}$$

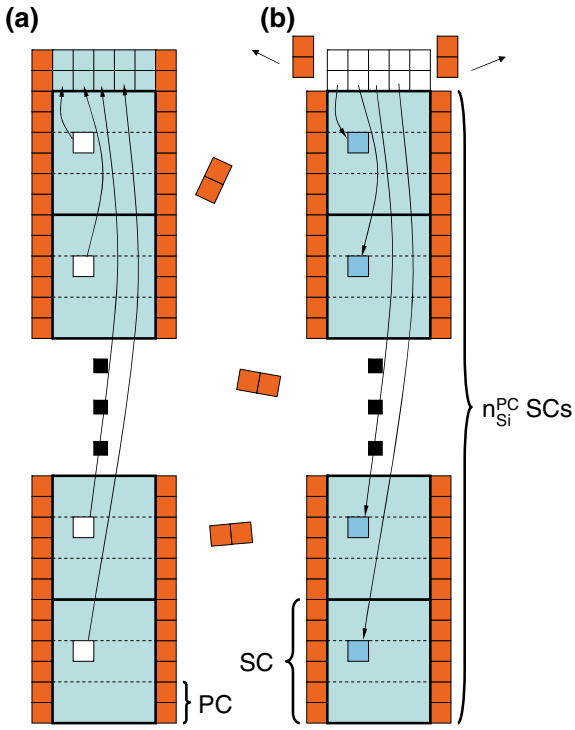

Fig. 4 Construction for dealing with defects in 1D semiconductor structures. **a** Vacancies and substitutionals: we create as many defects as necessary for adding an extra primitive cell to the wire. **b** Self-interstitials: we create as many defects as necessary for removing a primitive cell from the wire. Reprinted with permission from R. Rurali and X. Cartoixà, Nano Lett., **9**, 975–979 (2009), Ref. [30]. Copyright 2009 American Chemical Society

where $Si_n H_m$ denotes the composition of the clean nanowire supercell that will host the defect, and we have assumed that any not used passivating H atoms are released as molecular hydrogen gas.

With the above or analogous constructions, it is easy to see that a general expression for the formation energy of a given type of defect will be

$$E_{\text{form}}^{D^q} = E_{D^q} - N E_{NW}^{PC} - \sum n_X \mu_X - \frac{n_{Si}}{n_{Si}^{PC}} \left(E_{NW}^{PC} - n_H^{PC} \frac{E_{H_2}}{2} \right) + q(\varepsilon_v + \mu_e), \tag{16}$$

where N is the number of primitive cells used in the clean system calculation, E_{NW}^{PC} is the energy of the NW clean primitive cell, satisfying $E_{\text{prist}} = N E_{NW}^{PC}$, n_X is the number of non-host atoms of species X added to the clean system, μ_X is their chemical potential, n_{Si} is the number of Si atoms involved in the defect formation (e.g., $+1$ for a self-interstitial), n_H^{PC} is the number of passivating atoms in an NW primitive cell (taken to be hydrogens) and $E_{H_2}/2$ is the corresponding chemical potential. All quantities appearing in Eq. (16) are now well defined and easily extracted from a total energy calculation. Note as well that, in the bulk limit, $n_{Si}^{PC} \to \infty$ and Eq. (14) is recovered.

3.2 *Madelung Energies for Anisotropic Materials and Dielectric Screening*

As mentioned in Sect. 2.5, in charged defects with PBCs there is a spurious interaction energy between the defect replicas that must be corrected for. In the Makov–Payne scheme [18], the Madelung energy of a lattice of point charges immersed in a neutralizing background is scaled by the dielectric constant of the bulk host material in order to compute the spurious energy. For charged defects in NWs, and given that a NW is an obviously anisotropic system, its dielectric tensor will in general have different components along the diagonal, and low-symmetry NW growth directions might even introduce off-diagonal components. Thus, the expressions for the correction of the spurious energies must allow for a possible tensorial character of ε. We worked this out in Ref. [30], obtaining for the Madelung constant in the general case

$$\begin{aligned}\alpha = &\sum_{\mathbf{R}_i} \frac{1}{\sqrt{\det \varepsilon}} \frac{\operatorname{erfc}\left(\eta\sqrt{\mathbf{R}_i \cdot \varepsilon^{-1} \cdot \mathbf{R}_i}\right)}{\sqrt{\mathbf{R}_i \cdot \varepsilon^{-1} \cdot \mathbf{R}_i}} \\ &+ \sum_{\mathbf{G}_i} \frac{4\pi}{V_c} \frac{\exp(\mathbf{G}_i \cdot \varepsilon \cdot \mathbf{G}_i / 4\eta^2)}{\mathbf{G}_i \cdot \varepsilon \cdot \mathbf{G}_i} - \frac{2\eta}{\sqrt{\pi \det \varepsilon}} - \frac{\pi}{V_c \eta^2},\end{aligned} \tag{17}$$

where the sum over $\mathbf{R}_i$ ($\mathbf{G}_i$) extends over all vectors of the direct (reciprocal) lattice except for zero, η is a suitably chosen convergence factor, and V_c is the volume of the primitive cell, with the expression for the correction to leading order becoming

$$E_{\text{aper}} = E_{\text{per}} + \frac{q^2 \alpha}{2} + O(L^{-3}). \tag{18}$$

Focusing now on the dielectric screening, one must look closely at the different interactions taking place in order to make a sensible choice of ε. A first thought would be to use, for example, the modified Penn model [31] in order to obtain an approximation to the value of the dielectric constant for directions perpendicular to the growth axis. This would be indeed the correct approach if we were to study the physics of excitons in the NW. However, it must be kept in mind that two images corresponding to different instances of the NW will interact mainly through vacuum if enough buffer space is left. It is then reasonable to expect that the perpendicular components of the dielectric tensor, $\varepsilon_\perp = \varepsilon_{xx} = \varepsilon_{yy}$ will have a value of 1.

For the longitudinal direction of the NW, the discussion can start with the long-range behavior of the electrostatic interaction energy between two point charges inside a dielectric cylinder, but even this situation is not completely clear. Lugo et al. [33] provide expressions based on the image charge method, but a closer analysis indicates that their expressions are valid for a dielectric sphere, rather than a cylinder. Based on physical arguments, Diarra et al. argued [32] that, in a 1D system, screening is completely inefficient at distances z large compared to the cylinder radius R, and that the effective ϵ is thus one (see Fig. 5 for a graphical depiction of their argument

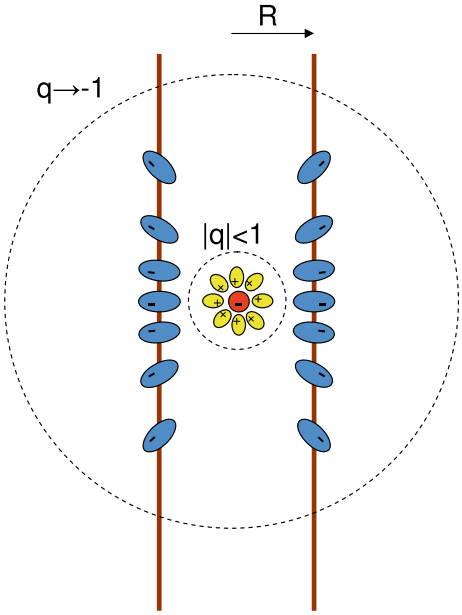

Fig. 5 Graphical depiction of Diarra et al.'s argument [32] for the inefficiency of dielectric screening in nanowires at axial distances much larger than the wire radius. A negative test charge (red sphere) is placed inside the NW. The electron cloud is repelled until it hits the surface (blue ellipses), leaving behind a positive background next to the test charge (yellow ellipses). A Gauss sphere with radius less than the NW radius probes a total interior charge of less than unity, while a Gauss sphere with radius much larger than the NW radius will probe an interior charge close to 1. Thus, points with $r < R$ see a (screened) effective charge $|q| < 1$, while for $z \gg R$ the effective charge is unscreened, $q \to -1$

and an explanation). Bányai et al. [34] and Slachmuylders and coworkers [35] have provided analytical expressions for the interaction energy in the general case, but these are in series form, and the asymptotic behavior is not apparent.

We obtained asymptotic expressions in Ref. [28] for the electrostatic interaction energy of two charges placed at the axis of an NW, separated distance z. For the case of an SiNW, the effective ε they experience is plotted in Fig. 6. We see how, in agreement with Diarra et al.'s [32] argument, the effective $\varepsilon_\parallel = \varepsilon_{zz}$ quickly drops when $z \gtrsim 2R$ to below 1, to then slowly recover to the asymptotic $\varepsilon_\parallel(z \to \infty) = 1$ value.

3.3 Al Substitutional in a Thin SiNW

We put together all these considerations to study the case of an Al substitutional in an Si nanowire (SiNW) [28, 30], which in bulk acts as an acceptor with an activation energy $E_{(0/-)} = 69$ meV [6]. The SiNW is grown along the [110] direction, with a

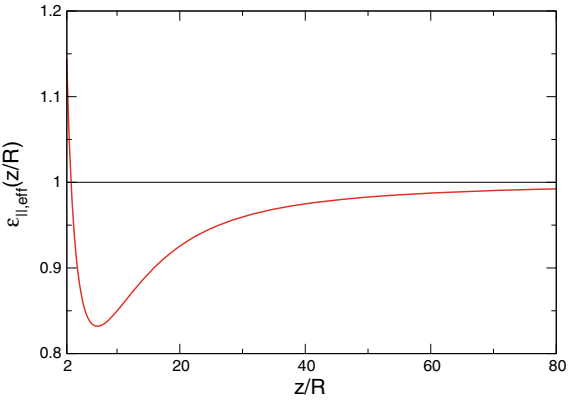

Fig. 6 Effective dielectric constant experienced by two point charges placed at the axis of a cylindrical silicon NW, a distance z apart

diameter of 1.0 nm, and the optimized length of the primitive cell along the wire axis is found to be 3.943 Å.

First, a study is carried out to find the required supercell size in the wire periodic direction, L_z, to obtain converged activation energies. We considered supercells made from 4 to 16 primitive cells, corresponding to a separation between the impurity and its closest replicas along the wire axis from ∼16 to ∼63 Å. The results are summarized in Fig. 7, where we plot the (Madelung corrected) formation energy E_{form} of the $\mathrm{Al}^{0}_{\mathrm{Si}}$ and $\mathrm{Al}^{-1}_{\mathrm{Si}}$ defects—the formation energies are evaluated at the top of the valence band (i.e., electron Fermi level μ_e set to zero) of the undoped wire, E_{VBM}, and $q\mu_e$ must be added to obtain the formation energies at different μ_e's and the transition level $(0/-)$. We use the definition of E_{form} for a 1D system given in Eq. (16). The transition level is simply obtained as follows:

$$E(0/-) = E(\mathrm{Al}^{-1}_{\mathrm{Si}}) - E(\mathrm{Al}^{0}_{\mathrm{Si}}) - E_{\mathrm{VBM}}, \tag{19}$$

where $E(\mathrm{Al}^{0}_{\mathrm{Si}})$ and $E(\mathrm{Al}^{-1}_{\mathrm{Si}})$ are the total energy of the system with a neutral and a charged Al defect, respectively.

As can be seen in Fig. 7a, the formation energy of the neutral defect is readily obtained with a supercell made of 5 primitive cells (amounting to a spacing of 24 Å between adjacent defects), whereas the ionized defect converges more slowly and 15–16 primitive cells are needed. Note that the $1/L_z$ behavior of the convergence is not completely removed with our Madelung-like correction, due to the previously mentioned point that the effective dielectric constant has a z dependence.

Figure 7b displays the transition level referred to the valence band edge (black squares), whose convergence is limited by the slowest term in Eq. (19), $E(\mathrm{Al}^{-1}_{\mathrm{Si}})$ in this case. In the same panel, we show the same quantity calculated without the Madelung correction (red triangles), converging more slowly and to an incorrect value. The reason for this is that a lateral supercell size of $L_x = L_y = 100$ Å was used for the L_z convergence study but, as seen in Fig. 8, this is not enough for

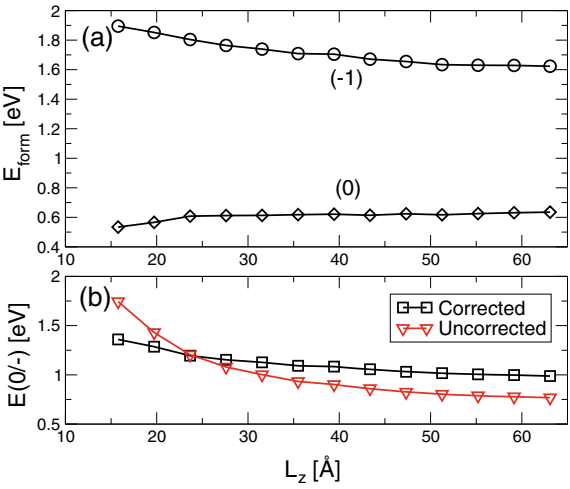

Fig. 7 **a** Formation energy E_F for the neutral (0) and charged (-1) impurity (Madelung corrected), and **b** ionization energy $E(0/-)$ as a function of the supercell size along the axial direction L_z. Supercells made of 4 to 16-PC are considered. Lines are a guide to the eye. Reprinted figure with permission from [R. Rurali et al., Phys. Rev. B, **81**, 235304 (2010)], Ref. [28]. Copyright 2010 by the American Physical Society

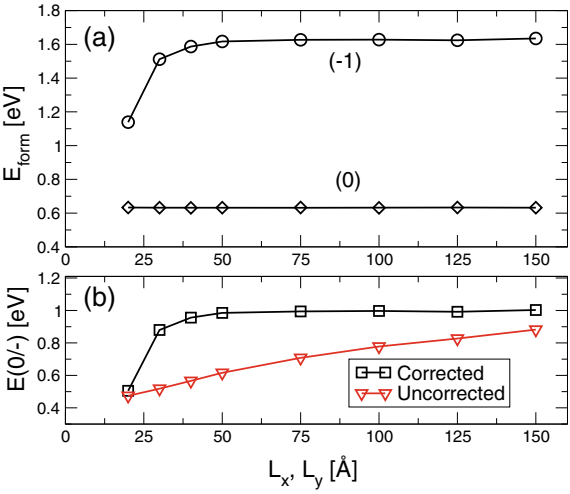

Fig. 8 **a** Formation energy E_F for the neutral (0) and charged (-1) impurity (Madelung corrected), and **b** ionization energy $E(0/-)$ as a function of the supercell size along the directions L_x, L_y perpendicular to the wire axis. As the diameter of the wire is 1 nm the vacuum buffer thickness amounts to $L_x - 10$ Å. Lines are a guide to the eye. Reprinted figure with permission from [R. Rurali et al., Phys. Rev. B, **81**, 235304 (2010)], Ref. [28]. Copyright 2010 by the American Physical Society

convergence in the uncorrected case. On the other hand, application of the correction in Eq. (18) readily provides converged magnitudes for a lateral separation as low as 50 Å.

We finally plot the formation energies for the Si bulk and thin NW case as a function of μ_e in Fig. 9. We observe, as in the convergence studies, that the transition level for the NW lies at energies much higher than the bulk, which renders substitutional doping in thin NWs unachievable. This is due to a combination of quantum confinement and dielectric mismatch effects on the excitonic wavefunction [35]. We also see that raising the chemical potential, i.e., charging the growth

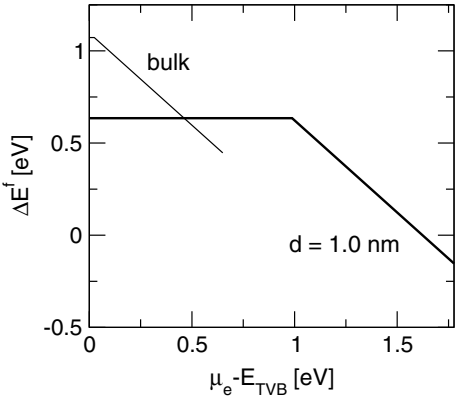

Fig. 9 Formation energy of an Al substitutional (Al_{Si}) point defect in [110] SiNW with a diameter of 1.0 nm and bulk. The Al_{Si} is at the center of the wire. The electron chemical potential μ_e spans the bandgap, which is taken to be the GGA value under the Perdew–Burke–Ernzerhof parametrization [36] for bulk

substrate negatively, will favor the incorporation of Al substutionals into the NW. Substrate bias has been considered in the context of physical and chemical vapor deposition [37, 38], but it seems that the influence of the substrate bias in the catalyst consumption/incorporation has received less attention.

4 Conclusions

In the last 10 years, the first-principles prediction of the properties of charged defects in bulk semiconductors has become a mature subject. For nanowires, technical difficulties related to the highly anisotropic character of an NW with periodic boundary conditions, together with the decrease of the effectiveness of screening prevent the straightforward application of the bulk methods. Here, we have reviewed how a few of these issues can be partially remedied, but there is still room for improvement up to the level of accuracy that the bulk methods can provide. With our capabilities so far, we have shown that standard substitutional doping yields too high activation energies for ultrathin NWs and that substrate bias should have a strong effect on the amount of Al incorporation into an Al-catalyzed VSS-grown NW, and is expected to have a similar effect in related systems.

Acknowledgements We acknowledge financial support by Spain's Ministerio de Economía, Industria y Competitividad (MINECO) under the Severo Ochoa Centers of Excellence Program under Grant No. SEV-2015-0496, and by the Generalitat de Catalunya under Grant No. 2017 SGR 1506.

References

1. W. Bullis, Solid-State Electron. **9**(2), 143 (1966). https://doi.org/10.1016/0038-1101(66)90085-2. http://www.sciencedirect.com/science/article/pii/0038110166900852
2. L. Forbes, Gold Bull. **10**(2), 49 (1977). https://doi.org/10.1007/BF03215429
3. M.W. Doherty, N.B. Manson, P. Delaney, F. Jelezko, J. Wrachtrup, L.C. Hollenberg, Phys. Rep. **528**(1), 1 (2013). https://doi.org/10.1016/j.physrep.2013.02.001. http://www.sciencedirect.com/science/article/pii/S0370157313000562.Thenitrogen-vacancy-colour-centre-in-diamond
4. C. Freysoldt, B. Grabowski, T. Hickel, J. Neugebauer, G. Kresse, A. Janotti, C.G. Van de Walle, Rev. Mod. Phys. **86**, 253 (2014). https://doi.org/10.1103/RevModPhys.86.253
5. G.D. Watkins, J.R. Troxell, Phys. Rev. Lett. **44**, 593 (1980). https://doi.org/10.1103/PhysRevLett.44.593
6. O.E. Madelung, *Semiconductors: Basic Data*, 2nd edn. (Springer-Verlag, Berlin, Germany, 1996)
7. E.G. Seebauer, M.C. Kratzer, *Charged Semiconductor Defects: Structure, Thermodynamics and Diffusion*, 1st edn. Engineering Materials and Processes (Springer-Verlag, London, 2009). https://doi.org/10.1007/978-1-84882-059-3
8. D.V. Lang, J. Appl. Phys. **45**(7), 3023 (1974). https://doi.org/10.1063/1.1663719
9. A. Walsh, A.A. Sokol, C.R.A. Catlow, Phys. Rev. B **83**, 224105 (2011). https://doi.org/10.1103/PhysRevB.83.224105
10. S.B. Zhang, J.E. Northrup, Phys. Rev. Lett. **67**, 2339 (1991)
11. R. Waser, M. Aono, Nat. Mater. **6**, 833 (2007). https://doi.org/10.1038/nmat2023
12. R. Waser, R. Dittmann, G. Staikov, K. Szot, Adv. Mater. **21**(25–26), 2632 (2009). https://doi.org/10.1002/adma.200900375
13. D.T.J. Hurle, J. Appl. Phys. **85**(10), 6957 (1999). https://doi.org/10.1063/1.370506
14. M.J. Puska, S. Pöykkö, M. Pesola, R.M. Nieminen, Phys. Rev. B **58**, 1318 (1998). https://doi.org/10.1103/PhysRevB.58.1318
15. G. Makov, R. Shah, M.C. Payne, Phys. Rev. B **53**, 15513 (1996). https://doi.org/10.1103/PhysRevB.53.15513
16. C.G. Van de Walle, J. Neugebauer, J. Appl. Phys. **95**(8), 3851 (2004). https://doi.org/10.1063/1.1682673
17. S. Lany, A. Zunger, Phys. Rev. B **78**, 235104 (2008). https://doi.org/10.1103/PhysRevB.78.235104
18. G. Makov, M.C. Payne, Phys. Rev. B **51**(7), 4014 (1995)
19. M. Leslie, N.J. Gillan, J. Phys. C: Solid State Phys. **18**(5), 973 (1985)
20. J.M. Ziman, *Principles of the Theory of Solids*, 2nd edn. (Cambridge University Press, Cambridge, UK, 1972)
21. P.P. Ewald, Annalen der Physik **369**(3), 253 (1921). https://doi.org/10.1002/andp.19213690304
22. C. Freysoldt, J. Neugebauer, C.G. Van de Walle, Phys. Rev. Lett. **102**, 016402 (2009). https://doi.org/10.1103/PhysRevLett.102.016402
23. C. Freysoldt, J. Neugebauer, C.G. Van de Walle, Phys. Status Solidi (b) **248**(5), 1067 (2011). https://doi.org/10.1002/pssb.201046289
24. J.P. Perdew, Int. J. Quantum Chem. **28**(S19), 497 (1985). https://doi.org/10.1002/qua.560280846
25. J. Heyd, G.E. Scuseria, M. Ernzerhof, J. Chem. Phys. **118**(18), 8207 (2003). https://doi.org/10.1063/1.1564060
26. E.R. Batista, J. Heyd, R.G. Hennig, B.P. Uberuaga, R.L. Martin, G.E. Scuseria, C.J. Umrigar, J.W. Wilkins, Phys. Rev. B **74**, 121102 (2006). https://doi.org/10.1103/PhysRevB.74.121102
27. W. Chen, A. Pasquarello, J. Phys. Condens. Matter **27**(13), 133202 (2015). https://doi.org/10.1088/0953-8984/27/13/133202
28. R. Rurali, M. Palummo, X. Cartoixà, Phys. Rev. B **81**(23), 235304 (2010). https://doi.org/10.1103/PhysRevB.81.235304

29. Y. Wang, V. Schmidt, S. Senz, U. Gösele, Nat. Nanotech. **1**(3), 186 (2006)
30. R. Rurali, X. Cartoixà, Nano Lett. **9**, 975 (2009). https://doi.org/10.1021/nl802847p
31. R. Tsu, D. Babić, L. Ioriatti, J. Appl. Phys. **82**(3), 1327 (1997). https://doi.org/10.1063/1.365762
32. M. Diarra, Y.M. Niquet, C. Delerue, G. Allan, Phys. Rev. B **75**(4), 045301 (2007). https://doi.org/10.1103/PhysRevB.75.045301
33. J.E. Lugo, J. Tagüeña-Martínez, J.A. del Río, Solid State Commun. **117**(9), 555 (2001). https://doi.org/10.1016/S0038-1098(00)00505-6
34. L. Bányai, I. Galbraith, C. Ell, H. Haug, Phys. Rev. B **36**(11), 6099 (1987). https://doi.org/10.1103/PhysRevB.36.6099
35. A.F. Slachmuylders, B. Partoens, W. Magnus, F.M. Peeters, Phys. Rev. B **74**(23), 235321 (2006). https://doi.org/10.1103/PhysRevB.74.235321
36. J.P. Perdew, K. Burke, M. Ernzerhof, Phys. Rev. Lett. **77**(18), 3865 (1996)
37. V. Kulikovsky, V. Vorlíček, P. Boháč, M. Stranyánek, R. Čtvrtlík, A. Kurdyumov, L. Jastrabik, Surf. Coat. Technol. **202**(9), 1738 (2008). https://doi.org/10.1016/j.surfcoat.2007.07.029
38. J. Ball, H.S. Reehal, Cryst. Eng. Comm. **18**, 2913 (2016). https://doi.org/10.1039/C6CE00403B

Applications

Nanowire Field-Effect Transistors

Junichi Motohisa and Shinjiro Hara

Abstract Vertical field-effect transistors (FETs) using semiconductor nanowires (NWs) formed by bottom-up approach are expected to outperform conventional planar transistors owing to their compatibility with surrounding-gate (SG) structures, possible heterogeneous integration with various kinds of materials including Si, and so on. In this chapter, basics, current status, and the possibility of vertical NW-FETs are described. We first introduce the importance of SG geometry from a viewpoint of the device application as well as the general advantage of vertical NW-FETs. Next, the fabrication of the NWs, where the site controllability is important for FET applications, are described with the main emphasis on the selective-area (SA) growth. Then, the current status and some of the issues for further development of their performances are explained. Some of the new directions including tunnel FETs (TFETs) and spin FETs to go beyond the classical limit of the FET will also be described before the summary of this chapter.

Keywords Semiconductor nanowire · Vertical field-effect transistor · Surrounding-gate structure · Selective-area growth · Tunnel FET · Spin FET

1 Introduction

When the understanding of physics in the two-dimensional electron system realized in the inversion layer of Si MOSFET (metal-oxide-semiconductor field-effect transistor) and semiconductor heterostructures were advancing in the 1970s and 1980s [1],

J. Motohisa (✉)
Graduate School of Information Science and Technology and Research Center for Integrated Quantum Electronics, Hokkaido University, North 14 West 9, Sapporo 060-0814, Japan
e-mail: motohisa@ist.hokudai.ac.jp

S. Hara
Research Center for Integrated Quantum Electronics, Hokkaido University, North 13 West 8, Sapporo 060-0813, Japan
e-mail: hara@rciqe.hokudai.ac.jp

© Springer Nature Singapore Pte Ltd. 2021

N. Fukata and R. Rurali (eds.), *Fundamental Properties of Semiconductor Nanowires*,
https://doi.org/10.1007/978-981-15-9050-4_9

interest in the one-dimensional electron system was initiated by a theoretical prediction on the suppression of scattering and possibility of ultrahigh mobility in quantum wires in 1980 [2]. In the same period, one of the topics in low-temperature physics was the electron transport in metal thin films or MOSFET with narrow channels from the viewpoint of Anderson localization or electron-electron interactions [3]. These narrow channel structures were fabricated by utilizing lithographic and etching techniques from much larger structures, and such "top-down" technique still continues to be developed with the advancement of Si-CMOS (complementary-MOS) technology. These two research interests merged and lead to a quest for physics, properties, and device applications of low-dimensional nanostructures such as quantum wires and quantum dots. To realize the system free from disorder, technology to realize them utilizing crystal growth was also developed as well as the top-down lithographic technique. In the 1990s, Hiruma and co-workers [4] shed light on the semiconductor whiskers with diameter less than 100 nm formed by vapor-liquid-solid (VLS) mechanism [5] as a novel electronic material to realize one-dimensional quantum wires. This pioneering research on thin one-dimensional structures formed with "bottom-up" technique has bloomed up as a research on nanowires (NWs) ever since the 2000s. It is noted that the research is supported not only by the advancement of the technology to realize NWs with various forms and variety of materials, but also the proposal and demonstration of various kinds of device applications.

Here in this chapter, we would like to review and outlook applications of NWs for field-effect transistors (FETs). The present electronics and society are supported by the advancement of integrated circuits (ICs) based on Si CMOS technology, and their advancement is brought forth by a simple principle; the smaller the transistors become, the faster they become, thus, the more denser and the more functional the ICs are. The guideline for shrinking the transistor size in the channel length is established as scaling rule, and the density of the transistors keeps increasing following the Moore's law. However, the advancement of the Si CMOS technology is facing a grand challenge owing to the physical limit in their size and material property of Si. In addition, along with the continuing requirements for high-performance ICs, reduction of power dissipation is also required to reduce the heat from the ICs and to be effective for energy-saving society. Various remedies have already been developed and introduced in the current Si CMOS technology, and FETs using vertical NWs are one of the candidates to be incorporated in the future Si CMOS technology for its continuous advancement.

Our focus in this chapter is mainly on the vertical FETs using NWs formed by the bottom-up approach, since they can fully utilize the advantage of NWs formed by the bottom-up approach. We also describe mainly on FETs made of III–V semiconductor NWs, which have higher electron mobility than Si and suitable for a replacement of channel material with Si. In Sect. 2, we summarize the advantages of vertical FETs utilizing NWs formed by bottom-up approaches. In particular, advantages of SG structures is explained in detail. In Sect. 3, fabrication of NWs and vertical NW-FETs are shown. We mainly explain selective-area (SA) metal-organic vapor phase epitaxy (MOVPE) for the growth of NWs, because the other chapters in this book are devoted to some extent to the NWs grown via vapor-liquid-solid (VLS) mechanism,

and an excellent site controllability of SA-grown NWs, which is important for FET applications. Next, we review the current status of vertical NW-FETs and some of the issues for further development of their performances are explained in Sect. 4. Before summarizing this chapter in Sect. 6, some of the new directions, for instance, tunneling FETs (TFETs) and spin FETs, to go beyond the classical limit of the FETs, and new materials and structures in Sect. 5, since the advantage of NWs is indeed in their shape, allowing the integration with various kind of materials and in a hope to giving birth to unexpected developments.

2 Basics of NW-FETs

2.1 Issues and Requirements for FETs in Modern Electronics

As we mentioned in the introduction, advancement of the performance of FETs following the scaling is facing various limits, and one of the grand challenges of FETs in the modern electronics is to reduce the power consumption without sacrificing their performance. This is particularly important for large-scale integrated circuits (LSIs) for digital logic circuit applications. The on- and off-state of MOSFETs can be switched by applying the gate voltage V_{GS} either V_{on} or V_{off} and $V_{off} < V_{th} < V_{on}$ for n-channel MOSFET, where V_{th} is the threshold voltage. In logic circuits, V_{off} is usually zero and V_{on} is equal to power supply voltage V_{DD} of the circuit. In this case, the power dissipation of the logic circuit is conceptually expressed as

$$P = [\eta I_{on} V_{on} + (1 - \eta) I_{off} V_{DD}] nf = [\eta C V_{DD}^2 + (1 - \eta) I_{off} V_{DD}] nf \qquad (1)$$

Here, I_{on} and I_{off} are the on-state and off-state current, respectively, C represents a capacitor of the circuit and is represented by a sum (per one FET) of the gate capacitance of an FET and parasitic capacitance, n is the number of FETs, f is the clock frequency, and η is a fraction of on-time of the FETs. The first term in the bracket represent the power dissipation in the on-state, and the second is that in the off-state. Note that on-state current I_{on} does not appear explicitly in the final form of this equation, but large I_{on} is important to reduce delay times (or transit time), which are given by $\tau = C V_{on}/I_{on}$. Equation (1) clearly shows that the reduction of supply voltage V_{DD} is of primary importance to reduce the power dissipation. The scaling, particularly, constant-field scaling is thus effective to minimize the increase of power consumption when the device size becomes smaller. The second term or the off-state power dissipation, however, becomes more and more important with the decrease of V_{DD}. If the switching is purely binary, I_{off} can be zero with input voltage of V_{off}, but finite current, called subthreshold current, flows at the off-state under $V_{GS} < V_{th}$, as shown in the red line of Fig. 1a. The characteristics of FETs at V_{GS} around V_{th} is characterized by subthreshold slope S, which is defined as

$$S = \frac{dV_{GS}}{d\log_{10} I_{DS}} . \quad (2)$$

This is a measure of the abruptness of switching in FETs and is limited by the thermal distribution of the carriers in conventional FETs, as explained later (Eq. (3)). Since S is finite and the logic swing $V_{on} - V_{off}$ is limited with $V_{on} = V_{DD}$ and $V_{off} = 0$, off-state current cannot be reduced without the cost of decreased on-state current, and decrease of I_{on} leads to the longer switching delay τ and low speed of the ICs.

Besides, the shorter channel length is important to achieve high-speed FETs since the transit time of the carrier through the channel determines its switching speed, but short channel length devices pose a number of problems, such as short channel effect, velocity saturation, high-field effect, and so on. In particular, the short channel effect, which represents the decrease of threshold voltage V_{th} in FETs with short channel length, is detrimental in reducing the power consumption. The short channel effect originates from the extension of the depletion layer from the source and drain into the channel region beneath the gate. It gives rise to the modification of surface potential at the semiconductor-insulator interface, thus, the electrostatic control of the channel potential via gate voltage becomes ineffective in short channel devices as compared with the long-channel devices. This results in an increase of S, as schematically shown in a blue line in Fig. 1a. In addition, shorter channel geometry results in the stronger influence of the field from the source and the drains than that from the gate, leading to the drain-induced barrier lowering (DIBL). This further reduces the effective threshold voltages with the drain bias V_{DS} and increase the drain current I_{DS}. As a result, I_{off} increases, as schematically shown in the blue dashed line in Fig. 1a at large V_{DS}, making an additional difficulty in decreasing V_{DD} and power consumption in ultra-scaled devices. Thus, to simultaneously achieve large I_{on} and small I_{off}, it is required to realize FET which are immune to the short channel effect and to maintain S as small as possible. Even more, it is demanded to realize smaller S than the classical limit in ultimately scaled FETs towards energy efficient ICs [6].

The requirements of FETs for the application to high-frequency analog amplifier are somewhat different from those for low-voltage logic. In general, source-common amplifiers (Fig. 1c) are used for high-power amplifiers with high gain and the operation of the circuits is analyzed with small signal analysis of the amplifier. The maximum achievable gain of the source-common amplifiers is called intrinsic gain and is given by g_m/g_D, where g_m is the transconductance ($=dI_{DS}/dV_{GS}$) and g_D is the drain conductance ($=dI_{DS}/dV_{DS}$), as shown in Fig. 1b (also, see Appendix 2 for detail). Note that g_D corresponds to the slope in the I_{DS}-V_{DS} characteristics. To achieve high gain, the transistors should be operated in the saturation region (namely, $V_{DS} > V_{GS} - V_{th} \equiv V_{DS,sat}$ where $V_{DS,sat}$ is a saturation drain voltage) to have large g_m and small g_D. In ideal MOSFETs, g_D is 0 in the saturation regions, but becomes finite due to the channel length modulation, which causes due to the expansion of depletion region from the drain into the channel. The channel length modulation becomes more important as the shrinkage of channel length. In addition, if the short channel effect sets in, the saturation behavior of the FETs becomes further weak, giving rise to the decrease of g_D as shown in the blue line in Fig. 1b. This results in

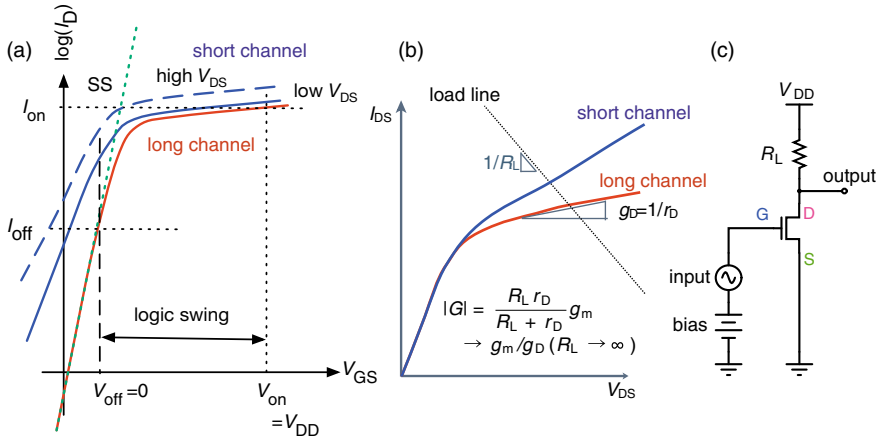

Fig. 1 Drain current characteristics of FETs and effect associated with short channel effect. Drain current I_{DS} is plotted as a function of gate voltage V_{GS} and shown in **a** a semi-logarithmic scale and **b** a linear scale. The characteristics of the long and short channel FETs are shown by red and blue lines, respectively. Increase of subthreshold slope S is detrimental in low-power digital logic application and increase of output drain conductance g_D reduces the gain of which is important analog amplifier application. **c** Circuit of a common-source amplifier

the reduction of the intrinsic gain. Since short gate channel device is required for fast and high-frequency operation, the inappropriate electrostatic control of the channel by the gate is a fatal problem to realize high-gain amplifier.

2.2 *Short Channel Effect in NW-FETs*

The requirements for modern FETs described in the previous section can largely be fulfilled by the introduction of multi-gate geometry [7, 8]. In conventional MOSFETs (Fig. 2a), S is expressed as [9]

$$S = \ln 10 \frac{k_B T}{q} \left(1 + \frac{C_D}{C_{OX}}\right) = 2.30 \frac{k_B T}{q} \left(1 + \frac{C_D}{C_{OX}}\right), \tag{3}$$

where k_B is the Boltzmann constant, q the elementary charge, T the temperature, C_{OX} the gate oxide capacitance, and C_D is the depletion capacitance in MOS structure. For cylindrical NWs with radius R (=$d/2$ where d is the diameter), C_{OX} per unit length along the NWs is given by

$$C_{OX} = \frac{2\pi \varepsilon_{OX} \varepsilon_0}{\ln\left(1 + \frac{t_{OX}}{R}\right)}, \tag{4}$$

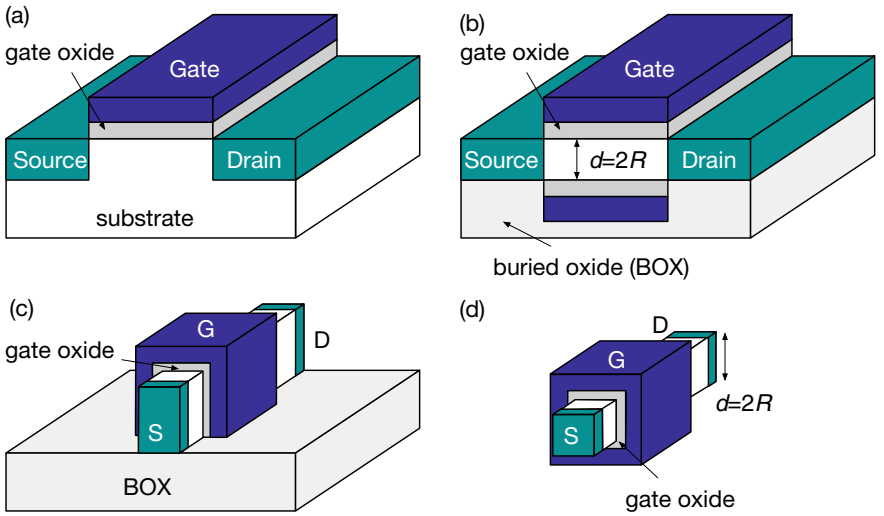

Fig. 2 Structure of planar MOSFET (**a**) and examples of multi-gate FETs. **b** double-gate MOSFET, **c** FINFET, and **d** NW SG MOSFET

where t_{OX} and ε_{OX} are the thickness and the dielectric constant of the gate oxide, respectively. If the substrate doping is sufficiently small, or if the thickness of the channel is sufficiently thinner than the depletion thickness as in the case of well-designed dual-gate (DG) MOSFET (Fig. 2b), the volume inversion [10] occurs and C_D can be negligible. In this case, S is very close to the classical limit of 60 mV/dec at room temperature. This ideal situation is also expected for FINFET (Fig. 2c or tri-gate structures, in which gate acts the channel from the three directions, or NWs with surrounding-gate (SG) or gate-all-around (GAA) geometry, in which gates wrap around the channel region of the NWs (Fig. 2d), if the width of the fin or the radius of the NWs is much thinner than the thickness of the depletion layer. More importantly, in multi-gate structures, the electrostatic control of the channel by the gate becomes much more effective owing simply to the geometrical reason, and FETs with the multi-gate geometry is more immune to the short channel effect as compared with single-gate FETs.

For a more quantitative understanding, the immunity for the short channel effect of the FETs is explained by the scaling theory and the concept of the natural length λ, which is a length measure for the electrostatic control of the channel by the gate, and the structure or materials with shorter λ is more immune to the short channel effect. For example, natural length λ_2 for the DG MOSFET with channel thickness $d = 2R$ is given by [11, 12]

$$\lambda_2 = \sqrt{\frac{\varepsilon_S}{\varepsilon_{OX}}\left(1 + \frac{\varepsilon_{OX} R}{2\varepsilon_S t_{OX}}\right) R t_{OX}} \tag{5}$$

Here, $\varepsilon_{\mathrm{OX}}$ is the dielectric constant of the gate oxide, ε_S is the dielectric constant of the channel semiconductor, and t_{OX} is the thickness of the gate oxide. On the other hand, for cylindrical SG NW-FETs with radius R (or the diameter $d = 2R$), it is given by [13]

$$\begin{aligned}\lambda_3 &= \sqrt{\frac{2\varepsilon_S R^2 \ln_2\left(1+\frac{t_{\mathrm{OX}}}{R}\right)+\varepsilon_{\mathrm{OX}}R^2}{4\varepsilon_{\mathrm{OX}}}} \\ &\sim \sqrt{\frac{\varepsilon_{\mathrm{S}}}{2\varepsilon_{\mathrm{OX}}}\left(1+\frac{\varepsilon_{\mathrm{OX}}R}{2\varepsilon_{\mathrm{S}}t_{\mathrm{OX}}}\right)Rt_{\mathrm{OX}}} \\ &= \lambda_2/\sqrt{2}\end{aligned} \tag{6}$$

The natural length for NW MOSFETs and DG MOSFETs for with InAs channel are shown in Fig. 3a for $\varepsilon_{OX} = 20\varepsilon_0$ and $t_{\mathrm{OX}} = 3$ nm. To maintain low S and small DIBL, the effective channel length L_{eff} is desired to satisfy $L_{\mathrm{eff}} \leq 5\lambda$ [13]. Therefore, NW-FETs are about a factor of 1.4 immune to the short channel effect as compared with the double-gate FETs with the same characteristic dimension. It also indicates that we can use thicker NWs with as compared with DG MOSFET under the same natural length, which is beneficial to avoid mobility degradation due to roughness scattering or to accommodate harmful quantum effects, which give rise to the increase of effective mass originating from nonparabolicity and confinement and decrease of channel charges due to the increase of quantized energy.

Figure 3b–d also show the roll-off of threshold voltage, subthreshold slope, and DIBL in SG NW-FETs with NW radius R of 5 and 15 nm calculate using an analytical model [14]. Calculation parameters are listed in Table 1. The natural lengths are 3.3 and 8.5 nm for $R = 5$ and 15 nm, respectively. All the plot shows that the immunity in the short channel effect in NW MOSFET and it is better for thinner NWs.

2.3 Modeling of NW-FETs

In this section, we show calculation results of modeling for the characteristics of NW-FETs to show and discuss their capability for high-performance logic applications. The performance of the NW-FETs for RF applications is discussed in Ref. [15]. The models for I–V characteristics explained here are a continuous model for long-channel MOSFETs with undoped NWs in SG structure [16] and a model for ballistic NW-FETs [15, 17–19]. The details of the models are given in Appendix 1. Before showing the detail of the calculation results, it is important to remind limitations of these models. The former is a classical model for the long-channel FETs and the short channel effect and velocity saturation is not considered. The roll-off of threshold voltages, increase of subthreshold slopes, and DIBL in short channel FETs can be considered in a different model described in Sect. 2.2, but cannot be included in the explicit modeling. Quantum effects, which are thought to be important for thin NWs

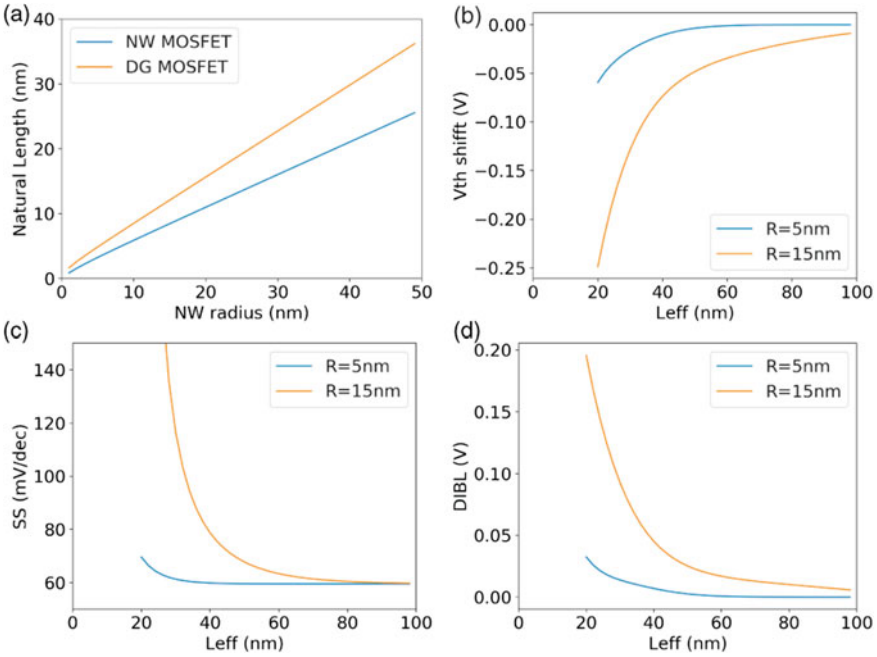

Fig. 3 **a** Natural length in NW MOSFET and DG MOSFET with InAs channel. **b** Threshold voltage roll-off, **c** subthreshold slope, and **d** DIBL in NW-FETs with NW diameter R of 5 and 15 nm. Drain voltage V_{DS} is 0.5 V. DIBL is defined as the difference of threshold voltage for $V_{DS} = 0.05$ and 0.5 V

with diameter d less than about 30 nm, are also not taken into account. The quantum confinement raises the bottom of the conduction band energy and limits the available number of states for the electrons. Thus, it is thought to overestimate the carrier density and drain current density in thin NWs as well as induces the positive shift of the threshold voltage. In the model of ballistic MOSFET, increase of subthreshold slopes and DIBL can be taken into account and appropriate analysis by comparison with experiments is possible. It is also possible to include the quantum effects and band nonparabolicity [15, 19]. However, the ballistic transport is expected only for very short channel devices and regarded as an upper bound for the drain current; In addition, thick NWs are hard to take into account the quantum effects appropriately because of too many numbers of confined states. The limited number of confined states in thin NWs should also limit the total carrier density in the channel, but it is not considered here. Readers interested in much advanced modeling should refer to Ref. [20].

The calculation was carried out for n-channel InAs NW-FETs. For classical continuous model, circular InAs NWs with diameter d is used as a channel of the SG MOSFET. In the model for a ballistic FETs, the InAs NW MOSFET has a rectangular cross section of NW size d with the same EOT (effective oxide thickness), and

Table 1 Calculation parameters for the characteristics of NW-FETs using classical and ballistic model

Effective mass m^*	$0.023\,m_e$
Band gap energy E_G	0.36 eV
Intrinsic carrier concentration n_i	10^{15} cm^{-3}
Mobility μ	1000 cm^2/Vs
Gate length L_G	1 μm
Dielectric constant of InAs ε_S	15.15
Dielectric constant of gate oxide ε_{OX}	20
Gate oxide thickness t_{OX}	3 nm
Temperature T	300 K

quantum effects and band nonparabolicity are considered following Lind [15]. Deterioration of subthreshold slopes and DIBL are not considered (namely, $\alpha_G = 1$ and $\alpha_D = 0$ in Eq. (38)). In both models, the drain voltages are set at $V_{DS} = 0.5\,\text{V} \equiv V_{DD}$ and the threshold voltage are set so that the off current I_{off} at $V_{GS} = V_{off} = 0$ is set at 100 nm/μm (normalized with the circumference of the NW). Parameters for the calculation are summarized in Table 1.

Figure 4a, b show transfer characteristics for $d = 30$ nm in linear and semi-logarithmic scales, respectively. Figure 4c shows the maximum of the drain current I_{DS} for $V_{DS} = V_{GS} = 0.5(=V_{DD})$ plotted as a function of the NW size d. The I_{DS} in the classical model can be much larger if the gate length L_G is shorter and mobility μ is larger, but both the model predicts a similar magnitude of I_{DS}. Based on the present modeling, it is reasonable to conclude that thin NWs are more capable of high current drivability for low-voltage logic application. As described in Sect. 4, the largest on current reported to date for NW-FETs is 555 and 360 μA/μm for a top-down lateral [21] and a bottom-up vertical NW-FET [22], respectively, at $V_{DS} = V_{on} - V_{off} = 0.5$ V with $I_{off} = 100$ nA/μm, and they are thought to be very close to the ballistic limit.

2.4 Advantages of Vertical NW-FETs with Bottom-Up NWs

The concept of vertical surrounding-gate (SG) transistors in the framework of Si-CMOS technology was first proposed and demonstrated by Matsuoka and co-workers [23], where they noted their high-packing ability, superior subthreshold characteristics, small substrate bias effect, and high reliability. Superior subthreshold characteristics owing to their immunity in the short channel effect of SG NW-FETs is already described in the previous sections. For the high-packing density, it is described in Ref. [23] that the occupied area of the CMOS inverter was predicted to be shrunk to 50% of that using planar transistors. More recently, Veloso et al. [24, 25] estimated an

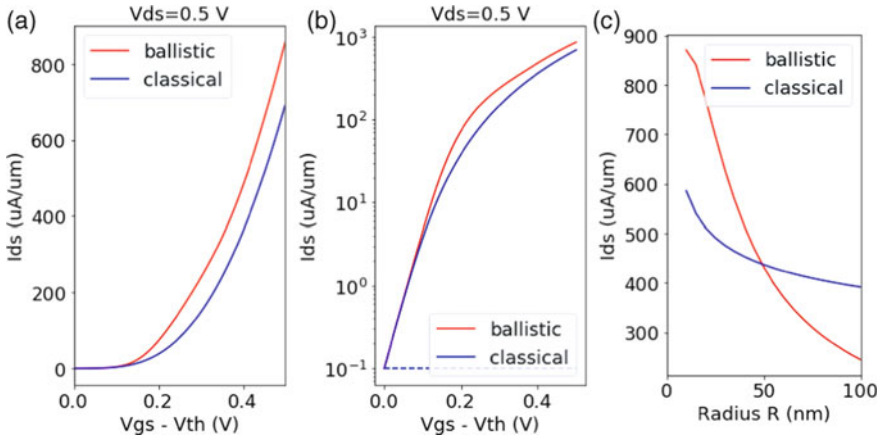

Fig. 4 **a**, **b** Calculated transfer characteristics of NW-FETs with size $d = 30$ nm. **c** Size dependence of maximum drain current I_{DS} at $V_{DS} = V_{GS} = 0.5$ V in NW-FETs

area reduction of 20–30% in 6-transistor SRAM (static random access memory) cells built with vertical NW-FETs as compared with those built with lateral NW-FETs in 5 nm node, and discuss the resulting advantage in the margin for the size tuning of memory cells on their performance. For these reasons, NW-FETs with SG structure is strongly demanded for the low-power ICs and high-frequency circuits, and are the one of the promising candidates as FETs for future ICs, as picked up in the IRDS (IEEE International Roadmap for Devices and Systems) roadmaps [26], and FETs utilizing NW structures, formed either by top-down or bottom-up approaches are investigated by many groups.

The main subject of this chapter is to introduce the capability of NW-FETs with NWs formed by bottom-up approaches, so, before concluding this section, we summarize the advantages of NW-FETs utilizing epitaxially grown NWs in addition to the advantages of NW-FETs with vertical SG structure discussed so far.

1. Vertical geometry allows easy implementation of surrounding-gate (SG) or gate-all around (GAA) structures, which is possible to suppress short channel effect and improve subthreshold characteristics owing to the strong electrostatic coupling of the channel and the gates.
2. Small footprint of NW allows high-density integration of FETs, whose size is limited by the area of the electrode. Integration could further be put forward if stacking of NW-FETs in the vertical direction becomes possible.
3. Epitaxially grown NWs are free from process-induced fabrication damages.
4. Small footprint also makes us free from constraints in the lattice-matching issues in the epitaxial growth and enables us the growth of NWs on highly lattice mismatched substrates or on dissimilar materials. This is particularly important in heterogeneous integration of FETs made of high-mobility III–V or Ge NWs with Si-MOSFET in CMOS technology on Si platforms.

5. Various kinds of heterostructures can be realized simply by controlling the material supply and growth conditions. The heterostructures include axial (vertical) and radial (lateral or core-shell) structures, and substrates and NWs with dissimilar materials just mentioned in (4). It gives additional freedom for the selection of materials and helps introducing new structures to improve the performance of FETs.
6. For GaN and related materials, NWs are surrounded by non-polar sidewall surfaces, that is, channels are free from strain or polarization-induced charges. This is important in realizing normally-off devices.

The advantages (1) and (2) are listed for completeness, and the other items in the list will be further explained in the following sections.

3 Fabrication of Nanowire Vertical FETs

3.1 Nanowire Growth

3.1.1 General Issues

The bottom-up NWs discussed here are grown mainly by utilizing metal-organic vapor phase epitaxy (MOVPE) or molecular beam epitaxy (MBE) with catalyst-assisted vapor-liquid-solid (VLS) mechanism or selective area (SA) epitaxially growth. In the case of an application for transistors, site control of NWs is important. The position of the NWs can be controlled by the position of catalyst in VLS growth or the mask opening in SA growth, and it is possible by patterning the catalyst or mask using the lithographic technique. The diameter of NWs is determined by the size of the catalyst or the mask opening. Thus, to form NWs with diameters around or less than 100 nm, the electron beam lithography is commonly used to define such fine patterns. It is also important to realize vertical NWs on the substrate. This is particularly important for III–V NWs, which are polar in nature, to grow on non-polar substrates, i.e., Si and Ge, as described later.

3.1.2 Selective-Area Growth of NWs

Since details of VLS-grown NWs are given in separate sections in this book, outline of SA growth of NWs is described below. Figure 5a shows a procedure for the selective area growth of NWs [27]. It is noted that it is a conventional epitaxial growth process for the growth of III–V and III-nitride semiconductors except for the use of the masked substrates. In MOVPE, SiO_2 or SiN is mainly used as masks and their typical thickness is 20–30 nm, Fig. 5b shows an SEM image of the mask fabricated by deposition of SiO_2, electron beam lithography, and etching of SiO_2. The materials we use for the growth of III–V NWs in SA-MOVPE are trimethylgallium (TMGa),

trimethylindium (TMIn), trimethylaluminum (TMAl) for group III precursors and arsine (AsH_3) and tertiarybutylphosphine (TBP) for group V materials.

There are two key issues for the successful SA growth of NWs. One is the selectivity of the growth of opening areas and masked areas. For ideal SA growth, nucleation and deposition on the mask should be eliminated. Generally, this can be achieved more easily in SA-MOVPE than in SA-MBE. This is because the growth process involves decomposition and chemical reaction of metal-organic molecules of group III sources on the surface in MOVPE (group V species have higher vapor pressure and usually growth is done under excess group V materials supply), and if the surface energy is sufficiently low on the masked area, such reactions cannot be promoted on the mask. In MBE, elemental group III atoms are supplied, and they deposited on the whole substrate. Thus, for successful SA growth, group III atoms deposited on the mask should diffuse to the opening area or thermally evaporated. This requires relatively high growth temperature, but too high-temperature results in the desorption of atoms on the opening area. For this reason, SA-MBE of III–V material was believed to be hard without using special growth sequences or techniques, such reported in Refs. [28, 29]. However, successful growth of InGaAs [30] and GaN [31] NWs are reported in SA-MBE, and this is thought to be owing to the relatively high growth temperature for NW growth as compared with their standard growth temperatures, enabling appropriate surface diffusion and re-evaporation of Ga and In.

The other is the direction of the growth. That is, it should proceed in the direction normal to the substrate and growth of tilt NWs should be minimized. As mentioned, the SA growth relies on the conventional epitaxial growth mechanism, so it means the growth rate in the vertical direction should be much faster than other directions. Thus, understanding the nature of the crystal growth and the choice of the appropriate orientation of the substrate is important. For GaAs, InAs and their alloys (InGaAs), NWs can be grown on (111)B-oriented substrates in SA-MOVPE when the growth temperature T_G is high and partial pressures of AsH_3 is low. This is because the growth in the [111]B directions can be promoted while the growth rate of the sidewall {110} surface is suppressed under these conditions, and we can obtain NWs of hexagonal column structures surrounded by $\{\bar{1}10\}$ facets perpendicular to the substrates. On the other hand, if the growth temperature becomes lower or AsH_3 partial pressure becomes higher, the growth rate of the (111)B surface is reduced and that of the {110} surface is enhanced, and results in the lateral or radial growth. The dependence of the growth rate on the growth condition is explained by the formation of arsenic trimer on (111)B surface, which formed due to excess As and prevent the adsorption of Ga, while both adsorption of Ga and As is required but binding of group V atoms are less strong in As-deficient conditions on $\{1\bar{1}0\}$ surfaces. Note that this growth condition dependence of the surface can be used to control the radial and axial growth and to form core-shell heterostructure NWs, as described later. Detail mechanisms of the SA-MOVPE growth of GaAs NWs with the atomistic model are described in Refs. [32–35]. Similarly, high-temperature and low TBP partial pressure is required for SA-MOVPE of InP NWs, but vertical NWs grow on (111)A oriented substrates [36–39]. It is noted that the InP NWs exhibit transition of crystal structures between wurtzite (WZ) and zincblende (ZB) depending on the growth conditions, as discussed

in Refs. [40–42]. GaN exhibits strong anisotropy in the growth rate, and GaN NWs spontaneously grow in the [0001] direction. This can be explained, in the first order, by the stability of non-polar sidewall surfaces (M-plane ($\{1\bar{1}00\}$) or A-plane ($\{11\bar{2}0\}$)) of wurtzite crystals, where stable adsorption of both Ga and N is required to promote the growth, and result in the lower sticking coefficient of Ga on those surfaces than on (0001) [43].

In reality, the size of the NWs was determined by the amount of the lateral growth as well as the size of the mask opening. The growth of high-temperature and low group V material supply ratio is thus important to realize small NWs. This growth condition in turn makes it difficult to form nuclei inside the mask opening when the opening size becomes very small. By reducing the size of the mask opening and optimizing growth conditions, or introducing two-step growth, the NW diameter down to 20–30 nm was realized by SA-MOVPE, as shown in Fig. 5d [44]. Template-assisted selective epitaxy, developed by the IBM group [45–47], is a variation of SA growth technique and is an alternative method to suppress the unwanted radial growth of NWs and to obtain vertical NWs on (001) Si.

3.1.3 III–V NWs on Si Substrates

As we described in Sect. 2.4, one of the advantages of the bottom-up NWs is the capability of heterogeneous integration, going beyond the constraints in the lattice constant and crystal structures. This is because the growth is restricted in areas with size less than a few hundreds or few tens of nanometers, and it allows strain relaxation in the lateral direction. This leads to the enhancement of critical layer thickness in the heteroepitaxial growth [48]. Its representing example is the direct heteroepitaxial growth of III–V NWs on Si substrates, and it is demonstrated that misfit dislocations are nearly confined at the interface between the substrate and NWs, and NWs free from misfit dislocations have been realized both in VLS and SA growth technique. Tomioka et al. [49] indeed showed that the density of misfit dislocations can be reduced from the values expected from the lattice mismatch in thin NWs.

For the growth of III–V semiconductors on Si, the other issue to be noted is "polar on non-polar" growth. As explained in the previous section, GaAs, InAs, and InGaAs NWs grow in the [111]B direction. On the other hand, Si (111) surface has four equivalent ⟨111⟩ directions, only one of which is vertical to the surface. Therefore, NWs can be formed randomly in the slanted direction as well as vertical directions, or results in the formation of antiphase boundaries and ill-shaped NWs such as hillocks. To tackle this problem, Tomioka et al. [50] explored procedures to replace topmost Si atoms of the (111) surface with As atoms to form As-incorporated (or As-terminated) Si^{3+} surface prior to the NW growth in SA-MOVPE. This method is firstly used for InAs NWs on Si, and later GaAs [51] and InGaAs [52, 53] NWs. Kim et al. [54] and Yao et al. [35] also succeeded in the growth of InGaAs and GaAs NWs on Si in SA-MOVPE, respectively. Their approaches seem to be simpler and detail of the recipe for the optimum growth seems to depend on the alloy composition in (InGa)As, but it seems that common and important ingredients are the high-temperature (∼900 °C)

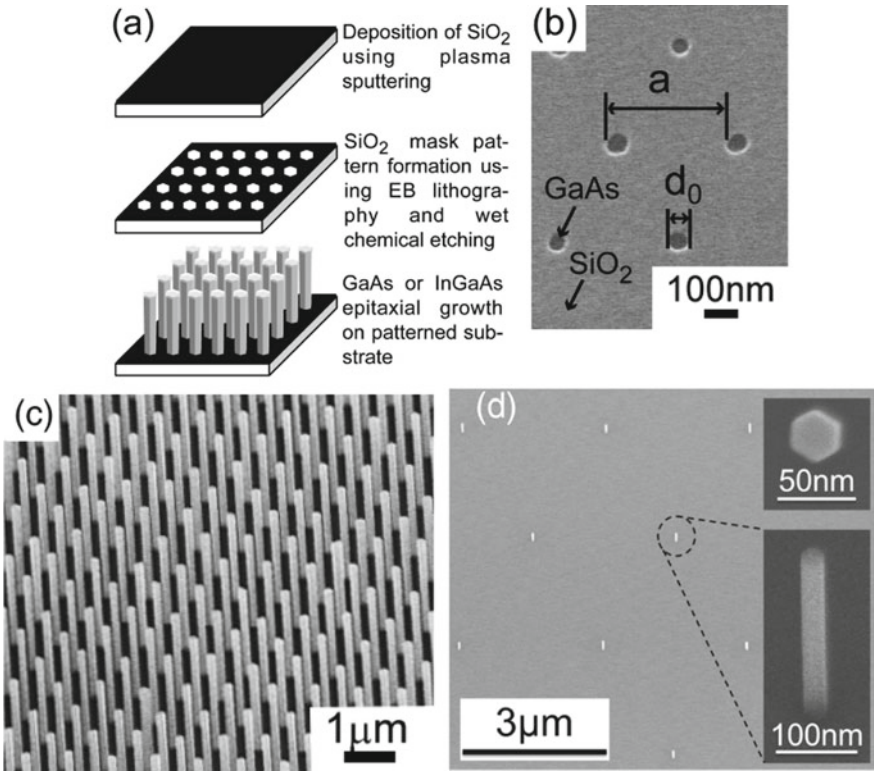

Fig. 5 **a** Growth process of NWs by selective-area (SA) growth. **b** Typical mask pattern for SA growth. **c** SEM image of GaAs NWs. Reproduced with permission from Ref. [27]. Copyright (2005) The American Institute of Physics. **d** SEM image of InGaAs NW with diameter about 30 nm. Reproduced with permission from Ref. [44]. Copyright (2013) Japan Society of Applied Physics

thermal cleaning in H_2 ambient and exposure to AsH_3 at the temperature close to the optimum growth temperature of NWs.

On the other hand, vertical InAs and InGaAs NWs on Si (111) are reported by Kollbmüller and co-workers in SA-MBE [30, 55, 56]. Interestingly, they achieved a very high yield of vertical NWs on Si, although it does not seem that some special treatment was carried out to mimic the polar surface of (111)B in the growth chamber, except for the removal of the native oxide in the mask opening before the loading of the substrate into MBE.

III–V NW growth on Si substrates was attempted by Au-catalyzed [57] or self-catalyzed [58, 59] growth at the early stage of the NW research. The challenge here is to achieve both high yield vertical growth and site controlled growth simultaneously. Attempts to optimize the growth as well as to disclose the fundamental growth mechanism are being carried out [60–65].

Another type of approach to integrate position controlled III–V NWs on Si is called template-assisted selective epitaxy (TASE), [45, 46] mentioned in Sect. 3.1.2. In TASE, the growth is guided and proceeds to fill SiO_2 tube with sub-micron diameter formed on Si substrates. This approach is effective to realize vertical NWs independent of the orientation of the Si substrates and to suppress parasitic lateral growth. Borg et al. demonstrated NWs with diameter down to 25 nm by selective growth using MOVPE [45], and the same IBM group demonstrated vertical tunnel FET [47]. A similar approach is also reported by Vukajlovic-Plestina et al. [66] using MBE. Finally, the Lund group utilizes site controlled InAs NWs on Si (111) substrate with epitaxially grown thin layer of InAs for FET application [67]. Though these indirect integration schemes require an additional step to grow InAs prior to the patterning of the substrate, following advantages can be pointed out if one reminds of realistic FET applications; (1) at the patterning of the epitaxial layer, wiring of NW-FETs, which is necessary for circuit application, can also be performed prior to the formation of NWs, and (2) large contact resistance between Si and InAs can be eliminated.

3.1.4 Growth of Heterostructured NWs

As described in Sect. 2.4, one of the important advantage of bottom-up NWs is an ability to realize heterostructures with abrupt interfaces. The NWs can have two types of heterostructures, namely, axial and radial (or core-shell) heterostructures. The axial structures can be realized simply by changing the material supply, while optimum growth of radial heterostructures requires more fine control of growth conditions. In SA-MOVPE, lower temperature and higher group V partial pressure are applied for the both for GaAs- and InP-based radial heterostructures. On the other hand in catalyst-assisted NWs, the epitaxial growth on the sidewalls of the NWs proceeds in a similar manner with conventional layer growth. Thus, as similar to the case of SA growth, lower temperature and higher group V material supply rate are usually employed for III–V NWs. To invoke radial growth, catalysts are generally removed, and in some cases, dopant gasses are supplied to change the preferential direction of the growth.

One of the examples for radial heterostructure NWs grown by SA-MOVPE are shown in Fig. 6 [68]. Here, InAs and InP shells are grown on the sidewall of InP NWs and core-multishell NWs are formed. In this material system, it was found to result sometimes in the uncontrollable bending of NWs or in the formation of InAs three-dimensional islands via Stranski-Krastanow (SK) growth mode owing to the lattice mismatch. To achieve uniform growth of InAs on the sidewalls of InP NWs, the growth temperature and growth rate was set lower than that for InP NWs. The outer InP shell is also grown under lower temperature and higher TBP pressure to promote the radial growth of InP. The details of the growth conditions are described in Refs. [68, 69].

For application in FETs, core-shell heterostructures are expected to be effective in FETs in order to reduce the interface density between the semiconductor surface

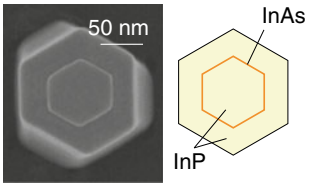

Fig. 6 SEM cross-sectional image of an InP/InAs/InP core-multishell NW observed after anisotropic dry etching and stain etching and its schematic illustration. Reproduced with permission from Ref. [68]. Copyright (2010) American Institute of Physics

and gate dielectrics. Besides, axial heterostructures are used to stack vertically the different channel materials or to introduce barriers in the channel [70]. The use of heterostructures in NW-FETs is described later in detail.

3.1.5 Doping in NWs

Intentional impurity doping is one of the critical step in the fabrication of various devices. High doping is required for the contact regions to reduce the parasitic resistance, while the introduction of the small amount of impurity is enough to control the threshold voltage of FETs. It also was shown to impact on the performance of tunnel FET (TFET) [71].

Usually, doping is carried out during the growth for III–V and III-nitride NWs. It is, however, very complicated because the growth dynamics of NWs itself is far more complicated than in the case of the growth of planar layer. Particularly in MOVPE growth, doping involves the vapor phase diffusion and chemical decomposition of dopant precursors and their interaction with main growth species and the semiconductor surface. Thus, doping in NWs raises some issues which are absent in the planar layer growth. The strongest effect is its influence in the growth dynamics. In VLS growth in MOVPE reactor, a drastic change of the axial and radial growth rate of NWs are confirmed depending on the type of dopant atoms and precursors (see, for instance, Ref. [72]); higher doping usually results in the promotion of the radial or shell growth, and are not ideal for NWs and formation of low-resistance contacts selectively on the top of the NWs. Doping is also known to introduce transition of crystal structures or change of the formation rate of ZB and WZ structures, as observed in Zn-doped InP NWs both grown in the VLS [73] and SA-MOVPE [74]. Tomioka et al. [49] furthermore pointed out that a small amount of impurity could result in a heavy doping in NWs with a small diameter and doping with continuous dopant supply could result in too high doping levels. Although some attempts are made by utilizing a multi-terminal measurement of the NW resistivity, a lack of reliable characterization method for the doping level and dopant activation efficiency makes the problems harder to clarify.

Under these circumstances, we here briefly show a method to overcome some of these problems carried out in SA-MOVPE. Tomioka and co-workers proposed a pulse

doping scheme in SA-MOVPE, in which dopant gas was supplied with intermission time. By introducing pulse doping of Zn in InAs, they succeeded in controlling the threshold voltage of FET (TFET) [49] by compensating unintentionally incorporated carbon donors. They furthermore demonstrated that pulse doping of Sn is effective to suppress the radial growth in InGaAs NWs and to obtain low series resistance between the contact and active region of the device for n-type layer [75].

3.1.6 Growth of Semiconductor/magnetic Material Hybrid Structures

As described in Sect. 3.1.4, one of the most important advantages of bottom-up NWs is an ability to create heterojunctions with atomically abrupt heterointerfaces in the semiconducting NWs. This is also the case in the selective-area growth of heterojunction NWs between magnetic metals and semiconductors. In addition to the application of semiconducting heterojunction NWs to vertical FETs discussed in previous sections, an extremely wide variety of future device applications of semiconducting heterojunction NWs has been reported in a large number of review articles. In particular, Yang et al. introduced semiconducting NW technologies in one of the most famous review articles [76]. However, the latest review articles on semiconducting NWs are mostly focusing on an introduction to a specific topic related to a specific materials property and/or device application. For example, progress in photovoltaic and energy applications [77–79], photonic and optical device applications [80, 81], electrical properties in the terahertz (THz) regime [82], biological and medical applications [83–85], and electronic device characteristics [15, 86] have been reported individually. The tendency of the latest review articles to focus on specific applications prominently indicates increasing expectations in now well established semiconducting NW technologies to deliver results of industrial importance. Only one of these review articles, however, discusses the electrical spin-injection and spin-transport in semiconducting NWs [87]. Thus, the attractive outlook of semiconducting NW devices in the context of magneto-nanoelectronic or nanospintronic device applications has, to the best of the authors' knowledge, not been reviewed yet.

Activities to create diluted magnetic semiconductors (DMS) [88] and the heterojunction between ferromagnetic metals and III–V compound semiconductors have recently attracted great attention in semiconductor nanospintronics research owing to possible additional functionalities that can be added to current semiconducting devices and integrated circuits. Among these approaches, granular hybrid structures, in which ferromagnetic nanoclusters (NCs) are embedded into III–V compound semiconducting layers, are one of the most attractive materials candidates for future nanospintronic devices due to their large magnetoresistance (MR) effects [89–93] and a comparatively long spin-relaxation time [94, 95]. Nanospintronic devices have been produced on semiconducting substrates mostly by conventional top-down fabrication techniques after low-temperature MBE of these materials. Various kinds of NWs based on the heterojunction between ferromagnetic metals and III–V compound semiconductors or DMS [96] have recently been synthesized to produce NW spintronic devices using several techniques based on the conventional VLS method

as a bottom-up fabrication approach, e.g., GaMnAs NWs [97, 98], GaAs/GaMnAs core-shell NWs, [99, 100] MnAs nanoparticles on InAs [101] and GaAs [102] NWs, GaAs/MnAs core-shell NWs [103, 104], GaN-related DMS NWs [96, 105, 106], heterojunction NWs between MnGe alloys and Ge [107, 108] and between MnSi alloys and Si [109], as well as vertical multiple-segment AuGe/Ge NWs [110]. However, it is also crucial to recognize, avoid, and overcome possible problems arising in the growth process which may limit the performance of current and future nanoelectronic and photonic NW devices discussed in other sections of this book chapter. One challenge, in particular when using conventional VLS methods in the NW growth, is to avoid metal impurities in the NW material originating from the metal catalysts employed. Therefore, the authors have developed a hybridization technique to grow ferromagnetic MnAs NCs [111] on vertical free-standing semiconducting NW templates grown by the authors' catalyst-free SA-MOVPE technique, which is introduced in previous subsections in this book chapter, in the research field of semiconductor nanospintronics, and reported on the formation and characterizations of MnAs NC/GaAs hybrid NWs [112, 113]. The SA-MOVPE process developed in the previous study essentially allows us to directly synthesize single-crystal ferromagnetic MnAs NCs on a semiconducting substrate [111]. The NCs formed by the SA-MOVPE process can be used as promising building blocks for fabricating future nanospintronic devices as they exhibit large angle-dependent MR effects [114, 115]. However, even when using the authors' hybridization techniques, it still remains challenging to control the crystal orientations of the MnAs NCs on a ⟨111⟩ B-oriented GaAs NW template [112, 113] and to obtain vertical heterojunction MnAs/GaAs NWs with atomically abrupt heterointerfaces between MnAs and GaAs. It is likely that the difficulties in forming vertical heterojunction NWs are mainly due to the rather stable crystal facet of the c-plane, i.e., the {0001}-oriented surface, of hexagonal NiAs-type MnAs NCs grown by SA-MOVPE [111, 112]. Such vertical heterojunctions would enable the spin-polarized carrier injection into semiconducting NW channels. [116] The authors believe that the combination of a magnetic tunnel junction electrode, e.g., CoFeB/MgO [117] and CoFe/MgO [118], and vertical ferromagnetic/semiconducting heterojunction NWs with atomically abrupt heterointerfaces [108] would possibly overcome major obstacles of conductance mismatch and poor controllability of the heterointerface formation in current spin-MOSFETs [119]. In addition, the {111}B-oriented semiconducting NW channels may also have a great advantage for enhancing spin lifetime in the channels of spin-MOSFETs [120].

Thus, in this subsection, the authors introduce recent technological developments for the synthesis of high-quality vertical ferromagnetic MnAs NC/semiconducting InAs heterojunction NWs with atomically abrupt heterointerfaces on semiconducting substrates utilizing the so-called endotaxy of MnAs NCs after the SA-MOVPE of host InAs NW templates. After the structural characterizations by transmission electron microscopy (TEM), the authors show a preliminary result of the magnetotransport properties of a single MnAs/InAs heterojunction NW. The temperature dependence of MR effects is investigated. The content of this subsection is mostly based on that of the previous articles [121–125].

Due to several reasons described above, in the current study, the InAs NW arrays were used as a template, which were fabricated hetero-epitaxially on GaAs {111}B substrates by utilizing the catalyst-free SA-MOVPE process for creating high-quality vertical ferromagnetic MnAs NC/semiconducting InAs heterojunction NWs [121–125]. The experimental details in this subsection are described in the previous articles [121–124]. Again, at first, the initial circular openings, which were arranged and defined in SiO_2 thin films by electron beam lithography, are prepared. There were typically two types of the observed diameter, d_0, of the initial circular openings: one was approximately 80–90 nm and the other was approximately 110–140 nm. The distances between the initial circular openings, or the pitch, were 0.5, 1.0, and 3.0 μm on the substrates. The SiO_2 thin films, whose typical thicknesses were estimated to be approximately 20–30 nm, were deposited on GaAs {111}B wafers by plasma sputtering. The growth temperature, T_g, and the growth time, t, for the InAs NWs were 580 °C and 30 min, respectively. Conventional organometallic and hydride sources, i.e., TMIn and AsH_3, diluted in H_2 carrier gas, were used in all the growth experiments. The estimated partial pressures of TMIn and AsH_3 diluted in H_2 carrier gas were 4.9×10^{-7} [126] and 1.3×10^{-4} atm, respectively, for the SA-MOVPE of undoped InAs NW templates. The phenomenon of the "endotaxy" of MnAs in InAs was utilized for MnAs NC growth after InAs NW growth. Endotaxy is associated with a diffusion process that leads to the redistribution of substances [127], i.e., MnAs NCs in a host crystal, which is the InAs NWs in this study, and the formation of new stable phases. This is the key technique for forming ferromagnetic NCs "inside" semiconducting NWs grown by SA-MOVPE. The authors have observed that a large number of single-crystal MnAs NCs grow in GaAs NW templates even without any supply of AsH_3 source gas as the result of endotaxy [112, 113]. During the endotaxy of MnAs NCs into the host InAs NW templates in this study, the authors only supplied the organometallic source of $(CH_3C_5H_4)_2Mn$ diluted in H_2 carrier gas. The T_g for the MnAs NCs was set to 580 °C, and the t was 1 min. The estimated partial pressure of $(CH_3C_5H_4)_2Mn$ was 3.0×10^{-6} atm. During the decrease in temperature during the purging process after the MnAs NC growth, AsH_3 diluted in H_2 carrier gas was supplied. Structural characterization in terms of the size and position of the MnAs NCs and the InAs NW templates was conducted by secondary electron microscopy (SEM) using a scanning electron microscope. Cross-sectional TEM was also used for obtaining lattice images of NCs and NWs. Detailed structural characterizations, such as the analyses of crystal structures and solid compositions of the NCs and NWs, were performed by electron diffraction (ED) measurements and energy dispersive X-ray (EDX) spectroscopy in combination with TEM, using an electron beam with a spot diameter of about 1 nm. All the TEM analyses in this subsection, including the ED measurements and EDX spectroscopy, were performed by a professional characterization company of Toray Research Center, Inc. [128].

A template structure of InAs NW arrays was grown by SA-MOVPE at first to fabricate vertical ferromagnetic MnAs NC/semiconducting InAs heterojunction NWs. Figure 7a shows a typical bird's-eye view obtained by SEM of the template array of InAs NWs before the MnAs NC endotaxy [121]. Prior to the SA-MOVPE, initial circular openings with d_0 of 110–140 nm and a pitch of 1.0 μm were prepared in

the SiO_2 thin films. The diameter of the resulting InAs NWs shown in Fig. 7a is estimated to be approximately 150 nm and their height is about 1.5 μm. For initial circular openings with d_0 between 80 and 90 nm, typically InAs NWs with a diameter of approximately 120 nm are grown. The inset in Fig. 7a is a highly magnified top view of one of the InAs NWs. The InAs NWs reveal a hexagonal prismatic shape surrounded by six $\{0\bar{1}1\}$ crystal facets and grow in the ⟨111⟩B direction on the GaAs {111}B substrates. The top of the NWs reveals that flat {111}B crystal facets surrounded by tilted $\{\bar{1}\bar{1}0\}$ ones are formed during the growth. Figure 7b shows typical ferromagnetic MnAs NC/semiconducting InAs hybrid NWs grown at a T_g of 580 °C for 1 min [121]. The NCs are formed on the top {111}B crystal facets of the InAs NWs, and also some additional NCs are grown around the middle parts of the NWs. The authors utilized the endotaxy of MnAs in InAs for the MnAs NC formation after the SA-MOVPE of the host crystals of InAs NWs [127]. The endotaxial nanoclustering of magnetic metals in semiconductors has also been observed in other materials system, e.g., MnSb:GaSb [129] and MnP:GaP [130] thin films.

Mn-doped semiconducting GaAs and InAs layers usually show p-type conductivity, as demonstrated so far, e.g., in the case of diluted magnetic III–V semiconductors [131]. As closely investigated in the previous study [113] to discuss the unintentional doping by Mn atoms to host undoped semiconducting NWs after the endotaxy of MnAs, the authors have characterized current and voltage (I-V) properties of MnAs/GaAs hybrid NWs using vertical two-terminal device structures of free-standing hybrid NWs. MnAs NCs were grown at a T_g of 600 °C for the MnAs/GaAs hybrid NWs on GaAs {111}B substrates. On the Zn-doped p-type GaAs {111}B substrates, I-V curves showed approximately linear characteristics, i.e., ohmic behavior. On the Si-doped n-type GaAs {111}B substrates, on the other hand, I-V curves showed marked rectifying properties. These results in Ref. [113] markedly showed that the MnAs/GaAs hybrid NWs had p-type conductivity. In addition, the authors reported in another study [92] the electrical and magnetotransport characteristics for the samples with MnAs NCs self-assembly formed on GaInAs/InP {111}B layers by conventional MOVPE, i.e., not by SA-MOVPE. The MnAs NCs were self-assembled on GaInAs {111}B surfaces at a T_g of 650 °C, and all the samples showed p-type conductivity with nearly the same carrier concentrations of approximately 1.7×10^{18} cm^{-3} estimated at 280 K [92]. Therefore, as in the case of the self-assembled formation of MnAs NCs on GaInAs {111}B surfaces, the Mn atoms provided during the endotaxy of MnAs NCs at a T_g of 600 °C thermally diffuse into the undoped GaAs NWs in Ref. [113]. And then, they are unintentionally incorporated as an acceptor yielding p-type GaAs layers, or possibly p-type paramagnetic dilute magnetic semiconductor layers of GaMnAs, near the NW surfaces. Therefore, it is reasonable that the unintentional doping of Mn atoms to the host InAs NWs after the endotaxy of MnAs at a T_g of 580 °C, whose T_g for the MnAs endotaxy is similar to the two cases above of the previous studies, [92, 113] also occurs in this study. Further experiments, however, should be conducted to conclude in an electrical conduction property and an unintentionally-doped carrier concentration in the current case of MnAs/InAs heterojunction NWs.

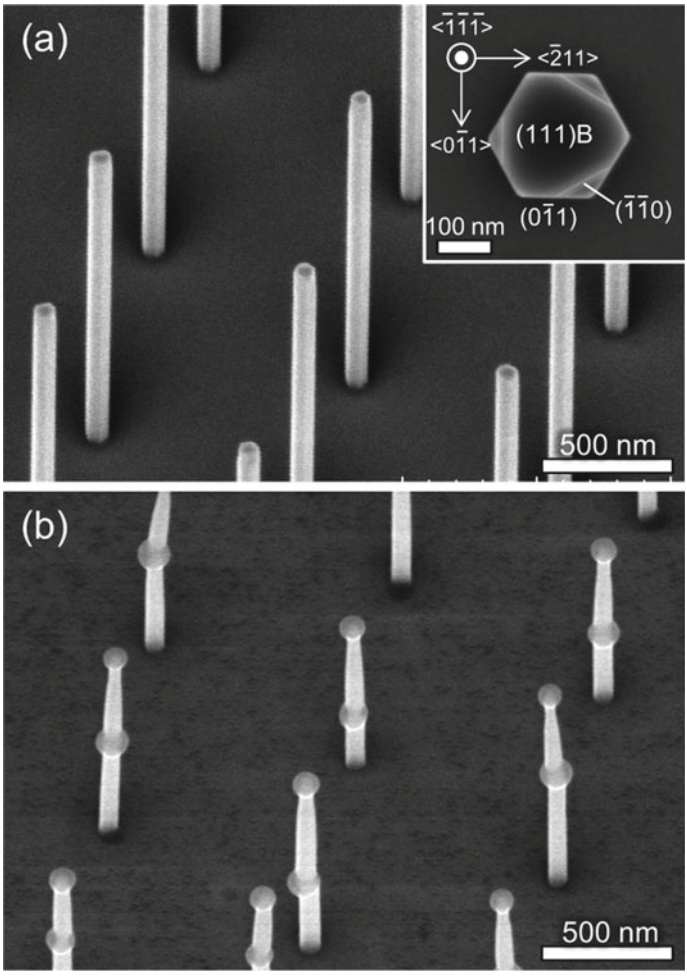

Fig. 7 Bird's-eye views of secondary electron microscope (SEM) images of a typical **a** host semiconducting InAs nanowire (NW) array template before the growth of magnetic MnAs nanostructures and **b** vertical MnAs/InAs heterojunction NWs. The inset of Fig. 7a is a top view of SEM image of the crystal facets typically formed on top of host InAs NWs. Reproduced with permission from Ref. [121]. Copyright (2016) the Japan Society of Applied Physics

Structural characterization was conducted by TEM for comparable hybrid NWs to carefully investigate the structural characteristics of the ferromagnetic MnAs NC/semiconducting InAs hybrid NWs shown in Fig. 7b. Figure 8a, b show highly magnified cross-sectional bright-field TEM images of the MnAs NCs that were formed in the middle and on the top {111}B crystal facets of the host InAs NWs, respectively [121]. The width and height of the NC in Fig. 8a were estimated to be approximately 85 and 55 nm, respectively, and those in Fig. 8b were estimated to be

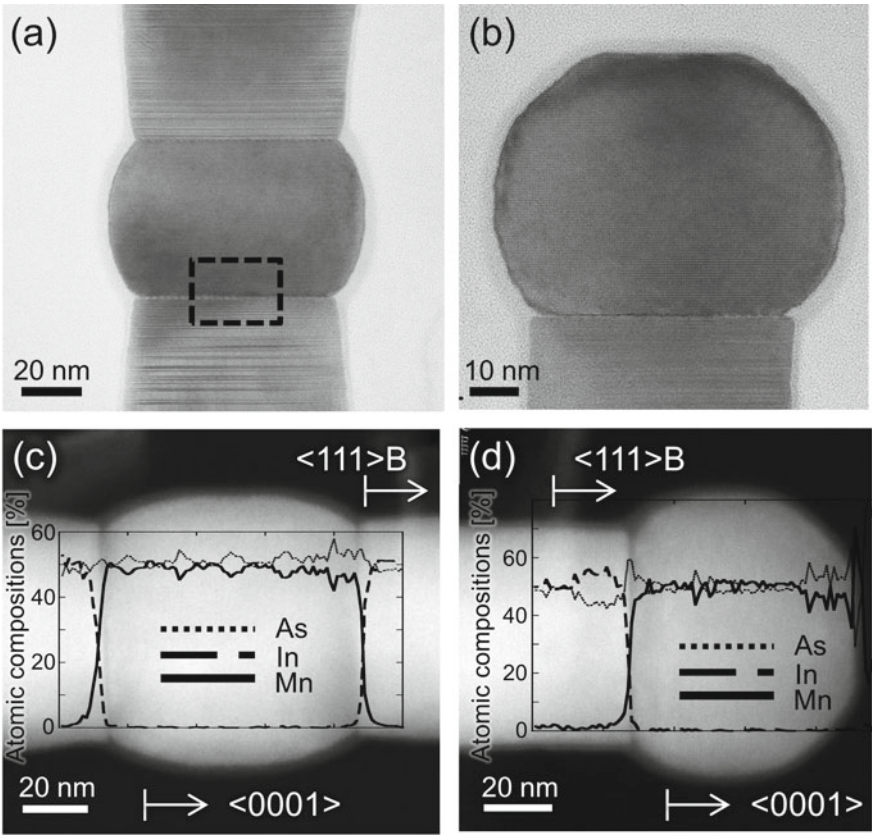

Fig. 8 Cross-sectional transmission electron microscope (TEM) images of magnetic MnAs nanostructures formed **a** in the middle and **b** on the top {111}B crystal facet of semiconducting InAs nanowires (NWs). Cross-sectional TEM images with corresponding line profile obtained by energy dispersive X-ray spectroscopy for **c** middle and **d** top of NW. The percentages of As, In, and Mn atoms were estimated by eliminating possible external contamination by chemicals or atoms, such as carbon, oxygen, and silicon, which were possibly introduced during the sample preparation processes and from materials of the sample holders used for TEM observations. Reproduced with permission from Ref. [121]. Copyright (2016) the Japan Society of Applied Physics

approximately 72 and 54 nm, respectively. TEM observations confirm that rotational twin defects are randomly formed in the InAs NWs, and that no dislocations or other defects, on the other hand, can be observed in the MnAs NCs. The characterization results of EDX spectroscopy of the corresponding MnAs NCs are shown in Fig. 8c and d, respectively [121]. The atomic compositions of the NCs and the NWs in terms of the three elements, i.e., As, In, and Mn were estimated from the line profiles obtained by EDX spectroscopy. This way the authors precisely determined the solid compositions of the NCs and NWs and eliminated possible external contamination by chemicals, or atoms, such as carbon, oxygen, and silicon, which were possibly

introduced during the sample preparation processes or originated from the materials of the sample holders used for the TEM observations. The atomic solid compositions in % of As, In, and Mn elements are found to correspond to approximately 52, 1.0, and 47%, respectively, in the regions of the NC positioned in the middle of the host InAs NWs, as shown in Fig. 8c. The MnAs NC formed on the top {111}B crystal facets of the host InAs NWs has similar atomic solid compositions of approximately 51, 0, and 49% of As, In, and Mn elements, respectively, as shown in Fig. 8d. Figure 9 shows a lattice image of the interface between the NW and the NC which was formed in the middle of the NW [121]. As shown in Fig. 9, atomically abrupt heterointerfaces are formed between MnAs NC and InAs NW. Similar results in terms of the heterointerfaces were obtained for the NCs formed on the top {111}B crystal facets of the NWs. The results of the structural characterization show that vertical ferromagnetic MnAs NC/semiconducting InAs heterojunction NWs with atomically abrupt heterointerfaces were successfully grown by utilizing the endotaxy of MnAs NCs at a T_g of 580 °C. In addition to the cross-sectional lattice images by TEM, the ED patterns from the MnAs NC, the host InAs NW, and the GaAs substrate were measured, as shown in Fig. 10 [121]. The ED patterns reveal that the MnAs NCs exhibit a hexagonal NiAs-type crystal structure, which is confirmed by the ED patterns of the points 1 and 3 in Fig. 10. The host InAs NW and the GaAs substrate, on the other hand, have a ZB-type crystal structure, as shown in the ED patterns of the points 2 and 4 in Fig. 10, respectively. The c-axis, i.e., the ⟨0001⟩ direction, of the NiAs-type MnAs NCs is approximately parallel to the ⟨111⟩B direction of the host ZB-type InAs NWs. The possible growth mechanism and the formation control of MnAs NCs in the host InAs NWs as the result of endotaxy are discussed in detail in the previous studies [121, 123].

As described in Sect. 3.1.5, in the cases of pure III–V compound semiconducting NWs, the transition of crystal structures from conventional ZB- to WZ-type have been theoretically and experimentally investigated [132, 133]. The structural transitions were exemplary observed both in the SA-MOVPE of InP and InP/AlInP NWs [40, 134] and in the VLS growth of InAs and GaAs NWs [135, 136]. A MnAs bulk crystal shows a first-order structural phase transition between the MnP-type β-MnAs (paramagnetic orthorhombic β-phase) and the NiAs-type α-MnAs and (ferromagnetic hexagonal α-phase) in the vicinity of room temperature. In addition, in the special case of MnAs NCs embedded in a ZB-type GaAs matrix, structural transition of MnAs NCs from NiAs- to ZB-type was observed [93, 137]. From the ED measurements by cross-sectional TEM in Fig. 10, the authors conclude that the MnAs NCs in the MnAs/InAs heterojunction NWs are α-MnAs with a hexagonal NiAs-type structure. Therefore, the authors have not observed any structural transition in the MnAs/InAs heterojunction NWs in this study. As observed in the cross-sectional lattice image around the heterointerface between MnAs and InAs in Fig. 9, atomically abrupt heterointerfaces are formed between MnAs NC and InAs NW. The authors have never observed any defect and dislocation in the lattice images of MnAs NCs in the MnAs/InAs heterojunction NWs. The MnAs NCs are single crystal with the lattice constant of a MnAs bulk crystal. It appears, however, in Fig. 9 that there is possibly a strain in the crystal lattice of only one or two monolayers of MnAs NCs

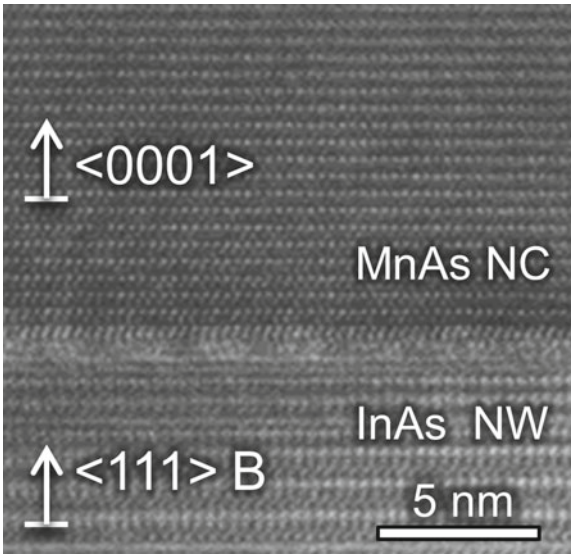

Fig. 9 Lattice image of an atomically abrupt heterointerface between InAs and MnAs that is formed in the middle of a MnAs/InAs heterojunction nanowire (NW). The observed area is indicated by a black dashed line in Fig. 8a. Reproduced with permission from Ref. [121]. Copyright (2016) the Japan Society of Applied Physics

at the interface, judging from the image contrasts of Fig. 9. It remains challenging to observe two-dimensionally any defects in the crystal lattice of MnAs NCs at the interfaces in detail. However, a small number of defects may be formed only at the interfaces, since the crystal structure of MnAs NCs is not identical to that of InAs NWs in this study. The Curie temperature, T_c, of the MnAs NCs in the InAs NWs have not been determined in this study. However, in the previous studies, measurements of the hysteresis curves [138] and the magnetization [92] reveal an increased T_c of 340 K for comparable samples with NiAs-type MnAs NCs on GaInAs {111}B layers. For different types of the samples with MnAs NCs formed in Mn-incorporated GaInAs {001} layers, a decrease of T_c from 320 to 290 K was observed, which was possibly caused by a change in the solid composition of the NCs from MnAs to MnP due to the existence of an undoped InP capping layers on top of GaInAs {001} layers with MnAs NCs [139]. Several researchers have also reported on MnAs NCs with a single magnetic domain, which were epitaxially grown on GaAs NWs. From measurements of the hysteresis curve of the MnAs NCs, they estimated a T_c of 313 K for the MnAs NCs on GaAs NWs [140]. Thus, the T_c of the MnAs NCs in the MnAs/InAs heterojunction NWs in this study can be expected to be larger than 320 K.

In addition, to roughly discuss carrier injection from a ferromagnetic metal nanostructure to a semiconducting NW, first-principles calculations based on the density functional theory were carried out using the Advance/PHASE software developed by Advance Soft Corp. [141], and the work function, φ, between the Fermi energy,

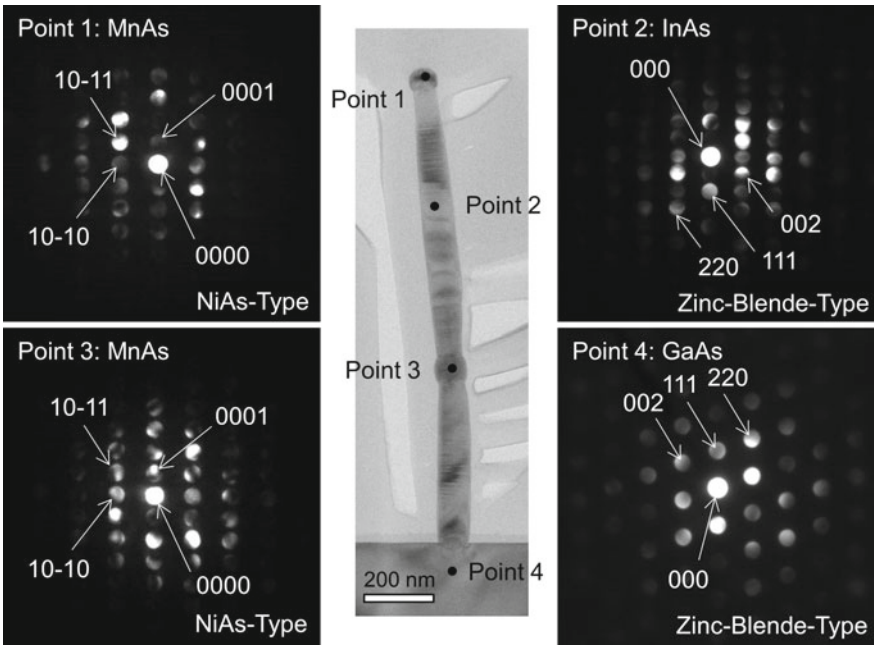

Fig. 10 Cross-sectional transmission electron microscope image and electron diffraction patterns of vertical magnetic MnAs nanostructures/semiconducting InAs heterojunction nanowires (NWs) on GaAs {111}B substrates: Points 1 and 3 for MnAs nanostructures, Point 2 for InAs NW, and Point 4 for GaAs {111} B substrate. Reproduced with permission from Ref. [121]. Copyright (2016) the Japan Society of Applied Physics

E_f, and the vacuum levels of a MnAs {0001} plane and the electron affinity, χ, between the conduction band edge, E_c, and the vacuum levels of InAs {111}A and B planes were obtained. The χ of the InAs {111}A, i.e., In-terminated, and {111}B, i.e., As-terminated, planes were to be 5.29 and 4.30 eV, respectively. The φ of the MnAs {0001} plane was calculated to be 3.40 to 4.93 eV. It is confirmed that it markedly depends on the surface termination, i.e., Mn-terminated ($\varphi = 3.40$ eV) or As-terminated ($\varphi = 4.93$ eV) surfaces, although it remains challenging to conclude which work function for the MnAs {0001} planes, i.e., the Mn- or As-terminated MnAs {0001} planes, should be taken into account in the actual case of the heterointerface between MnAs and InAs in the NWs. However, there may be two possible combinations between the φ of the MnAs {0001} plane and the χ of the InAs {111}A or B planes: (1) one is between $\varphi = 3.40$ eV for the Mn-terminated MnAs {0001} plane and $\chi = 4.30$ eV for the As-terminated InAs {111}B plane, and (2) the other is between $\varphi = 4.93$ eV for the As-terminated MnAs {0001} plane and $\chi = 5.29$ eV for the In-terminated InAs {111}A-plane since there are presumably one monolayer of As atoms at the heterointerface between MnAs and InAs. From the viewpoint of carrier injection from a ferromagnetic metal to a semiconductor, therefore, the results

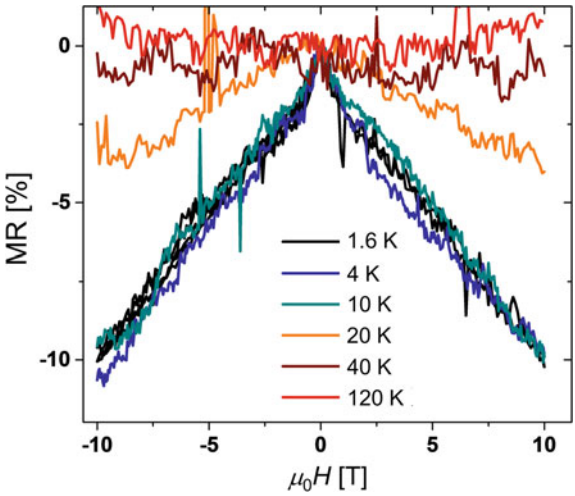

Fig. 11 Magnetoresistance (MR) of the MnAs/InAs heterojunction nanowire (NW) at different temperatures and a magnetic field oriented perpendicular to the NW axis. Reproduced with permission from Ref. [125]. Copyright (2019) the Materials Research Society

in this study show that the spin-polarized current injection from ferromagnetic metal MnAs NCs to semiconducting InAs NWs can be expected, although the precise band diagram between MnAs NCs and InAs NWs has not been determined yet. The strong influence of the incorporation of Mn into the NWs is found in the MR behavior of the MnAs/InAs heterojunction NW. A preliminary result of its MR effects is shown in Fig. 11 [125]. For temperatures below 40 K, the NW exhibits a large linear negative MR, and even at higher temperatures the large positive MR found in the case of the InAs NW completely vanishes. Interestingly, for temperatures below 10 K, i.e., where impurity band transport dominates, the MR effect is independent of temperature. The detailed discussion is described in the previously invited article [125]. However, further investigations are required to identify the underlying transport mechanisms in detail as well as to understand the influence of the MnAs NCs on the transport processes in the MnAs/InAs heterojunction NWs.

3.2 Fabrication of Vertical NW-FETs

Fabrication procedures for vertical surrounding-gate FETs are summarized in Fig. 12 and described as follows [142]. After the growth of NWs, whole NWs were covered with high-k dielectrics formed by atomic layer deposition (ALD). We mainly use $Hf_{0.8}Al_{0.2}O$, and its typical thickness was 10–20 nm, corresponding to equivalent oxide thickness (EOT) of 1.9–3.7 nm. Next, tungsten gate metal and its contacting-pads were formed by sputtering and defined using photolithography. Low-k benzocyclobutene resin (BCB, Dow chemical) was once spin-coated and then etched back to the desired thickness (∼300 nm) by reactive ion etching (RIE), followed by dry and wet etching of metal and high-k remained on the top portion of NW. At this step,

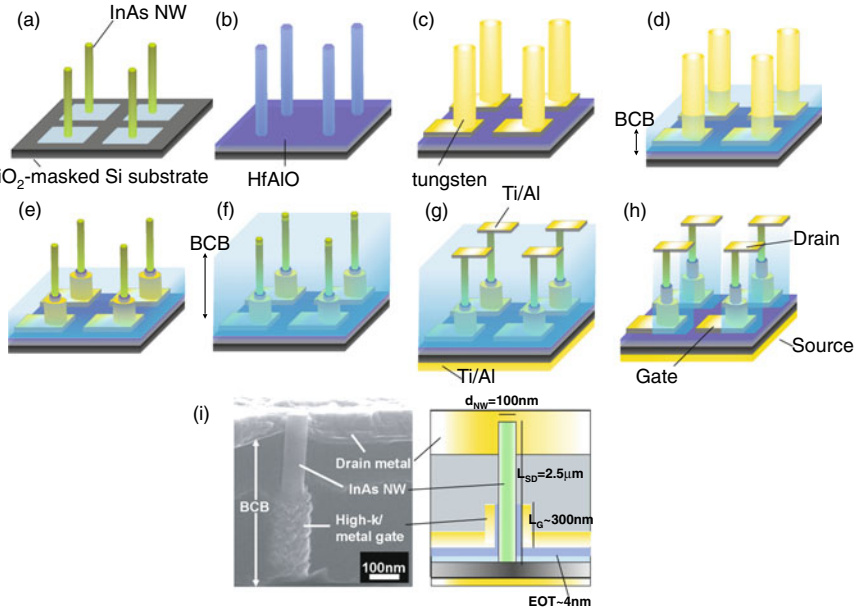

Fig. 12 Fabrication processes of vertical FETs. **a** SA-MOVPE growth of NWs. **b** Atomic layer deposition of high-k gate dielectrics. **c** Metal sputtering for gate electrode. **d** Planarization and etching using BCB. **e** Selective etching of metal and high-k dielectric. **f** Second plararization and echoing for the formation of separation layer. **g** Drain and source metal evaporation. **h** Gate contacting-pads exposure. **i** SEM image of the cross section of vertical SG NW-FET. Reproduced with permission from Ref. [142]. Copyright (2010) the Japan Society of Applied Physics

BCB layer works as protecting mask for etchings and defines the gate length, L_G. After that, the device was spin-coated again with BCB for electrical separation layer of the gate and the top drain electrode and etched back to the thickness so that only the top of the NWs was exposed. Finally, a stack of Ti and Al was evaporated on NW top and backside of the substrate, respectively, for drain and source contacts. Figure 12i shows a cross-sectional SEM image of vertical NW SG FET.

The process described here seems to be very standard to fabricate vertical NW-FETs. Lund group incorporated a method to introduce the spacer layer between the substrate (source electrode) and the gate to reduce the capacities coupling between each contact. This is important in reducing the parasitic capacitance and to allow operation in higher frequencies. They also attempted to form the source electrode at the bottom of NWs by the sputtering of Al and W from the top of the sample surface followed by their etch-back process to the desired thickness [143–145]. They also develop a gate-last process by control the gate length by introducing the electron beam

exposure process in silsesquioxane (HSQ) and NW diameter by digital etching [146, 147]. Gate last process is also developed by Lund group, as reported in Ref. [148].

4 Current Status of NW-FETs

4.1 Static Characteristics

The first vertical NW-FET using bottom-up NWs was reported in 2003, where CuSCN NWs were formed by electrodeposition in a polymer template with pores of nanoscale diameters [149]. Then, Nguyen and co-workers reported vertical FETs using catalyst-assisted grown In_2O_3 [150] and ZnO [151] NWs, followed by reports by Schmidt et al. [152] and by Goldberger et al. [153]. In these studies, although the modulation of drain current by gate electrode was confirmed, the saturation characteristics were insufficient. Bryllert et al. [154] reported the vertical NW-FETs using site controlled InAs NWs on an InAs substrate. Our first vertical NW-FET was reported in 2010 using InAs NWs grown on Si [142].

Figure 13a–c show benchmarks of NW-FETs reported to date. The benchmarks include FETs fabricated with bottom-up and top-down NWs, and both vertical and lateral structures. The results summarized in these figures are obtained by using InAs or InGaAs NWs for n-channel FET; this is owing to their high-mobility. Figure 13a shows g_m and S obtained for $V_{DS} = 0.5$ V, unless otherwise specified, in each reference, and the contour for the quality factor $Q = g_m/S$ is also shown. As explained in Sect. 2, the most important metrics for low-power logic are I_{on} and I_{off}. To emphasize this point, we extracted I_{on} at $V_{GS} = V_{on} = V_{off} + V_{DS}$ from the figures, where $V_{DS} = 0.5$ V and $I_{off} = 100\,\mathrm{nA}/\mu\mathrm{m}$ at $V_{GS} = V_{off}$ in Fig. 13b, and $I_{off} = 1\,\mathrm{nA}/\mu\mathrm{m}$ in 13c. The general trend is that the low S is required for large I_{on}, suggesting the importance of good electrostatic control of the gate. The largest on current reported to date for FETs with bottom-up is $360\,\mu\mathrm{A}/\mu\mathrm{m}$ (extracted from Fig. in Ref. [22]), while $555\,\mu\mathrm{A}/\mu\mathrm{m}$ is reported in lateral FETs with top-down NWs [21]. Though it is not clear from this benchmark, it also seems to be important to reduce leakage between source-drain leakage to reduce I_{off}. Suppression of gate leakage current is also important, but all the published results satisfy the required level for leakage of the gate current.

The major limiting factors for the performance of current NW-FETs are thought to be as follows. The first limitation originates from parasitic resistance at the source and drain. For instance, Tomioka et al. [22] reported one of the best characteristics with InAs vertical NW-FETs on Ge substrate, and they ascribed to the improvement as compared with NW-FETs on Si substrate to the reduction of series resistance between NW and substrates. The parasitic resistance includes contact resistance between the source/drain regions of the semiconductors and metals, and the access resistance between the channel and source/drain regions. This issue is being and could be tackled by, for example, optimization of doping in NWs, use of NWs on

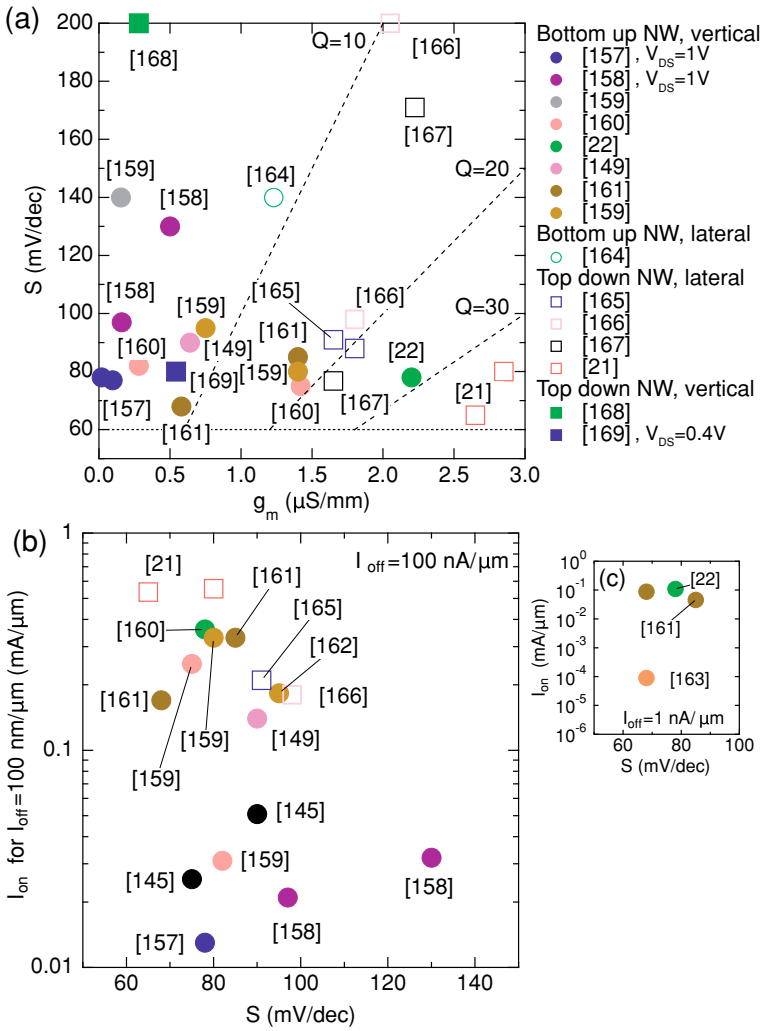

Fig. 13 Benchmark of III–V NW-FETs. **a** Maximum transconductance g_m versus subthreshold slope S. Both g_m and S are the date for $V_{DS} = 0.5$ V unless otherwise specified. **b** On current I_{on} vs S with V_{GS} swing of 0.5 V. The off current I_{off} is set at 100 nA/μm. **c** Same as Fig. (**b**) for $I_{off} = 1$ nA/μm. Data are extracted from Refs. [21, 22, 146, 148, 155–168]. Some values of I_{on} are extracted from the figure and small deviations from real measured data might be present

low-resistive InAs epitaxial layer, and so on. The second limitation is the leakage between source and drain, which arises because of the narrow gap semiconductors and limits I_{off}. The third, which is the most critical, is the interface states between the gate insulator and NWs. This increases the subthreshold slope as [9]

$$S = 2.30\frac{k_B T}{q}\left(1 + \frac{C_{\mathrm{D}} + C_{\mathrm{it}}}{C_{\mathrm{OX}}}\right). \tag{7}$$

Here, effect of interface states are considered by the capacitance associated with the trap density D_{it} and $C_{\mathrm{it}} = qD_{\mathrm{it}}$. The interface states make gate control ineffective in the linear and saturation regions of FETs, resulting in the reduction of I_{DS} and transconductance g_{m}.

Most of the FETs with bottom-up NWs shown here achieve high-performance utilizing heterostructures by tackling these problems mentioned above. These are described later in Sect. 4.3.

4.2 High-Frequency Characteristics

As described in Sect. 2, immunity in the short channel effect of SG NW-FETs is also promising as high-frequency devices. The metrics as a high-frequency FETs are the current gain h_{21} and power gains, such as maximum available power gain (MSG), maximum stable power gain (MSG), and unilateral power gain (U) [169, 170]. The figure of merit characterizing the frequency dependence of those gains are the transition frequency f_{T} and maximum oscillation frequency f_{max}. f_{T} is a frequency when current gain $|h_{21}|$ is unity, and f_{max} is defined as a frequency when MSG or U is unity.

Figure 14a schematically shows intrinsic and parasitic capacitive components of the vertical NW-FETs. Here $C_{\mathrm{GG,i}}$ is the intrinsic capacitor (per unit length along the NW), representing the charge accumulation in the channel by the gate voltage. $C_{\mathrm{GG,i}}$ is given by the series connection of oxide capacitance C_{OX}, quantum capacitance C_{Q}, and charge centroide capacitance C_{C} [15]. The other capacitive components are the parasitic ones; C_{DS} is the drain-source capacitance, $C_{\mathrm{GS,p}}$ is the gate-source capacitance, $C_{\mathrm{GD,p}}$ is the gate-drain capacitance, and $C_{\mathrm{GS,w}}$ and $C_{\mathrm{GD,w}}$ are the capacitance between gate and NWs in the source and drain side, respectively. In vertical NW-FETs, the $C_{\mathrm{GS,p}}$ and $C_{\mathrm{GD,p}}$ can be very large because of the large overlap of gate, source, and drain electrodes, as shown as an illustration of the pad contacts [171] in Fig. 14b. The small signal equivalent circuit of the FET is shown in Fig. 14c with parasitic gate, source, and drain resistances, denoted as R_{G}, R_{S}, and R_{D}, respectively. In this equivalent circuit, some capacitors shown in Fig. 14b are collected as $C_{\mathrm{GS}} = C_{\mathrm{GG,i}}L_{\mathrm{G}} + C_{\mathrm{GS,e}} + C_{\mathrm{GS,w}}$, $C_{\mathrm{GD}} = C_{\mathrm{GD,e}} + C_{\mathrm{GD,w}}$. Following this equivalent circuit model, approximate form of f_{T} is expressed as [169]

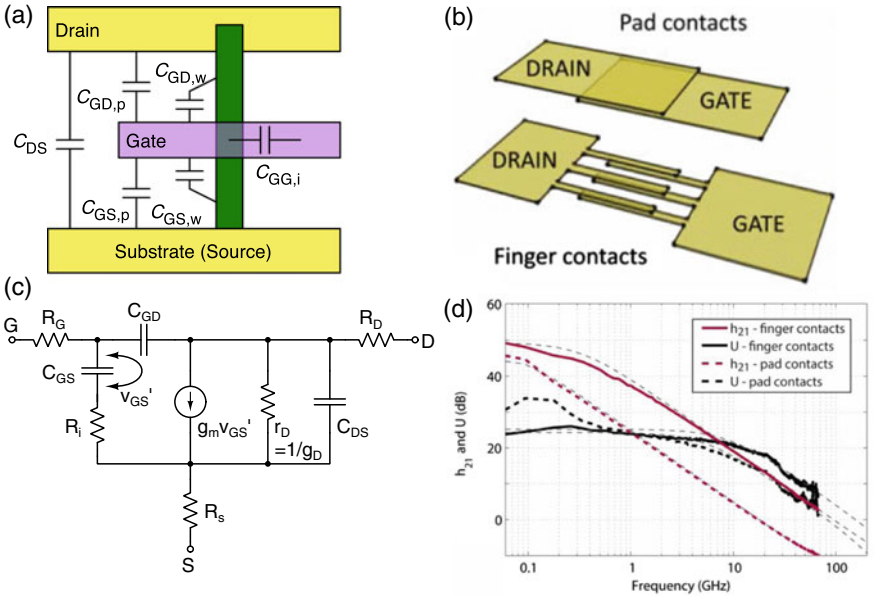

Fig. 14 **a** Side view of the NW-FETs and intrinsic and parasitic capacitance associated with FETs. **b** Geometry for the gate and source electrode. Finger contact is used to minimize parasitic capacitors ($C_{GS,p}$ and $C_{GD,p}$). Copyright @ IEEE. All rights reserved. Reprinted, with permission, from Ref. [171]. **c** Example of small signal equivalent circuit for FETs. **d** Measured frequency characteristics of current gain h_{21} and unilateral power gain U for vertical InAs NW-FETs. f_T and f_{max} are determined from exploration as shown in the dashed lines. Copyright @ IEEE. All rights reserved. Reprinted, with permission, from Ref. [171]

$$f_T \sim \frac{g_m}{2\pi(C_{GS} + C_{GD})} \tag{8}$$

and

$$f_{max} \sim \frac{f_T}{2\sqrt{(R_G + R_i + R_S)g_D + 2\pi f_T C_{GD}(R_i + R_S + 2R_G)}} \tag{9}$$

Details of these derivation is described in Appendix 2.

In Ref. [15], somewhat different expressions are given for f_T and f_{max} based on a different equivalent circuit and approximations as

$$f_T = \frac{1}{2\pi}\left(\frac{C_{GS}}{g_m} + (R_S + R_D)\left[C_{GS}\frac{g_D}{g_m} + C_{GD}\right]\right)^{-1} \tag{10}$$

and

$$f_{max} = \sqrt{\frac{f_T}{8\pi R_G\left(C_{GD} + C_{GS}\frac{g_D}{g_m}\right)}}\,. \tag{11}$$

In any case, it is important to minimize parasitic component as well as to achieve large transconductance g_m and small drain conductance g_D for high f_T and f_{max}.

The other important figure of merit is the noise figure F_{min} and is given, according to Refs. [172] or [173], as

$$F_{min} \sim 1 + K\sqrt{g_m(R_i + R_S)}\frac{f}{f_T} \tag{12}$$

where K is a fitting factor. This also indicates that reduction of parasitic components and large f_T are import for realizing low-noise amplifier.

Investigation of high-frequency characteristics of the vertical NW-FETs is extensively carried out by Lund group using InAs NWs. To date, the reported highest f_T and f_{max} of the vertical NW-FET is 103 GHz and 155 GHz, respectively, with a FET having the gate length $L_G = 0.15\mu$m [171], as shown in Fig. 14d. This is also the highest f_T and f_{max} among NW-based FETs. This record high cutoff frequency seems to result from various optimizations, and one of the optimizations is to use finger contacts (see Fig. 14b) to reduce parasitic capacitance $C_{GG,p}$. According to their estimation, the parasitic capacitance was reduced by 78% by the finger contacts as compared with pad contacts, and resulted in the impressive enhancement of f_T. The finger contacts also result in the increase of gate resistance R_G, resulting in the suppression of expected enhancement of f_{max} owing to the reduced parasitic capacitance, but could be improved by the optimization of the geometry of gate fingers. Furthermore, Lund group has carried out performance evaluation of vertical SG NW-FETs taking into device size scaling and various parasitic components and predicted $f_T = 2.72$ THz and $f_{max} = 1.79$ THz using InAs NW-FETs with NW diameter d of 8 nm and the gate length L_G of 11.1 nm [174].

4.3 Utilization of Heterostructures

As mentioned in Sect. 2.4, one of the most significant advantages of the bottom-up NWs is the possibility to realize various heterostructures, which are free from constraints of lattice matching in the epitaxial growth of thin films. Among them, NW-FETs with radial heterostructures or core-(multi)shell structures, in which the core with smaller bandgap material surrounded by the shell lager band gap materials, have been demonstrated to show significantly superior performances in InAs-based NW-FETs [156, 159, 175] and Ge/Si-based NWs [176–178] as compared with homostructure NW-FETs. Ganjipour et al. [179] reported GaSb/InGaSb core-shell NW-FETs, and thin InAs shell was found to improve on current and transconductance of p-type FETs with GaSb core as a channel. In addition, they found that the conduction changed from p-type to n-type with the increase of shell thickness.

Figure 15a shows an SEM image and a schematic illustration of InAs/ InAlAs core-shell NWs. Size of the InAs core d and the thickness of AlInAs shell was measured 80 and 20 nm, respectively. The InAlAs shell layer consists of undoped and doped

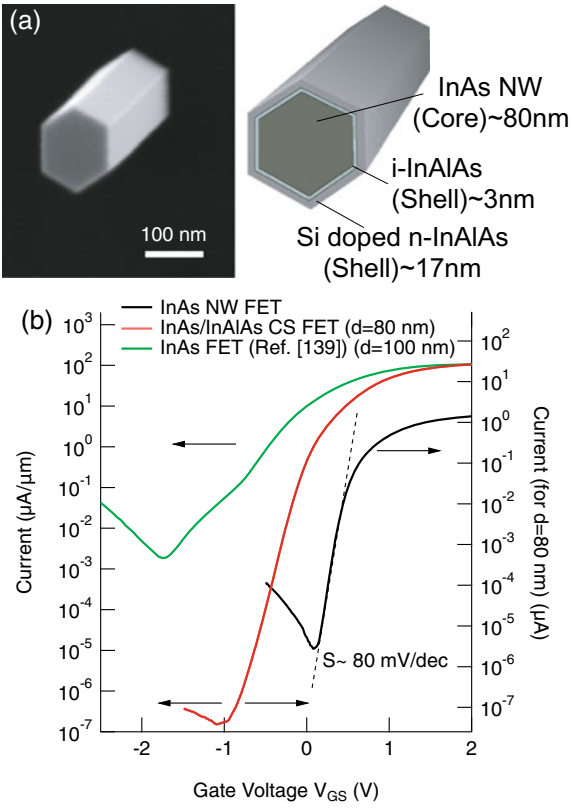

Fig. 15 **a** SEM image and schematic illustration of InAs/InAlAs core-shell NWs. **b** Transfer characteristics of InAs NW-FETs and InAs/InAlAs core-shell NW-FETs

layers, and their thickness was estimated to be 3 and 17 nm, respectively. Figure 15b shows representative transfer characteristics of InAs and InAs/InAsAs NW-FETs for $V_{DS} = 1$ V [180]. The core-shell NW-FET exhibited $I_{DS,max} = 100\,\mu A/\mu m$ at $V_{GS} = 1.5$ V and maximum transconductance g_m of $g_{m,max} = 91.5\,\mu S/\mu m$, which are normalized with πd ($d = 80$ nm). The on-off ratio measured 0.5 V above and below the threshold voltage $V_{th} = 0.5$ V was 10^7, and $S = 110$ mV/dec. In core-shell NW-FETs, the subthreshold slope is improved from the data published in Ref. [142], or maximum current and transconductance was increased from the InAs NWs with improved subthreshold characteristics. Though these are not data obtained in the state-of-art technology, this example clearly shows the improvement of FET characteristics by the introduction of core-shell structures.

The reason for the improved performance of FETs with core-shell structures is as follows. First, it is attributable to the reduction of surface state density. In general, high-density of interface states exists at the interface between III–V semiconductors and gate insulators. The charges associated with the interface states terminate electronic lines of force starting from the gate electrode, thus, they make the charge control in the channel via the gate ineffective and lead to the reduction of drain cur-

rent and transconductance and increase of S, which is expressed in Eq. (7). These interface states can be reduced by the introduction of large gap semiconductor layer as a passivation layer. Care must be taken, however, that the introduction of shell layer decreases the effective oxide capacitance. In a simple model, the total oxide capacitance $C_{\mathrm{OX,eff}}$ is given by the series connection of oxide and shell capacitance, that is,

$$C_{\mathrm{OX,eff}}^{-1} = {C'_{\mathrm{OX}}}^{-1} + C_{\mathrm{shell}}^{-1} \tag{13}$$

where

$$C_{\mathrm{shell}} = \frac{2\pi\varepsilon_{\mathrm{shell}}\varepsilon_0}{\ln\left(1+\frac{R}{t_{\mathrm{shell}}}\right)} \tag{14}$$

and

$$C'_{\mathrm{OX}} = \frac{2\pi\varepsilon_{\mathrm{OX}}\varepsilon_0}{\ln\left(1+\frac{R+t_{\mathrm{shell}}}{t_{\mathrm{OX}}}\right)} \tag{15}$$

The reduction of oxide capacitance leads to the increase of subthreshold slope without reduction of D_{it} (see Eq. (7)). It also reduces transconductance g_{m}. Thus, reduction of the interface between the shell semiconductor and insulator is none the less important in core-shell structures, and the introduction of shell layer is considered to allow us more candidates for the choice of material combination having good interface properties.

Second, insertion of the shell layer in between the gate insulator also result in the improvement of mobility due to the reduction of surface roughness scattering; this is partly ascribed to the reduction of the height of the roughness, and partly to the reduction of the height of the potential fluctuation originating from the reduction of band discontinuity between channel semiconductor and gate insulator, The shell with a higher bandgap than the core layer also works as a carrier supply layer, and, as similar to the n-AlGaAs/GaAs modulation doped structure (so-called HEMT structure), separation of charged impurity and carrier reduces the impurity scattering and improvement of the mobility. Strain effect is also considered as an origin for the improvement, via the increase the carrier density in the channel and the enhancement of the carrier mobility. As the third possibility, the surface passivation by the shell also results in the reduction of depletion layer thickness from the surface, and the increase of carrier density originating from these effects helps reducing parasitic resistance, such as contact resistance at the source and drain, and access resistance which exists between the channel and source/drain regions.

On the other hand, axial heterostructures are also introduced for NW-FETs to improve their performance, and its effectiveness is demonstrated in InAs-based NWs. InAs has a large electron mobility owing to its small effective mass and is the most promising as a channel material of the FETs. However, its small bandgap also results in the large band-to-band (BTB) tunneling and impact ionization, giving rise to the increase of the off-state current and deterioration of subthreshold slope S. Lind et al. [70, 181] introduced a segment of InAsP layer as barrier in the NW-FETs with InAs

channel, and obtained smaller S and I_{off} as compared with FETs without insertion of InAsP. Improvement of FET characteristics by the use of axial heterostructure was further demonstrated in Refs. [160, 161] for InAs/InGaAs NWs, in which higher bandgap material are inserted in the drain side and obtained small S and I_{off} less than $1\,\text{nA}/\mu\text{m}$.

5 Enhancement of Functionality of Vertical NW-FETs

5.1 Tunnel Field-Effect Transistors

As described in Sect. 2.1, transistors with small subthreshold slope S are required to reduce off-state current and power consumption in low-voltage circuits, while S in conventional FETs is given by Eq. (2) and is limited by the thermal distribution of the carriers and classical diffusion current. In order to go beyond this classical limit, some attempts are reported by introducing novel mechanisms in the operation of FETs. One of the most promising approaches is to utilize quantum mechanical tunneling, and various kinds of tunnel FET (TFETs) [182–184] realizing S smaller than thermal limit have been reported.

The basic structure of tunnel FET (TFET) is a reverse biased p^+-i-n^+ structure, and the basic operation of n-type TFET (Fig. 16a) is as follows. In n-type TFET, p^+ and n^+ region, respectively, correspond to the source and drain electrode, and no current flows for zero gate voltage V_{GS} (or V_{GS} below threshold voltage) from drain to source (Fig. 16b). By applying the positive gate voltage at around the junction between p^+ and i regions, the energy in the i-region is lowered, and the tunneling of an electron from the valence band in the p^+ region to the conduction band in the i-region takes place, indicating that the band-to-band (BTB) current is controlled by the gate voltage. Since the number of carriers contributing the conduction is determined by the energy width of the BTB tunneling probability T, the transport of electrons with higher energy, which exists due to thermal distribution is suppressed and the tunneling current becomes less dependent on the temperature and S is not limited by the thermal activation of the carries.

Under Wentzel-Kramar-Brillouin (WKB) approximation, the BTB tunneling probability T is expressed as [182]

$$T \propto \exp(-b/\xi) \tag{16}$$

where b is the material-dependent constants expressing the degree of BTB tunneling, and ξ is the field at the junction. Specifically, for triangular potential at the junction

$$b = \frac{4\sqrt{2m^*}E_G^{3/2}}{3q\hbar} \tag{17}$$

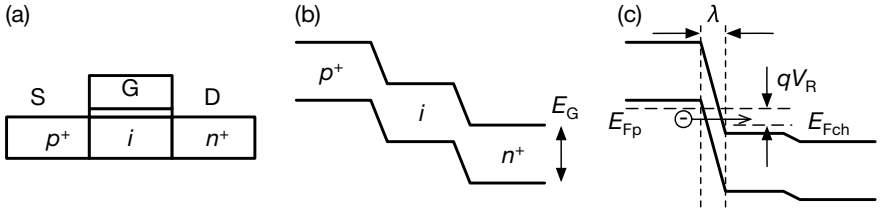

Fig. 16 **a** Schematic illustration of an n-type TFET. Band diagram of homojunction p^+-i-n^+ TFET under **b** off-state and **c** on-state

where m^* is the tunneling effective mass and E_G the band gap of the materials. The source-drain current I_{DS} is proportional to T and can be calculated as

$$I_{\mathrm{DS}} = aV_R\xi \exp\left(-\frac{b}{\xi}\right) \tag{18}$$

where $V_R = (E_{Fp} - E_{Fch})/q$ is the effective bias across the tunnel junctions, E_{Fp} and E_{Fch} is the Fermi level of the p^+ and channel regions (see Fig. 16c), and a is a constant. The subthreshold slope S is then given by [185]

$$S = \ln(10)\left[\frac{1}{V_R}\frac{dV_R}{dV_{\mathrm{GS}}} + \frac{\xi + b}{\xi^2}\frac{d\xi}{dV_{\mathrm{GS}}}\right]^{-1} \tag{19}$$

To realize small S, the denominator consisting of two terms should be enlarged. Maximizing the first term requires effective electrostatic control of the channel potential (E_{Fch}/q) by V_{GS}, and strong field ξ at the junction and effective gate control of ξ by decreasing the junction width λ with V_{GS} to maximize the second term. Note that this indicates the importance of good electrostatic control by the gate in TFETs.

It is also noted that S is not the only figure of merit for TFETs. Because the tunneling intrinsically limits the energy range and the number of carriers, the loss of the on current I_{on} as compared with classical FETs are inevitable, and low I_{on} results in the inferior performance for the logic ICs. Therefore, some compromises are necessary to achieve small S and large I_{on}. Equation (18) indicates that large ξ and materials with small b is required for large drain current. In homojunction TFET discussed above, however, the choice of materials is limited and electric field at the junction is mainly determined by the doping, making hard to obtain compromised TFET design for required S and I_{on}. This limitation can be overcome by using type-II heterostructures with staggered band alignment and band engineering.

These, namely, the requirements of the good gate controllability and necessity of band engineering, lead us to the conclusion that combining vertical NWs and TFETs is be very beneficial. Indeed, the advantages of NWs for TFET applications would be more than in the case of conventional FETs. In TFETs, good electrostatic control of the channel by the gate is a more stringent requirement to maintain S below the thermal limit. More freedom of the material choice in the NW structures

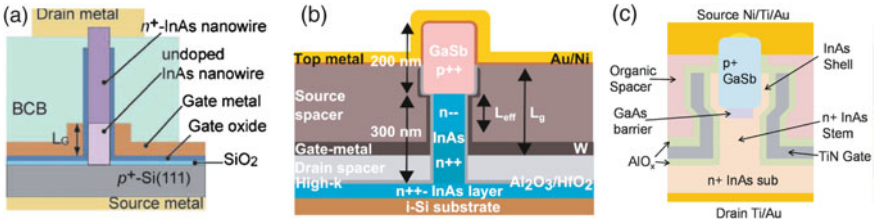

Fig. 17 Some of the reported TFETs utilizing vertical NWs. **a** With Si/InAs heterojunction with staggered type-II band alignment [188]. Reproduced with permission. Copyright (2011) Institute of Physics. **b** With vertical InAs/GaSb heterostructure. Copyright @ IEEE. All rights reserved. Reprinted, with permission, from Ref. [189]. **c** TFETs combining vertical/lateral heterostructure NWs. Reprinted from Ref. [190] by T. Vasen et al., licensed under CC BY 4.0

than in planar counterparts is advantageous for band engineering. Furthermore, a combination of radial and axial heterostructure can increase the on current for given footprints.

Figure 17 shows some of the vertical NW TFETs. The first NW-based TFET was reported by Bjork et al. [186] using Si NWs grown by VLS mechanisms, and later, Schmid et al. [187] and Tomioka and Fukui reported TFETs utilizing InAs/Si heterostructure, where staggered type-II band alignment is formed. Comprehensive investigations on TFETs implementing InGaAs/GaSb heterostructure NWs are reported by the Lund group.

Figure 18 shows a benchmark of some of the TFETs reported recently. Here, S is plotted as a function of I_{DS} for several types of TFETs including vertical NW TFETs. Note that the figure is just to show the current status of the TFETs in various technologies, and benchmarking TFET from published data is challenging because they are not compared under the similar measurement conditions, such as drain voltages. In addition, as mentioned earlier, S is not only a measure for the performance of the TFETs. Nevertheless, TFETs utilizing vertical NWs and heterostructures are promising candidates for steep-slope transistors with high on-state current density.

5.2 *p-Channel FETs and CMOS Structure*

CMOS logic, namely, complementary operation of n-channel and p-channel MOSFET in logic circuits is playing a very important role to reduce the power consumption, and circuits made of NW-FETs should also require a complementary operation, that is, both n-channel and p-channel FETs. Reports on the fabrication of p-channel FETs are much fewer than that on n-channel FETs. The p-channel vertical NW-FET was reported by Schmidt et al. [152] and by Goldberger et al. [153] using Si NWs. Besides, high-performance p-channel lateral FETs using Ge/Si core-shell NWs are reported [176, 177]. This Ge/Si NW MOSFET with $L_G =$ nm and $d \sim 15$ nm was analyzed to operate between 60 and 85% of the ballistic limit at $I_{on}/I_{off}1 = 100$

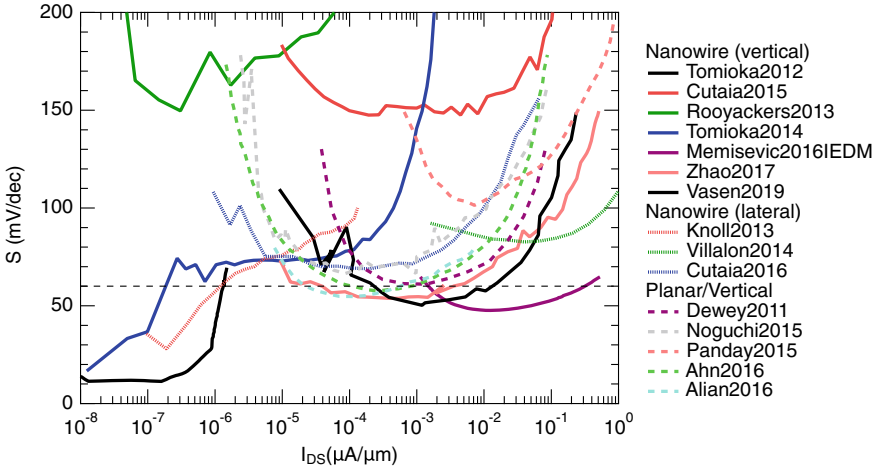

Fig. 18 Some of the resent results on the subthreshold slope S of TFETs realized in various technologies and materials. References: Tomioka 2012: [191] (traces is taken from [71]), Cutaia 2015: [47], Rooyackers 2013: [192] Tomioka 2014: [193] Memisevic 2016: [194], Zhao 2017: [195] Memisevic 2018: [196], Vasen 2019: [190], Knoll 2013: [197], Villalon 2014 [198], Cutaia 2016: [199], Dewey 2011: [200], Noguchi 2015: [201], Panday 2015: [202], Ahn 2016: [203], Alian 2016: [204]

after the extraction of the series resistance [205]. Later, vertical FET Ge/Si core-shell [206] were also reported, and they showed drain current of 750 μA/μm at $V_{DS} = V_{GS} = -2$ V with $V_{th} = +0.95$V, and $S = 125$ mV/dec from a device with gate length of 544 nm.

For III–V semiconductors, GaSb is the most promising material for p-channel FETs since it has the highest hole mobility among III–V semiconductors. p-channel FETs using GaSb NWs are reported in Ref. [147] in vertical geometry.

By combining n-channel and p-channel NW-FETs, some attempted are reported towards CMOS logic. A CMOS logic using n-channel InAs NW FET and p-channel Si/Ge NW-FET is reported by Nam et al. [207]. They fabricated lateral FETs using NWs transferred from original substrates and interconnect them to realize ring oscillators. The fabricated 3-stage ring oscillator with a maximum oscillation frequency of 108 MHz with supply voltage V_{DD} of 8 V, indicating the delay of 3 ns with a single-stage inverter. Dey et al. [208] reported on a CMOS inverter with InAs/GaSb heterostructure NWs.

In the application point of view, control and matching of the threshold voltages between n-channel and p-channel FETs is required, Much harder challenge for CMOS would be the matching of current between p- and n-channel transistors. Ge and GaSb are promising for p-channel FET owing to their high hole mobility, but it is not as good as electron mobility of InAs or InGaAs, which are the candidate for the n-channel FETs. Some breakthrough is required for more practical logic applications.

5.3 Spin-FETs

Spin-FETs and spin-MOSFETs have been introduced as a promising candidate for emerging research materials and new functional device applications, i.e., so-called "Beyond CMOS" technologies, in future industry of electronics, as reported periodically in the international roadmap for devices and systems (IRDS) by the Institute of Electrical and Electronics Engineers (IEEE) [209]. The idea of spin-FETs was originally proposed as so-called "Datta-Das-type spin-FETs", in which spin precession due to the spin-orbit coupling is controlled in a narrow gap semiconducting channel, e.g., InAs, InSb, and alloy semiconductors between them, with a relatively strong spin-orbit interaction [210]. After the proposal of the first spin-FETs, the device concept of spin-MOSFETs was demonstrated as so-called "Sugahara-Tanaka-type spin-MOSFETs", whose output characteristics are controlled by the relative magnetization configuration of ferromagnetic-semiconductor channel and ferromagnetic metal source/drain electrodes [119, 211]. So far, several attempts to investigate spin-FETs theoretically and experimentally have intensively been demonstrated using III–V compound semiconductors with a strong spin-orbit interaction and group IV semiconductors, such as Si and Ge, as channel materials of FETs [212–216]. The majority of the investigations is based on the conventional top-down-type fabrication technologies after the thin film growth of materials on semiconducting substrates. However, the recent efforts by Takase et al. have intensively been devoted to create "lateral" spin-NW-FETs using narrow gap III–V compound semiconducting NWs, which have been grown vertically by a VLS method using metal catalyst, detached mechanically from the substrates after the VLS growth, and finally put on insulating substrates to fabricate electrodes and gate oxides for transistors [217, 218]. The tremendous improvements in device performance of NW-FETs, which are intensively discussed in previous sections in this book chapter, can directly be introduced to the proposed spin-NW-FETs and spin-NW-MOSFETs in the current work as well as a possible high functionality proposed in the device concepts of spin-FETs and spin-MOSFETs based on the conventional top-down-type fabrication technologies after the thin film growth [119, 210, 211].

Using semiconducting NWs, on the other hand, most of the efforts in research have been devoted from the basic pure physical interests to characterize magnetotransport properties and magnetoresistance (MR) effects, including electronic phase coherence, weak (anti)localization (WL and WAL), and universal conductance fluctuations (UCF) under low-temperature and high magnetic field conditi1ons, as an ideal component of mesoscopic materials system [219–246]. A wide variety of semiconducting materials of NWs, e.g., InAs [217, 219–230], InSb [218, 231, 232], GaAs/InAs core/shell [233, 234], Mn-ion implanted GaAs [235, 236], GaN [237, 238], InN [239–242], Si/Ge [243–245], and InSnO [246] NWs, have been investigated for a deep understanding of a mesoscopic nature of semiconducting NWs. In the previous study, the authors have intensively investigated the magnetotransport properties of single ferromagnetic MnAs NC/semiconducting InAs heterojunction NWs [125] and host InAs NWs to deeply understand pure basic physical aspects

of semiconducting NWs with ferromagnetic nanomaterials for future device applications to vertical spin-NW-FETs and spin-NW-MOSFETs [230]. The authors have observed negative magnetoresistance effect of single InAs NWs hybridized with ferromagnetic MnAs NCs [125] and anomalous angle-dependent magnetotransport properties of single InAs NWs [230]. Therefore, the authors believe that the vertical ferromagnetic MnAs NC/semiconducting InAs heterojunction NWs in the current work are definitely exhibiting new possibilities and versatility for creating novel magneto-nanoelectronic or nanospintronic devices using vertical free-standing heterojunction NWs, e.g., spin-NW-FETs and spin-NW-MOSFETs, as well as spin-NW-light-emitting diode-arrays and NW-array-THz-wave-emitters, as was reported and discussed in the review articles [247, 248].

5.4 GaN-Based Vertical NW-FETs

GaN and related materials are promising candidates for FETs used in power electronics [249] and high-frequency power devices owing to their superior characteristics in high breakdown voltages and large saturation velocity as compared with Si and conventional III–V semiconductors. In particular, vertical devices, such as trench MOSFET [250, 251] and CAVET (current-aperture-vertical-electron-transistor) [252, 253], are attracting interest for their capability in low on-state resistance and large current density as well as high breakdown voltages. Very recently, vertical FETs implementing fins as a channel is proposed and demonstrated to show excellent characteristics in 0.9–1.2 kV class power devices [254–256]. This vertical FINFET eliminates p-type layer for current separation, whose quality is of one of the current issues, and utilized non-polar M-plane surfaces as a channel to realize normally-off devices.

In addition to the advantages of GaN related materials mentioned above, they have unique characteristics as compared with conventional III–V semiconductors as follows. First, the dielectric constant is smaller than Si and other III–V semiconductors. As shown in Eqs. (5) and (6), short natural length λ is expected for smaller dielectric constant, thus, GaN-based FETs are more immune to the short channel effect. Second, the effective mass of electrons is heavier than that in III–V semiconductor. This is an obstacle to obtain high injection velocity at the source end and to realize increment of the current density; however, the heavier effective mass associated with a larger bandgap also means small quantum effect and small nonparabolicity of the conduction band. Therefore, even in the ultimately scaled devices, deterioration of the FET performance is expected to be much less than in other III–V semiconductors. In this point of view, application of GaN-based NW-FET is discussed for logic application in Refs. [257, 258]. GaN-based TFET is also proposed in Ref. [259].

Position controlled GaN NWs are grown by SA-MOVPE [260–263] and SA-MBE [31, 264–268] using mask SiO_2, SiN, Ti, or Mo masks, mainly for the application to light-emitting devices. To date, there are some works on the lateral GaN FETs utilizing epitaxially GaN NWs [269–273], and vertical SG NW-FETs are fabricated

using NWs formed by lithography and etching, i.e., top-down method, from some groups [274–279]. Because the focus of this chapter is vertical FETs utilizing epitaxially grown NWs, we are not going into the detail of these works, but, because of advantages of GaN-based vertical NW devices and rich possible field of their application, technology to realize bottom-up NWs and that to fabricate vertical SG FETs are expected to merge in the near future.

6 Summary

In this chapter, we explained the features of FETs utilizing bottom-up NWs, and reviewed their current status, mainly in focus on the vertical FETs. The new structures and materials exploiting future directions are also shown together with the issues in the current technologies.

The geometry of NWs is advantageous for transistor application as we have explained. Furthermore, the heterogeneous combination with various materials is possible based on the geometry as well as the diversity of the constituent materials. New technologies may be merged and introduced in the present conventional technology based on planar transistors. For instance, implementation of negative capacitance [280, 281] would be straightforward in NWs. In the IRDS Roadmap issued in 2018, the NW vertical transistor is expected to be implemented in 2028 [26], and continuous developments in the fabrication technology are strongly demanded to the practical implementation.

Acknowledgements The authors thank Prof. Takashi Fukui, Prof. Kenji Hiruma, and Prof. Katsuhiro Tomioka at Hokkaido University, Japan, and Prof. Peter J. Klar and Dr. Matthias T. Elm in Justus-Liebig-University (JLU) Giessen, Germany, for collaborations and stimulating and productive discussions. The authors also address sincere and special thanks to our former and present graduate students, in particular, Dr. Jinichiro Noborisaka, Dr. Takuya Sato, Dr. Yoshinori Kohashi, Dr. Shinya Sakita, Dr. Ryutaro Kodaira, Mr. Tomotaka Tanaka, Mr. Yuta Kobayashi, Mr. Ryoma Horiguchi, Mr. Tetsuro Kadowaki, Mr. Kyohei Kabamoto, Mr. Hiromu Fujimagari, Mr. Masatoshi Yatago, as well as Mr. Patrick Uredat and Dr. Martin Fischer, graduate students in JLU Giessen, Germany, for carrying out and supporting experiments for growth, fabrication, characterization of NWs and NW-FETs. This work in part was financially supported by a Grant-in-aid for Scientific Research from the Japan Society for the Promotion of Science (JSPS). S. H. sincerely thanks the financial support of the JSPS via Grant-in-Aid for Scientific Research (B), KAKENHI Grant No. JP17H02727, and Grant-in-Aid for Challenging Exploratory Research, KAKENHI Grant No. JP16K13671, and gratefully acknowledges the financial support of the Murata Science Foundation in part.

Conflict of Interest The authors declare that they have no conflict of interest.

Appendix 1: Models for Current-Voltage Characteristics of Nanowire FETs

Explicit Continuous Model for Long-Channel FETs

In this appendix, we introduce two models for calculating current-voltage characteristics of NW-FETs. The first one is explicit continuous model for long-channel undoped SG MOSFETs with cylindrical cross section having radius R, which is derived by Iñíguez et al. [16]. The drain current I_{DS} in their model is calculated by the following equation;

$$I_{\mathrm{DS}} = \frac{2\pi R}{L_{\mathrm{G}}}\mu\left[2\varphi_{\mathrm{th}}(Q_{\mathrm{S}} - Q_{\mathrm{D}}) + \frac{Q_{\mathrm{S}}^2 - Q_{\mathrm{D}}^2}{2C_0} + \varphi_{\mathrm{th}}Q_0 \ln\left(\frac{Q_{\mathrm{D}} + Q_0}{Q_{\mathrm{S}} + Q_0}\right)\right], \quad (20)$$

where L_{G} is the gate length, μ is the mobility, and

$$Q_0 = \frac{4\varepsilon_{\mathrm{S}}\varepsilon_0}{R}\varphi_{\mathrm{th}}\,, \quad (21)$$

with $\varphi_{\mathrm{th}} = k_B T/q$, and ε_{S} is the dielectric constant of the channel material. C_0 is the oxide capacitance *per unit area* (=$C_{\mathrm{OX}}/2\pi R$ with C_{OX} given by Eq. (4)). Q_{D} and Q_{S} are inversion charges at source and drain and determined by solving the following equation for Q with $Q_{\mathrm{D}} = Q(V_{\mathrm{DS}})$ and $Q_{\mathrm{S}} = Q(0)$;

$$(V_{\mathrm{GS}} - \Delta\varphi - V) - \varphi_{\mathrm{th}} \ln\left(\frac{8}{\delta R^2}\right) = \frac{Q}{C_0} + \varphi_{\mathrm{th}} \ln\left(\frac{Q}{Q_0}\right) + \varphi_{\mathrm{th}} \ln\left(\frac{Q + Q_0}{Q_0}\right). \quad (22)$$

Here, $\Delta\varphi$ is the difference of work function between channel material and the gate metal and

$$\delta = \frac{q^2 n_i}{k_B T \varepsilon_{\mathrm{S}}\varepsilon_0} \quad (23)$$

with intrinsic carrier density n_i. This equation should be solved numerically, but a closed form for Q is also given in Ref. [16] as

$$Q = C_0\left(-\frac{2C_0\varphi_{\mathrm{th}}^2}{Q_0} + \sqrt{\left(\frac{2C_0\varphi_{\mathrm{th}}^2}{Q_0}\right)^2 + 4\varphi_{\mathrm{th}}^2 \ln^2\left(1 + \exp\left(\frac{V_{\mathrm{GS}} - V_{\mathrm{T}} + \Delta V_{\mathrm{T}} - V}{2\varphi_{\mathrm{th}}}\right)\right)}\right) \quad (24)$$

with

$$V_{\mathrm{T}} = V_0 + 2\varphi_{\mathrm{th}} \ln\left(1 + \frac{Q'}{Q_0}\right) \quad (25)$$

and

$$Q' = C_0 \left(-\frac{2C_0\varphi_{\rm th}^2}{Q_0} + \sqrt{\left(\frac{2C_0\varphi_{\rm th}^2}{Q_0}\right)^2 + 4\varphi_{\rm th}^2 \ln^2\left(1 + \exp\left(\frac{V_{\rm GS} - V_0 - V}{2\varphi_{\rm th}}\right)\right)} \right) \tag{26}$$

and

$$\Delta V_{\rm T} = \frac{2C_0\varphi_{\rm th}^2}{Q_0} \frac{Q'}{Q_0 + Q'} \tag{27}$$

and

$$V_0 = \Delta\varphi + \varphi_{\rm th} \ln\left(\frac{8}{\delta R^2}\right) \tag{28}$$

Model of Ballistic One-Dimensional Transistor

Next, a brief outline to calculate drain current in ballistic NW-FETs is described following the model of the ballistic transistor by Lundstrom and co-workers [17, 18]. The electron density in one-dimensional (1D) electron system is calculated as

$$n_{\rm 1D} = \int_{E_C}^{\infty} \frac{2m^*}{\pi\hbar} \frac{1}{\sqrt{E - E_C}} \frac{1}{1 + \exp\left(\frac{E - E_F}{k_B T}\right)} dE \tag{29}$$

$$= \mathcal{D}_{\rm 1D} F_{-1/2}\left(\frac{E_F - E_C}{k_B T}\right), \tag{30}$$

where E_F is the Fermi level, E_C represents the bottom of the conduction band, m^* is the density of state effective mass, $\mathcal{D}_{\rm 1D}$ is the effective density of state in 1D system given by

$$\mathcal{D}_{\rm 1D} = \frac{\sqrt{2m^* k_B T}}{\sqrt{\pi}\hbar}, \tag{31}$$

$F_j(\eta)$ is a Fermi-Dirac integral of the j-th order

$$F_j(\eta) = \frac{1}{\Gamma(j+1)} \int_0^{\infty} \frac{\eta_0^j}{1 + \exp(\eta_0 - \eta)} d\eta_0, \tag{32}$$

and $\Gamma(z)$ is the Gamma function. Drain current of the transistor in the ballistic regime is determined by the net carrier flow from source to drain with energy larger than the top of the barrier $U_{\rm SCF}$, shown in Fig. 19. $U_{\rm SCF}$ is determined in a self-consistent way by solving the following equation:

$$U_{\rm SCF} = -q(\alpha_{\rm G} V_{\rm G} + \alpha_{\rm D} V_{\rm D} + \alpha_{\rm S} V_{\rm S}) + \frac{q^2}{C_\Sigma} n_s \tag{33}$$

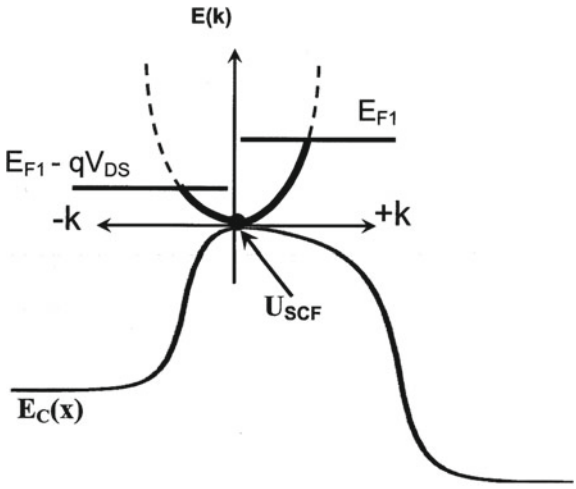

Fig. 19 Illustration to show how the top of the barrier is determined by the Fermi level in the drain and source. The carriers (electrons) from source to drain (or vice versa) has positive (negative) wavevector k and contribute to the positive drain current I_{DS}, and total carrier density at the top of the barrier is determined by the some of the carriers from source and drain. Copyright @ IEEE. All rights reserved. Reprinted, with permission, from Ref. [17]

Here n_s represents the electron density at the top of the barrier and given by the sum of the contribution from the source side and the drain side. Thus, using Eq. (30), n_s in 1D system is given by

$$n_s = \frac{\mathcal{D}_{1\mathrm{D}}}{2}\left[F_{-1/2}\left(\frac{E_F - U_{\mathrm{SCF}}}{k_B T}\right) + F_{-1/2}\left(\frac{E_F - qV_{\mathrm{D}} - U_{\mathrm{SCF}}}{k_B T}\right)\right] \tag{34}$$

Furthermore, V_i's (i = G, D, or S) are the voltage at the terminals of FETs, α_i's are the leverage factor of each terminals and given by the capacitance C_i associated with the each terminals as

$$\alpha_G = \frac{C_{\mathrm{G}}}{C_\Sigma}, \quad \alpha_{\mathrm{D}} = \frac{C_{\mathrm{D}}}{C_\Sigma}, \quad \alpha_{\mathrm{S}} = \frac{C_{\mathrm{S}}}{C_\Sigma}, \tag{35}$$

and

$$C_\Sigma = C_G + C_{\mathrm{D}} + C_{\mathrm{S}} \tag{36}$$

The values of these capacitors are set so that to fit with are used to fit the experimental data of S and DIBL, as described in Refs. [17, 205]. By setting $V_G = V_{\mathrm{GS}} + V_{\mathrm{S}}$ $V_{\mathrm{D}} = V_{\mathrm{DS}} + V_{\mathrm{S}}$, Eq. (33) reduces to

$$U_{UCF} + qV_{\mathrm{S}} = -q(\alpha_{\mathrm{G}} V_{\mathrm{GS}} + \alpha_{\mathrm{D}} V_{\mathrm{DS}}) + \frac{q^2}{C_\Sigma} n_s \tag{37}$$

using $\alpha_{\mathrm{G}} + \alpha_{\mathrm{D}} + \alpha_{\mathrm{S}} = 1$. By replacing $U_{\mathrm{SCF}} = E_0 - qV_{\mathrm{S}}$ and $E_F = E_{\mathrm{Fs}} - qV_{\mathrm{S}}$,

$$E_0 = -q(\alpha_{\mathrm{G}} V_{\mathrm{GS}} + \alpha_{\mathrm{D}} V_{\mathrm{DS}}) + \frac{q^2}{C_\Sigma} n_s \tag{38}$$

and

$$n_s = \mathcal{D}_{1D}\left[F_{-1/2}\left(\frac{E_{Fs}-E_0}{k_BT}\right)+F_{-1/2}\left(\frac{E_{Fs}-qV_{DS}-E_0}{k_BT}\right)\right] \tag{39}$$

Equation (38) is identical to Eq. (30) in Ref. [15], or Eq. (35) in [19], except for that multiple subbands and nonparabolicity are not considered in n_s given in Eq. (39). The drain current I_{DS} is calculated as [15, 18, 19]

$$I_{DS} = \frac{2qk_BT}{h}\left[F_0\left((E_{Fs}-E_0)/k_BT\right)-F_0\left((E_{Fs}-E_0-qV_{DS})/k_BT\right)\right] \tag{40}$$

$$= \frac{2qk_BT}{h}\left[\ln\left(1+\exp\left(\frac{E_{Fs}-E_0}{k_BT}\right)\right)-\ln\left(1+\exp\left(\frac{E_{Fs}-E_0-qV_{DS}}{k_BT}\right)\right)\right] \tag{41}$$

If one has to take into account multiple subbands in NWs, it is doable by considering quantized energy E_n and taking sum of the contribution from each subbands for n_s (Eq. 39) and I_{DS} (Eq. 41), as described in Refs. [15, 19].

Appendix 2: y-Parameters and Gain of FETs

Four-Terminal Network

Figure 20a represents a two-port or a four-terminal network. The port 1 consists of a pair of terminals 1 and 1′ and the port 2 consists of a pair of terminals 2 and 2′. The voltage at the port j is expressed as v_j, and the current i_j flows in (flows out) in terminal j (j'), with $j = 1, 2$. The y-parameters, or admittance parameters, are the parameter expressing the characteristics of a four-terminal network and correlate the input terminal 1–1′ and the output terminal 2–2′ with following relationship:

$$\begin{pmatrix} i_1 \\ i_2 \end{pmatrix} = \begin{pmatrix} y_{11} & y_{12} \\ y_{12} & y_{22} \end{pmatrix}\begin{pmatrix} v_1 \\ v_2 \end{pmatrix} \tag{42}$$

Amplifier is modeled as a four-terminal network with port 1 as an input and port 2 as an output, and a signal source e with a signal impedance z_S (or admittance $y_S = 1/z_S$) drives the input, and a load with impedance z_L (or admittance $y_L = 1/z_S$) is connected at the port 2, as shown in Fig. 20b. Important parameters for this 4-terminal network is the gains of the circuit, namely, current gain $G_i = -i_2/i_1$, voltage gain $G_v = v_2/v_1$, and power gain $G_p = \Re(G_v^* G_i)$, and input and output impedance, which are defined as $z_i = v_1/i_1$ and $z_o = v_2/i_2|_{e=0}$, respectively. In the presence of input source and load, we have following two equations;

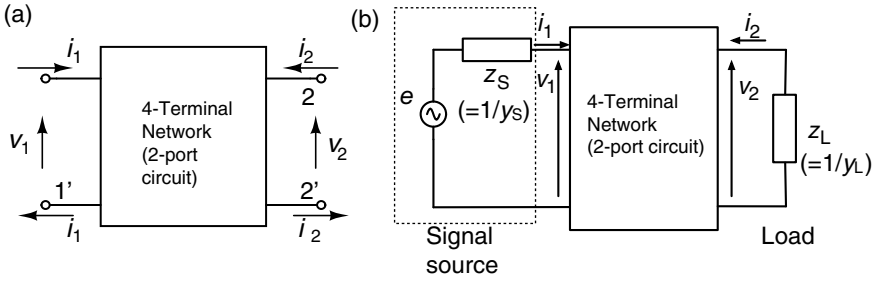

Fig. 20 **a** Two-port circuit or four-terminal network circuit. **b** Two-port circuit with signal source e with signal impedance z_S and load z_L

$$e - v_1 = z_s i_1 \tag{43}$$

$$-v_2 = z_L i_2 \tag{44}$$

With Eq. (42), we have four equations for v_1, v_2, i_1, and i_2, and we can express the gains and input/output impedance by the y-parameters as follows.

$$G_v = \frac{v_2}{v_1} = \frac{-y_{21}}{y_{22} + y_L} \tag{45}$$

$$G_i = -\frac{i_2}{i_1} = \frac{-y_{21} y_L}{(y_{11} y_{22} - y_{12} y_{21}) + y_{11} y_L} \tag{46}$$

$$G_p = -\frac{\Re(v_2^* i_2)}{\Re(v_1^* i_1)} = \frac{|y_{21}|^2 \Re y_L}{\Re[(y_{11} y_{22} - y_{12} y_{21}) + y_{11} y_L](y_{22} + y_L)^*} \tag{47}$$

$$z_i = \frac{v_1}{i_1} = \frac{1}{y_{11} - \frac{y_{12} y_{21}}{y_L + y_{22}}} \tag{48}$$

$$z_o = \left(\frac{v_2}{i_2}\right)_{e=0} = \frac{1}{y_{22} - \frac{y_{12} y_{21}}{y_S + y_{11}}} \tag{49}$$

For source-common amplifier shown is shown in Fig. 1c. the terminal 1–1′ corresponds to the gate-source, and terminal 2–2′ to the drain-source. To obtain of the gain of the amplifier, the circuit analysis is carried out by replacing the FET with a small signal model of and by deriving y-parameters from the circuit analysis. Then the gains and impedance are obtained using Eqs. (45)–(49). Figure 14a is a standard small signal equivalent circuit [282].

In Eqs. (45)–(49), parameters of the amplifier is expressed by the y-parameters of the FETs. Alternative expression is obtained by hybrid parameters or h-parameters defined by the following equation.

$$\begin{pmatrix} v_1 \\ i_2 \end{pmatrix} = \begin{pmatrix} h_{11} & h_{12} \\ h_{12} & h_{22} \end{pmatrix} \begin{pmatrix} i_1 \\ v_2 \end{pmatrix} \tag{50}$$

The y-parameters and h-parameters are not independent and related each other as follows;

$$y_{11} = \frac{1}{h_{11}} \tag{51}$$

$$y_{12} = -\frac{h_{12}}{h_{11}} \tag{52}$$

$$y_{21} = \frac{h_{21}}{h_{11}} \tag{53}$$

$$y_{22} = \frac{h_{11}h_{22} - h_{12}h_{21}}{h_{11}} \tag{54}$$

DC Gain of Source-Common Amplifier

For DC analysis, all the capacitive components can be neglected, and voltage gains are obtained as

$$|G_v| = g_{\mathrm{m}} \frac{r_{\mathrm{D}} z_{\mathrm{L}}}{r_{\mathrm{D}} + z_{\mathrm{L}}} \tag{55}$$

where g_{m} is the transconductance and $R_D = 1/g_D$ is the drain resistance. The voltage gain becomes large for large R_D and z_{L}, and, for $z_{\mathrm{L}} \to \infty$, $|G_v| x \to g_{\mathrm{m}} r_{\mathrm{D}} = g_{\mathrm{m}}/r_{\mathrm{D}}$. This is the maximally possible voltage gain in the source-common amplifier and is called intrinsic gain.

AC Analysis

In the case of AC analysis, both intrinsic and parasitic capacitors (and parasitic inductors if required but is neglected here) should be considered but the process is similar to what we have explained. Of particular importance here is the power gain G_p. The voltage gain G_v is maximum for $z_{\mathrm{L}} \to \infty$ (port 2 opened), while current gain is maximum for $z_{\mathrm{L}} = 0$ (port 2 shorted) and is given as $G_i = -y_{21}/y_{11}$ with y-parameters or $G_i = -h_{21}$ with h-parameters. Therefore, there is an optimum value for z_{L} to realize large G_v. Indeed, the maximum G_v is obtained when the impedance matching is satisfied, namely, $z_{\mathrm{L}} = z_o^*$. The same conditions is also required for input, thus $z_{\mathrm{S}} = z_i^*$. The gain obtained when both input and output impedance are matched, is called maximum available power gain (MAG) and by using the results given in Eq. (47), MAG is expressed by the y-parameters as follows;

$$\mathrm{MAG} = \frac{y_{21}}{y_{12}}(k - \sqrt{k^2 - 1}) \tag{56}$$

where k is a stability factor and given by

$$k = \frac{2\Re y_{11}\Re y_{22} - \Re(y_{12}y_{21})}{|y_{12}y_{21}|} \tag{57}$$

It is noted that the amplifier can be unstable and becomes an oscillator due to the feedback loop, and for the amplifier with FET, C_{GD} works as an intrinsic feedback element. That is, FET amplifier can be unstable due to C_{GD}. The stability of FET amplifier is judged by the stability factor k; if $k > 1$, the amplifier is stable, while it is unstable for $k < 1$ and Eq. (56) cannot be used. In this case, the figure of merit of the FET is given by the maximum stable power gain (MSG), which is given by $k = 1$ in Eq. (56):

$$\mathrm{MSG} = \frac{y_{21}}{y_{12}} \tag{58}$$

As mentioned, the source of instability is C_{GD}. To eliminate instability, we can parallelly connect a circuit which 'neutralizes' C_{GD} of the feedback loop. This process is called unilaterization, and the maximum available power gain U after unilateriza-iation is given by

$$\mathrm{U} = \frac{|y_{21}y_{12}|^2}{4(\Re y_{11}\Re y_{22} - \Re y_{12}\Re y_{21})} \tag{59}$$

which is called Mason's unilateral power gain.

As the impedance is dependent on frequency $f = 2\pi\omega$, the gains are also frequency dependent. Transition frequency f_{T} is defined by the frequency when maximum current gain $|y_{21}/y_{11}| = |h_{21}| = 1$. The frequency when MAG or U is unity is defined as maximum oscillation frequency $f_{\max}$, respectively.

Using the small signal equivalent circuit, f_{T} and $f_{\max}$ are calculated as follows. Neglecting R_G, R_S, and R_D, y-parameters based on the equivalent circuit of Fig. 14b are calculated as

$$y_{11} = \frac{R_i C_{\mathrm{GS}}^2 \omega}{D} + j\omega\left(\frac{C_{\mathrm{GS}}}{D} + C_{\mathrm{GD}}\right) \tag{60}$$

$$y_{12} = -j\omega C_{\mathrm{GD}} \tag{61}$$

$$y_{21} = \frac{g_{\mathrm{m}}}{1 + j\omega R_i C_{\mathrm{GS}}} C_{\mathrm{GD}} \tag{62}$$

$$y_{22} = g_D + j\omega(C_{\mathrm{GD}} + C_{DS}) \tag{63}$$

where

$$D = 1 + \omega^2 C_{\mathrm{GS}} R_i^2 \tag{64}$$

f_{T} is obtained from $|y_{21}/y_{11}| = 1$ and, neglecting higher order with respect to angular frequency ω, it is expressed as

$$f_{\mathrm{T}} = \frac{g_{\mathrm{m}}}{2\pi(C_{\mathrm{GS}} + C_{\mathrm{GD}})} \tag{65}$$

Calculation considering R_G, R_S, and R_D requires more elaboration but with reasonable approximation, it yields [169]

$$|\mathrm{MSG}| \sim \left| \frac{g_{\mathrm{m}}}{\omega C_{\mathrm{GD}}} \right| \tag{66}$$

and

$$\mathrm{MAG} \sim \left(\frac{f}{f_{\mathrm{T}}} \right)^2 [4g_{\mathrm{D}}(R_i + R_{\mathrm{S}} + R_{\mathrm{G}}) + 4\pi f_{\mathrm{T}} C_{\mathrm{GD}}(R_i + R_{\mathrm{S}} + R_{\mathrm{G}})] \tag{67}$$

Note that MAG rolls off with $1/f^2$, that is -6 dB/octave or -20 dB/decade. One also can see $f_{\max}$ is given by Eq. (9). U also roles off with -20 dB/decade. Mathematically, unity gain frequency is the same for both MAG and U but it requires some care for actual determination of $f_{\max}$ from the experiment of the high-frequency characteristics.

References

1. T. Ando, A.B. Fowler, F. Stern, Rev. Mod. Phys. **54**(2), 437 (1982). https://doi.org/10.1103/RevModPhys.54.437
2. H. Sakaki, Jpn. J. Appl. Phys. **19**(12), L735 (1980). https://doi.org/10.1143/JJAP.19.L735
3. P.A. Lee, T.V. Ramakrishnan, Rev. Mod. Phys. **57**(2), 287 (1985). https://doi.org/10.1103/RevModPhys.57.287
4. K. Hiruma, M. Yazawa, T. Katsuyama, K. Ogawa, K. Haraguchi, M. Koguchi, H. Kakibayashi, J. Appl. Phys. **77**(2), 447 (1995). https://doi.org/10.1063/1.359026
5. R.S. Wagner, W.C. Ellis, Appl. Phys. Lett. **4**(5), 89 (1964). https://doi.org/10.1063/1.1753975
6. T. Sakurai, in *IEEE/ACM International Symposium on Low Power Electronics and Design* (IEEE, 2011), pp. 57–58. https://doi.org/10.1109/ISLPED.2011.5993604
7. I. Ferain, C.A. Colinge, J.P. Colinge, Nature **479**(7373), 310 (2011). https://doi.org/10.1038/nature10676
8. J.P. Colinge, Solid State Electron. **48**(6), 897 (2004). https://doi.org/10.1016/j.sse.2003.12.020
9. S. Sze, K.K. Ng, *Physics of Semiconductor Devices*. Sze/Physics (Wiley, Hoboken, NJ, USA, 2006). https://doi.org/10.1002/0470068329
10. F. Balestra, S. Cristoloveanu, M. Benachir, J. Brini, T. Elewa, IEEE Electron Device Lett. **8**(9), 410 (1987). https://doi.org/10.1109/EDL.1987.26677
11. K. Suzuki, T. Tanaka, Y. Tosaka, H. Horie, Y. Arimoto, IEEE Trans. Electron Devices **40**(12), 2326 (1993). https://doi.org/10.1109/16.249482
12. R.H. Yan, A. Ourmazd, K. Lee, IEEE Trans. Electron Devices **39**(7), 1704 (1992). https://doi.org/10.1109/16.141237
13. C.P. Auth, J.D. Plummer, IEEE Electron Device Lett. **18**(2), 74 (1997). https://doi.org/10.1109/55.553049
14. B. Yu, Y. Yuan, J. Song, Y. Taur, IEEE Trans. Electron Devices **56**(10), 2357 (2009). https://doi.org/10.1109/TED.2009.2028048

15. E. Lind, Semicond. Sci. Technol. **31**(9), 093005 (2016). https://doi.org/10.1088/0268-1242/31/9/093005
16. B. Iniguez, D. Jimenez, J. Roig, H. Hamid, L. Marsal, J. Pallares, IEEE Trans. Electron Devices **52**(8), 1868 (2005). https://doi.org/10.1109/TED.2005.852892
17. A. Rahman, J. Guo, S. Datta, M. Lundstrom, IEEE Trans. Electron Devices **50**(9), 1853 (2003). https://doi.org/10.1109/TED.2003.815366
18. M. Lundstrom, J. Guo, *Nanoscale Transistors* (Kluwer Academic Publishers, Boston, 2006). https://doi.org/10.1007/0-387-28003-0
19. B. Yu, L. Wang, Y. Yuan, P.M. Asbeck, Y. Taur, IEEE Trans. Electron Devices **55**(11), 2846 (2008). https://doi.org/10.1109/TED.2008.2005163
20. https://nanohub.org/topics/negf
21. C.B. Zota, F. Lindelöw, L. Wernersson, E. Lind, in *2016 IEEE Symposium on VLSI Technology* (2016), pp. 1–2. https://doi.org/10.1109/VLSIT.2016.7573418
22. K. Tomioka, F. Izhizaka, T. Fukui, Nano Lett. **15**(11), 7253 (2015). https://doi.org/10.1021/acs.nanolett.5b02165
23. H. Takato, K. Sunouchi, N. Okabe, A. Nitayama, K. Hieda, F. Horiguchi, F. Masuoka, IEEE Trans. Electron Devices **38**(3), 573 (1991). https://doi.org/10.1109/16.75168
24. A. Veloso, E. Altamirano-Sanchez, S. Brus, B.T. Chan, M. Cupak, M. Dehan, C. Delvaux, K. Devriendt, G. Eneman, M. Ercken, T. Huynh-Bao, T. Ivanov, P. Matagne, C. Merckling, V. Paraschiv, S. Ramesh, E. Rosseel, L. Rynders, A. Sibaja-Hernandez, S. Suhard, Z. Tao, E. Vecchio, N. Waldron, D. Yakimets, K. De Meyer, D. Mocuta, N. Collaert, A. Thean, ECS Trans. **72**(4), 31 (2016). https://doi.org/10.1149/07204.0031ecst
25. A. Veloso, Z. Tao, W. Li, E. Altamirano-Sanchez, J.J. Versluijs, S. Brus, P. Matagne, N. Waldron, J. Ryckaert, D. Mocuta, N. Collaert, T. Huynh-Bao, E. Rosseel, V. Paraschiv, K. Devriendt, E. Vecchio, C. Delvaux, B.T. Chan, M. Ercken, in *2016 IEEE SOI-3D-Subthreshold Microelectronics Technology Unified Conference (S3S)* (IEEE, 2016), pp. 1–3. https://doi.org/10.1109/S3S.2016.7804409
26. IRDS. International Roadmap for Devices and Systems: 2018 Update; More Moore (2018)
27. J. Noborisaka, J. Motohisa, T. Fukui, Appl. Phys. Lett. **86**(21), 213102 (2005). https://doi.org/10.1063/1.1935038
28. F.E. Allegretti, T. Nishinaga, J. Cryst. Growth **156**(1–2), 1 (1995). https://doi.org/10.1016/0022-0248(95)00268-5
29. G. Bacchin, K. Tsunoda, T. Nishinaga, J. Cryst. Growth **174**(1–4), 616 (1997). https://doi.org/10.1016/S0022-0248(97)00018-3
30. G. Koblmüller, G. Abstreiter, physica status solidi (RRL)–Rapid Res. Lett. **8**(1), 11 (2014). https://doi.org/10.1002/pssr.201308207
31. H. Sekiguchi, K. Kishino, A. Kikuchi, Appl. Phys. Express **1**(12), 122837 (2008). https://doi.org/10.1002/pssb.200675628
32. K. Ikejiri, J. Noborisaka, S. Hara, J. Motohisa, T. Fukui, J. Cryst. Growth **298**(SPEC. ISS), 616 (2007). https://doi.org/10.1016/j.jcrysgro.2006.10.179
33. K. Ikejiri, T. Sato, H. Yoshida, K. Hiruma, J. Motohisa, S. Hara, T. Fukui, Nanotechnology **19**(26), 265604 (2008). https://doi.org/10.1088/0957-4484/19/26/265604
34. H. Yoshida, K. Ikejiri, T. Sato, S. Hara, K. Hiruma, J. Motohisa, T. Fukui, J. Cryst. Growth **312**(1), 52 (2009). https://doi.org/10.1016/j.jcrysgro.2009.10.006
35. M. Yao, C. Sheng, M. Ge, C.Y. Chi, S. Cong, A. Nakano, P.D. Dapkus, C. Zhou, ACS Nano **10**(2), 2424 (2016). https://doi.org/10.1021/acsnano.5b07232
36. M. Inari, J. Takeda, J. Motohisa, T. Fukui, Physica E **21**(2–4), 620 (2004). https://doi.org/10.1016/j.physe.2003.11.091
37. P. Mohan, J. Motohisa, T. Fukui, Nanotechnology **16**(12), 2903 (2005). https://doi.org/10.1088/0957-4484/16/12/029
38. Q. Gao, D. Saxena, F. Wang, L. Fu, S. Mokkapati, Y. Guo, L. Li, J. Wong-Leung, P. Caroff, H.H. Tan, C. Jagadish, Nano Lett. **14**(9), 5206 (2014). https://doi.org/10.1021/nl5021409
39. Q. Gao, V.G. Dubrovskii, P. Caroff, J. Wong-Leung, L. Li, Y. Gua, L. Fu, H.H. Tan, J. Chennupati, Nano Lett. **16**(7), 4361 (2016). https://doi.org/10.1021/acs.nanolett.6b01461

40. Y. Kitauchi, Y. Kobayashi, K. Tomioka, S. Hara, K. Hiruma, T. Fukui, J. Motohisa, Nano Lett. **10**(5), 1699 (2010). https://doi.org/10.1021/nl1000407
41. T. Yamashita, T. Akiyama, K. Nakamura, T. Ito, Jpn. J. Appl. Phys. **49**(5), 55003 (2010). https://doi.org/10.1143/JJAP.49.055003
42. T. Yamashita, T. Akiyama, K. Nakamura, T. Ito, Jpn. J. Appl. Phys. **50**(5), 055001 (2011). https://doi.org/10.1143/JJAP.50.055001
43. K.A. Bertness, A. Roshko, L.M. Mansfield, T.E. Harvey, N.A. Sanford, J. Cryst. Growth **310**(13), 3154 (2008). https://doi.org/10.1016/j.jcrysgro.2008.03.033
44. Y. Kohashi, S. Sakita, S. Hara, J. Motohisa, Appl. Phys. Express **6**(2), 025502 (2013). https://doi.org/10.7567/APEX.6.025502
45. M. Borg, H. Schmid, K.E. Moselund, G. Signorello, L. Gignac, J. Bruley, C. Breslin, P. Das Kanungo, P. Werner, H. Riel, Nano Lett. **14**(4), 1914 (2014). https://doi.org/10.1021/nl404743j
46. H. Schmid, M. Borg, K. Moselund, L. Gignac, C.M. Breslin, J. Bruley, D. Cutaia, H. Riel, Appl. Phys. Lett. **106**(23), 233101 (2015). https://doi.org/10.1063/1.4921962
47. D. Cutaia, K.E. Moselund, M. Borg, H. Schmid, L. Gignac, C.M. Breslin, S. Karg, E. Uccelli, H. Riel, IEEE J. Electron Devices Soc. **3**(3), 176 (2015). https://doi.org/10.1109/JEDS.2015.2388793
48. F. Glas, Phys. Rev. B, Cond. Matter **74**(12), 121302 (2006). https://doi.org/10.1103/PhysRevB.74.121302
49. K. Tomioka, M. Yoshimura, T. Fukui, Nano Lett. **13**(12), 5822 (2013). https://doi.org/10.1021/nl402447h
50. K. Tomioka, J. Motohisa, S. Hara, T. Fukui, Nano Lett. **8**(10), 3475 (2008). https://doi.org/10.1021/nl802398j
51. K. Tomioka, Y. Kobayashi, J. Motohisa, S. Hara, T. Fukui, Nanotechnology **20**(14), 145302 (2009). https://doi.org/10.1088/0957-4484/20/14/145302
52. K. Tomioka, T. Tanaka, S. Hara, K. Hiruma, T. Fukui, IEEE, J. Sel. Top. Quantum Electron. **17**(4), 1112 (2011). https://doi.org/10.1109/JSTQE.2010.2068280
53. K. Tomioka, T. Fukui, J. Phys. D Appl. Phys. **47**(39), 394001 (2014). https://doi.org/10.1088/0022-3727/47/39/394001
54. H. Kim, A.C. Farrell, P. Senanayake, W.J. Lee, D.L. Huffaker, Nano Lett. **16**(3), 1833 (2016). https://doi.org/10.1021/acs.nanolett.5b04883
55. S. Hertenberger, D. Rudolph, M. Bichler, J.J. Finley, G. Abstreiter, G. Koblmüller, J. Appl. Phys. **108**(11), 114316 (2010). https://doi.org/10.1063/1.3525610
56. S. Hertenberger, S. Funk, K. Vizbaras, A. Yadav, D. Rudolph, J. Becker, S. Bolte, M. Döblinger, M. Bichler, G. Scarpa, P. Lugli, I. Zardo, J.J. Finley, M.C. Amann, G. Abstreiter, G. Koblmüller, Appl. Phys. Lett. **101**(4), 043116 (2012). https://doi.org/10.1063/1.4738769
57. T. Mårtensson, C.P.T. Svensson, B.A. Wacaser, M.W. Larsson, W. Seifert, K. Deppert, A. Gustafsson, L.R. Wallenberg, L. Samuelson, Nano Lett. **4**(10), 1987 (2004). https://doi.org/10.1021/nl0487267
58. M. Mattila, T. Hakkarainen, H. Lipsanen, H. Jiang, E.I. Kauppinen, Appl. Phys. Lett. **89**(6), 063119 (2006). https://doi.org/10.1063/1.2336599
59. B. Mandl, J. Stangl, T. Mårtensson, A. Mikkelsen, J. Eriksson, L.S. Karlsson, G. Bauer, L. Samuelson, W. Seifert, Nano Lett. **6**(8), 1817 (2006). https://doi.org/10.1021/nl060452v
60. S. Plissard, G. Larrieu, X. Wallart, P. Caroff, Nanotechnology **22**(27), 275602 (2011). https://doi.org/10.1088/0957-4484/22/27/275602
61. S.J. Gibson, J.P. Boulanger, R.R. LaPierre, Semicond. Sci. Technol. **28**(10), 105025 (2013). https://doi.org/10.1088/0268-1242/28/10/105025
62. A.M. Munshi, D.L. Dheeraj, V.T. Fauske, D.C. Kim, J. Huh, J.F. Reinertsen, L. Ahtapodov, K.D. Lee, B. Heidari, A.T. Van Helvoort, B.O. Fimland, H. Weman, Nano Lett. **14**(2), 960 (2014). https://doi.org/10.1021/nl404376m
63. M.T. Robson, V.G. Dubrovskii, R.R. LaPierre, Nanotechnology **26**(46), 465301 (2015). https://doi.org/10.1088/0957-4484/26/46/465301

64. E. Russo-Averchi, J. Vukajlovic Plestina, G. Tütüncüoglu, F. Matteini, A. Dalmau-Mallorquí, M. De La Mata, D. Rüffer, H.A. Potts, J. Arbiol, S. Conesa-Boj, A. Fontcuberta I. Morral, Nano Lett. **15**(5), 2869 (2015). https://doi.org/10.1021/nl504437v
65. J. Vukajlovic-Plestina, W. Kim, L. Ghisalberti, G. Varnavides, G. Tütüncuoglu, H. Potts, M. Friedl, L. Güniat, W.C. Carter, V.G. Dubrovskii, A. Fontcuberta i Morral, Nat. Commun. **10**(1), 869 (2019). https://doi.org/10.1038/s41467-019-08807-9
66. J. Vukajlovic-Plestina, V.G. Dubrovskii, G. Tütüncuoglu, H. Potts, R. Ricca, F. Meyer, F. Matteini, J.B. Leran, A.F. i Morral, Nanotechnology **27**(45), 455601 (2016). https://doi.org/10.1088/0957-4484/27/45/455601
67. S.G. Ghalamestani, S. Johansson, B.M. Borg, E. Lind, K.A. Dick, L.E. Wernersson, Nanotechnology **23**(1), 015302 (2012). https://doi.org/10.1088/0957-4484/23/1/015302
68. P. Mohan, J. Motohisa, B.M. Borg, Appl. Phys. Lett. **88**(13), 133105 (2006). https://doi.org/10.1063/1.2189203
69. P. Mohan, J. Motohisa, T. Fukui, Appl. Phys. Lett. **88**(1), 13110 (2006). https://doi.org/10.1063/1.2161576
70. L. Froberg, C. Rehnstedt, C. Thelander, E. Lind, L. Wernersson, L. Samuelson, IEEE Electron Device Lett. **29**(9), 981 (2008). https://doi.org/10.1109/LED.2008.2001971
71. E. Memisevic, J. Svensson, E. Lind, L.E. Wernersson, Nanotechnology **29**(43), 435201 (2018). https://doi.org/10.1088/1361-6528/aad949
72. M.T. Borgström, J. Wallentin, M. Heurlin, S. Fält, P. Wickert, J. Leene, M.H. Magnusson, K. Deppert, L. Samuelson, IEEE, J. Sel. Top. Quantum Electron. **17**(4), 1050 (2011). https://doi.org/10.1109/JSTQE.2010.2073681
73. R.E. Algra, M.A. Verheijen, M.T. Borgström, L.F. Feiner, G. Immink, W.J.P. Van Enckevort, E. Vlieg, E.P.A.M. Bakkers, Nature **456**(7220), 369 (2008). https://doi.org/10.1038/nature07570
74. K. Ikejiri, F. Ishizaka, K. Tomioka, T. Fukui, Nano Lett. **12**(9), 4770 (2012). https://doi.org/10.1021/nl302202r
75. E. Nakai, M. Chen, M. Yoshimura, K. Tomioka, T. Fukui, Jpn. J. Appl. Phys. **54**, 15201 (2015). https://doi.org/10.7567/JJAP.54.015201
76. N.P. Dasgupta, J. Sun, C. Liu, S. Brittman, S.C. Andrews, J. Lim, H. Gao, R. Yan, P. Yang, Adv. Mater. **26**(14), 2137 (2014). https://doi.org/10.1002/adma.201305929
77. N.I. Goktas, P. Wilson, A. Ghukasyan, D. Wagner, S. McNamee, R.R. LaPierre, Appl. Phys. Rev. **5**(4), 41305 (2018). https://doi.org/10.1063/1.5054842
78. Z. Li, H.H. Tan, C. Jagadish, L. Fu, Adv. Mater. Technol. **3**(9), 1 (2018). https://doi.org/10.1002/admt.201800005
79. S. Mokkapati, C. Jagadish, Opt. Express **24**(15), 17345 (2016). https://doi.org/10.1364/oe.24.017345
80. S.W. Eaton, A. Fu, A.B. Wong, C.Z. Ning, P. Yang, Nat. Rev. Mater. **1**(6), 16028 (2016). https://doi.org/10.1038/natrevmats.2016.28
81. I. Holzman, Y. Ivry, Adv. Quantum Technol. **2**(3–4), 1800058 (2019). https://doi.org/10.1002/qute.201800058
82. H.J. Joyce, J.L. Boland, C.L. Davies, S.A. Baig, M.B. Johnston, Semicond. Sci. Technol. **31**(10), 103003 (2016). https://doi.org/10.1088/0268-1242/31/10/103003
83. Z. Wang, S. Lee, K. Koo, K. Kim, IEEE Trans. Nanobiosci. **15**(3), 186 (2016). https://doi.org/10.1109/TNB.2016.2528258
84. M.A. Doucey, S. Carrara, Trends Biotechnol. **37**(1), 86 (2019). https://doi.org/10.1016/j.tibtech.2018.07.014
85. Q. Li, N. Lu, L. Wang, C. Fan, Small Methods **2**(4), 1700263 (2018). https://doi.org/10.1002/smtd.201700263
86. T. Mikolajick, A. Heinzig, J. Trommer, T. Baldauf, W.M. Weber, Semicond. Sci. Technol. **32**(4), 43001 (2017). https://doi.org/10.1088/1361-6641/aa5581
87. J. Tang, K.L. Wang, Nanoscale **7**(10), 4325 (2015). https://doi.org/10.1039/c4nr07611g
88. C. Gould, K. Pappert, G. Schmidt, L. Molenkamp, Adv. Mater. **19**(3), 323 (2007). https://doi.org/10.1002/adma.200600126

89. M.T. Elm, P.J. Klar, S. Ito, S. Hara, Phys. Rev. B **83**(23), 235305 (2011). https://doi.org/10.1103/PhysRevB.83.235305
90. C. Michel, M.T. Elm, B. Goldlücke, S.D. Baranovskii, P. Thomas, W. Heimbrodt, P.J. Klar, Appl. Phys. Lett. **92**(22), 223119 (2008). https://doi.org/10.1063/1.2937128
91. P.J. Wellmann, J.M. Garcia, J.L. Feng, P.M. Petroff, Appl. Phys. Lett. **73**(22), 3291 (1998). https://doi.org/10.1063/1.122748
92. M.T. Elm, C. Michel, J. Stehr, D.M. Hofmann, P.J. Klar, S. Ito, S. Hara, H.A. Krug von Nidda, J. Appl. Phys. **107**(1), 13701 (2010). https://doi.org/10.1063/1.3275427
93. P.N. Hai, S. Ohya, M. Tanaka, S.E. Barnes, S. Maekawa, Nature **458**(7237), 489 (2009). https://doi.org/10.1038/nature07879
94. P.N. Hai, S. Ohya, M. Tanaka, Nat. Nanotechnol. **5**(8), 593 (2010). https://doi.org/10.1038/nnano.2010.130
95. M. Tanaka, S. Ohya, P. Nam Hai, Appl. Phys. Rev. **1**(1), 11102 (2014). https://doi.org/10.1063/1.4840136. https://doi.org/10.1063/1.4840136
96. P.V. Radovanovic, C.J. Barrelet, S. Gradečak, F. Qian, C.M. Lieber, Nano Lett. **5**(7), 1407 (2005). https://doi.org/10.1021/nl050747t
97. H.S. Kim, Y.J. Cho, K.J. Kong, C.H. Kim, G.B. Chung, J. Park, J.Y. Kim, J. Yoon, M.H. Jung, Y. Jo, B. Kim, J.P. Ahn, Chem. Mater. **21**(6), 1137 (2009). https://doi.org/10.1021/cm8033388
98. C. Borschel, M.E. Messing, M.T. Borgström, W. Paschoal, J. Wallentin, S. Kumar, K. Mergenthaler, K. Deppert, C.M. Canali, H. Pettersson, L. Samuelson, C. Ronning, Nano Lett. **11**(9), 3935 (2011). https://doi.org/10.1021/nl2021653
99. A. Rudolph, M. Soda, M. Kiessling, T. Wojtowicz, D. Schuh, W. Wegscheider, J. Zweck, C. Back, E. Reiger, Nano Lett. **9**(11), 3860 (2009). https://doi.org/10.1021/nl9020717
100. X. Yu, H. Wang, D. Pan, J. Zhao, J. Misuraca, S. von Molnár, P. Xiong, Nano Lett. **13**(4), 1572 (2013). https://doi.org/10.1021/nl304740k
101. D.G. Ramlan, S.J. May, J.G. Zheng, J.E. Allen, B.W. Wessels, L.J. Lauhon, Nano Lett. **6**(1), 50 (2006). https://doi.org/10.1021/nl0519276
102. M.F.H. Wolff, D. Görlitz, K. Nielsch, M.E. Messing, K. Deppert, Nanotechnology **22**(5), 55602 (2010). https://doi.org/10.1088/0957-4484/22/5/055602
103. M. Hilse, Y. Takagaki, J. Herfort, M. Ramsteiner, C. Herrmann, S. Breuer, L. Geelhaar, H. Riechert, Appl. Phys. Lett. **95**(13), 133126 (2009). https://doi.org/10.1063/1.3240405
104. J. Liang, J. Wang, A. Paul, B.J. Cooley, D.W. Rench, N.S. Dellas, S.E. Mohney, R. Engel-Herbert, N. Samarth, Appl. Phys. Lett. **100**(18), 182402 (2012). https://doi.org/10.1063/1.4710524
105. H.J. Choi, H.K. Seong, J. Chang, K.I. Lee, Y.J. Park, J.J. Kim, S.K. Lee, R. He, T. Kuykendall, P. Yang, Adv. Mater. **17**(11), 1351 (2005). https://doi.org/10.1002/adma.200401706
106. H.K. Seong, J.Y. Kim, J.J. Kim, S.C. Lee, S.R. Kim, U. Kim, T.E. Park, H.J. Choi, Nano Lett. **7**(11), 3366 (2007). https://doi.org/10.1021/nl0716552
107. J.L. Lensch-Falk, E.R. Hemesath, L.J. Lauhon, Nano Lett. **8**(9), 2669 (2008). https://doi.org/10.1021/nl800933s
108. J. Tang, C.Y. Wang, M.H. Hung, X. Jiang, L.T. Chang, L. He, P.H. Liu, H.J. Yang, H.Y. Tuan, L.J. Chen, K.L. Wang, ACS Nano **6**(6), 5710 (2012). https://doi.org/10.1021/nn301956m
109. Y.C. Lin, Y. Chen, A. Shailos, Y. Huang, Nano Lett. **10**(6), 2281 (2010). https://doi.org/10.1021/nl101477q
110. X. Li, G. Meng, S. Qin, Q. Xu, Z. Chu, X. Zhu, M. Kong, A.P. Li, ACS Nano **6**(1), 831 (2012). https://doi.org/10.1021/nn2043466
111. S. Hara, D. Kawamura, H. Iguchi, J. Motohisa, T. Fukui, J. Cryst. Growth **310**(7–9), 2390 (2008). https://doi.org/10.1016/j.jcrysgro.2007.12.026
112. M. Yatago, H. Iguchi, S. Sakita, S. Hara, Jpn. J. Appl. Phys. **51**(2), 02BH01 (2012). https://doi.org/10.1143/jjap.51.02bh01
113. S. Hara, S. Sakita, M. Yatago, Jpn. J. Appl. Phys. **51**(11S), 11PE01 (2012). https://doi.org/10.1143/JJAP.51.11PE01. Open access

114. M.T. Elm, P.J. Klar, S. Ito, S. Hara, H.A. Krug von Nidda, Phys. Rev. B **84**(3), 35309 (2011). https://doi.org/10.1103/PhysRevB.84.035309
115. M. Fischer, M.T. Elm, S. Sakita, S. Hara, P.J. Klar, Appl. Phys. Lett. **106**(3), 32401 (2015). https://doi.org/10.1063/1.4906036
116. F.A. Zwanenburg, D.W. van der Mast, H.B. Heersche, L.P. Kouwenhoven, E.P.A.M. Bakkers, Nano Lett. **9**(7), 2704 (2009). https://doi.org/10.1021/nl901184m
117. T. Inokuchi, T. Marukame, M. Ishikawa, H. Sugiyama, Y. Saito, Appl. Phys. Express **2**, 23006 (2009). https://doi.org/10.1143/apex.2.023006
118. X. Jiang, R. Wang, R.M. Shelby, R.M. Macfarlane, S.R. Bank, J.S. Harris, S.S.P. Parkin, Phys. Rev. Lett. **94**(5), 56601 (2005). https://doi.org/10.1103/PhysRevLett.94.056601
119. S. Sugahara, J. Nitta, Proc. IEEE **98**(12), 2124 (2010). https://doi.org/10.1109/JPROC.2010.2064272
120. K. Biermann, A. Hernández-Mínguez, R. Hey, P.V. Santos, J. Appl. Phys. **112**(8), 83913 (2012). https://doi.org/10.1063/1.4759241
121. R. Kodaira, S. Hara, K. Kabamoto, H. Fujimagari, Jpn. J. Appl. Phys. **55**(7), 75503 (2016). https://doi.org/10.7567/JJAP.55.075503. Open access
122. K. Kabamoto, R. Kodaira, S. Hara, J. Cryst. Growth **464**, 80 (2017). https://doi.org/10.1016/j.jcrysgro.2016.11.044
123. R. Kodaira, K. Kabamoto, S. Hara, Jpn. J. Appl. Phys. **56**(6S1), 06GH03 (2017). https://doi.org/10.7567/JJAP.56.06GH03
124. R. Kodaira, R. Horiguchi, S. Hara, J. Cryst. Growth **507**, 241 (2019). https://doi.org/10.1016/j.jcrysgro.2018.11.023
125. S. Hara, M.T. Elm, P.J. Klar, J. Mater. Res. **34**(23), 3863 (2019). https://doi.org/10.1557/jmr.2019.333. Invited paper
126. D.V. Shenai-Khatkhate, R.L. DiCarlo, R.A. Ware, J. Cryst. Growth **310**(7), 2395 (2008). https://doi.org/10.1016/j.jcrysgro.2007.11.196. D. V. Shenai-Khatkhate et al. reported on an update on the vapor pressure (P) equation of TMIn, i.e, $\log P(\text{Torr}) = 10.98 - 3204/T(\text{K})$. In this study, however, the authors used the estimated partial pressure for TMIn obtained using a conventionally used old equation, i.e., $\log P(\text{Torr}) = 10.52 - 3014/T(\text{K})$, for comparison with the previous articles
127. I. Bonev, Acta Crystallogr. Sect. A **28**(6), 508 (1972). https://doi.org/10.1107/S0567739472001391
128. Commissioned analysis conducted by Toray Research Center, Inc., Japan, https://www.toray-research.co.jp/en/businesses/analysis/
129. W. Braun, A. Trampert, V.M. Kaganer, B. Jenichen, D.K. Satapathy, K.H. Ploog, J. Cryst. Growth **301-302**, 50 (2007). http://www.sciencedirect.com/science/article/pii/S0022024806008633
130. N. Nateghi, D. Ménard, R.A. Masut, J. Appl. Phys. **116**(13), 133512 (2014). https://doi.org/10.1063/1.4896910
131. H. Munekata, H. Ohno, R.R. Ruf, R.J. Gambino, L.L. Chang, J. Cryst. Growth **111**(1), 1011 (1991). https://doi.org/10.1016/0022-0248(91)91123-R
132. T. Akiyama, K. Sano, K. Nakamura, T. Ito, Jpn. J. Appl. Phys. **45**(No. 9), L275 (2006). https://doi.org/10.1143/jjap.45.l275
133. F. Glas, J.C. Harmand, G. Patriarche, Phys. Rev. Lett. **99**(14), 146101 (2007). https://doi.org/10.1103/PhysRevLett.99.146101
134. F. Ishizaka, Y. Hiraya, K. Tomioka, J. Motohisa, T. Fukui, Nano Lett. **17**(3), 1350 (2017). https://doi.org/10.1021/acs.nanolett.6b03727
135. H.J. Joyce, J. Wong-Leung, Q. Gao, H.H. Tan, C. Jagadish, Nano Lett. **10**(3), 908 (2010). https://doi.org/10.1021/nl903688v
136. M. Paladugu, J. Zou, Y.N. Guo, X. Zhang, H.J. Joyce, Q. Gao, H.H. Tan, C. Jagadish, Y. Kim, Nanoscale Res. Lett. **4**(8), 846 (2009). https://doi.org/10.1007/s11671-009-9326-6
137. M. Yokoyama, H. Yamaguchi, T. Ogawa, M. Tanaka, J. Appl. Phys. **97**(10), 10D317 (2005). https://doi.org/10.1063/1.1852214
138. S. Hara, T. Fukui, Appl. Phys. Lett. **89**(11), 113111 (2006). https://doi.org/10.1063/1.2349309

139. S. Hara, M. Lampalzer, T. Torunski, K. Volz, W. Treutmann, W. Stolz, J. Cryst. Growth **261**(2–3), 330 (2004). https://doi.org/10.1016/j.jcrysgro.2003.11.064
140. J. Hubmann, B. Bauer, H.S. Körner, S. Furthmeier, M. Buchner, G. Bayreuther, F. Dirnberger, D. Schuh, C.H. Back, J. Zweck, E. Reiger, D. Bougeard, Nano Lett. **16**(2), 900 (2016). https://doi.org/10.1021/acs.nanolett.5b03658
141. Commissioned theoretical calculation carried out by Advance Soft Corp., Japan, using the Advance/PHASE software, http://www.advancesoft.jp/product/advance_phase/
142. T. Tanaka, K. Tomioka, S. Hara, J. Motohisa, E. Sano, T. Fukui, Appl. Phys. Express **3**(2), 025003 (2010). https://doi.org/10.1143/APEX.3.025003
143. M. Egard, S. Johansson, A.C. Johansson, K.M. Persson, A.W. Dey, B.M. Borg, C. Thelander, L.E. Wernersson, E. Lind, Nano Lett. **10**(3), 809 (2010). https://doi.org/10.1021/nl903125m
144. C. Rehnstedt, T. Martensson, C. Thelander, L. Samuelson, L. Wernersson, IEEE Trans. Electron Devices **55**(11), 3037 (2008). https://doi.org/10.1109/TED.2008.2005179
145. C. Thelander, L. FrobergFroberg, C. Rehnstedt, L. Samuelson, L. Wernersson, IEEE Electron Device Lett. **29**(3), 206 (2008). https://doi.org/10.1109/LED.2007.915374
146. M. Berg, K.M. Persson, O.P. Kilpi, J. Svensson, E. Lind, L.E. Wernersson, in *2015 IEEE International Electron Devices Meeting (IEDM)* (IEEE, 2015), pp. 31.2.1–31.2.4. https://doi.org/10.1109/IEDM.2015.7409806
147. A. Jonsson, J. Svensson, L.E. Wernersson, IEEE Electron Device Lett. **39**(7), 935 (2018). https://doi.org/10.1109/LED.2018.2837676
148. M. Berg, O.P. Kilpi, K.M. Persson, J. Svensson, M. Hellenbrand, E. Lind, L.E. Wernersson, IEEE Electron Device Lett. **37**(8), 966 (2016). https://doi.org/10.1109/LED.2016.2581918
149. J. Chen, R. Könenkamp, Appl. Phys. Lett. **82**(26), 4782 (2003). https://doi.org/10.1063/1.1587258
150. P. Nguyen, H.T. Ng, T. Yamada, M.K. Smith, J. Li, J. Han, M. Meyyappan, Nano Lett. **4**(4), 651 (2004). https://doi.org/10.1021/nl0498536
151. H.T. Ng, J. Han, T. Yamada, P. Nguyen, Y.P. Chen, M. Meyyappan, Nano Lett. **4**(7), 1247 (2004). https://doi.org/10.1021/nl049461z
152. V. Schmidt, H. Riel, S. Senz, S. Karg, W. Riess, U. Gösele, Small **2**(1), 85 (2006). https://doi.org/10.1002/smll.200500181
153. J. Goldberger, A.I. Hochbaum, R. Fan, P. Yang, Nano Lett. **6**(5), 973 (2006). https://doi.org/10.1021/nl060166j
154. T. Bryllert, L.E. Wernersson, L. Froberg, L. Samuelson, IEEE Electron Device Lett. **27**(5), 323 (2006). https://doi.org/10.1109/LED.2006.873371
155. C. Thelander, C. Rehnstedt, L.E. Froberg, E. Lind, T. Martensson, P. Caroff, T. Lowgren, B.J. Ohlsson, L. Samuelson, L.E. Wernersson, IEEE Trans. Electron Devices **55**(11), 3030 (2008). https://doi.org/10.1109/TED.2008.2005151
156. K. Tomioka, K. Ikejiri, T. Tanaka, J. Motohisa, S. Hara, K. Hiruma, T. Fukui, J. Mater. Res. **26**(17), 2127 (2011). https://doi.org/10.1557/jmr.2011.103. Invited paper
157. K. Tomioka, M. Yoshimura, T. Fukui, Technical Digest—International Electron Devices Meeting, IEDM **1**(111), 33.3.1 (2011). https://doi.org/10.1109/IEDM.2011.6131663
158. K.M. Persson, M. Berg, M. Borg, J. Wu, H. Sjöland, E. Lind, L.E. Wernersson, Device Research Conference-Conference Digest. DRC **479**(7373), 195 (2012). https://doi.org/10.1109/DRC.2012.6256966
159. K. Tomioka, M. Yoshimura, T. Fukui, Nature **488**(7410), 189 (2012). https://doi.org/10.1038/nature11293
160. O.P. Kilpi, J. Wu, J. Svensson, E. Lind, L.E. Wernersson, in *2017 Symposium on VLSI Technology* (IEEE, 2017), pp. T36–T37. https://doi.org/10.23919/VLSIT.2017.7998191
161. O.P. Kilpi, J. Svensson, J. Wu, A.R. Persson, R. Wallenberg, E. Lind, L.E. Wernersson, Nano Lett. **17**(10), 6006 (2017). https://doi.org/10.1021/acs.nanolett.7b02251
162. H. Gamo, K. Tomioka, J. Cryst. Growth **500**, 58 (2018). https://doi.org/10.1016/j.jcrysgro.2018.07.035
163. A.W. Dey, C. Thelander, E. Lind, K.A. Dick, B.M. Borg, M. Borgstrom, P. Nilsson, L.E. Wernersson, IEEE Electron Device Lett. **33**(6), 791 (2012). https://doi.org/10.1109/LED.2012.2190132

164. J.J. Gu, X.W. Wang, H. Wu, J. Shao, A.T. Neal, M.J. Manfra, R.G. Gordon, P.D. Ye, in *2012 International Electron Devices Meeting* (IEEE, 2012), pp. 27.6.1–27.6.4. https://doi.org/10.1109/IEDM.2012.6479117
165. C.B. Zota, G. Roll, L.E. Wernersson, E. Lind, IEEE Trans. Electron Devices **61**(12), 4078 (2014). https://doi.org/10.1109/TED.2014.2363732
166. G. Doornbos, M. Holland, G. Vellianitis, M.J.H. Van Dal, B. Duriez, R. Oxland, A. Afzalian, T.K. Chen, G. Hsieh, M. Passlack, Y.C. Yeo, IEEE J. Electron Devices Soc. **4**(5), 253 (2016). https://doi.org/10.1109/JEDS.2016.2574203
167. X. Zhao, J. Lin, C. Heidelberger, E.A. Fitzgerald, J.A. Del Alamo, Technical Digest—International Electron Devices Meeting, IEDM (2013), pp. 695–698. https://doi.org/10.1109/IEDM.2013.6724710
168. S. Ramesh, T. Ivanov, E. Camerotto, N. Sun, J. Franco, A. Sibaja-Hernandez, R. Rooyackers, A. Alian, J. Loo, A. Veloso, A. Milenin, D. Lin, P. Favia, H. Bender, N. Collaert, A.V. Thean, K. De Meyer, Digest of Technical Papers—Symposium on VLSI Technology **2016**(Sept), 1 (2016). https://doi.org/10.1109/VLSIT.2016.7573419
169. M. Fukuta, K. Suyama, H. Suzuki, H. Ishikawa, IEEE Trans. Electron Devices **23**(4), 388 (1976). https://doi.org/10.1109/T-ED.1976.18416
170. M.S. Gupta, IEEE Trans. Microw. Theory Tech. **40**(5), 864 (1992). https://doi.org/10.1109/22.137392
171. S. Johansson, E. Memisevic, L.E. Wernersson, E. Lind, IEEE Electron Device Lett. **35**(5), 518 (2014). https://doi.org/10.1109/LED.2014.2310119
172. H. Fukui, IEEE Trans. Electron Devices **26**(7), 1032 (1979). https://doi.org/10.1109/T-ED.1979.19541
173. M. Pospieszalski, IEEE Trans. Microw. Theory Tech. **37**(9), 1340 (1989). https://doi.org/10.1109/22.32217
174. K. Jansson, E. Lind, L.E. Wernersson, IEEE Trans. Electron Devices **59**(9), 2375 (2012). https://doi.org/10.1109/TED.2012.2204757
175. X. Jiang, Q. Xiong, S. Nam, F. Qian, Y. Li, C.M. Lieber, Nano Lett. **7**(10), 3214 (2007). https://doi.org/10.1021/nl072024a
176. J. Xiang, W. Lu, Y. Hu, Y. Wu, H. Yan, C.M. Lieber, Nature **441**(7092), 489 (2006). https://doi.org/10.1038/nature04796
177. Y. Hu, J. Xiang, G. Liang, H. Yan, C.M. Lieber, Nano Lett. **8**(3), 925 (2008). https://doi.org/10.1021/nl073407b
178. D.C. Dillen, K. Kim, E.S. Liu, E. Tutuc, Nat. Nanotechnol. **9**(2), 116 (2014). https://doi.org/10.1038/nnano.2013.301
179. B. Ganjipour, M. Ek, B. Mattias Borg, K.A. Dick, M.E. Pistol, L.E. Wernersson, C. Thelander, Appl. Phys. Lett. **101**(10), 103501 (2012). https://doi.org/10.1063/1.4749283
180. T. Tanaka. Unpublished
181. E. Lind, A.I. Persson, L. Samuelson, L.E. Wernersson, Nano Lett. **6**(9), 1842 (2006). https://doi.org/10.1021/nl052468b
182. A.C. Seabaugh, Q. Zhang, Proc. IEEE **98**(12), 2095 (2010). https://doi.org/10.1109/JPROC.2010.2070470
183. H. Lu, A. Seabaugh, IEEE J. Electron Devices Soc. **2**(4), 44 (2014). https://doi.org/10.1109/JEDS.2014.2326622
184. C. Convertino, C.B. Zota, H. Schmid, A.M. Ionescu, K.E. Moselund, J. Phys. Condens. Matter **30**(26), 264005 (2018). https://doi.org/10.1088/1361-648X/aac5b4
185. Q. Zhang, W. Zhao, A. Seabaugh, IEEE Electron Device Lett. **27**(4), 297 (2006). https://doi.org/10.1109/LED.2006.871855
186. M.T. Björk, J. Knoch, H. Schmid, H. Riel, W. Riess, Appl. Phys. Lett. **92**(19), 193504 (2008). https://doi.org/10.1063/1.2928227
187. H. Schmid, K.E. Moselund, M.T. Björk, M. Richter, H. Ghoneim, C.D. Bessire, H. Riel, Device Research Conference-Conference Digest. DRC **29**, 181 (2011). https://doi.org/10.1109/DRC.2011.5994479

188. K. Tomioka, T. Fukui, Appl. Phys. Lett. **98**(8), 083114 (2011). https://doi.org/10.1063/1.3558729
189. E. Memisevic, J. Svensson, M. Hellenbrand, E. Lind, L.E. Wernersson, IEEE Electron Device Lett. **37**(5), 549 (2016). https://doi.org/10.1109/LED.2016.2545861
190. T. Vasen, P. Ramvall, A. Afzalian, G. Doornbos, M. Holland, C. Thelander, K.A. Dick, L.E. Wernersson, M. Passlack, Sci. Rep. **9**(1), 202 (2019). https://doi.org/10.1038/s41598-018-36549-z
191. K. Tomioka, M. Yoshimura, T. Fukui, in *2012 Symposium on VLSI Technology (VLSIT)* (IEEE, 2012), 2010, pp. 47–48. https://doi.org/10.1109/VLSIT.2012.6242454
192. R. Rooyackers, A. Vandooren, A.S. Verhulst, A. Walke, K. Devriendt, S. Locorotondo, M. Demand, G. Bryce, R. Loo, A. Hikavyy, T. Vandeweyer, C. Huyghebaert, N. Collaert, A. Thean, Technical Digest—International Electron Devices Meeting, IEDM (2013), pp. 4.2.1–4.2.4. https://doi.org/10.1109/IEDM.2013.6724558
193. K. Tomioka, T. Fukui, Appl. Phys. Lett. **104**(7), 073507 (2014). https://doi.org/10.1063/1.4865921
194. E. Memisevic, J. Svensson, M. Hellenbrand, E. Lind, L.E. Wernersson, Technical Digest—International Electron Devices Meeting, IEDM (2017), pp. 19.1.1–19.1.4. https://doi.org/10.1109/IEDM.2016.7838450
195. X. Zhao, A. Vardi, J.A. Del Alamo, IEEE Electron Device Lett. **38**(7), 855 (2017). https://doi.org/10.1109/LED.2017.2702612
196. E. Memisevic, J. Svensson, E. Lind, L.E. Wernersson, IEEE Electron Device Lett. **39**(7), 1089 (2018). https://doi.org/10.1109/LED.2018.2836862
197. L. Knoll, Q.T. Zhao, A. Nichau, S. Trellenkamp, S. Richter, A. Schäfer, D. Esseni, L. Selmi, K.K. Bourdelle, S. Mantl, IEEE Electron Device Lett. **34**(6), 813 (2013). https://doi.org/10.1109/LED.2013.2258652
198. A. Villalon, C. Le Royer, P. Nguyen, S. Barraud, F. Glowacki, A. Revelant, L. Selmi, S. Cristoloveanu, L. Tosti, C. Vizioz, J.M. Hartmann, N. Bernier, B. Prévitali, C. Tabone, F. Allain, S. Martinie, O. Rozeau, M. Vinet, Digest of Technical Papers-Symposium on VLSI Technology **49**(2010), 2013 (2014). https://doi.org/10.1109/VLSIT.2014.6894369
199. D. Cutaia, K.E. Moselund, H. Schmid, M. Borg, A. Olziersky, H. Riel, Digest of Technical Papers—Symposium on VLSI Technology (619509), 1 (2016). https://doi.org/10.1109/VLSIT.2016.7573444
200. E. Memisevic, J. Svensson, E. Lind, L.e. Wernersson, IEEE Trans. Electron Devices **64**(11), 4746 (2017). https://doi.org/10.1109/TED.2017.2750763
201. M. Noguchi, S. Kim, M. Yokoyama, O. Ichikawa, T. Osada, M. Hata, M. Takenaka, S. Takagi, J. Appl. Phys. **118**(4), 045712 (2015). https://doi.org/10.1063/1.4927265
202. R. Pandey, H. Madan, H. Liu, V. Chobpattana, M. Barth, B. Rajamohanan, M.J. Hollander, T. Clark, K. Wang, J.H. Kim, D. Gundlach, K.P. Cheung, J. Suehle, R. Engel-Herbert, S. Stemmer, S. Datta, Digest of Technical Papers-Symposium on VLSI Technology **T206**, 2015 (2013). https://doi.org/10.1109/VLSIT.2015.7223676
203. D.H. Ahn, S.M. Ji, M. Takenaka, S. Takagi, Digest of Technical Papers-Symposium on VLSI Technology 1–2 (2016). https://doi.org/10.1109/VLSIT.2016.7573443
204. A. Alian, Y. Mols, C.C.M. Bordallo, D. Verreck, A. Verhulst, A. Vandooren, R. Rooyackers, P.G.D. Agopian, J.A. Martino, A. Thean, D. Lin, D. Mocuta, N. Collaert, Appl. Phys. Lett. **109**(24), 243502 (2016). https://doi.org/10.1063/1.4971830
205. G. Liang, J. Xiang, N. Kharche, G. Klimeck, C.M. Lieber, M. Lundstrom, Nano Lett. **7**(3), 642 (2007). https://doi.org/10.1021/nl062596f
206. L. Chen, F. Cai, U. Otuonye, W.D. Lu, Nano Lett. **16**(1), 420 (2016). https://doi.org/10.1021/acs.nanolett.5b04038
207. S. Nam, X. Jiang, Q. Xiong, D. Ham, C.M. Lieber, Proc. Natl. Acad. Sci. **106**(50), 21035 (2009). https://doi.org/10.1073/pnas.0911713106
208. A.W. Dey, J. Svensson, B.M. Borg, M. Ek, L.E. Wernersson, Nano Lett. **12**(11), 5593 (2012). https://doi.org/10.1021/nl302658y
209. The HP of the IEEE IRDS, https://irds.ieee.org/

210. S. Datta, B. Das, Appl. Phys. Lett. **56**(7), 665 (1990). https://doi.org/10.1063/1.102730
211. S. Sugahara, M. Tanaka, J. Appl. Phys. **97**(10), 10D503 (2005). https://doi.org/10.1063/1.1852280
212. K.C. Hall, W.H. Lau, K. Gündoğdu, M.E. Flatté, T.F. Boggess, Appl. Phys. Lett. **83**(14), 2937 (2003). https://doi.org/10.1063/1.1609656
213. M.E. Flatté, G. Vignale, Appl. Phys. Lett. **78**(9), 1273 (2001). https://doi.org/10.1063/1.1348317
214. J. Schliemann, J.C. Egues, D. Loss, Phys. Rev. Lett. **90**(14), 146801 (2003). https://doi.org/10.1103/PhysRevLett.90.146801
215. B. Huang, D.J. Monsma, I. Appelbaum, Appl. Phys. Lett. **91**(7), 72501 (2007). https://doi.org/10.1063/1.2770656
216. Y. Fujita, M. Yamada, Y. Nagatomi, K. Yamamoto, S. Yamada, K. Sawano, T. Kanashima, H. Nakashima, K. Hamaya, Jpn. J. Appl. Phys. **55**(6), 63001 (2016). https://doi.org/10.7567/jjap.55.063001
217. K. Takase, Y. Ashikawa, G. Zhang, K. Tateno, S. Sasaki, Sci. Rep. **7**(1), 930 (2017). https://doi.org/10.1038/s41598-017-01080-0
218. K. Takase, K. Tateno, S. Sasaki, Appl. Phys. Express **12**(11), 117002 (2019). https://doi.org/10.7567/1882-0786/ab460f
219. S. Wirths, K. Weis, A. Winden, K. Sladek, C. Volk, S. Alagha, T.E. Weirich, M. von der Ahe, H. Hardtdegen, H. Lüth, N. Demarina, D. Grützmacher, T. Schäpers, J. Appl. Phys. **110**(5), 53709 (2011). https://doi.org/10.1063/1.3631026
220. C. Blömers, M.I. Lepsa, M. Luysberg, D. Grützmacher, H. Lüth, T. Schäpers, Nano Lett. **11**(9), 3550 (2011). https://doi.org/10.1021/nl201102a
221. D. Liang, J. Du, X.P.A. Gao, Phys. Rev. B **81**(15), 153304 (2010). https://doi.org/10.1103/PhysRevB.81.153304
222. S. Estévez Hernández, M. Akabori, K. Sladek, C. Volk, S. Alagha, H. Hardtdegen, M.G. Pala, N. Demarina, D. Grützmacher, T. Schäpers, Phys. Rev. B **82**(23), 235303 (2010). https://doi.org/10.1103/PhysRevB.82.235303
223. A.E. Hansen, M.T. Björk, C. Fasth, C. Thelander, L. Samuelson, Phys. Rev. B **71**(20), 205328 (2005). https://doi.org/10.1103/PhysRevB.71.205328
224. P. Roulleau, T. Choi, S. Riedi, T. Heinzel, I. Shorubalko, T. Ihn, K. Ensslin, Phys. Rev. B **81**(15), 155449 (2010). https://doi.org/10.1103/PhysRevB.81.155449
225. S. Dhara, H.S. Solanki, V. Singh, A. Narayanan, P. Chaudhari, M. Gokhale, A. Bhattacharya, M.M. Deshmukh, Phys. Rev. B **79**(12), 121311 (2009). https://doi.org/10.1103/PhysRevB.79.121311
226. L.B. Wang, J.K. Guo, N. Kang, D. Pan, S. Li, D. Fan, J. Zhao, H.Q. Xu, Appl. Phys. Lett. **106**(17), 173105 (2015). https://doi.org/10.1063/1.4919390
227. D. Liang, M.R. Sakr, X.P.A. Gao, Nano Lett. **9**(4), 1709 (2009). https://doi.org/10.1021/nl900424k
228. D. Liang, X.P.A. Gao, Nano Lett. **12**(6), 3263 (2012). https://doi.org/10.1021/nl301325h
229. F. Vigneau, Z. Zeng, W. Escoffier, P. Caroff, R. Leturcq, Y.M. Niquet, B. Raquet, M. Goiran, Phys. Rev. B **97**(12), 125308 (2018). https://doi.org/10.1103/PhysRevB.97.125308
230. P. Uredat, R. Kodaira, R. Horiguchi, S. Hara, A. Beyer, K. Volz, P.J. Klar, M.T. Elm, Nano Lett. **20**(1), 618 (2020). https://doi.org/10.1021/acs.nanolett.9b04383
231. J. Kammhuber, M.C. Cassidy, H. Zhang, Ö. Gül, F. Pei, M.W.A. de Moor, B. Nijholt, K. Watanabe, T. Taniguchi, D. Car, S.R. Plissard, E.P.A.M. Bakkers, L.P. Kouwenhoven, Nano Lett. **16**(6), 3482 (2016). https://doi.org/10.1021/acs.nanolett.6b00051
232. F. Vigneau, Ö. Gül, Y.M. Niquet, D. Car, S.R. Plissard, W. Escoffier, E.P.A.M. Bakkers, I. Duchemin, B. Raquet, M. Goiran, Phys. Rev. B **94**(23), 235303 (2016). https://doi.org/10.1103/PhysRevB.94.235303
233. F. Haas, T. Wenz, P. Zellekens, N. Demarina, T. Rieger, M. Lepsa, D. Grützmacher, H. Lüth, T. Schäpers, Sci. Rep. **6**(1), 24573 (2016). https://doi.org/10.1038/srep24573
234. F. Haas, P. Zellekens, M. Lepsa, T. Rieger, D. Grützmacher, H. Lüth, T. Schäpers, Nano Lett. **17**(1), 128 (2017). https://doi.org/10.1021/acs.nanolett.6b03611

235. W. Paschoal, S. Kumar, C. Borschel, P. Wu, C.M. Canali, C. Ronning, L. Samuelson, H. Pettersson, Nano Lett. **12**(9), 4838 (2012). https://doi.org/10.1021/nl302318f
236. S. Kumar, W. Paschoal, A. Johannes, D. Jacobsson, C. Borschel, A. Pertsova, C.H. Wang, M.K. Wu, C.M. Canali, C. Ronning, L. Samuelson, H. Pettersson, Nano Lett. **13**(11), 5079 (2013). https://doi.org/10.1021/nl402229r
237. M.T. Elm, P. Uredat, J. Binder, L. Ostheim, M. Schäfer, P. Hille, J. Müßener, J. Schörmann, M. Eickhoff, P.J. Klar, Nano Lett. **15**(12), 7822 (2015). https://doi.org/10.1021/acs.nanolett.5b02332
238. P. Uredat, P. Hille, J. Schörmann, M. Eickhoff, P.J. Klar, M.T. Elm, Phys. Rev. B **100**(8), 85409 (2019). https://doi.org/10.1103/PhysRevB.100.085409
239. S. Alagha, S.E. Hernández, C. Blömers, T. Stoica, R. Calarco, T. Schäpers, J. Appl. Phys. **108**(11), 113704 (2010). https://doi.org/10.1063/1.3516216
240. T. Richter, C. Blömers, H. Lüth, R. Calarco, M. Indlekofer, M. Marso, T. Schäpers, Nano Lett. **8**(9), 2834 (2008). https://doi.org/10.1021/nl8014389
241. R. Frielinghaus, S. Estévez Hernández, R. Calarco, T. Schäpers, Appl. Phys. Lett. **94**(25), 252107 (2009). https://doi.org/10.1063/1.3159626
242. C. Blömers, T. Schäpers, T. Richter, R. Calarco, H. Lüth, M. Marso, Appl. Phys. Lett. **92**(13), 132101 (2008). https://doi.org/10.1063/1.2905268
243. C. Kloeffel, M.J. Rančić, D. Loss, Phys. Rev. B **97**(23), 235422 (2018). https://doi.org/10.1103/PhysRevB.97.235422
244. S. Zhang, S.A. Dayeh, Y. Li, S.A. Crooker, D.L. Smith, S.T. Picraux, Nano Lett. **13**(2), 430 (2013). https://doi.org/10.1021/nl303667v
245. J. Sun, R.S. Deacon, R. Wang, J. Yao, C.M. Lieber, K. Ishibashi, Nano Lett. **18**(10), 6144 (2018). https://doi.org/10.1021/acs.nanolett.8b01799
246. P.Y. Yang, L.Y. Wang, Y.W. Hsu, J.J. Lin, Phys. Rev. B **85**(8), 85423 (2012). https://doi.org/10.1103/PhysRevB.85.085423
247. M.T. Elm, S. Hara, Adv. Mater. **26**(48), 8079 (2014). https://doi.org/10.1002/adma.201403136. Review paper
248. P. Uredat, M.T. Elm, R. Horiguchi, P.J. Klar, S. Hara, J. Phys. D: Appl. Phys. 53(33), 333002 (2020). Invited topical review paper. https://doi.org/10.1088/1361-6463/ab88e8
249. T. Ueda, Jpn. J. Appl. Phys. **58**(SC), SC0804 (2019). https://doi.org/10.7567/1347-4065/ab12c9
250. H. Otake, K. Chikamatsu, A. Yamaguchi, T. Fujishima, H. Ohta, Appl. Phys. Express **1**(1), 11105 (2008). https://doi.org/10.1143/APEX.1.011105
251. R. Li, Y. Cao, M. Chen, R. Chu, IEEE Electron Device Lett. **37**(11), 1466 (2016). https://doi.org/10.1109/LED.2016.2614515
252. S. Chowdhury, M.H. Wong, B.L. Swenson, U.K. Mishra, IEEE Electron Device Lett. **33**(1), 41 (2011). https://doi.org/10.1109/LED.2011.2173456
253. H. Nie, Q. Diduck, B. Alvarez, A.P. Edwards, B.M. Kayes, M. Zhang, G. Ye, T. Prunty, D. Bour, I.C. Kizilyalli, IEEE Electron Device Lett. **35**(9), 939 (2014). https://doi.org/10.1109/LED.2014.2339197
254. Y. Zhang, M. Sun, D. Piedra, J. Hu, Z. Liu, Y. Lin, X. Gao, K. Shepard, T. Palacios, in *2017 IEEE International Electron Devices Meeting (IEDM)* (IEEE, 2017), pp. 9.2.1–9.2.4. https://doi.org/10.1109/IEDM.2017.8268357
255. M. Sun, Y. Zhang, X. Gao, T. Palacios, IEEE Electron Device Lett. **38**(4), 509 (2017). https://doi.org/10.1109/LED.2017.2670925
256. Y. Zhang, M. Sun, J. Perozek, Z. Liu, A. Zubair, D. Piedra, N. Chowdhury, X. Gao, K. Shepard, T. Palacios, IEEE Electron Device Lett. **40**(1), 75 (2019). https://doi.org/10.1109/LED.2018.2880306
257. N. Chowdhury, T. Palacios, in *2017 IEEE Compound Semiconductor Integrated Circuit Symposium (CSICS)* (IEEE, 2017), pp. 1–3. https://doi.org/10.1109/CSICS.2017.8240466
258. N. Chowdhury, G. Iannaccone, G. Fiori, D.A. Antoniadis, T. Palacios, IEEE Electron Device Lett. **38**(7), 859 (2017). https://doi.org/10.1109/LED.2017.2703953

259. W. Li, L. Cao, C. Lund, S. Keller, P. Fay, Physica Status Solidi(a) **213**(4), 905 (2015). https://doi.org/10.1002/pssa.201532564
260. S.D. Hersee, X. Sun, X. Wang, Nano Lett. **6**(8), 1808 (2006). https://doi.org/10.1021/nl060553t
261. K. Choi, M. Arita, Y. Arakawa, J. Cryst. Growth **357**(C), 58 (2012). https://doi.org/10.1016/j.jcrysgro.2012.07.025
262. Y. Robin, S.Y. Bae, T.V. Shubina, M. Pristovsek, E.A. Evropeitsev, D.A. Kirilenko, V.Y. Davydov, A.N. Smirnov, A.A. Toropov, V.N. Jmerik, M. Kushimoto, S. Nitta, S.V. Ivanov, H. Amano, Sci. Rep. **8**(1), 7311 (2018). https://doi.org/10.1038/s41598-018-25473-x
263. S. Kamiyama, W. Lu, T. Takeuchi, M. Iwaya, I. Akasaki, ECS J. Solid State Sci. Technol. **9**(1), 015007 (2020). https://doi.org/10.1149/2.0252001JSS
264. K.A. Bertness, A.W. Sanders, D.M. Rourke, T.E. Harvey, A. Roshko, J.B. Schlager, N.A. Sanford, Adv. Funct. Mater. **20**(17), 2911 (2010). https://doi.org/10.1002/adfm.201000381
265. T. Schumann, T. Gotschke, F. Limbach, T. Stoica, R. Calarco, Nanotechnology **22**(9), 95603 (2011). https://doi.org/10.1088/0957-4484/22/9/095603
266. A. Bengoechea-Encabo, F. Barbagini, S. Fernandez-Garrido, J. Grandal, J. Ristić, M.A. Sanchez-Garcia, E. Calleja, U. Jahn, E. Luna, A. Trampert, J. Ristic, M.A. Sanchez-Garcia, E. Calleja, U. Jahn, E. Luna, A. Trampert, J. Cryst. Growth **325**(1), 89 (2011). https://doi.org/10.1016/j.jcrysgro.2011.04.035
267. A. Urban, J. Malindretos, J.H. Klein-Wiele, P. Simon, A. Rizzi, New J. Phys. **15**(5), 53015 (2013). https://doi.org/10.1088/1367-2630/15/5/053045
268. J.E. Kruse, L. Lymperakis, S. Eftychis, A. Adikimenakis, G. Doundoulakis, K. Tsagaraki, M. Androulidaki, A. Olziersky, P. Dimitrakis, V. Ioannou-Sougleridis, P. Normand, T. Koukoula, T. Kehagias, P. Komninou, G. Konstantinidis, A. Georgakilas, J. Appl. Phys. **119**(22), 224305 (2016). https://doi.org/10.1063/1.4953594
269. Y. Huang, X. Duan, Y. Cui, C.M. Lieber, Nano Lett. **2**(2), 101 (2002). https://doi.org/10.1021/nl015667d
270. Y. Li, J. Xiang, F. Qian, S. Gradečak, Y. Wu, H. Yan, D.A. Blom, C.M. Lieber, Nano Lett. **6**(7), 1468 (2006). https://doi.org/10.1021/nl060849z
271. J.W. Yu, P.C. Yeh, S.L. Wang, Y.R. Wu, M.H. Mao, H.H. Lin, L.H. Peng, Appl. Phys. Lett. **101**(18), 183501 (2012). https://doi.org/10.1063/1.4764554
272. Ž. Gačević, D. López-Romero, T. Juan Mangas, E. Calleja, Appl. Phys. Lett. **108**(3), 033101 (2016). https://doi.org/10.1063/1.4940197
273. W. Li, M.D. Brubaker, B.T. Spann, K.A. Bertness, P. Fay, IEEE Electron Device Lett. **39**(2), 184 (2018). https://doi.org/10.1109/LED.2017.2785785
274. F. Yu, D. Rümmler, J. Hartmann, L. Caccamo, T. Schimpke, M. Strassburg, A.E. Gad, A. Bakin, H.H. Wehmann, B. Witzigmann, H.S. Wasisto, A. Waag, Appl. Phys. Lett. **108**(21), 213503 (2016). https://doi.org/10.1063/1.4952715
275. F. Yu, S. Yao, F. Römer, B. Witzigmann, T. Schimpke, M. Strassburg, A. Bakin, H.W. Schumacher, E. Peiner, H.S. Wasisto, A. Waag, Nanotechnology **28**(9), 95206 (2017). https://doi.org/10.1088/1361-6528/aa57b6
276. F. Yu, K. Strempel, M.F. Fatahilah, H. Zhou, F. Römer, A. Bakin, B. Witzigmann, H.W. Schumacher, H.S. Wasisto, A. Waag, IEEE Trans. Electron Devices **65**(6), 2439 (2018). https://doi.org/10.1109/TED.2018.2824985
277. D.H. Son, Y.W. Jo, J.H. Seo, C.H. Won, K.S. Im, Y.S. Lee, H.S. Jang, D.H. Kim, I.M. Kang, J.H. Lee, Solid-State Electronics **145**, 1 (2018). https://doi.org/10.1016/j.sse.2018.03.001
278. M.F. Fatahilah, F. Yu, K. Strempel, F. Römer, D. Maradan, M. Meneghini, A. Bakin, F. Hohls, H.W. Schumacher, B. Witzigmann, A. Waag, H.S. Wasisto, Sci. Rep. **9**(1), 10301 (2019). https://doi.org/10.1038/s41598-019-46186-9
279. M.F. Fatahilah, K. Strempel, F. Yu, S. Vodapally, A. Waag, H.S. Wasisto, Micro Nano Eng. **3**(March), 59 (2019). https://doi.org/10.1016/j.mne.2019.04.001
280. S. Salahuddin, S. Datta, Nano Lett. **8**(2), 405 (2008). https://doi.org/10.1021/nl071804g

281. M. Kobayashi, Appl. Phys. Express **11**(11), 110101 (2018). https://doi.org/10.7567/APEX.11.110101
282. M. Berroth, R. Bosch, IEEE Trans. Microw. Theory Tech. **38**(7), 891 (1990). https://doi.org/10.1109/22.55781

InP/InAs Quantum Heterostructure Nanowires Toward Telecom-Band Nanowire Lasers

Guoqiang Zhang, Kouta Tateno, Takehiko Tawara, and Hideki Gotoh

Abstract One challenge for compound semiconductor nanowires has been the development of a complementary metal–oxide–semiconductor (CMOS)-compatible synthesis approach which can produce semiconductor heterostructure nanowires with excellent optical properties in technologically important telecom-band range. This remains challenging mostly because gold (Au), which is widely used as a catalyst particle for nanowire synthesis with the vapor–liquid–solid (VLS) approach [1], is not allowable in the mainstream CMOS process [2, 3]. Here, we describe the growth, structural, and optical properties of InP/InAs heterostructure nanowires by developing an Au-free self-catalyzed VLS approach. Indium material, one of the elements of InP and InAs materials, is used as the catalyst particle to catalyze the growth of InP, InAs, and further InP/InAs heterostructure nanowires. The heterostructure nanowire exhibits excellent optical property, enabling lasing operation with a tunable lasing wavelength in telecom band at room temperature. An approach is then described to form site-defined InP/InAs nanowires by combining bottom-up self-assembly process with top-down photolithography techniques. A unique growth phenomenon of self-catalyzed VLS approach is then revealed that the catalyst particle size (thus, the nanowire diameter) can be tailored by modulating V/III flow ratio during growth. Finally, we give a summary of InP/InAs quantum heterostructure nanowires.

Keywords Semiconductor · Nanowire · Heterostructure · Laser · Telecommunication

1 Introduction

One challenge for compound semiconductor nanowires has been the development of a complementary metal–oxide–semiconductor (CMOS)-compatible synthesis approach which can produce semiconductor heterostructure nanowires with excellent optical properties in technologically important telecom-band range. This remains

G. Zhang (✉) · K. Tateno · T. Tawara · H. Gotoh
NTT Basic Research Laboratories, NTT Corporation, 3-1 Morinosato-Wakamiya, Atsugi 243-0198, Kanagawa, Japan
e-mail: guoqiang.zhang.ta@hco.ntt.co.jp

© Springer Nature Singapore Pte Ltd. 2021

N. Fukata and R. Rurali (eds.), *Fundamental Properties of Semiconductor Nanowires*,
https://doi.org/10.1007/978-981-15-9050-4_10

challenging, on one hand, mostly because gold (Au), which is widely used as a catalyst particle for nanowire synthesis with the vapor–liquid-solid (VLS) approach [1], is not permitted in the mainstream CMOS process as Au is highly detrimental to the performance of minority carrier electronic devices [2, 3]. On the other hand, the telecom-band wavelength range (1.2–1.6 μm) is technologically important in optical fiber communication systems. Despite significant progress of nanowire lasers working in ultraviolet, visible, and near infrared (<1 μm) range [4–15], there are few reports about nanowire lasers in telecom-band wavelength range [15–18]. Instead of wide-banggap GaAs(P) nanowires, we have focused on indium-contained InP/InAs quantum heterostructure nanowires (Fig. 1) [19, 20]. The InP/InAs quantum heterostructure potentially cover a long wavelength range including telecom band by quantum confinement effect in InAs quantum disk (QDisk) along the axial direction (Fig. 1b).

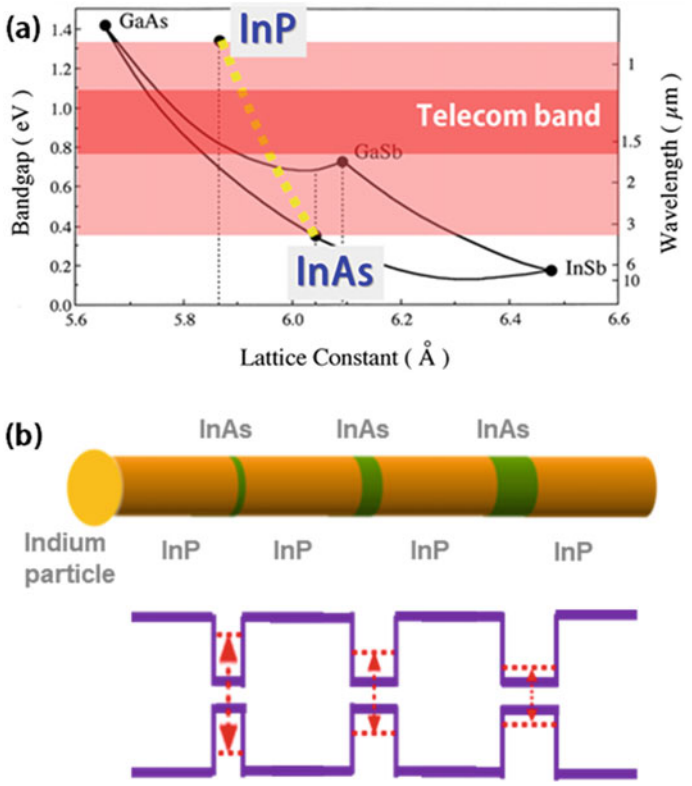

Fig. 1 **a** Bandgap and lattice constant of several III–V compound semiconductors. InP/InAs can potentially cover a long wavelength range including telecom band. **b** Schematic diagram of an InP/InAs heterostructure nanowire connected by a single indium catalyst particle through VLS growth mode. By quantum confinement effect along the axial direction, the real bandgap of InAs layer can be modulated by its thickness

Due to the lattice mismatch as high as 3.1% of InP/InAs, the conventional epitaxy in the film structure usually results in high-density dislocations in InAs active layers (Fig. 2a–c). This makes it extremely challenging to form dislocation-free InAs active layers with the superior optical property. For the nanowire structure, this is not the case. Because of their nanoscale diameter of nanowires, the nanowire crystalline lattice can deform laterally to a large extent to relax the strain induced by lattice mismatch (Fig. 2d). In comparison with multi-quantum well (MQW) planar film structures, which could produce dislocations due to the 3.1% high lattice mismatch of InP/InAs, the nanowire heterostructure could endure large lattice mismatch [21] and thus has the advantage of producing dislocation-free active region (Fig. 2d) [22]. From this point of view, the nanowire structure opens up new opportunities developing new heterostructure with high crystalline quality by breaking the limitation of lattice match in film structure.

About nanowire synthesis approach, because of its high controllability in terms of composition, heterostructure, doping, diameter, etc., the VLS mode has been widely utilized (Fig. 3). The Au particle-catalyzed VLS mode has been mostly used in the synthesis of various nanowires including GaP, GaAs, InAs, and InP nanowires [11, 17, 23–25]. But the use of Au material is not compatible with the mainstream Si-based complementaryCMOS technology and thus hinder the integration of optically active III–V compound semiconductor nanowires into CMOS process [26]. For III–V compound semiconductor nanowires, one alternative way is to use one of the elements, mostly, group-III elements, as catalyst particle materials and to grow nanowires in self-catalyzed VLS mode. The self-catalyzed VLS approach shows high potential in the field of Si-based integrated optoelectronics for the CMOS-compatible process feature [22, 26–28], i.e., Au-free characteristics.

Here, we chose indium-contained InP/InAs material combination. On one hand, indium-contained InP/InAs materials enable to use self-catalyzed, i.e., indium-catalyzed, VLS approach for the heterostructure formation along the axial direction

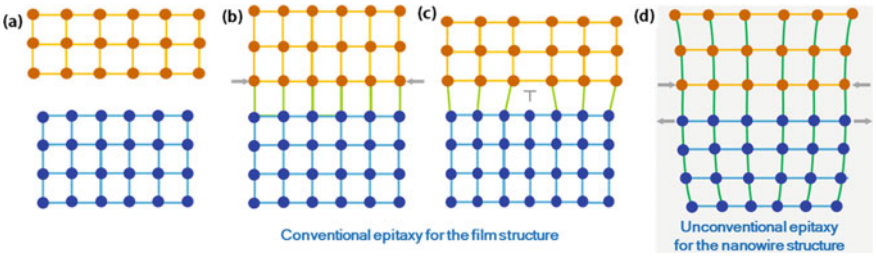

Fig. 2 Schematic diagram of strain relaxation for crystal materials with lattice mismatch. **a** Lattices of crystal materials before epitaxy. **b** Coherent growth by elastic deformation of the epilayer lattice; **c** Incoherent growth (strain relaxation by mismatch dislocations); **d** Coherent growth by elastic deformation of both lattices. In contrast to the planar film structure, the lattice in the nanowire structure can deform much more along the radial direction because of its microscale or nanoscale diameter and thus can endure higher strain induced by the lattice mismatch

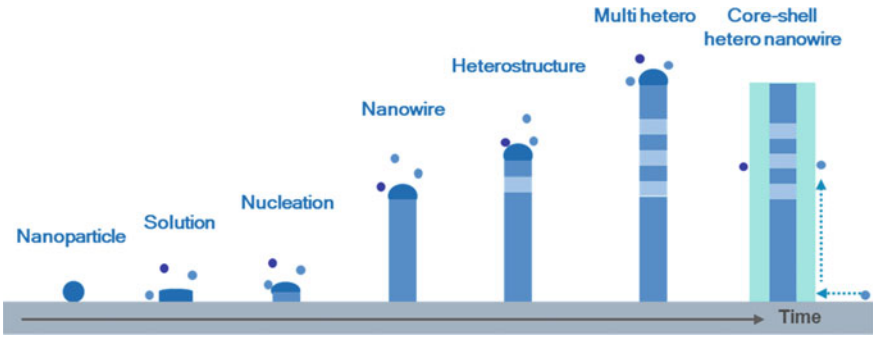

Fig. 3 Schematic diagram of VLS growth mode. InAs and InP nanowires can be grown by self-catalyzed VLS mode using indium particles. This enables InAs/InP quantum heterostructure nanowires along the axial direction (Fig. 1b)

(Fig. 1b) [22, 27–29]. On the other hand, the InAs QDisk can function as wavelength-tunable gain medium covering a wide wavelength range including telecom band by quantum confinement effect along the axial direction [30].

In this chapter, we firstly describe growth and structure of InP and InAs nanowires via the self-catalyzed VLS mode [27, 28]. Then we present the InP/InAs heterostructure nanowires, including growth, structural, and interface analysis, tuning emission wavelength by the thickness of InAs QDisks [22]. The nanowire exhibits excellent optical property, enabling lasing operation with tunable lasing wavelength range in full telecom band at room temperature [30]. We present a novel approach to form the site-defined InP/InAs nanowires by combining bottom-up self-assembly with a top-down micro-photolithography technique [31]. Finally, we describe a distinct growth phenomenon of self-catalyzed VLS approach that the catalyst particle size (thus, the nanowire diameter) can be tailored by modulating V/III flow ratio during the growth process [29].

2 InP and InAs Nanowires Grown by Self-Catalyzed VLS Mode

In this section, we describe the growth and structural properties of InP and InAs nanowires grown in the self-catalyzed VLS mode through self-assembled indium particles. We synthesize these nanowires in a metalorganic vapor phase epitaxy (MOVPE) system. indium particles are formed on InP (111)B by introducing trimethylindium (TMIn) source material at 360 °C for 15–300 s at a flow rate of 3.0 μmol/min. The temperature is then reduced to the growth temperature (330–350 °C) and growth is initiated by introducing TMIn and tertiarybutylarsenic (TBA), or tertiarybutylphosphine (TBP) simultaneously.

For the InP nanowire growth, the flow rates of TMIn and TBP are 2.12–3.03 and 803.6 μmol/min, respectively. For the InAs segment growth, the flow rates of TMIn and TBA are 1.5–7.2 and 44.6–446 μmol/min respectively. We also used the flow rate unit of sccm (standard cubic centimeters per minute). The mole flow rate of TMIn and TBP (or TBA) materials with 1 sccm corresponds to 1.5×10^{-7} mol/min and 4.46×10^{-5} mol/min, respectively.

Figure 4 shows SEM images of vertically aligned InP nanowires grown on an InP (111)B substrate and TEM compositional analysis images for the particle tip region. The nanowire has a diameter of 200 ± 20 nm. We analyze the structure and composition using the TEM–XEDS equipment (Fig. 4). The InP nanowire exhibits a ZB crystalline structure with some stacking faults along the growth direction. A clear contrast can be seen between the nanowire and the particle. The nanowire region is composed of indium and P, but the particle is composed only of indium. A quantitative analysis of the particle indicates that it is composed of pure indium. This is direct evidence that the InP nanowire is grown via the self-catalyzed VLS mode.

For InAs nanowires, there has been some argument whether it is available to grow InAs nanowires by self-catalyzed VLS mode [32]. We consider that two factors are important to realize self-catalyzed InAs nanowire growth, one is V/III ratio, the other is growth temperature. We have revealed that V/III ratio has a substantial

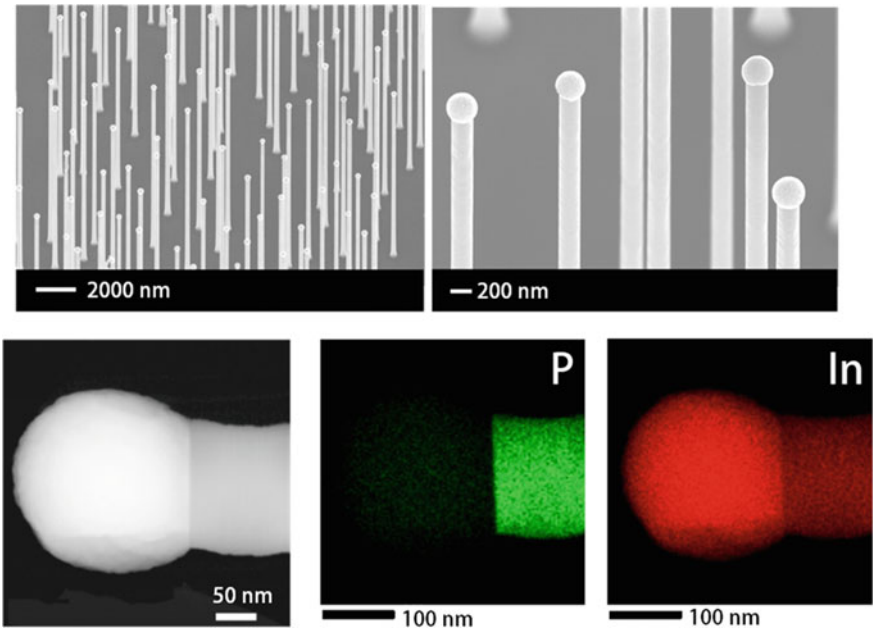

Fig. 4 SEM images (tilt: 38°) of InP nanowires grown on InP(111)B substrate and TEM compositional analysis for the particle–nanowire region. InP nanowires are vertically aligned on the substrate. A particle is visible at each nanowire tip. The mapping images indicate an indium composition in the tip particle. (Figure from Ref. [28]. Reprinted with permission from IOP Publishing)

effect on the morphology of InAs nanowires (or nanostructures) [27]. As the III/V mole ratio is increased, there is a continuous change in the nanowire shape, from a tapering shape to a uniform shape, and then a reversely tapering shape. The increased supply of indium source material enables the indium particle-catalyzed VLS growth. Growth temperature shows a considerable influence on nanowire growth mode. High temperature (>400 °C) facilitates the usual VPE growth, while low temperature (~330–350 °C) disables the usual VPE growth and facilitates the catalyzed VLS growth. Temperature plays a key role in the competitive growth of the two modes. Under low V/III ratio and low growth temperature (330 °C), we grow InAs nanowires with an indium particle at each nanowire tip (Fig. 5).

The experimental results shown in this section confirm the feasibility of self-catalyzed VLS growth of both InP and InAs nanowires. This makes it available to form InP/InAs axial-heterostructure nanowires by the self-catalyzed VLS mode.

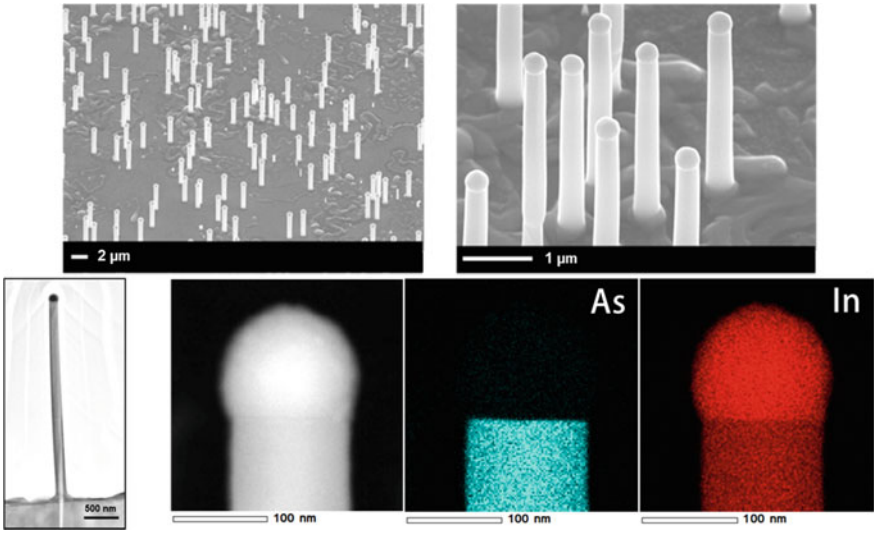

Fig. 5 SEM images (tilt: 38°) of InAs nanowires grown on InP(111)B substrate and TEM compositional analysis for the particle–nanowire region. InAs nanowires are vertically aligned on the substrate. A particle is visible at each nanowire tip. Quantitative compositional analysis indicates that the particle at the tip is pure indium. The reality that there is an indium particle at each nanowire tip indicates that these InAs nanowires are grown in the self-catalyzed VLS mode. (Figure from Ref. [27])

3 InP/InAs Heterostructure Nanowires by Self-Catalyzed VLS Mode

In this section, we describe the structural analysis and optical property of multi-stacked InAs/InP heterostructure nanowires. The InP/InAs axial-heterostructure nanowire is realized by indium particle-catalyzed VLS mode. The heterostructure nanowire exhibits an atomically abrupt InP/InAs interface. The luminescence range is tailored by the thickness of InAs QDisks and cover the telecommunication window range.

InP/InAs nanowires are grown with growth times for InAs segments of 0.5, 1, and 1.5 s. TEM images of the nanowire (Fig. 6) clearly indicate the formation of InP/InAs multi-heterostructure with three InAs QDisks. Figure 6e schematically shows the heterostructure and band structure of the multi-stacked InAs/InP nanowire. The different thickness should result in different energies between the ground level of electron and hole (E_1, E_2, and E_3) by quantum confinement effect along the axial direction.

Interface abruptness is a key factor in heterostructures to precisely engineer the carrier distribution for functional devices. To determine the interface abruptness, we analyze the nanowire with an aberration-corrected scanning TEM (Cs-STEM) system. The system has a very small electron beam probe size (angstrom level) [33]. This makes it a powerful tool for interface analysis with atomic layer resolution.

The InAs/InP heterostructure nanowire has two different switching sequences, i.e., InP → InAs and InAs → InP. Both interfaces have been analyzed to clarify the influence of the switching sequence on the interface abruptness. The InAs → InP interface exhibits a compositionally graded InAsP layer. The thickness is estimated to be 3–4 monolayers. In contrast with this, the InP → InAs interface exhibits a sharp contrast, implying a very abrupt interface (Fig. 7).

Quantitative analysis for the InP → InAs interface has further been performed (Fig. 7). There is a sharp change in the spot intensity of the V-group atoms. The As(P) exhibits a uniform intensity profile in the InAs(P) segment. In contrast, the intensity between the As and P spots changes sharply at the interface. The result shows that the InP → InAs interface is atomically abrupt.

An atomically abrupt interface has been considered to be extremely difficult to realize by VLS synthesis approach due to the catalyst particle-induced reservoir effect [34]. One effective way to suppress the reservoir effect is to use a low growth temperature. Solubility of other materials in catalyst particles usually decreases with temperature and the reservoir effect can thus be suppressed by low growth temperature. Here, the indium particle-catalyzed VLS synthesis approach allows a very low growth temperature (330–350 °C) because of the low melting point of indium (156.6 °C). The other advantage of the low growth temperature is that the atomic diffusion in the interface region can be significantly suppressed. Noting that the growth temperature is quite low compared with the usual growth temperature (>500 °C) of InP and InAs films in conventional VPE mode. InP → InAs and InAs → InP heterostructures have distinctly different interface properties since As is more

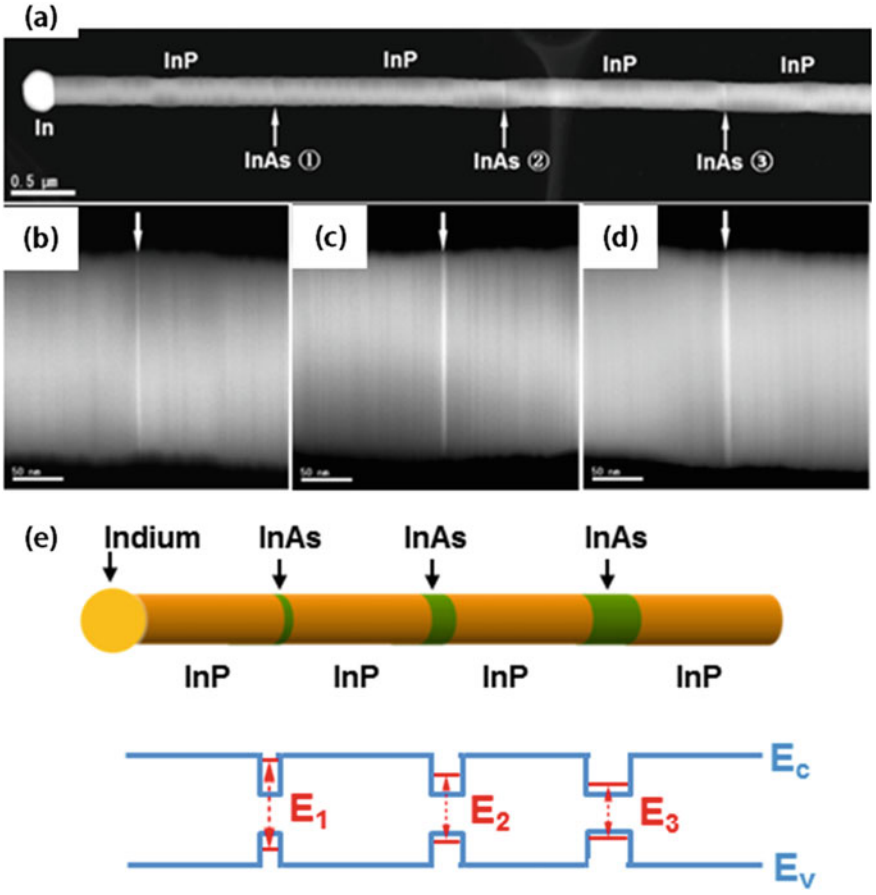

Fig. 6 TEM analysis of a single InP/InAs heterostructure nanowire with three InAs QDisks. **a** HAADF-STEM image of a nanowire. **b–d** HAADF-STEM images of three InP/InAs/InP double heterointerfaces. **e** Schematic diagrams of the composition and band structures of the heterostructure nanowire. (Figure from Ref. [22]. Reprinted with permission from IOP Publishing)

soluble in indium particles than P, which consequently causes an enhanced reservoir effect.

It is necessarily important to tune the luminescence wavelength, in particular, in the telecommunication window (1.2–1.6 μm). Because the ground (or ground and excited) state energy can be directly modulated by the thickness for quantum confinement effect, the optical emission energy should be thickness dependent. The dependence is clarified by directly correlating the thickness with the emission energy of each InAs QDisk. Cathodoluminescence (CL) measurement in an SEM system is performed. In contrast to the conventional micro-photoluminescence with microscale resolution, the combination of CL with an SEM system enables nanoscale spatial resolution as the pumping source is an electron beam.

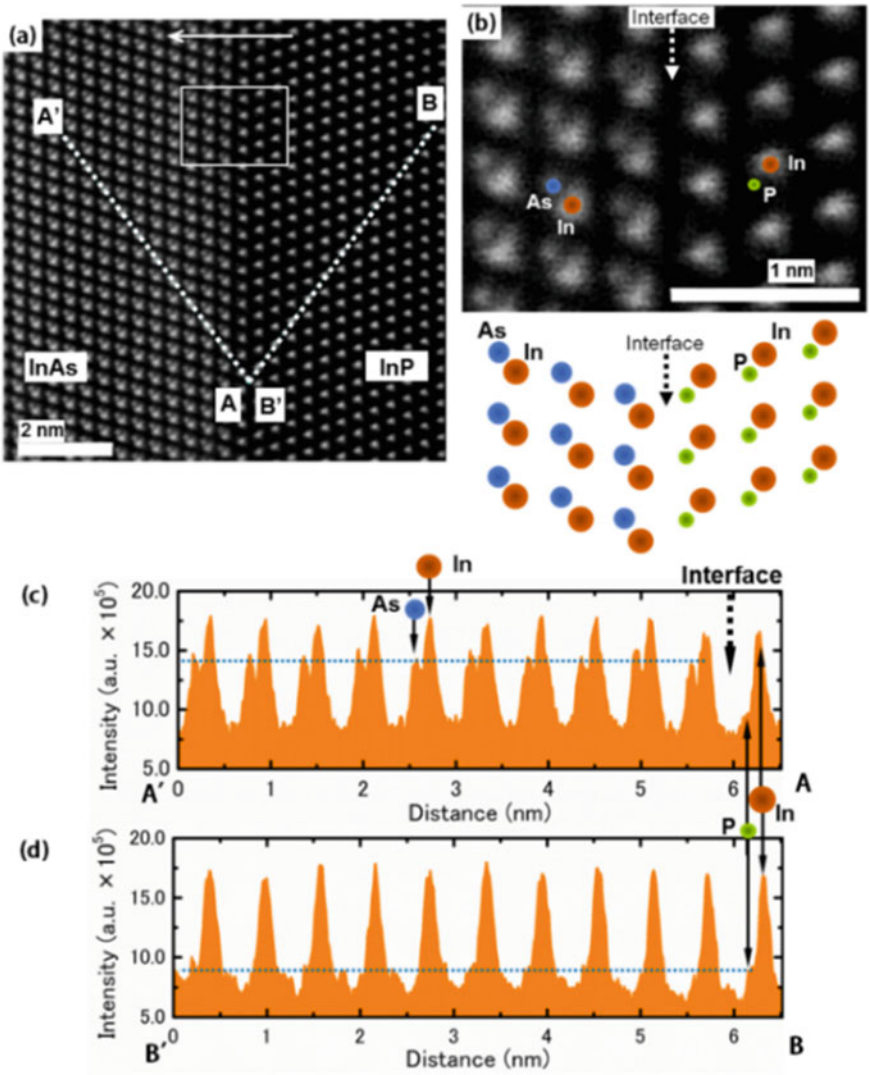

Fig. 7 Interface analysis with Cs-STEM. **a** and **b** High-resolution HAADF-STEM image of the InP → InAs interface. The <111> growth direction is indicated by a white arrow. The interface region in the white rectangle is shown in (**b**). The atomic model schematic is shown below. **c** and **d** The intensity profiles along the A′A and B′B lines in (**a**). As(P) shows the uniform intensity profile in the InAs(P) segment. The intensity of As(P) exhibits a sharp change at the interface. (Figure from Ref. [22]. Reprinted with permission from IOP Publishing)

For the CL measurement, the nanowires are transferred to a Si substrate covered with a thin Au film. The highly conductive Au film favorably avoids charge up during measurement. Samples are analyzed with an SEM (JEOL, JSM-7800F) equipped with a CL (Gatan, MonoCL4) system [22]. The sample stage is cooled to 8 K with liquid helium. The luminescence is collected by a parabolic mirror and guided to a grating and is finally detected with a photomultiplier.

The luminescence spectrum of a single nanowire consisted of four peaks (Fig. 8a). Four long bright spots with the emission at 1.4187 eV are from InP segments. The other three dark spots indicate the locations of InAs segments in the nanowire. The InAs segments ①, ②, and ③ have emission peak energies at 1.117, 0.946, and 0.826 eV, respectively. Telecom-band window (1.2–1.6 μm) can be covered through quantum confinement effect along the nanowire axial direction by tuning thickness of each InAs QDisk.

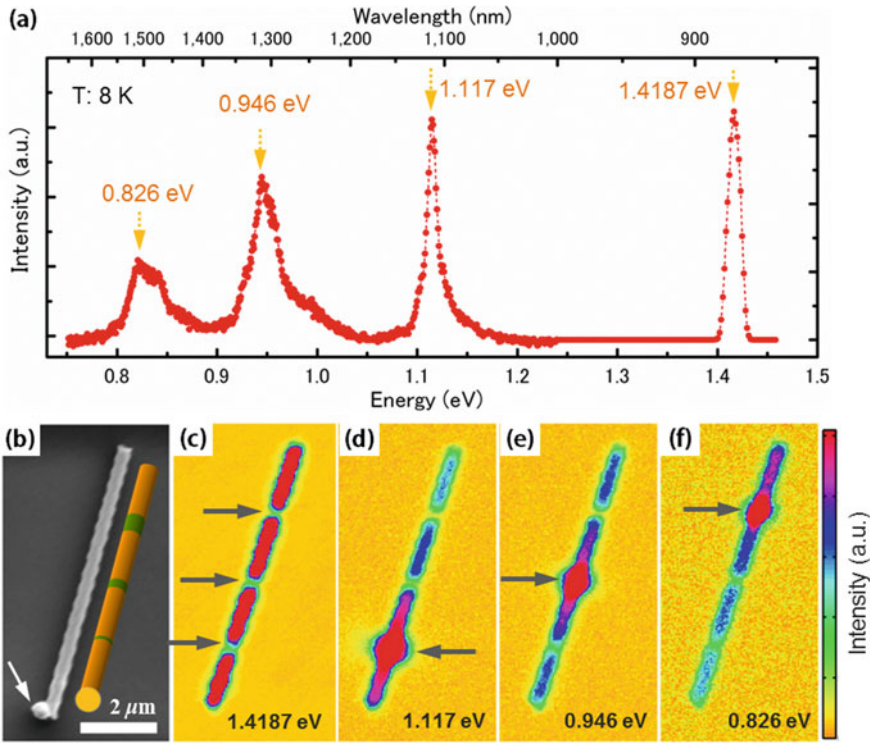

Fig. 8 CL spectra and images of a single nanowire at 8 K (Liquid helium). **a** CL spectra of a single InP/InAs nanowire. **b** SEM image of a single nanowire. The white arrow indicates an indium particle at the nanowire tip. The position was a little bit moved in the dispersion process. The inset is a schematic diagram of the nanowire structure. **c–f** Monochromatic CL images of the nanowire at each peak energy shown in (**a**). (Figure from Ref. [22]. Reprinted with permission from IOP Publishing)

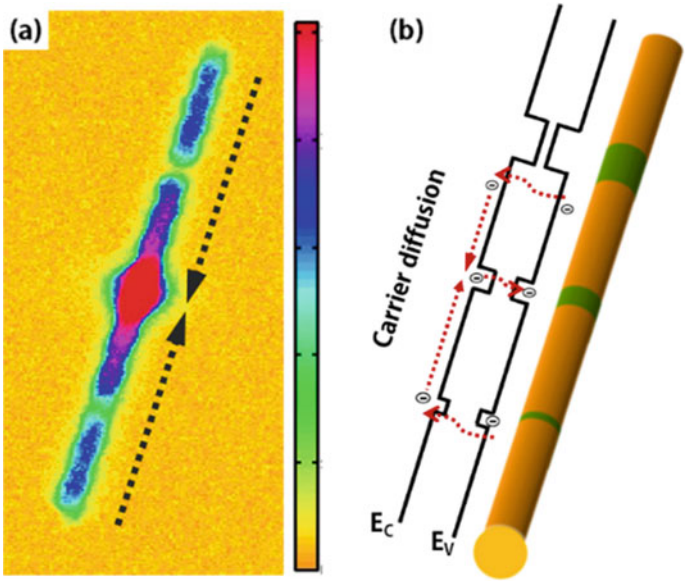

Fig. 9 Carrier diffusion effect on monochromatic mapping measurement result. **a** Monochromatic CL image of the nanowire at 0.946 eV, which corresponds to the emission energy of the middle InAs QDisk. The arrows indicate the carrier diffusion direction from the excited area other than the middle InAs QDisk. **b** Schematic diagram of the carrier diffusion effect. The inset shows the nanowire structure

The InP barrier segments also exhibit the luminescence in the emission range of the InAs segments. Part of the carriers excited on the InP barrier will diffuse and reach the InAs segments before recombination in InP segments, and eventually recombine in the photon emission with the energy of the ground (or ground and excited) states of the InAs QDisk (Fig. 9). The monochromatic mapping measurement attributes the luminescence to the excited InP spot area. Even the thinnest InAs QDisk is excited, some carriers with high energy can diffuse and reach the middle InAs QDisk, and eventually recombine with light emission in the energy of the real bandgap of the middle QDisk.

4 Telecom-Band Lasing in Single InP/InAs Nanowires

In this section, we describe telecom-band single-nanowire lasers operating at room temperature based on multi-quantum disk (MQD) InP/InAs heterostructure nanowires. The establishment of formation technique of InP/InAs heterostructure nanowires with high controllability enables to add more InAs QDisks into InP nanowires with luminescence in the telecom-band wavelength range (Fig. 10a). These nanowires are mechanically dispersed onto foreign substrates. The indium particles

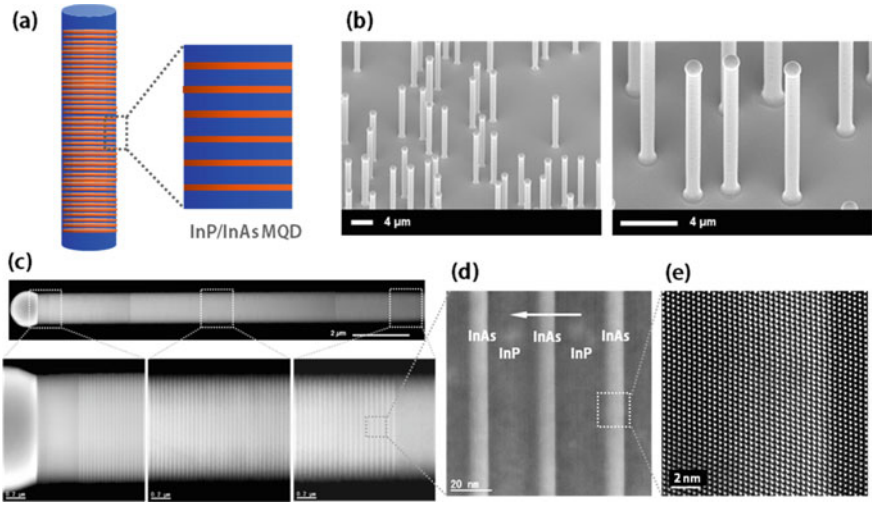

Fig. 10 InP/InAs MQD nanowires. **a** Schematic diagram of MQD heterostructure nanowires. The red color indicates the InAs layer. **b** SEM images (tilt: 38°) of vertically aligned InP/InAs MQD nanowires. **c** HAADF-STEM images of an InP/InAs MQD nanowire taken along the [011] zone axis. The nanowire contains 400 units of InP/InAs heterostructure. **d** and **e** Aberration-corrected HAADF-STEM images. (Figure from Ref. [30])

at nanowire tips can be removed from the nanowire in the mechanical dispersion process. Hence, two (111) facet mirrors can be made at both ends of a nanowire. The structure constructs a Fabry–Pérot cavity because of the refractive index difference between the InP medium and surrounding air. The lasing behavior can then be expected by optically pumping the InP/InAs MQD nanowire.

To increase the gain material volume of InAs QDisks, we put 400 units of InAs QDisks into each InP nanowire. HAADF-STEM measurement directly reveals the MQD stacking along the growth direction. The nanowire is dominated by the growth via the VLS mode along the axial direction with negligible uncatalyzed growth occurring on the sidewall because of the low growth temperature.

Despite a 3.1% lattice mismatch of InP/InAs and a relatively large diameter (~1 μm), the growth is coherent in a dislocation-free InAs/InP interface. The InP → InAs interface (Fig. 10e) is atomically abrupt, while InAs → InP interface exhibits a grade layer due to the strong reservoir effect of arsenic in indium catalyst particles. Both InAs QDisks and InP barrier layer have a zinc-blende crystalline structure without any stacking faults in Fig. 10e.

The coherent interface of InP/InAs MQD structure indicates a relatively high strain due to the lattice mismatch as high as 3.1%. Because a single InP barrier layer is quite thicker than a single InAs QDisk, high compressive strain is applied on InAs QDisks. The lattice along the *y*-direction remains compressively coherent, while the lattice along *z*-direction is elongated in the InAs QDisk to relax strain energy. The large strain present in InAs gain material favorably increases gain.

The optical properties of the InP/InAs MQD nanowires are characterized by micro-PL. For optical measurement, the nanowires are mechanically dispersed onto Au-coated SiO_2/Si substrate (Fig. 11a). The pump laser spot with a circular shape was focused down to 2.0 μm diameter using ×50 lens. PL spectrum of individual nanowires shows a relatively broad spontaneous emission with a peak wavelength at 1.57–1.59 μm (Fig. 11b). As power density increases, the emission intensity increases rapidly and then become dominant. Above the excitation power of 2.15 mJ cm^{-2}, the peak collapses into a narrow peak centered on 1573 nm. The feature together with other measurements (L–L curve and decay evolution) clearly indicate a lasing behavior [30].

The MQD heterostructure provides the capability to tune the photon emission energy range by the thickness of single InAs QDisks in a wide wavelength range (Fig. 12a). The thickness can be tuned by the parameter of flow rate of source materials. PL results show that the dominant peak is shifted up to the high-energy (short wavelength) side with reduced thickness of single InAs QDisks (Fig. 12b). The stimulated emission is then seen for a number of nanowires by increasing excitation power (Fig. 12c). The lasing wavelength of nanowires grown under each flow rate is located in different ranges (O, E, C, and L). These results indicate a high capability

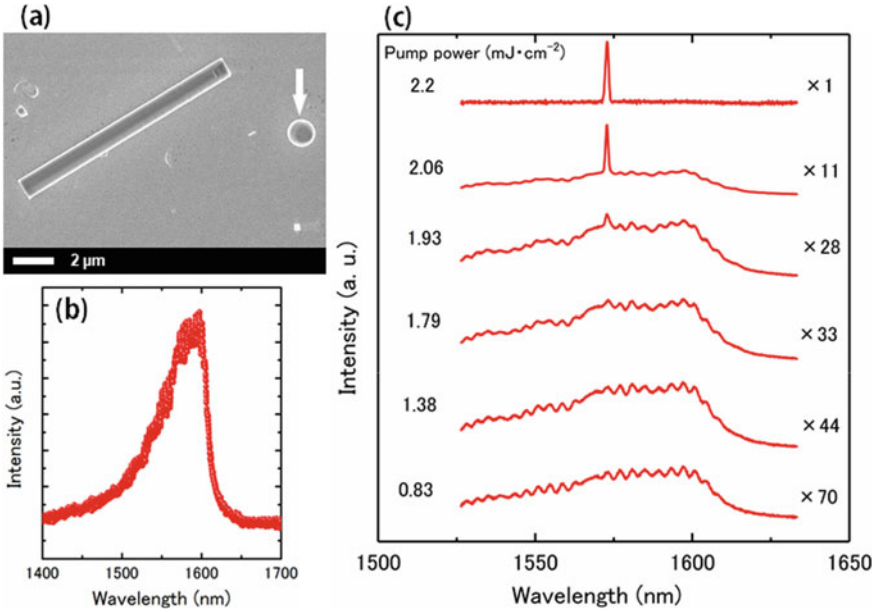

Fig. 11 Optical characterization by micro-PL at room temperature. **a** SEM image of a nanowire mechanically dispersed onto SiO_2/Si substrates covered with 200-nm-thick gold film. The white arrow indicates an indium particle mechanically removed from a nanowire. **b** PL spectrum of a single nanowire under a pump laser power of 0.83 mJ cm^{-2}. **c** PL spectra of the nanowire with increasing pump power. Spectra are offset for clarity. (Figure from Ref. [30])

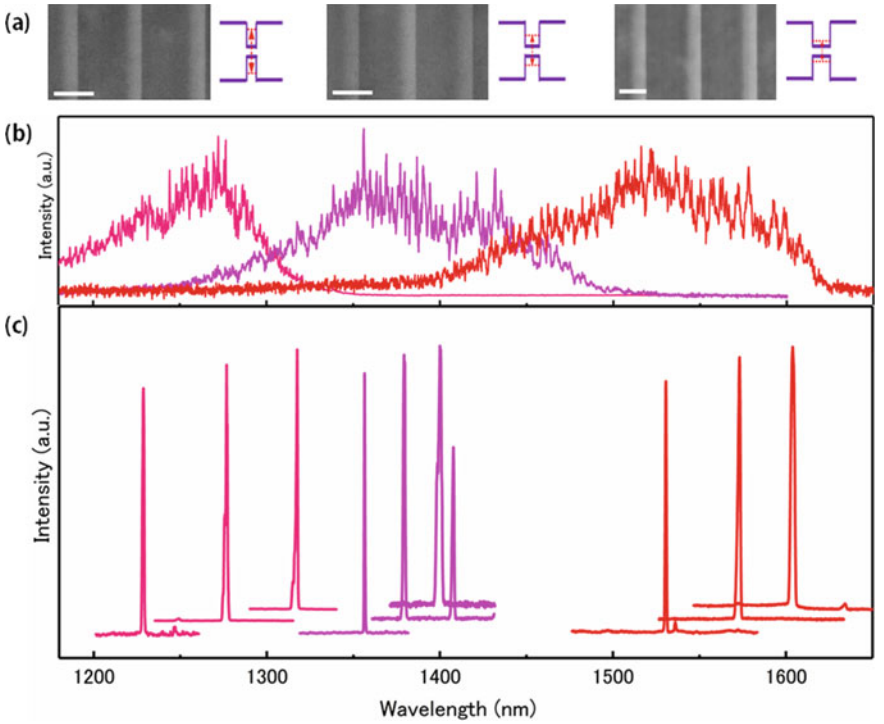

Fig. 12 Tuning the lasing wavelength range in full telecom band. **a** HAADF-STEM images of InP/InAs MQD nanowires grown under varied flow rates. The flow rates of TMIn:TBA are (μmol/min): 0.75:223, 0.98:290, and 1.5:447 from left-hand to right-hand sides. The corresponding thickness of a single InAs QDisk is 6.8 ± 0.8 nm, 7.5 ± 0.8 nm, 9.0 ± 1 nm, respectively. All scale bars denote 20 nm. **b** Corresponding spontaneous PL spectra of individual nanowires. **c** Corresponding PL spectra in stimulated emission. Spectra are offset for clarity. A wide wavelength range is covered in the whole telecom band, including two technologically important telecom-band windows of 1.3 and 1.55 μm. (Figure from Ref. [30])

of MQD heterostructure nanowires to modulate the lasing wavelength in a broad range simply by thickness.

5 Site Control of InP/InAs Heterostructure Nanowires

In this section, we describe a bottom-up self-assembly way to realize site-defined InP/InAs heterostructure nanowire array. The conventional way to realize site-defined nanowires via particle-catalyzed VLS approach is to define the particle position by

lithography process and then grow nanowires initiating growth from these particles. Instead of this conventional way, we have developed a new approach for site-defined nanowires by combining top-down lithography and bottom-up self-assembly techniques [31].

The growth procedure is a two-step ("seed and grow") process. In seed step, indium adatoms are allowed to diffuse on amorphous masking film and reach the open windows of an exposed InP substrate. These indium adatoms in open windows accumulate into nanoparticles and form an indium nanoparticle array under optimized temperature and window spacing conditions (Fig. 13). In the growth step, site-defined InP nanowires can then be grown in the indium-particle-catalyzed VLS mode by using the indium nanoparticle array. This first step is crucial because the success of the nanowire growth step is directly determined by the location of the indium particles on the substrate.

The diffusion of indium adatoms on the substrate surface will be temperature-dependent following an Arrhenius-type relationship. For a single atom diffusing on a 2D substrate, using Einstein's diffusion length relation, $\lambda = \sqrt{D\tau}$, the displacement from the arrival site to the eventual incorporation site can be written as follows:

$$\lambda = \sqrt{D\tau} = \lambda_0 \exp[-E_d/(2\kappa_B T)],$$

where τ being the mean surface diffusion time [35, 36]. In this equation, the pre-exponential factor λ_0 is the merged effective jump distance, E_d is the diffusion barrier of a single jump, and κ_B is Boltzmann's constant. Based on this equation, the diffusion length is temperature-dependent and simply increases with temperature. The temperature and pitch size (window spacing) are therefore key parameters for deciding the alignment of seed particles in the open windows.

The ideal seeding conditions are found by varying the temperature and the window spacing on the substrate while keeping other deposition condition (Fig. 14). If the window spacing (L) is short enough, the indium adatoms can diffuse to the exposed area (open windows) and then form indium particles inside the window; otherwise, they form particles on the SiO_2 masking film. Within a single open window, the indium adatoms form single or multi-indium particles. Multi-particles may coalescence into a single particle with enough supply of indium source material.

The alignment of the indium particles directly affects the subsequent InP nanowire growth. For L of 5 and 6 μm, indium particles present on the SiO_2 film lead to irregular nanowire growth. For an L of 4 μm, there is very little growth on the SiO_2 film, but still some irregular growth from the window area [31]. Figure 15 shows a well-aligned uniform nanowire array grown from particles deposited at 480 °C on L 3-μm substrate, without the formation of other unwanted crystal growth features.

Compared with site-defined catalyst particles directly by lithography technique, the indium particles by a combination of lithography and self-assembly process are not precisely defined in open windows (Fig. 14). We have continued to develop and improve the technique for high site precision and selectivity. Currently, we have been able to grow InP/InAs heterostructure nanowire array with high precision, high homogeneity, and high selectivity (unpublished).

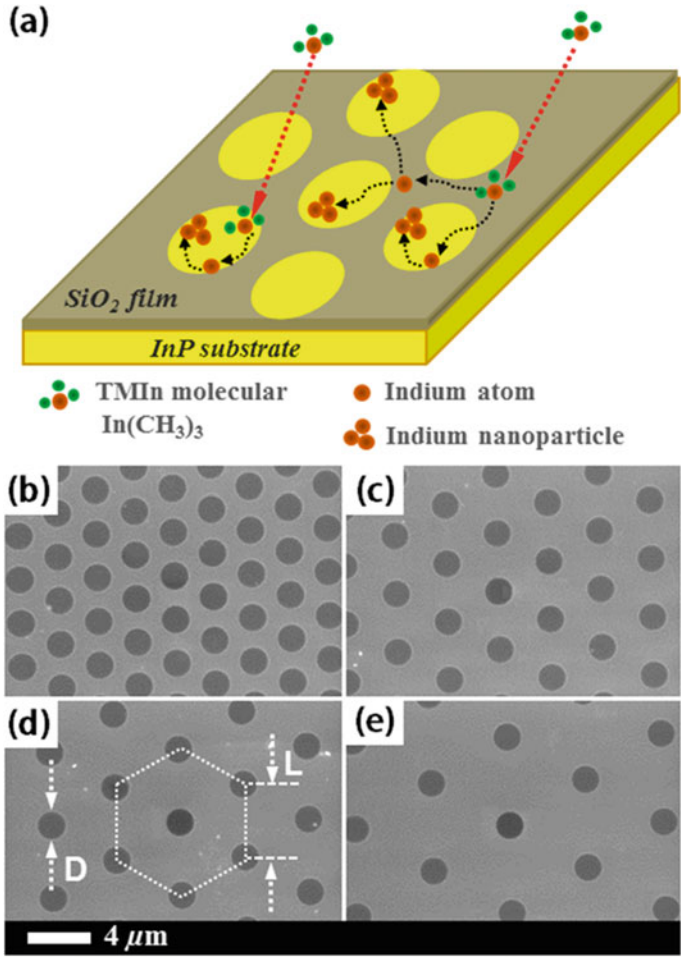

Fig. 13 **a** Schematic diagram of absorption and decomposition of source materials, surface diffusion, and accumulation of indium adatoms on SiO_2 masking film surface and open windows. TMIn molecules are firstly absorbed on the heated substrate surface and decompose into indium atoms. Most indium adatoms directly desorb from the masking film surface. Other indium adatoms diffuse on the surface and reach open windows with the crystalline surface. These indium adatoms preferentially accumulate into particles on open windows to minimize the surface energy. **b–e** InP substrates with different pitch size (L). The circular window is the exposed InP crystalline surface after SiO_2 film removal. The diameters of the circular open windows, D, are all the same (2 μm). **b** L: 3 μm, **c** L: 4 μm, **d** L: 5 μm, **e** L: 6 μm. (Figure from Ref. [31]. Reprinted with permission from American Chemical Society)

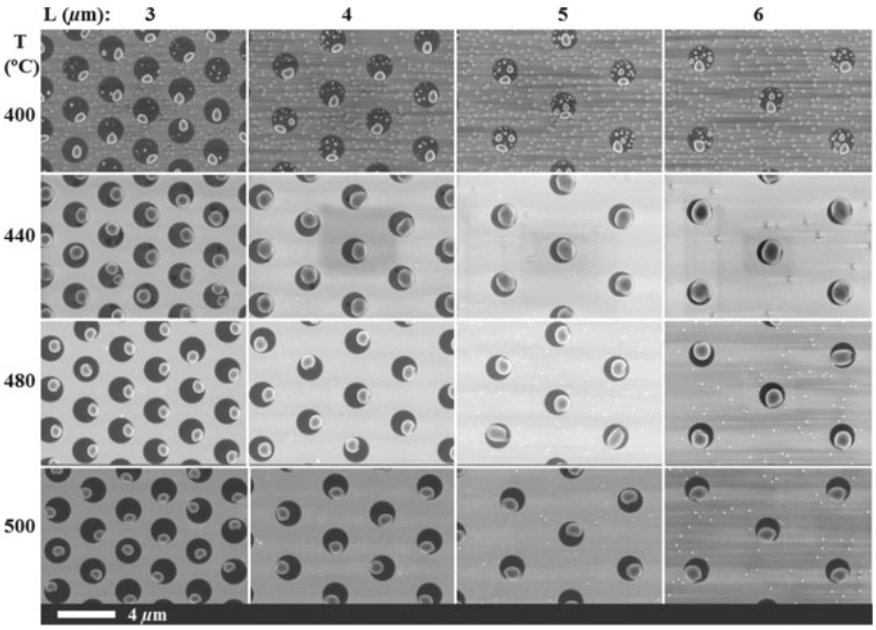

Fig. 14 Indium particles deposited at different temperatures on InP (211)B substrate with different size open windows. With increasing substrate temperature, less indium particles form on the amorphous SiO_2 masking film. With decreasing window spacing (L), more indium adatoms can diffuse, then reach the InP open window area, eventually accumulate into particles. Temperature-dependent diffusion length of indium adatoms plays a key role in deciding the regular alignment of indium particles. (Figure from Ref. [31]. Reprinted with permission from American Chemical Society)

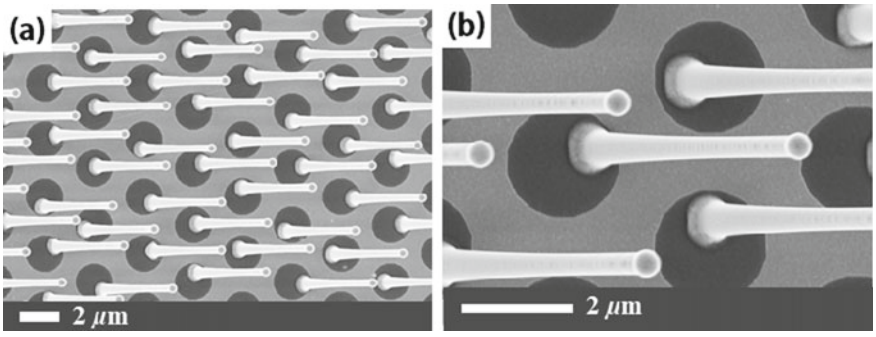

Fig. 15 Top view SEM images of InP nanowire array grown from site-defined indium particles. Indium particles defined inside open windows initiate the nanowire growth. No growth occurs on the masking film. There is an indium particle at each nanowire tip. (Figure from Ref. [31]. Reprinted with permission from American Chemical Society)

6 In Situ Tuning Nanowire Diameter

In this section, we reveal a distinct phenomenon in the nanowire growth by the self-catalyzed VLS mode, i.e., tunable catalyst particle size by V/III precursor ratio. The phenomenon enables a new function of in situ tuning nanowire diameter with high controllability [29].

The self-catalyzed VLS approach uses one of element material in a compound, usually group-III materials (indium, gallium, etc.), as the catalyst material to grow the compound nanowires in the catalyzed mode, e.g., Ga for GaAs and GaP nanowires [37, 38] and indium for InP and InAs nanowires [39]. According to the Gibbs phase rule, a system with two elements and three phases has only one degree of freedom. If the temperature is specified, then the partial pressures of the two components cannot be freely varied, i.e., with unique values. This suggests that during self-catalyzed VLS growth the liquid droplet is inherently unstable and tends to grow or shrink, as predicted in a theoretical study by Tersoff [40]. This may make it possible to tune the seed particle size, thus nanowire diameter, by modulating the flow rate of the source material, or V/III ratio, during growth in a wide range. The shrinking (growing) indium droplet particle results in a decrease (increase) in the nanowire diameter. Conveniently, one can expect to tune the nanowire diameter by modulating the flow rate of indium source material. Nanowire shape can therefore be tailored with various shapes simply by flow rate (or V/III ratio) profile (Fig. 16).

Experiments have been designed and carried out to demonstrate the diameter modulation ability in a wide-scale range from microscale to nanoscale (Fig. 17). The results shown in Fig. 17 indicate that the nanowire diameter can be continuously tuned by modulating the flow rate of the indium source material. The uniform nanowire shape is varied from a needle-like shape with a sharp tip to a shape resembling a baseball bat (Fig. 17). This approach can also be used to enlarge the nanowire diameter during growth (reversely tapered) [29]. These results shown here also provide direct evidences to the theoretical work describing dynamic diameter tuning [40] and self-equilibration growth phenomenon [41].

The fabrication of site-specified nanostructures in the nanoscale range realized by conventional photolithography with microscale resolution has considered to be a challenge for many applications that require low-cost and high-throughput manufacturing processes. The diameter modulation technique described here provides a new approach to bridge the micro-nanoscale gap between the microscale-featured photolithographic and nanoscale-featured nanolithographic processes.

By the technique described in the last section, indium particles are selectively deposited in microscale-featured circular windows made by photolithography process (Fig. 18a–c). Both III- and V-group source materials are then introduced into the growth chamber to initiate nanowire growth selectively from indium particles in the self-catalyzed VLS mode. The array of InP nanowires with tapering diameters are obtained under optimized growth condition (Fig. 18d–f). While the initial indium particle size is 1-μm diameter, the nanowire diameter shrinks with length, and the diameter close to the nanowire tip decreases to ~0.2 μm. If the flow rate for the

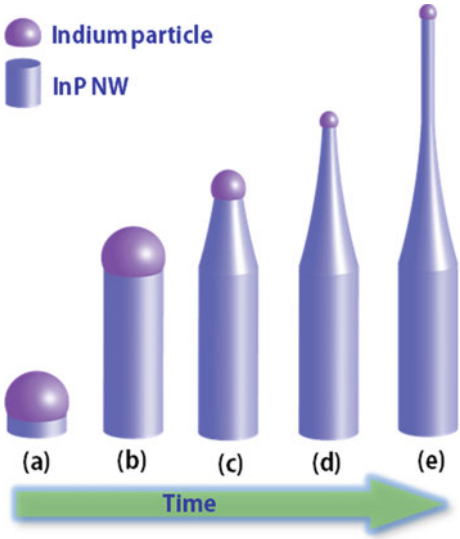

Fig. 16 Schematic diagram of tunable nanowire diameter with self-catalyzed VLS approach. In contrast to Au-catalyzed VLS approach with three components (so two degrees of freedom), the system with two components has only one degree of freedom. If growth temperature is specified, gas pressure corresponds to a unique nanowire diameter to be energetically stable, otherwise, it would be unstable. Therefore, the indium droplet particle size can be tuned by modulating the indium source material supply. In principle, the nanowire shape can be tuned from uniform (**a** and **b**) to tapering (**c** and **d**) and a combination of tapering and uniform shapes (**e**) by modulating the flow rate of the indium source material (or V/III ratio). (Figure from Ref. [29]. Reprinted with permission from IOP Publishing)

tapering diameter is kept, the indium particle at the tip will eventually vanish and catalyzed growth will stop. Here, the nanowire diameter is continuously modulated from a microscale size (1 μm) to a nanoscale size (~200 nm, even down to <50 nm) simply by tuning the indium source material flow rate. This indeed enables the fabrication of site-specified nanowires with a nanoscale diameter (potentially with InAs quantum dots by heterostructure) by using microscale-featured photolithography.

The scalability of this nanowire diameter tuning technique is essentially different from other particle-catalyzed VLS [1, 42] and selective area growth (SAG) techniques [43, 44]. The approach includes seeding, positioning, growing, and dimensional tuning in a single growth chamber simply by the flow rate. This method also overcomes the need to pre-select the size by seeding various sizes of catalyst particles or to select the exposed substrate window size as is common in other SAG methods.

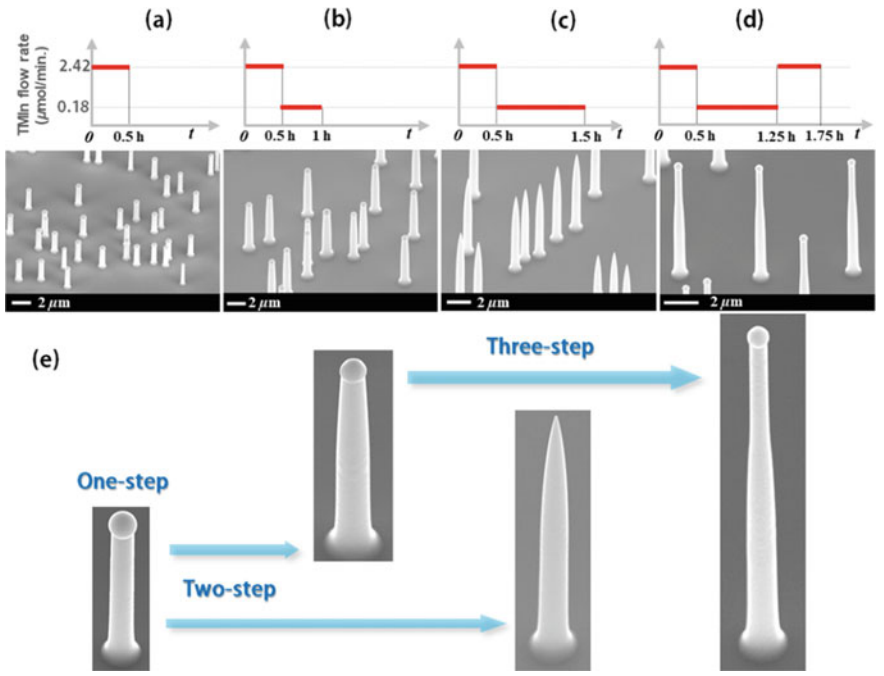

Fig. 17 InP nanowires grown with different TMIn flow rate profiles. (**a**–**d**) TMIn flow rate profiles and corresponding SEM images (tilt: 38°) of InP nanowires grown under different profiles. **e** Close-up views of single nanowires grown with the four profiles. (Figure from Ref. [29]. Reprinted with permission from IOP Publishing)

7 Summary

In this chapter, we have described the growth, structural, and optical properties, and site control of InP, InAs, and InP/InAs heterostructure nanowires by developing a CMOS-compatible Au-free self-catalyzed VLS approach. The InP/InAs nanowire exhibits excellent optical property, enabling lasing operation with tunable lasing wavelength range in telecom band at room temperature. A novel approach is presented for site-defined InP/InAs nanowires by the combination of bottom-up self-assembly process with top-down micro-photolithography technique. A distinct growth phenomenon of self-catalyzed VLS approach is described. This provides a new approach for nanowire diameter tuning during growth by modulating V/III flow ratio.

The synthesis approach of InP/InAs heterostructure nanowires grown by self-catalyzed VLS approach has two significant advantages: Au-free and low growth temperature (<350 °C). The approach has high potential to integrate optically active InP/InAs materials and related functional optical devices into Si-based integrated optoelectronics for the CMOS-compatible process feature.

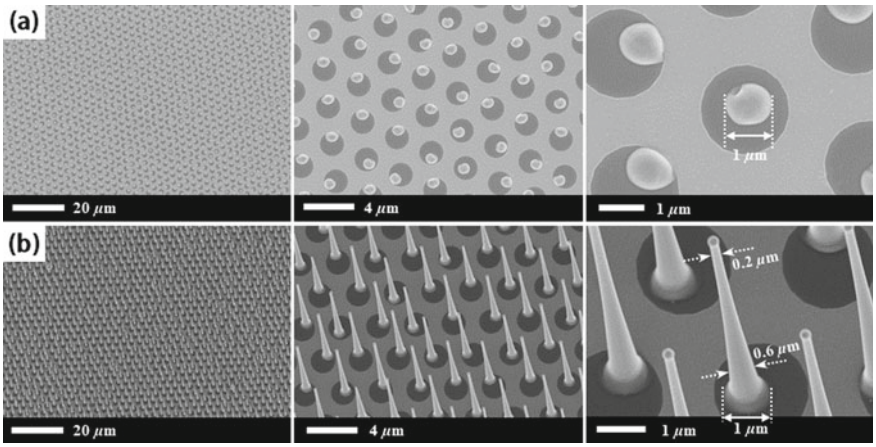

Fig. 18 Site-specified InP nanowires epitaxially grown on InP (211)B substrate with nanowire diameter modulated from microscale to nanoscale. **a** Top-view SEM images of indium particles selectively deposited in circular open windows. **b** Top-view SEM images of InP nanowires grown from the indium particles shown in (**a**). The <111>-oriented nanowires are inclined to the InP (211)B substrate. One can see a clear difference between the diameters of the root and the tip, as indicated in the figure. (Figure from Ref. [29]. Reprinted with permission from IOP Publishing)

References

1. R.S. Wagner, W.C. Ellis, Appl. Phys. Lett. **4**, 89–90 (1964)
2. W.M. Bullis, Solid·State Electron. **9**, 143–168 (1966)
3. G.J. Sprokel, J.M. Fairfield, J. Electrochem. Soc. **112**, 200–203 (1965)
4. M.H. Huang, S. Mao, H. Feick, H. Yan, Y. Wu, H. Kind, E. Weber, R. Russo, P. Yang, Science **292**, 1897–1899 (2001)
5. J.C. Johnson, H.Q. Yan, R.D. Schaller, L.H. Haber, R.J. Saykally, P.D. Yang, J. Phys. Chem. B **105**, 11387–11390 (2001)
6. R. Agarwal, C.J. Barrelet, C.M. Lieber, Nano Lett. **5**, 917–920 (2005)
7. P.J. Pauzauskie, D.J. Sirbuly, P. Yang, Phys. Rev. Lett. **96**, 143903 (2006)
8. A.H. Chin, S. Vaddiraju, A.V. Maslov, C.Z. Ning, M.K. Sunkara, M. Meyyappan, Appl. Phys. Lett. **88**, 163115 (2006)
9. R. Chen, T.T.D. Tran, K.W. Ng, W.S. Ko, L.C. Chuang, F.G. Sedgwick, C. Chang-Hasnain, Nat. Photonics **5**, 170–175 (2011)
10. B. Mayer, D. Rudolph, J. Schnell, S. Morkotter, J. Winnerl, J. Treu, K. Muller, G. Bracher, G. Abstreiter, G. Koblmuller, J.J. Finley, Nat Commun **4**, 2931 (2013)
11. D. Saxena, S. Mokkapati, P. Parkinson, N. Jiang, Q. Gao, H.H. Tan, C. Jagadish, Nat. Photonics **7**, 963–968 (2013)
12. J. Tatebayashi, S. Kako, J.F. Ho, Y. Ota, S. Iwamoto, Y. Arakawa, Nat. Photonics **9**, 501–505 (2015)
13. S. Zhao, X. Liu, S.Y. Woo, J. Kang, G.A. Botton, Z. Mi, Appl. Phys. Lett. **107**, 043101 (2015)
14. H. Zhu, Y. Fu, F. Meng, X. Wu, Z. Gong, Q. Ding, M.V. Gustafsson, M.T. Trinh, S. Jin, X.Y. Zhu, Nat Mater **14**, 636–642 (2015)
15. M. Takiguchi, A. Yokoo, K. Nozaki, M.D. Birowosuto, K. Tateno, G. Zhang, E. Kuramochi, A. Shinya, M. Notomi, N. M., N. K., S. A., M. S., K. E., APL Photonics **2**, 046106 (2017)
16. H. Kim, W.-J. Lee, A.C. Farrell, A. Balgarkashi, D.L. Huffaker, Nano Lett. **17**, 5244–5250 (2017)

17. A. Yokoo, M. Takiguchi, M.D. Birowosuto, K. Tateno, G. Zhang, E. Kuramochi, A. Shinya, H. Taniyama, M. Notomi, ACS Photonics **4**, 355–362 (2017)
18. M.D. Birowosuto, A. Yokoo, G. Zhang, K. Tateno, E. Kuramochi, H. Taniyama, M. Takiguchi, M. Notomi, Nat. Mater. **13**, 279–285 (2014)
19. M.S. Gudiksen, L.J. Lauhon, J. Wang, D.C. Smith, C.M. Lieber, Nature (London) **415**, 617–620 (2002)
20. Y. Wu, R. Fan, P. Yang, Nano Lett. **2**, 83–86 (2002)
21. E. Ertekin, P.A. Greaney, D.C. Chrzan, T.D. Sands, J. Appl. Phys. **97**, 114325 (2005)
22. G. Zhang, K. Tateno, M.D. Birowosuto, M. Notomi, T. Sogawa, H. Gotoh, Nanotechnology **26**, 115704 (2015)
23. J.J. Hannah, J.D. Callum, G. Qiang, H.H. Tan, J. Chennupati, L.-H. James, M.H. Laura, B.J. Michael, Nanotechnology **24**, 214006 (2013)
24. D. Saxena, N. Jiang, X. Yuan, S. Mokkapati, Y. Guo, H.H. Tan, C. Jagadish, Nano Lett. **16**, 5080–5086 (2016)
25. G. Zhang, K. Tateno, H. Gotoh, T. Sogawa, H. Nakano, Jpn. J. Appl. Phys. **49**, 015001 (2010)
26. H. Riel, L.-E. Wernersson, M. Hong, J.A. del Alamo, MRS Bull. **39**, 668–677 (2014)
27. G. Zhang, S. Sasaki, K. Tateno, H. Gotoh, T. Sogawa, AIP Adv. **3**, 052107 (2013)
28. G. Zhang, K. Tateno, H. Gotoh, T. Sogawa, Appl. Phys. Express **5**, 055201 (2012)
29. G. Zhang, K. Tateno, T. Sogawa, H. Gotoh, Nanotechnology **29**, 155202 (2018)
30. G. Zhang, M. Takiguchi, K. Tateno, T. Tawara, M. Notomi, H. Gotoh, Sci. Adv. **5**, eaat8896 (2019)
31. G. Zhang, C. Rainville, A. Salmon, M. Takiguchi, K. Tateno, H. Gotoh, ACS Nano **9**, 10580–10589 (2015)
32. S. Hertenberger, D. Rudolph, S. Bolte, M. Döblinger, M. Bichler, D. Spirkoska, J.J. Finley, G. Abstreiter, G. Koblmüller, Appl. Phys. Lett. **98**, 123114 (2011)
33. M. Varela, A.R. Lupini, K.V. Benthem, A.Y. Borisevich, M.F. Chisholm, N. Shibata, E. Abe, S.J. Pennycook, Annu. Rev. Mater. Res. **35**, 539–569 (2005)
34. K.A. Dick, J. Bolinsson, B.M. Borg, J. Johansson, Nano Lett. **12**, 3200–3206 (2012)
35. H. Ibach, *Physics of Surfaces and Interfaces* (Springer, 2006)
36. U. Pohl,*Methods of Epitaxy, Epitaxy of Semiconductors* (Springer, Berlin, Heidelberg, 2013), pp. 171–224
37. J. Kasahara, K. Kajiwara, T. Yamada, J. Cryst. Growth **38**, 23–28 (1977)
38. A.F.I. Morral, C. Colombo, G. Abstreiter, J. Arbiol, J.R. Morante, Appl. Phys. Lett. **92**, 063112 (2008)
39. C.J. Novotny, P.K.L. Yu, Appl. Phys. Lett. **87**, 203111 (2005)
40. J. Tersoff, Nano Lett. **15**, 6609–6613 (2015)
41. V.G. Dubrovskii, T. Xu, A.D. Álvarez, S.R. Plissard, P. Caroff, F. Glas, B. Grandidier, Nano Lett. **15**, 5580–5584 (2015)
42. L. Samuelson, Mater. Today **6**, 22–31 (2003)
43. J. Motohisa, J. Noborisaka, J. Takeda, M. Inari, T. Fukui, J. Cryst. Growth **272**, 180–185 (2004)
44. J. Noborisaka, J. Motohisa, T. Fukui, Appl. Phys. Lett. **86**, 213102 (2005)